Multimetallic Models of the Nitrogenase Active Site

Thesis by
Charles H. Arnett

In Partial Fulfillment of the Requirements
for the Degree of Doctor of Philosophy

CALIFORNIA INSTITUTE OF TECHNOLOGY
Division of Chemistry and Chemical Engineering
Pasadena, California
2020
(Defended on August 28th, 2020)

Charles H. Arnett
ORCID: 0000-0002-1272-3797

ACKNOWLEDGEMENTS

Hindsight is perfect, and from that perspective I can now survey the critical roles played by so many different people in shaping who I am today. The foregoing will not be an exhaustive list, but simply a remembrance of those who have made my graduate studies possible. Since this is my own history, I choose to thank all of you in chronological order. Each person's contribution was vital at that very moment in time, so that is how I want to acknowledge you.

First and foremost, I thank my Lord and Savior Jesus Christ. He knew me before I knew myself, before time began. He has been with me and guided me through every challenge I faced in life. This document and all the work it describes is dedicated to Him because without Him it would not have happened.

Secondly, I thank my family, but especially my mom. She was faithful to bring me up in the knowledge of God and loved me even when I went astray. She sacrificed everything she was in order that I may be who I am today. It shall never be forgotten.

I thank my undergraduate advisor Prof. Tim Warren, who cultivated my enthusiasm for synthetic chemistry. Even as an undergraduate, he gave me considerable latitude with my project. That independence prepared me for graduate study by training me to steer my own research, to identify gaps in the literature, and, develop novel approaches to solve those problems. He remains a mentor to this day.

I thank Prof. Jonas Peters, who welcomed me into his lab as a summer undergraduate research fellow before my senior year at Georgetown. It was during that time that I developed an interest in bioinorganic chemistry, particularly as it pertains to the nitrogenase enzyme. I had the great fortune of overlapping with some amazing chemists in his lab that summer, including Dave Lacy, with whom I worked directly, and Jon Rittle, who stoked my interest in

nitrogenase. I enjoyed my time in his lab so much that it was a foregone conclusion in my mind that I would attend Caltech if I was accepted. Although I ultimately decided not to join his lab as a graduate student, Jonas has continued to be a mentor as well as the chair of my thesis committee.

I am beyond indebted to Theo for his support and mentorship as my thesis advisor over the past five years. I joined his lab as a summer research assistant on June 29, 2015, and there is not one day since that time that I regret. As graduate students, I think we all feel some apprehension approaching our advisors with research problems or changes in career plans because we don't know exactly how they will respond. Early on, however, I found Theo to be very approachable, eager to understand, and deeply insightful. This was a great encouragement to me and enabled me to take risks and persist through challenges in my research where perhaps I would not have if my advisor had been less patient.

I would also like to thank all the member of the Agapie group, past and present. Special thanks go to HB, Graham, and Chris who shared in training me as I developed as a chemist. Chris and I, in particular, shared a glovebox for four years. We had our share of misunderstandings and frustrations, but I always looked up to him (literally and figuratively) as a model chemist. Since Chris graduated, I have had the honor of sharing a glovebox with Manar, who is both a gentle giant and an incredibly talented scientist. He made my last year at Caltech enjoyable, and I will miss our candid conversations about current events.

I thank Prof. Brian Stoltz and Prof. Harry Gray, who are both members of my thesis committee and were each instructor of one of my first year courses. Perhaps my fondest memory from graduate school is the afternoon that Brian came to our lab and made diazomethane for us. We wanted to use it as a carbide precursor, but, as we learned, there was no one else on campus who had experience preparing it. It was quite an honor to be in the lab with Brian! On top of that, Brian also introduced me to several practicing intellectual property attorneys in the course of my job search and helped me secure employment at Jones Day.

During the course of my studies, I had the opportunity to collaborate with some amazing scientists. Special thanks go to Paul Oyala for his hard work and invaluable insight, without which Chapters 5 and 6 of this thesis would not have been possible. I also thank Matthew Chalkley, Dirk Schild, and Nik Thompson in the Peters group for assistance using the Mössbauer spectrometer. I am also immensely grateful to Mike and Larry for their help with crystallography. Mike was always in the lab early in the morning and streamlined many a crystal for me. Although Larry's natural work hours were later than mine, it was never difficult to find or e-mail him to set up a time to mount. Without his continued efforts, I doubt any of the instruments in the X-ray lab would remain operable for long – they always seem to be in need of repair! Our conversations while crystal hunting were always interesting and fun. I also thank Dave and Mona for maintaining amazing NMR and Mass Spec. facilities.

Last but not least, I am grateful to the National Science Foundation for providing financial support for my graduate education.

ABSTRACT

Motivated by the lack of an atomic-level understanding of the reduction of small molecule substrates by nitrogenase, this dissertation describes the synthesis, characterization and reactivity of well-defined model clusters of the enzyme active site.

Chapter 2 describes a series of site-differentiated, high spin iron clusters which reversibly bind carbon monoxide in redox states Fe^{II}_4 through $Fe^{II}Fe^{III}_3$. Detailed spectroscopic and thermochemical studies reveal that this remarkable reactivity can be attributed to the ability of remote metal centers to shuttle reducing equivalents to the small molecule binding site.

Chapter 3 further explores the consequences of internal electron transfer events on the thermodynamics of small molecule binding by site-differentiated, tetranuclear iron clusters. To systematically tune the electronic properties of the cluster, a Hammett series was prepared. Counterintuitively, introduction of electron-donating substituents *suppresses* the first CO binding event but *enhances* the second. Detailed spectroscopic studies revealed that the origin of this behavior can be traced to the effect of the substituents on the redox reorganization energy associated with internal electron transfer.

Chapter 4 presents the synthesis and characterization of the first open-shell diiron μ-carbyne complex, which also features a biologically relevant Fe(μ-C)(μ-H)Fe core. This electronically unusual species could be activated toward binding of N_2 upon addition of H^+/e, which initially involves an iron-carbene intermediate.

Chapter 5 describes the synthesis and spectroscopic investigation of the first carbon-bridged, bimetallic complexes featuring odd numbers of valence electrons as spectroscopic models of the critical E_4(4H) intermediate of nitrogenase. Detailed pulse EPR studies revealed

the effects of electronic localization on the spectroscopic signatures of the μ-hydride motif and provide insight into the electronic distribution in a reduced state of FeMoco.

Chapter 6 describes the synthesis and characterization of terminal iron-carbene complexes, including EPR characterization of open-shell variants.

Appendix A describes unpublished efforts to prepared site-differentiated models of FeMoco featuring carbon- or sulfur-based donors.

Appendix B presents unpublished work towards modelling the cooperative activation and reduction of N_2 by diiron complexes featuring carbon-based bridging ligands.

PUBLISHED CONTENT AND CONTRIBUTIONS

Parts of this thesis have been adapted from published articles co-written by the author.

The following articles were reproduced in part with permission from the American Chemical Society:

"A Thermodynamic Model for Redox-Dependent Binding of Carbon Monoxide at Site-Differentiated, High Spin Iron Clusters" **Arnett, C.H.**; Chalkley, M.J.; Agapie, T. *J. Am. Chem. Soc.* **2018***, 140,* 5569-5578. DOI: 10.1021/jacs.8b01825

M.J.C. performed He-tempertaure magnetic Mossbauer measurements. C.H.A. conducted all other research and spectroscopic studies. C.H.A. and T.A. conceived and designed the research and co-wrote the manuscript.

"Remote Ligand Modifications Tune Electronic Distribution and Reactivity in Site-Differentiated, High Spin Iron Clusters: Flipping Scaling Relationships" **Arnett, C.H.**; Kaiser, J.; Agapie, T. *Inorg. Chem.* **2019***, 58,* 15971-15982.

J.K. performed and analyzed positionally-resolved X-ray diffraction studies. C.H.A. conducted all other research and spectroscopic studies. C.H.A. and T.A. conceived and designed the research and co-wrote the manuscript.

"Activation of an Open Shell, Carbyne-Bridged Diiron Complex Toward Binding of Dinitrogen" **Arnett, C.H.**; Agapie, T. *J. Am. Chem. Soc.* **2020***, 142,* 10059–10068.

C.H.A. conducted all research, spectroscopic, and computational studies. C.H.A. and T.A. conceived and designed the research and co-wrote the manuscript.

TABLE OF CONTENTS

CHAPTER 1

GENERAL INTRODUCTION

INTRODUCTION

A Tale of Two Processes: Industrial vs. Biological Nitrogen Fixation. The availability of reactive sources of nitrogen, an essential component of all proteins and nucleic acids, is one of the most important factors that limits agricultural production and population growth.[1] The industrial Haber-Bosch process supplies *c.a.* 50% of the fixed nitrogen that is consumed globally, but it is unsustainable in its present form.[2-3] Using iron catalysts, ammonia (NH_3) is produced by the reduction of dinitrogen (N_2) with dihydrogen (H_2), derived from fossil fuels, as the source of electrons and protons at elevated temperatures (400-500 °C) and high pressures (150-200 atm).[4] Alone, the Haber-Bosch process consumes *c.a.* 1% of the annual global energy supply and contributes to *c.a.* 3% of total CO_2 emissions per annum.[5-6] As such, there is broad interest in developing more sustainable technologies for nitrogen fixation using renewable energy and carbon-neutral sources of electrons and protons.

Inspiration towards this goal can be drawn from the biological generation of NH_3 from atmospheric N_2 by the nitrogenase enzymes. Prior to the development of industrial methods for NH_3 synthesis, this class of nitrogen-fixing enzymes, present in only *c.a.* 5% of bacterial genera, was responsible for supplying nearly all bioavailable nitrogen[7] and operates using ATP as an energy source, cellular reductants, and protons from water.[8-10] Although significant advances have been made in elucidating the resting-state structure of the nitrogenase active sites, the mechanism of NH_3 production is still not well understood. The Mo-nitrogenase enzyme is a heterotetrameric protein complex whose active site is a complicated [7Fe-9S-Mo-C-*R*-homocitrate] cluster (the iron-molybdenum cofactor, FeMoco, Figure 1) composed of [4Fe-3S] and [3Fe-Mo-3S] subunits fused together by three bridging sulfides and an interstitial carbon atom, a structural element that is unique to FeMoco among all other biological Fe-S clusters.[11-12] During one turnover, at least eight sequential proton-electron transfers, coupled by complex protein conformational changes to ATP cleavage, occur at the active site, releasing two equivalents of NH_3 and at least one equivalent of H_2.[9, 13]

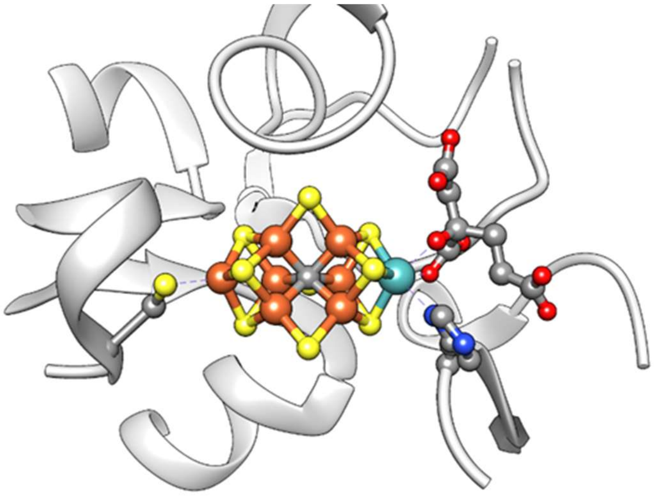

Figure 1. The [7Fe-9S-Mo-C-R-homocitrate] FeMoco of Nitrogenase (PDB 4WES).

A Kinetic Model of Biological Nitrogen Fixation: Linking Intermediates. To develop a mechanistic description of nitrogenase catalysis, in the mid-1980's, Lowe and Thorneley derived a model for the reduction of N_2 by the Mo-nitrogenase enzyme from simulations of the kinetics of NH_3 production and H_2 evolution.[14-17] Although their investigations did not provide any insight into the structure of the proposed intermediates, the kinetic model developed by Lowe and Thorneley provides a framework for the assignment of reduced states of FeMoco. Within the context of the Lowe-Thorneley model (Figure 2), these intermediate states are described by the notation E_n, where the index "n" refers to the number of electrons the active site has accumulated relative to the resting state E_0. On the basis of their extensive studies, it is believed that nitrogenase catalysis is divided into two distinct phases – an initial "electron-loading" phase and a subsequent N_2 reduction phase.[8] During the initial electron-loading phase, the active site displays low affinity for N_2 binding and, thus, reducing equivalents accumulate at the active site without substrate modification. After the active site has been reduced by at least three electrons relative to its resting state, N_2 binding occurs and substrate functionalization commences. Although the reduction potentials associated with each E_n/E_{n+1} redox couple are unknown,[18] the same reductant is employed for each electron transfer.[19] This implies that charge does not build up at the active site,[20] but instead that proton transfer is coupled to the reduction of FeMoco.

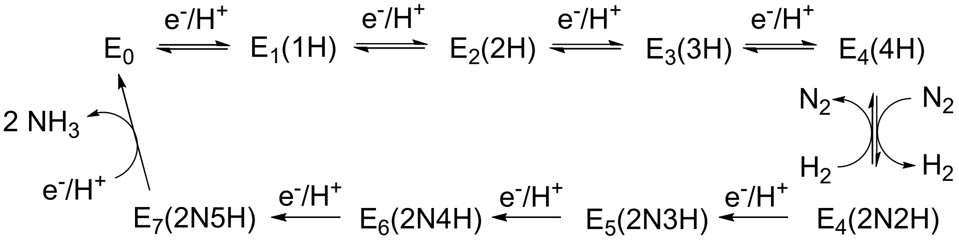

Figure 2. Simplified Lowe-Thorneley scheme for the reduction of N_2 by nitrogenase.

Over the ensuing decades, efforts have been directed towards characterizing and interrelating the putative E_n intermediates of FeMoco, an undertaking that has been challenged by the inability to synchronously trigger the conversion of each respective E_n state to the E_{n+1} level. However, detailed EPR investigations by Hoffman and coworkers have provided significant insight into the mechanism of N_2 reduction by the Mo-nitrogenase enzyme and have experimentally validated the basic tenets of the Lowe-Thorneley model.[8, 21-22] The inherent selectivity of EPR measurements for half-integer spin species renders the odd-numbered E_n states of FeMoco spectroscopically silent. Although this precludes the detection of some intermediates, by minimizing the number of overlapping signals, it facilitates a more thorough characterization of the observable even-numbered E_n states. To assign the E_n level of intermediates trapped in a frozen matrix by EPR, Hoffman and coworkers developed a cryoannealing protocol, which prevents further reduction of the active site but allows intermediates E_2-E_4 to relax back to the resting state E_0 in two-electron steps by the loss of H_2.[23-24] Although conventional continuous-wave EPR experiments generally provide little structural information, advanced pulse EPR studies reported by Hoffman reveal the presence of two bridging hydrides ligands in the E_4 state of FeMoco.[25-26] This four-electron reduced state can reversibly bind N_2 to generate a spectroscopically observable intermediate, the accumulation of which is promoted by a high partial pressure of N_2 but a low partial pressure of H_2.[27] These observations suggest that N_2 binding is coupled to the reductive elimination of the hydride ligands observed in the E_4 state, a mechanistic hypothesis which is further supported by the dependence of H/D scrambling on the presence of N_2.[28]

Towards an Atomic-Level Mechanistic Description. Although the Lowe-Thorneley model provides a general framework for understanding nitrogenase catalysis, it does not yield atomic-level insight into the mechanism by which FeMoco converts N_2 to NH_3. Obtaining such atomic-level detail has proven challenging, in part because N_2 binding does not occur until the cofactor has been reductively activated to at least the E_3 level and the effect of the activation process on the structure of the cofactor has yet to be fully determined. As a result, neither the location nor the mode of N_2 binding to FeMoco was known prior to this year, though an accumulated body of experimental evidence had implicated the Fe2-S2B-Fe6 edge of the cofactor (Figure 3, S2B in red) as the most likely site of substrate binding.[22, 29-32] These S_3C-ligated "belt" iron centers do not display any affinity for binding N_2 in the resting state of the cofactor, but reductive elimination of H_2 from either the E_3 or E_4 state may generate a low-valent iron site capable of binding N_2.[28] In one potential mode of substrate activation (Figure 3, top left), coordination of a terminal N_2 ligand may be accommodated by an elongation of one Fe-C interaction, similar to what is observed for a propargyl alcohol bound state of FeMoco.[32] In the context of this model, N_2 reduction may occur at a single iron site,[33] with protons delivered to the N_2 unit by either alternating or distal-first pathways. However, recent crystallographic studies highlight the potential role of metal-metal cooperativity in substrate activation and reduction by FeMoco. The first crystal structure of the cofactor coordinated by a substrate-analog revealed selective substitution of a bridging sulfide (S2B) by carbon monoxide, with CO bridging Fe2 and Fe6.[34] During turnover with selenocyanate, an alternative nitrogenase substrate, quantitative incorporation of selenium into the S2B site was also observed.[35] More recently, a putative intermediate in the reduction of N_2 by a V-containing analog of FeMoco was crystallographically characterized, which revealed an imido (-NH) ligand bridging Fe2 and Fe6, with S2B located as a hydrosulfide anion ($^{-}$SH) 7 Å away from the cofactor.[36] These observations suggest that FeMoco may be activated by displacement of S2B following electron loading, generating a reactive site for cooperative binding and reduction of N_2 along the Fe2/Fe6 edge of the cofactor (Figure 3, right).[37-38] Experimental support for this hypothesis was recently obtained by Ribbe and Hu, who crystallized an N_2 bound form of FeMoco.[39] Notably, their structure demonstrated that N_2 can potentially displace more than one of the belt sulfide ligands, highlighting the role of cofactor dynamics in nitrogenase catalysis.

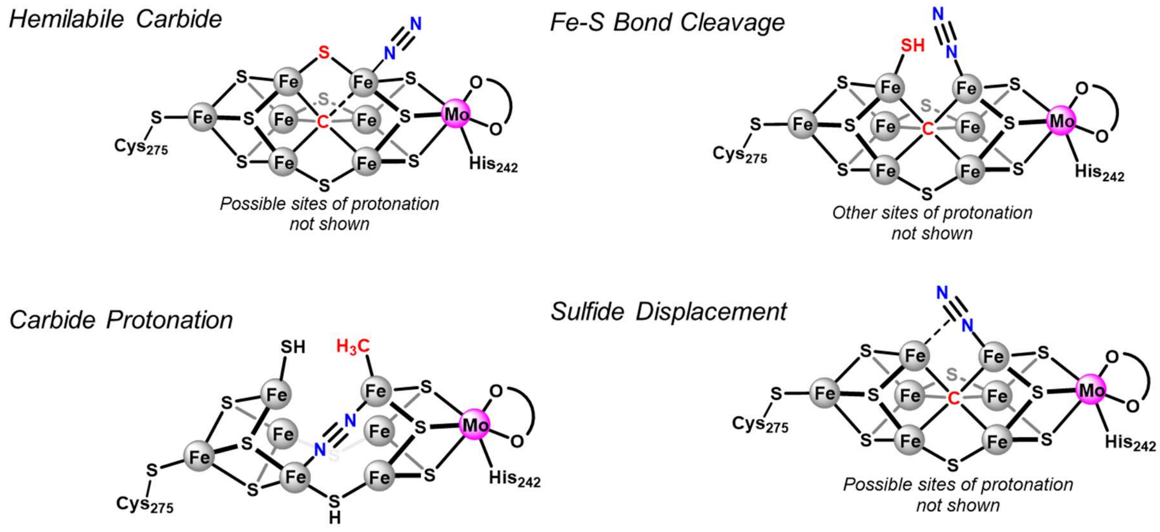
Hemilabile Carbide

Possible sites of protonation not shown

Fe-S Bond Cleavage

Other sites of protonation not shown

Carbide Protonation

Sulfide Displacement

Possible sites of protonation not shown

Figure 3. Atomic-level mechanisms proposed for cofactor activation.[20, 40]

Synthetic Complexes Related to the Fe-Mo Cofactor (FeMoCo) of Nitrogenase. While synthetic model systems have been useful for understanding the structure and function of many inorganic cofactors in biology, efforts to evaluate cooperative N_2 reduction mechanisms with small molecule mimics of FeMoco have been impeded by the scarcity of appropriate models.[20] Substantial effort has been directed toward the preparation of a faithful structural mimic of the FeMo cofactor itself, yielding several close approximations,[41-43] albeit none which incorporate a bridging carbide motif. However, it is not obvious whether the isolation of a synthetic [7Fe-9S-Mo-C] cluster would in fact lead to an improved understanding of nitrogenase catalysis. Indeed, the FeMo cofactor can be extracted intact from the enzyme,[44] but it is not capable of reducing N_2 *in vitro*, indicating that the protein host has a significant influence on the reactivity of the cluster. Moreover, like FeMoco, synthetic Fe-S clusters are structurally dynamic.[45] In the absence of a supporting protein matrix, oligomerization to form higher nuclearity clusters occurs upon reduction rather than binding of N_2.[46-47] Although some synthetic Fe-S clusters have been reported to catalytically reduce alternative substrates (among others, CO, ^-CN, and CO_2) of nitrogenase,[48-51] the mechanistic details of these transformations have not been reported and the structure of the active catalyst is not known. Instead, to mimic the stabilizing influence of the protein scaffold, several groups have sought to obtain insight into the role of cooperativity in the activation of small molecule substrates of nitrogenase using multinuclear iron complexes that are supported by rigid ligand frameworks.[52-56] This approach has been successfully applied by others in the study of diazene and hydrazine reduction,[57-60] but has yet to yield direct mechanistic insight into the reduction of N_2 by multimetallic iron complexes.[61-62] Our own group has employed this strategy using modularly assembled site-differentiated iron clusters to evaluate the influence of remote metal centers on the activation of small molecules.[63-64] The work detailed in Chapter 2 and 3 herein leverages this approach to understand the thermodynamic consequences of internal electron transfer events involving remote metal centers on substrate binding. Using polynucleating ligand scaffolds, it is possible to target the synthesis of small molecule models which mimic only a small portion of the FeMo cofactor, such as the Fe-(μ-C)(μ-H)-Fe complexes discussed in Chapter 4 and 5, which are mechanistically and spectroscopically more tractable than the cofactor itself.

References

1. Smil, V., *Enriching the Earch: Fritz Haber, Carl Bosch, and the Transformation of World Food Production*. The MIT Press: Cambridge, MA, 2001.
2. Canfield, D. E.; Glazer, A. N.; Falkowski, P. G., The Evolution and Future of Earth's Nitrogen Cycle. *Science*, **2010,** *330* (6001), 192-196.
3. Gruber, N.; Galloway, J. N., An Earth-system perspective of the global nitrogen cycle. *Nature* **2008,** *451*, 293.
4. Kandemir, T.; Schuster, M. E.; Senyshyn, A.; Behrens, M.; Schlögl, R., The Haber–Bosch Process Revisited: On the Real Structure and Stability of "Ammonia Iron" under Working Conditions. *Angew. Chem. Int. Ed.* **2013,** *52* (48), 12723-12726.
5. Smith, B. E., Nitrogenase Reveals Its Inner Secrets. *Science* **2002,** *297* (5587), 1654-1655.
6. Milton, R. D.; Cai, R.; Abdellaoui, S.; Leech, D.; De Lacey, A. L.; Pita, M.; Minteer, S. D., Bioelectrochemical Haber–Bosch Process: An Ammonia-Producing H_2/N_2 Fuel Cell. *Angew. Chem. Int. Ed.* **2017,** *56* (10), 2680-2683.
7. Thamdrup, B., New Pathways and Processes in the Global Nitrogen Cycle. *Ann. Rev. Ecol. Evol. Syst.* **2012,** *43* (1), 407-428.
8. Hoffman, B. M.; Lukoyanov, D.; Yang, Z.-Y.; Dean, D. R.; Seefeldt, L. C., Mechanism of Nitrogen Fixation by Nitrogenase: The Next Stage. *Chem. Rev.* **2014,** *114* (8), 4041-4062.
9. Burgess, B. K.; Lowe, D. J., Mechanism of Molybdenum Nitrogenase. *Chem. Rev.* **1996,** *96* (7), 2983-3012.
10. Burgess, B. K., The iron-molybdenum cofactor of nitrogenase. *Chem. Rev.* **1990,** *90* (8), 1377-1406.
11. Lancaster, K. M.; Roemelt, M.; Ettenhuber, P.; Hu, Y.; Ribbe, M. W.; Neese, F.; Bergmann, U.; DeBeer, S., X-ray Emission Spectroscopy Evidences a Central Carbon in the Nitrogenase Iron-Molybdenum Cofactor. *Science* **2011,** *334* (6058), 974-977.
12. Spatzal, T.; Aksoyoglu, M.; Zhang, L.; Andrade, S. L. A.; Schleicher, E.; Weber, S.; Rees, D. C.; Einsle, O., Evidence for Interstitial Carbon in Nitrogenase FeMo Cofactor. *Science* **2011,** *334* (6058), 940-940.
13. Lowe, D. J.; Thorneley, R. N., The mechanism of Klebsiella pneumoniae nitrogenase action. Pre-steady-state kinetics of H_2 formation. *Biochem. J.* **1984,** *224* (3), 877-886.
14. Lowe, D. J.; Thorneley, R. N., The mechanism of Klebsiella pneumoniae nitrogenase action. Pre-steady-state kinetics of H_2 formation. *Biochem. J.* **1984,** *224* (3), 877-886.
15. Lowe, D. J.; Thorneley, R. N. F., The mechanism of Klebsiella pneumoniae nitrogenase action. The determination of rate constants required for the simulation of the kinetics of N_2 reduction and H_2 evolution. *Biochem. J.* **1984,** *224* (3), 895-901.
16. Thorneley, R. N. F.; Lowe, D. J., The mechanism of Klebsiella pneumoniae nitrogenase action. Pre-steady-state kinetics of an enzyme-bound intermediate in N_2 reduction and of NH_3 formation. *Biochem. J.* **1984,** *224* (3), 887-894.
17. Thorneley, R. N. F.; Lowe, D. J., The mechanism of Klebsiella pneumoniae nitrogenase action. Simulation of the dependences of H_2-evolution rate on component-protein concentration and ratio and sodium dithionite concentration. *Biochem. J.* **1984,** *224* (3), 903-909.
18. Watt, G. D.; Burns, A.; Lough, S.; Tennent, D. L., Redox and spectroscopic properties of oxidized MoFe protein from Azotobacter vinelandii. *Biochemistry* **1980,** *19* (21), 4926-4932.

19. J. C.; Dean, D. R.; Seefeldt, L. C., MECHANISTIC FEATURES OF THE MO-CONTAINING NITROGENASE. *Ann. Rev. Plant Phys. Mol. Biol.* **2001,** *52* (1), 269-295.

20. Čorić, I.; Holland, P. L., Insight into the Iron–Molybdenum Cofactor of Nitrogenase from Synthetic Iron Complexes with Sulfur, Carbon, and Hydride Ligands. *J. Am. Chem. Soc.* **2016,** *138* (23), 7200-7211.

21. Hoffman, B. M.; Lukoyanov, D.; Dean, D. R.; Seefeldt, L. C., Nitrogenase: A Draft Mechanism. *Acc. Chem. Res.* **2013,** *46* (2), 587-595.

22. Dos Santos, P. C.; Igarashi, R. Y.; Lee, H.-I.; Hoffman, B. M.; Seefeldt, L. C.; Dean, D. R., Substrate Interactions with the Nitrogenase Active Site. *Acc. Chem. Res.* **2005,** *38* (3), 208-214.

23. Lukoyanov, D.; Yang, Z.-Y.; Duval, S.; Danyal, K.; Dean, D. R.; Seefeldt, L. C.; Hoffman, B. M., A Confirmation of the Quench-Cryoannealing Relaxation Protocol for Identifying Reduction States of Freeze-Trapped Nitrogenase Intermediates. *Inorg. Chem.* **2014,** *53* (7), 3688-3693.

24. Lukoyanov, D.; Barney, B. M.; Dean, D. R.; Seefeldt, L. C.; Hoffman, B. M., Connecting nitrogenase intermediates with the kinetic scheme for N_2 reduction by a relaxation protocol and identification of the N_2 binding state. *Proc. Natl. Acad. Sci. - USA* **2007,** *104* (5), 1451-1455.

25. Igarashi, R. Y.; Laryukhin, M.; Dos Santos, P. C.; Lee, H.-I.; Dean, D. R.; Seefeldt, L. C.; Hoffman, B. M., Trapping H- Bound to the Nitrogenase FeMo-Cofactor Active Site during H_2 Evolution: Characterization by ENDOR Spectroscopy. *J. Am. Chem. Soc.* **2005,** *127* (17), 6231-6241.

26. Hoeke, V.; Tociu, L.; Case, D. A.; Seefeldt, L. C.; Raugei, S.; Hoffman, B. M., High-Resolution ENDOR Spectroscopy Combined with Quantum Chemical Calculations Reveals the Structure of Nitrogenase Janus Intermediate E_4(4H). *J. Am. Chem. Soc.* **2019,** *141* (30), 11984-11996.

27. Lukoyanov, D.; Yang, Z.-Y.; Khadka, N.; Dean, D. R.; Seefeldt, L. C.; Hoffman, B. M., Identification of a Key Catalytic Intermediate Demonstrates That Nitrogenase Is Activated by the Reversible Exchange of N_2 for H_2. *J. Am. Chem. Soc.* **2015,** *137* (10), 3610-3615.

28. Lukoyanov, D.; Khadka, N.; Yang, Z.-Y.; Dean, D. R.; Seefeldt, L. C.; Hoffman, B. M., Reductive Elimination of H_2 Activates Nitrogenase to Reduce the N≡N Triple Bond: Characterization of the E_4(4H) Janus Intermediate in Wild-Type Enzyme. *J. Am. Chem. Soc.* **2016,** *138* (33), 10674-10683.

29. Lee, H.-I.; Igarashi, R. Y.; Laryukhin, M.; Doan, P. E.; Dos Santos, P. C.; Dean, D. R.; Seefeldt, L. C.; Hoffman, B. M., An Organometallic Intermediate during Alkyne Reduction by Nitrogenase. *J. Am. Chem. Soc.* **2004,** *126* (31), 9563-9569.

30. Benton, P. M. C.; Laryukhin, M.; Mayer, S. M.; Hoffman, B. M.; Dean, D. R.; Seefeldt, L. C., Localization of a Substrate Binding Site on the FeMo-Cofactor in Nitrogenase: Trapping Propargyl Alcohol with an α-70-Substituted MoFe Protein. *Biochemistry* **2003,** *42* (30), 9102-9109.

31. Sarma, R.; Barney, B. M.; Keable, S.; Dean, D. R.; Seefeldt, L. C.; Peters, J. W., Insights into substrate binding at FeMo-cofactor in nitrogenase from the structure of an α-70Ile MoFe protein variant. *J. Inorg. Biochem.* **2010,** *104* (4), 385-389.

32. George, S. J.; Barney, B. M.; Mitra, D.; Igarashi, R. Y.; Guo, Y.; Dean, D. R.; Cramer, S. P.; Seefeldt, L. C., EXAFS and NRVS Reveal a Conformational Distortion of the FeMo-cofactor in the MoFe Nitrogenase Propargyl Alcohol Complex. *J. Inorg. Biochem.* **2012,** *112*, 85-92.

33. Del Castillo, T. J.; Thompson, N. B.; Peters, J. C., A Synthetic Single-Site Fe Nitrogenase: High Turnover, Freeze-Quench ^{57}Fe Mössbauer Data, and a Hydride Resting State. *J. Am. Chem. Soc.* **2016,** *138* (16), 5341-5350.

34. Spatzal, T.; Perez, K. A.; Einsle, O.; Howard, J. B.; Rees, D. C., Ligand binding to the FeMo-cofactor: Structures of CO-bound and reactivated nitrogenase. *Science* **2014,** *345* (6204), 1620-1623.

35. Spatzal, T.; Perez, K. A.; Howard, J. B.; Rees, D. C., Catalysis-dependent selenium incorporation and migration in the nitrogenase active site iron-molybdenum cofactor. *eLife* **2015,** *4*, e11620.

36. Sippel, D.; Rohde, M.; Netzer, J.; Trncik, C.; Gies, J.; Grunau, K.; Djurdjevic, I.; Decamps, L.; Andrade, S. L. A.; Einsle, O., A bound reaction intermediate sheds light on the mechanism of nitrogenase. *Science* **2018,** *359* (6383), 1484-1489.

37. Rohde, M.; Sippel, D.; Trncik, C.; Andrade, S. L. A.; Einsle, O., The Critical E_4 State of Nitrogenase Catalysis. *Biochemistry* **2018,** *57* (38), 5497-5504.

38. Dance, I., How feasible is the reversible S-dissociation mechanism for the activation of FeMo-co, the catalytic site of nitrogenase? *Dalton Trans.* **2019,** *48* (4), 1251-1262.

39. Kang, W.; Lee, C. C.; Jasniewski, A. J.; Ribbe, M. W.; Hu, Y., Structural evidence for a dynamic metallocofactor during N_2 reduction by Mo-nitrogenase. *Science* **2020,** *368* (6497), 1381-1385.

40. Buscagan, T. M.; Rees, D. C., Rethinking the Nitrogenase Mechanism: Activating the Active Site. *Joule* **2019,** *3* (11), 2662-2678.

41. Zhang, Y.; Holm, R. H., Synthesis of a Molecular $Mo_2Fe_6S_9$ Cluster with the Topology of the P^N Cluster of Nitrogenase by Rearrangement of an Edge-Bridged $Mo_2Fe_6S_8$ Double Cubane. *J. Am. Chem. Soc.* **2003,** *125* (13), 3910-3920.

42. Ohki, Y.; Ikagawa, Y.; Tatsumi, K., Synthesis of New [8Fe-7S] Clusters: A Topological Link between the Core Structures of P-Cluster, FeMo-co, and FeFe-co of Nitrogenases. *J. Am. Chem. Soc.* **2007,** *129* (34), 10457-10465.

43. Ohta, S.; Ohki, Y.; Hashimoto, T.; Cramer, R. E.; Tatsumi, K., A Nitrogenase Cluster Model $[Fe_8S_6O]$ with an Oxygen Unsymmetrically Bridging Two Proto-Fe_4S_3 Cubes: Relevancy to the Substrate Binding Mode of the FeMo Cofactor. *Inorg. Chem.* **2012,** *51* (21), 11217-11219.

44. Lydon, B. R.; Lee, C. C.; Tanifuji, K.; Sickerman, N. S.; Newcomb, M. P.; Hu, Y.; Ribbe, M. W.; Yang, J. Y., Electrochemical Characterization of Isolated Nitrogenase Cofactors from Azotobacter vinelandii. *ChemBioChem* **2019**, *20*, 1-7.

45. Holm, R. H.; Lo, W., Structural Conversions of Synthetic and Protein-Bound Iron–Sulfur Clusters. *Chem. Rev.* **2016,** *116* (22), 13685-13713.

46. Lee, S. C.; Lo, W.; Holm, R. H., Developments in the Biomimetic Chemistry of Cubane-Type and Higher Nuclearity Iron–Sulfur Clusters. *Chem. Rev.* **2014,** *114* (7), 3579-3600.

47. Venkateswara Rao, P.; Holm, R. H., Synthetic Analogues of the Active Sites of Iron−Sulfur Proteins. *Chem. Rev.* **2004,** *104* (2), 527-560.

48. Sickerman, N. S.; Tanifuji, K.; Lee, C. C.; Ohki, Y.; Tatsumi, K.; Ribbe, M. W.; Hu, Y., Reduction of C_1 Substrates to Hydrocarbons by the Homometallic Precursor and Synthetic Mimic of the Nitrogenase Cofactor. *J. Am. Chem. Soc.* **2017,** *139* (2), 603-606.

49. Tanifuji, K.; Sickerman, N.; Lee, C. C.; Nagasawa, T.; Miyazaki, K.; Ohki, Y.; Tatsumi, K.; Hu, Y.; Ribbe, M. W., Structure and Reactivity of an Asymmetric Synthetic Mimic of Nitrogenase Cofactor. *Angew. Chem. Int. Ed.* **2016,** *55* (50), 15633-15636.

50. Malinak, S. M.; Demadis, K. D.; Coucouvanis, D., Catalytic Reduction of Hydrazine to Ammonia by the VFe_3S_4 Cubanes. Further Evidence for the Direct Involvement of the Heterometal in the Reduction of Nitrogenase Substrates and Possible Relevance to the Vanadium Nitrogenases. *J. Am. Chem. Soc.* **1995,** *117* (11), 3126-3133.

51. Coucouvanis, D.; Demadis, K. D.; Malinak, S. M.; Mosier, P. E.; Tyson, M. A.; Laughlin, L. J., Catalytic and stoichiometric multielectron reduction of hydrazine to ammonia and acetylene to ethylene with clusters that contain the MFe_3S_4 cores (M=Mo, V). Relevance to the function of nitrogenase. *J. Mol. Catal. A: Chem.* **1996,** *107* (1), 123-135.

52. Creutz, S. E.; Peters, J. C., Diiron Bridged-Thiolate Complexes That Bind N_2 at the $Fe^{II}Fe^{II}$, $Fe^{II}Fe^{I}$, and $Fe^{I}Fe^{I}$ Redox States. *J. Am. Chem. Soc.* **2015,** *137* (23), 7310-7313.

53. Rittle, J.; McCrory, C. C. L.; Peters, J. C., A 10^6-Fold Enhancement in N_2-Binding Affinity of an $Fe_2(\mu\text{-}H)_2$ Core upon Reduction to a Mixed-Valence $Fe^{II}Fe^{I}$ State. *J. Am. Chem. Soc.* **2014,** *136* (39), 13853-13862.

54. Ferreira, R. B.; Murray, L. J., Cyclophanes as Platforms for Reactive Multimetallic Complexes. *Acc. Chem. Res.* **2019,** *52* (2), 447-455.

55. Hernández Sánchez, R.; Zheng, S.-L.; Betley, T. A., Ligand Field Strength Mediates Electron Delocalization in Octahedral $[(^{H}L)_2Fe_6(L')_m]^{n+}$ Clusters. *J. Am. Chem. Soc.* **2015,** *137* (34), 11126-11143.

56. Bartholomew, A. K.; Teesdale, J. J.; Hernández Sánchez, R.; Malbrecht, B. J.; Juda, C. E.; Ménard, G.; Bu, W.; Iovan, D. A.; Mikhailine, A. A.; Zheng, S.-L.; Sarangi, R.; Wang, S. G.; Chen, Y.-

S.; Betley, T. A., Exposing the inadequacy of redox formalisms by resolving redox inequivalence within isovalent clusters. *Proc. Natl. Acad. Sci. - USA* **2019,** *116* (32), 15836-15841.

57. Li, Y.; Li, Y.; Wang, B.; Luo, Y.; Yang, D.; Tong, P.; Zhao, J.; Luo, L.; Zhou, Y.; Chen, S.; Cheng, F.; Qu, J., Ammonia formation by a thiolate-bridged diiron amide complex as a nitrogenase mimic. *Nat. Chem.* **2013,** *5*, 320.

58. Powers, T. M.; Betley, T. A., Testing the Polynuclear Hypothesis: Multielectron Reduction of Small Molecules by Triiron Reaction Sites. *J. Am. Chem. Soc.* **2013,** *135* (33), 12289-12296.

59. Bellows, S. M.; Arnet, N. A.; Gurubasavaraj, P. M.; Brennessel, W. W.; Bill, E.; Cundari, T. R.; Holland, P. L., The Mechanism of N–N Double Bond Cleavage by an Iron(II) Hydride Complex. *J. Am. Chem. Soc.* **2016,** *138* (37), 12112-12123.

60. DeRosha, D. E.; Chilkuri, V. G.; Van Stappen, C.; Bill, E.; Mercado, B. Q.; DeBeer, S.; Neese, F.; Holland, P. L., Planar three-coordinate iron sulfide in a synthetic [4Fe-3S] cluster with biomimetic reactivity. *Nat. Chem.* **2019,** *11* (11), 1019-1025.

61. Rodriguez, M. M.; Bill, E.; Brennessel, W. W.; Holland, P. L., N_2 Reduction and Hydrogenation to Ammonia by a Molecular Iron-Potassium Complex. *Science* **2011,** *334* (6057), 780-783.

62. Lee, Y.; Sloane, F. T.; Blondin, G.; Abboud, K. A.; García-Serres, R.; Murray, L. J., Dinitrogen Activation Upon Reduction of a Triiron(II) Complex. *Angew. Chem. Int. Ed.* **2015,** *54*, 1499-1503.

63. Reed, C. J.; Agapie, T., Tetranuclear Fe Clusters with a Varied Interstitial Ligand: Effects on the Structure, Redox Properties, and Nitric Oxide Activation. *Inorg. Chem.* **2017,** *56* (21), 13360-13367.

64. de Ruiter, G.; Thompson, N. B.; Lionetti, D.; Agapie, T., Nitric Oxide Activation by Distal Redox Modulation in Tetranuclear Iron Nitrosyl Complexes. *J. Am. Chem. Soc.* **2015,** *137* (44), 14094-14106.

CHAPTER 2

A THERMODYNAMIC MODEL FOR REDOX-DEPENDENT BINDING OF CARBON MONOXIDE AT SITE-DIFFERENTIATED, HIGH SPIN IRON CLUSTERS

The text for this chapter was reproduced in part from:

Arnett, C.H.; Chalkley, M.J.; Agapie, T. *J. Am. Chem. Soc.* **2018***, 140,* 5569-5578.

ABSTRACT

Binding of N_2 and CO by the FeMo-cofactor of nitrogenase depends on the redox level of the cluster, but the extent to which pure redox chemistry perturbs the affinity of high spin iron clusters for π-acids is not well understood. Here, we report a series of site-differentiated iron clusters which reversibly bind CO in redox states Fe^{II}_4 through $Fe^{II}Fe^{III}_3$. One-electron redox events result in small changes in the affinity for (at most ~400-fold) and activation of CO (at most 28 cm^{-1} for ν_{CO}). The small influence of redox chemistry on the affinity of these high spin, valence-localized clusters for CO is in stark contrast to the large enhancements (10^5-10^{22} fold) in π-acid affinity reported for monometallic and low spin bimetallic iron complexes, where redox chemistry occurs exclusively at the ligand binding site. While electron-loading at metal centers *remote* from the substrate binding site has minimal influence on the CO binding energetics (~1 kcal·mol^{-1}), it provides a conduit for CO binding at an Fe^{III} center. Indeed, internal electron transfer from these *remote* sites accommodates binding of CO at an Fe^{III}, with a small energetic penalty arising from redox reorganization (~ 2.6 kcal·mol^{-1}). The ease with which these clusters redistribute electrons in response to ligand binding highlights a potential pathway for coordination of N_2 and CO by FeMoco, which may occur on an oxidized edge of the cofactor.

INTRODUCTION

The Mo-nitrogenase enzyme mediates the multielectron reductions of N_2[1] and CO[2] at a unique heterometallic [7Fe-9S-Mo-C-*R*-homocitrate] active site, the iron-molybdenum cofactor (FeMoco, Figure 1a).[3-4] In both cases, catalysis involves an electron loading phase prior to substrate binding, suggesting that coordination of both N_2 and CO is sensitive to the redox level of the cofactor. While atomic level details remain elusive, binding of N_2 does not occur until FeMoco has been reduced by at least three electrons relative to its resting state,[5] whereas only one or two reducing equivalents are required to initiate CO binding.[6-8] As both a substrate and reversible inhibitor of catalysis, CO is an excellent reporter of substrate interactions with FeMoco. While an N_2-bound form of the cofactor has yet to be unambiguously characterized, both terminal and bridging CO adducts of FeMoco have been spectroscopically detected during turnover.[9-11] One of these intermediates has recently been crystallographically characterized, demonstrating that CO bridges between Fe2 and Fe6.[12] Several spectroscopic and biochemical studies support a central role for these two belt iron sites in the binding of CO in several proposed intermediates,[7, 11, 13] as well as other substrates,[14-16] including perhaps N_2.[17]

Despite progress towards their spectroscopic and structural characterization, no information is currently available about the distribution of oxidation states in CO-bound forms of FeMoco. In addition to controlling substrate access to the cofactor,[18] it has been suggested that the local protein environment can induce some degree of valence localization within the cluster. Notably, spatially resolved anomalous dispersion refinement of FeMoco in its resting state revealed that the specific iron centers which have been implicated as CO binding sites lie on a more oxidized edge of the cofactor.[19] Depending on the location of hydride accumulation, which has been proposed to occur during the electron loading phase of catalysis,[10] internal electron transfer events may be required for CO to bind at this oxidized edge.

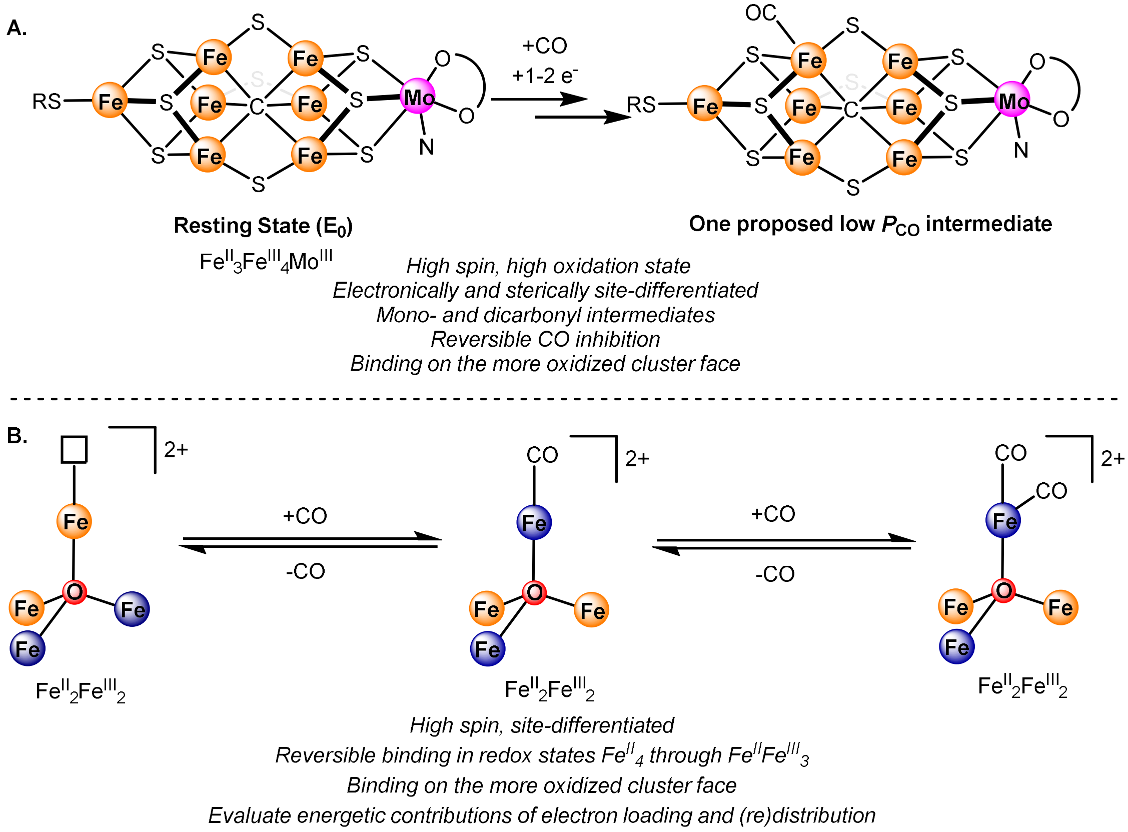

Figure 1. Iron-Molybdenum cofactor (FeMoco) of nitrogenase and synthetic model complexes. (A) Redox-dependent binding of CO by FeMoco. (B) Inorganic core of synthetic model clusters which reversibly bind CO in four isostructural redox states.

Although clearly electron loading of FeMoco plays a key role in allowing the cofactor to bind π-acids, it is challenging to untangle the effects of pure redox chemistry from concomitant structural changes that may occur upon reduction. Moreover, the energetic consequences of internal redox rearrangements which may accommodate substrate binding have not been experimentally determined. Despite capturing essential structural features of the biological system,[20-22] synthetic high spin iron(II/III) clusters generally lack site-differentiation due to reliance on self-assembly strategies, complicating studies of ligand binding at discrete reactive site(s). Furthermore, large structural changes and redistribution of ligands often occur upon redox changes or CO binding in iron cluster models.[23-26] While well-defined multimetallic systems which exhibit reactivity relevant to nitrogenase have been reported,[21, 27-38] to date there are no reported studies on the energetics of CO binding in multiple, isostructural redox states of a synthetic, high spin iron cluster.

In order to evaluate the influence of redox chemistry on ligand binding and activation phenomena, our group has recently developed synthetic strategies to access site-differentiated tetranuclear clusters featuring a coordinatively unsaturated metal center.[39-41] Here, we report the synthesis of a redox series of high spin, site-differentiated iron clusters which reversibly bind CO in four redox states (Fe^{II}_4 through $Fe^{II}Fe^{III}_3$). We observe that coordination of CO to both the $Fe^{II}_2Fe^{III}_2$ and $Fe^{II}Fe^{III}_3$ redox state of the cluster involves an internal redox reorganization; binding of CO at the apical Fe^{III} site induces an internal electron transfer from a distal Fe^{II} center. Studying the energetics of CO binding, we observe only small enhancements (at most ~400-fold) in the affinity for CO due to pure redox chemistry in these high spin, valence localized iron clusters, in contrast to the large enhancements ($> 10^5$-fold) in π-acid affinity reported for monometallic and low spin, bimetallic iron complexes, where redox chemistry occurs exclusively at the ligand binding site. Deconvoluting the effect of redox at specific sites within the cluster, we demonstrate that electron-loading at metal centers *remote* from the substrate binding site has a relatively small influence on the CO binding energetics. Additionally, a small energetic cost is associated with redistribution of electrons in response to ligand binding which explains why coordination of CO at an oxidized face of the cluster remains facile.

RESULTS AND DISCUSSION

A Redox Series of Site-Differentiated, Tetranuclear Iron Clusters. In order to evaluate the effect of electron loading and (re)distribution on CO binding in high spin iron clusters, we targeted the synthesis of imidazolate bridged congeners of our previously reported[41] pyrazolate bridged iron clusters. The differences in the electronic properties of the ligands were probed by DFT calculations (B3LYP/6-31G+(d,p)) for 3-methylpyrazolate and 1-methylimidazolate as simplified models. The frontier orbitals of 3-methylpyrazolate include two N-based donor molecular orbitals (MOs) of σ-symmetry (HOMO-3 and HOMO-4) with respect to interactions with individual metals. Nearly equal contributions from atomic orbitals localized on either nitrogen atom (Figure 2A) are observed. This is in contrast to 1-methylimidazolate where the analogous σ-donor orbitals are spatially distinct, with the HOMO largely localized on C (Figure 2B). Moreover, the energy separation between the two σ-donor orbitals (relative to the HOMO) is larger for 1-methylimidazolate and, due to the lower electronegativity of C, these orbitals lie at higher energy than those of 3-methylpyrazolate. By tuning the steric bulk of the imidazolates to orient the ligand with its C-donors binding the apical metal, this electronic desymmetrization of the bridging ligand was anticipated to enhance the electron density of the apical metal (relative to the distal triiron core). This electronic effect increases the propensity for oxidation at the apical metal site with imidazolate compared to pyrazolate ligands.

The desired clusters are accessible in three steps (Scheme 1) from the triiron precursor $LFe_3(OAc)_3$.[42] Complete acetate removal was effected by treatment of $LFe_3(OAc)_3$ with an excess of Me_3SiOTf in dichloromethane, affording the precursor $LFe_3(OTf)_3$ (**1**, Structures Figure 1) with more labile triflate ligands. Addition of 1-phenyl imidazole (PhIm-H, 3.3 equiv.) and iodosobenzene (PhIO) to a suspension of **1** in tetrahydrofuran affords the PhIm-H coordinated species $[\mathrm{LFe_3O(PhIm\text{-}H)_3}][\mathrm{OTf}]_3$ (**2**, Structures Figure 2). Deprotonation of **2** with sodium hexamethyldisilazide ($\mathrm{Na[N(SiMe_3)_2]}$, 3.2 equiv.) followed by addition of $\mathrm{FeCl_2}$ affords the desired species $[\mathrm{LFe_3O(PhIm)_3Fe}][\mathrm{OTf}]_2$ (**3**). A single crystal X-ray diffraction study confirms the formation of a tetranuclear iron cluster (Figure 3a), where the bond metrics within the $\mathrm{Fe_4(\mu_4\text{-}O)}$ motif are diagnostic of metal oxidation states.[39-41] For the structurally homologous pyrazolate bridged clusters $[\mathrm{LFe_3O(PhPz)_3Fe}][\mathrm{OTf}]_n$ (n = 1-3), the distances between the distal, six-coordinate iron centers (Fe1, Fe2, Fe3, respectively) and the interstitial oxygen atom (O1) elongate upon reduction (average Fe1/2/3-O1 distances: 1.96 Å for $\mathrm{Fe^{III}}$ and 2.07 Å for $\mathrm{Fe^{II}}$).[41] The observation of two long (2.1480(19) and 2.093(2) Å) and one short (1.983(2) Å) bond distance between the interstitial oxygen (O1) and the iron centers Fe1, Fe2, and Fe3 suggests a valence localized $[\mathrm{Fe^{II}}_2\mathrm{Fe^{III}}]$ assignment for the basal triiron core of **3**. This indicates an $\mathrm{Fe^{III}}$ assignment for the apical Fe4 center, consistent with its short Fe4-O1 distance (1.8128(19) Å).

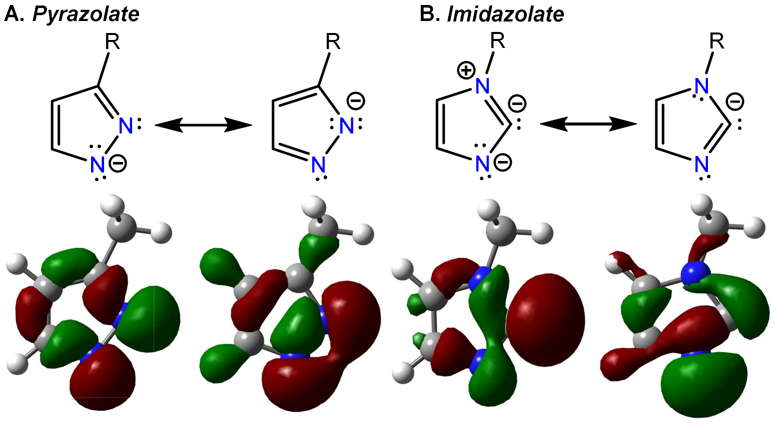

Figure 2. (A) Calculated σ-donor MO's for 3-methylpyrazolate (B) Calculated σ-donor MO's for 1-methylimidazolate. Orbital energies (relative to the HOMO, respectively) are given in parentheses, and isosurfaces are shown at the 0.04 e Å $^{-3}$ level. For both pyrazolate and imidazolate anions, there is an additional, higher energy resonance structure (not depicted).

Scheme 1. Synthesis of tetranuclear iron clusters[43].

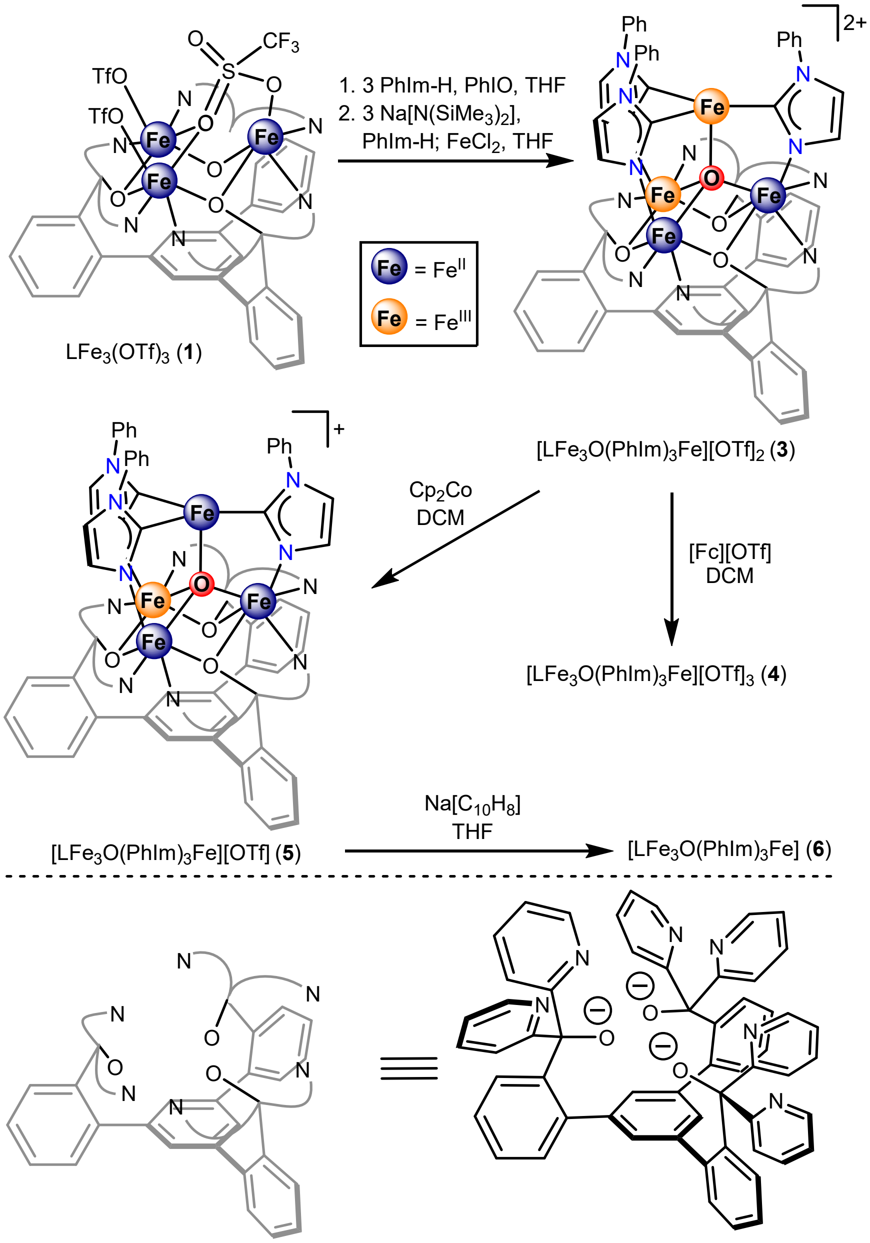

For comparison, the isoelectronic pyrazolate bridged cluster [LFe$_3$O(PhPz)$_3$Fe][OTf]$_2$ features a significantly longer Fe4-O1 distance (1.972(2) Å), consistent with its assignment as Fe^{II} based on ^{57}Fe Mössbauer spectroscopy.[41] This indicates that, unlike **3**, both of the ferric centers in [LFe$_3$O(PhPz)$_3$Fe][OTf]$_2$ are localized within the basal triiron core (Fe1-O1: 1.932(2) Å, Fe2-O1: 1.998(2) Å for [LFe$_3$O(PhPz)$_3$Fe][OTf]$_2$).[41] Consistent with our computational studies, these results demonstrate that substitution of the 3-phenyl pyrazolate ligands by 1-phenyl imidazolate indeed makes the apical binding site more electron rich, facilitating oxidation at Fe4. For the pyrazolate bridged clusters, [LFe$_3$O(PhPz)$_3$Fe][OTf]$_n$ (n = 1-3), oxidation of the apical Fe4 center was not observed in the absence of an additional anionic donor.[41]

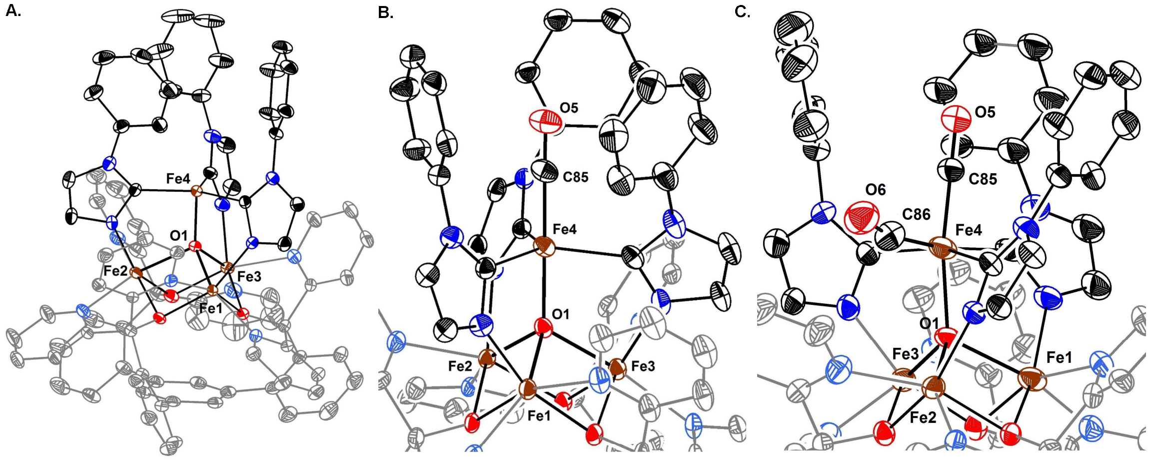

Figure 3. Solid state structures of **3**, **5-CO** and **3-(CO)₂**. Hydrogen atoms and outer sphere counterions not shown for clarity. (A) [LFe$_3$O(PhIm)$_3$Fe][OTf]$_2$ (**3**). (B) [LFe$_3$O(PhIm)$_3$Fe(CO)][OTf] (**5-CO**) (C) [LFe$_3$O(PhIm)$_3$Fe(CO)$_2$][OTf]$_2$ (**3-(CO)$_2$**).

In order to interrogate the effect of the imidazolate ligands on the electronic properties of the cluster as a whole, the CV of **3** was recorded in dichloromethane (Figure 4). Three (quasi)-reversible one-electron redox events are observed at -1.013 V, -0.200 V, and +0.450 V (all vs. Fc/Fc$^+$). The first two electrochemical events are assigned to the $\mathrm{Fe^{II}_3Fe^{III}/Fe^{II}_2Fe^{III}_2}$ (-1.013 V) and $\mathrm{Fe^{II}_2Fe^{III}_2/Fe^{II}Fe^{III}_3}$ (-0.200 V) redox couples. These potentials are cathodically shifted by 286 mV and 182 mV, respectively, relative to the analogous redox events for the pyrazolate bridged homolog [LFe$_3$O(PhPz)$_3$Fe][OTf]$_2$, [41] demonstrating the enhanced donor properties of 1-phenyl imidazolate relative to 3-phenyl pyrazolate (Figure 5). The final quasi-reversible electrochemical event at +0.450 V is assigned to the $\mathrm{Fe^{II}Fe^{III}_3/Fe^{III}_4}$ couple. Notably, the corresponding oxidation was not observed in the CV of [LFe$_3$O(PhPz)$_3$Fe][OTf]$_2$ at potentials up to +1 V. However, the CV of [LFe$_3$O(PhPz)$_3$Fe][OTf]$_2$ in dichloromethane exhibits an additional reduction at -1.733 V assigned to the Fe$^{II}_4$/Fe$^{II}_3$Fe^{III} redox event.[41] At similar potentials, the CV of **3** exhibits a large reductive wave, suggesting that the all-ferrous cluster reacts with dichloromethane. Notwithstanding, the Fe$^{II}_4$/Fe$^{II}_3$Fe^{III} redox event becomes (quasi)-reversible (-1.868 V) when the CV of **3** is recorded in tetrahydrofuran (Figure 4).

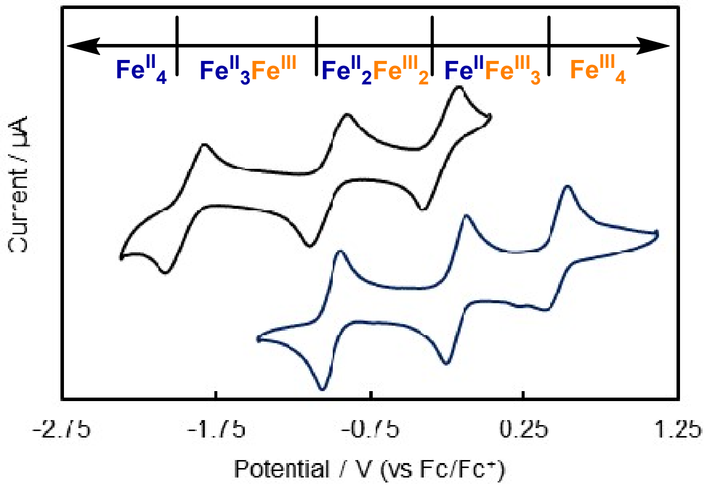

Figure 4. Cyclic voltammetry of **3** in THF (top, black) and CH$_2$Cl$_2$ (bottom, blue) with 0.1 M [*n*Bu$_4$N][PF$_6$] at a scan rate of 100 mV/s. For the Fe^{II}Fe$^{III}_3$/Fe$^{III}_4$ couple, two reductive features are observed and they become better resolved with faster scan rates. This may arise from reversible triflate binding, interconverting [LFe$_3$O(PhIm)$_3$Fe][OTf]$_4$ and [LFe$_3$O(PhIm)$_3$Fe(OTf)][OTf]$_3$.

Consistent with its electrochemical behavior, treatment of **3** with [Fc][OTf] in dichloromethane affords a new paramagnetic species which, following crystallization, was structurally characterized as [LFe$_3$O(PhIm)$_3$Fe][OTf]$_3$ (**4**). Addition of Cp$_2$Co to a solution of **3** in dichloromethane cleanly affords the reduced species [LFe$_3$O(PhIm)$_3$Fe][OTf] (**5**). Further reduction of **5** with sodium napthalenide (Na[C$_{10}$H$_8$]) in tetrahydrofuran affords an insoluble blue powder, assigned as the all-ferrous cluster, [$LFe_3O(PhIm)_3Fe$] (**6**), on the basis of Mössbauer spectroscopy (Mössbauer, Figure 5).[44]

The solid-state structures of **4** and **5** (Structures, Figures 3-4) demonstrate that the basic geometric features of **3** are maintained throughout the redox series, where the bond metrics within the $Fe_4(\mu_4\text{-}O)$ motif reveal the primary locus of redox chemistry. Oxidation of **3** to **4** results in a significant contraction of the Fe3-O1 distance from 2.092(2) Å to 1.983(4) Å, consistent with oxidation within the basal triiron core. Conversely, reduction of **3** to **5** results in an elongation of the Fe4-O1 distance from 1.8128(19) Å to 1.883(4) Å, suggesting reduction of the apical iron from Fe^{III} to Fe^{II}. The insolubility of **6** precludes structural characterization.

The crystallographic assignment of redox distributions in **3**-**6** is further corroborated by zero field ^{57}Fe Mössbauer spectroscopy. The 80 K Mössbauer spectrum of **3** (Mössbauer, Figure 1) was best fit with four quadrupole doublets, corresponding to four inequivalent iron centers. Two quadrupole doublets with isomer shifts of 1.03 mm/s and 1.14 mm/s ($|\Delta E_Q|$ of 3.13 mm/s and 3.22 mm/s, respectively) are characteristic of six-coordinate, high spin ferrous centers, while the quadrupole doublet with an isomer shift of 0.39 mm/s ($|\Delta E_Q|$ = 0.37 mm/s) is consistent with the presence of one octahedral ferric ion.[39-41] This results in an assignment of the core oxidation level as [$Fe^{II}_2Fe^{III}$], which is identical to that inferred from the solid state structure. The remaining quadrupole doublet, with an isomer shift of 0.19 mm/s ($|\Delta E_Q|$ = 1.11 mm/s), is attributed to the apical iron. Similar parameters have been observed for four-coordinate, high-spin ferric centers.[20]

Compared to the spectrum of **3**, the relative intensity of the diagnostic basal core Fe^{II} resonance near 3 mm/s decreases in **4**, consistent with oxidation within the triiron core. The spectrum of **4** was best fit with four quadrupole doublets with parameters indicating the presence of only one six-coordinate, high-spin ferrous center, maintenance of the apical, high-spin Fe^{III}, and two high-spin, six-coordinate ferric centers (Mössbauer, Figure 3). Conversely, upon reduction of **3** to **5**, there is no change in the relative intensity of the Lorentzian feature near 3 mm/s (Mössbauer, Figure 4). Instead, a substantial change in the isomer shift of the quadrupole doublet assigned to the apical iron is observed (δ = 0.19 mm/s in **3** vs. δ = 0.89 mm/s in **5**), suggesting one electron reduction of Fe4.

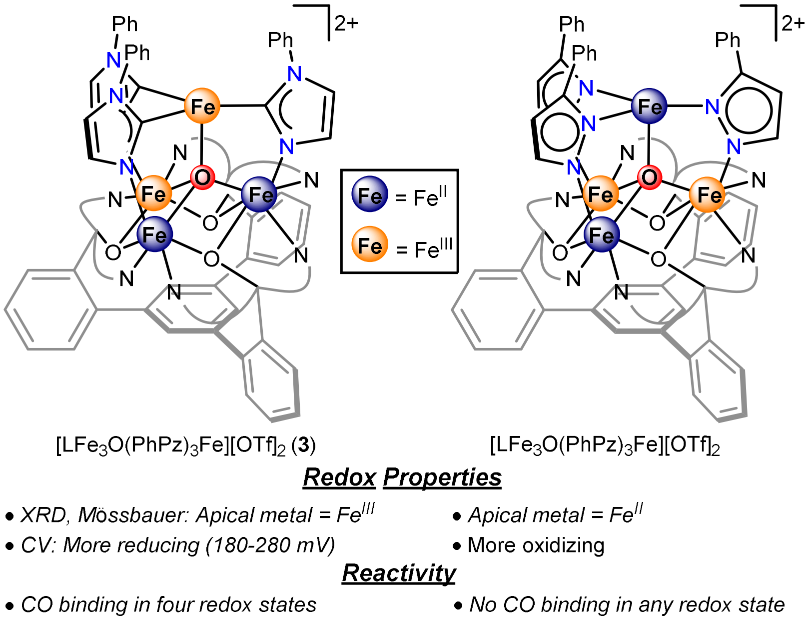

Figure 5. Comparison of the redox properties and reactivity of [LFe$_3$O(PhIm)$_3$Fe][OTf]$_2$ (**3**, left) and [LFe$_3$O(PhPz)$_3$Fe] [OTf]$_2$ (right).

Electronic Structure of 3. In order to confirm the high spin assignment of the apical, four-coordinate Fe^{III} centers of **3** and **4** inferred from Mössbauer studies, additional spectroscopic studies were undertaken, with a focus on **3** which features the shortest Fe4-O1 bond length. To assess the nature of the exchange coupling and the spin ground state, variable temperature (VT) magnetic susceptibility and variable temperature-variable field (VTVH) magnetization data were collected. The VT magnetic susceptibility data for **3** obtained between 1.8 K and 300 K at 0.1 T (Figure 6a) indicates overall ferromagnetic coupling and an $S = 4$ spin ground state. A plateau in the susceptibility is observed between 10-20 K at a value of ~9.1 cm^3 K mol^{-1} which decreases gradually to 6.4 cm^3 K mol^{-1} at 300 K. Below 10 K, a drop in $\chi_M T$ is also observed, likely a result of zero-field splitting. The susceptibility data for **3** was fit between 1.8 and 300 K according to the spin Hamiltonian $H = D(S_{z,i}^{2}\text{-}1/3(S_i(S_i+1)+gu_B S_i\cdot H)\} - 2J_{ij}(S_i\cdot S_j)$. A satisfactory simulation of the experimental data is obtained assuming all metal centers are *locally* high spin with isotropic exchange constants: J_{14} = -29.2 cm^{-1}, J_{24} = -63.9 cm^{-1}, J_{34} = -28.8 cm^{-1}, $J_{12} = J_{23}$ = -8.2 cm^{-1} and J_{13} = -9.5 cm^{-1}. From these simulated parameters, the observed ferromagnetic behavior may be rationalized. Strong antiferromagnetic interactions of the apical Fe^{III} (Fe4) with each of the metal centers of the triiron core ($|J_{\text{apical-core}}| \geq 3|J_{\text{core-core}}|$) results in ferromagnetic alignment of the spins on Fe1/Fe2/Fe3 at low temperatures, affording an $S = 4$ ground state.

Consistent with this spin coupling scheme, VTVH magnetization data collected between 1.8 and 9 K at fields of 1 to 7 T (Figure 6b) were well simulated with the system spin Hamiltonian $H = DS_z^2 + E(S_x^2 + S_y^2) + gu_B\mathbf{S}\cdot\mathbf{H}$. Due to the presence of zero field splitting, the VTVH magnetization data for **3** saturates near 5.4μ_B at 1.8 K and 7 T, below the expected M = gS limit for g = 2.0. However, the experimental data is well reproduced assuming an S = 4 ground state with g = 2.00, D = -3.65 cm^{-1}, and $|E/D|$ = 0.33. Consistent with its assignment as a non-Kramer's system with $D < 0$,[45] the Mössbauer spectrum of **3** at 2.3 K exhibits pronounced magnetic hyperfine splitting with well-resolved features between -7 and 8 mm/s in an applied field of only 50 mT (Mössbauer, Figure 2). The parallel mode EPR spectrum of **3** in a propionitrile/butryonitrile (4:5) glass exhibits a sharp feature with g ~17.2 at 4.5 K which is assigned to a transition within the M_s = +/- 4 doublet (EPR, Figure 1).

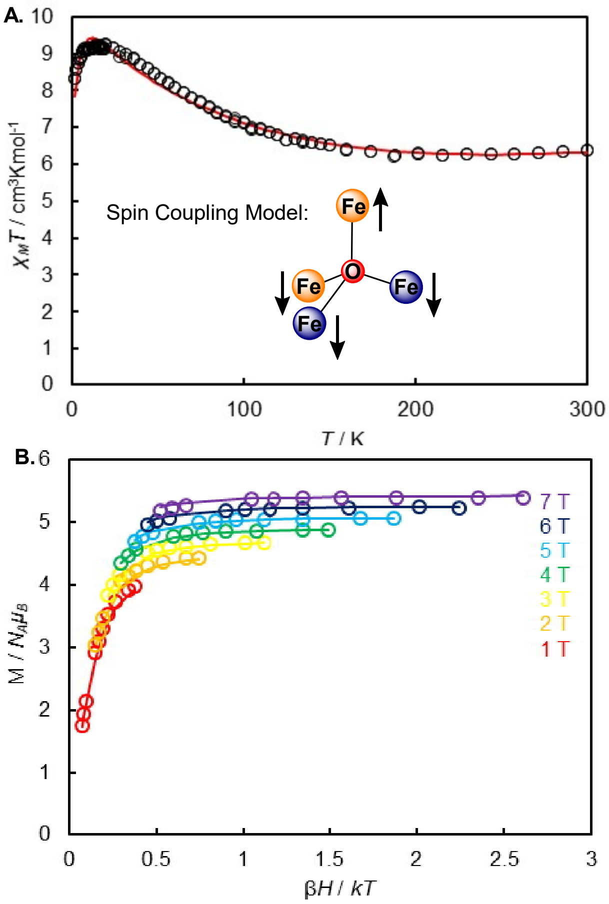

Figure 6. (A) Variable temperature direct current magnetic susceptibility data for $[LFe_3O(PhIm)_3Fe][OTf]_2$ (**3**) obtained between 1.8 K and 300 K at 0.1 T. Simulated according to the spin Hamiltonian $H = \Sigma\{D(S_{z,i}^2 - 1/3(S_i(S_i+1) + g\mu_B S_i \cdot H)\} - 2J_{ij}(S_i \cdot S_j)$ with all metal centers *locally* high spin. For full simulation parameters, see the Supporting Information. (B) Variable temperature-variable field magnetization data for $[LFe_3O(PhIm)_3Fe][OTf]_2$ (**3**) between 1.8 and 9 K at fields of 1 to 7 T. Simulated according to the system spin Hamiltonian $H = DS_z^2 + E(S_x^2 + S_y^2) + g\mu_B\mathbf{S}\cdot\mathbf{H}$ with $g = 2.00$, $D = -3.65$ cm^{-1}, and $|E/D| = 0.33$.

CO Binding Equilibria of 3. Having confirmed the high spin assignment of the apical Fe^{III} center in **3**, we explored its reactivity with CO (Figure 7). In this regard, variable temperature IR spectroscopy indicated the formation of both mono- (**3**-**CO**) and dicarbonyl- (**3**-**(CO)$_2$**) adducts of **3**. The IR spectrum of **3** measured at 195 K in CO-saturated dichloromethane (Figure 7c) following an Ar purge exhibited an intense feature at 1944 cm^{-1} (**3-CO**) in addition to weaker features at 2014 cm^{-1} and 1960 cm^{-1} (**3-(CO)$_2$**). Warming the solution to 273 K with stirring under Ar results in loss of the features at 2014 and 1960 cm^{-1} and a decrease of intensity at 1944 cm^{-1}. Upon further warming to room temperature, no CO vibrational features were observed.

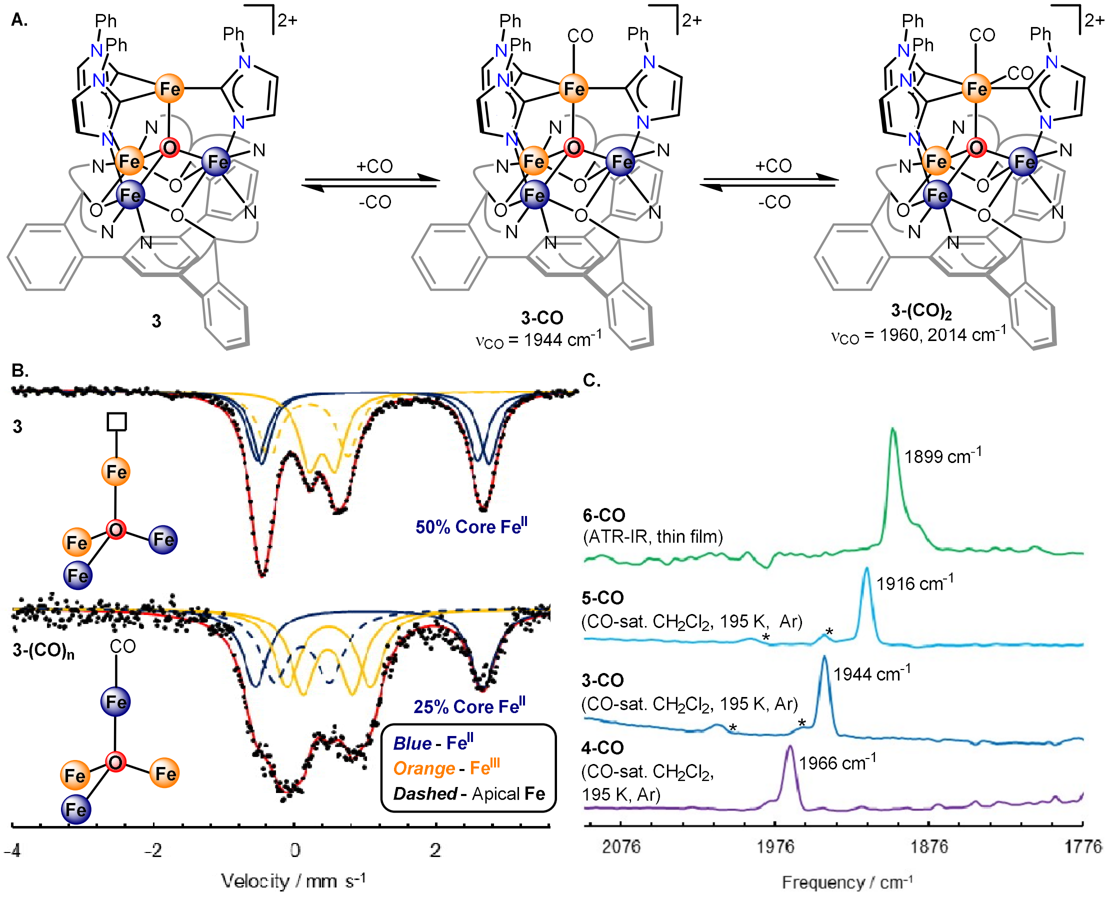

Figure 7. Binding of CO by [$LFe_3O(PhIm)_3Fe$][OTf]$_2$ (3) induces an internal electron transfer. (A) Cooling solutions of [$LFe_3O(PhIm)_3Fe$][OTf]$_2$ (**3**) under CO initially affords the monocarbonyl [$LFe_3O(PhIm)_3Fe(CO)$][OTf]$_2$ (**3-CO**). Further cooling converts **3-CO** into the dicarbonyl [$LFe_3O(PhIm)_3Fe(CO)_2$][OTf]$_2$ (**3-(CO)$_2$**). (B) Top: Zero field ^{57}Fe Mössbauer spectrum (80 K, microcrystalline material) of [$LFe_3O(PhIm)_3Fe$](OTf)$_2$ confirms the presence of two core Fe^{II} centers (50% total iron). (Bottom): Mössbauer spectrum of [$LFe_3O(PhIm)_3Fe(CO)_n$][OTf]$_2$ (**3-(CO)$_n$**) in CO-saturated 2,6-lutidine (*f.p.* = -5 ^{o}C) demonstrates that binding of CO results in a change of the core redox level from [$Fe^{II}_2Fe^{III}$] to [$Fe^{II}Fe^{III}_2$], with electron transfer to the site of CO binding. See the Supporting Information for full simulation details. (C) IR spectroscopy illustrates the influence of redox chemistry on ν_{CO} for the

monocarbonyl complexes described herein. The observed shifts in ν_{CO} of only 20-30 cm^{-1} (**6-CO**: 1899 cm^{-1}, **5-CO**: 1916 cm^{-1}, **3-CO**: 1944 cm^{-1}, **4-CO**: 1966 cm^{-1}) support an Fe^{II}-CO assignment across the series, implying that redox reorganization accompanies CO binding in **3** and **4**. An asterisk denotes features associated with the dicarbonyl complexes.

The temperature dependent formation of both **3-CO** and **3-(CO)$_2$** was confirmed by ^{1}H-NMR studies. Cooling solutions of **3** in either dichloromethane-*d*$_2$ (NMR, Figure 15) or acetone-*d*$_6$ (NMR, Figure 21) under an atmosphere of CO from room temperature initially affords **3-CO** as the major species, though an additional species simultaneously grows in. Further cooling results in the loss of **3-CO** and complete conversion to this more asymmetric species, assigned as **3-(CO)$_2$**. Confirmation of this assignment was obtained by crystallization from solutions of **3** at low temperature under an atmosphere of CO, which afforded crystals of **3-(CO)$_2$** suitable for XRD. The solid state structure of **3-(CO)$_2$** confirms that both CO ligands bind Fe4 (Figure 3c). Warming solutions of **3-(CO)$_2$** from 198 K back to room temperature confirms that these temperature-dependent CO binding events are fully reversible.

In the absence of redox reorganization, binding of CO by **3** would afford an apical Fe^{III}-CO unit in **3-CO** (Table 1). However, with few exceptions,[46-49] Fe^{III} centers generally display no affinity for CO.[50] Alternatively, we envisioned that an internal electron transfer (*i*-ET) from a distal Fe^{II} site might accommodate coordination of CO (Figure 7a). Based on the diagnostic features associated with the basal core Fe^{II} centers in these clusters,[39-41] Mössbauer spectroscopy serves as a convenient tool to determine whether redox reorganization accompanies CO binding.[51] The zero field Mössbauer spectrum (80 K) obtained by freezing a CO-saturated solution of **3** in 2,6-lutidine (*f.p.* = -5 ºC) reveals a significant loss of basal Fe^{II} intensity (Mössbauer, Figure 6). The spectrum can be satisfactorily fit to a mixture of **3-(CO)$_n$** (61%) and **3** (39%) (Mössbauer, Figure 7). The Mössbauer spectrum of **3-(CO)$_n$** (Figure 7b, bottom) obtained following subtraction of residual **3** reveals a single quadrupole doublet (25% total iron) with an isomer shift near 1 mm/s (δ = 1.05 mm/s, $|\Delta E_Q|$ = 3.22 mm/s), indicating the presence of a single core ferrous center and a change in the core redox level from [$Fe^{II}_2Fe^{III}$] to [$Fe^{II}Fe^{III}_2$] following binding of CO. The simulated Mössbauer parameters associated with the apical iron center of **3-(CO)$_n$** (δ = 0.10 mm/s, $|\Delta E_Q|$ = 3.22 mm/s) are consistent with the formation of an *S* = 1 trigonal bipyramidal Fe^{II}-CO complex following internal electron transfer.[52] In contrast to the well-defined reactivity of **3**, reactions of CO with synthetic, high spin iron(II/III) clusters typically result in cluster fragmentation and the formation of reduced, low spin iron carbonyl clusters,[23-24] further illustrating the advantages of employing robust ligand scaffolds to interrogate chemistry relevant to nitrogenase.[29, 36]

Reversible CO Binding Across Four Redox States. Encouraged by the reactivity of **3** with CO, we investigated the dependence of CO binding on the redox state of the cluster. Remarkably, binding of CO remains reversible for **4**-**6**. Cooling solutions of **4** in dichloromethane-*d*$_2$ under an atmosphere of CO affords **4-CO** (NMR, Figure 12), an assignment confirmed by the observation of a single CO stretching frequency (ν_{CO} = 1966 cm^{-1}) in its IR spectrum (CO-saturated dichloromethane at 195 K, Figure 7c). Oxidation of **4** with [$N(C_6H_4Br\text{-}4)_3$][OTf] in dichloromethane-*d*$_2$ affords the all-ferric cluster [$LFe_3O(PhIm)_3Fe$][OTf]$_4$ (**7**), with ^{1}H-NMR (NMR, Figure 24) and UV-Vis spectral features which are identical under N_2 or CO, suggesting that at least one Fe^{II} center is necessary for CO binding.

Under an atmosphere of CO, **5** converts predominately to [$LFe_3O(PhIm)_3Fe(CO)$][OTf] (**5-CO**) at room temperature based on IR (ν_{CO} = 1916 cm^{-1}) and ^{1}H-NMR spectroscopy. Further cooling converts **5-CO** to **5-(CO)$_2$**, which exhibits diagnostic features at 1994 and 1944 cm^{-1} in its low temperature IR spectrum (CO-saturated dichloromethane at 195 K, Figure 7c). By ^{1}H-NMR spectroscopy, heating **5-CO** under CO in chlorobenzene-*d*$_5$ (NMR, Figure 23) or exposing it to an atmosphere of N_2 returns **5**, demonstrating that binding of CO is reversible. Single crystals of **5-CO** amenable to XRD were obtained from solutions of **5** under CO and confirm its identity as a monocarbonyl adduct featuring a trigonal bipyramidal coordination environment at Fe4 (Figure 3b).

Unfortunately, the insolubility of **6** precludes direct solution monitoring of its reactivity with CO. However, changes in the ATR-IR spectrum following addition of an atmosphere of CO to a suspension of **6** in tetrahydrofuran supports the formation of both mono- (**6-CO**, ν_{CO} = 1899 cm^{-1}) and dicarbonyl (**6-(CO)$_2$**, ν_{CO} = 1980 and 1891 cm^{-1}) adducts. The formation of these CO bound species is reversible; removing the CO atmosphere results in gradual loss of the Fe-CO stretching frequencies for both **6-CO** and **6-(CO)$_2$** and formation of an insoluble blue material with IR spectral features indicative of **6**.

Table 1. Summary of redox distribution assignments for 3-(CO)$_n$-7-(CO)$_n$.

Complex	Distal Metals	Apical Metal
$[LFe_3O(PhIm)_3Fe][OTf]_4$ (**7**)	$[Fe^{III}_3]$	Fe^{III}
$[LFe_3O(PhIm)_3Fe][OTf]_3$ (**4**)	$[Fe^{II}Fe^{III}_2]$	Fe^{III}
$[LFe_3O(PhIm)_3Fe][OTf]_2$ (**3**)	$[Fe^{II}_2Fe^{III}]$	Fe^{III}
$[LFe_3O(PhIm)_3Fe][OTf]$ (**5**)	$[Fe^{II}_2Fe^{III}]$	Fe^{II}
$[LFe_3O(PhIm)_3Fe]$(**6**)	$[Fe^{II}_3]$	Fe^{II}
$[LFe_3O(PhIm)_3Fe(CO)][OTf]_2$ (**4-CO**)	$[Fe^{III}_3]$	Fe^{II}
$[LFe_3O(PhIm)_3Fe(CO)][OTf]_2$ (**3-CO**)	$[Fe^{II}Fe^{III}_2]$	Fe^{II}
$[LFe_3O(PhIm)_3Fe(CO)][OTf]$ (**5-CO**)	$[Fe^{II}_2Fe^{III}]$	Fe^{II}
$[LFe_3O(PhIm)_3Fe(CO)]$(**6-CO**)	$[Fe^{II}_3]$	Fe^{II}
$[LFe_3O(PhIm)_3Fe(CO)_2][OTf]_2$ (**3-(CO)$_2$**)	$[Fe^{II}Fe^{III}_2]$	Fe^{II}
$[LFe_3O(PhIm)_3Fe(CO)_2][OTf]$ (**5-(CO)$_2$**)	$[Fe^{II}_2Fe^{III}]$	Fe^{II}
$[LFe_3O(PhIm)_3Fe(CO)_2]$(**6-(CO)$_2$**)	$[Fe^{II}_3]$	Fe^{II}

For the monocarbonyl complexes described herein, shifts in ν_{CO} of only 20-30 cm^{-1} are observed per redox event (**6-CO**: 1899 cm^{-1}, **5-CO**: 1916 cm^{-1}, **3-CO**: 1944 cm^{-1}, **4-CO**: 1966 cm^{-1}, Figure 7c). These shifts are similar in magnitude to those which arise from *remote* redox chemistry in related tetranuclear iron nitrosyl clusters[39, 41] and are significantly smaller than expected for redox chemistry centered at the Fe-CO unit (~100 cm^{-1} per redox event).[48-49, 53-54] Moreover, the observed Fe-CO stretching frequencies are within the range reported for other trigonal bipyramidal Fe^{II} monocarbonyl complexes. Combined with the observation of a change in the core redox level of **3** by Mössbauer spectroscopy,[55] these results suggest an Fe^{II}-CO assignment across the redox series (**3-CO** to **6-CO**). This implies that coordination of CO induces an internal electron transfer from one of the distal Fe^{II} centers to the apical Fe^{III} site in both **3** and **4**. Ligand-induced redox reorganizations (LIRR) related to those observed for **3** and **4** have been reported for monometallic compounds featuring redox active supporting ligands,[56-59] as well as complexes with pendant ferrocenyl substituents.[60-61] Notwithstanding, we are not aware of precedence for a reversible, internal electron transfer involving metal centers within a multinuclear cluster which is induced by small molecule binding. Changes in the identity of an ancillary ligand (DMF, MeCN, or ^{-}CN) have been shown to modulate the extent of valence delocalization in a series of hexairon clusters.[62] However, the site-differentiated nature of the clusters examined here allows us to distinguish the effects of CO binding on the electronic properties of the binding site from those on *remote* metal centers.

CO Binding Energetics. In order to quantify the effect of redox chemistry on the affinity of **3**-**6** for CO, we evaluated their CO binding energetics by ^{1}H-NMR spectroscopy, which facilitated accurate identification of speciation in the reaction mixtures.[63] At 303 K, the CO binding constant for **3** (K_1(**3**) = 0.15 atm^{-1}, dichloromethane-d_2, P_{CO} = 1 atm.) is at least 10^3-fold lower than for most Fe^{II} complexes (Table 2),[64-66] though a sterically encumbered, trigonal monopyrimidal Fe^{II} complex with a similar affinity for CO (K_{298K} = 6.9 atm^{-1}) has been reported.[67] The thermodynamic parameters associated with the formation of **3-CO** (ΔH = -13.6(8) $kcal\cdot mol^{-1}$, ΔS = -48(3) $cal\cdot mol^{-1}\cdot K^{-1}$) suggest that this low CO affinity derives from an unusually large entropic penalty, which we attribute to loss of rotational freedom in the flanking aryl substituents upon CO binding. While a complete study on the energetics of forming **5-CO** in dichloromethane (*b.p.* = 39.6 °C) was not possible due to temperature constraints, at 303 K the affinity of the apical Fe^{II} of **5** for CO (K_1(**5**)) was determined to be 59 atm^{-1}, an enhancement of only ~400-fold ($\Delta\Delta G_{303K}$ ~ 3.6 $kcal{\cdot}mol^{-1}$) relative to **3**, which features an apical Fe^{III}.

Table 2. Thermodynamics of diatomic binding for 3-5 in dichloromethane and selected reference compounds.

Complex	Ligand	K_{303K} (atm^{-1})	ΔH ($kcal\ mol^{-1}$)	ΔS ($cal\ mol^{-1}\ K^{-1}$)
chelated protoheme[a]	CO	1.6×10^{6}	-17.5	-34
$Fe^{II}(TPP)(1,2\text{-}Me_2Im)$[a]	CO	3.4×10^{3}	-12.8	-26.1
$Fe^{II}(PocPiv)(1,2\text{-}Me_2Im)$[a]	CO	8.2×10^{3}	-13.9	-28
$K[N(CH_2C(O)N^{i}Pr)_3Fe^{II}]$[b]	CO	6.9	---	---
$[Fe^{II}(P_4N_2)][B(C_6F_5)_4]_2$[c]	N_2	$<4 \times 10^{-23}$	---	---
$[Fe^{I}(P_4N_2)][B(C_6F_5)_4]$[c]	N_2	0.4	-6.5	-23.4
$[Fe^{0}(P_4N_2)]$[c]	N_2	$\sim 4 \times 10^{4}$	---	---
$[(N_2)Fe^{II}(\mu\text{-}H)_2Fe^{II}]$[d]	N_2	1.1 M^{-1}	-9	-30
$[(N_2)Fe^{1.5}(\mu\text{-}H)_2Fe^{1.5}]$[d]	N_2	$\sim 2.9 \times 10^{6}$ M^{-1}	---	---
4	CO	0.2[e]	-12.1	-47
3	CO	0.2	-13.6	-48
5	CO	59	-17.2[f]	---
3-CO	CO	0.1[e]	-8.3	-32[g]
5-CO	CO	0.2[e]	-9.2	-34[g]

In contrast to the relatively small difference in the CO affinities of **3** and **5** (~400-fold), significantly larger enhancements (>10^5-fold) in binding affinities have previously been reported to accompany 1e^- redox chemistry (Table 2). For example, reduction of a square planar iron tetraphosphine complex from iron(II) to iron(I) and then to iron(0) results in successive ~10^{22}-fold and 10^5-fold enhancements in its affinity for N_2.[68] Reduction of a low spin $(N_2)Fe^{II}(\mu\text{-}H)_2Fe^{II}$ complex to its valence-delocalized $(N_2)Fe^{I}(\mu\text{-}H)_2Fe^{II}$ congener results in a 10^6-fold enhancement in its affinity for a second molecule of N_2.[35] Notably, computational studies revealed that the SOMO of both $(N_2)Fe^{I}(\mu\text{-}H)_2Fe^{II}$ and $(N_2)Fe^{I}(\mu\text{-}H)_2Fe^{II}(N_2)$ complexes are valence-delocalized, suggesting that minimal redox reorganization accompanies N_2 binding, and the large effect on binding is due to the formal difference in oxidation state at the N_2 binding site.

The small influence which reduction of **3** to **5** has on the CO binding energetics seems inconsistent with the low affinity Fe^{III} typically exhibits toward CO[50] and the large changes in binding affinity seen in other systems upon $1e^-$ reduction. We propose instead that the internal electron transfer (*i*-ET) which accompanies coordination of CO to **3** facilitates this otherwise unfavorable binding event. From this perspective, **3** contains a masked apical Fe^{II} site whose affinity for CO is modulated relative to **5** by two terms, one accounting for the energetic cost of redox reorganization and the other for the effect of changes in redox states of the remote metals (Figure 8). Although our data for these and related clusters[39-41, 69-70] is most consistent with a valence-localized assignment, an analogous scheme can be constructed for a valence-delocalized system, where the internal electron transfer (*i*-ET) term is replaced by a term accounting for the energetic penalty of trapping an electron at Fe4, assuming the CO bound product is valence-localized.

Despite the simplicity of this thermodynamic model, it adequately accounts for trends in the energetics of CO binding in **3**-**5**. The difference in enthalpy ($\Delta\Delta H$) for the second CO binding event in **3** and **5**, the formation of **3-(CO)$_2$** and **5-(CO)$_2$**, respectively, is only 0.9(6) kcal·mol^{-1}. This small $\Delta\Delta H$ reflects the relatively small influence that the redox states of the *remote* metal sites have on CO binding in these high-spin, valence-localized iron clusters in the absence of redox reorganization. In contrast, the first CO binding event for **3** and **5**, the formation of **3-CO** and **5-CO**, respectively, has a larger $\Delta\Delta H$ (3.6 kcal·mol^{-1}). Assuming that changes in the redox state of the *remote* metals have an effect on CO binding similar to that observed in the dicarbonyl series (~1 kcal·mol^{-1}), the redox reorganization penalty must be on the order of 2.6(6) kcal·mol^{-1} (RRE = -nFΔE, ΔE ~ -110 mV).

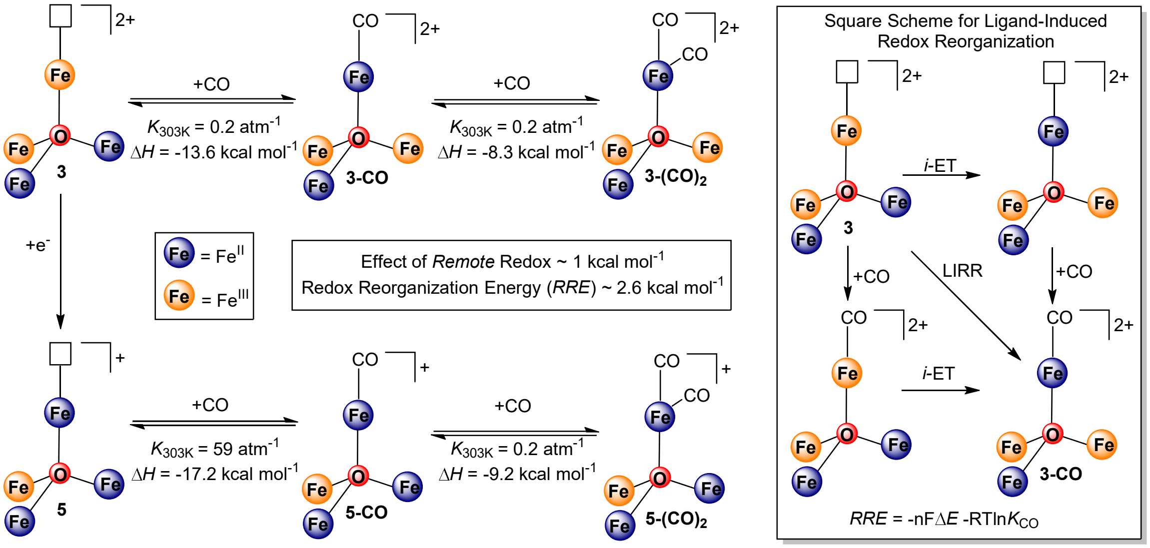

Figure 8. Thermodynamics of ligand-induced redox reorganization. The difference in the CO binding enthalpy for **3-CO** and **5-CO** ($\Delta\Delta H$ ~ 1 kcal·mol^{-1}) corresponds to the effect of *remote* redox chemistry on the CO affinity of the apical Fe^{II} center. A similar value is obtained comparing **3** and **4** ($\Delta\Delta H$ ~ 1.5 kcal·mol^{-1}). The larger difference in the enthalpy of CO binding to **3** vs. **5** ($\Delta\Delta H$ ~ 3.6 kcal·mol^{-1}) arises from the energetic penalty associated with internal electron transfer in **3**. From this, we can estimate a redox reorganization energy (RRE) of ~ 2.6 kcal·mol^{-1}. Right: Thermodynamic square scheme for ligand-induced redox organization (LIRR). Note, electron transfer is coupled to structural rearrangements, especially within the $Fe_4(\mu_4\text{-}O)$ motif (Supplementary Table 4), such that the redox sites and their relative potentials are not fully independent.

As in **3**, the formation of **4-CO** must involve a redox reorganization and hence, the difference in ΔH for CO binding between them should reflect only the *remote* redox effect if the above model is correct. The observation of a $\Delta\Delta H$ of ~1.5 kcal/mol for the formation of **3-CO** and **4-CO** is thus in agreement with this model. This further implies that the redox reorganization in **4** has a similar energetic penalty ($\Delta\Delta E$ ~ 0 vs. **3**) despite the more oxidized basal triiron core. While oxidation of **3** to **4** does elongate the Fe3-O1 distance from 2.1480(19) Å to 2.215(4) Å, increasing its local reduction potential, the influence of this structural rearrangement on ΔE must be largely levelled by a concomitant increase in the Fe4-O1 distance from 1.8128(19) to 1.855(4) Å. Given the valence-localized nature of these clusters, it is not surprising that the local redox potentials of the core $\mathrm{Fe^{II}}$ sites (relative to the apical $\mathrm{Fe^{III}}$ center) remain mostly invariant to cluster redox chemistry. As such, the redox reorganization energy associated with internal electron transfer (*RRE* ~ 2.6 $\mathrm{kcal{\cdot}mol^{-1}}$) is not significantly perturbed by redox state. This levelling of ΔE in valence-localized clusters leads us to the conclusion that the most drastic differences in ligand binding affinities between oxidized and reduced species will be observed at the point where redox reorganization ceases to be required, as observed for **3-5**.

CONCLUSIONS

In summary, for high spin, valence-localized iron clusters such as those described herein, small enhancements (at most ~400-fold) in the affinity for π-acids arise from pure redox chemistry, despite a notable effect on the degree of CO activation (67 $\mathrm{cm^{-1}}$ over three redox events). Deconvoluting the effect of redox at specific sites within the cluster, we demonstrate that electron-loading at metal centers *remote* from the substrate binding site has a relatively small influence on the CO binding energetics (~ 1 $\mathrm{kcal{\cdot}mol^{-1}}$). Nonetheless, availability of reducing equivalents and internal electron transfers from these *remote* metal sites facilitate binding of π-acids at the apical $\mathrm{Fe^{III}}$ center due to the relatively small energetic penalty arising from redox reorganization (*RRE* ~ 2.6 $\mathrm{kcal{\cdot}mol^{-1}}$). The ease with which these valence-localized, high spin iron clusters redistribute electrons in response to ligand binding provides insight into redox-dependent binding of N_2 and CO by FeMoco, especially in light of a recent report which suggests that substrate binding interactions may occur on an oxidized edge of the cofactor.[19]

EXPERIMENTAL DETAILS

General Considerations. All reactions were performed at room temperature in a nitrogen filled M. Braun glovebox or using standard Schlenk techniques unless otherwise specified. Glassware was oven dried at 140°C for at least two hours prior to use, and allowed to cool under vacuum. PhIm-H was prepared according to a literature procedure,[71] dried over calcium hydride, and distilled at 130°C under vacuum. $LFe_3(OAc)_3$ was prepared according to a literature procedure[42] and purified by recrystallization. [Fc][OTf][72] and $Na[BAr^F{}_{24}]$[73] were prepared according to literature procedures. $[Fc^*][OTf]$ was prepared by oxidation of Fc^* with [Fc][OTf] in dichloromethane followed by crystallization from dichloromethane/pentane. $[Cp_2Co][OTf]$ was prepared by oxidation of Cp_2Co with AgOTf. All other reagents were obtained commercially unless otherwise noted and typically stored over activated 4 Å molecular sieves. Tetrahydrofuran was dried using sodium/benzophenone ketyl, degassed with three freeze-pump-thaw cycles, vacuum transferred, and stored over 3 Å molecular sieves prior to use. Dichloromethane, diethyl ether, benzene, acetonitrile, hexanes, and pentane were dried by sparging with nitrogen for at least 15 minutes, then passed through a column of activated A2 alumina under positive nitrogen pressure. Acetone and acetone-d_6 were dried using calcium sulfate (Drierite), degassed with three freeze-pump-thaw cycles, vacuum transferred, and stored over 3 Å molecular sieves prior to use. Dichloromethane-d_2 was dried over calcium hydride, degassed by three freeze-pump-thaw cycles, and vacuum transferred prior to use. Chlorobenzene-d_5 was degassed by three-pump-thaw cycles and dried over 3 Å molecular sieves prior to use. ^1H and ^{19}F NMR spectra were recorded on a Varian 300 or 400 MHz spectrometer. All chemical shifts (δ) are reported in ppm, and coupling constants (*J*) are in hertz. The ^{1}H-NMR spectra were referenced using residual H impurity in the deuterated solvent, whereas the ^{19}F chemical shifts are reported relative to the internal lock signal. UV-Vis spectra were recorded on a Varian Cary Bio 50 spectrophotometer. Infrared (ATR-IR) spectra were recorded on a Bruker ALPHA ATR-IR spectrometer. Solution ATR-IR spectra were recorded on a Mettler Toledo iC10 ReactIR. Elemental analyses were performed at Caltech.

Physical Methods.

Mössbauer Measurements. Zero field ^{57}Fe Mössbauer spectra were recorded in constant acceleration on a spectrometer from See Co (Edina, MN) equipped with an SVT-400 cryostat (Janis, Wilmington, WA). The quoted isomer shifts are relative to the centroid of the spectrum of α-Fe foil at room temperature. Unless otherwise noted, samples were prepared by grinding polycrystalline (20-50 mg) into a fine powder and pressed into a homogenous pellet with boron nitride in a cup fitted with a screw cap. The data were fitted to Lorentzian lineshapes using the program WMOSS (www.wmoss.org).

EPR Spectroscopy. X-band EPR spectra were collected on a Bruker EMX spectrometer equipped with a He flow cryostat. Samples of 3 were prepared as frozen glasses in 4:5 propionitrile/butyronitrile (2 mM). Spectra were collected with microwave powers ranging from 2 mW to 8 mW with modulation amplitudes of 4 Gauss. Variable temperature spectra were plotted with SpinCount (Prof. Michael Hendrich).

Magnetic Measurements. Magnetic measurements for 3 were conducted with a Quantum Design MPMS3 SQUID Magnetometer at the University of California, Los Angeles. A polycrystalline sample of 3 was wrapped in plastic film and placed in a gelatin capsule. The capsule was then inserted into a plastic straw. Magnetization data at 100 K from 0 to 4 T were collected to confirm the absence of ferromagnetic impurities. Direct current variable temperature magnetic susceptibility measurements were collected between 1.8 and 300 K with a 0.1 T field. Reduced magnetization data was collected between 1.8 and 9 K at fields between 1 and 7 T. Magnetic susceptibility data was corrected for diamagnetism of the sample, estimated using Pascal's constants. Magnetic susceptibility data was simulated with julX (Prof. Eckhard Bill) and reduced magnetization data was simulated with PHI.[74]

Electrochemical Measurements. CVs were recorded with a Pine Instrument Company AFCBP1 bipotentiostat using the AfterMath software package. All measurements were performed in a three-electrode cell, which consisted of (1) a glassy carbon working electrode, (2) a Pt wire counter electrode, and (3) a Ag wire reference electrode. Dry solvent that contained 0.1 M $n\mathrm{Bu}_4\mathrm{NPF}_6$ was employed as the electrolyte solution for all electrochemical measurements. All electrochemical measurements were performed at room temperature in an M. Braun nitrogen filled glovebox or in specialized glassware on the Schlenk line. The ferrocene/ferrocenium ($\mathrm{Fc/Fc^+}$) redox couple was used as an internal standard for all measurements.

X-ray Crystallography. For compounds 1-2, 4-5, 3-$(\mathrm{CO})_2$ and 5-CO low-temperature (100 K) diffraction data (φ-and ω-scans) were collected on a Bruker AXS D8 VENTURE KAPPA diffractometer coupled to a PHOTON 100 CMOS detector with Mo Kα radiation (λ = 0.71073 Å) or with Cu Kα (λ = 1.54178 Å). For compound 3, low-temperature (100 K) diffraction data (φ-and ω-scans) were collected on a Bruker AXS KAPPA APEX II diffractometer coupled to an APEX II CCD detector with graphite monochromated Mo Kα radiation (λ = 0.71073 Å). All diffractometer manipulations, including data collection, integration, and scaling were carried out using the Bruker APEXII software.[75] Absorption corrections were applied using SADABS.[76] Structures were solved by direct methods using SHELXS[77] and refined against $F2$ on all data by full-matrix least squares with SHELXL-2014[78] interfaced with Olex2-1.2.8[79] and using established refinement techniques. All non-hydrogen atoms were refined anisotropically, except heavily disordered solvent in some cases. All hydrogen atoms were included into the model at geometrically calculated positions and refined using a riding model. The isotropic displacement parameters of all hydrogen atoms were fixed to 1.2 times the *U* value of the atoms they are linked to (1.5 times for methyl groups). All disordered atoms were refined with the help of similarity restraints on the 1,2- and 1,3-distances and displacement parameters as well as enhanced rigid bond restraints for anisotropic displacement parameters. Due to the size of the compounds, most crystals included solvent accessible voids, which tended to contain disordered solvent. In most cases, this disorder could be modeled satisfactorily. Furthermore, the long-range order of these crystals and amount of high angle data was in some cases not ideal, due to desolvation of the crystals and/or solvent disorder.

DFT Calculations. Gaussian09 was used for all calculations.[80] Geometry optimizations for 3-methylpyrazolate and 1-methylimidazolate were performed with the BP86 functional with a double-ζ basis set and one set of polarization functions (6-31G+(d,p)). Initial geometries were taken from the X-ray crystal structures of $[LFe_3O(PhPz)_3Fe][OTf]_2$ and $[LFe_3O(PhIm)_3Fe][OTf]_2$ (3), respectively, by removing all atoms except for one of the bridging ligands and exchanging the aryl substituent for a methyl group. Single point energy calculations were then performed with the B3LYP functional, also with the 6-31G+(d,p) basis set. Molecular orbitals were visualized with Gaussview.

Synthetic Procedures. *Synthesis of* $LFe_3(OTf)_3$, (1). Trimethylsilyl triflate (4.10 mL, 22.65 mmol, 10 equiv.) was added dropwise to a suspension of $LFe_3(OAc)_3$ (2.72 g, 2.26 mmol, 1 equiv.) in dichloromethane (80 mL), affording a golden yellow solution. After stirring for 30 minutes, the volatiles were removed in vacuo affording $LFe_3(OTf)_3$ as a pale yellow solid. The material can be triturated with dichloromethane to remove most of the impurities. After trituration,

$LFe_3(OTf)_3$ is collected on a course frit as a light yellow solid (2.59 g, 78% yield). Crystals suitable for X-ray diffraction were grown by diffusion of diethyl ether into a concentrated dichloromethane solution of the compound. We have not been able to obtain a satisfactory elemental analysis for $LFe_3(OTf)_3$, possibly due to its extreme air and moisture sensitivity. However, structural analysis confirms its identity, which is satisfactory for its use as a precursor to 2. ^1H NMR (300 MHz, CD_2Cl_2) δ 112.96 (s), 97.06 (s), 84.67 (s), 45.45 (s), 37.18 (s), 35.38 (s), 26.25 (s), 16.68 (s), 7.84 (s), 3.81 (s), -2.35 (b), -3.16 (s), -7.32 (s). ^{19}F NMR (300 MHz, CD_2Cl_2) δ – 41.79 (b). UV-Vis (CH_2Cl_2) [ε (M^{-1} cm^{-1})]: 372 nm (2.91 x 10^3).

Synthesis of *$[LFe_3O(PhIm\text{-}H)_3][OTf]_3$*, (2). A solution of PhIm (838 mg, 5.82 mmol, 3.3 equiv.) in tetrahydrofuran (13 mL) was added dropwise to a stirring suspension of $LFe_3(OTf)_3$ (2.59 g, 1.76 mmol, 1.0 equiv.) in tetrahydrofuran (43 mL). The resulting orange solution was allowed to stir for one hour, at which point a suspension of PhIO (388 mg, 1.76 mmol, 1.0 equiv.) in tetrahydrofuran (20 mL) was added. The solution immediately darkened, and a dark brown precipitate formed gradually. After stirring overnight, the precipitate was collected on a bed of Celite, washed with additional tetrahydrofuran, and then eluted with dichloromethane. The volatiles were removed under reduced pressure to afford $[LFe_3O(PhIm\text{-}H)_3][OTf]_3$ as a dark brown solid (3.02 g, 97% yield). Crystals suitable for X-ray diffraction were grown by diffusion of diethyl ether into a concentrated dichloromethane solution of the compound. Unfortunately, we have not been able to obtain satisfactory elemental analysis for this compound. ^1H NMR (300 MHz, CD_2Cl_2) δ 103.79 (b), 100.89 (b), 98.12 (b), 82.04 (s), 78.36 (b), 68.19 (s), 66.99 (s), 66.58 (s), 59.35 (s), 51.73 (s), 49.32 (s), 48.89 (s), 47.62 (s), 46.74 (s), 45.35 (s), 44.51 (s), 42.11 (b), 18.16 (b), 17.02 (s), 15.14 (b), 14.04 (b), 13.31 (s), 12.80 (b), 11.88 (s), 10.69 (s), 9.19 (b), 8.36 (b), 7.93 (s), 6.61 (s), 4.81 (s), 4.40 (s), 2.90 (s), 1.13 (b), -2.88 (b), -

6.15 (b). ^{19}F NMR (300 MHz, CD_2Cl_2) δ -9.21 (3F), -77.58 (6F). UV-Vis (CH_2Cl_2) [ε (M^{-1} cm^{-1})]: 408 nm (2.60 x 10^3), 531 nm (7.74 x 10^2).

Synthesis of [LFe$_3$O(PhIm)$_3$Fe][OTf]$_2$, (3). In a 20-mL scintillation vial charged with a stir bar and wrapped in foil, [LFe$_3$O(PhIm-H)$_3$][OTf]$_3$ (1.06 g, 0.55 mmol, 1.0 equiv.) and PhIm (87.1 mg, 0.60 mmol, 1.1 equiv.) were suspended in 5 mL of tetrahydrofuran and frozen in a cold well along with a solution of Na[N(SiMe$_3$)$_2$] (334 mg, 1.83 mmol, 3.3 equiv.) in 1.5 mL of tetrahydrofuran. Upon sufficient thawing for the mixture to begin stirring, the Na[N(SiMe$_3$)$_2$] solution was added dropwise in the dark. After stirring for 1 hour, the solution was frozen in the cold well. Upon sufficient thawing for the mixture to begin stirring, a thawing slurry of $FeCl_2$ (80.2 mg, 0.64 mmol, 1.2 equiv.) in 3.5 mL of tetrahydrofuran was added dropwise. After stirring for 22 hours, the mixture was filtered over a bed of Celite and the precipitate was eluted with dichloromethane. The volatiles were removed under reduced pressure to afford [LFe$_3$O(PhIm)$_3$Fe][OTf]$_2$ as a dark brown solid (230 mg, 23% yield). Crystals suitable for X-ray diffraction were grown by layering a dilute solution of the compound with diethyl ether at -35°C. ^{1}H NMR (300 MHz, CD_2Cl_2) δ 117.34 (b), 76.82 (s), 74.75 (s), 70.70 (b), 51.84 (s), 47.54 (s), 47.08 (s), 20.98 (b), 20.40 (s), 14.68 (s), 12.89 (s), 12.42 (s), 7.25 (s), 6.34 (s), 5.52 (s), 4.93 (s), 4.60 (s), 3.32 (s), 2.99 (s), 2.42 (s), 1.05 (s), -4.58 (b), -6.98 (s). ^{19}F NMR (300 MHz, CD_2Cl_2) δ -78.32. UV-Vis (CH_2Cl_2) [ε (M^{-1} cm^{-1})]: 252 nm (9.56 x 10^4), 464 nm (1.04 x 10^4). ESI-MS (m/z): 762 ([LFe$_3$O(PhIm)$_3$Fe]$^{2+}$) Anal. Calcd (%) for $C_{86}H_{60}F_6Fe_4N_{12}O_{10}S_2$: C, 56.66; H, 3.32; N, 9.22. Found: C, 56.38; H, 3.40; N, 9.09.

Synthesis of [LFe$_3$O(PhIm)$_3$Fe][OTf]$_3$ (4). In a 20-mL scintillation vial charged with a stir bar, a dichloromethane solution of [Fc][OTf] (26.8 mg, 0.08 mmol, 1.0 equiv.) was added dropwise to a stirring solution of [LFe$_3$O(PhIm)$_3$Fe][OTf]$_2$ (145.9 mg, 0.08 mmol, 1.0 equiv.) in 2 mL of dichloromethane. After 30 minutes, the volatiles were removed under reduced pressure and the pink-purple residue was triturated with diethyl ether. The suspension was filtered over Celite, and the remaining pink-purple powder was washed with additional diethyl ether before eluting with dichloromethane. The volatiles were removed under reduced pressure to afford [LFe$_3$O(PhIm)$_3$Fe][OTf]$_3$ as a pink-purple solid (110 mg, 70% yield). Crystals suitable for X-ray diffraction were obtained by diffusion of diethyl ether into a dilute solution of 4 in dichloromethane. ^{1}H NMR (400 MHz, CD$_2$Cl$_2$) δ 139.84 (b), 101.61 (b), 87.16 (s), 65.70 (s), 63.96 (s), 57.17 (s), 32.93 (b), 14.58 (s), 12.39 (s), 11.70 (s), 10.99 (s), 6.33 (s), 4.97 (b), 3.99 (s), -2.30 (b), -12.29 (b). ^{19}F NMR (300 MHz, CD$_2$Cl$_2$) δ -78.53. UV-Vis (CH$_2$Cl$_2$) [ε (M^{-1} cm^{-1})]: 379 nm (8.88 x 10^3), 494 nm (8.37 x 10^3). Anal. Calcd (%) for $C_{87}H_{60}F_9Fe_4N_{12}O_{13}S_3$: C, 52.99; H, 3.07; N, 8.52. Found: C, 52.65; H, 3.17; N, 8.46.

Synthesis of [LFe$_3$O(PhIm)$_3$Fe][OTf], (5). (A) By reduction of 3: In a 20-mL scintillation vial charged with a stir bar, a dichloromethane solution of Cp$_2$Co (10.6 mg, 0.056 mmol, 1.0 equiv.) was added dropwise to a stirring solution of [LFe$_3$O(PhIm)$_3$Fe][OTf]$_2$ (102 mg, 0.056 mmol, 1.0 equiv.) in 3 mL of dichloromethane. After one hour, the volatiles were removed under reduced pressure, and the dark purple residue was then triturated in dimethoxyethane (DME) overnight. The purple precipitate was collected on a bed of Celite, washed with additional DME, and then eluted with dichloromethane. The volatiles were removed under reduced pressure to afford [LFe$_3$O(PhIm)$_3$Fe][OTf] as a dark purple solid (69.5 mg, 74% yield). Crystals suitable for X-ray diffraction were obtained by diffusion of diethyl ether into a dilute solution of 5 in 1:1 dichloromethane:acetonitrile. (B) By oxidation of 6: To a suspension of [LFe$_3$O(PhIm)$_3$Fe] (31.5 mg, 0.021 mmol) in tetrahydrofuran (1 mL) was added a suspension of [Cp$_2$Co][OTf] (10.5 mg, 0.031 mmol, 1.5 equiv.). The mixture immediately changes color from blue to purple. After stirring for 45 minutes, the mixture was concentrated under vacuum. The ^{1}H-NMR spectrum (CD$_2$Cl$_2$) of the crude product mixture revealed clean re-generation of 5. ^{1}H NMR (300 MHz, CD_2Cl_2) δ 101.23 (b), 57.39 (s), 56.72 (s), 40.91 (b), 38.06 (s), 36.00 (s), 31.58 (s), 24.16 (s), 13.54 (s), 12.66 (s), 11.92 (s), 8.26 (s), 7.22 (s), -4.45 (b). ^{19}F NMR (300 MHz, CD_2Cl_2) δ -78.89. UV-Vis (CH_2Cl_2) [ε (M^{-1} cm^{-1})]: 413 nm (4.28×10^2), 513 nm (3.39×10^3). Anal. Calcd (%) for $C_{85}H_{60}F_3Fe_4N_{12}O_7S$: C, 60.99; H, 3.61; N, 10.04. Found: C, 60.14; H, 3.66; N, 10.51.

Synthesis of [LFe$_3$O(PhIm)$_3$Fe] (6). A solution of naphthalene (32.6 mg, 0.25 mmol, 5.0 equiv.) in 8 mL of tetrahydrofuran was added dropwise to a suspension of sodium metal in 10 mL of tetrahydrofuran (45 mg, 1.96 mmol, 39.2 equiv.), affording a dark green solution. After stirring for two hours, the solution was filtered over Celite and added dropwise to a stirring solution of [LFe$_3$O(PhIm)$_3$Fe][OTf] (86.1 mg, 0.05 mmol, 1.0 equiv.) and Na[BAr$^F_{24}$] (45.6 mg, 0.05 mmol, 1.0 equiv.). After stirring overnight, the precipitate was collected on a fine frit and washed with additional tetrahydrofuran (2x5 mL), affording [LFe$_3$O(PhIm)$_3$Fe] as a metallic blue powder (50.5 mg, 66% yield). We have not been able to obtain satisfactory elemental analysis for 6, likely due to its air sensitivity.

Synthesis of [LFe$_3$O(PhIm)$_3$Fe(CO)] (6-CO). A suspension of [LFe$_3$O(PhIm)$_3$Fe] (27.5 mg, 0.018 mmol) in 2.7 mL of tetrahydrofuran was transferred to 20 mL Schlenk tube. The suspension was degassed by three freeze-pump-thaw cycles, and an atmosphere of CO was admitted at room temperature. After stirring for five hours, an IR spectrum of the green suspension was collected. The mixture was then frozen, evacuated once, and exposed to N_2 (without thawing). After stirring for two hours or overnight, only the vibrational feature assigned to [LFe$_3$O(PhIm)$_3$Fe(CO)] was observed (ν_{CO} = 1899 cm^{-1}). The green precipitate was collected by filtration at the 2-3 hr. time point to minimize CO loss (20 mg, 72%).

Synthesis of [LFe$_3$O(PhIm)$_3$Fe][OTf]$_4$ (7). For ^{1}H-NMR: A solution of [LFe$_3$O(PhIm)$_3$Fe][OTf]$_3$ (4, 18 mg) was prepared in 0.7 mL CD_2Cl_2. An aliquot (0.35 mL) was added to a J Young tube, and the solution was frozen in the cold well. A solution of $[N(C_6H_4Br\text{-}4)_3][OTf]$ (7 mg) was prepared in 2 mL of CD_2Cl_2. An aliquot (0.2 mL) of this $[N(C_6H_4Br\text{-}4)_3][OTf]$ solution was added to the frozen solution of 4 and mixed thawing, affording a dark orange-brown solution and a considerable amount of a dark precipitate. ^{1}H-NMR spectra were collected at 298 K, 223 K and 198 K which confirmed the formation of one (or more) new species. The tube was then degassed by three freeze-pump-thaw cycles and CO (1 atm.) was admitted at 293 K. ^{1}H-NMR spectra collected under an atmosphere of CO matched those under N_2, demonstrating that CO does not bind the dissolved, NMR-active fraction of the material. Subsequently, the tube was degassed by three freeze-pump-thaw cycles. A solution of ferrocene (5.7 mg) was prepared in 0.2 mL CD_2Cl_2. Addition of an aliquot (0.12 mL) of this ferrocene solution to the degassed tube cleanly returns 4, suggesting that the oxidized product(s) retains the core geometry of 4 and most likely corresponds to the all-ferric cluster $[LFe_3O(PhIm)_3Fe][OTf]_4$ (7), though more detailed characterization of this compound has not been possible to date. It is possible that triflate binds the apical Fe^{III} of $[LFe_3O(PhIm)_3Fe][OTf]_4$ (7), which could also suppress CO binding.

For UV-Vis: A solution of $[LFe_3O(PhIm)_3Fe][OTf]_3$ (4, 7.2 mg) was prepared in dichloromethane (19 mL). A 50-μM solution was prepared by diluting 2.5 mL of this stock solution to 10 mL with dichloromethane. A 3-mL aliquot of this 50 μM solution was charged into a Kontes-valve sealed cuvette. A solution of $[N(C_6H_4Br\text{-}4)_3][OTf]$ (8.4 mg) was prepared in 5 mL of dichloromethane. To the stirring solution of 4 in the cuvette was added a 0.1 mL aliquot of the $[N(C_6H_4Br\text{-}4)_3][OTf]$ stock solution (1.5 equiv.). The UV-Vis spectrum of $[LFe_3O(PhIm)_3Fe][OTf]_4$ (7) was then recorded under N_2 between 198 and 298 K. Then the sample was degassed by three freeze-pump-thaw cycles, and CO (1 atm.) was admitted at room temperature. The UV-Vis spectrum of $[LFe_3O(PhIm)_3Fe][OTf]_4$ (7) was then recorded under

CO between 198 and 298. Other than a loss in signal intensity (presumably due to a small amount of decomposition of 7), there is no difference in the VT behavior under N_2 or CO.

Summary Tables

Table 3: Spectroscopic, Mössbauer, and structural parameters for complexes **3-CO, 4-CO, 5-CO and 6-CO** together with other monometallic trigonal bipyrimidal (TBP) Fe-complexes containing a single axial CO ligand.[53-54, 67, 81-82]

Complex	S =	ν(CO) (cm^{-1})	δ (mm/s)	$\lvert\Delta E_q\rvert$ (mm/s)	d(Fe-C) (Å)	d(C-O) (Å)
$(Et_4N)[N(CH_2CH_2S)_3Fe(CO)]$	1	1885	0.22	0.99	1.720(14)	1.154(14)
[LFe$_3$O(PhIm)$_3$Fe(CO)] (6-CO)	**1**	1899	0.16	0.97	---	---
[LFe$_3$O(PhIm)$_3$Fe(CO)](OTf) (5-CO)	**1**	1916	0.06	0.7	1.773	1.149
$[C(SiMe_2CH_2PPh_2)_3Fe(CO)](BAr^F{}_{24})$	1	1937	0.28	1.87	1.786	1.155
$K[N(CH_2C(O)N^iPr)_3Fe(CO)]$	1	1940	0.26	1.07	1.749	1.155
$(Et_4N)[ArS_3{}^PFe(CO)]$	1	1940	0.25	2.31	1.883*	1.001*
[LFe$_3$O(PhIm)$_3$Fe(CO)](OTf)$_2$ (3-CO)	**1**	1944	0.10	0.78	----	----
$[P_3{}^{Si}Fe(CO)](BAr^F{}_{24})$	1	1959	0.31	4.12	1.842	1.104
[LFe$_3$O(PhIm)$_3$Fe(CO)](OTf)$_3$ (4-CO)	**1**	1966	---	---	----	----

Table 4: Selected bond distances and angles for complexes **3-7, 3-(CO)$_2$ and 5-CO**

Bond Distance (Å)	Complex **3**	Complex **4**	Complex **5**	Complex **5-CO**	Complex **3-(CO)$_2$**
Fe1-O1	2.1480(19)	2.215(4)	2.032(4)	2.121(3)	2.135(5)
Fe2-O1	1.983(2)	1.978(4)	1.980(4)	1.927(3)	1.919(4)
Fe3-O1	2.093(2)	1.981(4)	2.067(4)	2.098(3)	2.023(4)
Fe4-O1	1.8128(19)	1.855(4)	1.883(4)	1.906(3)	2.006(4)
Fe4-C60	2.068(3)	2.045(6)	2.098(6)	2.052(4)	2.012(6)
Fe4-C69	2.063(3)	2.059(6)	2.092(6)	2.069(5)	2.019(8)
Fe4-C78	2.063(3)	2.055(6)	2.096(6)	2.053(4)	2.010(6)
Fe4-C85	-		-	1.775(5)	1.741(6)
Fe4-C86	-		-	-	1.824(8)
C85-O5	-		-	1.148(6)	1.147(8)
C86-O6	-		-	-	1.173(10)
Bond Angles (°)					
C60-Fe4-C69	119.11(11)	121.7(3)	119.7(2)	116.43(16)	104.5(3)
C69-Fe4-C78	121.68(11)	120.7(3)	121.1(2)	118.43(16)	97.9(3)
C60-Fe4-C78	118.74(11)	117.3(3)	118.5(2)	124.26(16)	153.5(2)
Fe4-C85-O5	-		-	178.3(4)	175.7(7)
Fe4-C86-O6	-		-	-	167.6(7)

Table 5: Mössbauer parameters for complexes **3-6, 3-CO, 5-CO, 6-CO**.

No.	Complex	δ (mm/s)	|ΔE_q| (mm/s)	Occupancy (%)
3	$[LFe_3O(PhIm)_3Fe](OTf)_2$	1.03	3.13	25
		1.14	3.22	25
		0.39	0.38	25
		0.19	1.11	25
4	$[LFe_3O(PhIm)_3Fe(CO)](OTf)_3$	0.89	3.34	25
		0.50	0.56	25
		0.48	1.05	25
		0.17	1.07	25
5	$[LFe_3O(PhIm)_3Fe](OTf)$	1.09	3.17	25
		1.10	3.41	25
		0.53	1.11	25
		0.89	2.29	25
6	$[LFe_3O(PhIm)_3Fe]$	1.13	3.19	75
		0.68	2.08	25
6-CO	$[LFe_3O(PhIm)_3Fe(CO)]$	1.09	3.14	75
		0.16	0.97	25
3-CO	$[LFe_3O(PhIm)_3Fe(CO)_n](OTf)_2$	1.05	3.22	25
		0.47	0.71	25
		0.48	1.18	25
		0.10	0.78	25
5-CO	$[LFe_3O(PhIm)_3Fe(CO)](OTf)$	1.04	2.89	25
		1.13	3.39	25
		0.53	1.09	25
		0.06	0.70	25

Table 6: Crystal and refinement data for precursor complexes **1** and **2.**

	Complex **1**	Complex **2**
CCDC	1816163	1816164
Empirical formula	$C_{60.51}H_{40.06}Cl_{1.01}F_9Fe_3N_6O_{12}S_3$	$C_{87.5}H_{64}ClF_9Fe_3N_{12}O_{13}S_3$
Formula weight	1513.64	1961.68
Temperature/K	100	100
Crystal system	triclinic	trigonal
Space group	P-1	P-3
a/Å	12.5224(6)	23.4333(11)
b/Å	12.8854(6)	23.4333(11)
c/Å	21.9843(11)	9.7960(5)
α/°	93.576(2)	90
β/°	103.138(2)	90
γ/°	118.3998(18)	120
Volume/$Å^3$	2977.9(3)	4658.5(5)
Z	2	2
$\rho_{calc}g/cm^3$	1.688	1.398
μ/mm^{-1}	0.97	0.64
F(000)	1531	2002
Crystal size/mm^3	0.34 × 0.28 × 0.19	0.23 × 0.23 × 0.11
Radiation	MoKα (λ = 0.71073)	MoKα (λ = 0.71073)
2Θ range for data collection/°	4.478 to 66.282	4.618 to 59.184
Index ranges	$-19 \leq h \leq 19$, $-17 \leq k \leq 19$, $-31 \leq l \leq 33$	$-30 \leq h \leq 32$, $-32 \leq k \leq 27$, $-13 \leq l \leq 13$
Reflections collected	98544	91999
Independent reflections	22669 [R_{int} = 0.0476, R_{sigma} = 0.0500]	8466 [R_{int} = 0.0596, R_{sigma} = 0.0340]
Data/restraints/parameters	22669/143/941	8466/143/419
Goodness-of-fit on F^2	1.02	1.033
Final R indexes [I>=2σ (I)]	R_1 = 0.0428, wR_2 = 0.0999	R_1 = 0.0626, wR_2 = 0.1678
Final R indexes [all data]	R_1 = 0.0693, wR_2 = 0.1113	R_1 = 0.0886, wR_2 = 0.1836
Largest diff. peak/hole / e $Å^{-3}$	1.44/-0.70	1.00/-0.65

Table 7: Crystal and refinement data for tetranuclear complexes **3** and **5.**

	Complex **3**	Complex **5**
CCDC	1816165	1816166
Empirical formula	$C_{90.6}H_{68.17}Cl_{4.26}F_6Fe_4N_{12}O_{10.62}S_2$	$C_{90.34}H_{60}F_3Fe_4N_{14.67}O_7S$
Formula weight	2047.49	1775.37
Temperature/K	100	100.03
Crystal system	triclinic	monoclinic
Space group	P-1	C2/c
a/Å	15.486(2)	40.403(4)
b/Å	15.4964(18)	17.5931(17)
c/Å	19.448(2)	25.468(3)
α/°	100.128(2)	90
β/°	93.878(4)	115.389(6)
γ/°	93.078(3)	90
Volume/$Å^3$	4573.6(10)	16355(3)
Z	2	8
$\rho_{calc}g/cm^3$	1.487	1.442
μ/mm^{-1}	0.87	6.422
F(000)	2086	7262
Crystal size/mm^3	0.44 × 0.28 × 0.13	0.9 × 0.38 × 0.16
Radiation	MoKα (λ = 0.71073)	CuKα (λ = 1.54178)
2Θ range for data collection/°	2.134 to 69.866	5.576 to 133.094
Index ranges	$-24 \le h \le 24, -24 \le k \le 24, -31 \le l \le 31$	$-48 \le h \le 48, -20 \le k \le 20, -29 \le l \le 30$
Reflections collected	200849	115838
Independent reflections	39977 [R_{int} = 0.0614, R_{sigma} = 0.0524]	14365 [R_{int} = 0.1060, R_{sigma} = 0.0565]
Data/restraints/parameters	39977/294/1231	14365/26/1071
Goodness-of-fit on F^2	1.049	1.032
Final R indexes [I>=2σ (I)]	R_1 = 0.0807, wR_2 = 0.2239	R_1 = 0.0847, wR_2 = 0.2283
Final R indexes [all data]	R_1 = 0.1245, wR_2 = 0.2577	R_1 = 0.1124, wR_2 = 0.2541
Largest diff. peak/hole / e $Å^{-3}$	2.98/-2.09	1.25/-1.69

Table 8: Crystal and refinement data for tetranuclear cluster **4.**

	Complex **4**
CCDC	1816169
Empirical formula	$C_{96}H_{72}Cl_2F_9Fe_4N_{12}O_{15}S_3$
Formula weight	2195.13
Temperature/K	99.99
Crystal system	triclinic
Space group	P-1
a/Å	14.3206(12)
b/Å	19.6847(14)
c/Å	20.858(2)
α/°	115.463(6)
β/°	109.048(5)
γ/°	94.165(6)
Volume/Å^3	4859.2(8)
Z	2
ρ_{calc}g/cm^3	1.5
μ/mm^{-1}	6.552
F(000)	2238
Crystal size/mm^3	0.212 × 0.142 × 0.106
Radiation	CuKα (λ = 1.54178)
2Θ range for data collection/°	5.112 to 160.954
Index ranges	$-18 \leq h \leq 17$, $-23 \leq k \leq 25$, $-26 \leq l \leq 26$
Reflections collected	68612
Independent reflections	20695 [R_{int} = 0.0888, R_{sigma} = 0.0809]
Data/restraints/parameters	20695/468/1316
Goodness-of-fit on F^2	1.029
Final R indexes [I>=2σ (I)]	R_1 = 0.0947, wR_2 = 0.2515
Final R indexes [all data]	R_1 = 0.1376, wR_2 = 0.2932
Largest diff. peak/hole / e Å^{-3}	2.89/-1.16

Table 9: Crystal and refinement data for carbonyl adducts **3-(CO)$_2$** and **5-CO.**

	Complex **3-(CO)$_2$**	Complex **5-CO**
CCDC	1816168	1816167
Empirical formula	$C_{91.07}H_{66.15}Cl_{6.15}F_6Fe_4N_{12}O_{12}S_2$	$C_{92}H_{65}F_3Fe_4N_{15}O_8S$
Formula weight	2140.23	1821.05
Temperature/K	99.97	100
Crystal system	monoclinic	triclinic
Space group	$P2_1/c$	P-1
a/Å	14.4988(5)	12.349(4)
b/Å	45.032(2)	15.527(7)
c/Å	14.6559(7)	21.471(8)
α/°	90	78.351(13)
β/°	106.580(2)	79.352(12)
γ/°	90	88.530(13)
Volume/Å^3	9171.2(7)	3962(3)
Z	4	2
ρ_{calc}g/cm^3	1.55	1.526
μ/mm^{-1}	7.732	0.823
F(000)	4349	1866
Crystal size/mm^3	0.21 × 0.19 × 0.15	0.3 × 0.25 × 0.15
Radiation	CuKα (λ = 1.54178)	MoKα (λ = 0.71073)
2Θ range for data collection/°	6.36 to 161.064	4.268 to 61.386
Index ranges	$-18 \leq h \leq 18$, $-56 \leq k \leq 56$, $-18 \leq l \leq 18$	$-17 \leq h \leq 17$, $-22 \leq k \leq 22$, $-30 \leq l \leq 30$
Reflections collected	150997	145591
Independent reflections	19794 [R_{int} = 0.0813, R_{sigma} = 0.0472]	24232 [R_{int} = 0.0856, R_{sigma} = 0.0597]
Data/restraints/parameters	19794/151/1230	24232/96/1180
Goodness-of-fit on F^2	1.05	1.035
Final R indexes [I>=2σ (I)]	R_1 = 0.1018, wR_2 = 0.2745	R_1 = 0.0877, wR_2 = 0.2192
Final R indexes [all data]	R_1 = 0.1225, wR_2 = 0.2913	R_1 = 0.1309, wR_2 = 0.2596
Largest diff. peak/hole / e Å^{-3}	2.44/-1.11	2.05/-1.61

Special Refinement Details for $LFe_3(OTf)_3$ (1). Compound **1** crystallizes in the triclinic space group P-1 with one molecule in the asymmetric unit along with one half of a molecule of co-crystallized dichloromethane. The co-crystallized dichloromethane molecule is located near a special position (inversion center) and was modelled with the aid of a similarity restraint on the 1,2 distances (C61-Cl1, 1.734(6) Å and C61-Cl2, 1.758(5) Å) and enhanced rigid bond restraints on all components of the disorder. Additionally, one of the triflates is disordered (over two positions with occupancies of 93% and 7%) and was modelled with the help of similarity restraints on the 1,2 distances and enhanced rigid bond restraints on all components of the disorder. Only the major component is shown in Figure S65.

Special Refinement Details for $[LFe_3O(PhIm\text{-}H)_3][OTf]_3$ (2). Compound **2** crystallizes in the trigonal space group P-3 with one-third of one molecule in the asymmetric unit along with one outer sphere triflate. The triflate counterion is heavily disordered and was modelled over two positions (occupancies of 72% and 28%, respectively) with the aid of similarity restraints on all 1,2 distances and enhanced rigid bond restraints. Additionally, there is a large solvent accessible void which contains one molecule of dichloromethane disordered over six positions close a three-fold rotoinversion axis.

Special Refinement Details for $[LFe_3O(PhIm)_3Fe][OTf]_2$ (3). Compound **3** crystallizes in the triclinic space group P-1 with one molecule in the asymmetric unit along with two outer sphere triflate counter ions, 2.15 co-crystallized molecules of dichloromethane, and 0.62 molecules of co-crystallized diethyl ether. One of the triflate counter ions is disordered over two distinct positions (occupancies of 62% and 38%). The first position is otherwise occupied by dichloromethane (38%), whereas the second position is otherwise occupied by diethyl ether (62%). There are two additional molecules of co-crystallized dichloromethane, one of which was modelled as disordered over two positions. The second is heavily disordered and was modelled isotropically. There is significant residual electron density close to this molecule of dichloromethane which could not sufficiently be modelled any further. There is additional solvent disorder which could not be satisfactorily modelled and was masked in Olex2. The volume of the solvent accessible void space was found to be 129.7 Å^3 in which 44.6 e$^-$ were located.

Special Refinement Details for [LFe$_3$O(PhIm)$_3$Fe(CO)$_2$][OTf]$_2$ (3-(CO)$_2$). Compound **3-(CO)$_2$** crystallizes in the monoclinic space group P2$_1$/*c* with one molecule in the asymmetric unit along with two outer sphere triflate counter ions and 3.1 molecules of co-crystallized dichloromethane. The triflate counterions and the co-crystallized dichloromethane were modelled with the help of similarity restraints on the 1,2-distances and anisotropic displacement parameters. There is some residual electron density close to a disordered dichloromethane molecules which could not be sufficiently modelled any further.

Special Refinement Details for [LFe$_3$O(PhIm)$_3$Fe][OTf]$_3$ (4). Compound **4** crystallizes in the triclinic space group P-1 with one molecule in the asymmetric unit along with three outer sphere triflate counter ions, one co-crystallized molecule of dichloromethane, and one molecule of co-crystallized diethyl ether. One of the triflate counter ions is heavily disordered over two distinct positions (occupancies of 62% and 38%). Both components were modelled as a rigid group, using structural parameters derived from one of the non-disordered triflates. There is significant residual electron density close to this heavily disordered triflate which could not sufficiently be modelled any further. The co-crystallized diethyl ether molecule is heavily disordered and was modelled isotropically as disordered over two positions.

Special Refinement Details for [LFe$_3$O(PhIm)$_3$Fe][OTf] (5). Compound **5** crystallizes in the monoclinic space group C2/*c* with one molecule in the asymmetric unit along with one outer sphere triflate counter ion and 2.7 molecules of co-crystallized acetonitrile. There are large solvent accessible channels in the crystal which have been modelled as containing co-crystallized acetonitrile molecules. However, the solvent in those channels appears to be heavily disordered, and the co-crystallized acetonitrile molecules were modelled isotropically. All 1,2 and 1,3 distances in the disordered solvent molecules were fixed (C_1-N: 1.157(1) Å, C_1-C_2: 1.458(1) Å, C_2-N: 2.71(1) Å).

Special Refinement Details for [LFe$_3$O(PhIm)$_3$Fe(CO)][OTf] (5-CO). Compound **5-CO** crystallizes in the triclinic space group P-1 with one molecule in the asymmetric unit along with one outer sphere triflate and three co-crystallized acetonitrile molecules. The triflate counter ion is disordered over two positions (occupancies of 75% and 25%). There is significant disorder associated with the co-crystallized acetonitrile molecules. Two of the co-crystallized acetonitrile molecules are disordered over special positions. One was heavily disordered and was refined isotropically. The second was further disordered over two positions (occupancies of 56% and 44%). In close proximity, there is an additional acetonitrile molecule which is disordered over two positions (occupancies of 44% and 56%, such that the two molecules do not occupy the same void space) All disordered molecules were modelled with the help of similarity restraints on the 1,2 and 1,3 distances and on the anisotropic displacement parameters. There are also residual electron density peaks close to the iron centers, but they are too close (~0.9 Å) to be another atom. The possibility of non-merohedral twinning was evaluated through cell_now, but a significant twin component could not be identified. While the residual density could be due to disorder which cannot be satisfactorily modelled, their proximity to the heavy metals suggests they may arise due to absorption problems or truncation errors instead.

References

1. Burgess, B. K.; Lowe, D. J., Mechanism of Molybdenum Nitrogenase. *Chem. Rev.* **1996,** *96* (7), 2983-3012.

2. Hu, Y.; Ribbe, M. W., Nitrogenases—A Tale of Carbon Atom(s). *Angew. Chem. Int. Ed.* **2016,** *55* (29), 8216-8226.

3. Spatzal, T.; Aksoyoglu, M.; Zhang, L.; Andrade, S. L. A.; Schleicher, E.; Weber, S.; Rees, D. C.; Einsle, O., Evidence for Interstitial Carbon in Nitrogenase FeMo Cofactor. *Science* **2011,** *334* (6058), 940-940.

4. Lancaster, K. M.; Roemelt, M.; Ettenhuber, P.; Hu, Y.; Ribbe, M. W.; Neese, F.; Bergmann, U.; DeBeer, S., X-ray Emission Spectroscopy Evidences a Central Carbon in the Nitrogenase Iron-Molybdenum Cofactor. *Science* **2011,** *334* (6058), 974-977.

5. Hoffman, B. M.; Lukoyanov, D.; Yang, Z.-Y.; Dean, D. R.; Seefeldt, L. C., Mechanism of Nitrogen Fixation by Nitrogenase: The Next Stage. *Chem. Rev.* **2014,** *114* (8), 4041-4062.

6. Pickett, C. J.; Vincent, K. A.; Ibrahim, S. K.; Gormal, C. A.; Smith, B. E.; Best, S. P., Electron-Transfer Chemistry of the Iron–Molybdenum Cofactor of Nitrogenase: Delocalized and Localized Reduced States of FeMoco which Allow Binding of Carbon Monoxide to Iron and Molybdenum. *Chem. Eur. J.* **2003,** *9* (1), 76-87.

7. Yan, L.; Pelmenschikov, V.; Dapper, C. H.; Scott, A. D.; Newton, W. E.; Cramer, S. P., IR-Monitored Photolysis of CO-Inhibited Nitrogenase: A Major EPR-Silent Species with Coupled Terminal CO Ligands. *Chem. Eur. J.* **2012,** *18* (51), 16349-16357.

8. Paengnakorn, P.; Ash, P. A.; Shaw, S.; Danyal, K.; Chen, T.; Dean, D. R.; Seefeldt, L. C.; Vincent, K. A., Infrared spectroscopy of the nitrogenase MoFe protein under electrochemical control: potential-triggered CO binding. *Chem. Sci.* **2017,** *8* (2), 1500-1505.

9. Lee, H.-I.; Cameron, L. M.; Hales, B. J.; Hoffman, B. M., CO Binding to the FeMo Cofactor of CO-Inhibited Nitrogenase: ^{13}CO and ^{1}H Q-Band ENDOR Investigation. *J. Am. Chem. Soc.* **1997,** *119* (42), 10121-10126.

10. Tolland, J. D.; Thorneley, R. N. F., Stopped-Flow Fourier Transform Infrared Spectroscopy Allows Continuous Monitoring of Azide Reduction, Carbon Monoxide Inhibition, and ATP Hydrolysis by Nitrogenase. *Biochemistry* **2005,** *44* (27), 9520-9527.

11. Scott, A. D.; Pelmenschikov, V.; Guo, Y.; Yan, L.; Wang, H.; George, S. J.; Dapper, C. H.; Newton, W. E.; Yoda, Y.; Tanaka, Y.; Cramer, S. P., Structural Characterization of CO-Inhibited Mo-Nitrogenase by Combined Application of Nuclear Resonance Vibrational Spectroscopy, Extended X-ray Absorption Fine Structure, and Density Functional Theory: New Insights into the Effects of CO Binding and the Role of the Interstitial Atom. *J. Am. Chem. Soc.* **2014,** *136* (45), 15942-15954.

12. Spatzal, T.; Perez, K. A.; Einsle, O.; Howard, J. B.; Rees, D. C., Ligand binding to the FeMo-cofactor: Structures of CO-bound and reactivated nitrogenase. *Science* **2014,** *345* (6204), 1620-1623.

13. Yang, Z.-Y.; Seefeldt, L. C.; Dean, D. R.; Cramer, S. P.; George, S. J., Steric Control of the Hi-CO MoFe Nitrogenase Complex Revealed by Stopped-Flow Infrared Spectroscopy. *Angew. Chem. Int. Ed.* **2011,** *50* (1), 272-275.

14. Lee, H.-I.; Igarashi, R. Y.; Laryukhin, M.; Doan, P. E.; Dos Santos, P. C.; Dean, D. R.; Seefeldt, L. C.; Hoffman, B. M., An Organometallic Intermediate during Alkyne Reduction by Nitrogenase. *J. Am. Chem. Soc.* **2004,** *126* (31), 9563-9569.

15. Benton, P. M. C.; Laryukhin, M.; Mayer, S. M.; Hoffman, B. M.; Dean, D. R.; Seefeldt, L. C., Localization of a Substrate Binding Site on the FeMo-Cofactor in Nitrogenase: Trapping Propargyl Alcohol with an α-70-Substituted MoFe Protein. *Biochemistry* **2003,** *42* (30), 9102-9109.

16. George, S. J.; Barney, B. M.; Mitra, D.; Igarashi, R. Y.; Guo, Y.; Dean, D. R.; Cramer, S. P.; Seefeldt, L. C., EXAFS and NRVS Reveal a Conformational Distortion of the FeMo-cofactor in the MoFe Nitrogenase Propargyl Alcohol Complex. *J. Inorg. Biochem.* **2012,** *112*, 85-92.

17. Sarma, R.; Barney, B. M.; Keable, S.; Dean, D. R.; Seefeldt, L. C.; Peters, J. W., Insights into substrate binding at FeMo-cofactor in nitrogenase from the structure of an α-70Ile MoFe protein variant. *J. Inorg. Biochem.* **2010,** *104* (4), 385-389.

18. Dos Santos, P. C.; Igarashi, R. Y.; Lee, H.-I.; Hoffman, B. M.; Seefeldt, L. C.; Dean, D. R., Substrate Interactions with the Nitrogenase Active Site. *Acc. Chem. Res.* **2005,** *38* (3), 208-214.

19. Spatzal, T.; Schlesier, J.; Burger, E.-M.; Sippel, D.; Zhang, L.; Andrade, S. L. A.; Rees, D. C.; Einsle, O., Nitrogenase FeMoco investigated by spatially resolved anomalous dispersion refinement. *Nat. Commun.* **2016,** *7*, 10902.

20. Venkateswara Rao, P.; Holm, R. H., Synthetic Analogues of the Active Sites of Iron−Sulfur Proteins. *Chem. Rev.* **2004,** *104* (2), 527-560.

21. Tanifuji, K.; Sickerman, N.; Lee, C. C.; Nagasawa, T.; Miyazaki, K.; Ohki, Y.; Tatsumi, K.; Hu, Y.; Ribbe, M. W., Structure and Reactivity of an Asymmetric Synthetic Mimic of Nitrogenase Cofactor. *Angew. Chem. Int. Ed.* **2016,** *55* (50), 15633-15636.

22. Ohta, S.; Ohki, Y.; Hashimoto, T.; Cramer, R. E.; Tatsumi, K., A Nitrogenase Cluster Model [Fe_8S_6O] with an Oxygen Unsymmetrically Bridging Two Proto-Fe_4S_3 Cubes: Relevancy to the Substrate Binding Mode of the FeMo Cofactor. *Inorg. Chem.* **2012,** *51* (21), 11217-11219.

23. Al-Ani, F. T.; Hughes, D. L.; Pickett, C. J., From an {Fe_4S_4}-cluster to {Fe_2S_2}- and {Fe_3S}-carbonyls. Crystal structure of $[Fe_3S(CO)_9]^{2-}$. *J. Organomet. Chem.* **1986,** *307* (2), C31-C34.

24. Han, J.; Coucouvanis, D., Synthesis and structure of the organometallic $MFe_2(\mu_3\text{-}S)_2$ clusters (M = Mo or Fe). *Dalton Trans.* **2005,** (7), 1234-1240.

25. Eames, E. V.; Betley, T. A., Site-Isolated Redox Reactivity in a Trinuclear Iron Complex. *Inorg. Chem.* **2012,** *51* (19), 10274-10278.

26. Kuppuswamy, S.; Wofford, J. D.; Joseph, C.; Xie, Z.-L.; Ali, A. K.; Lynch, V. M.; Lindahl, P. A.; Rose, M. J., Structures, Interconversions, and Spectroscopy of Iron Carbonyl Clusters with an Interstitial Carbide: Localized Metal Center Reduction by Overall Cluster Oxidation. *Inorg. Chem.* **2017,** *56* (10), 5998-6012.

27. Sickerman, N. S.; Tanifuji, K.; Lee, C. C.; Ohki, Y.; Tatsumi, K.; Ribbe, M. W.; Hu, Y., Reduction of C_1 Substrates to Hydrocarbons by the Homometallic Precursor and Synthetic Mimic of the Nitrogenase Cofactor. *J. Am. Chem. Soc.* **2017,** *139* (2), 603-606.

28. Ohki, Y.; Araki, Y.; Tada, M.; Sakai, Y., Synthesis and Characterization of Bioinspired [Mo_2Fe_2]–Hydride Cluster Complexes and Their Application in the Catalytic Silylation of N_2. *Chem. Eur. J.* **2017,** *23* (53), 13240-13248.

29. Anderton, K. J.; Knight, B. J.; Rheingold, A. L.; Abboud, K. A.; Garcia-Serres, R.; Murray, L. J., Reactivity of hydride bridges in a high-spin $[Fe_3(\mu\text{-}H)_3]^{3+}$ cluster: reversible H_2/CO exchange and Fe-H/B-F bond metathesis. *Chem. Sci.* **2017,** *8* (5), 4123-4129.

30. MacLeod, K. C.; McWilliams, S. F.; Mercado, B. Q.; Holland, P. L., Stepwise N-H bond formation from N_2-derived iron nitride, imide and amide intermediates to ammonia. *Chem. Sci.* **2016,** *7* (9), 5736-5746.

31. Bellows, S. M.; Arnet, N. A.; Gurubasavaraj, P. M.; Brennessel, W. W.; Bill, E.; Cundari, T. R.; Holland, P. L., The Mechanism of N–N Double Bond Cleavage by an Iron(II) Hydride Complex. *J. Am. Chem. Soc.* **2016,** *138* (37), 12112-12123.

32. Lee, Y.; Sloane, F. T.; Blondin, G.; Abboud, K. A.; García-Serres, R.; Murray, L. J., Dinitrogen Activation Upon Reduction of a Triiron(II) Complex. *Angew. Chem. Int. Ed.* **2015,** *54*, 1499-1503.

33. Creutz, S. E.; Peters, J. C., Diiron Bridged-Thiolate Complexes That Bind N_2 at the $Fe^{II}Fe^{II}$, $Fe^{II}Fe^{I}$, and $Fe^{I}Fe^{I}$ Redox States. *J. Am. Chem. Soc.* **2015,** *137* (23), 7310-7313.

34. Arnet, N. A.; Dugan, T. R.; Menges, F. S.; Mercado, B. Q.; Brennessel, W. W.; Bill, E.; Johnson, M. A.; Holland, P. L., Synthesis, Characterization, and Nitrogenase-Relevant Reactions of an Iron Sulfide Complex with a Bridging Hydride. *J. Am. Chem. Soc.* **2015,** *137* (41), 13220-13223.

35. Rittle, J.; McCrory, C. C. L.; Peters, J. C., A 10^6-Fold Enhancement in N_2-Binding Affinity of an $Fe_2(\mu\text{-}H)_2$ Core upon Reduction to a Mixed-Valence $Fe^{II}Fe^{I}$ State. *J. Am. Chem. Soc.* **2014,** *136* (39), 13853-13862.

36. Powers, T. M.; Betley, T. A., Testing the Polynuclear Hypothesis: Multielectron Reduction of Small Molecules by Triiron Reaction Sites. *J. Am. Chem. Soc.* **2013,** *135* (33), 12289-12296.

37. Li, Y.; Li, Y.; Wang, B.; Luo, Y.; Yang, D.; Tong, P.; Zhao, J.; Luo, L.; Zhou, Y.; Chen, S.; Cheng, F.; Qu, J., Ammonia formation by a thiolate-bridged diiron amide complex as a nitrogenase mimic. *Nat. Chem.* **2013,** *5*, 320.

38. Rodriguez, M. M.; Bill, E.; Brennessel, W. W.; Holland, P. L., N_2 Reduction and Hydrogenation to Ammonia by a Molecular Iron-Potassium Complex. *Science* **2011,** *334* (6057), 780-783.

39. Reed, C. J.; Agapie, T., Tetranuclear Fe Clusters with a Varied Interstitial Ligand: Effects on the Structure, Redox Properties, and Nitric Oxide Activation. *Inorg. Chem.* **2017,** *56* (21), 13360-13367.

40. de Ruiter, G.; Carsch, K. M.; Gul, S.; Chatterjee, R.; Thompson, N. B.; Takase, M. K.; Yano, J.; Agapie, T., Accelerated Oxygen Atom Transfer and C−H Bond Oxygenation by Remote Redox Changes in Fe_3Mn-Iodosobenzene Adducts. *Angew. Chem. Int. Ed.* **2017,** *56* (17), 4772-4776.

41. de Ruiter, G.; Thompson, N. B.; Lionetti, D.; Agapie, T., Nitric Oxide Activation by Distal Redox Modulation in Tetranuclear Iron Nitrosyl Complexes. *J. Am. Chem. Soc.* **2015,** *137* (44), 14094-14106.

42. Tsui, E. Y.; Kanady, J. S.; Day, M. W.; Agapie, T., Trinuclear first row transition metal complexes of a hexapyridyl, trialkoxy 1,3,5-triarylbenzene ligand. *Chem. Commun.* **2011,** *47* (14), 4189-4191.

43. In this and all subsequent figures, we have chosen to represent the bonding within the imidazolate bridging ligands with a delocalized N-C-N pi system. We prefer this representation based on the structural features of 3-5. The presence of delocalized N-C-N pi bonding is evidenced by the planarity of the imidazolate rings, by a sum of the angles around the aryl-substituted nitrogens near 360 degrees, and by the similarity observed in the two C-N bond lengths within each respective ring.

44. Due to the insolubility of 6, we are unable to fully characterize this material by standard solution- and solid-state techniques. However, in addition to the Mossbauer spectrum, we note that the blue color of 6 is characteristic of the all-ferrous redox state of the analogous pyrazolate bridged clusters (see ref. 41). Also, re-oxidation of this materical with $[Cp_2Co][OTf]$ cleanly returns 5, suggesting 6 is not a decomposition product. Moreover, the reactivity of 6 with CO and the electronic properties of its CO adducts are consistent with its assignment as $[LFe_3O(PhIm)_3Fe]$.

45. Münck, E.; Ksurerus, K.; Hendrich, M. P., [17] Combining Mössbauer spectroscopy with integer spin electron paramagnetic resonance. In *Methods Enzymol.*, Academic Press: 1993; Vol. 227, pp 463-479.

46. Therien, M. J.; Trogler, W. C., Mechanism of oxidatively induced migratory insertion of carbon monoxide. Evidence for a nineteen-electron intermediate. *J. Am. Chem. Soc.* **1987,** *109* (17), 5127-5133.

47. Etzenhouser, B. A.; Cavanaugh, M. D.; Spurgeon, H. N.; Sponsler, M. B., Mixed-Valence Diiron Complexes with Butadienediyl Bridges. *J. Am. Chem. Soc.* **1994,** *116* (5), 2221-2222.

48. Hsu, H.-F.; Koch, S. A.; Popescu, C. V.; Münck, E., Chemistry of Iron Thiolate Complexes with CN- and CO. Models for the $[Fe(CO)(CN)_2]$ Structural Unit in Ni−Fe Hydrogenase Enzymes. *J. Am. Chem. Soc.* **1997,** *119* (35), 8371-8372.

49. Nakae, T.; Hirotsu, M.; Aono, S.; Nakajima, H., Visible-light-induced release of CO by thiolate iron(iii) carbonyl complexes bearing N,C,S-pincer ligands. *Dalton Trans.* **2016,** *45* (41), 16153-16156.

50. Benito-Garagorri, D.; Lagoja, I.; Veiros, L. F.; Kirchner, K. A., Reactivity of coordinatively unsaturated iron complexes towards carbon monoxide: to bind or not to bind? *Dalton Trans.* **2011,** *40* (18), 4778-4792.

51. In an effort to obtain additional information about the electronic structure of 3-CO, we have measured the parallel and perpendicular mode EPR spectra (at 5 K) upon flash quenching samples of 3 prepared at various temperatures under CO. Unfortunately, the only spectral change observed is the loss of the sharp EPR feature associated with 3; no new features are observed. The instability of 3-(CO)n toward CO loss precludes a study of its magnetic properties by SQUID magnetometry.

52. The spectrum of 3-CO presented in Figure 7b (and in the SI) lacks the necessary resolution between -1 mm/s and 1.5 mm/s necessary to obtain a truly unique fit. The distal, six-coordinate ferric centers and the apical S = 1 Fe(II)-CO are expected to exhibit overlapping resonances in that region of the spectrum which complicates deconvolution of these features. However, the simulations

presented for 3-CO are constrained by the relative intensity of the diagnostic feature near 3 mm/s associated with the six-coordinate, high spin Fe(II) centers, which serves as a sensitive probe of the relative redox level of the distal triiron core. The simulation shown affords Mossbauer parameters for the apical iron of 3-(CO)n consistent with those observed for 5-CO and 6-CO. An alternative simulation can be obtained which infers the presence of three ferric ions (and thus, one electron oxidation relative to 3). However, this fit is not considered chemically reasonable as our 1H-NMR studies indicate that the only species formed upon reaction of 3 with CO are 3-CO and 3-(CO)2 (along with residual 3). Moreover, our vibrational data supports sed internal redox reorganization and an Fe(II)-CO assignment for the apical iron of 3-(CO).

53. Lee, Y.; Peters, J. C., Silylation of Iron-Bound Carbon Monoxide Affords a Terminal Fe Carbyne. *J. Am. Chem. Soc.* **2011,** *133* (12), 4438-4446.

54. Rittle, J.; Peters, J. C., Fe–N_2/CO complexes that model a possible role for the interstitial C atom of FeMo-cofactor (FeMoco). *Proc. Natl. Acad. Sci. U. S. A.* **2013,** *110* (40), 15898-15903.

55. Unfortunately, we are unable to generate 4-CO in non-chlorinated solvents. The trication 4 decomposes rapidly via reduction to 3 in the presence of polar, coordinating solvents such as acetone or acetonitrile. Chlorinated solvents cannot be used for frozen solution Mossbauer spectroscopy due to the strong absorption of gamma rays by heavier atoms such as Cl.

56. Gagne, R. R.; Ingle, D. M., Intramolecular electron transfer and valence isomerization in mononuclear nickel-macrocyclic ligand complexes: formation of paramagnetic nickel(I)-carbonyl complexes. *J. Am. Chem. Soc.* **1980,** *102* (4), 1444-1446.

57. Gagne, R. R.; Ingle, D. M., One-electron-reduced nickel(II)-macrocyclic ligand complexes. Four-coordinate nickel(I) species and nickel(II)-ligand radical species which form paramagnetic, five-coordinate nickel(I) adducts. *Inorg. Chem.* **1981,** *20* (2), 420-425.

58. Lewis, J.; Schroder, M., Reduction of Schiff-base macrocyclic complexes. Stabilisation of nickel(I) conjugated macrocyclic complexes via a reversible ligand-to-metal electron-transfer process. *J. Chem. Soc., Dalton Trans.* **1982,** (6), 1085-1089.

59. Sullivan, E. P.; Strauss, S. H., Reversible carbon monoxide binding to iron(III) isobacteriochlorins. *Inorg. Chem.* **1989,** *28* (16), 3093-3095.

60. Kourkine, I. V.; Slone, C. S.; Mirkin, C. A.; Liable-Sands, L. M.; Rheingold, A. L., Small Molecule-Induced Intramolecular Electron “Pitch and Catch” in a RhodiumI Complex with Substitutionally Inert Redox-Active Ligands. *Inorg. Chem.* **1999,** *38* (12), 2758-2759.

61. Camara, J. M.; Rauchfuss, T. B., Combining acid–base, redox and substrate binding functionalities to give a complete model for the [FeFe]-hydrogenase. *Nat. Chem.* **2011,** *4*, 26.

62. Hernández Sánchez, R.; Zheng, S.-L.; Betley, T. A., Ligand Field Strength Mediates Electron Delocalization in Octahedral $[(HL)_2Fe_6(L')_m]^{n+}$ Clusters. *J. Am. Chem. Soc.* **2015,** *137* (34), 11126-11143.

63. In addition to direct spectroscopic technques, ligand binding affinities are commonly measured using electrochemical techniques, especially where one or more of the binding constants is too large or small to measure directly. For our clusters, we are able to directly measure the CO binding constants in three redox states by ^{1}H-NMR spectroscopy. We prefer these direct measurements for our system because they do not require any assumptions about cluster speciation at given temperature, concentration and pressure. By ^{1}H-NMR spectroscopy, we can directly quantify the relevant species in the binding equilibria. We have measured the electrochemistry of 3 under CO (see the SI), but a full understanding of the changes in the electrochemical profile would require CV simulations involving two successive binding equilibria at each redox couple and assumptions about cluster speciation and relative rates of chemical and electron transfer events.

64. David, S.; James, B. R.; Dolphin, D.; Traylor, T. G.; Lopez, M. A., Dioxygen and carbon monoxide binding to apolar cyclophane hemes: durene-capped hemes. *J. Am. Chem. Soc.* **1994,** *116* (1), 6-14.

65. Suslick, K. S.; Reinert, T. J., The synthetic analogs of O_2-binding heme proteins. *J. Chem. Educ.* **1985,** *62* (11), 974.

66. Collman, J. P.; Brauman, J. I.; Iverson, B. L.; Sessler, J. L.; Morris, R. M.; Gibson, Q. H., Dioxygen and carbonyl binding to iron(II) porphyrins: a comparison of the "picket fence" and "pocket" porphyrins. *J. Am. Chem. Soc.* **1983,** *105* (10), 3052-3064.

67. Ray, M.; Golombek, A. P.; Hendrich, M. P.; Young, V. G.; Borovik, A. S., Synthesis and Structure of a Trigonal Monopyramidal Fe(II) Complex and Its Paramagnetic Carbon Monoxide Derivative. *J. Am. Chem. Soc.* **1996,** *118* (25), 6084-6085.

68. Prokopchuk, D. E.; Wiedner, E. S.; Walter, E. D.; Popescu, C. V.; Piro, N. A.; Kassel, W. S.; Bullock, R. M.; Mock, M. T., Catalytic N_2 Reduction to Silylamines and Thermodynamics of N_2 Binding at Square Planar Fe. *J. Am. Chem. Soc.* **2017,** *139* (27), 9291-9301.

69. de Ruiter, G.; Thompson, N. B.; Takase, M. K.; Agapie, T., Intramolecular C–H and C–F Bond Oxygenation Mediated by a Putative Terminal Oxo Species in Tetranuclear Iron Complexes. *J. Am. Chem. Soc.* **2016,** *138* (5), 1486-1489.

70. Herbert, D. E.; Lionetti, D.; Rittle, J.; Agapie, T., Heterometallic Triiron-Oxo/Hydroxo Clusters: Effect of Redox-Inactive Metals. *J. Am. Chem. Soc.* **2013,** *135* (51), 19075-19078.

71. de Lange, B.; Lambers-Verstappen, M. H.; Schmieder-van de Vondervoort, L.; Sereinig, N.; de Rijk, R.; de Vries, A. H. M.; de Vries, J. G., Aromatic Amination of Aryl Bromides Catalysed by Copper/β-Diketone Catalysts: The Effect of Concentration. *Synlett* **2006,** *2006* (18), 3105-3109.

72. Bailey, B. C.; Basuli, F.; Huffman, J. C.; Mindiola, D. J., Terminal Titanium(IV) (Trimethylsilyl)imides Prepared by Oxidatively Induced Trimethylsilyl Abstraction. *Organometallics* **2006,** *25* (11), 2725-2728.

73. Del Castillo, T. J.; Thompson, N. B.; Peters, J. C., A Synthetic Single-Site Fe Nitrogenase: High Turnover, Freeze-Quench ^{57}Fe Mössbauer Data, and a Hydride Resting State. *J. Am. Chem. Soc.* **2016,** *138* (16), 5341-5350.

74. Chilton, N. F.; Anderson, R. P.; Turner, L. D.; Soncini, A.; Murray, K. S., PHI: A powerful new program for the analysis of anisotropic monomeric and exchange-coupled polynuclear d- and f-block complexes. *J. Comput. Chem.* **2013,** *34* (13), 1164-1175.

75. *APEX-II Version 2 User Manual, M86-E01078*. Bruker Analytical X-ray Systems: Madison, WI, 2006.

76. Sheldrick, G., *SADABS (version 2008/1): Program for Absorption Correction for Data from Area Detector Frames*. University of Göttingen: 2008.

77. Sheldrick, G., A short history of SHELX. *Acta Crystall. Sec. A* **2008,** *64* (1), 112-122.

78. Sheldrick, G., Crystal structure refinement with SHELXL. *Acta Crystall. Sec. C* **2015,** *71* (1), 3-8.

79. Dolomanov, O. V.; Bourhis, L. J.; Gildea, R. J.; Howard, J. A. K.; Puschmann, H., OLEX2: a complete structure solution, refinement and analysis program. *J. Appl. Crystallogr.* **2009,** *42* (2), 339-341.

80. M. J. Frisch, G. W. T., H. B. Schlegel, G. E. Scuseria, M. A. Robb, J. R. Cheeseman, G. Scalmani, V. Barone, B. Mennucci, G. A. Petersson, H. Nakatsuji, M. Caricato, X. Li, H. P. Hratchian, A. F. Izmaylov, J. Bloino, G. Zheng, J. L. Sonnenberg, M. Hada, M. Ehara, K. Toyota, R. Fukuda, J. Hasegawa, M. Ishida, T. Nakajima, Y. Honda, O. Kitao, H. Nakai, T. Vreven, J. A. Montgomery, Jr., J. E. Peralta, F. Ogliaro, M. Bearpark, J. J. Heyd, E. Brothers, K. N. Kudin, V. N. Staroverov, R. Kobayashi, J. Normand, K. Raghavachari, A. Rendell, J. C. Burant, S. S. Iyengar, J. Tomasi, M. Cossi, N. Rega, J. M. Millam, M. Klene, J. E. Knox, J. B. Cross, V. Bakken, C. Adamo, J. Jaramillo, R. Gomperts, R. E. Stratmann, O. Yazyev, A. J. Austin, R. Cammi, C. Pomelli, J. W. Ochterski, R. L. Martin, K. Morokuma, V. G. Zakrzewski, G. A. Voth, P. Salvador, J. J. Dannenberg, S. Dapprich, A. D. Daniels, O. Farkas, J. B. Foresman, J. V. Ortiz, J. Cioslowski, and D. J. Fox, Gaussian 09. Gaussian, Inc.: Wallingford CT, 2009.

81. Nguyen, D. H.; Hsu, H.-F.; Millar, M.; Koch, S. A.; Achim, C.; Bominaar, E. L.; Münck, E., Nickel(II) Thiolate Complex with Carbon Monoxide and Its Fe(II) Analog: Synthetic Models for CO Adducts of Nickel−Iron-Containing Enzymes. *J. Am. Chem. Soc.* **1996,** *118* (37), 8963-8964.

82. C. Davies, S.; L. Hughes, D.; L. Richards, R.; Roger Sanders, J., Iron complexes of the $N(CH_2CH_2S)_3^{3-}$ ligand; a paramagnetic, trigonal bipyramidal Fe(II) CO complex as a chelate ligand. *Chem. Commun.* **1998,** (24), 2699-2700.

CHAPTER 3

REMOTE LIGAND MODIFICATIONS TUNE ELECTRONIC DISTRIBUTION AND REACTIVITY IN SITE-DIFFERENTIATED, HIGH SPIN IRON CLUSTERS: FLIPPING SCALING RELATIONSHIPS

The text for this chapter was reproduced in part from:

Arnett, C.H.; Kaiser, J.; Agapie, T. *Inorg. Chem.* **2019***, 58,* 15971-15982.

ABSTRACT

We report the synthesis, characterization and reactivity of [LFe$_3$O(^{R}ArIm)$_3$Fe][OTf]$_2$, the first Hammett series of a site-differentiated cluster. The cluster reduction potentials and CO stretching frequencies shift as expected based on the electronic properties of the ligand: electron-donating substituents result in more reducing clusters and weaker C-O bonds. However, unusual trends in the energetics of their two sequential CO-binding events with the substituent σ_p parameters are observed. Specifically, introduction of electron-donating substituents *suppresses* the first CO binding event ($\Delta\Delta H$ as much as 7.9 kcal·mol^{-1}) but *enhances* the second ($\Delta\Delta H$ as much as 1.9 kcal·mol^{-1}). X-ray crystallography, including multiple-wavelength anomalous diffraction, Mössbauer spectroscopy, and SQUID magnetometry reveal that these substituent effects result from changes in the energetic penalty associated with electronic redistribution within the cluster, which occurs during the CO binding event.

INTRODUCTION

The reactivity of transition metal ions is sensitive to their local environment,[1-2] enabling the rational development and optimization of catalysts based on established structure-function relationships. However, because many of the thermodynamic properties central to their reactivity are highly correlated,[3-5] ligand modifications which enhance one measure of reactivity (*e.g.* reduction potential) may adversely affect another (*e.g.* acidity, hydricity, ligand binding affinity).[6-8] Breaking, or inverting, these traditional scaling relationships can prove advantageous in fine tuning the reactivity and/or selectivity of transition metal-based catalysts.[9-13] For example, incorporation of trimethylanilinium groups into the backbone of a tetraphenylporphyrin results in electrocatalysts for CO_2 reduction which operate with higher efficiency at lower overpotential due to stabilization of the initial Fe^0-CO_2 adduct, breaking the correlation between activity and overpotential.[11]

In comparison to monometallic systems, the influence of changes in the first and second coordination sphere on the properties of metal clusters are poorly understood,[14-16] despite the fact that catalysts which incorporate multiple metal centers are common in biological systems and mediate challenging multielectron transformations.[17-22] Although only a subset of the metal ions within the cluster are believed to be involved in substrate binding and functionalization, the remote metals may significantly impact the properties and activity of the reactive site.[23-28] For example, varying the identity of the pendant group 13 metal in a series of heterobimetallic [MNi] (M = Al, Ga, In) complexes tunes their H_2 and N_2 binding affinities[23] as well as their activity towards olefin hydrogenation.[29] A heterobimetallic Zr/Co complex activates O_2[25] and organic azides[26] at a Zr^{IV} center, with electrons delivered to the substrate by the remote redox-active cobalt center. Conversely, proximal redox-inactive metals have been shown to induce inverse linear free energy relationships in the rates of C-H oxidation[9] and $Mn^{V}N$ coupling.[10] Studies from our laboratory demonstrate that remote metal sites influence small molecule activation,[30-32] bond dissociation free energies,[33-34] and oxygen atom transfer[35] without formally changing the oxidation state of the metal site directly involved in substrate binding. The close proximity of multiple redox-active metal centers in a site-differentiated clusters may afford unique opportunities to challenge traditional scaling relationships, though such an approach has not been realized because of the synthetic challenges associated with controlling cluster nuclearity and geometry in common self-assembly reactions.[36]

To facilitate (electronic) structure-function studies[37-41], our group and others employ polynucleating ligands scaffolds to template the organization of multiple metal centers.[42-47] Herein, we report the synthesis and characterization of a unique Hammett series of a site-differentiated cluster, $[LFe_3O(^{R}ArIm)_3Fe][OTf]_2$ (Figure 1), which reversibly binds up to two molecules of CO. The redox properties of the cluster are dependent on the electronic nature of the substituent ($\Delta E_{1/2}$ = 270-310 mV), with electron-releasing substituents resulting in cathodic shifts. Unexpectedly, introduction of electron-donating substituents *suppresses* the first CO binding event of the cluster ($\Delta\Delta H$ as much as 7.9 $kcal{\cdot}mol^{-1}$). Even more surprising, the opposite trend is observed for the second CO binding event, which is *enhanced* by electron-donating substituents ($\Delta\Delta H$ as much as 1.9 $kcal{\cdot}mol^{-1}$). Crystallographic, spectroscopic and magnetic studies enabled us to deconvolute the effect of ligand modification at specific sites within the cluster. These studies suggest that electron-releasing substituents enlarge the energetic penalty associated with electronic redistribution within the cluster, an essential feature of the first CO binding event. Binding of the second molecule of CO does not require an internal electron transfer, which explains why the second binding constant increases as the clusters become more electron-rich.

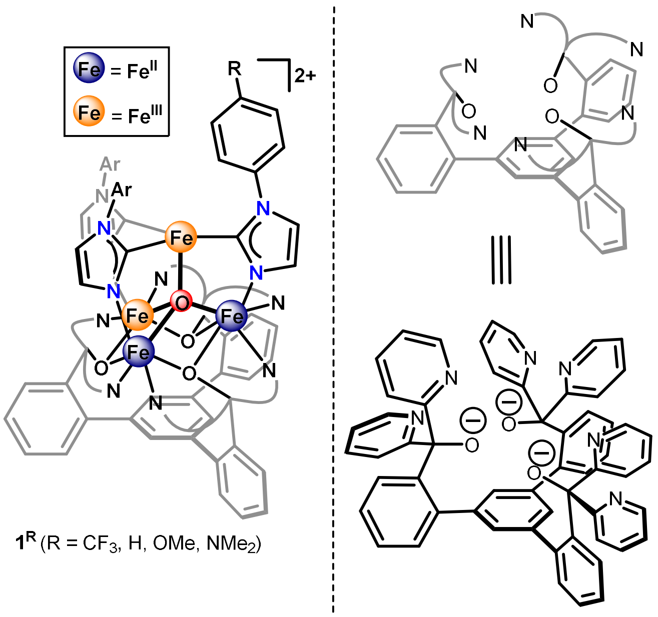

$\mathbf{1^R}$ (R = CF_3, H, OMe, NMe_2)

FIGURE 1. General molecular structure of $[LFe_3O(^{R}ArIm)_3Fe][OTf]_2$, supported by imidazolates and a 1,3,5- triarylbenzene-based ligand. The inset shows the coloring scheme for the metal oxidation states.

RESULTS AND DISCUSSION

Synthesis and Electrochemistry. Complexes $[LFe_3O(^{pCF3}ArIm)_3Fe][OTf]_2$ ($\mathbf{1^{CF3}}$), $[LFe_3O(^{pOMe}ArIm)_3Fe][OTf]_2$ ($\mathbf{1^{OMe}}$) and $[LFe_3O(^{pNMe2}ArIm)_3Fe][OTf]_2$ ($\mathbf{1^{NMe2}}$) were synthesized in a manner similar to that recently described for $[LFe_3O(PhIm)_3Fe][OTf]_2$ ($\mathbf{1^H}$) (Scheme 1).[30] Although high quality crystal structures could not be obtained for $\mathbf{1^{OMe}}$ or $\mathbf{1^{NMe2}}$, their ^{1}H-NMR spectra are strikingly similar to those of the structurally characterized clusters $\mathbf{1^{CF3}}$ and $\mathbf{1^H}$ (NMR, Figure 46). Moreover, the ESI mass spectra of $\mathbf{1^{OMe}}$ and $\mathbf{1^{NMe2}}$ feature peaks at m/z = 809 and 827, respectively, consistent with $[LFe_3O(^{pOMe}ArIm)_3Fe]^{2+}$ and $[LFe_3O(^{pNMe2}ArIm)_3Fe]^{2+}$ formulations.

The effect of remote ligand modification on the electrochemical properties of $[LFe_3O(^{R}ArIm)_3Fe][OTf]_2$ was interrogated by cyclic voltammetry. In dichloromethane, $\mathbf{1^R}$ (R = CF3, H, OMe, NMe_2) exhibits two quasireversible electrochemical events: a reduction assigned to $Fe^{II}{}_3Fe^{III}/Fe^{II}{}_2Fe^{III}{}_2$ redox couple (average $E_{1/2}$ ~ -1 V) and an oxidation assigned to $Fe^{II}_2Fe^{III}_2/Fe^{II}Fe^{III}_3$ redox couple (average $E_{1/2}$ ~ -0.11 V, Figure 2A). The potentials associated with both redox events are dependent on the electronic nature of the substituent, illustrated by the linear correlation of the measured $E_{1/2}$ values with their Hammett σ_p parameters (Figure 2B).[48] The half wave potentials of the $Fe^{II}_3Fe^{III}/Fe^{II}_2Fe^{III}_2$ redox event are shifted over a 310 mV range from -0.87 V for $\mathbf{1}^{\mathbf{CF3}}$ to -1.18 V for $\mathbf{1}^{\mathbf{NMe2}}$, suggesting a significant effect of remote ligand substitution on the energy of the redox active orbital(s) associated with $[Fe_3(\mu_4\text{-}O)Fe]$ core. Likewise, the half wave potentials of the $Fe^{II}_2Fe^{III}_2/Fe^{II}Fe^{III}_3$ redox event are tuned over a similar range (270 mV) from +0.02 V for $\mathbf{1}^{\mathbf{CF3}}$ to -0.25 V for $\mathbf{1}^{\mathbf{NMe2}}$.

Scheme 1. Modular Synthesis of Site-Differentiated Iron Clusters with Variable Remote Substituents.

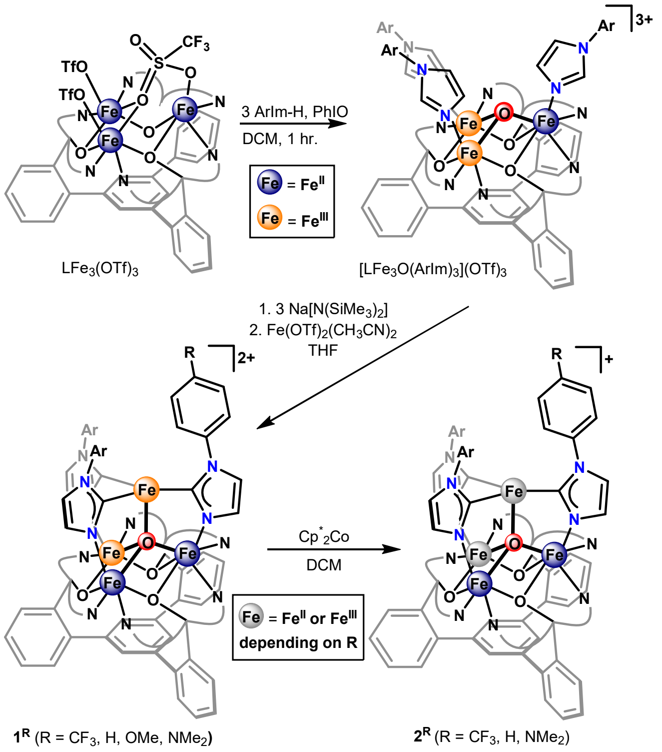

Spectroscopic Studies of $[LFe_3O(^{R}ArIm)_3Fe]^{2+}$ *Clusters.* Although the electrochemical properties of $\mathbf{1}^{\mathbf{R}}$ (R = CF3, H, OMe, NMe_2) trend with the substituent σ_p parameters, spectroscopic studies reveal only subtle differences in their electronic ground state.[49] The zero field ^{57}Fe Mössbauer spectra of $\mathbf{1}^{\mathbf{CF3}}$ (Mössbauer, Figure 8) and $\mathbf{1}^{\mathbf{NMe2}}$ (Mössbauer, Figure 9) are qualitatively similar to that of $\mathbf{1^{H}}$.[50] Spectral simulations reveal the presence of two iron subsites (50% total iron) with Mössbauer parameters (δ ~ 1 mm/s, $|\Delta E_Q|$ ~ 3 mm/s) diagnostic of high spin, six-coordinate Fe^{II} centers, [30-32, 34-35, 51] indicating a $[Fe^{II}_2Fe^{III}]$ assignment of the redox state of the triiron core. Moreover, the isomer shifts associated with the apical iron center of $\mathbf{1^{CF3}}$, $\mathbf{1^{H}}$ and $\mathbf{1^{NMe2}}$ (δ = 0.19-0.22 mm/s) are consistent with an Fe^{III} formulation.[52] The EPR spectra of $\mathbf{1^{CF3}}$ and $\mathbf{1^{NMe2}}$ (EPR, Figure 2), collected in parallel mode at 4.5 K in a propionitrile/butyronitrile (4:5) glass all exhibit a feature at g ~ 17.2 assigned to a transition within the M_s = +/- 4 doublet of an S = 4 spin system (D < 0). [53-58] This assignment is consistent with variable temperature magnetic susceptibility measurements on $\mathbf{1^{CF3}}$ (Figure S1) and $\mathbf{1^{NMe2}}$ (Figure S2), which plateau ($\mathbf{1^{CF3}}$: ~8.8 cm^3 K mol^{-1}, $\mathbf{1^{NMe2}}$: ~9.3 cm^3 K mol^{-1}) near the expected spin-only value for an isolated S = 4 center (10 cm^3 K mol^{-1}).

Synthesis and X-ray Diffraction Studies of $[LFe_3O(^{R}ArIm)_3Fe]^+$ Clusters. Consistent with their electrochemical behavior, $\mathbf{1^{CF3}}$, $\mathbf{1^{H}}$, and $\mathbf{1^{NMe2}}$ can be reduced with 1 equiv. of Cp^*_2Co, affording complexes with nearly identical ^{1}H-NMR features (NMR, Figure 47). Structural characterization confirmed the identity of these paramagnetic compounds as $[LFe_3O(^{pCF3}ArIm)_3Fe][OTf]$ ($\mathbf{2^{CF3}}$, Figure 3A), $[LFe_3O(PhIm)_3Fe][BF_4]$ ($\mathbf{2^{H}}$, prepared by reduction of $\mathbf{2^{H}}$ to the all-ferrous cluster followed by re-oxidation with $[Cp_2Co][BF_4]$, Figure 3B) and $[LFe_3O(^{pNMe2}ArIm)_3Fe][BF_4]$ ($\mathbf{2^{NMe2}}$, Figure 3C), respectively. Upon reduction, the Fe4-O1 distance of $\mathbf{1^{CF3}}$ (*c.a.* 1.80 Å) elongates to 1.897(1) Å (Table 1), suggesting a ferrous oxidation state assignment for the apical iron in $\mathbf{2^{CF3}}$. Moreover, the long Fe1-O1 (2.068(2) Å) and Fe3-O1 (2.074(2) Å) distances and short Fe2-O1 (1.933(2) Å) bond length of $\mathbf{2^{CF3}}$ are consistent with maintaining the $[Fe^{II}_2Fe^{III}]$ redox level of the basal triiron core observed in $\mathbf{1^{CF3}}$. Similar Fe-O1 bond lengths are observed for $\mathbf{2^{H}}$ (Table 1), indicating that incorporation of electron withdrawing trifluoromethyl substituents does not significantly perturb the ground state electron distribution within $[Fe_3(\mu_4\text{-}O)Fe]^{7+}$ core.

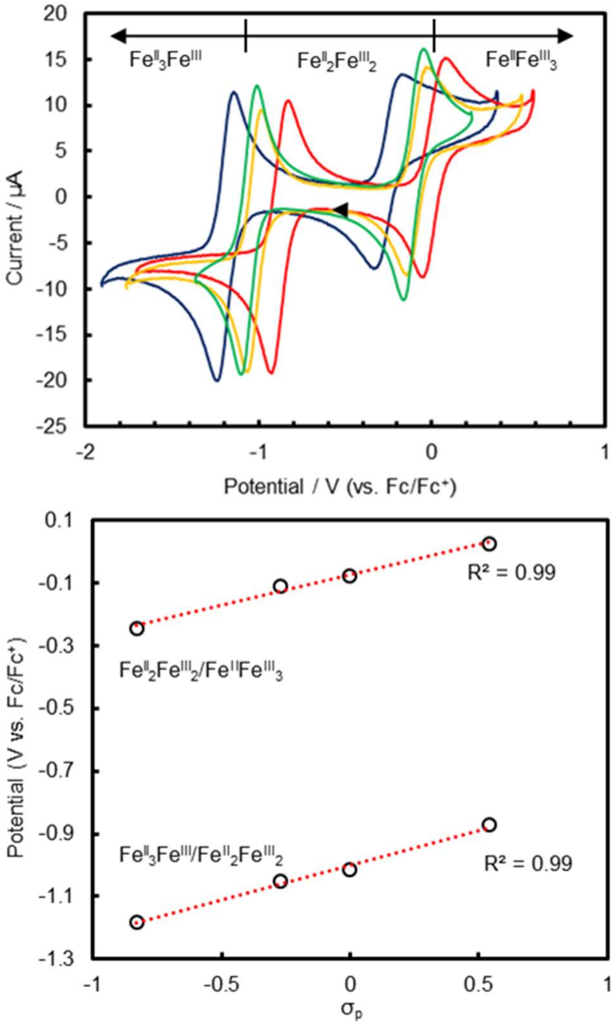

Figure 2. (A) Cyclic voltammograms of $\mathbf{1}^{\mathbf{CF3}}$ (red), $\mathbf{1}^{\mathbf{H}}$ (orange), $\mathbf{1}^{\mathbf{OMe}}$ (green), and $\mathbf{1}^{\mathbf{NMe2}}$ (blue) in CH_2Cl_2 (0.1 M $[n\text{Pr}_4\text{N}][\text{BAr}^{\text{F}}_{24}]$ supporting electrolyte). Scan rate: 100 mV/s. (B) Plot of $E_{1/2}(Fe^{II}_2Fe^{III}_2/Fe^{II}Fe^{III}_3)$ (top) and $E_{1/2}(Fe^{II}_3Fe^{III}/Fe^{II}_2Fe^{III}_2)$ (bottom) vs. Hammett substituent constants (σ_p) for $\mathbf{1}^{\mathbf{R}}$ (R = CF3, H, OMe, NMe_2), respectively.

Remarkably, however, the solid state structure of $\mathbf{2}^{\mathbf{NMe2}}$ reveals a significant influence of remote ligand modification on the redox distribution of $[Fe_3(\mu_4\text{-}O)Fe]^{7+}$ cluster. The Fe4-O1 bond length of $\mathbf{2}^{\mathbf{NMe2}}$ (1.839(2) Å, Table 1) is substantially shorter than those of $\mathbf{2}^{\mathbf{CF3}}$ (1.897(1) Å) or $\mathbf{2}^{\mathbf{H}}$ (1.881(1) Å), suggesting that incorporation of electron donating dimethylamino substituents favors localization of ferric character at the apical iron center. This shift in the electron distribution is supported by an elongation in the Fe2-O1 distance from 1.933(2) Å in **2**$^{\mathbf{CF3}}$ or 1.881(1) Å in **2**$^{\mathbf{H}}$ to 1.986(2) Å in **2**$^{\mathbf{NMe2}}$ (Table 1), indicating a more reduced [Fe^{II}_3] triiron core in **2**$^{\mathbf{NMe2}}$. Consistent with this assignment, an elongation of the [Fe1|Fe2|Fe3] centroid-O1 distance is observed from 0.957(2) Å in **2**$^{\mathbf{H}}$ to 1.015(2) Å in **2**$^{\mathbf{NMe2}}$. Admittedly, the Fe2-O1 distance of **2**$^{\mathbf{NMe2}}$ remains somewhat short compared to other core Fe^{II}-O1 distances (average ~ 2.07 Å),[30, 32] though this may simply be a manifestation of the rigidity of the supporting ligand. Despite differences in the Fe-O1 bond lengths of **2**$^{\mathbf{CF3}}$ and **2**$^{\mathbf{NMe2}}$, the volume of the tetrametallic core remains nearly constant (average Fe-Fe separations: 3.36(4) vs. 3.37(3) Å). The constrained volume of [$Fe_3(\mu_4$-O)Fe] core may prevent a more dramatic elongation of the Fe2-O1 distance of **2**$^{\mathbf{NMe2}}$ in response to charge redistribution induced by remote modification of the ligand. The higher sensitivity of the apical iron to the electronic nature of the remote substituents likely results from the fact that, while these substituted imidazolates bridge Fe4 to the basal triiron core, only Fe4 is bound to all three.

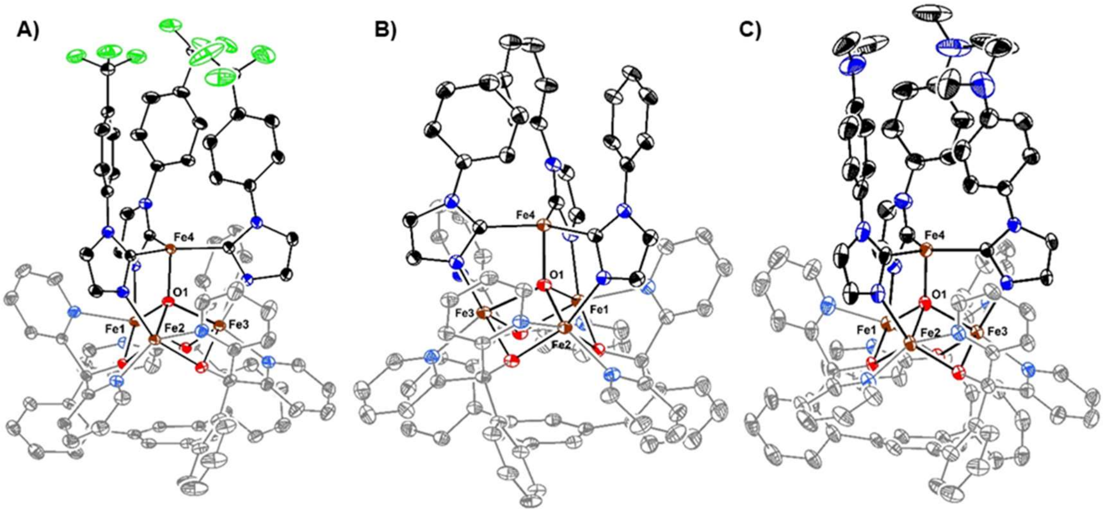

Figure 3. Solid state structures of **2**$^{\mathbf{CF3}}$, **2**$^{\mathbf{H}}$ and **2**$^{\mathbf{NMe2}}$. Hydrogen atoms and outer sphere counterions not shown for clarity. (A) [$LFe_3O(^{pCF3}ArIm)_3Fe$][OTf] (**2**$^{\mathbf{CF3}}$). (B) [$LFe_3O(PhIm)_3Fe$][BF_4] (**2**$^{\mathbf{H}}$) (C) [$LFe_3O(^{pNMe2}ArIm)_3Fe$][BF_4] (**2**$^{\mathbf{NMe2}}$).

Table 1. Summary of Selected Bond Lengths.

Bond Distance (Å)	$\mathbf{1}^{\mathrm{H}}$ [a]	$\mathbf{2}^{\mathrm{CF3}}$	$\mathbf{2}^{\mathrm{H}}$	$\mathbf{2}^{\mathrm{NMe2}}$
Fe1-O1	2.148(2)	2.068(2)	2.091(1)	2.063(2)
Fe2-O1	1.983(2)	1.933(2)	1.881(1)	1.986(2)
Fe3-O1	2.093(2)	2.074(2)	2.108(1)	2.097(2)
Fe4-O1	1.813(2)	1.897(1)	1.881(1)	1.839(2)
Fe1-N11	2.144(3)	2.145(2)	2.164(2)	2.164(2)
Fe2-N9	2.131(2)	2.133(2)	2.121(2)	2.156(2)
Fe3-N7	2.137(3)	2.169(2)	2.174(2)	2.178(2)
Fe4-C60	2.068(3)	2.087(2)	2.093(2)	2.071(2)
Fe4-C69	2.063(3)	2.107(2)	2.102(2)	2.075(3)
Fe4-C78	2.063(3)	2.084(2)	2.082(2)	2.082(3)

[a] Data taken from ref. 30.

^{57}Fe Mössbauer spectroscopy of $[LFe_3O(^{R}ArIm)_3Fe]^+$ Clusters. In order to obtain additional insight into the effect of remote ligand modifications on electron distribution, $\mathbf{2}^{\mathbf{CF3}}$ and $\mathbf{2}^{\mathbf{NMe2}}$ were studied by ^{57}Fe Mössbauer spectroscopy. The Mössbauer spectrum of $\mathbf{2}^{\mathbf{CF3}}$ (80 K, Figure 4 top) features only three well-resolved resonances, albeit with discernable shoulders near the Lorentzian features around -0.5 mm/s and 3 mm/s, respectively. A satisfactory simulation of the experimental spectrum requires at least three distinct iron subsites which, based on the relative intensity of the resonance near 3 mm/s, occur in a 2:1:1 ratio. Two reasonable simulations were obtained, both of which afford Mössbauer parameters for one subsite (50% total iron) which are consistent with the presence of two high-spin, six-coordinate Fe$^{\mathrm{II}}$ centers (δ ~ 1.1 mm/s, $|\Delta E_{\mathrm{Q}}|$ ~ 3.2 mm/s) within the triiron core.[30-32, 34-35, 51] The relative intensity of the sharp resonance near 1 mm/s indicates the presence of one ferric ion whose isomer shift and quadrupole splitting depend on how the Lorentzian feature near -0.5 mm/s is modelled, with δ bounded between 0.34-0.47 mm/s. Isomer shifts in this range are common for high-spin, six-coordinate ferric centers in O/N rich ligand environments,[59-63] suggesting a $[\mathrm{Fe^{II}}_2\mathrm{Fe^{III}}]$

redox level for the triiron core identical to that inferred from the solid state structure. The shoulder observed to the left of the Lorentzian feature around 3 mm/s is attributed a third ferrous site with a lower isomer shift (δ ~ 0.8 mm/s) and lower quadrupole splitting ($|\Delta E_Q|$ ~ 2.7 mm/s). A similar shoulder is observed in the Mössbauer spectra of **2^H^**[30] and [LFe$_3$O(PhPz)$_3$Fe][OTf][32]. This shoulder, which is absent in the spectrum of the one-electron oxidized cluster **1^{CF3}** (Mössbauer, Figure 8) has been assigned to a resonance of the apical Fe^{II} center.[30, 32] Due to its lower coordination number and softer (C rich) ligand environment, a smaller isomer shift is anticipated for the apical ferrous site compared to the pseudo-octahedral Fe^{II} centers of the triiron core.[64] The final model (Table 2) affords an isomer shift of 0.73 mm/s ($|\Delta E_Q|$ ~ 2.76 mm/s) for the trigonal pyramidal ferrous site of **2^{CF3}**, a value similar to those reported for four-coordinate, high-spin Fe^{II} centers supported by multidentate *N*-heterocyclic carbene ligand scaffolds.[65-66]

On the other hand, the Mössbauer spectrum of **2^{NMe2}** (Figure 4, bottom) is distinct from those of **2^{CF3}** and **2^{H}**, indicating a change in the electronic structure. Most notably, the sharp resonance near 1 mm/s observed in the spectra of **2^{CF3}**, **2^{H}**, and [LFe$_3$O(PhPz)$_3$Fe][OTf][32] is absent. Instead, a sharp, nearly isotropic signal is observed at 0.11 mm/s, indicating a significantly lower isomer shift for the ferric subsite of **2^{NMe2}**. Six-coordinate, high-spin Fe^{III} complexes are not known to exhibit isomer shifts lower than ~0.35 mm/s. As such, the quadrupole doublet for the ferric subsite does not originate from within the triiron core. Isomer shifts of ~0.20 mm/s are commonly observed for four-coordinate, high spin ferric iron complexes in soft ligand environments, suggesting an Fe^{III} assignment for the apical metal center.[52] Consistent with this assignment, the isomer shift of the apical iron center in **2^{NMe2}** (δ = 0.11 mm/s) does not differ significantly from that in **1^{NMe2}** (δ = 0.22 mm/s, Mössbauer, Figure 9). For comparison, a substantially larger difference is observed in the isomer shifts associated with the apical iron center in $\mathbf{2}^{\mathbf{CF3}}$ (δ = 0.73 mm/s) compared to $\mathbf{1}^{\mathbf{CF3}}$ (δ = 0.19 mm/s). Furthermore, the presence of three six-coordinate, high spin ferrous centers in the triiron core of $\mathbf{2}^{\mathbf{NMe2}}$ is supported by the Mössbauer parameters of the remaining subsite (δ = 1.10 mm/s, $|\Delta E_Q|$ = 3.23 mm/s, 75% total iron, Table 2).

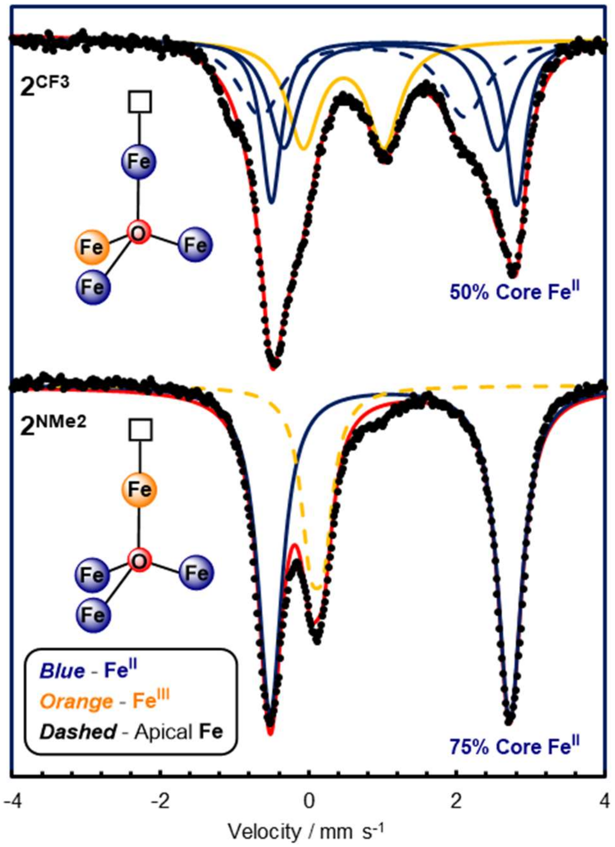

Figure 4. Remote ligand modifications tune redox distribution in a series of site-differentiated $[LFe_3O(^{R}ArIm)_3Fe]^+$ clusters. Top: Zero field ^{57}Fe Mössbauer spectrum (80 K, microcrystalline material) of $[LFe_3O(^{pCF3}ArIm)_3Fe][OTf]$ ($\mathbf{2}^{\mathbf{CF3}}$). (Bottom): Zero field ^{57}Fe Mössbauer spectrum (80 K, microcrystalline material) of $[LFe_3O(^{pNMe2}ArIm)_3Fe][OTf]$ ($\mathbf{2}^{\mathbf{NMe2}}$). For additional simulation details, see the Supporting Information.

Table 2. Summary of Mössbauer Parameters.

No.	Complex	δ	$\lvert \Delta E_Q \rvert$	%
$\mathbf{1}^{\mathbf{CF_3}}$	$\mathrm{[LFe_3O(^{pCF_3}ArIm)_3Fe][OTf]_2}$	1.10	3.17	25
		1.16	2.80	25
		0.39	0.39	25
		0.19	1.24	25
$\mathbf{1}^{\mathbf{NMe_2}}$	$\mathrm{[LFe_3O(^{pNMe_2}ArIm)_3Fe][OTf]_2}$	1.02	2.89	25
		1.09	3.30	25
		0.39	0.45	25
		0.22	1.10	25
$\mathbf{2}^{\mathbf{CF_3}}$	$\mathrm{[LFe_3O(^{pCF_3}ArIm)_3Fe][OTf]}$	1.11	2.88	25
		1.15	3.31	25
		0.47	1.09	25
		0.73	2.76	25
$\mathbf{2}^{\mathbf{NMe_2}}$	$\mathrm{[LFe_3O(^{pNMe_2}ArIm)_3Fe][OTf]}$	1.10	3.23	75
		0.11	0.18	25

Multiple-Wavelength Anomalous Diffraction. Further insight into the electronic structure of $\mathbf{2}^{\mathbf{CF3}}$ was sought by multiple-wavelength anomalous X-ray diffraction (MAD). Inelastic scattering of X-rays results in a wavelength dependence of the atomic scattering factors: $\mathrm{f_i}(\lambda) = \mathrm{f_i^0} + \mathrm{f_i'}(\lambda) + i\mathrm{f_i''}(\lambda)$, where $\mathrm{f_i'}(\lambda)$ and $\mathrm{f_i''}(\lambda)$ are the real and imaginary components of the anomalous scattering due to the absorption of X-rays by element i.[67-68] Thus, MAD experiments can provide information on metal oxidation state and coordination geometry, similar to XANES, but in a site-specific manner for individual metal sites within a cluster.[15, 69] Unfortunately, however, only $\mathrm{f_i''}(\lambda)$ is directly proportional to absorption, and for centrosymmetric crystals, such as the clusters discussed herein, $\mathrm{f_i''}(\lambda)$ cannot be refined directly. In principle, analysis of the $\mathrm{f_i'}(\lambda)$ spectra could provide similar site-specific information, however their interpretation is not straightforward, and studies of well-defined model clusters are limited.[70-73] A plot of the refined $\mathrm{f_i'}(\lambda)$ values for Fe1 - Fe4 as a function of energy for $\mathbf{2}^{\mathbf{CF3}}$ (Figure 5) clearly distinguishes the unique coordination environment of Fe4 from Fe1-Fe3. The $f_i'(\lambda)$ curves of the six-coordinate, high-spin ferrous sites Fe1 and Fe3 are broader and have a lower energy minima than that of the six-coordinate ferric site Fe2. Although the effects of radiation damage are apparent in the higher energy data sets, the MAD data for $\mathbf{2^{CF3}}$ correlates well with the oxidation state distribution inferred by traditional X-ray crystallography and ^{57}Fe Mössbauer spectroscopy, which indicate an Fe(II) formulation for both Fe1 and Fe3.

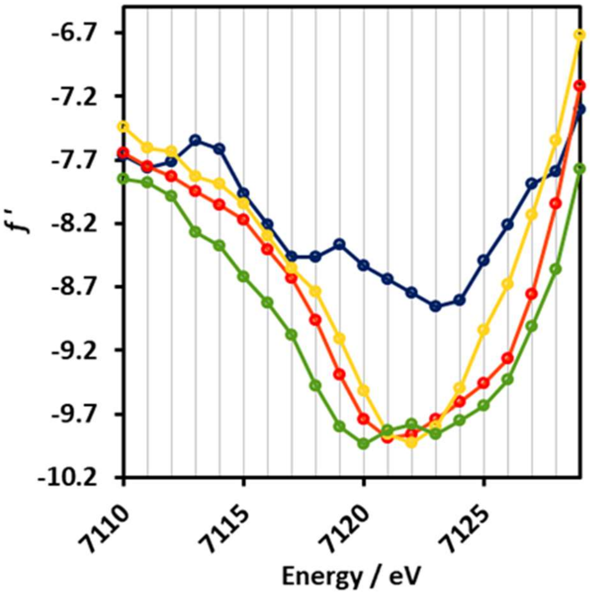

Figure 5. Plot of refined *f'* values for Fe1 (green), Fe2 (yellow), Fe3 (red) and Fe4 (blue) as a function of energy for $\mathbf{2^{CF3}}$. Atom labels are the same as those used in the structure of $\mathbf{2^{CF3}}$ in Figure 3A. Selected bond lengths are included Table 1. For additional refinement details, see the Supporting Information.

SQUID Magnetometry for $[LFe_3O(^{R}ArIm)_3Fe]^+$ *Clusters.* To elucidate the effect of redox distribution on the exchange coupling, variable temperature magnetic susceptibility measurements were performed on $\mathbf{2^{CF3}}$, $\mathbf{2^{H}}$, and $\mathbf{2^{NMe2}}$ in the temperature range 1.8-300 K at 0.1 T (Figure 6). The value of $\chi_M T$ for 2^{NMe2} at 300 K (6.35 cm^3 K mol^{-1}) deviates significantly from the spin-only value (13.38 cm^3 K mol^{-1}) anticipated for uncoupled Fe^{II} (S = 2) and Fe^{III} (S = 5/2) centers, indicating the presence of antiferromagnetic coupling. However, $\chi_M T$

increases gradually as the temperature is lowered (Figure 6, blue trace), eventually reaching a plateau (7.87 cm^3 K mol^{-1}) between 10-40 K corresponding to the expected spin-only value for an isolated $S = 7/2$ center ($g = 2.00$). The near-ideal Curie behavior observed between 10-40 K suggests that excited states with $S \neq 7/2$ are not thermally accessible. An exchange coupling model ($J_{14} = J_{34}$; $J_{12} = J_{23}$, numerical subscripts chosen to be consistent with atom labels in the crystal structures) based on the *pseudo*-C$_s$ symmetry of the [Fe$_3$(μ_4-O)Fe] core was employed to simulate the experimental data according to the spin Hamiltonian $H = -2\sum J_{ij}(S_i \cdot S_j)$. The effective exchange coupling constants obtained from these simulations ($J_{14} = J_{34} = -29$ cm^{-1}, $J_{24} = -40$ cm^{-1}, $J_{12} = J_{23} = -3.4$ cm^{-1}, $J_{13} = -0.8$ cm^{-1}) reveal that the $S = 7/2$ ground state originates from spin frustration of the triiron core due to strong antiferromagnetic interactions of Fe1/Fe2/Fe3 with the apical Fe^{III} center. The larger value of J_{24} (compared to $J_{14} = J_{34}$) is consistent with the shorter Fe2-O1 distance observed in the solid state structure. Consistent with the $S = 7/2$ ground state inferred from magnetic susceptibility measurements, magnetization saturation for $\mathbf{2^{NMe2}}$ occurs at 6.6μ_B at 1.8 K and 7 T, near the expected M = gS limit for $g = 2.00$. Simulations according to the system spin Hamiltonian $H = DS_z^2 + E(S_x^2 + S_y^2) + g\mu_B \mathrm{S}\cdot\mathrm{H}$ best reproduce the experimental data, assuming $S = 7/2$ with $g = 1.92$, $D = -0.21$ cm^{-1}, and $|E/D| = 0$ (Supplementary Fig. 69).

In contrast to the gradual rise in χ_MT observed for $\mathbf{2^{NMe2}}$, the molar susceptibilities of $\mathbf{2^{CF3}}$ (Figure 6, red trace) and $\mathbf{2^{H}}$ (Figure 6, orange trace) decrease monotonically with temperature, reaching values of 3.16 cm^3 K mol^{-1} and 1.81 cm^3 K mol^{-1}, respectively, at 1.8 K. No plateau is observed in the χ_MT values down to 1.8-5 K, suggesting that neither $\mathbf{2^{CF3}}$ nor $\mathbf{2^{H}}$ possess a well-isolated spin ground state. Simulations of the experimental data reveal significantly smaller $J_{14} = J_{34}$ coupling constants for $\mathbf{2^{CF3}}$ and $\mathbf{2^{H}}$ (-2.1 cm^{-1} and -5 cm^{-1}, respectively) compared to $\mathbf{2^{NMe2}}$ (-29 cm^{-1}). While the intracore exchange coupling remains weak ($J_{12} = J_{23} =$ -2.3 cm^{-1}, $J_{13} =$ -0.6 cm^{-1} for $\mathbf{2^{CF3}}$; $J_{12} = J_{23} =$ -4.8 cm^{-1}, $J_{13} =$ -1.3 cm^{-1} for $\mathbf{2^{H}}$), the smaller values of $J_{14} = J_{34}$ are no longer large enough to spin frustrate the triiron core. As a result, the calculated energy level diagrams for $\mathbf{2^{CF3}}$ and $\mathbf{2^{H}}$ indicate multiple low-lying excited states with energies as low as *c.a.* 0.3 cm^{-1} and 0.6 cm^{-1}, respectively (equivalent temperatures 0.4 K and 0.9 K). This is in stark contrast to $\mathbf{2^{NMe2}}$ for which the first excited sextet state is predicted at *c.a.* 120 cm^{-1} (equivalent temperature 173 K).

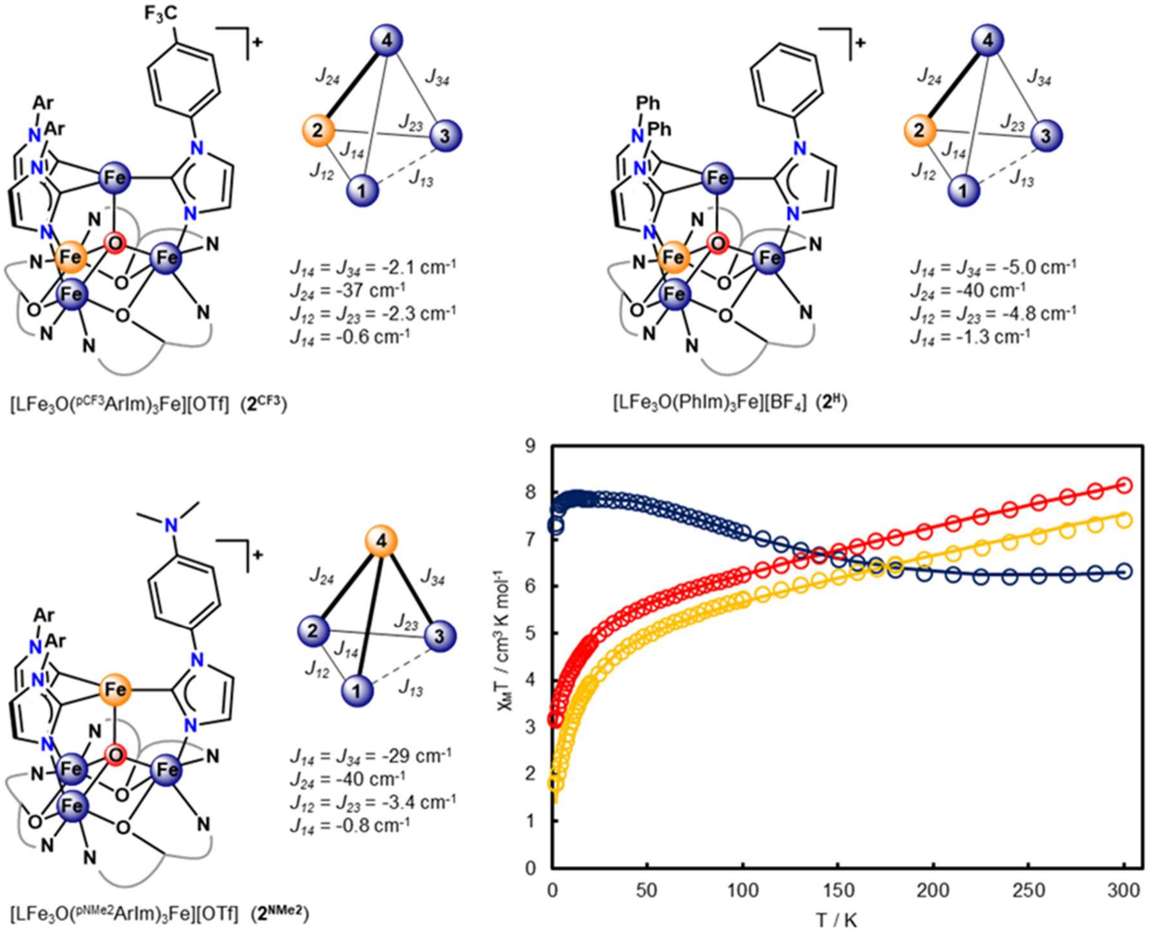

Figure 6. Redox distribution governs the magnetic properties in a series of site-differentiated [LFe$_3$O(^{R}ArIm)$_3$Fe]$^+$ clusters. Exchange coupling model, fit parameters, and variable temperature magnetic susceptibility data for $\mathbf{2^{CF3}}$ (red trace), $\mathbf{2^{H}}$ (orange trace), and $\mathbf{2^{NMe2}}$ (blue trace). For additional simulation details, see the Supporting Information.

Based on the sensitivity of the spin ladder to $J_{14} = J_{34}$, the presence (or absence) of a well-isolated, high-spin ground state appears to be directly correlated with the oxidation state of the apical iron center. The dominant superexchange pathways within $[Fe_3(\mu_4\text{-}O)Fe]^{7+}$ core are likely through the monoatomic-bridging oxo ligand, and the strength of these interactions are highly sensitive to the Fe-O bond lengths.[74-76] For $\mathbf{2^{CF3}}$ and $\mathbf{2^{H}}$ which feature apical Fe^{II} centers, the Fe4-O1 distance is elongated (0.04-0.06 Å) relative to $\mathbf{2^{NMe2}}$, which features an apical ferric site. The nearly identical values for J_{24} determined for $\mathbf{2^{CF3}}$ (-37 cm^{-1}), $\mathbf{2^{H}}$ (-40 cm^{-1}) and $\mathbf{2^{NMe2}}$ (-40 cm^{-1}) suggest that changes in the Fe^{II}-Fe^{III} coupling constant due to elongation in the Fe4-O1 distance are largely compensated for by contraction of the Fe2-O1 bond length. However, elongation in the Fe4-O1 distance modulates the extent to which Fe4 is magnetically coupled with the ferrous centers of the triiron core (Fe1 and Fe3), thereby dictating whether or not the triiron core will be ferromagnetically aligned at low temperatures. Overall, our magnetostructural studies indicate that the spin ground state of site-differentiated iron clusters and its energetic isolation from excited states are indicators of electronic distribution, which we have shown can be systematically tuned by remote ligand modifications.

CO Reactivity: IR Spectroscopy. Crystallographic, spectroscopic, and magnetic studies indicate that localization of ferric character at the unique apical iron is preferred in the ground state of $[LFe_3O(^{R}ArIm)_3Fe]^{2+}$ clusters. Notwithstanding, we have previously shown that binding of CO induces an internal electron transfer from a distal Fe^{II} center, resulting in an apical Fe^{II}-CO motif as supported by Mössbauer and IR spectroscopy.[30] While internal electron transfer from a *remote* metal site accommodates coordination of CO at Fe^{III}, measurements of the CO binding energetics revealed that redox reorganization introduces a small energetic penalty to ligand binding. Based on the sensitivity of the redox distribution of $\mathbf{1^{R}}$ (R = CF3, H, OMe, NMe_2) to remote ligand modification, we reasoned that remote ligand modifications may also tune the propensity of $[LFe_3O(^{R}ArIm)_3Fe]^{2+}$ core to *redistribute* electron density, the extent of which may be determined by measuring the CO binding energetics of $\mathbf{1^{R}}$ (R = CF3, H, OMe, NMe_2). As such, we investigated the effect of remote ligand modifications on the reactivity of the Hammett series $\mathbf{1^{R}}$ (R = CF3, H, OMe, NMe_2) with CO. The IR spectrum of $\mathbf{1^{CF3}}$ at 195 K in CO-saturated dichloromethane (3.3 mM) following an Ar purge is qualitatively similar to that of $\mathbf{2^{H}}$ (Figure 7B). An intense feature attributed to the formation of the monocarbonyl adduct $\mathbf{1^{CF3}}$**-CO** is observed at 1947 cm^{-1} (compared to 1944 cm^{-1} for $\mathbf{1^{H}}$**-CO**). Additionally, weak features at 1961 and 2015 cm^{-1} indicate formation of a dicarbonyl complex $\mathbf{1^{CF3}\text{-}(CO)_2}$ (1960 and 2014 cm^{-1} for $\mathbf{1^{H}\text{-}(CO)_2}$).[77] Upon warming the solution to 273 K under Ar, the Fe-CO vibration of $\mathbf{1^{CF3}}$**-CO** at 1947 cm^{-1} remains intense. In analogous experiments with $\mathbf{1^{H}}$**-CO**, no diagnostic Fe-CO vibrations were discernable at 273 K,[30] suggesting that formation of the monocarbonyl complex is thermodynamically more favorable for $\mathbf{1^{CF3}}$ compared to $\mathbf{1^{H}}$.

On the other hand, the IR spectrum of $\mathbf{1^{OMe}}$ (Figure 7B) in CO-saturated dichloromethane under nearly identical conditions (3.1 mM, 195 K) exhibits three intense Fe-CO vibrational features. The lowest energy feature (1942 cm^{-1}) is attributable to the monocarbonyl complex $\mathbf{1^{OMe}}$**-CO**, with the remaining features at 1955 and 2013 cm^{-1} assigned to the dicarbonyl adduct $\mathbf{1^{OMe}\text{-}(CO)_2}$. The higher relative intensity of these features indicates a larger binding constant for coordination of the second CO to $\mathbf{1^{OMe}}$ compared $\mathbf{1^{CF3}}$ or $\mathbf{1^{H}}$. For the most electron-rich cluster $\mathbf{1^{NMe2}}$, no well-defined features assignable to the monocarbonyl complex $\mathbf{1^{NMe2}}$**-CO** are observed, only those corresponding to the dicarbonyl adduct $\mathbf{1^{NMe2}\text{-}(CO)_2}$ at 1957 and 2013 cm^{-1}. The CO stretching frequencies of the mono- and dicarbonyl complexes are affected only slightly by the ligand changes (1942-1947 cm^{-1} for $\mathbf{1^{R}}$**-CO**, R = CF_3, H, OMe, 1984-1988 cm^{-1} as the average for $\mathbf{1^{R}\text{-}(CO)_2}$, R = CF_3, H, OMe, NMe_2). The monocarbonyl species show increased activation of CO, as expected, with the more electron-rich ligands. For dicarbonyl species, the same trend holds for **1^{R}-(CO)$_2$**, R = CF_3, H, OMe, NMe_2). However, the opposing trends in the proportion of mono- and dicarbonyl species generated as a function of different ligands is unexpected. Despite the higher binding affinity of **1^{OMe}** and **1^{NMe2}** for two molecules of CO at 195 K, neither exhibit discernable Fe-CO vibrational features upon warming to 273 K, suggesting a lower overall affinity for CO compared to **1^{CF3}** at this temperature.

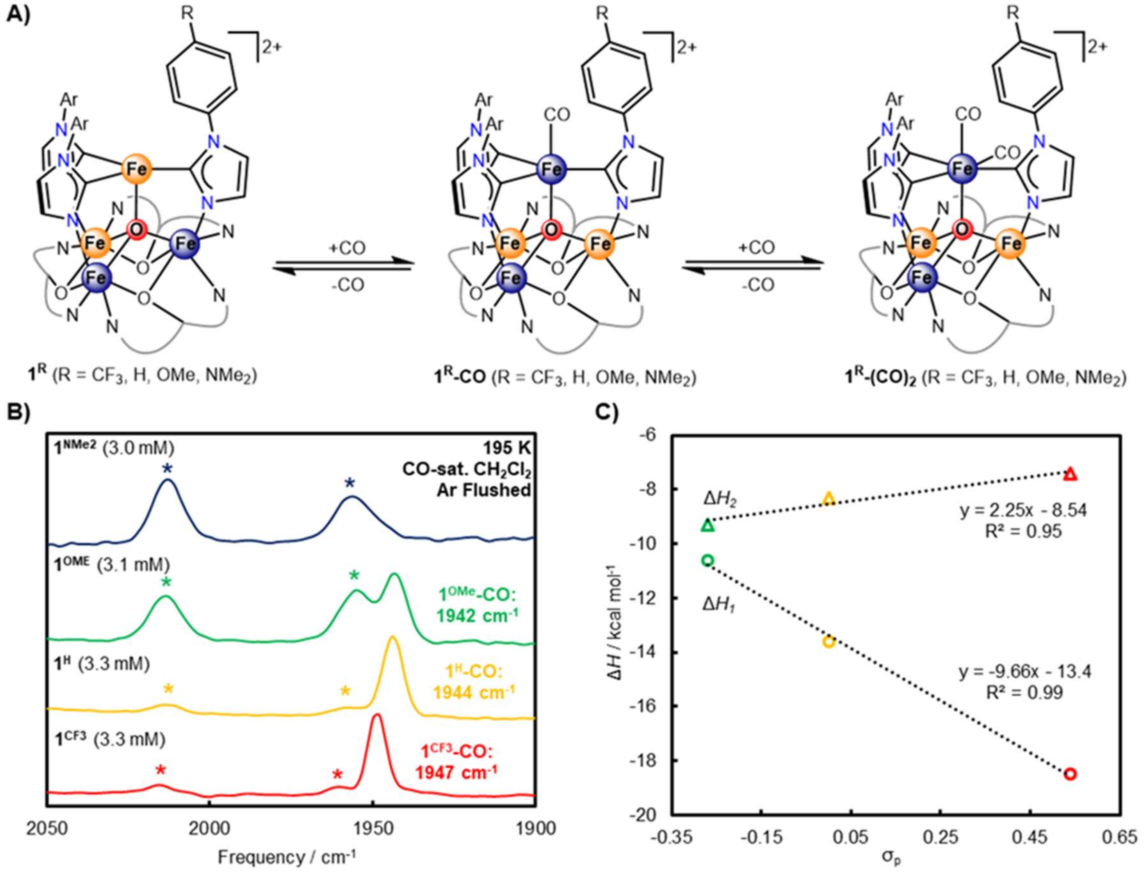

Figure 7. Ligand-Dependent CO Binding Trends. (A) Clusters **1^{R}** (R = CF_3, H, OMe, NMe_2) successively bind two molecules of CO at the apical Fe4 site. For structural characterization of representative examples of mono- and dicarbonyl adducts, see ref. 30. (B) Low temperature IR spectroscopy illustrates the influence of ligand modifications on the affinity of **1^{R}** (R = CF_3, H, OMe, NMe_2) for binding one vs. two molecules of CO. Asterisks denote features associated with the corresponding dicarbonyl species **1^{R}-(CO)$_2$** (R = CF_3, H, OMe, NMe_2). For experimental details and variable temperature data, see the Supporting Information. (C) Plot of the measured Δ*H* values for the first (bottom, circles) and second (top, triangles) CO binding events of **1^{CF3}** (red), **1^{H}** (orange), and **1^{OMe}** (green) vs. the substituent Hammett σ_p parameters.

CO Binding Energetics. The ligand-dependent trends in CO binding were confirmed by ^{1}H-NMR spectroscopy. Cooling solutions of $\mathbf{1^{CF3}}$ in dichloromethane-d_2 under an atmosphere of CO from 298 K to 268 K predominately affords the monocarbonyl complex $\mathbf{1^{CF3}}$**-CO** as the major species (84% at 268 K, NMR, Figure 48). Cooling beyond 268 K gradually converts $\mathbf{1^{CF3}}$**-CO** to the dicarbonyl complex $\mathbf{1^{CF3}\text{-}(CO)_2}$ (100% at 203 K). Compared to $\mathbf{1^{CF3}}$, significantly lower conversion of $\mathbf{1^{OMe}}$ to $\mathbf{1^{OMe}}$**-CO** is observed between 278-298 K (13% vs. 82% at 278K, NMR, Figure 49) under an atmosphere of CO under identical conditions (8.8 mM in CD_2Cl_2, P_{CO} = 1 atm). Moreover, the presence of $\mathbf{1^{OMe}}$ (>5%) in solution down to 243 K indicates that $\mathbf{1^{OMe}}$ has a lower overall affinity for CO than $\mathbf{1^{CF3}}$ in the temperature range 243-298 K. Whereas substantial amounts of $\mathbf{1^{CF3}}$**-CO** accumulate before significant quantities of $\mathbf{1^{CF3}\text{-}(CO)_2}$ are observed, appearance of $\mathbf{1^{OMe}}$**-CO** and $\mathbf{1^{OMe}\text{-}(CO)_2}$ occurs almost simultaneously (19% vs. 18%, respectively, at 268 K). As a result, full conversion of $\mathbf{1^{OMe}}$ to the dicarbonyl complex $\mathbf{1^{OMe}\text{-}(CO)_2}$ is achieved at higher temperatures (223 K compared to 203 K for $\mathbf{1^{CF3}\text{-}(CO)_2}$). For the more electron-rich $\mathbf{1^{NMe2}}$, ^{1}H-NMR features associated with the corresponding monocarbonyl adduct $\mathbf{1^{NMe2}}$**-CO** are not observed at any temperature, and full conversion to $\mathbf{1^{NMe2}\text{-}(CO)_2}$ occurs between 233-243 K (NMR, Figure 50). This does not simply result from a large binding constant associated with the second coordination event (with K_1 being constant) because, like $\mathbf{1^{OMe}}$, the onset temperature for CO binding (*c.a.* 268-278 K) is much lower than for $\mathbf{1^{CF3}}$ (>298 K). Thus, qualitatively, our variable temperature ^{1}H-NMR and IR studies indicate that the electronic effect of the remote ligand modifications have a disparate influence on the first and second CO binding events. Formation of the monocarbonyl adducts $[LFe_3O(^{R}ArIm)_3Fe(CO)]^{2+}$ is *suppressed* by electron-donating substituents, whereas formation of the dicarbonyl complexes $[LFe_3O(^{R}ArIm)_3Fe(CO)_2]^{2+}$ is *enhanced.*

To quantify the electronic effect of the remote ligand modifications, the CO-binding energetics of $\mathbf{1^{R}}$ (R = CF_3, H, OMe, NMe_2) were determined by ^{1}H-NMR spectroscopy with [Fc*][OTf] as an internal standard in a sealed capillary tube. At 278 K,[78] the CO binding constants of $\mathbf{1^{R}}$**-(CO)**$_2$ (R = CF_3, H, OMe) span nearly two orders of magnitude, decreasing monotonically from 9.3 atm^{-1} for $\mathbf{1^{CF3}}$ to 1.7 atm^{-1} for $\mathbf{1^{H}}$ and 0.2 atm^{-1} for $\mathbf{1^{OMe}}$ (all in dichloromethane-*d*$_2$, P_{CO} = 1 atm., Table 3). Van't Hoff analysis reveals that formation of the monocarbonyl adducts $\mathbf{1^{R}}$**-(CO)** (R = CF_3, H, OMe) is associated with a large entropic penalty, which has previously been explained by the loss of rotational freedom in the flanking aryl substituents upon binding of CO.[30] By comparison, the smaller entropic penalty associated with formation of the dicarbonyl adducts $\mathbf{1^{R}}$**-(CO)**$_2$ (R = CF_3, H, OMe) suggests that CO binding is cooperative, due to rotational "locking" of the aryl substituents following formation of the corresponding monocarbonyl adduct.

Table 3. Thermodynamics of CO Binding to $\mathbf{1^{R}}$ (R = CF_3, H, OMe, NMe_2) in dichloromethane.

Complex[a]	Ligand	$K_{278\,K}$ (atm^{-1})[b]	Δ*H* (kcal mol^{-1})	Δ*S* (cal mol^{-1} K^{-1})
$\mathbf{1^{CF3}}$ [c]	CO	9.3	-18.5(4)	-62(2)
$\mathbf{1^{H}}$ [d]	CO	1.7	-13.6(8)	-48(3)
$\mathbf{1^{OMe}}$ [e]	CO	0.2	-10.6(2)	-42(1)
$\mathbf{1^{NMe2}}$ [f]	2 CO	0.1	-23.2(9)	-88(4)
$\mathbf{1^{CF3}}$**-CO** [g]	CO	0.1	-7.4(1)	-31(1)
$\mathbf{1^{H}}$**-CO** [c]	CO	0.2	-8.3(5)	-32(2)
$\mathbf{1^{OMe}}$**-CO** [f]	CO	0.5	-9.3(3)	-35(1)

[a] Standard state: 1 atm. CO unless noted otherwise. [b] Binding energetics of $\mathbf{1^{R}}$ (R = CF_3, H, OMe, NMe_2) were determined by ^{1}H-NMR spectroscopy with [Fc*][OTf] as an internal standard in a sealed capillary tube. See supporting information for more details. [c] Binding constants measured between 263-308 K. [d] Data taken from ref. 30. [e] Binding constants measured between 243-283 K. [f] Binding constants measured between 243-278 K. [g] Binding constants measured between 213-278 K.

Insights into Ligand-Dependent CO Binding Trends. The linear correlation of the measured Fe-CO vibrational features with the Hammett substituent constants indicates that an electronic rearrangement occurs in $\mathbf{1^{CF3}}$ and $\mathbf{1^{OMe}}$ upon CO binding, analogous to that reported previously for $\mathbf{1^{H}}$.[30] We have proposed a thermodynamic model for ligand-induced redox reorganization which quantitatively describes the binding of CO at the apical Fe^{III} center of $\mathbf{1^{R}}$ (R = CF_3, H, OMe, NMe_2).[30] The measured ΔH values for the formation of $\mathbf{1^{R}}$**-CO** (R = CF_3, H, OMe) can be decomposed into two terms, one arising from the energetic cost of redox reorganization and the other from the intrinsic affinity of the incipient localized Fe^{II} site for CO (Figure 8B). The sensitivity of the first CO binding event to the substituent σ_p parameter ($\Delta\Delta H$ = -4.9 kcal·mol^{-1} for $\mathbf{1^{CF3}}$ and +3.0 kcal·mol^{-1} for $\mathbf{1^{OMe}}$, relative to $\mathbf{1^{H}}$) indicates that the redox reorganization energy is significantly perturbed by remote ligand modifications.

Importantly, the second CO binding event of 1^{R}, R = CF_3, H, OMe (formation of $\mathbf{1^{R}}$**-(CO)**$_2$, R = CF_3, H, OMe from $\mathbf{1^{R}}$**-CO**, R = CF_3, H, OMe) serves as an internal reference for remote substituent effect on CO binding *in the absence of redox reorganization.*[79] The small $\Delta\Delta H$ values calculated for the second CO binding events of of 1^{R}, R = CF_3, H, OMe (+0.9 kcal/mol for $\mathbf{1^{CF3}}$ and -1.0 kcal·mol^{-1} for $\mathbf{1^{OMe}}$, relative to $\mathbf{1^{H}}$) demonstrate that this intrinsic substituent influence is small, but the trend is consistent with the expectation that more reducing metal complexes should have a higher affinity for π-acids.[30, 80-81] Assuming that the intrinsic substituent effect is similar for both the first and second CO binding events, the effect of remote ligand modification on the redox reorganization energy (*RRE*, relative to that for $\mathbf{1^{H}}$) must be on the order of -5.8 kcal·mol^{-1} for $\mathbf{1^{CF3}}$ and +4.0 kcal·mol^{-1} for $\mathbf{1^{OMe}}$. Thus, incorporation of electron-donating substituents stabilizes ferric character at the apical metal site and increases the penalty associated with internal electronic rearrangements within the cluster, which would formally reduce Fe4, resulting in an inverted linear free energy relationship for CO binding (Figure 8b(ii)).

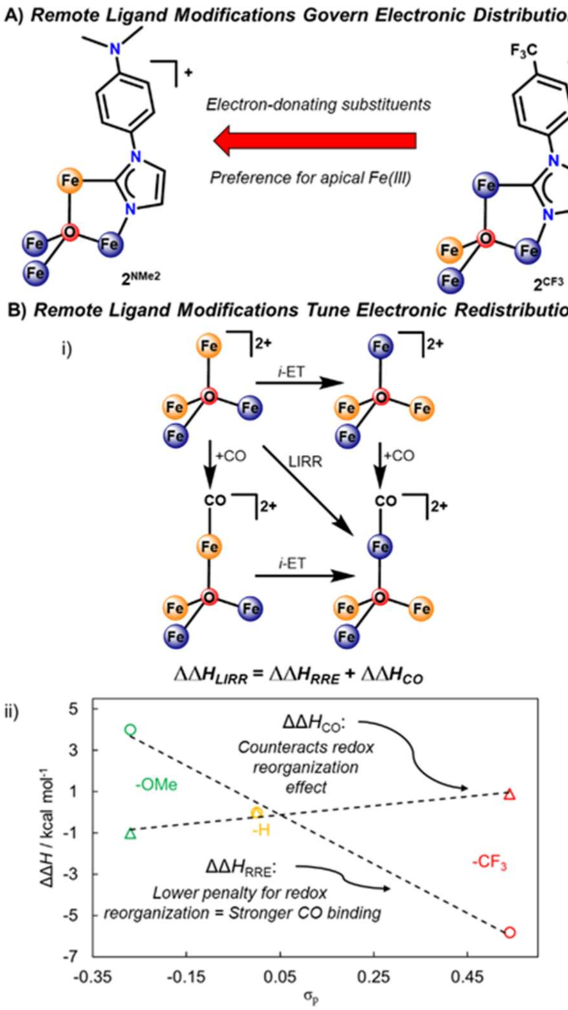

Figure 8. (A) Summary of the effect of remote ligand modifications on the electronic distribution of $\mathbf{1}^{\mathbf{R}}$ (R = CF_3, H, OMe, NMe_2). (B) (i) Thermodynamic model for binding of CO to $\mathbf{1}^{\mathbf{R}}$ (R = CF_3, H, OMe, NMe_2), coupled to an internal redox reorganization, which can be used to estimate the effect of remote ligand substitution of the redox reorganization energies of $\mathbf{1}^{\mathbf{R}}$ (R = CF_3, H, OMe, NMe_2).. (ii) Plot of the $\Delta\Delta H_{\mathrm{RRE}}$ (circles) and $\Delta\Delta H_{\mathrm{CO}}$ (triangles) values for $\mathbf{1}^{\mathbf{CF3}}$ (red), $\mathbf{1}^{\mathbf{H}}$ (orange) and $\mathbf{1}^{\mathbf{OMe}}$ (green) vs. the substituent Hammett σ_p parameters ($\mathbf{1}^{\mathbf{H}}$ is set to 0 for reference). Abbreviations: *iET* = internal electron transfer/redox reorganization, *LIRR* = ligand-induced redox reorganization, *RRE* = redox reorganization energy.

CONCLUSIONS

In summary, a series of site-differentiated iron clusters [$LFe_3O(^{R}ArIm)_3Fe$][OTf]$_2$ with tunable electronic properties was synthesized, and binding of up to two molecules of CO was observed. The cluster's redox properties and CO stretching shift as expected based on the electronic properties of the ligand: electron-donating substituents result in more reducing clusters and weaker C-O bonds. Moreover, the electronic character of a remote ligand substituent was found to significantly affect the energetics of CO binding ($\Delta\Delta H$ as much as 7.9 kcal·mol^{-1}) at a single ferric iron site within the cluster. Surprisingly, however, electron-donating substituents *suppress* the first CO binding event but *enhance* the second. Spectroscopic studies reveal that these substituent effects result from changes in the penalty associated with electronic redistribution, which is an essential feature of the first CO binding event. To the best of our knowledge, the clusters discussed herein are the first to simultaneously exhibit "normal" and inverted free energy relatioships for CO binding. This unique feature of multimetallic complexes which must undergo electronic rearrangement to accomodate small molecule binding could be potentially useful in controlling product selectivity, for example in the reduction of CO to hydrocarbons, by providing a means to independently tune sequential CO binding constants.[82] More broadly, the unusual ligand-dependent trends in diatomic binding reported herein highlight how the first and/or second coordination sphere of a transition metal cluster could be rationally tuned to flip traditional thermodynamic scaling relationships towards controlling small molecule activation.

EXPERIMENTAL DETAILS

General Considerations. All reactions were performed at room temperature in a nitrogen filled M. Braun glovebox or using standard Schlenk techniques unless otherwise specified. Glassware was oven dried at 140°C for at least two hours prior to use, and allowed to cool under vacuum. The *N*-substituted aryl imidazoles ^{pOMe}ArIm and ^{pNMe2}ArIm were synthesized from the corresponding anilines, glyoxal, formaldehyde, and aqueous ammonia based on a literature procedure.[83] ^{pCF3}ArIm was prepared from the corresponding aniline, thiophosgene and aminoacetylaldehyde diethyl acetal based on an adapted literature procedure.[83] All aryl imidazoles were further purified by sublimation at 100°C under vacuum. $Fe(OTf)_2(MeCN)_2$,[84] [Fc][OTf][85] and $Na[BAr^F_{24}]$[86] were prepared according to literature procedures. $[Fc^*][OTf]$ was prepared by oxidation of Fc^* with [Fc][OTf] in dichloromethane followed by crystallization from dichloromethane/pentane. $LFe_3(OTf)_3$, $[LFe_3O(PhIm)_3Fe][OTf]_2$ (1^H) and $[LFe_3O(PhIm)_3Fe]$ were prepared as previously described.[30] All other reagents were obtained commercially unless otherwise noted and typically stored over activated 4 Å molecular sieves. Tetrahydrofuran was dried using sodium/benzophenone ketyl, degassed with three freeze-pump-thaw cycles, vacuum transferred, and stored over 3 Å molecular sieves prior to use. Dichloromethane, diethyl ether, benzene, acetonitrile, hexanes, and pentane were dried by sparging with nitrogen for at least 15 minutes, then passing through a column of activated A2 alumina under positive nitrogen pressure. Dichloromethane-d_2 was dried over calcium hydride, degassed by three freeze-pump-thaw cycles, and vacuum transferred prior to use. ^1H and ^{19}F NMR spectra were recorded on a Varian 300 or 400 MHz spectrometer. All chemical shifts (δ) are reported in ppm, and coupling constants (J) are in hertz. The ^1H-NMR spectra were referenced using residual H impurity in the deuterated solvent, whereas the ^{19}F chemical shifts are reported relative to the internal lock signal. UV-Vis spectra were recorded on a Varian Cary Bio 50 spectrophotometer. Infrared (ATR-IR) spectra were recorded on a Bruker ALPHA ATR-IR spectrometer. Solution ATR-IR spectra were recorded on a Mettler Toledo iC10 ReactIR. Elemental analyses were performed at Caltech.

Physical Methods

Mössbauer Measurements. Zero field ^{57}Fe Mössbauer spectra were recorded in constant acceleration on a spectrometer from See Co (Edina, MN) equipped with an SVT-400 cryostat (Janis, Wilmington, WA). The quoted isomer shifts are relative to the centroid of the spectrum of α-Fe foil at room temperature. Unless otherwise noted, samples were prepared by grinding polycrystalline (20-50 mg) into a fine powder and pressed into a homogenous pellet with boron nitride in a cup fitted with a screw cap. The data were fitted to Lorentzian lineshapes using the program WMOSS (www.wmoss.org).

EPR Spectroscopy. X-band EPR spectra were collected on a Bruker EMX spectrometer equipped with a He flow cryostat. Samples were prepared as frozen glasses in 4:5 propionitrile/butyronitrile or 2-MeTHF. Spectra were collected with microwave powers ranging from 0.5 mW to 8 mW with modulation amplitudes of 4 Gauss. Spectral simulations were conducted with EasySpin.[87]

Magnetic Measurements. Magnetic measurements were conducted with a Quantum Design MPMS3 SQUID Magnetometer at the University of California, Los Angeles. Polycrystalline samples were wrapped in plastic film and placed in a gelatin capsule. The capsule was then inserted into a plastic straw. Magnetization data at 100 K from 0 to 4 T were collected to confirm the absence of ferromagnetic impurities. Direct current variable temperature magnetic susceptibility measurements were collected between 1.8 and 300 K with a 0.1 T field. Reduced magnetization data was collected between 1.8 and 9 K at fields between 1 and 7 T. Magnetic susceptibility data was corrected for diamagnetism of the sample, estimated using Pascal's constants, as well as the sample holder. Magnetic susceptibility and reduced magnetization data was simulated with PHI.[88]

Electrochemical Measurements. CVs were recorded with a Pine Instrument Company AFCBP1 bipotentiostat using the AfterMath software package. All measurements were performed in a three-electrode cell, which consisted of (1) a glassy carbon working electrode, (2) a Pt wire counter electrode, and (3) a Ag wire reference electrode. Dry solvent that contained 0.1 M *n*Bu_4NPF_6 was employed as the electrolyte solution for all electrochemical measurements. All electrochemical measurements were performed at room temperature in an M. Braun nitrogen filled glovebox. The ferrocene/ferrocenium (Fc/Fc^+) redox couple was used as an internal standard for all measurements.

X-ray Crystallography. For compounds 1^{CF3}, 1^{H}, 2^{CF3}, 1^{H}, and 1^{NMe2}, low-temperature (100 K) diffraction data (φ-and ω-scans) were collected on a Bruker AXS D8 VENTURE KAPPA diffractometer coupled to a PHOTON 100 CMOS detector with Mo Kα radiation (λ = 0.71073 Å) or with Cu Kα (λ = 1.54178 Å). All diffractometer manipulations, including data collection, integration, and scaling were carried out using the Bruker APEXII software.[89] Absorption corrections were applied using SADABS.[90] Structures were solved by direct methods using SHELXS[91] and refined against *F*2 on all data by full-matrix least squares with SHELXL-2014[92] interfaced with Olex2-1.2.8[93] and using established refinement techniques. All non-hydrogen atoms were refined anisotropically, except heavily disordered solvent in some cases. All hydrogen atoms were included into the model at geometrically calculated positions and refined using a riding model. The isotropic displacement parameters of all hydrogen atoms were fixed to 1.2 times the *U* value of the atoms they are linked to (1.5 times for methyl groups). All disordered atoms were refined with the help of similarity restraints on the 1,2- and 1,3-distances and displacement parameters as well as enhanced rigid bond restraints for anisotropic displacement parameters. Due to the size of the compounds, most crystals included solvent accessible voids, which tended to contain disordered solvent. In most cases, this disorder could be modeled satisfactorily. Furthermore, the long-range order of these crystals and amount of high-angle data was in some cases not ideal, due to desolvation of the crystals and/or solvent disorder.

Positionally Resolved X-ray Crystallography. Radiation damage was a significant issue (Supplementary Fig. 89), and we have only been able to obtain acceptable quality data for 2^{CF3}. For 2^{CF3}, anomalous diffraction data was collected at SSRL beamline 12-2. Samples were mounted at 100K and subjected to a "MAD-scan" at the Fe K-edge. Wavelenghts for subsequent datasets were chosen as +/-10eV around the inflection point. A dataset at 17keV was collected on a PILATUS 6M detector at a distance of 188mm to serve as a reference. Subsequently, full spheres of diffraction data were collected across the edge from low to high energy. The data were processed with XDS and brought on a common scale with XSCALE.[94] Structures previously solved and refined using SHELX were converted into PDB format using MERCURY. This file was used in combination with the XDS_ASCII.HKL from the 17keV dataset to refine the structure in PHENIX.[95] Setting the geometry target weight wc to zero allows for unrestrained refinement and results in an R-factor (5.35%) comparable to the original refinement in SHELXL. This refined model was then subjected to refinement against datasets at the energies across the Fe K-edge. The only parameters refined were f' and f" for the individual Fe atoms.

Synthetic Procedures. *Preparation of* $[LFe_3O(ArIm\text{-}H)_n(OTf)_{3-n}][OTf]_n$ *Precursors.* A solution of the *N*-aryl imidazole ArIm-H (2.34 mmol, 3.1 equiv.) in dichloromethane (3 mL) was added dropwise to a stirring suspension of $LFe_3(OTf)_3$ (1.01 g, 0.689 mmol, 1 equiv.) in dichloromethane (5 mL). The resulting orange solution was allowed to stir for one hour, at which point it was frozen in a glovebox cold well. The frozen mixture was removed from the cold well, and iodosobenzene (152 mg, 0.689 mmol, 1 equiv.) was added upon thawing. After stirring for one hour, the resulting dark brown solution was concentrated under vacuum. Tetrahydrofuran was added to the residue, and the suspension was stirred overnight. The precipitate was then collected on a bed of Celite, washed with additional tetrahydrofuran, and then eluted with dichloromethane. The volatiles were removed under reduced pressure. Prior to use in subsequent reactions, the trimetallic precursors [LFe$_3$O(ArIm)$_n$(OTf)$_{3-n}$][OTf]$_n$ were crystallized by diffusion of diethyl ether in concentrated dichloromethane solutions of the compound.

[LFe$_3$O(^{pCF3}ArIm-H)$_3$][OTf]$_3$, (A). ^{1}H NMR (300 MHz, CD$_2$Cl$_2$) δ 102.04 (b), 99.56 (b), 97.30 (b), 79.75 (b), 77.62 (b), 74.10 (b), 68.77 (b), 67.29 (b), 65.72 (b), 64.94 (b), 58.13 (b), 49.75 (b), 48.96 (b), 47.17 (b), 46.14 (b), 44.44 (b), 44.00 (b), 39.36 (b), 16.23 (b), 15.08 (b), 13.81 (b), 13.12 (b), 12.17 (b), 10.75 (b), 9.11 (b), -1.07 (b), -4.23 (b), -6.97 (b). ^{19}F NMR (300 MHz, CD$_2$Cl$_2$) δ -9.16 (s), -63.05 (s), -78.23 (s).

[LFe$_3$O(^{pOMe}ArIm-H)$_3$][OTf]$_3$, (B). ^{1}H NMR (300 MHz, CD$_2$Cl$_2$) δ 101.64 (b), 99.07 (b), 96.59 (b), 79.68 (s), 78.40 (b), 77.12 (b), 76.14 (b), 69.14 (b), 66.81 (s). 66.20 (s), 63.56 (s), 57.44 (s), 50.27 (s), 48.93 (b), 47.57 (s), 46.12 (s), 44.30 (s), 43.76 (s), 42.80 (s), 41.75 (b), 26.24 (b), 17.06 (s), 16.10 (s), 15.49 (s), 14.37 (s), 13.98 (b), 13.16 (s), 12.24 (s), 11.33 (b), 10.64 (s), 9.95 (s), 9.68 (b), 8.54 (s), 6.89 (s), 6.52 (s), 0.68 (b), -1.31 (b), -3.48 (b), -6.86 (b). ^{19}F NMR (300 MHz, CD$_2$Cl$_2$) δ -10.12 (s), -78.01 (s).

[LFe$_3$O(^{pNMe2}ArIm-H)$_3$][OTf]$_3$, (C). ^{1}H NMR (300 MHz, CD$_2$Cl$_2$) δ 102.23 (b), 100.31 (b), 97.97 (b), 95.10 (b), 79.19 (b), 76.20 (b), 73.29 (b), 68.60 (b), 67.29 (s), 65.21 (s), 63.74 (b), 60.72 (b), 55.83 (s), 49.62 (s), 48.48 (b), 45.87 (s), 45.30 (b), 43.42 (s), 42.69 (s), 41.54 (s), 26.69 (b), 16.04 (s), 15.49 (s), 15.21 (s), 13.88 (s), 13.67 (s), 13.39 (s), 12.23 (s), 11.85 (s), 10.85 (s), 10.24 (s), 9.25 (s), 8.54 (b), -0.01 (b), -2.16 (b), -4.53 (b), -8.23 (b). ^{19}F NMR (300 MHz, CD$_2$Cl$_2$) δ -8.79 (b), -78.10 (s).

Preparation of [LFe$_3$O(ArIm)$_3$Fe][OTf]$_2$. A solution of ArIm-H (0.40 mmol, 1 equiv.) in 3 mL tetrahydrofuran was added to a suspension of [LFe$_3$O(ArIm-H)$_3$][OTf]$_3$ (0.40 mmol, 1 equiv.) 3 mL of tetrahydrofuran. The mixture was then frozen in a glovebox cold well. The frozen mixture was removed from the cold well and a thawing solution of Na[N(SiMe$_3$)$_2$] (232 mg, 1.27 mmol, 3.2 equiv.) in 2 mL of tetrahydrofuran was added dropwise. After stirring for 1 hour at room temperature, the mixture was once again frozen in the cold well. The frozen mixture was then removed from the cold well, and a thawing slurry of Fe(OTf)$_2$(MeCN)$_2$ (182 mg, 0.42 mmol, 1.05 equiv.) in 3.5 mL of tetrahydrofuran was added dropwise. After stirring for 22 hours at room temperature, the mixture was filtered over a bed of Celite, washed with additional tetrahydrofuran, and eluted with dichloromethane. The volatiles were removed under reduced pressure to afford [LFe$_3$O(ArIm)$_3$Fe][OTf]$_2$ as a dark brown solid.

[LFe$_3$O(^{pCF3}ArIm)$_3$Fe][OTf]$_2$, (1^{CF3}). (285 mg, 35% yield). Crystals suitable for X-ray diffraction were grown by diffusion of diethyl ether into a dilute solution of the compound in dichloromethane/acetonitrile (1:1). ^{1}H NMR (300 MHz, CD$_2$Cl$_2$) δ 114.11 (b), 74.98 (s). 72.14 (s), 67.45 (b), 49.60 (s), 46.99 (s), 42.82 (s), 26.35 (b), 19.06 (s), 13.48 (s), 12.78 (s), 12.52 (s), -1.23 (s), -4.76 (s). ^{19}F NMR (300 MHz, CD$_2$Cl$_2$) δ -78.83 (s), -62.93 (s). UV-Vis (CH$_3$CN) [ε (M^{-1} cm^{-1})]: 447 nm (7.4 x 10^3). Anal. Calcd (%) for C$_{89}$H$_{57}$F$_{15}$Fe$_4$N$_{12}$O$_{10}$S$_2$: C, 52.74; H, 2.83; N, 8.29. Found: C, 52.57; H, 3.02; N, 8.26.

[LFe$_3$O(^{pOMe}ArIm)$_3$Fe][OTf]$_2$, (1^{OMe}). (100 mg, 13% yield). Crystals suitable for X-ray diffraction were grown by diffusion of diethyl ether into a dilute solution of the compound in dichloromethane/acetonitrile (1:1). ^{1}H NMR (300 MHz, CD$_2$Cl$_2$) δ 116.47 (b), 75.69 (s), 73.99 (s), 70.55 (b), 51.42 (s), 47.08 (s), 46.35 (s), 21.36 (b), 20.18 (s), 14.67 (s), 12.29 (s), -4.30 (s), -6.33 (s). ^{19}F NMR (300 MHz, CD$_2$Cl$_2$) δ -78.32. UV-Vis (CH$_2$Cl$_2$) [ε (M^{-1} cm^{-1})]: 461 nm (8.14

x 10^3). Anal. Calcd (%) for $C_{89}H_{66}F_6Fe_4N_{12}O_{13}S_2$: C, 55.88; H, 3.48; N, 8.79. Found: C, 55.54; H, 3.66; N, 8.51.

[LFe$_3$O(^{pNMe2}ArIm)$_3$Fe][OTf]$_2$, (1^{NMe2}). (79.4 mg, 10% yield). Crystals suitable for X-ray diffraction were grown by diffusion of diethyl ether into a dilute solution of the compound in dichloromethane/acetonitrile (1:1). ^{1}H NMR (300 MHz, CD_2Cl_2) δ 115.72 (b), 74.71 (s), 73.37 (s), 70.44 (b), 51.16 (s), 46.76 (s), 45.61 (s), 21.71 (b), 20.46 (s), 14.88 (s), 12.35 (s), -3.58 (b), -7.05 (s). ^{19}F NMR (300 MHz, CD_2Cl_2) δ -79.33. UV-Vis (acetone) [ε (M^{-1} cm^{-1})]: 443 nm (7.85 x 10^3), 598 nm (2.90 x 10^3). Anal. Calcd (%) for $C_{92}H_{75}F_6Fe_4N_{15}O_{10}S_2$: C, 56.60; H, 3.87; N, 10.76. Found: C, 56.00; H, 4.05; N, 10.46.

Preparation of [LFe$_3$O(^{pCF3}ArIm)$_3$Fe][OTf], (2^{CF3}). A solution of Cp*$_2$Co (22.3 mg, 0.068 mmol, 1.0 equiv.) in 1 mL tetrahydrofuran was added dropwise to a stirring suspenion of [LFe$_3$O(^{pCF3}ArIm)$_3$Fe][OTf]$_2$ (137.5 mg, 0.068 mmol, 1.0 equiv.) in 4 mL of tetrahydrofuran. After one hour, the reaction mixture was filtered over a bed of Celite to remove [Cp$^*_2$Co][OTf]. The volatiles were removed under reduced pressure to afford [LFe$_3$O(^{pCF3}ArIm)$_3$Fe][OTf] as a pink-purple solid (110 mg, 86% yield). Crystals suitable for X-ray diffraction were obtained by diffusion of diethyl ether into a dilute solution of the compound in 1:1 dichloromethane:acetonitrile. ^{1}H NMR (300 MHz, CD_2Cl_2) δ 95.46 (b), 59.28 (s), 56.86 (s), 39.91 (b), 37.38 (s), 34.98 (s), 29.19 (s), 23.58 (s), 12.84 (s), 12.31 (s), 11.45 (s), 9.75 (s), -4.75 (s). ^{19}F NMR (300 MHz, CD_2Cl_2) δ -77.53 (s), -60.10 (s). UV-Vis (CH_2Cl_2) [ε (M^{-1} cm^{-1})]: 502 nm (4.05 x 10^3). Anal. Calcd (%) for $C_{88}H_{57}F_{12}Fe_4N_{12}O_7S$: C, 56.28; H, 3.06; N, 8.95. Found: C, 56.33; H, 3.58; N, 8.98.

Preparation of [LFe$_3$O(PhIm)$_3$Fe][BF$_4$], (2^H). A solution of [Cp$_2$Co][BF$_4$] (10.3 mg, 0.037 mmol, 1 equiv.) in minimal acetonitrile was added to a suspension of freshly prepared [LFe$_3$O(PhIm)$_3$Fe] (108.8 mg, 0.071 mmol) in thawing tetrahydrofuran (5 mL). After stirring for one hour, the volatiles were removed under vacuum, and the residue washed with diethyl ether to remove Cp_2Co, affording $[LFe_3O(PhIm)_3Fe][BF_4]$ as a dark purple solid (102 mg, 89% yield). Crystals suitable for X-ray diffraction were obtained by diffusion of diethyl ether into a dilute solution of the compound in dichloromethane. ^1H NMR (300 MHz, CD_2Cl_2): identical to that for $[LFe_3O(PhIm)_3Fe][OTf]$ (2-OTf). ^{19}F NMR (300 MHz, CD_2Cl_2) δ -151.70.

Preparation of $[LFe_3O(^{pNMe2}ArIm)_3Fe][OTf]$, ($2^{NMe2}$-OTf). A solution of $Cp^*{}_2Co$ (10.8 mg, 0.033 mmol, 1.0 equiv.) in 1 mL tetrahydrofuran was added dropwise to a stirring suspenion of $[LFe_3O(^{pNMe2}ArIm)_3Fe][OTf]_2$ (63.9 mg, 0.033 mmol, 1.0 equiv.) in 4 mL of tetrahydrofuran. After stirring for four hours, the resulting black-purple precipitate was collected on a bed of Celite and eluted with 1,2-dimethoxyethane. The combined filtrates were concentrated to dryness under reduced pressure to afford $[LFe_3O(^{pNMe2}ArIm)_3Fe][OTf]$ as a black-purple solid (54 mg, 91% yield). ^1H NMR (300 MHz, CD_2Cl_2) δ 108.95 (b), 57.97 (s), 43.61 (b), 40.23 (s), 37.57 (s), 35.13 (s), 25.44 (s), 14.68 (s), 13.33 (s), 12.41 (s), 10.90 (b), -4.94 (b). ^{19}F NMR (300 MHz, CD_2Cl_2) δ -78.95. UV-Vis (CH_2Cl_2) [ε ($M^{-1}\,cm^{-1}$)]: 566 nm (4.64×10^3), 443 nm (5.60×10^3). Anal. Calcd (%) for $C_{92}H_{77}Cl_2F_3Fe_4N_{15}O_7S$: C, 58.53; H, 4.11; N, 11.83. Found: C, 58.75; H, 4.56; N, 11.30.

Preparation of $[LFe_3O(^{pNMe2}ArIm)_3Fe][BF_4]$, ($2^{NMe2}$-$BF_4$). A suspension of $[LFe_3O(pNMe_2ArIm)_3Fe]$ $[OTf]_2$ (126.5 mg, 0.065 mmol, 1 equiv.) in 5 mL of tetahydrofuran was added to a suspension of 2% Na(Hg) amalgam (7.5 mg Na, 0.32 mmol, 5 equiv.) in 5 mL of tetrahydrofuran. After stirring for four hours, the suspension was decanted from the Na(Hg) amalgam and filtered through a fine frit. The metallic blue precipitate was washed with copious amounts of tetrahydrofuran, affording $[LFe_3O(^{pNMe2}ArIm)_3Fe]$ (61.5 mg, 0.037 mmol, 57% yield) which was used immediately without further purification.

A solution of $[Cp_2Co][BF_4]$ (10.3 mg, 0.037 mmol, 1 equiv.) in minimal acetonitrile was added to a suspension of freshly prepared $[LFe_3O(^{pNMe2}ArIm)_3Fe]$ (31.5 mg, 0.021 mmol) in thawing tetrahydrofuran (1 mL). After stirring for one hour, the volatiles were removed under vacuum and the residue washed with diethyl ether to remove Cp_2Co, affording $[LFe_3O(^{pNMe2}ArIm)_3Fe][BF_4]$ as a black-purple solid (59 mg, 92% yield). Crystals suitable for X-ray diffraction were obtained by diffusion of diethyl ether into a dilute solution of the compound in dichloromethane. ^{1}H NMR (300 MHz, CD_2Cl_2): identical to that for $[LFe_3O(^{pNMe2}ArIm)_3Fe][OTf]$ (2^{NMe2}-OTf). ^{19}F NMR (300 MHz, CD_2Cl_2) δ -152.91.

Supplemental Figures

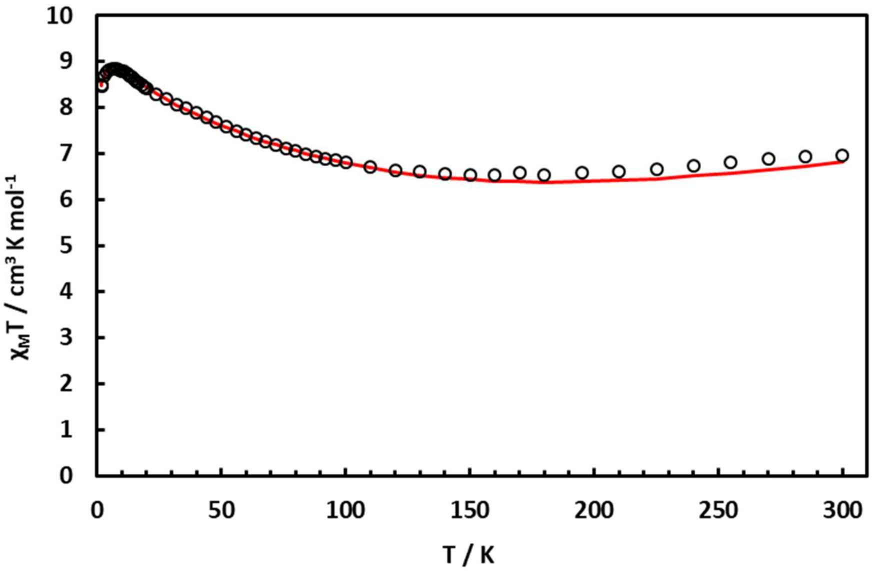

Figure S1. Direct current variable temperature magnetic susceptibility measurements for $[LFe_3O(^{pCF3}ArIm)_3Fe][OTf]_2$ (1^{CF3}) collected between 1.8 and 300 K with a 0.1 T field after diamagnetic correction (black circles). Full Fit parameters: $S_1 = S_3 = 2$, $S_2 = S_4 = 5/2$; $g_1 = g_2 = g_3 = g_4 = 2.00$; $|D_1| = |D_3| = 0.77$ cm^{-1}, $|D_2| = 1.99$ cm^{-1}, $|D_4| = 1.96$ cm^{-1}; $J_{14} = J_{34} = -22.7$ cm^{-1}, $J_{24} = -32.2$ cm^{-1}, $J_{12} = J_{23} = -0.1$ cm^{-1}, $J_{13} = -13.5$ cm^{-1}.

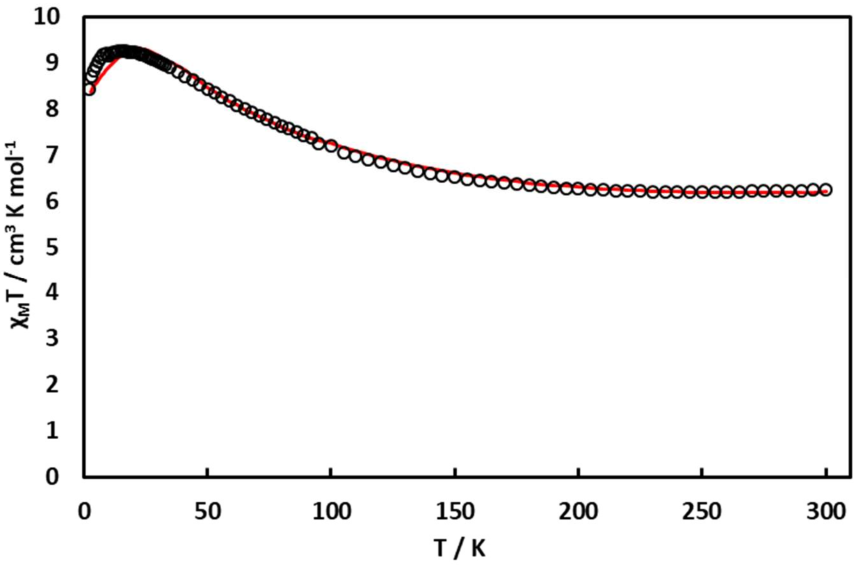

Figure S2. Direct current variable temperature magnetic susceptibility measurements for $[LFe_3O(^{pNMe2}ArIm)_3Fe][OTf]_2$ (1^{NMe2}) collected between 1.8 and 300 K with a 0.1 T field after diamagnetic correction (black circles). Best fit parameters including zero-field splitting effects: $S_1 = S_3 = 2$, $S_2 = S_4 = 5/2$; $g_1 = g_2 = g_3 = g_4 = 2.00$; $|D_1| = |D_3| = 5.8$ cm^{-1}, $|D_2| = 0$ cm^{-1}, $|D_4| = 0.8$ cm^{-1}; $J_{14} = J_{34} = -26.1$ cm^{-1}, $J_{24} = -69.4$ cm^{-1}, $J_{12} = J_{23} = -4.5$ cm^{-1}, $J_{13} = -10$ cm^{-1}.

Summary Tables

Table 3: Crystal and refinement data for precursor complexes $\mathbf{1^{CF3}}$ and $\mathbf{2^{CF3}}$.

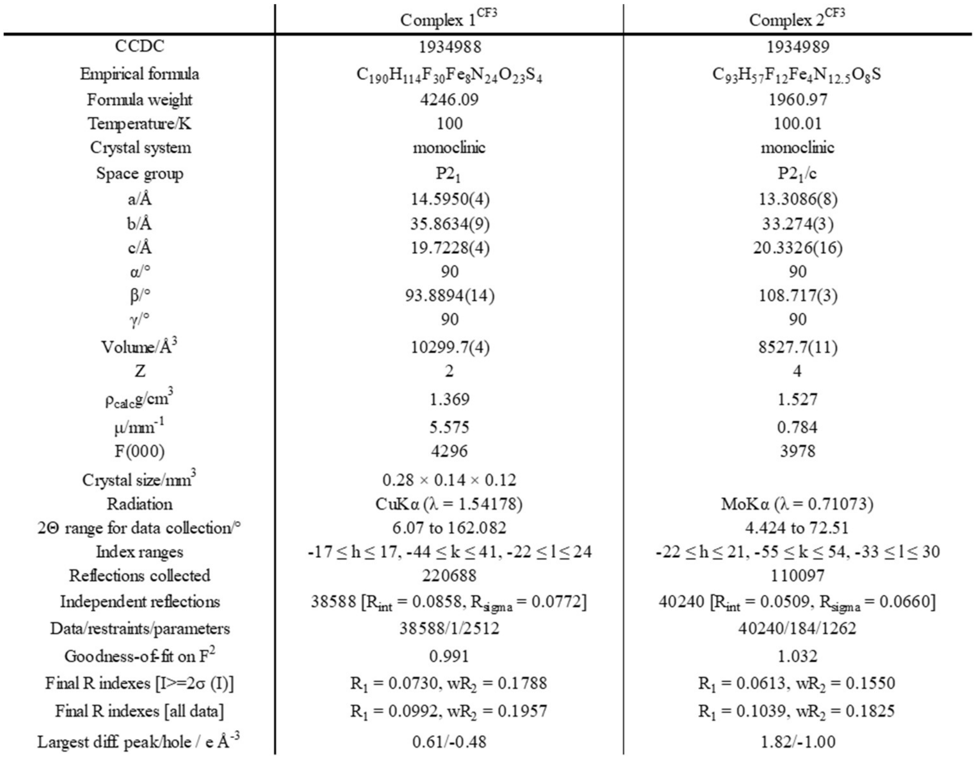

	Complex 1^{CF3}	Complex 2^{CF3}
CCDC	1934988	1934989
Empirical formula	$C_{190}H_{114}F_{30}Fe_8N_{24}O_{23}S_4$	$C_{93}H_{57}F_{12}Fe_4N_{12.5}O_8S$
Formula weight	4246.09	1960.97
Temperature/K	100	100.01
Crystal system	monoclinic	monoclinic
Space group	$P2_1$	$P2_1/c$
a/Å	14.5950(4)	13.3086(8)
b/Å	35.8634(9)	33.274(3)
c/Å	19.7228(4)	20.3326(16)
α/°	90	90
β/°	93.8894(14)	108.717(3)
γ/°	90	90
Volume/Å^3	10299.7(4)	8527.7(11)
Z	2	4
ρ_{calc}g/cm^3	1.369	1.527
μ/mm^{-1}	5.575	0.784
F(000)	4296	3978
Crystal size/mm^3	0.28 × 0.14 × 0.12	
Radiation	CuKα (λ = 1.54178)	MoKα (λ = 0.71073)
2Θ range for data collection/°	6.07 to 162.082	4.424 to 72.51
Index ranges	$-17 \le h \le 17$, $-44 \le k \le 41$, $-22 \le l \le 24$	$-22 \le h \le 21$, $-55 \le k \le 54$, $-33 \le l \le 30$
Reflections collected	220688	110097
Independent reflections	38588 [R_{int} = 0.0858, R_{sigma} = 0.0772]	40240 [R_{int} = 0.0509, R_{sigma} = 0.0660]
Data/restraints/parameters	38588/1/2512	40240/184/1262
Goodness-of-fit on F^2	0.991	1.032
Final R indexes [I>=2σ (I)]	R_1 = 0.0730, wR_2 = 0.1788	R_1 = 0.0613, wR_2 = 0.1550
Final R indexes [all data]	R_1 = 0.0992, wR_2 = 0.1957	R_1 = 0.1039, wR_2 = 0.1825
Largest diff. peak/hole / e Å^{-3}	0.61/-0.48	1.82/-1.00

Table 4: Crystal and refinement data for precursor complexes $\mathbf{2^{H}}$ and $\mathbf{2^{NMe2}}$.

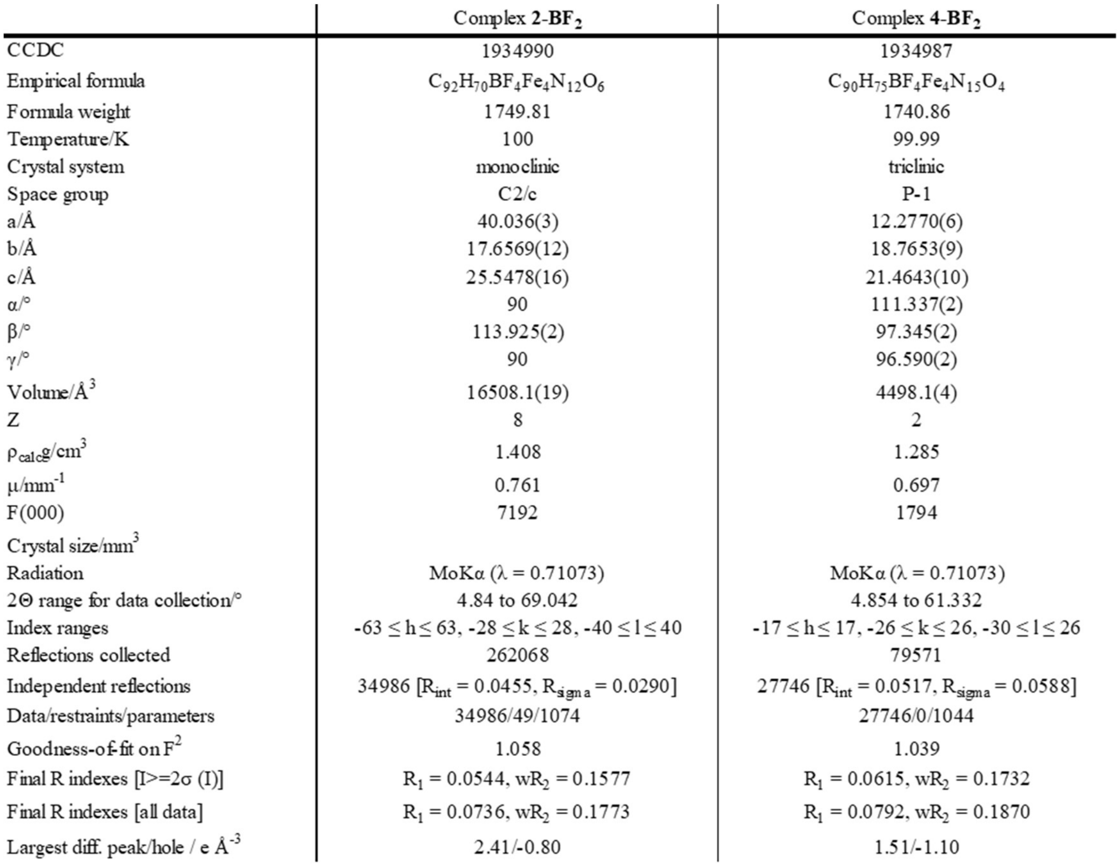

	Complex **2-BF$_2$**	Complex **4-BF$_2$**
CCDC	1934990	1934987
Empirical formula	$C_{92}H_{70}BF_4Fe_4N_{12}O_6$	$C_{90}H_{75}BF_4Fe_4N_{15}O_4$
Formula weight	1749.81	1740.86
Temperature/K	100	99.99
Crystal system	monoclinic	triclinic
Space group	C2/c	P-1
a/Å	40.036(3)	12.2770(6)
b/Å	17.6569(12)	18.7653(9)
c/Å	25.5478(16)	21.4643(10)
α/°	90	111.337(2)
β/°	113.925(2)	97.345(2)
γ/°	90	96.590(2)
Volume/Å^3	16508.1(19)	4498.1(4)
Z	8	2
ρ_{calc}g/cm^3	1.408	1.285
μ/mm^{-1}	0.761	0.697
F(000)	7192	1794
Crystal size/mm^3		
Radiation	MoKα (λ = 0.71073)	MoKα (λ = 0.71073)
2Θ range for data collection/°	4.84 to 69.042	4.854 to 61.332
Index ranges	$-63 \leq h \leq 63$, $-28 \leq k \leq 28$, $-40 \leq l \leq 40$	$-17 \leq h \leq 17$, $-26 \leq k \leq 26$, $-30 \leq l \leq 26$
Reflections collected	262068	79571
Independent reflections	34986 [R_{int} = 0.0455, R_{sigma} = 0.0290]	27746 [R_{int} = 0.0517, R_{sigma} = 0.0588]
Data/restraints/parameters	34986/49/1074	27746/0/1044
Goodness-of-fit on F^2	1.058	1.039
Final R indexes [I>=2σ (I)]	R_1 = 0.0544, wR_2 = 0.1577	R_1 = 0.0615, wR_2 = 0.1732
Final R indexes [all data]	R_1 = 0.0736, wR_2 = 0.1773	R_1 = 0.0792, wR_2 = 0.1870
Largest diff. peak/hole / e Å^{-3}	2.41/-0.80	1.51/-1.10

Special Refinement Details for [LFe$_3$O(^{pCF3}ArIm)$_3$Fe][OTf]$_2$. Compound 1^{CF3} crystallizes in the monoclinic space group *P*2$_1$ with two molecules in the asymmetric unit along with three molecules of co-crystallized diethyl ether. One molecule has disorder in one of the trifluoromethyl substituents. The diffraction data is not of sufficient quality for a discussion of bond lengths. However, it is enough to positively identify 1^{CF3} as [LFe$_3$O(^{pCF3}ArIm)$_3$Fe][OTf]$_2$.

Special Refinement Details for [LFe$_3$O(^{pCF3}ArIm)$_3$Fe][OTf]. Compound 2^{CF3} crystallizes in the monoclinic space group *P*2$_1$/c with one molecule in the asymmetric unit along co-crystallized diethyl ether and acetonitrile. The co-crystallized acetonitrile molecule is located near a special position (inversion center) and was modelled with the aid of a similarity restraint on the 1,2 distances and enhanced rigid bond restraints on all components of the disorder.

Additionally, the triflate counterion is disordered over two positions with occupancies of 63% and 37% and was modelled with the help of similarity restraints on the 1,2 distances and enhanced rigid bond restraints on all components of the disorder.

Special Refinement Details for [$LFe_3O(PhIm)_3Fe$][BF_4]. Compound 2^H crystallizes in the monoclinic space group C2/c with one molecule in the asymmetric unit along co-crystallized diethyl ether. One molecule of diethyl ether is disordered near a special position and was modelled isotropically with the aid of enhanced rigid bond restraints on all components of the disorder. Additionally, the tetrafluoroborate anion is disordered and was modelled with the help of similarity restraints on the 1,2 distances and enhanced rigid bond restraints on all components of the disorder.

Special Refinement Details for [$LFe_3O(^{pNMe2}ArIm)_3Fe$][BF_4]. Compound 2^{NMe2} crystallizes in the triclinic space group P-1 with one molecule in the asymmetric unit. Additionally, the tetrafluoroborate anion is significantly disordered and was modelled isotropically. There is additional solvent disorder which could not be satisfactorily modelled and was masked in Olex2. The volume of the solvent accessible void space was found to be 897.0 $Å^3$ in which 179.4 e^- were located.

References

1. Cook, S. A.; Borovik, A. S., Molecular Designs for Controlling the Local Environments around Metal Ions. *Acc. Chem. Res.* **2015,** *48* (8), 2407-2414.
2. Mirts, E. N.; Bhagi-Damodaran, A.; Lu, Y., Understanding and Modulating Metalloenzymes with Unnatural Amino Acids, Non-Native Metal Ions, and Non-Native Metallocofactors. *Acc. Chem. Res.* **2019,** *52* (4), 935-944.
3. Barlow, J. M.; Yang, J. Y., Thermodynamic Considerations for Optimizing Selective CO_2 Reduction by Molecular Catalysts. *ACS Cent. Sci.* **2019,** *5* (4), 580-588.
4. Warren, J. J.; Tronic, T. A.; Mayer, J. M., Thermochemistry of Proton-Coupled Electron Transfer Reagents and its Implications. *Chem. Rev.* **2010,** *110* (12), 6961-7001.
5. Ostericher, A. L.; Waldie, K. M.; Kubiak, C. P., Utilization of Thermodynamic Scaling Relationships in Hydricity To Develop Nickel Hydrogen Evolution Reaction Electrocatalysts with Weak Acids and Low Overpotentials. *ACS Catal.* **2018,** *8* (10), 9596-9603.
6. Azcarate, I.; Costentin, C.; Robert, M.; Savéant, J.-M., Dissection of Electronic Substituent Effects in Multielectron–Multistep Molecular Catalysis. Electrochemical CO_2-to-CO Conversion Catalyzed by Iron Porphyrins. *J. Phys. Chem. C* **2016,** *120* (51), 28951-28960.

7. Pegis, M. L.; McKeown, B. A.; Kumar, N.; Lang, K.; Wasylenko, D. J.; Zhang, X. P.; Raugei, S.; Mayer, J. M., Homogenous Electrocatalytic Oxygen Reduction Rates Correlate with Reaction Overpotential in Acidic Organic Solutions. *ACS Cent. Sci.* **2016,** *2* (11), 850-856.

8. Passard, G.; Ullman, A. M.; Brodsky, C. N.; Nocera, D. G., Oxygen Reduction Catalysis at a Dicobalt Center: The Relationship of Faradaic Efficiency to Overpotential. *J. Am. Chem. Soc.* **2016,** *138* (9), 2925-2928.

9. Chantarojsiri, T.; Ziller, J. W.; Yang, J. Y., Incorporation of redox-inactive cations promotes iron catalyzed aerobic C–H oxidation at mild potentials. *Chem. Sci.* **2018,** *9* (9), 2567-2574.

10. Chantarojsiri, T.; Reath, A. H.; Yang, J. Y., Cationic Charges Leading to an Inverse Free-Energy Relationship for N−N Bond Formation by Mn^{VI} Nitrides. *Angew. Chem. Int. Ed.* **2018,** *57* (43), 14037-14042.

11. Azcarate, I.; Costentin, C.; Robert, M.; Savéant, J.-M., Through-Space Charge Interaction Substituent Effects in Molecular Catalysis Leading to the Design of the Most Efficient Catalyst of CO_2-to-CO Electrochemical Conversion. *J. Am. Chem. Soc.* **2016,** *138* (51), 16639-16644.

12. Pegis, M. L.; Wise, C. F.; Koronkiewicz, B.; Mayer, J. M., Identifying and Breaking Scaling Relations in Molecular Catalysis of Electrochemical Reactions. *J. Am. Chem. Soc.* **2017,** *139* (32), 11000-11003.

13. Waidmann, C. R.; Miller, A. J. M.; Ng, C.-W. A.; Scheuermann, M. L.; Porter, T. R.; Tronic, T. A.; Mayer, J. M., Using combinations of oxidants and bases as PCET reactants: thermochemical and practical considerations. *Energy Environ. Sci.* **2012,** *5* (7), 7771-7780.

14. Rebelein, J. G.; Lee, C. C.; Newcomb, M.; Hu, Y.; Ribbe, M. W., Characterization of an M-Cluster-Substituted Nitrogenase VFe Protein. *mBio* **2018,** *9* (2), e00310-18.

15. Spatzal, T.; Schlesier, J.; Burger, E.-M.; Sippel, D.; Zhang, L.; Andrade, S. L. A.; Rees, D. C.; Einsle, O., Nitrogenase FeMoco investigated by spatially resolved anomalous dispersion refinement. *Nat. Commun.* **2016,** *7*, 10902.

16. Spatzal, T.; Einsle, O.; Andrade, S. L. A., Analysis of the Magnetic Properties of Nitrogenase FeMo Cofactor by Single-Crystal EPR Spectroscopy. *Angew. Chem. Int. Ed.* **2013,** *52* (38), 10116-10119.

17. Hoffman, B. M.; Lukoyanov, D.; Yang, Z.-Y.; Dean, D. R.; Seefeldt, L. C., Mechanism of Nitrogen Fixation by Nitrogenase: The Next Stage. *Chem. Rev.* **2014,** *114* (8), 4041-4062.

18. McEvoy, J. P.; Brudvig, G. W., Water-Splitting Chemistry of Photosystem II. *Chem. Rev.* **2006,** *106* (11), 4455-4483.

19. Lubitz, W.; Ogata, H.; Rüdiger, O.; Reijerse, E., Hydrogenases. *Chem. Rev.* **2014,** *114* (8), 4081-4148.

20. Ragsdale, S. W., Metals and Their Scaffolds To Promote Difficult Enzymatic Reactions. *Chem. Rev.* **2006,** *106* (8), 3317-3337.

21. Hakulinen, N.; Kiiskinen, L.-L.; Kruus, K.; Saloheimo, M.; Paananen, A.; Koivula, A.; Rouvinen, J., Crystal structure of a laccase from Melanocarpus albomyces with an intact trinuclear copper site. *Nat Struct Mol Biol* **2002,** *9* (8), 601-605.

22. Ferguson-Miller, S.; Babcock, G. T., Heme/Copper Terminal Oxidases. *Chem. Rev.* **1996,** *96* (7), 2889-2908.

23. Cammarota, R. C.; Xie, J.; Burgess, S. A.; Vollmer, M. V.; Vogiatzis, K. D.; Ye, J.; Linehan, J. C.; Appel, A. M.; Hoffmann, C.; Wang, X.; Young, V. G.; Lu, C. C., Thermodynamic and kinetic studies of H_2 and N_2 binding to bimetallic nickel-group 13 complexes and neutron structure of a Ni(η2-H2) adduct. *Chem. Sci.* **2019**, *10*, 7029.

24. Cammarota, R. C.; Clouston, L. J.; Lu, C. C., Leveraging molecular metal–support interactions for H2 and N2 activation. *Coord. Chem. Rev.* **2017,** *334*, 100-111.

25. Zhang, H.; Hatzis, G. P.; Moore, C. E.; Dickie, D. A.; Bezpalko, M. W.; Foxman, B. M.; Thomas, C. M., O_2 Activation by a Heterobimetallic Zr/Co Complex. *J. Am. Chem. Soc.* **2019**.

26. Krogman, J. P.; Bezpalko, M. W.; Foxman, B. M.; Thomas, C. M., Multi-electron redox processes at a Zr(iv) center facilitated by an appended redox-active cobalt-containing metalloligand. *Dalton Trans.* **2016,** *45* (27), 11182-11190.

27. Xue, G.; De Hont, R.; Münck, E.; Que Jr, L., Million-fold activation of the $[Fe_2(\mu\text{-}O)_2]$ diamond core for C–H bond cleavage. *Nat. Chem.* **2010,** *2*, 400.

28. Camara, J. M.; Rauchfuss, T. B., Combining acid–base, redox and substrate binding functionalities to give a complete model for the [FeFe]-hydrogenase. *Nat. Chem.* **2011,** *4*, 26.

29. Cammarota, R. C.; Lu, C. C., Tuning Nickel with Lewis Acidic Group 13 Metalloligands for Catalytic Olefin Hydrogenation. *J. Am. Chem. Soc.* **2015,** *137* (39), 12486-12489.

30. Arnett, C. H.; Chalkley, M. J.; Agapie, T., A Thermodynamic Model for Redox-Dependent Binding of Carbon Monoxide at Site-Differentiated, High Spin Iron Clusters. *J. Am. Chem. Soc.* **2018,** *140* (16), 5569-5578.

31. Reed, C. J.; Agapie, T., Tetranuclear Fe Clusters with a Varied Interstitial Ligand: Effects on the Structure, Redox Properties, and Nitric Oxide Activation. *Inorg. Chem.* **2017,** *56* (21), 13360-13367.

32. de Ruiter, G.; Thompson, N. B.; Lionetti, D.; Agapie, T., Nitric Oxide Activation by Distal Redox Modulation in Tetranuclear Iron Nitrosyl Complexes. *J. Am. Chem. Soc.* **2015,** *137* (44), 14094-14106.

33. Reed, C. J.; Agapie, T., A Terminal Fe^{III}–Oxo in a Tetranuclear Cluster: Effects of Distal Metal Centers on Structure and Reactivity. *J. Am. Chem. Soc.* **2019**, *141*, 9479.

34. Reed, C. J.; Agapie, T., Thermodynamics of Proton and Electron Transfer in Tetranuclear Clusters with $Mn–OH_2/OH$ Motifs Relevant to H_2O Activation by the Oxygen Evolving Complex in Photosystem II. *J. Am. Chem. Soc.* **2018,** *140* (34), 10900-10908.

35. de Ruiter, G.; Carsch, K. M.; Gul, S.; Chatterjee, R.; Thompson, N. B.; Takase, M. K.; Yano, J.; Agapie, T., Accelerated Oxygen Atom Transfer and C−H Bond Oxygenation by Remote Redox Changes in Fe_3Mn-Iodosobenzene Adducts. *Angew. Chem. Int. Ed.* **2017,** *56* (17), 4772-4776.

36. Holm, R. H.; Lo, W., Structural Conversions of Synthetic and Protein-Bound Iron–Sulfur Clusters. *Chem. Rev.* **2016,** *116* (22), 13685-13713.

37. Hernández Sánchez, R.; Zheng, S.-L.; Betley, T. A., Ligand Field Strength Mediates Electron Delocalization in Octahedral $[(^{H}L)_2Fe6(L')_m]^{n+}$ Clusters. *J. Am. Chem. Soc.* **2015,** *137* (34), 11126-11143.

38. Eames, E. V.; Harris, T. D.; Betley, T. A., Modulation of magnetic behavior via ligand-field effects in the trigonal clusters $(^{Ph}L)Fe_3L^*_3$ (L* = thf, py, PMe2Ph). *Chem. Sci.* **2012,** *3* (2), 407-415.

39. Anderton, K. J.; Ermert, D. M.; Quintero, P. A.; Turvey, M. W.; Fataftah, M. S.; Abboud, K. A.; Meisel, M. W.; Čižmár, E.; Murray, L. J., Correlating Bridging Ligand with Properties of Ligand-Templated $[Mn^{II}_3X_3]^{3+}$ Clusters (X = Br–, Cl–, H–, MeO–). *Inorg. Chem.* **2017,** *56* (19), 12012-12022.

40. Lee, H. B.; Agapie, T., Redox Tuning via Ligand-Induced Geometric Distortions at a YMn3O4 Cubane Model of the Biological Oxygen Evolving Complex. *Inorg. Chem.* **2019**, *58*, 14998.

41. Lee, H. B.; Shiau, A. A.; Oyala, P. H.; Marchiori, D. A.; Gul, S.; Chatterjee, R.; Yano, J.; Britt, R. D.; Agapie, T., Tetranuclear $[Mn^{III}Mn_3^{IV}O_4]$ Complexes as Spectroscopic Models of the S_2 State of the Oxygen Evolving Complex in Photosystem II. *J. Am. Chem. Soc.* **2018,** *140* (49), 17175-17187.

42. Stack, T. D. P.; Holm, R. H., Subsite-differentiated analogs of biological $[4Fe\text{-}4S]^{2+}$ clusters: synthesis, solution and solid-state structures, and subsite-specific reactions. *J. Am. Chem. Soc.* **1988,** *110* (8), 2484-2494.

43. Stack, T. D. P.; Holm, R. H., Subsite-specific functionalization of the $[4Fe\text{-}4S]^{2+}$ analog of iron-sulfur protein clusters. *J. Am. Chem. Soc.* **1987,** *109* (8), 2546-2547.

44. Zhao, Q.; Harris, T. D.; Betley, T. A., $[(^{H}L)_2Fe_6(NCMe)_m]^{n+}$ (m = 0, 2, 4, 6; n = −1, 0, 1, 2, 3, 4, 6): An Electron-Transfer Series Featuring Octahedral Fe6 Clusters Supported by a Hexaamide Ligand Platform. *J. Am. Chem. Soc.* **2011,** *133* (21), 8293-8306.

45. Zhao, Q.; Betley, T. A., Synthesis and Redox Properties of Triiron Complexes Featuring Strong Fe–Fe Interactions. *Angew. Chem. Int. Ed.* **2011,** *50* (3), 709-712.

46. Guillet, G. L.; Sloane, F. T.; Ermert, D. M.; Calkins, M. W.; Peprah, M. K.; Knowles, E. S.; Čižmár, E.; Abboud, K. A.; Meisel, M. W.; Murray, L. J., Preorganized assembly of three iron(ii) or manganese(ii) β-diketiminate complexes using a cyclophane ligand. *Chem. Commun.* **2013,** *49* (59), 6635-6637.

47. McSkimming, A.; Suess, D. L. M., Selective Synthesis of Site-Differentiated Fe_4S_4 and Fe_6S_6 Clusters. *Inorg. Chem.* **2018,** *57* (23), 14904-14912.

48. Hansch, C.; Leo, A.; Taft, R. W., A survey of Hammett substituent constants and resonance and field parameters. *Chem. Rev.* **1991,** *91* (2), 165-195.

49. We have elected to conduct thorough spectroscopic studies at the extremes of the Hammett series in order to elucidate the effects of the ligand substituents on the electronic structure of the clusters.

50. Full spectroscopic characterization was performed on the extremes of the Hammett series.

51. de Ruiter, G.; Thompson, N. B.; Takase, M. K.; Agapie, T., Intramolecular C–H and C–F Bond Oxygenation Mediated by a Putative Terminal Oxo Species in Tetranuclear Iron Complexes. *J. Am. Chem. Soc.* **2016,** *138* (5), 1486-1489.

52. Venkateswara Rao, P.; Holm, R. H., Synthetic Analogues of the Active Sites of Iron−Sulfur Proteins. *Chem. Rev.* **2004,** *104* (2), 527-560.

53. Chakrabarti, M.; Deng, L.; Holm, R. H.; Münck, E.; Bominaar, E. L., Mössbauer, Electron Paramagnetic Resonance, and Theoretical Studies of a Carbene-Based All-Ferrous Fe_4S_4 Cluster: Electronic Origin and Structural Identification of the Unique Spectroscopic Site. *Inorg. Chem.* **2009,** *48* (7), 2735-2747.

54. Yoo, S. J.; Angove, H. C.; Burgess, B. K.; Hendrich, M. P.; Münck, E., Mössbauer and Integer-Spin EPR Studies and Spin-Coupling Analysis of the $[4Fe\text{-}4S]^0$ Cluster of the Fe Protein from Azotobacter vinelandii Nitrogenase. *J. Am. Chem. Soc.* **1999,** *121* (11), 2534-2545.

55. Angove, H. C.; Yoo, S. J.; Burgess, B. K.; Münck, E., Mössbauer and EPR Evidence for an All-Ferrous Fe_4S_4 Cluster with S = 4 in the Fe Protein of Nitrogenase. *J. Am. Chem. Soc.* **1997,** *119* (37), 8730-8731.

56. Münck, E.; Ksurerus, K.; Hendrich, M. P., Combining Mössbauer spectroscopy with integer spin electron paramagnetic resonance. In *Methods Enzymol.*, Academic Press: 1993; Vol. 227, pp 463-479.

57. Surerus, K. K.; Hendrich, M. P.; Christie, P. D.; Rottgardt, D.; Orme-Johnson, W. H.; Munck, E., Moessbauer and integer-spin EPR of the oxidized P-clusters of nitrogenase: POX is a non-Kramers system with a nearly degenerate ground doublet. *J. Am. Chem. Soc.* **1992,** *114* (22), 8579-8590.

58. Hendrich, M. P.; Debrunner, P. G., Integer-spin electron paramagnetic resonance of iron proteins. *Biophys. J. 56* (3), 489-506.

59. Sutradhar, M.; Carrella, L. M.; Rentschler, E., A Discrete μ4-Oxido Tetranuclear Iron(III) Cluster. *Eur. J. Inorg. Chem.* **2012,** *2012* (27), 4273-4278.

60. Murali, M.; Nayak, S.; Costa, J. S.; Ribas, J.; Mutikainen, I.; Turpeinen, U.; Clémancey, M.; Garcia-Serres, R.; Latour, J.-M.; Gamez, P.; Blondin, G.; Reedijk, J., Discrete Tetrairon(III) Cluster Exhibiting a Square-Planar Fe4(μ4-O) Core: Structural and Magnetic Properties. *Inorg. Chem.* **2010,** *49* (5), 2427-2434.

61. Singh, A. K.; Jacob, W.; Boudalis, A. K.; Tuchagues, J.-P.; Mukherjee, R., A Tetragonal Core with Asymmetric Iron Environments Supported Solely by Bis(μ-OH){μ-(O–H···O)} Bridging and Terminal Pyridine Amide (N, O) Coordination: A New Member of the Tetrairon(III) Family. *Eur. J. Inorg. Chem.* **2008,** *2008* (18), 2820-2829.

62. Chardon-Noblat, S.; Horner, O.; Chabut, B.; Avenier, F.; Debaecker, N.; Jones, P.; Pécaut, J.; Dubois, L.; Jeandey, C.; Oddou, J.-L.; Deronzier, A.; Latour, J.-M., Spectroscopic and Electrochemical Characterization of an Aqua Ligand Exchange and Oxidatively Induced Deprotonation in Diiron Complexes. *Inorg. Chem.* **2004,** *43* (5), 1638-1648.

63. Borovik, A. S.; Murch, B. P.; Que, L.; Papaefthymiou, V.; Munck, E., Models for iron-oxo proteins: a mixed valence iron(II)-iron(III) complex. *J. Am. Chem. Soc.* **1987,** *109* (23), 7190-7191.

64. Gütlich, P.; Bill, E.; Trautwein, A. X., *Mössbauer Spectroscopy and Transition Metal Chemistry: Fundamentals and Applications*. Springer: Berlin, 2011.

65. Smith, J. M.; Mayberry, D. E.; Margarit, C. G.; Sutter, J.; Wang, H.; Meyer, K.; Bontchev, R. P., N–O Bond Homolysis of an Iron(II) TEMPO Complex Yields an Iron(III) Oxo Intermediate. *J. Am. Chem. Soc.* **2012,** *134* (15), 6516-6519.

66. Vogel, C.; Heinemann, F. W.; Sutter, J.; Anthon, C.; Meyer, K., An Iron Nitride Complex. *Angew. Chem. Int. Ed.* **2008,** *47* (14), 2681-2684.

67. Einsle, O.; Andrade, S. L. A.; Dobbek, H.; Meyer, J.; Rees, D. C., Assignment of Individual Metal Redox States in a Metalloprotein by Crystallographic Refinement at Multiple X-ray Wavelengths. *J. Am. Chem. Soc.* **2007,** *129* (8), 2210-2211.

68. Hendrickson, W., Determination of macromolecular structures from anomalous diffraction of synchrotron radiation. *Science* **1991,** *254* (5028), 51-58.

69. Wenke, B. B.; Spatzal, T.; Rees, D. C., Site-Specific Oxidation State Assignments of the Iron Atoms in the $[4Fe{:}4S]^{2+/1+/0}$ States of the Nitrogenase Fe-Protein. *Angew. Chem. Int. Ed.* **2019,** *58* (12), 3894-3897.

70. Hernández Sánchez, R.; Champsaur, A. M.; Choi, B.; Wang, S. G.; Bu, W.; Roy, X.; Chen, Y.-S.; Steigerwald, M. L.; Nuckolls, C.; Paley, D. W., Electron Cartography in Clusters. *Angew. Chem. Int. Ed.* **2018,** *57* (42), 13815-13820.

71. Wu, G.; Zhang, Y.; Ribaud, L.; Coppens, P.; Wilson, C.; Iversen, B. B.; Larsen, F. K., Multitemperature Resonance-Diffraction and Structural Study of the Mixed-Valence Complex $[Fe_3O(OOCC(CH_3)_3)_6(C_5H_5N)_3]$. *Inorg. Chem.* **1998,** *37* (23), 6078-6083.

72. Gao, Y.; Frost-Jensen, A.; Pressprich, M. R.; Coppens, P.; Marquez, A.; Dupuis, M., Valence contrast by synchrotron resonance scattering: application to a mixed-valence manganese compound. *J. Am. Chem. Soc.* **1992,** *114* (23), 9214-9215.

73. Bartholomew, A. K.; Teesdale, J. J.; Hernández Sánchez, R.; Malbrecht, B. J.; Juda, C. E.; Ménard, G.; Bu, W.; Iovan, D. A.; Mikhailine, A. A.; Zheng, S.-L.; Sarangi, R.; Wang, S. G.; Chen, Y.-S.; Betley, T. A., Exposing the inadequacy of redox formalisms by resolving redox inequivalence within isovalent clusters. *Proc. Natl. Acad. Sci. U. S. A.* **2019,** *116* (32), 15836-15841.

74. Mitchell, K. J.; Abboud, K. A.; Christou, G., Magnetostructural Correlation for High-Nuclearity Iron(III)/Oxo Complexes and Application to Fe_5, Fe_6, and Fe_8 Clusters. *Inorg. Chem.* **2016,** *55* (13), 6597-6608.

75. Weihe, H.; Güdel, H. U., Angular and Distance Dependence of the Magnetic Properties of Oxo-Bridged Iron(III) Dimers. *J. Am. Chem. Soc.* **1997,** *119* (28), 6539-6543.

76. Gorun, S. M.; Lippard, S. J., Magnetostructural correlations in magnetically coupled (.mu.-oxo)diiron(III) complexes. *Inorg. Chem.* **1991,** *30* (7), 1625-1630.

77. We have previously reported structural characterization of the analogous dicarbonyl complex 1^{H}-$(CO)_2$ and demonstrated that both CO molecules bind Fe4. The ^{1}H-NMR features of the monocarbonyl complex 1^{H}-CO are nearly identical to the isoelectronic, structurally homologous pyrazolate-bridged nitrosyl compound $[LFe_3O(PhPz)_3Fe][OTf_2]$, which has been structurally characterized. Moreover, the 1e- reduced monocarbonyl 2^{H}-CO has been structurally characterized, revealing that CO binds trans to O1 as expected. Thus, variable temperature ^{1}H-NMR and IR spectroscopies in combination with XRD studies have defined the spectroscopic signatures expected for the carbonyl adducts discussed herein.

78. This temperature was selected for comparison because it is the highest temperature for which the first and second CO binding constants of 1^{R} (where relevant) may be measured directly.

79. The Mossbauer spectrum of 1^{H}-$(CO)_2$ is consistent with an Fe(II) formulation for the apical iron center, indicating the overall redox distribution in the dicarbonyl complexes is the same as that in the monocarbonyl complexes. See ref. 7a.

80. Fujita, E.; Creutz, C.; Sutin, N.; Szalda, D. J., Carbon dioxide activation by cobalt(I) macrocycles: factors affecting carbon dioxide and carbon monoxide binding. *J. Am. Chem. Soc.* **1991,** *113* (1), 343-353.

81. Guo, R.-H.; Liu, C.-F.; Wei, T.-C.; Hu, C.-C., Electrochemical behavior of CO_2 reduction on palladium nanoparticles: Dependence of adsorbed CO on electrode potential. *Electrochem. Commun.* **2017,** *80*, 24-28.

82. Lee, C. C.; Wilcoxen, J.; Hiller, C. J.; Britt, R. D.; Hu, Y., Evaluation of the Catalytic Relevance of the CO-Bound States of V-Nitrogenase. *Angew. Chem. Int. Ed.* **2018,** *57* (13), 3411-3414.

83. Perry, M. C.; Cui, X.; Powell, M. T.; Hou, D.-R.; Reibenspies, J. H.; Burgess, K., Optically Active Iridium Imidazol-2-ylidene-oxazoline Complexes: Preparation and Use in Asymmetric Hydrogenation of Arylalkenes. *J. Am. Chem. Soc.* **2003,** *125* (1), 113-123.

84. Hagadorn, J. R.; Que, L.; Tolman, W. B., N-Donor Effects on Carboxylate Binding in Mononuclear Iron(II) Complexes of a Sterically Hindered Benzoate Ligand. *Inorg. Chem.* **2000,** *39* (26), 6086-6090.

85. Bailey, B. C.; Basuli, F.; Huffman, J. C.; Mindiola, D. J., Terminal Titanium(IV) (Trimethylsilyl)imides Prepared by Oxidatively Induced Trimethylsilyl Abstraction. *Organometallics* **2006,** *25* (11), 2725-2728.

86. Del Castillo, T. J.; Thompson, N. B.; Peters, J. C., A Synthetic Single-Site Fe Nitrogenase: High Turnover, Freeze-Quench ^{57}Fe Mössbauer Data, and a Hydride Resting State. *J. Am. Chem. Soc.* **2016,** *138* (16), 5341-5350.

87. Stoll, S.; Schweiger, A., EasySpin, a comprehensive software package for spectral simulation and analysis in EPR. *J. Magn. Res.* **2006,** *178* (1), 42-55.

88. Chilton, N. F.; Anderson, R. P.; Turner, L. D.; Soncini, A.; Murray, K. S., PHI: A powerful new program for the analysis of anisotropic monomeric and exchange-coupled polynuclear d- and f-block complexes. *J. Comput. Chem.* **2013,** *34* (13), 1164-1175.

89. *APEX-II Version 2 User Manual, M86-E01078*. Bruker Analytical X-ray Systems: Madison, WI, 2006.

90. Sheldrick, G., *SADABS (version 2008/1): Program for Absorption Correction for Data from Area Detector Frames*. University of Göttingen: 2008.

91. Sheldrick, G., A short history of SHELX. *Acta Crystall. Sec. A* **2008,** *64* (1), 112-122.

92. Sheldrick, G., Crystal structure refinement with SHELXL. *Acta Crystall. Sec. C* **2015,** *71* (1), 3-8.

93. Dolomanov, O. V.; Bourhis, L. J.; Gildea, R. J.; Howard, J. A. K.; Puschmann, H., OLEX2: a complete structure solution, refinement and analysis program. *J. Appl. Crystallogr.* **2009,** *42* (2), 339-341.

94. Kabsch, W., XDS. *Acta Crystallogr. Sect. D. Biol. Crystallogr.* **2010,** *66*, 125-132.

95. Adams, P. D.; Afonine Pavel, V.; Bunkóczi, G.; Chen, V. B.; Davis, I. W.; Echols, N.; Headd, J. J.; Hung, L.-W.; Kapral, G. J.; Grosse-Kunstleve, R. W.; McCoy, A., J.; Moriarty, N. W.; Oeffner, R.; Read, R. J.; Richardson, D. C.; Richardson, J. S.; Terwilligere, T. T.; Zwarta, P. H., PHENIX: a comprehensive Python-based system for macromolecular structure solution. *Acta Crystallogr. Sect. D. Biol. Crystallogr.* **2010,** *66*, 213-221.

CHAPTER 4

ACTIVATION OF AN OPEN SHELL, CARBYNE-BRIDGED DIIRON COMPLEX TOWARD BINDING OF DINITROGEN

The text for this chapter was reproduced in part from:

Arnett, C.H.; Agapie, T. *J. Am. Chem. Soc.* **2020***, 142,* 10059–10068.

ABSTRACT

Binding of N_2 by nitrogenase requires a reductive activation of the FeMo-cofactor, but the precise structure and atomic composition of FeMoco in its activated form is not well understood. However, recent crystallographic studies suggest that N_2 reduction may occur at a carbon-bridged diiron subunit of FeMoco. Toward modeling the activation of a Fe-(μ-C)-Fe site toward N_2 binding, we synthesized a new dinucleating, hexaphosphine ligand derived from a 2,6-disubstituted toluene platform. Activation of the central methyl group of the ligand affords the diiron μ-carbyne complex $(P_6ArC)Fe_2(\mu\text{-}H)$ featuring a biologically relevant Fe(μ-carbyne)(μ-H)Fe motif. SQUID magnetometry, Mössbauer spectroscopy, and DFT calculations reveal that $(P_6ArC)Fe_2(\mu\text{-}H)$ has a well-isolated $S = 1$ ground state, distinguishing it from all other diiron μ-carbyne complexes which are diamagnetic. Upon the addition of sources of H^+/e^- (H_2, TEMPO-H or HCl), $(P_6ArC)Fe_2(\mu\text{-}H)$ is activated toward N_2 binding, with concomitant protonation of the carbyne ligand. Although reaction with H_2 ultimately leads to complete protonation of the carbyne moiety, mechanistic investigations indicate that formation of a single C-H bond, with concomitant cleavage of one Fe-C bond, generates an iron-carbene intermediate capable of coordinating N_2.

INTRODUCTION

Reduction of atmospheric N_2 by the Mo-nitrogenase enzyme requires an initial activation phase[1]: the active site [7Fe-9S-Mo-C-*R*-homocitrate] cluster[2-5] (the iron molybdenum cofactor, FeMoco, Figure 1, top) must first be reduced by 3-4 electrons before substrate binds. Although pulsed EPR measurements indicate that bridging hydrides accumulate on the cofactor during this process,[6-7] the precise structure and atomic composition of FeMoco in its activated form is not well understood.[8-9] Structural rearrangements are common for iron-sulfur clusters,[10-11] and recent crystallographic studies reveal that a μ_2-sulfide ligand in the "belt" region of FeMoco can be displaced to expose a binding site for substrates and intermediates.[12-14] Computational and synthetic modelling studies demonstrate that Fe-S bond cleavage is a feasible mechanism for cofactor activation,[15-17] though even more dramatic rearrangements of FeMoco may be required.[18-20] For example, one computational study suggests that N_2 binds in the central cavity of the cofactor, following protonation of the interstitial carbide to a methyl ligand.[19] Despite ambiguity in the atomic-level details, the foregoing studies intimate a central role for a carbon-bridged diiron subunit of FeMoco in mediating the reduction of N_2.

Synthetic modelling studies have the potential to provide mechanistic insight into the activation of a carbon-bridged diiron site toward N_2 binding. To date, however, efforts in this regard have been largely restricted to the study of monometallic iron complexes with terminal arene,[17, 21] alkyl,[22-24] or carbene-based donors.[25-28] Although these studies have revealed a role for Fe-C hemilability in the activation of N_2,[23-24] they do not address proposals involving carbide protonation and Fe-C bond cleavage or the potential for cooperative N_2 binding to two metals. A number of diiron μ-carbyne complexes have been reported which feature a biologically relevant Fe-(μ-C)-Fe motif,[29-37] though none of these have been studied in the context of biological nitrogen fixation. The vast majority of these complexes are derivatives of the Fp anion and contain multiple π-acidic CO ligands (Figure 1, bottom), rendering the carbyne highly electrophilic.[32, 38-44] Moreover, all diiron μ-carbynes reported thus far are closed-shell, diamagnetic species, in stark contrast to the paramagnetic nature of FeMoco. In fact, there are only a handful of complexes featuring an Fe-(μ-CR$_x$)-Fe (x = 2 or 3) motif which exhibit an open-shell configuration.[45-49]

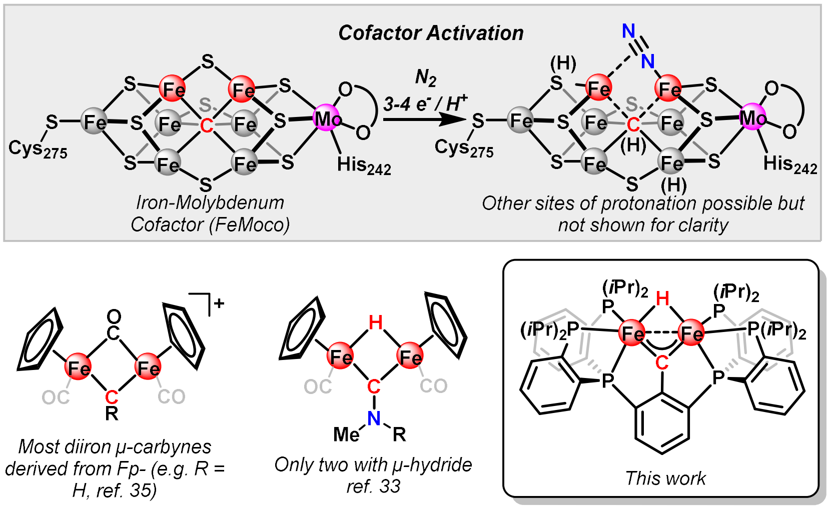

Most diiron μ-carbynes derived from Fp- (e.g. R = H, ref. 35)

Only two with μ-hydride ref. 33

This work

FIGURE 1. Binding of N$_2$ by the iron-molybdenum cofactor (FeMoco) of nitrogenase requires reductive activation of the cofactor, resulting in ill-defined structural changes (top). Diiron μ-carbyne complexes are structural models of a carbon-bridged diiron subunit of FeMoco, proposed to be central to catalysis.

Inspired by the mechanism through which the interstitial carbide is installed into FeMoco,[50-52] we envisioned that the Fe-(μ-CR)-Fe linkage might alternatively be accessed by templating two iron centers in the proximity of a methyl substituent, facilitating direct C-H activation. Toward this end, we have designed a dinucleating, hexaphosphine ligand derived from a 2,6-disubstituted toluene platform. Although this phosphine-rich supporting ligand is electronically distinct from the sulfide-rich environment of the iron centers in FeMoco, activation of the central methyl group affords an unusual open shell, carbyne-bridged diiron complex (Figure 1, bottom) which can be activated for binding of N$_2$ upon addition of H$_2$.

RESULTS AND DISCUSSION

Template-Assisted Synthesis of a Diiron μ-Carbyne Complex. The desired proligand was synthesized in two steps from 2,6-dibromotoluene (Scheme 1). Lithiation with 1 equiv. of *n*BuLi followed by addition of bis(*o*-diisopropylphosphinophenyl)-chlorophosphine (P_2P^{Cl}) yields the triphosphine intermediate P_3ArCH_3 (**1**). Although lithium-halogen exchange of **1** is dominated by self-quenching, generation of the Grignard reagent with Mg followed by treatment with P_2P^{Cl} proceeds cleanly, affording the desired ligand in 81% yield after workup. Metalation of P_6ArCH_3 (**2**) with two equivalents of $FeBr_2$ in tetrahydrofuran precipitates a yellow-green powder, believed to correspond to the diiron(II) tetrabromide complex $(P_6ArCH_3)Fe_2Br_4$ (**3**, Figure S7). Reduction of **3** with Cp^*_2Co in benzene affords the diiron(I) congener $(P_6ArCH_3)Fe_2Br_2$ (**4**) as a brick red solid. The iron centers of **4** are four coordinate with Fe-P bond lengths of 2.254(5) Å (Fe1-P1), 2.318(6) Å (Fe1-P2), and 2.330(6) Å (Fe1-P3). Most notably, in the solid state, **3** adopts a geometry appropriate for C-H activation (Figure S9) - both iron centers are directed toward the central methyl group, resulting in a reasonably short Fe1-C1 distance of 3.834 Å (Table S7).

Treatment of **4** with 2 equiv. of MeMgBr in tetrahydrofuran followed by refluxing in benzene generates a new paramagnetic species. X-ray diffraction studies revealed the formation of the desired diiron μ-carbyne complex $(P_6ArC)Fe_2(\mu\text{-}H)$ (**5**, Figure 2). Each iron site of **5** adopts *pseudo*-trigonal bipyramidal geometry with one short Fe-P distance (2.1307(7) Å, Table S7) and two long Fe-P bond lengths (Fe1-P2: 2.2627(8) Å, Fe1-P3: 2.2522(6) Å). Similar to reported carbyne-bridged complexes, **5** features a short Fe1-C1 distance of 1.792(1) Å. Notably, the diffraction data is of sufficient quality to unambiguously locate a single hydride bridging the two iron sites, with an Fe1-H1 bond length of 1.76(3) Å. The Fe-Fe distance within the Fe(μ-CAr)(μ-H)Fe diamond core of **5** is short (2.6776(6) Å), close to the range expected for an Fe-Fe single bond (ave. 2.6(1) Å).[45] To accommodate this short Fe-Fe separation, the ligand framework must distort, resulting in a P1-C3-C4 angle (141.42(1)°) which deviates significantly from expected value.

Scheme 1. Ligand synthesis and metalation.

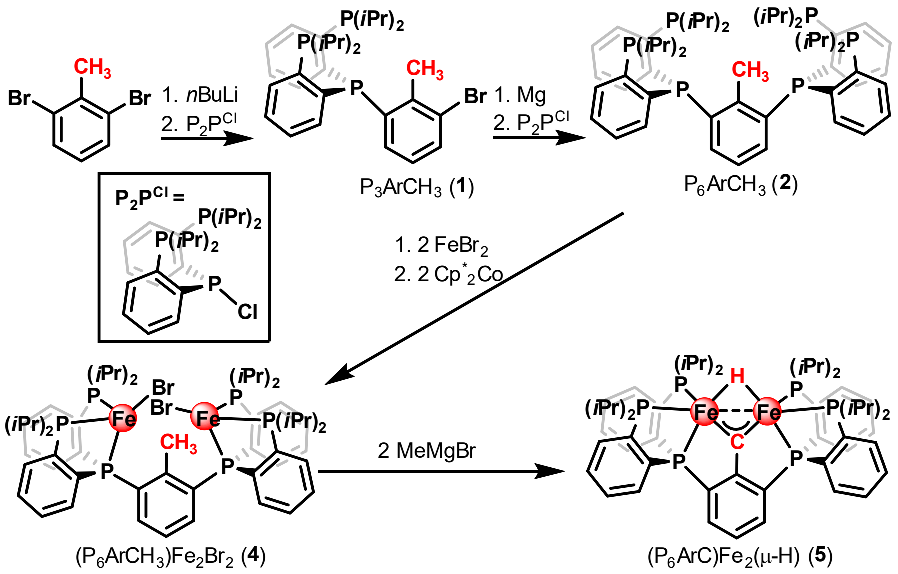

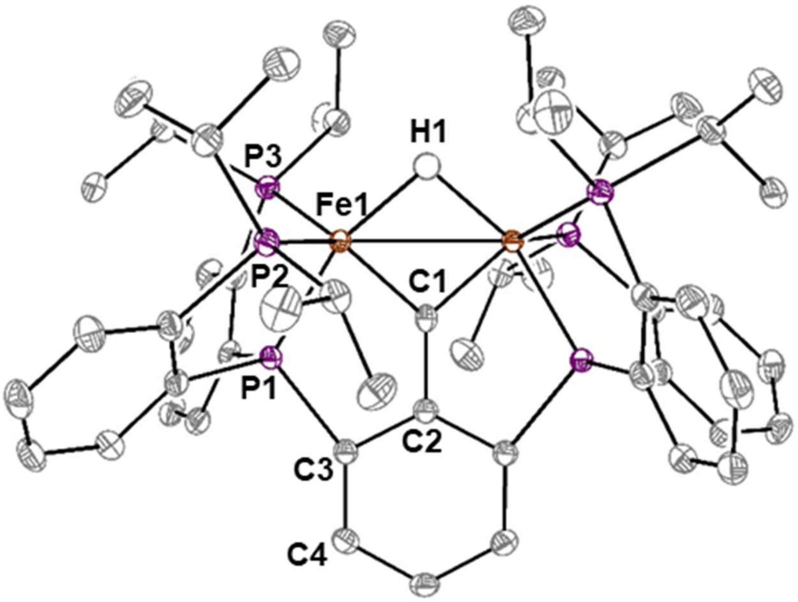

Figure 2. Crystal structure of $(P_6ArC)Fe_2(\mu\text{-}H)$ (**5**). Hydrogen atoms on the ligand are omitted for clarity. Thermal ellipsoids shown at 50% probability.

*Spectroscopic and Computational Characterization of **5**.* Given the strong-field donor set of **5**, the observation of broad, paramagnetically shifted resonances in its ^{1}H NMR spectrum (Figure S13) is notable. The position of these resonances exhibits ideal Curie behavior between 198 – 298 K (Figure S15), suggesting an open-shell configuration rather than thermal population of a low-lying paramagnetic excited state. Indeed, variable-temperature magnetic susceptibility measurements reveal that the χT value of **5** (1.01 cm^3 K mol^{-1}, 298 K, equivalent to μ_{eff} = 2.84 μ_B) is nearly constant between 5 – 298 K (Figure 3a), indicating a thermally isolated S = 1 ground state (expected: μ_{eff} = 2.83 μ_B). Although a number of open-shell diiron μ-hydride complexes have been reported,[53-59] **5** is the first paramagnetic diiron species featuring a μ-carbyne ligand.

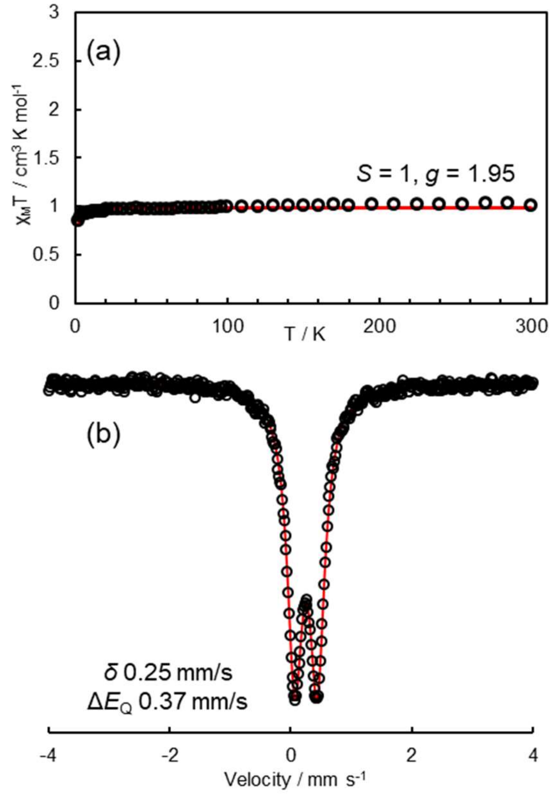

Figure 3. Characterization of (P_6ArC)Fe_2(μ-H) (**5**). Variable temperature magnetic susceptibility studies reveal a thermally isolated S = 1 ground state (a). ^{57}Fe Mössbauer spectrum (80 K, polycrystalline sample) of **5** (b).

Additional insight into the unusual electronic structure of **5** was obtained from DFT calculations. Consistent with experiment, computational studies reveal a triplet ground state for **5** (Table S2) with metrical parameters that closely resemble those in the solid state structure (Table S1). The calculated frontier molecular orbitals include ten orbitals with significant Fe 3*d* character and nearly equal distribution onto each iron site (Figure S74). As a result of the contraction of the axial Fe1-P1 bond length (Fe1-P1: 2.1307(7) Å), the Fe $3d_{xz}$ orbitals are higher in energy than orbitals of Fe $3d_{yz}$ parentage (Figure 4a) which are involved in σ-bonding with the equatorial phosphines (Fe1-P2: 2.2627(8) Å and Fe1-P3: 2.2522(6) Å). Additionally, the Fe $3d_{xz}$ orbitals are engaged in σ-bonding with both the μ-hydride and μ-carbyne ligands. A single Fe-H-Fe σ bonding orbital can be located below the *d* set (HOMO-9, Figure 4c), leading to a half-bond order for each Fe-H interaction (Löwdin bond order = 0.47). The two Fe-C σ-bonding orbitals are non-degenerate – one is relatively high-lying (HOMO-8), whereas the other is much lower in energy (HOMO-33). Mixing of $3d_{xy}$ character into the symmetric combination of the $3d_{yz}$ orbitals facilitates a highly covalent π bonding interaction with the carbyne ligand (HOMO-7). The presence of strong Fe-C π-bonding results in an empty Fe-C π^* orbital (LUMO, Figure 4b,c) and rationalizes the inaccessibility of higher spin states (e.g. $S = 2$). This orbital analysis implies delocalized multiple bond character, with a formal Fe-C bond order of 1.5 (Löwdin bond order = 1.34).

The antisymmetric combination of the Fe $3d_{yz}$ orbitals (HOMO) does not have appropriate symmetry to interact with either the μ-hydride or the μ-carbyne ligands. As a result of the longer Fe1-P2 and Fe1-P3 distances, this orbital is energetically accessible and is singly occupied (HOMO) in the ground state of **5**. The remaining singly-occupied orbital is of $3d_{x2-y2}$ parentage and has δ-symmetry relative to the Fe-Fe vector (HOMO-1, Figure 4b,c). Five additional iron-based orbitals with predominantly Fe $3d_{xy}$, $3d_{x2-y2}$ and $3d_{z2}$ character are found with lower energy and are fully populated (Figure S74). These filled orbitals include both the Fe-Fe σ (HOMO-6) and σ^* (HOMO-3) orbitals, suggesting that σ-bonding should not contribute significantly to the Fe-Fe interaction. Rather, the short Fe-Fe separation (2.6776(6) Å) appears to be a consequence of the constrained ligand environment, with electronic communication mediated by 3-center, 2-electron bonding across the Fe-C-Fe and the Fe-H-Fe motifs, leading to an Fe-Fe Löwdin bond order of 0.58.

Validation of this theoretical model can be obtained by comparison of the calculated (δ = 0.24 mm s^{-1}, $|\Delta E_Q|$ = 0.38 mm s^{-1}) and experimental (δ = 0.25 mm s^{-1}, $|\Delta E_Q|$ = 0.37 mm s^{-1}, Figure 3b) Mössbauer parameters, which are accurately reproduced only in the triplet state (Table S3).[60] Assuming a closed-shell configuration for the bridging carbyne ligand, the electronic structure of **5** can be formulated as $\{Fe^{II}_2(\mu\text{-}CAr^{3-})(\mu\text{-}H^-)\}$. Under this assumption, the 12 Fe 3*d* electrons occupy molecular orbitals that are delocalized across both iron centers, as well as the ligand. This situation is analogous to that recently described for the formally $Ni^{II}_2(\mu\text{-}H)_2$ dimer $[Cp'Ni(\mu\text{-}H)]_2$ (Cp' = 1,2,3,4-tetraisopropylcyclopentadienyl), which also adopts an S = 1 configuration.[61] However, due to delocalization and covalency, the physical oxidation state of **5** may be lower than Fe^{II}. Although there are few pertinent reference compounds against which the Mössbauer parameters may be benchmarked, the isomer shift of **5** (δ = 0.25 mm s^{-1}) falls between those reported for a related S = 1 iron(II)-carbonyl complex $[(SiP_3)Fe(CO)]^+$ (δ = 0.31 mm s^{-1}) and its iron(I) congener $[(SiP_3)Fe(CO)]$ (δ = 0.21 mm s^{-1}).[62] In light of these ambiguities, explicit reference to the formal oxidation state of **5** shall be avoided.

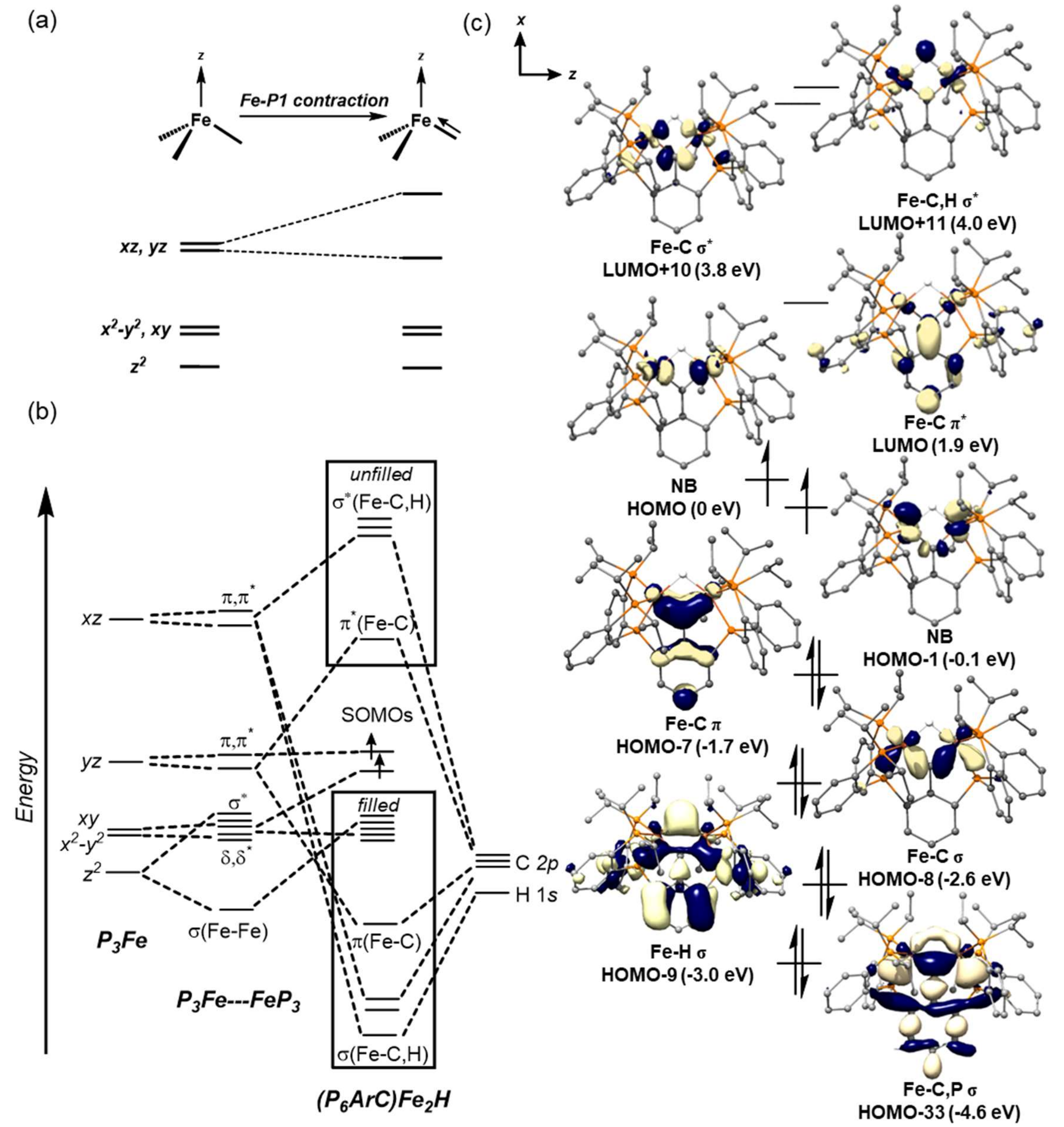

Figure 4. Electronic structure of (P_6ArC)Fe_2(μ-H) (**5**). (a) Illustration of the effect of the contraction of the Fe1-P1 distance on the FMO's of the P_3Fe fragment. (b) Qualitative MO diagram for (P_6ArC)Fe_2(μ-H) (**5**). (c) Calculated valence MOs (P_6ArC)Fe_2(μ-H) (**5**) highlighting the SOMO's and key Fe-C interactions. Isosurfaces are shown at the 0.03 eÅ^3 level and orbital energies (relative to the HOMO) are provided.

*Activation of **5** Toward N_2 Binding.* Complex **5** is a unique entry point for developing model chemistry relevant to the activation of FeMoco, especially in light of spectroscopic data that indicates bridging hydride ligands accumulate on the cofactor prior to N_2 binding.[6-7] For this reason, we investigated whether addition of H^+/e^- or, alternatively, H_2 promotes coordination of N_2. Exposure of **5** to a roughly equimolar mixture of H_2 and N_2 slowly converges to a single diamagnetic product (Figure S47-48) with spectroscopic parameters consistent with $(P_6ArCH_3)Fe_2(H_2)_2(H)_4$ (**6-H₂**) formulation. (Scheme 2). The ^{31}P NMR spectrum of **6-H₂** exhibits two distinct resonances at 124.9 ppm (d, *J* = 15 Hz, 4P) and 110.0 ppm (t, *J* = 19 Hz, 2 P). A resonance at -12.9 ppm (t, *J* =28 Hz) is observed in the ^1H NMR spectrum of **6-H₂** which corresponds to 8 protons (Figure S22). Under an H_2/N_2 atmosphere, these protons relax quickly (T_1 = 48 ms, Figure S25), characteristic of a metal-dihydrogen adduct.[63] Cooling the sample to 198 K partially resolves this signal into three distinct hydridic/Fe-H_2 resonances (Figure S24), suggesting that the hydride/H_2 ligands rapidly interconvert. Although similar reactivity is observed if **5** is exposed to an atmosphere of H_2, the reaction does not proceed cleanly. Significant quantities of dissociated ligand are observed by ^{31}P NMR, implying that N_2 stabilizes one or more of the intermediates.

Complex **6-H₂** is not stable under an atmosphere of N_2, converting gradually to the N_2 congener $(P_6ArCH_3)Fe_2(N_2)_2(H)_4$ (**6-N₂**, Figure S53-55). This transformation is accompanied by the loss of the resonance at -12.9 ppm in the ^1H NMR spectrum of **6-H₂** and the appearence of new features at -9.8 ppm (2H, T_1 = 382 ms) and -20.5 ppm (2H, T_1 = 380 ms). The ATR-IR spectrum of **6-N₂** features diagnostic vibrational features at 2073 cm^{-1} and 1790 cm^{-1} (Figure S35), corresponding to the N_2 and hydride ligands, respectively. Diffraction studies on **6-N₂** (Figure 5) confirm that the central carbon has been fully hydrogenated (Fe1-C1: 3.983(3) Å, Table S7). Each iron center in **6-N₂** is six-coordinate, with one hydride bisecting the equatorial phosphine donors (P2-F1-P3: 146.72(5)°). The other hydride is *trans* to the unique phosphine ligand P1.

Overall, the formation of **6** involves the addition of 3 equiv. of H_2 to **5**. To better understand the activation process, we sought to identify relevant intermediates. *In situ* monitoring of the reaction via ^{31}P NMR spectroscopy facilitates detection of one diamagnetic intermediate (Figure S48). This species exhibits three distinct ^{31}P resonances (δ = 126.4 ppm, 2P; 121.3 ppm; 2P, 110.8 ppm, 2P), indicating a loss of front-back mirror symmetry with respect to **5**. Although this intermediate cannot be isolated directly from the reaction of **5** with H_2, a compound with identical ^{1}H and ^{31}P NMR features can be independently prepared (Scheme 3). This species is accessed by reaction of **4** with 2 equiv. of *n*BuLi, and was identified as the diiron(I) μ-κ^1:κ^1-N_2 dihydride complex $[P_6ArCH_3](FeH)_2(\mu\text{-}N_2)$ (**7**) by XRD analysis (Figure 6a). The most noteworthy feature of the solid state structure of **7** is the ligand distortion (C1-C2-C3-P1 torsion angle: 29.8(5)°, Table S7) necessary to accommodate the Fe-N_2-Fe linkage. Otherwise, it resembles a previously reported, untethered congener, which also reacts with H_2 to generate an $Fe(H)_2(N_2)$ complex following exposure to N_2.[64-65] The singlet ground state of **7** likely arises from antiferromagnetic coupling of two low spin Fe(I) centers through the linear N_2 bridge.[64] Generation of the intermediate **7** requires the addition of 2 equiv. of H_2 to **5**, with the central carbyne ligand being fully protonated.

Scheme 2. Mechanism for the activation of **5** toward N_2 binding.

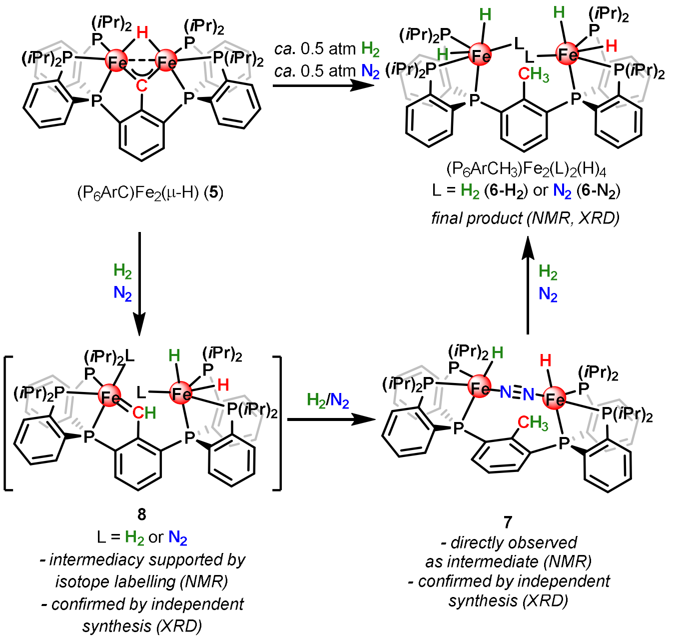

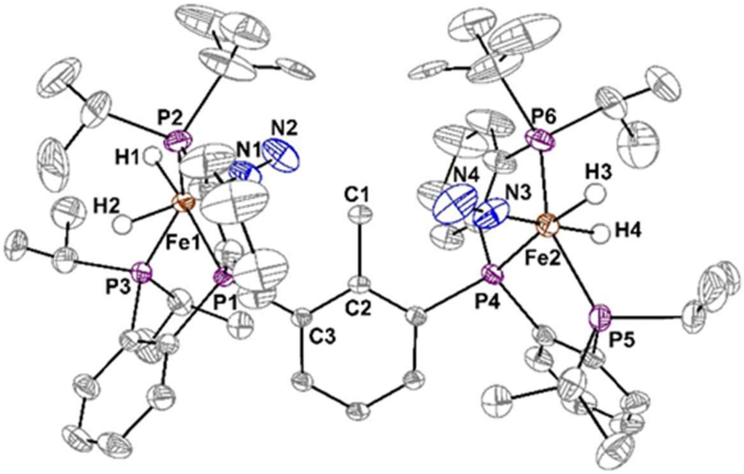

Figure 5. Crystal structure of $(P_6ArCH_3)Fe_2(N_2)_2(H)_4$ (**6**). Hydrogen atoms on the ligand are omitted for clarity. Thermal ellipsoids shown at 50% probability.

Efforts to directly observe the intermediate resulting from addition of only 1 equiv. of H_2 to **5** during the course of the reaction were not fruitful. However, isotope labelling experiments provide insight into the mechanism of this transformation. When **5** is exposed to a mixture of D_2 and N_2, a feature at -12.9 ppm integrating to one proton is observed in the ^1H NMR spectrum of the product **6** (Figure S52). Moreover, no signal corresponding to a $–CHD_2$

group is observed, demonstrating that D_2 adds regioselectively across one Fe-C bond with the original hydride ligand of **5** remaining bound to Fe. At room temperature under ambient light, this reaction is not reversible, and the original hydride ligand of **5** does not exchange with D_2 in the headspace.

The foregoing experiment indicates that the intermediate arising from addition of 1 equiv. of H_2 to **5** has formed at least one C-H bond and has at least one iron-bound hydride. Such a species can be independently synthesized by reduction of the diiron(I) dibromide **4** with excess Na/Hg amalgam (Scheme 3), affording the diiron(II) carbene, dihydride complex $(P_6ArCH)Fe_2(N_2)_2(H)_2$ (**8**, Figure 6b). One iron site has trigonal bipyramidal symmetry, with an N_2 ligand located *trans* to P1. The central carbon is bound to this iron via a terminal Fe=C(*H*)Ar linkage, characterized by a short Fe1-C1 distance (1.911(4) Å, Table S7). A detailed investigation of the electronic structure of **8** is beyond the scope of the present study, but we note the relatively long iron-carbene bond length that may implicate an unusual electron configuration at Fe1.[66] The other iron center is six coordinate, with a *cis*-dihydride motif. One hydride ligand bisects the P5-Fe2-P6 angle (151.36(5)°) while the other is *trans* to P4.

Scheme 3. Independent synthesis of **7** and **8.**

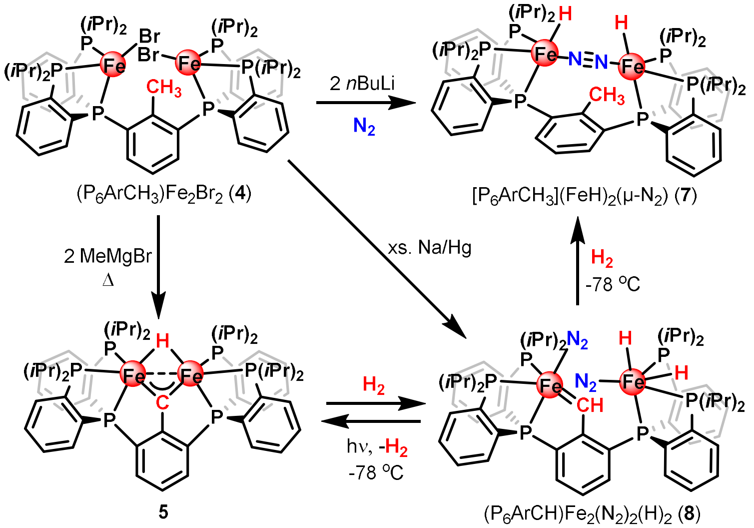

The presence of a terminal Fe=C(*H*)Ar motif in **8** is indicated by a diagnostic resonance at δ = 11.0 ppm (s, 1H) in the ^{1}H NMR spectrum (Figure S40). The carbon atom of Fe=*C*(H)R linkage gives rise to a strongly upfield shifted resonance, which appears as a 1:2:2:2:1 quintet at δ = 224 ppm in the ^{13}C{^{1}H} NMR spectrum due to coupling to two inequivalent classes of phosphorus nuclei ($^2J_{\text{C-P}}$ = 40 Hz, 1P; $^2J_{\text{C-P}}$ = 20 Hz, 2P). This feature becomes a doublet of quintets in the gate-decoupled ^{13}C NMR spectrum (Figure S44) due to coupling to the Fe=C(*H*)R proton ($^1J_{\text{C-H}}$ = 134 Hz). Spectroscopic confirmation of the presence of two iron-bound hydride ligands is obtained from the ^{1}H NMR spectrum of **8**, which features characteristic resonances at δ = -9.7 ppm and -20.6 ppm each corresponding to one proton (Figure S40-41). The hydride ligands are also detectable by IR spectroscopy, giving rise to a broad $\nu_{\text{Fe-H}}$ feature at 1789 cm^{-1}. Additional resonances at 2006 and 2070 cm^{-1} arise from the two molecules of N_2 observed in the solid state structure of **8**, one at each iron (Figure S45). Beyond its relevance to the activation of **5** toward coordination of N_2, **8** is a rare example of an N_2-bound iron-carbene or alkylidene complex, with only one series of compounds reported previously.[27]

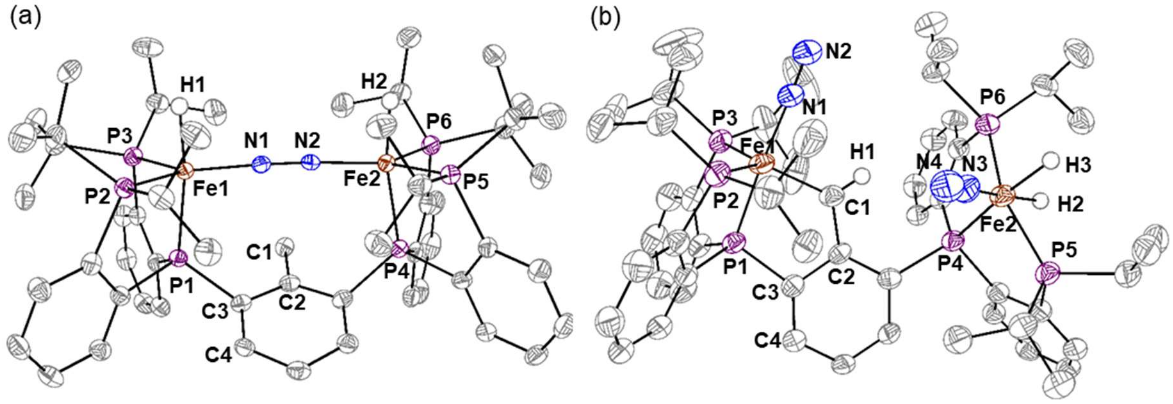

Figure 6. Independent synthesis of $[P_6ArCH_3](FeH)_2(\mu\text{-}N_2)$ (**7**) and $(P_6ArCH)Fe_2(N_2)_2(H)_2$ (**8**) from $(P_6ArCH_3)Fe_2Br_2$ (**4**). (a) Crystal structure of $[P_6ArCH_3](FeH)_2(\mu\text{-}N_2)$ (**7**). (b) Crystal structure of $(P_6ArCH)Fe_2(N_2)_2(H)_2$ (**8**). Hydrogen atoms on the ligand are omitted for clarity. Thermal ellipsoids shown at 50% probability.

The carbene complex **8** is a kinetically competent intermediate in the hydrogenation of **5**. Reaction of **8** with an equimolar mixture of H_2 and N_2 proceeds much more rapidly than the corresponding reaction of **5** (Figure S59-60). However, the initial product of this transformation is not **6-H₂**, but rather an equivalent species exhibiting mixed H_2/N_2 coordination (**6-H_2/N_2**). Evidently, N_2 does not readily exchange with H_2 under the experimental conditions. This notion is supported by the fact that **6-H_2/N_2** gradually converts to **6-N_2** upon exposure to an atmosphere of N_2 (Figure S61-62), similar to what is observed for **6-H_2**. Additional support for the intermediacy[67] of **8** in the hydrogenation of **5** was obtained by demonstrating that the reverse process, liberation of H_2 to generate **5**, is feasible under photolytic conditions (Scheme 3 and Figure S64). If the photolysis of **8** is conducted at -78 °C, both **5** and **7** are produced simultaneously (Figure S65-66). The most probable origin of **7** in these experiments is from addition of H_2 (liberated during the photolysis) to residual **8**, rather than addition of 2 equiv. of H_2 to **5** (Scheme 3). Indeed, independent studies show that **5** does not react with H_2/N_2 at low temperatures. Attempts to stoichiometrically add H_2 to **8** otherwise have consistently led to over-reaction to **6**. However, slow *in situ* generation of

H_2 via photolysis was a convenient strategy to observe conversion of **8** to **7**, the next intermediate in sequence.

Consequences for H_2 and N_2 Activation. Paramagnetic complexes which bind[68-70] and cleave[63, 71-73] H_2 remain rare. In a well-characterized example, Rh^{II} porphyrin complexes split H_2 via a linear, termolecular $[M\cdots H\cdot\cdot H\cdots M]^‡$ transition state.[74-75] This linear transition state facilitates homolytic cleavage by optimizing both M···H interactions in a manner similar to that implicated for other radical-type atom abstraction reactions.[75] In contrast, the spin-carrying orbitals of **5** are orthogonal (Figure 4), which precludes direct diradical activation of H_2 from **5**. Instead, H-H cleavage by **5** likely involves a transient σ-complex (Scheme 4). This intermediate may undergo bimetallic oxidative addition[76] followed rapidly by C-H bond formation (reductive elimination/H-migration) to avoid the accumulation of a spectroscopically observable trihydride intermediate, affording **8** (pathway a in Scheme 4). Moreover, this OA/RE sequence has to be irreversible (*i.e.* RE must be fast relative to OA), otherwise, the original μ-hydride ligand would scramble and be statistically incorporated into the incipient methyl group, which is not observed experimentally. This scenario would be in contrast with the rapid interconversion of hydride and H_2 ligands that occurs in **6-H₂**.

An alternative mechanism for the formation of **8** involves concerted cleavage of H_2 and formation of the C-H bond (pathway b in Scheme 4). In this mechanism, displacement of the μ-hydride facilitates an intramolecular formal deprotonation of H_2 by the μ-carbyne ligand (or, as an alternative, a σ-bond metathesis, which would involve a similar transition state), converting **5** directly to the carbene-dihydride complex **8**. The lack of H/D scrambling into CH_3 substituent implies that this deprotonation is irreversible, at least under thermal conditions, suggesting that the basicity of the μ-carbyne ligand may drive the reaction.

Scheme 4. Plausible mechanisms for H_2 activation by **5**.

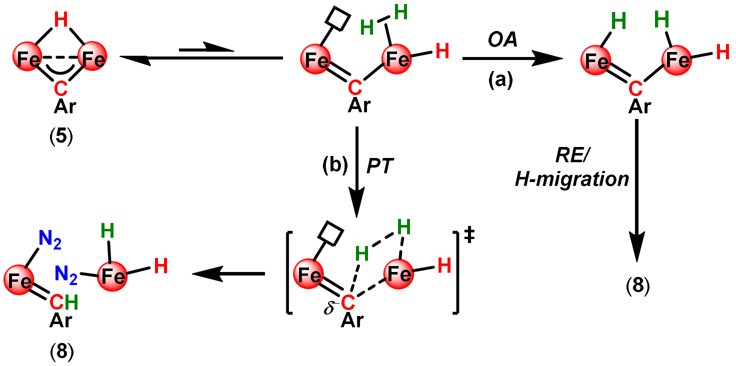

Although hydrogenation of **5** is thermodynamically favorable, it is a remarkably slow process, proceeding to completion only over the course of days. In contrast, cleavage of H_2 by the diamagnetic tetrairon μ₄-carbide cluster $[Fe_4C(CO)_{12}]^{2-}$ proceeds rapidly, even at lower temperatures.[77] Likwise, a diamagnetic diiron(II) μ-nitride complex $[([PhBP_3]Fe)_2(\mu\text{-}N)][Na(THF)_5]$, readily activates H_2, with full conversion to the μ-imide, μ-hydride species $[([PhBP_3]Fe)_2(\mu\text{-}NH)(\mu\text{-}H)][Na(THF)_5]$ within 30 minutes.[59] This latter species, although isoelectronic to **5**, appears to be inert to H_2, consistent with the suggestion that the enhanced basicity of the μ-carbyne is crucial for the observed reactivity.

The experimental data suggests that conversion of the open-shell diiron μ-carbyne complex **5** to the diamagnetic iron-carbene species **8** is the rate-limiting step in the overall transformation of **5** to **6**. As such, the slow overall reaction kinetics may result from the spin-forbidden character of this first H_2 activation step (see Figure S76 for a representation of the initial σ-interaction of the incoming H_2 ligand with the $3d_{x2\text{-}y2}$-derived orbital HOMO-1, a potential site of incoming ligand coordination). Along the reaction coordinate for ligand binding in **5**, the ground state may mix with a singlet excited state in which this orbital is unoccupied, thereby introducing a spin-induced kinetic barrier.[78-79] Such barriers are avoided in the interconversion of $2H^+/H_2$ by the *hydrogenase* enzymes due to the low-spin character of the active sites, which are stabilized by their CO and $^-$CN rich coordination environment.[80]

Delivery of reducing equivalents to paramagnetic active sites via discrete $1H^+/1e^-$ transfer events may be kinetically advantageous as it avoids additional barriers due to changes in overall spin state. Indeed, reductive activation of FeMoco involves discrete proton/electron transfer events,[1] though several reduced forms of the cofactor can also be reversibly interconverted via addition/loss of H_2.[81-85] Preliminary experiments demonstrate that addition of PCET reagents (e.g. TEMPO-H) or acids (e.g. HCl) to **5** also yields species which bind N_2 concomitant with Fe-C bond cleavage and C-H bond formation (Scheme 5). For example, treatment of **5** with TEMPO-H affords a mixture of species, only one of which exhibits well-defined ^{31}P NMR signals. The ^1H NMR of the reaction mixture reveals a diagnostic Fe=C(*H*)R resonance at 11.7 ppm for this diamagnetic species (Figure S69). Coordination of N_2 by this compound is suggested by the observation of a feature at 2076 cm^{-1} in the IR spectrum (Figure S71). On the other hand, protonation of **5** with HCl proceeds more cleanly, yielding a new paramagnetic species identified as the alkyliron(II)-N_2, iron(I)-chloride complex $(P_6ArCH_2)Fe(N_2)FeCl$ (**9**) by XRD analysis (Figure S73). Although reaction of **5** with HCl proceeds rapidly, hydrogen atom abstraction from TEMPO-H is considerably slower. While the slower kinetics of this latter reaction may be partially attributed to a spin-induced kinetic barrier, the effects of sterics and polarity are difficult to assess. As a final comment, one has to note that the intriguing speculations above regarding the impact of spin state on the chemistry of **5** would require rigorous investigations to prove, which are beyond the scope of this report.

Scheme 5. One or two C-H protonation events, with cleavage of one Fe-C linkage, promotes N_2 binding.

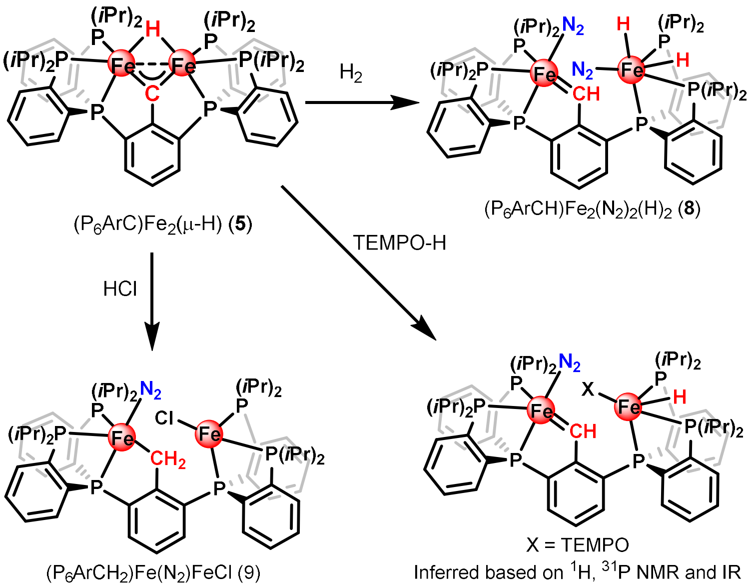

The absence of direct N_2 coordination by **5** is also noteworthy. One can envision an isomer of **5** featuring a terminal hydride ligand that binds N_2 in an end-on fashion (analogous to the H_2 σ-complex illustrated in Scheme 4) or cooperatively between the two iron sites. This scenario seems all the more plausible given that a series of thiolate-bridged diiron complexes structurally related to **5** have been reported which readily bind N_2.[86] If such an isomer were the lowest in energy, it seems likely that it would be accessible at the elevated reaction temperatures employed in the synthesis of **5**. Although spin-blocking might rationalize slow N_2 binding kinetics, there is evidently a thermodynamic perference for the μ-hydride ligand in **5**, in spite of the distortions it imposes on the ligand framework. Whether this thermodynamic bias against N_2 binding is predominantly electronic or steric in origin, our studies clearly demonstrate that displacement of the μ-hydride via C-H bond formation is a viable mechanism to promote an otherwise unfavorable N_2 coordination event.

CONCLUSIONS

Although it is difficult to harmonize the entirety of Siegbahn's mechanism[19] with the fact that the interstitial carbide is neither exchanged nor lost during turnover,[87] our studies demonstrate that Fe-C bond cleavage and C-H bond formation is a feasible mechanism for activation of a carbon-bridged diiron site toward binding N_2. The open-shell diiron μ-carbyne complex **5** does not bind N_2 on its own, emphasizing the robustness of the $Fe(\mu\text{-}X)_2Fe$ (X = C, H, or S) diamond core motif. Coordination of N_2 at such a subsite evidently requires cleavage of at least one Fe-X bond, though the effect of the higher coordination number of **5** and its sterically congested environment on N_2 binding remain under investigation. While intermediates such as **7** featuring a fully protonated carbon bind N_2, a single C-H protonation event, with concomitant cleavage of one Fe-C bond, is sufficient to generate a site which coordinates N_2. Given that the $\mu_6\text{-}C^{4-}$ ligand of FeMoco is installed via C-H activation, monoprotonation of the carbide may be reversible and generate an intermediate sufficiently reactive that it has avoided direct spectroscopic detection to date.

EXPERIMENTAL DETAILS

General Considerations. All reactions were performed at room temperature in a nitrogen filled M. Braun glovebox or using standard Schlenk techniques unless otherwise specified. Glassware was oven dried at 140°C for at least two hours prior to use, and allowed to cool under vacuum. Bis(*o*-diisopropylphosphinophenyl)-chlorophosphine (P_2P^{Cl}) was prepared as described elsewhere.[88] All other reagents were obtained commercially unless otherwise noted and typically stored over activated 4 Å molecular sieves. Tetrahydrofuran, toluene-d_8 and benzene-d_6 were dried using sodium/benzophenone ketyl, degassed with three freeze-pump-thaw cycles, vacuum transferred, and stored over 3 Å molecular sieves prior to use. Diethyl ether, benzene, toluene, acetonitrile, hexanes, and pentane were dried by sparging with nitrogen for at least 15 minutes, then passing through a column of activated A2 alumina under positive nitrogen pressure. ^{1}H and ^{31}P NMR spectra were recorded on a Varian 300 or 400 MHz spectrometer. All chemical shifts (δ) are reported in ppm, and coupling constants (*J*) are in hertz. The ^{1}H-NMR spectra were referenced using residual H impurity in the deuterated solvent. UV-Vis spectra were recorded on a Varian Cary Bio 50 spectrophotometer. Infrared (ATR-IR) spectra were recorded on a Bruker ALPHA ATR-IR spectrometer. Elemental analyses were performed at Caltech.

Physical Methods

Mössbauer Measurements. Zero field ^{57}Fe Mössbauer spectra were recorded in constant acceleration on a spectrometer from See Co (Edina, MN) equipped with an SVT-400 cryostat (Janis, Wilmington, WA). The quoted isomer shifts are relative to the centroid of the spectrum of α-Fe foil at room temperature. Unless otherwise noted, samples were prepared by grinding polycrystalline (20-50 mg) into a fine powder and pressed into a homogenous pellet with boron nitride in a cup fitted with a screw cap. The data were fitted to Lorentzian lineshapes using the program WMOSS (www.wmoss.org).

Magnetic Measurements. Magnetic measurements for 5 were conducted with a Quantum Design MPMS3 SQUID Magnetometer at the University of California, Los Angeles. A polycrystalline sample of 5 was wrapped in plastic film and placed in a gelatin capsule. The capsule was then inserted into a plastic straw. Magnetization data at 100 K from 0 to 4 T were collected to confirm the absence of ferromagnetic impurities. Direct current variable temperature magnetic susceptibility measurements were collected between 1.8 and 300 K with a 0.1 T field. Magnetic susceptibility data was corrected for diamagnetism of the sample, estimated using Pascal's constants. Magnetic susceptibility data was simulated with PHI.[89]

X-ray Crystallography. For compounds 4-8, low-temperature (100 K) diffraction data (φ-and ω-scans) were collected on a Bruker AXS D8 VENTURE KAPPA diffractometer coupled to a PHOTON 100 CMOS detector with Mo Kα radiation (λ = 0.71073 Å) or with Cu Kα (λ = 1.54178 Å). All diffractometer manipulations, including data collection, integration, and scaling were carried out using the Bruker APEXII software.[90] Absorption corrections were applied using SADABS.[91] Structures were solved by direct methods using SHELXS[92] and refined against *F*2 on all data by full-matrix least squares with SHELXL-2014[93] interfaced with Olex2-1.2.8[94] and using established refinement techniques. All non-hydrogen atoms were refined anisotropically, except heavily disordered solvent in some cases. Hydrogen atoms were included into the model at geometrically calculated positions and refined using a riding model, except for the hydride ligands in 5, 7, and 8 and the carbene C-*H* in 8. The isotropic displacement parameters of all hydrogen atoms were fixed to 1.2 times the *U* value of the atoms they are linked to (1.5 times for methyl groups).

DFT Calculations. Calculations were carried out using version 4.0.2 of the ORCA package.[95] Gas phase geometry optimizations were conducted using both the BP86 and TPSS functionals in combination with the scalar relativistically recontracted versions of the def2-SVP (ZORA-def2-SVP) basis set on most C and H atoms. An enlarged basis set (ZORA-def2-TZVP) was employed for the Fe and P atoms, the iron-bound C and H ligands as well as any C atoms of the central aryl linker which undergo significant distortion in the solid state structure. For all atoms, the general-purpose segmented all-electron relativistically contracted auxiliary Coulomb-fitting basis (SARC/J) was employed. Optimizations were followed by a frequency calculation to ensure a true minimum. In general, geometries obtained using the meta-GGA functional TPSS correlated better with the solid state structure. As such, single point calculations were carried out on these optimized geometries, using either the TPSSh, PBE0, or B3LYP functionals and an enlarged basis set (ZORA-def2-TZVPP) on the Fe and P atoms, the iron-bound C and H ligands as well as any C atoms of the central aryl linker which undergo significant distortion in the solid state structure. For all functionals employed, the $S = 1$ state was predicted to be lowest in energy, consistent with experiment. Orbital and spin density plots were rendered using UCSF Chimera.[96]

For DFT calculations of Mössbauer parameters,[60] the TPSSh functional was used in combination with the def2-TZVP basis set on most C and H atoms. The CP(PPP) basis set was employed for Fe and the IGLO-III basis set was utilized for P and the iron-bound C and H ligands as well as any C atoms of the central aryl linker which undergo significant distortion in the solid state structure. The general purpose def2/J Coulomb fitting basis was employed on atoms using the def2-TZVPbasis, while the AutoAux feature of ORCA was used to generate auxiliary bases for the other atoms. All auxiliary bases were fully decontracted. To capture core polarization effects, the radial integration accuracy was increased around the Fe, P, and the iron-bound C and H ligands (IntAcc 7). A previously-reported calibration[97] was used to convert the computed Fe core electron density to the isomer shift (δ) in units of mm s^{-1}; estimates of the uncertainty in the computed values of δ and ΔE_Q were obtained from this calibration. The Mössbauer parameters calculated from the $S = 1$ geometry correlated best with the experimental data.

Synthetic Procedures. *Preparation of (3-bromo-2-methylphenyl)(bis(2-diisopropylphenylphosphino)phosphine, (1).* A solution of *n*BuLi (2.4 mL, 3.87 mmol, 1.05 equiv.) was added dropwise to stirring solution of 2,6-dibromotoluene (919 mg, 3.68 mmol, 1 equiv.) in 35 mL of diethyl ether at -78 ºC. After stirring for 105 minutes at -78 ºC, the resulting colorless suspension was removed from the cold bath and stirred for an additional 7 minutes. The resulting colorless solution was then cooled back to -78 ºC. *CAUTION*: *DO NOT*

CONCENTRATE TO DRYNESS! The monolithiated species reacts exothermically if concentrated to dryness, causing glass failure and implosion of the reaction flask. A suspension of bis(*o*-diisopropylphosphinophenyl)-chlorophosphine (1.76 g, 3.87 mmol, 1.05 equiv.) in 12 mL of toluene was then added dropwise. The cold bath was removed and the orange suspension was allowed to warm to room temperature. After stirring for three hours, the resulting pale yellow suspension was filtered over Celite and concentrated in vacuo. The residue was washed with copious amounts of acetonitrile followed by pentane (2 x 5 mL) to afford 1 as an off-white powder (1.70 g, 78% yield). ^{1}H NMR (400 MHz, C_6D_6) δ = 7.41 (d, *J* = 8.1 Hz, 1H), 7.31 (m, 2H), 7.06 (t, *J* = 7.0 Hz, 2H), 6.97 (m, 2H), 6.91 (t, *J* = 7.6 Hz, 3H), 6.59 (t, *J* = 7.7 Hz, 1H), 2.72 (s, 3H), 2.11 (m, 2H), 1.95 (m, 2H), 1.12 (m, 12H), 0.87 (m, 12H). ^{31}P NMR (162 MHz, C_6D_6) δ = -0.7 (d, *J* = 156 Hz, 2P), -17.6 (t, *J* = 156 Hz, 1P). ^{13}C NMR (101 MHz, C_6D_6) δ = 147.32 (m), 147.06 (m), 146.98 (m), 142.74 (dd, *J* = 76 Hz, 124 Hz), 142.28 (t, *J* = 32 Hz), 142.07 (t, *J* = 28 Hz), 141.76 (s), 141.49 (s), 134.91 (s), 132.65 (s), 129.07 (b), 127.08 (b), 126.67 (d, *J* = 16 Hz), 25.90 (b), 24.31 (b), 21.96 (s), 21.71 (s), 20.45 (m), 19.73 (b).

Preparation of 2,6-bis[bis(2-diisopropylphenylphosphino)phosphino)]toluene, (2). Excess magnesium turnings (1.94, 79.6 mmol, 10 equiv.) were added to a solution of 1 (4.67 g, 7.96 mmol, 1 equiv.) in 35 mL of tetrahydrofuran. After stirring for 8 hours, the solution was filtered and cooled to -78 °C. A solution of bis(*o*-diisopropylphosphinophenyl)-chlorophosphine (3.78 g, 8.36 mmol, 1.05 equiv.) in 5 mL of tetrahydrofuran was then added dropwise. The cold bath was removed and the yellow solution was allowed to warm to room temperature. After stirring overnight, excess 1,4-dioxane (20 equiv.) was added, resulting in precipitation of a colorless solid. After stirring for 30 minutes, the mixture was concentrated to dryness. The oily residue was triturated once with hexanes and reconcentrated dryness. The resulting yellow solid was extracted with toluene, affording a yellow suspension which was filtered over Celite. After concentrating *in vacuo*, the residue was washed with acetonitrile (3 x 20 mL) and pentane (3 x 6 mL), affording 2 as a white powder (5.97 g, 81% yield). ^{1}H NMR (400 MHz, C_6D_6) δ = 7.35 (b, 4H), 7.20-7.00 (b, 12H), 6.98 (d, *J* = 8 Hz, 2 H), 6.79 (t, *J* = 8 Hz, 1H), 3.02 (s, 3H), 2.11 (b, 4 H), 1.95 (b, 4H), 1.15 (b, 24H), 0.88 (b, 24H). ^{31}P NMR (162 MHz, C_6D_6) δ = -1.48 (d, *J* = 159 Hz, 4P), -20.32 (t, *J* = 152 Hz, 2P). ^{13}C NMR (101 MHz, C_6D_6) δ = 148.33 (m), 147.03 (b), 142.48 (m), 142.53 (m), 139.21 (m), 137.82 (s), 136.26 (broad s), 134.90 (broad s), 132.44 (broad s), 129.27 (s), 128.80 (broad m), 128.51 (s), 125.87 (s), 125.64 (s), 25.78 (broad m), 23.78 (broad m), 21.41 (s), 20.77 (s), 20.57 (s), 20.33 (m), 19.18 (broad m).

Preparation of (P_6ArCH_3)Fe_2Br_4, (3). A solution of 2 (5.97 g, 6.46 mmol, 1.0 equiv.) in tetrahydrofuran (10 mL) was added to a suspension of $FeBr_2$ (2.78 g, 12.9 mmol, 2.0 equiv.) in tetrahydrofuran (40 mL). After stirring for overnight, the resulting precipitate was collected on a fine frit and washed with additional tetrahydrofuran, affording a species tentatively assigned as 3 as a yellow-green powder (8.23 g, 94% yield) which was used in subsequent reactions without further purification. ^{1}H NMR (400 MHz, CD_2Cl_2) δ = 166.66 (b), 161.79 (b), 71.19 (b), 44.96 (s), 38.34 (b), 28.86 (b), 16.25 (b), 14.59 (b), 14.08 (b), 12.44 (b), 11.98 (b), 10.76 (b), 8.17 (b), 6.94 (b), 2.85 (b), 0.55 (b), -8.56 (s).

Preparation of (P_6ArCH_3)Fe_2Br_2 (4). A suspension of Cp^*_2Co (3.88 g, 11.8 mmol, 2.0 equiv.) in minimal tetrahydrofuran (~10 mL) was added to a suspension of 3 (7.99 g, 5.9 mmol, 1.0 equiv.) in benzene/tetrahydrofuran (3:1, 130 mL). After stirring for three hours, the resulting brick red suspension was filtered over Celite and concentrated *in vacuo*. The residue was resuspended in 60 mL of benzene and stirred vigorously. Pentane (~100 mL) was added slowly to precipitate a red solid. The precipitate was collected on a fine frit and washed with additional pentane, affording 4 as a brick red powder (3.4 g, 48% yield). Crystals suitable for X-ray diffraction were obtained by diffusion of pentane into a concentrated benzene solution of 4. ^{1}H NMR (400 MHz, C_6D_6) δ = 185.84 (b), 111.73 (b), 71.82 (b), 48.77 (s), 24.69 (b), 9.84 (b), 8.40 (b), 5.48 (b), -5.02 (b), -14.10 (b), -32.32 (b). UV-Vis (THF) [ε (M^{-1} cm^{-1})]: 345 nm (5.3 x 10^3), 404 nm (5.6 x 10^3), 845 nm (4.0 x 10^2). Anal. Calcd (%) for $C_{55}H_{78}Br_2Fe_2P_6$: C, 55.21; H, 6.57; N, 0.00. Found: C, 55.22; H, 5.92; N, -0.03.

Preparation of $(P_6ArC)Fe_2(H)$ (5). A solution of 4 (443.3 mg, 0.37 mmol, 1.0 equiv.) in 12 mL of tetrahydrofuran was chilled to -78 ºC in a dry ice/acetone bath. A diluted solution of MeMgBr (0.3 M, 1.9 mL, 0.74 mmol, 2.0 equiv.) was added dropwise, and the mixture was stirred for 4 hours at -78 ºC before the cold bath was removed. After stirring 20 hours at room temperature, the resulting brown solution was concentrated *in vacuo*. The residue was extracted with benzene and filtered over Celite. The filtrate was then charged into a Schlenk tube and heated at reflux for 24 hours. Excess 1,4-dioxane (1 mL) was then added. After stirring for 30 minutes, the solution was filtered over Celite and then concentrated to dryness. The residue was extracted with toluene, filtered over Celite and then concentrated under vacuum. The residue was then washed with pentane (4 x 8 mL) and diethyl ether (2 x 8 mL) and then eluted with copious amounts of benzene/pentane (1/1). The filtrate was concentrated en vacuo, affording 5 as a black-brown powder (220 mg, 56%). X-ray quality crystals can be obtained by diffusion of pentane vapors into a concentrated solution of 5 in benzene. We note that on occasion 4 is not completely consumed in the reaction. In that case, the crude mixture obtained after thermolysis was stirred for 4 hours over excess Na/Hg (2%) and then worked up as described. ^{1}H NMR (400 MHz, C_6D_6) δ = 42.18 (b), 35.47 (b), 28.38 (b), 12.05 (b), 10.39 (b), 9.20 (b), 5.45 (b), 4.66 (b), 4.25 (b), 0.09 (b), -2.28 (b), -15.28 (b). UV-Vis (THF) [ε (M^{-1} cm^{-1})]: 313 nm (1.51 x 10^4), 366 nm (1.46 x 10^4), 479 nm (8.7 x 10^3), 788 nm (3.9 x 10^3). Anal. Calcd (%) for $C_{55}H_{76}Fe_2P_6$: C, 63.84; H, 7.40; N, 0.00. Found: C, 63.20; H, 6.99; N, 0.02.

Preparation of *(P_6ArCH_3)$Fe_2(H_2)_2(H)_4$, (6-H_2).* A J Young NMR tube was charged with 5 (12.5 mg, 0.012 mmol) and dissolved in C_7D_8 (0.45 mL). The tube was degassed on the Schlenk line with three freeze-pump-thaw cycles. A mixture of H_2/N_2 (*c.a.*50:50) was admitted to the tube at room temperature. This was rotated slowly until ^{1}H and ^{31}P NMR measurements indicated full consumption of 5, generally seven-eight days. Characterization of 6-H_2 was conducted on samples prepared *in situ*, as exposure to a N_2 atmosphere converts 6-H_2 irreversibly (at room temperature in ambient light) to 6-N_2. ^{1}H NMR (400 MHz, C_7D_8) δ = 7.60 (t, *J* = 8 Hz, 4H), 7.39 (d, *J* = 8 Hz, 4H), 7.12 (s, 2H), 6.95-7.03 (m, 6H), 6.74 (t, *J* = 8 Hz, 2H), 6.54 (t, *J* = 8 Hz, 1H), 2.40 (m, 4H), 2.05 (s, 3H), 1.91 (m, 4H), 1.32 (dd, *J* = 8 Hz, 16 Hz, 12H), 1.09 (dd, *J* = 8 Hz, 12 Hz, 12H), 0.97 (dd, *J* = 8 Hz, 12 Hz, 12H), 0.62 (dd, *J* = 8 Hz, 12 Hz, 12H), -12.92 (t, *J* = 28 Hz, 8H). ^{31}P{^{1}H} NMR (162 MHz, C_6D_6) δ = 124.91 (broad d, *J* = 15 Hz, 4P), 110.00 (t, *J* = 19 Hz, 2P).

Preparation of *(P_6ArCH_3)$Fe_2(N_2)_2(H)_4$, (6-N_2).* A J Young NMR tube was charged with 5 (12.5 mg, 0.012 mmol) and dissolved in C_6D_6 (0.45 mL). The tube was degassed on the Schlenk line with three freeze-pump-thaw cycles. A mixture of H_2/N_2 (*c.a.*50:50) was admitted to the tube at room temperature. This was rotated slowly until ^{1}H NMR measurements indicated full consumption of 5, generally seven-eight days. At this point, the tube was once again degassed via three freeze-pump-thaw cycles and an atmosphere of N_2 was admitted. After mixing for 24 hours, this process was repeated, resulting in complete conversion to 6 as indicated by ^{1}H and ^{31}P NMR spectroscopy. Yellow crystals suitable for X-ray diffraction were obtained by slow evaporation of a solution of 6 in tetrahydrofuran/hexamethyldisiloxane (1:1). ^{1}H NMR (400 MHz, C_7D_8) δ = 7.77 (dd, *J* = 4Hz, 12 Hz, 4H), 7.51 (broad d, *J* = 4 Hz, 4H), 7.27 (s, 2H), 7.24 (m, 6H), 6.97 (t, *J* = 8 Hz, 2H), 6.78 (t, *J* = 8 Hz, 1H), 2.56 (m, 8H), 2.30 (s, 3H), 1.51 (dd, *J* = 8 Hz, 16 Hz, 12H), 1.36 (dd, *J* = 8 Hz, 12 Hz, 12H), 1.31 (dd, *J* = 8 Hz, 12 Hz, 12H), 0.59 (dd, *J* = 8 Hz, 12 Hz, 12H), -9.75 (m, 2H), -20.47 (m, 2H). $^{31}P\{^1H\}$ NMR (162 MHz, C_6D_6) δ = 115.60 (broad d, 4P), 105.30 (broad t, *J* = 13 Hz, 2P). IR (thin film from benzene): 2073 cm^{-1} (ν_{N-N}), 1790 cm^{-1} (ν_{Fe-H}).

Preparation of $[P_6ArCH_3](FeH)_2(\mu\text{-}N_2)$*, (7).* A suspension of 4 (41.8 mg, 0.035 mmol, 1 equiv.) in toluene (6 mL) was chilled to -78 °C in a glovebox cold well. A solution of *n*BuLi (43 µL, 1.61 M, 2 equiv.) was added, resulting in a gradual darkening of the solution. After stirring in the cold well for four hours, the vial was warmed to room temperature, leading to an immediate color change to green. The mixture was then filtered over Celite and concentrated to dryness. The green residue was washed with pentane (3 x 1 mL) and diethyl ether (3 x 1 mL), affording 7 in spectroscopically pure form. Complex 7 is thermally sensitive, decomposing fully in solution over the course of 6-8 hours at room temperature. Crystals suitable for X-ray diffraction were obtained by cooling a dilute toluene/hexamethyldisiloxane solution of 7 to -35 °C. ^1H NMR (400 MHz, C_6D_6) δ = 8.31 (broad m, 2H), 8.17 (broad m, 2H), 7.51 (dd, *J* = 8 Hz, 16 Hz, 4H), 6.89-7.07 (m, 11H), 2.19 (septet, *J* = 4 Hz, 4H), 1.86 (m, 6H), 1.75 (septet, *J* = 4 Hz, 4H), 1.67 (dd, *J* = 8 Hz, 16 Hz, 6H), 1.62 (s, 3H), 1.51 (m, 6H), 1.02 (dd, *J* = 4 Hz, 16 Hz, 6H), 0.88 (t, *J* = 8 Hz, 6H), 0.38 (dd, *J* = 4 Hz, 16 Hz, 6H), -0.08 (dd, *J* = 4 Hz, 16 Hz, 6H), -0.36 (dd, 4 Hz, 12 Hz, 6H), -3.96 (b, 2H). $^{31}P\{^1H\}$ NMR (162 MHz, C_6D_6) δ = 126.37 (b, 2P), 121.33 (d, *J* = 42 Hz, 2P), 110.83 (broad dd, *J* = 19 Hz, 44 Hz, 2P).

Preparation of $(P_6ArCH)Fe_2(N_2)(H)_2$*, (8).* A 2% mixture of sodium amalgam was prepared by adding Hg via syringe to Na (25.9 mg, 10 equiv.) smeared along the side of a one dram vial. The sodium amalgam was poured into a thawing solution of **4** (134.6 mg, 0.112 mmol, 1 equiv.) in tetrahydrofuran (14 mL). After stirring for an additional three hours under nitrogen atmosphere, the orange-brown solution was filtered over Celite and concentrated *in vacuo*. The residue was triturated twice with hexanes and then extracted with toluene. The filtrate was concentrated *in vacuo* and washed with pentane (3 x 2 mL), affording **8** (100 mg, 84%) in >90% purity as a brown powder. Crystals suitable for X-ray diffraction were obtained by slow evaporation of a concentrated solution of **8** in pentane/diethyl ether (1:1). ^{1}H NMR (400 MHz, C_6D_6) δ = 11.03 (s, 1H), 7.97 (t, *J* = 8 Hz, 2H), 7.58 (t, *J* = 8 Hz, 2H), 7.50 (d, *J* = 8 Hz, 2H), 7.32 (m, 2H), 6.92-7.02 (m, 6H), 6.84 (t, *J* = 8 Hz, 4H), 6.70 (t, *J* = 8 Hz, 1H), 2.83 (m, 2H), 2.63 (m, 2H), 2.12 (m, 2H), 2.00 (m, 2H), 1.55 (m, 12H), 1.41 (m, 6H), 1.15 (m, 6H), 0.97 (m, 6H), 0.89 (m, 6H), 0.51 (m, 6H), 0.32 (m, 6H), -9.74 (m, 1H), -20.65 (m, 1H). ^{31}P{^{1}H} NMR (162 MHz, C_6D_6) δ = 126.1 (t, *J* = 21 Hz, 1P), 114.7 (broad d, *J* = 45 Hz, 2P), 103.6 (b, 1P), 93.8 (d, *J* = 21 Hz, 2P). ^{13}C{^{1}H} NMR (101 MHz, C_6D_6) δ 224.62 – 223.56 (m), 167.10 (d, *J* = 10.5 Hz), 166.57 (d, *J* = 10.6 Hz), 150.85 (dt, *J* = 38.6, 19.3 Hz), 149.67 (dt, *J* = 45.0, 16.4 Hz), 147.91 – 146.72 (m), 145.78 – 143.86 (m), 138.87 (d, *J* = 8.6 Hz), 130.81 – 130.21 (m), 129.73 (d, *J* = 16.9 Hz), 129.17 – 128.49 (m), 123.41, 65.56, 34.09, 31.32, 30.49 (d, *J* = 3.1 Hz), 30.27 – 29.28 (m), 24.46 (td, *J* = 16.8, 7.6 Hz), 22.37, 20.43, 20.01, 19.54 (dd, *J* = 8.5, 4.3 Hz), 18.92 (q, *J* = 3.6, 3.0 Hz), 15.26, 13.95. IR (thin film from benzene): 2070 cm^{-1} (ν_{N-N}), 2006 cm^{-1} (ν_{N-N}), 1789 cm^{-1} (ν_{Fe-H})

Supplemental Figures

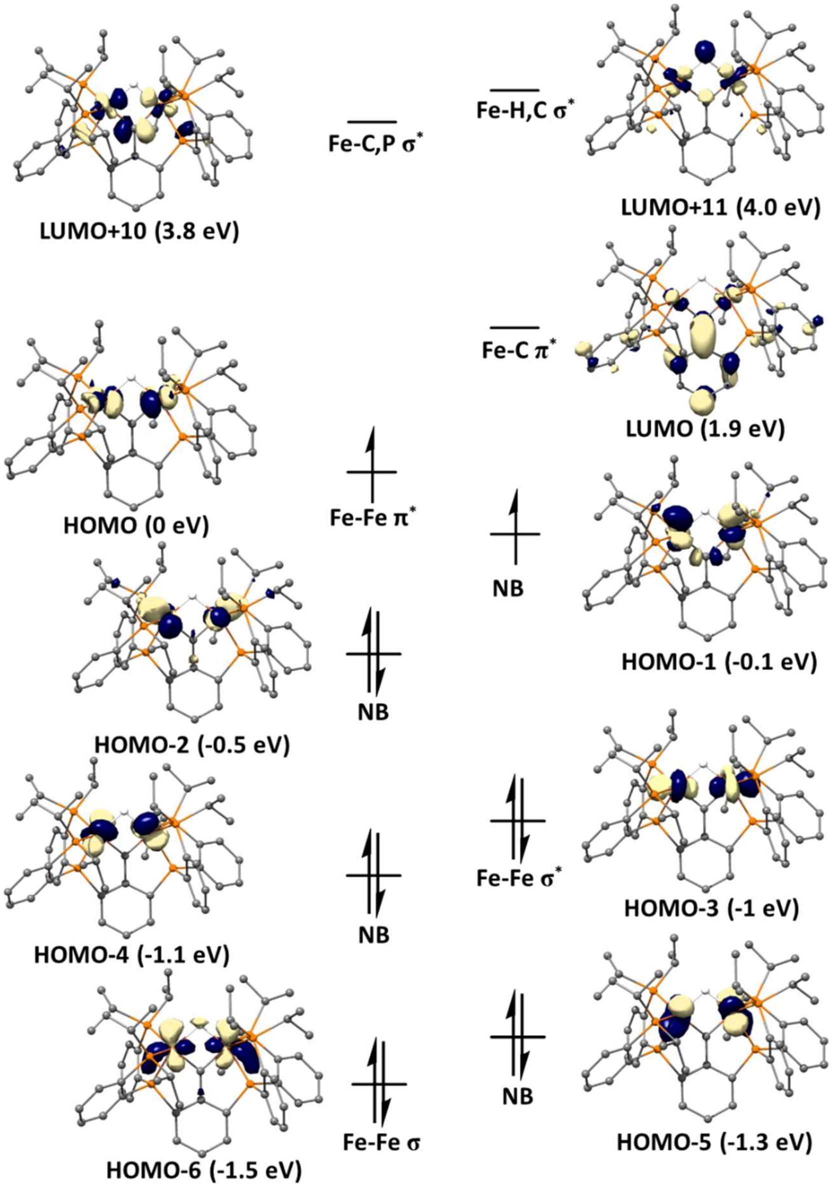

Figure S1. Calculated MO energy diagram and valence MOs for $(P_6ArC)Fe_2(\mu\text{-}H)$. Isosurfaces are shown at the 0.03 eÅ^{3} level and orbital energies (relative to the HOMO) are provided. Fe-Fe axial symmetry labels are a guide for the shape of the orbitals only.

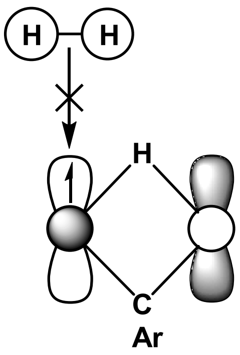

Figure S2. Illustration of the origin of spin-blocking in the activation of H_2 by **5**.

Summary Tables

Table 1. Summary of relevant metric parameters for complexes **4-8**.

	Complex				
	4	**5**	**6**	**7**	**8**
Fe1-C1	3.834(3)	1.792(1)	3.983(3)	3.811	1.911(4)
Fe1-H1	---	1.76(3)	---	1.52(5)	---
Fe1-P1	2.254(5)	2.1307(7)	2.1547(1)	2.145(1)	2.113(1)
Fe1-P2	2.330(6)	2.2627(8)	2.1584(2)	2.161(1)	2.221(1)
Fe1-P3	2.318(6)	2.2522(6)	2.1688(2)	2.186(1)	2.217(1)
Fe1-Fe2	7.666(6)	2.6776(6)	7.966(5)	4.758(1)	5.8861(9)
Fe1-Br1	2.351(4)	---	---	---	---
Fe1-N1	---	---	---	1.794(3)	1.821(3)
N1-N2	---	---	1.107(5)	1.167(4)	1.113(5)
Fe2-P4	---	---	---	2.142(1)	2.179(1)
Fe2-P5	---	---	---	2.160(1)	2.157(1)
Fe2-P6	---	---	---	2.182(1)	2.178(1)
Fe2-H2	---	---	---	1.47(5)	1.54(3)
Fe2-H3	---	---	---	---	1.53(3)
Fe2-N2	---	---	---	1.804(3)	---
Fe2-N3	---	---	---	---	1.800(3)
N3-N4	---	---	---	---	1.115(5)
Fe1-C1-Fe2	---	96.66(1)	---	---	---
H1-Fe1-C1	---	82.3(8)	---	---	---
P2-Fe1-P3	121.7(2)	116.14(3)	146.72(5)	106.28(5)	123.68(5)
P5-Fe2-P6	---	---	---	107.95(5)	151.36(5)
P1-C3-C4	123.1(1)	141.42(1)	120.0(2)	---	128.6(3)
C1-C2-C3	118.7(1)	117.52(9)	119.86(2)	120.1(3)	116.1(3)
P1-Fe1-N1	---	---	105.22(1)	99.6(1)	176.2(1)
C1-C2-C3-P1	5.9(1)	0.36(8)	0.8(2)	29.8(5)	5.3(4)

Table 2. Comparison of Experimental and Calculated Structural Metrics for $(P_6ArC)Fe_2(\mu\text{-}H)$.

		TPSS			BP86		
	Exp.	S = 0	S = 1	S = 2	S = 0	S = 1	S = 2
Fe1-C1	1.792(1)	1.785	1.788	1.837	1.784	1.787	1.831
Fe1-H1	1.76(3)	1.755	1.759	1.739	1.757	1.759	1.742
Fe1-P1	2.1307(7)	2.119	2.129	2.185	2.124	2.133	2.183
Fe1-P2	2.2627(8)	2.243	2.262	2.323	2.251	2.267	2.321
Fe1-P3	2.2522(6)	2.231	2.258	2.310	2.235	2.262	2.310
Fe-Fe	2.6776(6)	2.692	2.697	2.730	2.700	2.705	2.727

Table 3. Single point energies for TPSS-optimized geometries of $(P_6ArC)Fe_2(\mu\text{-}H)$.

	Energy / kJ mol^{-1}		
Functional	$S = 0$	$S = 1$	$S = 2$
B3LYP	57	0	13
PBE0	68	0	5
TPSSh	53	0	46

Table 4. Comparison of experimental and calculated Mössbauer parameters for $(P_6ArC)Fe_2(\mu\text{-}H)$.

	Exp.	$S = 0$	$S = 1$	$S = 2$
ρ (0)		11820.828	11820.651	11820.318
δ / mm s^{-1}	0.25	0.17	0.24	0.38
$\lvert\Delta E_Q\rvert$ / mm s^{-1}	0.37	2.68	0.38	0.63

Table 5. Summary of statistics for diffraction data relevant for complexes **4-5**.

	4	**5**
CCDC	1997107	1997108
Empirical formula	$C_{55}H_{56}P_6Fe_2Br_2$	$C_{65}H_{100}Fe_2P_6$
Formula weight	1174.33	1178.96
Temperature/K	99.99	100
Crystal system	monoclinic	monoclinic
Space group	C2/c	C2/c
a/Å	31.847(10)	14.878(4)
b/Å	11.095(2)	16.350(5)
c/Å	16.608(4)	25.612(5)
α/°	90	90
β/°	93.410(15)	90.577(15)
γ/°	90	90
Volume/Å^3	5858(3)	6230(3)
Z	4	4
ρ_{calc}g/cm^3	1.332	1.257
μ/mm^{-1}	7.365	5.469
F(000)	2392	2528
Crystal size/mm^3	0.18 × 0.1 × 0.01	0.301 × 0.25 × 0.24
Radiation	CuKα (λ = 1.54178)	CuKα (λ = 1.54178)
2Θ range for data collection/°	5.56 to 152.342	6.902 to 160.822
Index ranges	$-37 \leq h \leq 39$, $-13 \leq k \leq 13$, $-20 \leq l \leq 18$	$-18 \leq h \leq 18$, $-20 \leq k \leq 20$, $-29 \leq l \leq 32$
Reflections collected	41187	58255
Independent reflections	5568 [Rint = 0.1228, Rsigma = 0.0826]	6723 [Rint = 0.0496, Rsigma = 0.0260]
Data/restraints/parameters	5568/0/303	6723/0/343
Goodness-of-fit on F^2	1.076	1.024
Final R indexes [I>=2σ (I)]	R1 = 0.1876, wR2 = 0.3857	R1 = 0.0296, wR2 = 0.0738
Final R indexes [all data]	R1 = 0.2340, wR2 = 0.4128	R1 = 0.0315, wR2 = 0.0749
Largest diff. peak/hole / e Å^{-3}	2.17/-1.20	0.36/-0.27

Table 6. Summary of statistics for diffraction data relevant for complexes **6-7**.

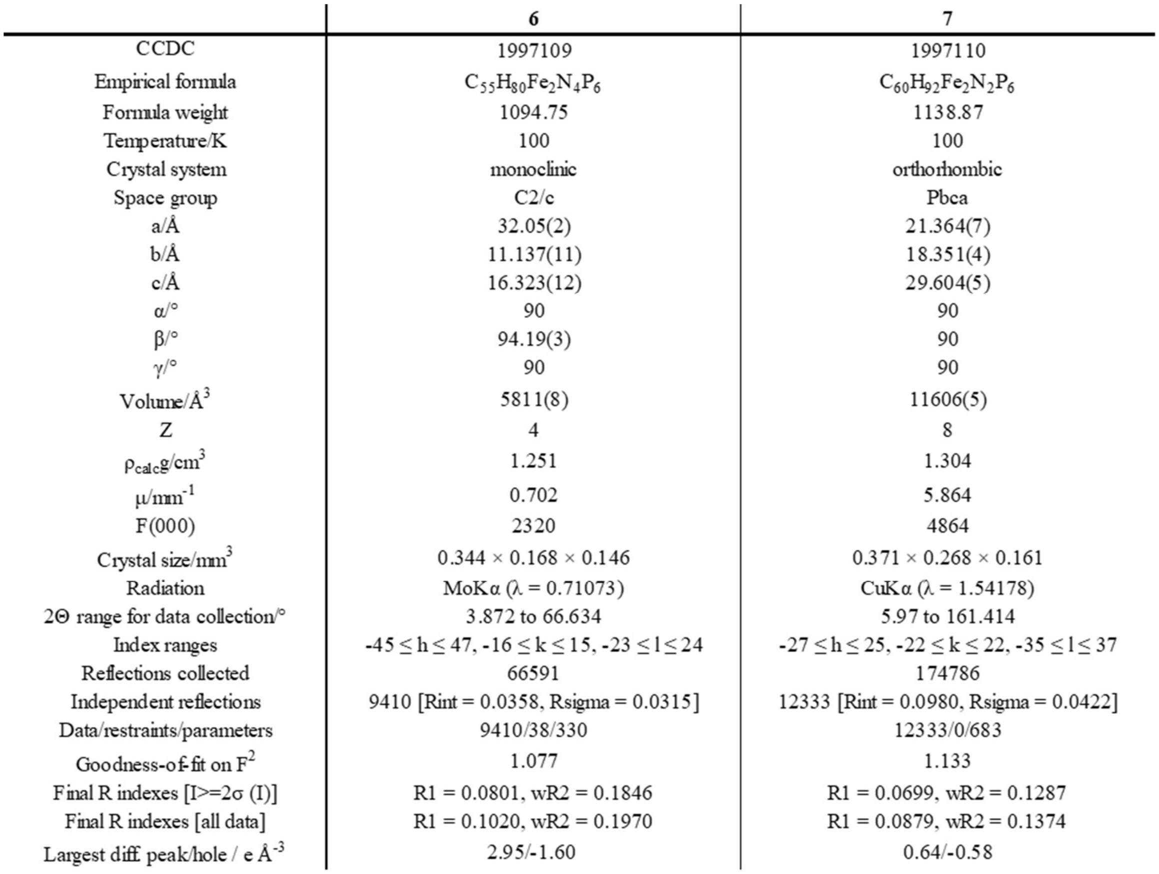

	6	**7**
CCDC	1997109	1997110
Empirical formula	$C_{55}H_{80}Fe_2N_4P_6$	$C_{60}H_{92}Fe_2N_2P_6$
Formula weight	1094.75	1138.87
Temperature/K	100	100
Crystal system	monoclinic	orthorhombic
Space group	C2/c	Pbca
a/Å	32.05(2)	21.364(7)
b/Å	11.137(11)	18.351(4)
c/Å	16.323(12)	29.604(5)
α/°	90	90
β/°	94.19(3)	90
γ/°	90	90
Volume/Å^3	5811(8)	11606(5)
Z	4	8
ρ_{calc}g/cm^3	1.251	1.304
μ/mm^{-1}	0.702	5.864
F(000)	2320	4864
Crystal size/mm^3	0.344 × 0.168 × 0.146	0.371 × 0.268 × 0.161
Radiation	MoKα (λ = 0.71073)	CuKα (λ = 1.54178)
2Θ range for data collection/°	3.872 to 66.634	5.97 to 161.414
Index ranges	$-45 \le h \le 47$, $-16 \le k \le 15$, $-23 \le l \le 24$	$-27 \le h \le 25$, $-22 \le k \le 22$, $-35 \le l \le 37$
Reflections collected	66591	174786
Independent reflections	9410 [Rint = 0.0358, Rsigma = 0.0315]	12333 [Rint = 0.0980, Rsigma = 0.0422]
Data/restraints/parameters	9410/38/330	12333/0/683
Goodness-of-fit on F^2	1.077	1.133
Final R indexes [I>=2σ (I)]	R1 = 0.0801, wR2 = 0.1846	R1 = 0.0699, wR2 = 0.1287
Final R indexes [all data]	R1 = 0.1020, wR2 = 0.1970	R1 = 0.0879, wR2 = 0.1374
Largest diff. peak/hole / e Å^{-3}	2.95/-1.60	0.64/-0.58

Table 7. Summary of statistics for diffraction data relevant for complex **8**.

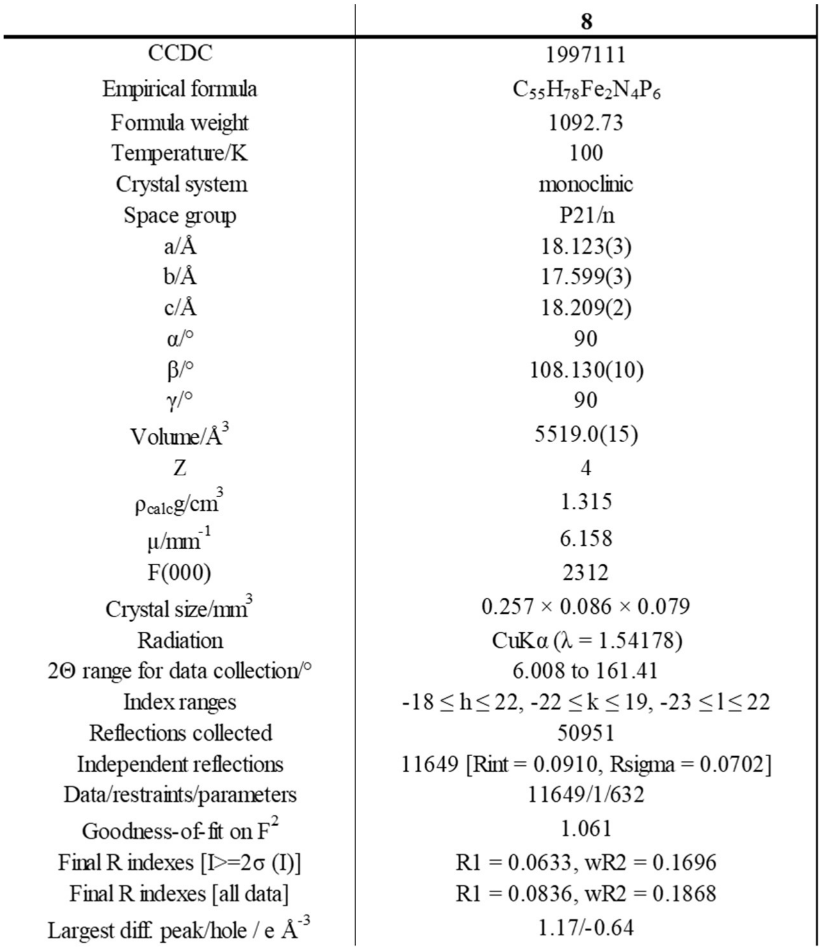

	8
CCDC	1997111
Empirical formula	$C_{55}H_{78}Fe_2N_4P_6$
Formula weight	1092.73
Temperature/K	100
Crystal system	monoclinic
Space group	P21/n
a/Å	18.123(3)
b/Å	17.599(3)
c/Å	18.209(2)
α/°	90
β/°	108.130(10)
γ/°	90
Volume/Å^3	5519.0(15)
Z	4
ρ_{calc}g/cm^3	1.315
μ/mm^{-1}	6.158
F(000)	2312
Crystal size/mm^3	0.257 × 0.086 × 0.079
Radiation	CuKα (λ = 1.54178)
2Θ range for data collection/°	6.008 to 161.41
Index ranges	$-18 \leq h \leq 22$, $-22 \leq k \leq 19$, $-23 \leq l \leq 22$
Reflections collected	50951
Independent reflections	11649 [Rint = 0.0910, Rsigma = 0.0702]
Data/restraints/parameters	11649/1/632
Goodness-of-fit on F^2	1.061
Final R indexes [I>=2σ (I)]	R1 = 0.0633, wR2 = 0.1696
Final R indexes [all data]	R1 = 0.0836, wR2 = 0.1868
Largest diff. peak/hole / e Å^{-3}	1.17/-0.64

Special Refinement Details for (P_6ArCH_3)Fe_2Br_2. Compound 4 crystallizes in the monoclinic space group *C*2/*c* with half of the molecule in the asymmetric unit. The molecule crystallizes with a two-fold rotation axis along the C1-C2 bond, such that the hydrogen substituents of the methyl group are disordered over a special position. These were refined with an AFIX 133 command.

Special Refinement Details for (P_6ArC)Fe_2H. Compound 5 crystallizes in the monoclinic space group *C*2/*c* with half of the molecule in the asymmetric unit. The data was of sufficient quality to unambiguously locate the bridging hydride ligand in the Fourier difference map.

Special Refinement Details for (P_6ArCH_3)$Fe_2(N_2)_2(H)_4$. Compound 6-N_2 crystallizes in the monoclinic space group *C2/c* with half of the molecule in the asymmetric unit. The molecule crystallizes with a two-fold rotation axis along the C1-C2 bond, such that the hydrogen substituents of the methyl group are disordered over a special position. These were refined with an AFIX 133 command. There is one isopropyl group which is also disordered over two positions. Electron density corresponding to the hydride ligands could be located in the Fourier diffraction map. However, stable refinement with reasonable bond lengths required imposing a fixed Fe-H distance of 1.54(2) Å. There is residual electron density close to the iron centers, but they are too close (~0.8 Å) to be another atom. The possibility of non-merohedral twinning was evaluated through cell_now, but a significant twin component could not be identified. While the residual density could be due to disorder which cannot be satisfactorily modelled, their proximity to the heavy metals suggests they may arise due to absorption problems or truncation errors instead.

Special Refinement Details for [P_6ArCH_3]$(FeH)_2(\mu\text{-}N_2)$. Compound 7 crystallizes in the orthorhombic space group *Pbca* with one molecule in the asymmetric unit along with one molecule of co-crystallized pentane. The co-crystallized pentane is disordered over two positions (52% and 48% relative occupancies). Electron density corresponding to two hydride ligands could be located directly in the Fourier difference map, which were refined with the aid of a similarity restraint on their 1,2-distances to Fe1 and Fe2, respectively.

Special Refinement Details for (P_6ArCH)$Fe_2(N_2)_2(H)_2$. Compound **8** crystallizes in the monoclinic space group *$P2_1/n$* with one molecule in the asymmetric unit. Electron density corresponding to two hydride ligands could be located directly in the Fourier difference map, which were refined with the aid of a similarity restraint on their 1,2-distances to Fe2. The difference map also revealed electron density corresponding to one proton on C1, which was allowed to freely refine.

References

1. Hoffman, B. M.; Lukoyanov, D.; Yang, Z.-Y.; Dean, D. R.; Seefeldt, L. C., Mechanism of Nitrogen Fixation by Nitrogenase: The Next Stage. *Chem. Rev.* **2014,** *114* (8), 4041-4062.
2. Spatzal, T.; Aksoyoglu, M.; Zhang, L.; Andrade, S. L. A.; Schleicher, E.; Weber, S.; Rees, D. C.; Einsle, O., Evidence for Interstitial Carbon in Nitrogenase FeMo Cofactor. *Science* **2011,** *334* (6058), 940-940.
3. Einsle, O.; Tezcan, F. A.; Andrade, S. L. A.; Schmid, B.; Yoshida, M.; Howard, J. B.; Rees, D. C., Nitrogenase MoFe-Protein at 1.16 Å Resolution: A Central Ligand in the FeMo-Cofactor. *Science* **2002,** *297* (5587), 1696-1700.
4. Kirn, J.; Rees, D. C., Crystallographic structure and functional implications of the nitrogenase molybdenum–iron protein from Azotobacter vinelandii. *Nature* **1992,** *360*, 553.
5. Lancaster, K. M.; Roemelt, M.; Ettenhuber, P.; Hu, Y.; Ribbe, M. W.; Neese, F.; Bergmann, U.; DeBeer, S., X-ray Emission Spectroscopy Evidences a Central Carbon in the Nitrogenase Iron-Molybdenum Cofactor. *Science* **2011,** *334* (6058), 974-977.
6. Igarashi, R. Y.; Laryukhin, M.; Dos Santos, P. C.; Lee, H.-I.; Dean, D. R.; Seefeldt, L. C.; Hoffman, B. M., Trapping H- Bound to the Nitrogenase FeMo-Cofactor Active Site during H_2 Evolution: Characterization by ENDOR Spectroscopy. *J. Am. Chem. Soc.* **2005,** *127* (17), 6231-6241.
7. Lukoyanov, D.; Yang, Z.-Y.; Dean, D. R.; Seefeldt, L. C.; Hoffman, B. M., Is Mo Involved in Hydride Binding by the Four-Electron Reduced (E_4) Intermediate of the Nitrogenase MoFe Protein? *J. Am. Chem. Soc.* **2010,** *132* (8), 2526-2527.
8. Buscagan, T. M.; Rees, D. C., Rethinking the Nitrogenase Mechanism: Activating the Active Site. *Joule* **2019,** *3* (11), 2662-2678.
9. Čorić, I.; Holland, P. L., Insight into the Iron–Molybdenum Cofactor of Nitrogenase from Synthetic Iron Complexes with Sulfur, Carbon, and Hydride Ligands. *J. Am. Chem. Soc.* **2016,** *138* (23), 7200-7211.
10. Lee, S. C.; Lo, W.; Holm, R. H., Developments in the Biomimetic Chemistry of Cubane-Type and Higher Nuclearity Iron–Sulfur Clusters. *Chem. Rev.* **2014,** *114* (7), 3579-3600.
11. Venkateswara Rao, P.; Holm, R. H., Synthetic Analogues of the Active Sites of Iron−Sulfur Proteins. *Chem. Rev.* **2004,** *104* (2), 527-560.
12. Spatzal, T.; Perez, K. A.; Einsle, O.; Howard, J. B.; Rees, D. C., Ligand binding to the FeMo-cofactor: Structures of CO-bound and reactivated nitrogenase. *Science* **2014,** *345* (6204), 1620-1623.
13. Spatzal, T.; Perez, K. A.; Howard, J. B.; Rees, D. C., Catalysis-dependent selenium incorporation and migration in the nitrogenase active site iron-molybdenum cofactor. *eLife* **2015,** *4*, e11620.
14. Sippel, D.; Rohde, M.; Netzer, J.; Trncik, C.; Gies, J.; Grunau, K.; Djurdjevic, I.; Decamps, L.; Andrade, S. L. A.; Einsle, O., A bound reaction intermediate sheds light on the mechanism of nitrogenase. *Science* **2018,** *359* (6383), 1484-1489.
15. Varley, J. B.; Wang, Y.; Chan, K.; Studt, F.; Nørskov, J. K., Mechanistic insights into nitrogen fixation by nitrogenase enzymes. *PCCP* **2015,** *17* (44), 29541-29547.
16. Dance, I., How feasible is the reversible S-dissociation mechanism for the activation of FeMo-co, the catalytic site of nitrogenase? *Dalton Trans.* **2019,** *48* (4), 1251-1262.
17. Čorić, I.; Mercado, B. Q.; Bill, E.; Vinyard, D. J.; Holland, P. L., Binding of dinitrogen to an iron–sulfur–carbon site. *Nature* **2015,** *526*, 96.
18. Siegbahn, P. E. M., The mechanism for nitrogenase including all steps. *PCCP* **2019,** *21* (28), 15747-15759.

19. Siegbahn, P. E. M., Model Calculations Suggest that the Central Carbon in the FeMo-Cofactor of Nitrogenase Becomes Protonated in the Process of Nitrogen Fixation. *J. Am. Chem. Soc.* **2016,** *138* (33), 10485-10495.

20. McKee, M. L., A New Nitrogenase Mechanism Using a CFe_8S_9 Model: Does H_2 Elimination Activate the Complex to N_2 Addition to the Central Carbon Atom? *The Journal of Physical Chemistry A* **2016,** *120* (5), 754-764.

21. Speelman, A. L.; Čorić, I.; Van Stappen, C.; DeBeer, S.; Mercado, B. Q.; Holland, P. L., Nitrogenase-Relevant Reactivity of a Synthetic Iron–Sulfur–Carbon Site. *J. Am. Chem. Soc.* **2019,** *141* (33), 13148-13157.

22. Hickey, A. K.; Muñoz, S. B.; Lutz, S. A.; Pink, M.; Chen, C.-H.; Smith, J. M., Arrested α-hydride migration activates a phosphido ligand for C–H insertion. *Chem. Commun.* **2017,** *53* (2), 412-415.

23. Creutz, S. E.; Peters, J. C., Catalytic Reduction of N_2 to NH_3 by an Fe–N_2 Complex Featuring a C-Atom Anchor. *J. Am. Chem. Soc.* **2014,** *136* (3), 1105-1115.

24. Rittle, J.; Peters, J. C., Fe–N_2/CO complexes that model a possible role for the interstitial C atom of FeMo-cofactor (FeMoco). *Proc. Natl. Acad. Sci. U. S. A.* **2013,** *110* (40), 15898-15903.

25. Reiners, M.; Baabe, D.; Zaretzke, M.-K.; Freytag, M.; Walter, M. D., Reversible dinitrogen binding to [Cp'Fe(NHC)] associated with an N2-induced spin state change. *Chem. Commun.* **2017,** *53* (53), 7274-7277.

26. Ouyang, Z.; Cheng, J.; Li, L.; Bao, X.; Deng, L., High-Spin Iron(I) and Iron(0) Dinitrogen Complexes Supported by N-Heterocyclic Carbene Ligands. *Chem. Eur. J.* **2016,** *22* (40), 14162-14165.

27. Lindley, B. M.; Jacobs, B. P.; MacMillan, S. N.; Wolczanski, P. T., Neutral Fe(iv) alkylidenes, including some that bind dinitrogen. *Chem. Commun.* **2016,** *52* (20), 3891-3894.

28. Ung, G.; Peters, J. C., Low-Temperature N_2 Binding to Two-Coordinate L_2Fe^0 Enables Reductive Trapping of $L_2FeN_2^-$ and NH_3 Generation. *Angew. Chem. Int. Ed.* **2015,** *54* (2), 532-535.

29. Marchetti, F., Constructing Organometallic Architectures from Aminoalkylidyne Diiron Complexes. *Eur. J. Inorg. Chem.* **2018,** *2018* (36), 3987-4003.

30. Vollmer, G. Y.; Wallasch, M. W.; Saurenz, D.; Eger, T. R.; Bauer, H.; Wolmershäuser, G.; Prosenc, M. H.; Sitzmann, H., Benzylidyne Bridges from Diphenylacetylene and a Methylidyne Bridge from Methylmagnesium Chloride. *Organometallics* **2015,** *34* (3), 644-652.

31. Xiao, N.; Xu, Q.; Sun, J.; Chen, J., Synthesis, structure and reactivity of novel pyridazine-coordinated diiron bridging carbene complexes. *Dalton Trans.* **2005,** (19), 3250-3258.

32. Chen, J.; Wang, R., Remarkable reactions of cationic carbyne complexes of manganese, rhenium, and diiron with carbonylmetal anions. *Coord. Chem. Rev.* **2002,** *231* (1), 109-149.

33. Albano, V. G.; Busetto, L.; Monari, M.; Zanotti, V., Reactions of acetonitrile di-iron μ-aminocarbyne complexes; synthesis and structure of [Fe2(μ-$CNMe_2$)(μ-H)$(CO)_2(Cp)_2$]. *J. Organomet. Chem.* **2000,** *606* (2), 163-168.

34. Holton, J.; Lappert, M. F.; Pearce, R.; Yarrow, P. I. W., Bridged hydrocarbyl or hydrocarbon binuclear transition metal complexes: classification, structures, and chemistry. *Chem. Rev.* **1983,** *83* (2), 135-201.

35. Casey, C. P.; Fagan, P. J.; Miles, W. H., Synthesis and interconversions of dinuclear iron complexes with μ-methyl, μ-methylene, and μ-methylidyne ligands. *J. Am. Chem. Soc.* **1982,** *104* (4), 1134-1136.

36. Nitay, M.; Priester, W.; Rosenblum, M., Lithium ion promotion in the synthesis of novel dinuclear iron-carbyne complexes. *J. Am. Chem. Soc.* **1978,** *100* (11), 3620-3622.

37. Casey, C. P.; Roddick, D. M., Formation of a bridging methylidyne complex and of a bridging vinyl complex from the reaction of $[(C_5H_5)Fe(NO)]_2$(μ-CH_2) with trityl cation. *Organometallics* **1986,** *5* (3), 436-438.

38. Busetto, L.; Zanotti, V., Carbene ligands in diiron complexes. *J. Organomet. Chem.* **2005,** *690* (24), 5430-5440.

39. Casey, C. P.; Vosejpka, P. C.; Crocker, M., Reactions of nucleophiles with cationic bridging alkylidyne complexes. *J. Organomet. Chem.* **1990,** *394* (1), 339-347.

40. Casey, C. P.; Meszaros, M. W.; Fagan, P. J.; Bly, R. K.; Marder, S. R.; Austin, E. A., Hydrocarbation-formation of diiron μ-alkylidyne complexes from the addition of the carbon-hydrogen bond of a .mu.-methylidyne complex across alkenes. *J. Am. Chem. Soc.* **1986,** *108* (14), 4043-4053.

41. Bursten, B. E.; Cayton, R. H., Electronic structure of piano-stool dimers. 3. Relationships between the bonding and reactivity of the organically bridged iron dimers $[CpFe(CO)]_2(\mu\text{-}CO)(\mu\text{-}L)$ (L = CO, CH_2, $C{=}CH_2$, CH^+). *J. Am. Chem. Soc.* **1986,** *108* (26), 8241-8249.

42. Casey, C. P.; Fagan, P. J.; Miles, W. H.; Marder, S. R., Reactions of a cationic bridging methylidyne-iron complex with carbon monoxide and with alkenes. *J. Mol. Catal.* **1983,** *21* (1), 173-188.

43. Casey, C. P.; Fagan, P. J.; Day, V. W., Formation of the bridging acylium complex $(C_5H_5)_2Fe_2(CO)_2(\mu\text{-}CO)(\mu\text{-}CHCO)^+ PF_6^-$ by addition of carbon monoxide to a bridging methylidyne-iron complex. *J. Am. Chem. Soc.* **1982,** *104* (25), 7360-7361.

44. Casey, C. P.; Fagan, P. J., Hydrocarbation: addition of the carbon-hydrogen bond of a cationic bridging iron-methylidyne complex to alkenes. *J. Am. Chem. Soc.* **1982,** *104* (18), 4950-4951.

45. Reesbeck, M. E.; Grubel, K.; Kim, D.; Brennessel, W. W.; Mercado, B. Q.; Holland, P. L., Diazoalkanes in Low-Coordinate Iron Chemistry: Bimetallic Diazoalkyl and Alkylidene Complexes of Iron(II). *Inorg. Chem.* **2017,** *56* (3), 1019-1022.

46. Yogendra, S.; Weyhermüller, T.; Hahn, A. W.; DeBeer, S., From Ylides to Doubly Yldiide-Bridged Iron(II) High Spin Dimers via Self-Protolysis. *Inorg. Chem.* **2019,** *58* (14), 9358-9367.

47. Sun, C.-L.; Krause, H.; Fürstner, A., A Practical Procedure for Iron-Catalyzed Cross-Coupling Reactions of Sterically Hindered Aryl-Grignard Reagents with Primary Alkyl Halides. *Adv. Synth. Catal.* **2014,** *356* (6), 1281-1291.

48. Ni, C.; Power, P. P., Methyl-Bridged Transition Metal Complexes (M = Cr−Fe) Supported by Bulky Terphenyl Ligands. *Organometallics* **2009,** *28* (22), 6541-6545.

49. Klose, A.; Solari, E.; Floriani, C.; Chiesi-Villa, A.; Rizzoli, C.; Re, N., Magnetic Properties Diagnostic for the Existence of Iron(II)-Iron(II) Bonds in Dinuclear Complexes Which Derive from Stepwise Insertion Reactions on Unsupported Iron-Aryl Bonds. *J. Am. Chem. Soc.* **1994,** *116* (20), 9123-9135.

50. Rettberg, L. A.; Wilcoxen, J.; Lee, C. C.; Stiebritz, M. T.; Tanifuji, K.; Britt, R. D.; Hu, Y., Probing the coordination and function of Fe4S4 modules in nitrogenase assembly protein NifB. *Nat. Commun.* **2018,** *9* (1), 2824.

51. Wiig, J. A.; Hu, Y.; Ribbe, M. W., Refining the pathway of carbide insertion into the nitrogenase M-cluster. *Nat. Commun.* **2015,** *6* (1), 8034.

52. Wiig, J. A.; Hu, Y.; Lee, C. C.; Ribbe, M. W., Radical SAM-Dependent Carbon Insertion into the Nitrogenase M-Cluster. *Science* **2012,** *337* (6102), 1672-1675.

53. Hickey, A. K.; Greer, S. M.; Valdez-Moreira, J. A.; Lutz, S. A.; Pink, M.; DeGayner, J. A.; Harris, T. D.; Hill, S.; Telser, J.; Smith, J. M., A Dimeric Hydride-Bridged Complex with Geometrically Distinct Iron Centers Giving Rise to an S = 3 Ground State. *J. Am. Chem. Soc.* **2019**.

54. Yang, D.; Li, Y.; Wang, B.; Zhao, X.; Su, L.; Chen, S.; Tong, P.; Luo, Y.; Qu, J., Synthesis and Electrocatalytic Property of Diiron Hydride Complexes Derived from a Thiolate-Bridged Diiron Complex. *Inorg. Chem.* **2015,** *54* (21), 10243-10249.

55. Lee, Y.; Anderton, K. J.; Sloane, F. T.; Ermert, D. M.; Abboud, K. A.; García-Serres, R.; Murray, L. J., Reactivity of Hydride Bridges in High-Spin [3M–3(μ-H)] Clusters (M = Fe^{II}, Co^{II}). *J. Am. Chem. Soc.* **2015,** *137* (33), 10610-10617.

56. Arnet, N. A.; Dugan, T. R.; Menges, F. S.; Mercado, B. Q.; Brennessel, W. W.; Bill, E.; Johnson, M. A.; Holland, P. L., Synthesis, Characterization, and Nitrogenase-Relevant Reactions of an Iron Sulfide Complex with a Bridging Hydride. *J. Am. Chem. Soc.* **2015,** *137* (41), 13220-13223.

57. Rittle, J.; McCrory, C. C. L.; Peters, J. C., A 10^6-Fold Enhancement in N_2-Binding Affinity of an $Fe_2(\mu\text{-}H)_2$ Core upon Reduction to a Mixed-Valence $Fe^{II}Fe^{I}$ State. *J. Am. Chem. Soc.* **2014,** *136* (39), 13853-13862.

58. Wang, W.; Nilges, M. J.; Rauchfuss, T. B.; Stein, M., Isolation of a Mixed Valence Diiron Hydride: Evidence for a Spectator Hydride in Hydrogen Evolution Catalysis. *J. Am. Chem. Soc.* **2013,** *135* (9), 3633-3639.

59. Brown, S. D.; Mehn, M. P.; Peters, J. C., Heterolytic H2 Activation Mediated by Low-Coordinate L_3Fe-(μ-N)-FeL_3 Complexes to Generate Fe(μ-NH)(μ-H)Fe Species. *J. Am. Chem. Soc.* **2005,** *127* (38), 13146-13147.

60. Neese, F., Prediction and interpretation of the ^{57}Fe isomer shift in Mössbauer spectra by density functional theory. *Inorg. Chim. Acta* **2002,** *337*, 181-192.

61. Yao, S. A.; Corcos, A. R.; Infante, I.; Hillard, E. A.; Clérac, R.; Berry, J. F., An "Intermediate Spin" Nickel Hydride Complex Stemming from Delocalized Ni_2(μ-H)$_2$ Bonding. *J. Am. Chem. Soc.* **2014,** *136* (39), 13538-13541.

62. Lee, Y.; Peters, J. C., Silylation of Iron-Bound Carbon Monoxide Affords a Terminal Fe Carbyne. *J. Am. Chem. Soc.* **2011,** *133* (12), 4438-4446.

63. Prokopchuk, D. E.; Chambers, G. M.; Walter, E. D.; Mock, M. T.; Bullock, R. M., H_2 Binding, Splitting, and Net Hydrogen Atom Transfer at a Paramagnetic Iron Complex. *J. Am. Chem. Soc.* **2019,** *141* (5), 1871-1876.

64. Buscagan, T. M.; Oyala, P. H.; Peters, J. C., N_2-to-NH_3 Conversion by a triphos–Iron Catalyst and Enhanced Turnover under Photolysis. *Angew. Chem. Int. Ed.* **2017,** *56* (24), 6921-6926.

65. Schild, D. J.; Peters, J. C., Light Enhanced Fe-Mediated Nitrogen Fixation: Mechanistic Insights Regarding H_2 Elimination, HER, and NH_3 Generation. *ACS Catal.* **2019,** *9* (5), 4286-4295.

66. Russell, S. K.; Hoyt, J. M.; Bart, S. C.; Milsmann, C.; Stieber, S. C. E.; Semproni, S. P.; DeBeer, S.; Chirik, P. J., Synthesis, electronic structure and reactivity of bis(imino)pyridine iron carbene complexes: evidence for a carbene radical. *Chem. Sci.* **2014,** *5* (3), 1168-1174.

67. It is most likely that under the experimental conditions (equimolar H2/N2) for hydrogenation of 5 that intermediate 8 binds H_2 rather than N_2. If N_2 were to be bound, 6-H_2/N_2 or 6-N_2 rather than 6-H_2 would be the expected product.

68. Lee, Y.; Kinney, R. A.; Hoffman, B. M.; Peters, J. C., A Nonclassical Dihydrogen Adduct of S = 1/2 Fe(I). *J. Am. Chem. Soc.* **2011,** *133* (41), 16366-16369.

69. Suess, D. L. M.; Tsay, C.; Peters, J. C., Dihydrogen Binding to Isostructural S = 1/2 and S = 0 Cobalt Complexes. *J. Am. Chem. Soc.* **2012,** *134* (34), 14158-14164.

70. Doyle, L. R.; Scott, D. J.; Hill, P. J.; Fraser, D. A. X.; Myers, W. K.; White, A. J. P.; Green, J. C.; Ashley, A. E., Reversible coordination of N_2 and H_2 to a homoleptic S = 1/2 Fe(i) diphosphine complex in solution and the solid state. *Chem. Sci.* **2018,** *9* (37), 7362-7369.

71. Dugan, T. R.; Holland, P. L., New routes to low-coordinate iron hydride complexes: The binuclear oxidative addition of H2. *J. Organomet. Chem.* **2009,** *694* (17), 2825-2830.

72. Halpern, J.; Pribanic, M., Hydrogenation of pentacyanocobaltate(II) at high pressures. *Inorg. Chem.* **1970,** *9* (11), 2616-2618.

73. Tannenbaum, R.; Dietler, U. K.; Bor, G.; Ungváry, F., Fundamental metal carbonyl equilibria, V1Reference [29][b] should be considered as Part IV; for Part III see reference [1].1:: Reinvestigation of the equilibrium between dicobalt octacarbonyl and cobalt tetracarbonyl hydride under hydrogen pressure. *J. Organomet. Chem.* **1998,** *570* (1), 39-47.

74. Cui, W.; Wayland, B. B., Activation of C−H / H−H Bonds by Rhodium(II) Porphyrin Bimetalloradicals. *J. Am. Chem. Soc.* **2004,** *126* (26), 8266-8274.

75. Wayland, B. B.; Ba, S.; Sherry, A. E., Reactions of hydrogen or deuterium molecule with a rhodium(II) metalloradical: kinetic evidence for a four-centered transition state. *Inorg. Chem.* **1992,** *31* (1), 148-150.

76. Manz, D.-H.; Duan, P.-C.; Dechert, S.; Demeshko, S.; Oswald, R.; John, M.; Mata, R. A.; Meyer, F., Pairwise H_2/D_2 Exchange and H_2 Substitution at a Bimetallic Dinickel(II) Complex Featuring Two Terminal Hydrides. *J. Am. Chem. Soc.* **2017,** *139* (46), 16720-16731.

77. Davis, J. H.; Beno, M. A.; Williams, J. M.; Zimmie, J.; Tachikawa, M.; Muetterties, E. L., Structure and chemistry of a metal cluster with a four-coordinate carbide carbon atom. *Proc. Natl. Acad. Sci. U. S. A.* **1981,** *78* (2), 668-671.

78. Carreón-Macedo, J.-L.; Harvey, J. N., Do Spin State Changes Matter in Organometallic Chemistry? A Computational Study. *J. Am. Chem. Soc.* **2004,** *126* (18), 5789-5797.

79. Poli, R.; Harvey, J. N., Spin forbidden chemical reactions of transition metal compounds. New ideas and new computational challenges. *Chem. Soc. Rev.* **2003,** *32* (1), 1-8.

80. Gordon, J. C.; Kubas, G. J., Perspectives on How Nature Employs the Principles of Organometallic Chemistry in Dihydrogen Activation in Hydrogenases. *Organometallics* **2010,** *29* (21), 4682-4701.

81. Lukoyanov, D. A.; Krzyaniak, M. D.; Dean, D. R.; Wasielewski, M. R.; Seefeldt, L. C.; Hoffman, B. M., Time-Resolved EPR Study of H_2 Reductive Elimination from the Photoexcited Nitrogenase Janus E4(4H) Intermediate. *J. Phys. Chem. B* **2019,** *123* (41), 8823-8828.

82. Lukoyanov, D.; Khadka, N.; Dean, D. R.; Raugei, S.; Seefeldt, L. C.; Hoffman, B. M., Photoinduced Reductive Elimination of H_2 from the Nitrogenase Dihydride (Janus) State Involves a FeMo-cofactor-H2 Intermediate. *Inorg. Chem.* **2017,** *56* (4), 2233-2240.

83. Lukoyanov, D.; Khadka, N.; Yang, Z.-Y.; Dean, D. R.; Seefeldt, L. C.; Hoffman, B. M., Reductive Elimination of H_2 Activates Nitrogenase to Reduce the N≡N Triple Bond: Characterization of the E_4(4H) Janus Intermediate in Wild-Type Enzyme. *J. Am. Chem. Soc.* **2016,** *138* (33), 10674-10683.

84. Lukoyanov, D.; Khadka, N.; Yang, Z.-Y.; Dean, D. R.; Seefeldt, L. C.; Hoffman, B. M., Reversible Photoinduced Reductive Elimination of H_2 from the Nitrogenase Dihydride State, the E_4(4H) Janus Intermediate. *J. Am. Chem. Soc.* **2016,** *138* (4), 1320-1327.

85. Lukoyanov, D.; Barney, B. M.; Dean, D. R.; Seefeldt, L. C.; Hoffman, B. M., Connecting nitrogenase intermediates with the kinetic scheme for N_2 reduction by a relaxation protocol and identification of the N2 binding state. *Proc. Natl. Acad. Sci. U. S. A.* **2007,** *104* (5), 1451-1455.

86. Creutz, S. E.; Peters, J. C., Diiron Bridged-Thiolate Complexes That Bind N_2 at the $Fe^{II}Fe^{II}$, $Fe^{II}Fe^{I}$, and $Fe^{I}Fe^{I}$ Redox States. *J. Am. Chem. Soc.* **2015,** *137* (23), 7310-7313.

87. Wiig, J. A.; Lee, C. C.; Hu, Y.; Ribbe, M. W., Tracing the Interstitial Carbide of the Nitrogenase Cofactor during Substrate Turnover. *J. Am. Chem. Soc.* **2013,** *135* (13), 4982-4983.

88. Mankad, N. P.; Rivard, E.; Harkins, S. B.; Peters, J. C., Structural Snapshots of a Flexible Cu_2P_2 Core that Accommodates the Oxidation States $Cu^{I}Cu^{I}$, $Cu^{1.5}Cu^{1.5}$, and $Cu^{II}Cu^{II}$. *J. Am. Chem. Soc.* **2005,** *127* (46), 16032-16033.

89. Chilton, N. F.; Anderson, R. P.; Turner, L. D.; Soncini, A.; Murray, K. S., PHI: A powerful new program for the analysis of anisotropic monomeric and exchange-coupled polynuclear d- and f-block complexes. *J. Comput. Chem.* **2013,** *34* (13), 1164-1175.

90. *APEX-II Version 2 User Manual, M86-E01078*. Bruker Analytical X-ray Systems: Madison, WI, 2006.

91. Sheldrick, G., *SADABS (version 2008/1): Program for Absorption Correction for Data from Area Detector Frames*. University of Göttingen: 2008.

92. Sheldrick, G., A short history of SHELX. *Acta Crystall. Sec. A* **2008,** *64* (1), 112-122.

93. Sheldrick, G., Crystal structure refinement with SHELXL. *Acta Crystall. Sec. C* **2015,** *71* (1), 3-8.

94. Dolomanov, O. V.; Bourhis, L. J.; Gildea, R. J.; Howard, J. A. K.; Puschmann, H., OLEX2: a complete structure solution, refinement and analysis program. *J. Appl. Crystallogr.* **2009,** *42* (2), 339-341.

95. Neese, F., The ORCA program system. *WIREs Comput. Mol. Sci.* **2012,** *2* (1), 73-78.

96. Pettersen, E. F.; Goddard, T. D.; Huang, C. C.; Couch, G. S.; Greenblatt, D. M.; Meng, E. C.; Ferrin, T. E., UCSF Chimera—A visualization system for exploratory research and analysis. *J. Comput. Chem.* **2004,** *25* (13), 1605-1612.

97. Thompson, N. B.; Green, M. T.; Peters, J. C., Nitrogen Fixation via a Terminal Fe(IV) Nitride. *J. Am. Chem. Soc.* **2017,** *139* (43), 15312-15315.

CHAPTER 5

MIXED-VALENT DIIRON μ-CARBYNE, μ-HYDRIDE COMPLEXES: IMPLICATIONS FOR NITROGENASE

The text for this chapter was reproduced in part from:

Arnett, C.H.; Bogacz, I.; Chatterjee, R.; Yano, J.; Oyala, P.H.; Agapie, T. *J. Am. Chem. Soc.* **2020***, In Revision*.

ABSTRACT

Binding of N_2 by the FeMo-cofactor of nitrogenase is believed to occur after transfer of 4 e^- and 4 H^+ equivalents to the active site. Although pulse EPR studies indicate the presence of two Fe-(μ-H)-Fe moieties, the structural and electronic features of this mixed valent intermediate remain poorly understood. Toward an improved understanding of this bioorganometallic cluster, we report herein the diiron μ-carbyne complex $(P_6ArC)Fe_2(\mu\text{-}H)$ can be oxidized and reduced, allowing for the first-time spectral characterization of two EPR-active Fe(μ-C)(μ-H)Fe model complexes linked by a 2 e^- transfer which bear some resemblance to a pair of E_n and E_{n+2} states of nitrogenase. Both species populate S = ½ states at low temperatures, and the influence of valence (de)localization on the spectroscopic signature of the μ-hydride ligand was evaluated by ^1H pulse EPR studies. Compared to analogous data for the $\{Fe_2(\mu\text{-}H)\}_2$ state of FeMoco (E_4(4H)), the data and analysis presented herein suggest that the hydride ligands in E_4(4H) bridge isovalent (most probably Fe^{III}) metal centers. Although electron transfer involves metal-localized orbitals, investigations of $[(P_6ArC)Fe_2(\mu\text{-}H)]^{+1}$ and $[(P_6ArC)Fe_2(\mu\text{-}H)]^{-1}$ by ^{13}C pulse EPR revealed that redox chemistry induces significant changes in Fe-C covalency (-44% upon 2 e^- reduction), a conclusion further supported by X-ray absorption spectroscopy, ^{57}Fe Mössbauer studies, and DFT calculations. Combined, our studies demonstrate that changes in covalency buffer against the accumulation of excess charge density on the metals by partially redistributing it to the bridging carbon, thereby facilitating multi-electron transformations.

INTRODUCTION

The active sites of the nitrogenase enzymes comprise a unique class of organometallic cofactors which incorporate a μ_6-C^{4-} ligand within a [7Fe-9S-M-C-*R*-homocitrate] (M = Mo, V, or Fe) cluster scaffold.[1-6] Spectroscopic and computational studies indicate that the resting state of the Mo-containing isoform (FeMoco, Figure 1, top left) is best formulated as a mixed valent Mo(III) 3Fe(II) 4Fe(III) cluster,[7-9] though the extent of valence localization is still a matter of debate.[10-13] Substrate binding and reduction requires an initial electron loading phase during which the cofactor may undergo structural rearrangements.[14-17] The accumulation of reducing equivalents at FeMoco is presumably coupled to proton transfer.[18] If protonation occurs at iron (*vide infra*), this would imply that the active site may cycle through only two formal oxidation states during catalysis,[19] both of which are mixed valent. The influence of the interstitial μ_6-C donor on the electronic structure and catalytic properties of the cofactor remains poorly understood.[20] Radiolabelling studies demonstrate that the carbide ligand is not lost or exchanged during catalysis.[21] However, this does not rule out an active role for the interstitial atom in bond-breaking and bond-making steps (which has been speculated previously).[22-24]

In contrast to water oxidation by photosystem II,[25] there is currently no general strategy which can generate intermediate states of FeMoco in a stepwise fashion for spectroscopic study. Sample heterogeneity complicates application of common bulk spectroscopic methods (XAS, XES or ^{57}Fe Mössbauer) to the study of reduced states of FeMoco.[13, 26-27] On the other hand, CW-EPR and pulse EPR/ENDOR spectroscopies can selectively interrogate nitrogenase intermediates with half-integer spin states.[28-30] In combination with cryoannealing protocols,[31-32] these techniques have been employed to characterize a variety of putative intermediates, most notably one which has accumulated 4 e^-

and 4 H^+ in the form of two Fe-(μ-H)-Fe moieties (Figure 1, top right).[33-34] It has been suggested that this state is the key activated intermediate generated just prior to N_2 binding.[35-36] As such, an improved understanding of its electronic structure and geometrical features could provide crucial insight into the activation process.

Synthetic model complexes which reproduce key structural features of proposed nitrogenase intermediates can provide insight into their spectroscopic signatures. This approach has motivated EPR studies of a variety of metal complexes containing nitrogenous ($Fe\text{-}N_xH_y$)[37-41] and organometallic (*e.g.* iron-alkene or iron-hydride) ligands.[42-45] Additionally, several paramagnetic diiron μ-hydride complexes have been reported,[46-53] two of which have been studied in detail using pulse EPR techniques.[54-55] These investigations elucidated the ^1H ENDOR signatures expected for the μ-hydride motif, at least for fully delocalized (Robin-Day Class III[56]) dimers. However, analogous studies for systems containing an Fe-(μ-C)-Fe linkage are not known, apart from a single report of ^{13}C pulse EPR data for the $S = 3/2$ resting state of FeMoco.[1] Carbon-bridged, multimetallic iron complexes are not uncommon,[57-65] but, with few exceptions,[66-71] these species have closed-shell electronic configurations. Those that are paramagnetic all exhibit integer spin states and, thus, are not readily characterized by pulse EPR methods.[66-71] To the best of our knowledge, only one synthetic iron complex featuring a carbon-based, X_n-type ($n = 1,2,3$) ligand, namely a terminal iron(V)-carbyne complex, has been interrogated by ^{13}C pulse EPR.[44] Enzymatic iron-alkyl species have been isotopically labelled and investigated by ENDOR and/or HYSCORE spectroscopy,[72-74] but none have been structurally characterized, and questions remain regarding their electronic structure.[75-76] As such, there remains a lack of well-defined reference compounds useful for comparisons against pulse EPR data reported for FeMoco or other bioorganometallic enzymes.

Recently, we reported the synthesis and reactivity of the arylcarbyne-bridged diiron complex, (P_6ArC)Fe_2(μ-H), which features a biologically relevant Fe(μ-C)(μ-H)Fe core (Figure 1, bottom).[66] Remarkably, SQUID magnetometry revealed that (P_6ArC)Fe_2(μ-H) features a thermally well-isolated $S = 1$ ground state. The unusual preference of (P_6ArC)Fe_2(μ-H) to adopt an open-shell configuration in spite of its strong field donor set suggested that related, mixed-valence compounds might be accessible. Herein, we demonstrate that (P_6ArC)Fe_2(μ-H) can indeed be oxidized and reduced, allowing for the first time spectral characterization of two EPR-active Fe(μ-C)(μ-H)Fe model complexes linked by a 2 e^- transfer which bear some resemblance to a pair of E_n and E_{n+2} states of nitrogenase (Figure 1, bottom).

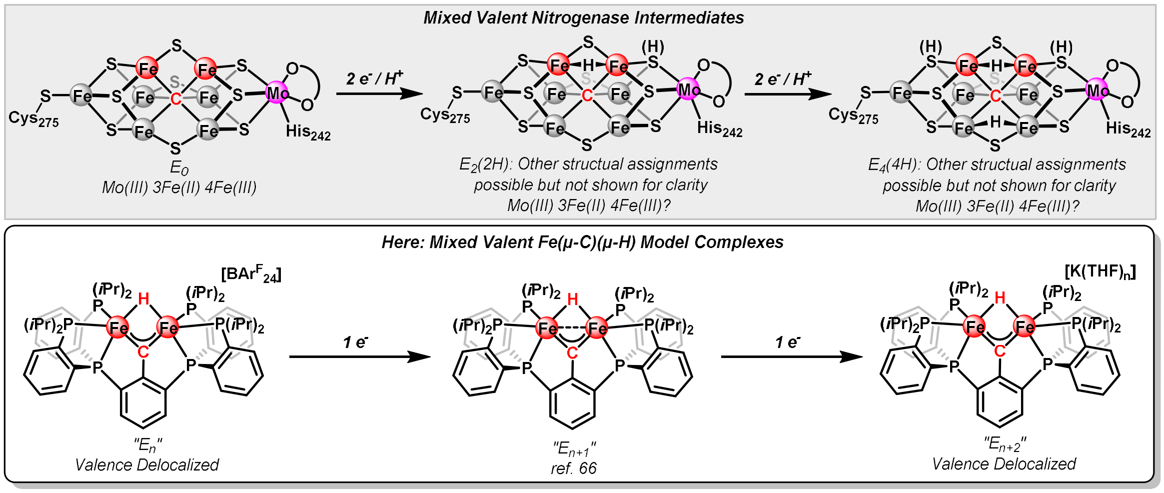

Figure 1. Mixed valent states are prevalent for the iron-molybdenum cofactor (FeMoco) of nitrogenase (top). Mixed valent diiron μ-carbyne complexes are structural and electronic models of a carbon-bridged diiron subunit of FeMoco, proposed to be central to catalysis, as well as a model of the conversion of E_n to E_{n+2} (bottom).

RESULTS AND DISCUSSION

Isolation and Characterization of a Stable {Fe_2(μ-CAr)}^{17} Complex. Towards accessing EPR-active model complexes featuring a biologically relevant Fe_2(μ-C) motif, the $S = 1$ diiron μ-carbyne complex ($(P_6ArC)Fe_2(\mu\text{-}H)$) was studied by cyclic voltammetry (CV). The CV of $(P_6ArC)Fe_2(\mu\text{-}H)$ in tetrahydrofuran (Figure 2) exhibits two quasi-reversible electrochemical events: a reduction with $E_{1/2}$ = -2.78 V (vs. Fc/Fc^+) attributed to the formation of the anionic species $[(P_6ArC)Fe_2(\mu\text{-}H)]^{1-}$ and an oxidation with $E_{1/2}$ = -1.65 V (vs. Fc/Fc^+) assigned to the generation of the corresponding cation $[(P_6ArC)Fe_2(\mu\text{-}H)]^{1+}$.[77] Although formally these electrochemical features correspond to the $Fe^{II}_2/Fe^{I}Fe^{II}$ and $Fe^{II}Fe^{III}/Fe^{II}_2$ redox couples of $(P_6ArC)Fe_2(\mu\text{-}H)$, the prospect of significant covalency within the iron-carbon bonding renders assignments of oxidation state ambiguous.[44, 78-86] Inverted ligand-field arrangements are characteristic of Fischer-type carbene and carbyne complexes, though it is commonly assumed this requires heteroatom substitution to stabilize the sub-octet configuration at carbon.[87] Delocalization with the aryl substituent in $\mathbf{\{Fe_2(\mu\text{-}CAr)\}^{17\text{-}19}}$ may impart some degree of Fischer-type character to the μ-carbyne, formally corresponding to a resonance structure of the form $\{Fe^0_2(\mu\text{-}CAr^+)(\mu\text{-}H^-)\}$ for $\mathbf{\{Fe_2(\mu\text{-}CAr)\}^{18}}$ (Figure 3). However, in light of the high covalency of the Fe-C bonding, a resonance form that falls between the extremes of a Fischer-type or Schrock-type description –$\{Fe^I_2(\mu\text{-}CAr^+)(\mu\text{-}H^-)\}$ – also warrants consideration. To account for this ambiguity, the valence electron count of the $[(P_6ArC)Fe_2(\mu\text{-}H)]^{-1/0/+1}$ redox series can be described by considering both the iron 3*d* and carbyne $\sigma+\pi$ electrons (denoted *n* in $\{Fe_2(\mu\text{-}CAr)\}^n$ representation, see Figure 3 for resonance description), which is analogous to the Enemark-Feltam notation used for metal-nitrosyl complexes.[88] Thus, in this framework the formally $Fe^{II}Fe^{III}$ complex $[(P_6ArC)Fe_2(\mu\text{-}H)]^{1+}$ has a valence electron count of $\mathbf{\{Fe_2(\mu\text{-}CAr)\}^{17}}$, whereas the $Fe^{I}Fe^{II}$ species $[(P_6ArC)Fe_2(\mu\text{-}H)]^{1-}$ is represented as $\mathbf{\{Fe_2(\mu\text{-}CAr)\}^{19}}$ (Table 1).

Table 1. Summary of Formulas for $\{Fe_2(\mu\text{-CAr})\}^{17-19}$.

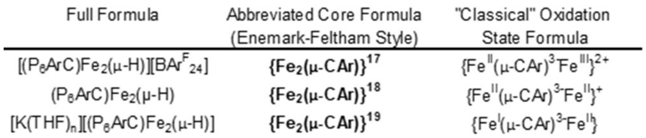

Full Formula	Abbreviated Core Formula (Enemark-Feltham Style)	"Classical" Oxidation State Formula
$[(P_6ArC)Fe_2(\mu\text{-H})][BAr^F_{24}]$	$\mathbf{\{Fe_2(\mu\text{-CAr})\}^{17}}$	$\{Fe^{II}(\mu\text{-CAr})^{3-}Fe^{III}\}^{2+}$
$(P_6ArC)Fe_2(\mu\text{-H})$	$\mathbf{\{Fe_2(\mu\text{-CAr})\}^{18}}$	$\{Fe^{II}(\mu\text{-CAr})^{3-}Fe^{II}\}^{+}$
$[K(THF)_n][(P_6ArC)Fe_2(\mu\text{-H})]$	$\mathbf{\{Fe_2(\mu\text{-CAr})\}^{19}}$	$\{Fe^{I}(\mu\text{-CAr})^{3-}Fe^{II}\}$

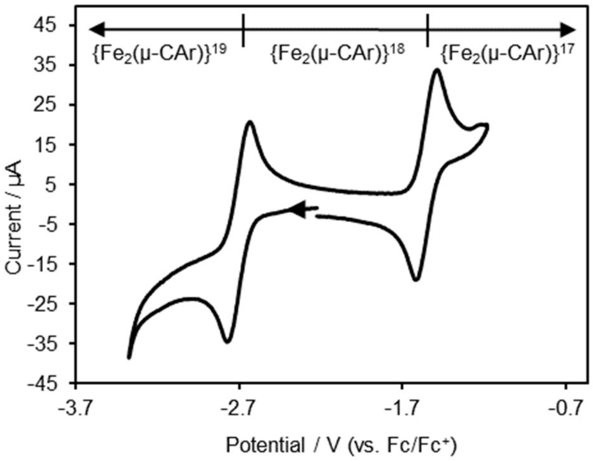

Figure 2. Cyclic voltammogram of $(P_6ArC)Fe_2(\mu\text{-H})$ (**$\{Fe_2(\mu\text{-CAr})\}^{18}$**) in tetrahydrofuran (0.4 M $[^nBu_4N][PF_6]$ supporting electrolyte). Scan rate: 100 mV/s.

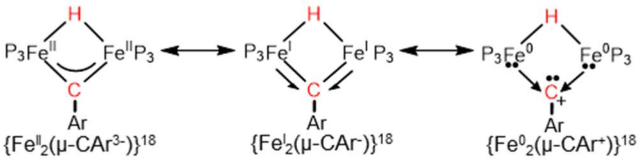

Figure 3. Limiting resonance structures for $(P_6ArC)Fe_2(\mu\text{-H})$ (**$\{Fe_2(\mu\text{-CAr})\}^{18}$**).

Chemical oxidation of $(P_6ArC)Fe_2(\mu\text{-H})$ (**$\{Fe_2(\mu\text{-CAr})\}^{18}$**) with $[Cp_2Co][BAr^F_{24}]$ in tetrahydrofuran (Figure 4a) proceeds cleanly, affording a new paramagnetic species detected by ^1H NMR spectroscopy (NMR, Figure 97). Single-crystal X-ray diffraction (XRD) studies confirm the identity of this compound as the desired $\{Fe_2(\mu\text{-CAr})\}^{17}$ species $[(P_6ArC)Fe_2(\mu\text{-H})][BAr^F_{24}]$ (**$\{Fe_2(\mu\text{-CAr})\}^{17}$**, Figure 4b). Compared to **$\{Fe_2(\mu\text{-CAr})\}^{18}$**, oxidized **$\{Fe_2(\mu\text{-CAr})\}^{17}$** shows an elongation of the Fe-P bond lengths attributed to attenuated π-backbonding (Table 2). This effect is more pronounced for the equatorial P donors (Δd_{ave} = 0.066(3) Å) than for the more tightly bound P1/P4 ligands (Δd_{ave} = 0.035(3) Å). The Fe-C1 distances in

{Fe$_2$(μ-CAr)}^{17} (Fe1-C1: 1.791(6) Å, Fe2-C1: 1.800(6) Å) are similar to those in **{Fe$_2$(μ-CAr)}^{18}** (Fe1/2-C1: 1.792(1) Å), indicating that the redox active orbital is essentially non-bonding with respect to the carbyne ligand.

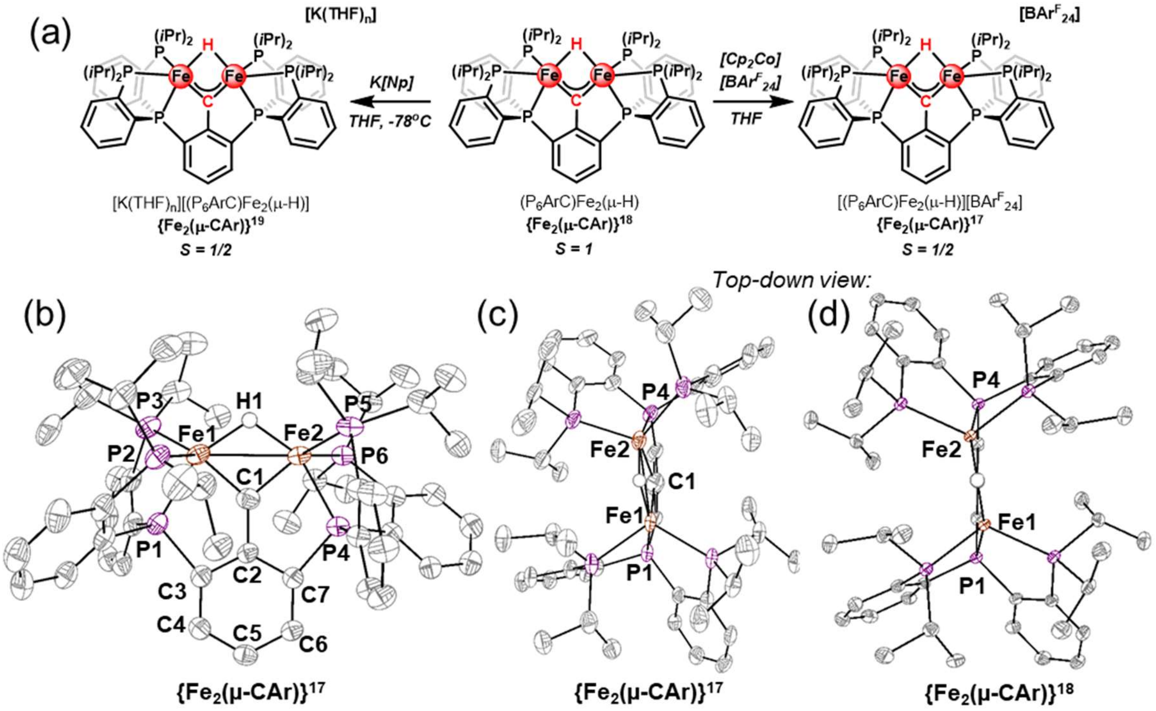

Figure 4. (a). Synthesis of [(P$_6$ArC)Fe$_2$(μ-H)][BAr$^F{}_{24}$] (**{Fe$_2$(μ-CAr)}^{17}**) and [K(THF)$_n$][(P$_6$ArC)Fe$_2$(μ-H)] (**{Fe$_2$(μ-CAr)}^{19}**) (b). Crystal structure of [(P$_6$ArC)Fe$_2$(μ-H)][BAr$^F{}_{24}$] (**{Fe$_2$(μ-CAr)}^{17}**). Hydrogen atoms on the ligand and counterion omitted for clarity. Thermal ellipsoids shown at 50% probability (c). Top down view illustrating the loss of C_2 symmetry in [(P$_6$ArC)Fe$_2$(μ-H)][BAr$^F{}_{24}$] (**{Fe$_2$(μ-CAr)}^{17}**) (d). Comparison to P$_6$ArC)Fe$_2$(μ-H)(**{Fe$_2$(μ-CAr)}^{18}**, ref. 66)

Unlike its one-electron reduced congener, **{Fe$_2$(μ-CAr)}^{17}** does not have crystallographically-imposed symmetry. The two iron sites of **{Fe$_2$(μ-CAr)}^{18}** are related by a C_2 axis along the C1-C2 vector (Figure 4d), which positions the metal centers on opposite faces of the central carbyne linker without any significant distortion of the C1-C2-C3-P1 torsion angle (0.36(8)°). In contrast, the solid-state structure of the oxidized compound reveals that both P$_3$ arms have rotated such that the iron centers of **{Fe$_2$(μ-CAr)}^{17}** are oriented on the same side of ligand (Figure 4c). This is accompanied by a deviation of the C1-C2-C3-P1 torsion angle (4.4(6)°) away from planarity.

Table 2. Comparison of Selected Bond Lengths and Angles for $\{Fe_2(\mu\text{-CAr})\}^{17\text{-}19}$.

Bonds (Å)	**$\{Fe_2(\mu\text{-CAr})\}^{17}$**	**$\{Fe_2(\mu\text{-CAr})\}^{18}$ [a]**	**$\{Fe_2(\mu\text{-CAr})\}^{19}$ [b]**
Fe1-C1	1.791(6)	1.792(1)	1.796
Fe1-P1	2.156(2)	2.1307(7)	2.076
Fe1-P2	2.292(2)	2.2627(8)	2.217
Fe1-P3	2.358(2)	2.2522(6)	2.206
Fe2-C1	1.800(6)	1.792(1)	1.796
Fe2-P4	2.176(2)	2.1307(7)	2.078
Fe2-P5	2.329(2)	2.2627(8)	2.217
Fe2-P6	2.311(2)	2.2522(6)	2.206
Fe1-Fe2	2.691(2)	2.6776(6)	2.795
Angles (°)			
Fe1-C1-Fe2	97.0(2)	96.66(1)	102.2
Fe1-C1-C2	130.4(5)	131.67(5)	128.9
Fe2-C1-C2	130.5(5)	131.67(5)	128.9
Sum	357.9(7)	360.00(7)	360.0
P1-C3-C4	138.1(4)	141.42(1)	141.0
P4-C7-C6	138.2(4)	141.42(1)	140.8
Torsions (°)			
C1-C2-C3-P1	4.4(6)	0.36(8)	0.2
C1-C2-C7-P4	0.4(6)	-0.36(8)	-0.3

[a] Previously reported, ref. 66. [b] Structural metrics for **$\{Fe_2(\mu\text{-CAr})\}^{19}$** derived from DFT geometry optimization (TPSS/def2-TZVP on Fe)).

Variable temperature ^1H NMR spectroscopy indicates that **$\{Fe_2(\mu\text{-CAr})\}^{17}$** also adopts a low symmetry structure in solution, at least below 228 K. At 298 K, the ^1H NMR spectrum of **$\{Fe_2(\mu\text{-CAr})\}^{17}$** exhibits 16 sharp, paramagnetically-shifted resonances between -20 and 85 ppm (NMR, Figure 97), consistent with C_2 symmetry or an exchange process. As expected for an open-shell species, cooling a solution of **$\{Fe_2(\mu\text{-CAr})\}^{17}$** in tetrahydrofuran-$d_8$ causes these features to shift substantially, with significant broadening of the signals down to 228 K (Figure 5). However, cooling below 228 K leads to decoalescence and sharpening of these features. The number of resonances (>30) observed at 188 K is roughly double that at 298 K, indicating C_1 symmetry at low temperature, in good agreement with what is observed in the solid state (T_{XRD} = 100 K). For comparison, the 1e$^-$ reduced compound **$\{Fe_2(\mu\text{-CAr})\}^{18}$** does not display the same behavior by variable temperature ^1H NMR spectroscopy[66] and, thus, either maintains a static, higher-symmetry geometry in solution or possesses a lower barrier to structural interconversion. Although the structure of **{Fe$_2$(μ-CAr)}^{17}** is clearly fluxional at elevated temperatures in solution, below ~188 K the conformational changes are slow on the NMR time scale. Notably, spectroscopic studies on **{Fe$_2$(μ-CAr)}^{17}** were conducted on samples maintained at or below liquid nitrogen temperature (77 K) and, therefore, likely reflect the electronic structure of the low symmetry geometry.

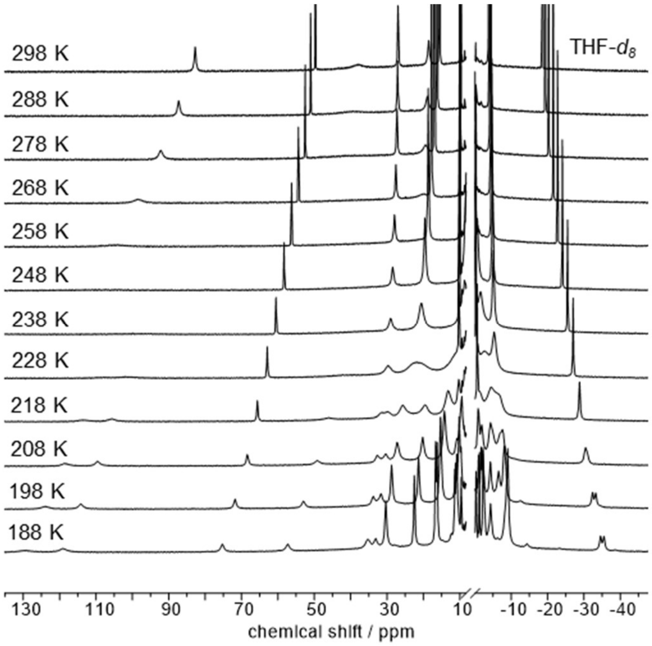

Figure 5. Variable temperature ^{1}H NMR spectra of [(P$_6$ArC)Fe$_2$(μ-H)][BAr$^F{}_{24}$] (**{Fe$_2$(μ-CAr)}^{17}**) in tetrahydrofuran-d_8 reveal fluxional behavior and a loss of symmetry at low temperatures.

Characterization of **{Fe$_2$(μ-CAr)}^{17}** by EPR spectroscopy intimates that the iron sites are antiferromagnetically coupled, leading to a doublet ground state for the dimer. The X-band ($\nu \approx 9.6$ GHz) continuous wave (CW) EPR spectrum of **{Fe$_2$(μ-CAr)}^{17}** at 5 K exhibits a nearly isotropic signal centered at $g \sim 2.09$ (Figure 6, top left), with no resolved hyperfine coupling. Measurement at Q-band ($\nu \approx 34$ GHz) via spin echo-detected field sweep resolves the small g anisotropy (Figure 6, bottom left), with simulations affording the rhombic g tensor $g = [2.114, 2.097, 2.054]$. For spin-coupled dimers in the limit of strong coupling and low zero-field splitting: $g_i = (g_1 + g_2)/2 + (g_1 - g_2)/2S(S + 1)[S_1(S_1 + 1) - S_2(S_2 + 1)$.[89-90] Thus, under the assumption of low spin Fe(II), the g tensor of the dimer would reflect the anisotropy of the Fe(III) site.[91] However, low spin Fe(III) complexes commonly exhibit highly anisotropic low spin signals.[92-96] Direct comparison can be made to the isoelectronic diiron μ-imide, μ-hydride complex [([PhBP$_3$]Fe)$_2$(μ-NH)(μ-H)] which reveals the g anisotropy ($g_{\|} = 2.54$ $g_{\perp} \sim 2.04$) expected for a low spin Fe^{II}/low spin Fe^{III} spin coupled system.[55] In contrast, **{Fe$_2$(μ-CAr)}^{17}** exhibits small g anisotropy and atypical symmetry within its g tensor ($g_{\perp} > g_{\|}$), both of which are inconsistent with a low spin Fe(II)/low spin Fe(III) formulation.

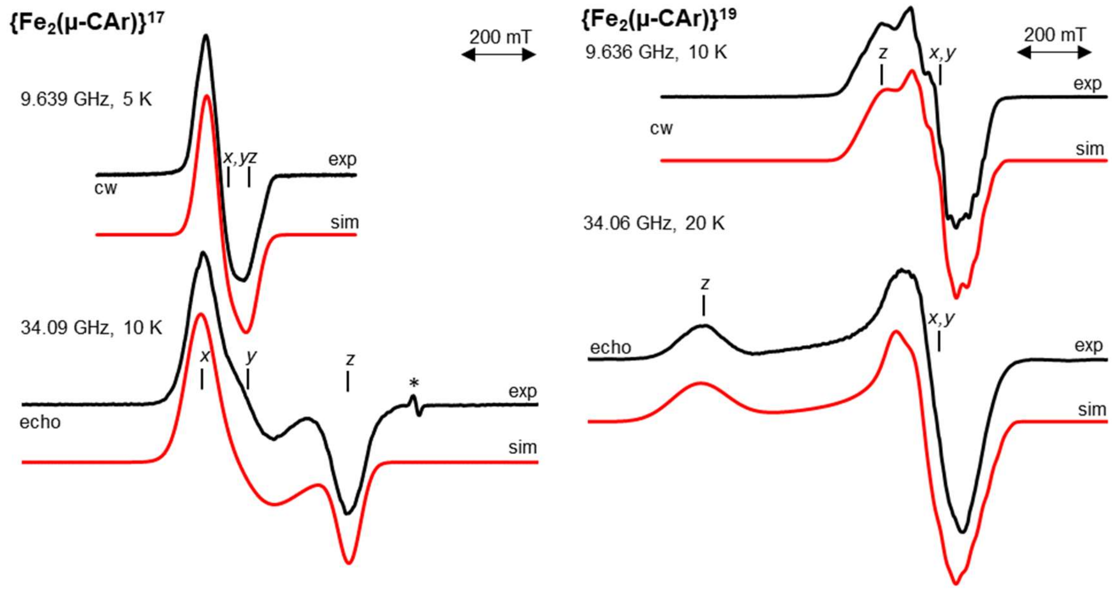

Figure 6. Left: X-band (top) and pseudomodulated[97] Q-band ESE-EPR (bottom) CW EPR Spectra of [(P$_6$ArC)Fe$_2$(μ-H)][BAr$^F{}_{24}$] (**{Fe$_2$(μ-CAr)}^{17}**) in 2-MeTHF (2 mM). Experimental data shown in black and simulations for $S = ½$, $g = [2.114, 2.097, 2.054]$ are shown in red. The asterisk denotes a background signal present in the Q-band resonator, not in the sample. X-band acquisition parameters: temperature = 5 K; MW frequency = 9.639 GHz; MW power = 2 mW; modulation frequency = 100 kHz; modulation amplitude = 0.4 mT; conversion time = 82 ms. Q-band Acquisition parameters: temperature = 10 K; MW frequency = 34.09 GHz. Right: X-band (top) and pseudomodulated[97] Q-band ESE-EPR (bottom) CW EPR Spectra of [K(THF)$_n$][(P$_6$ArC)Fe$_2$(μ-H)] (**{Fe$_2$(μ-CAr)}^{19}**) in 2-MeTHF (2 mM). Experimental data shown in black

and simulations for $S = ½$, g = [2.0890 2.036 2.026] are shown in red. X-band Acquisition parameters: temperature = 10 K; MW frequency = 9.636 GHz; MW power = 2 mW; modulation frequency = 100 kHz; modulation amplitude = 0.4 mT; conversion time = 82 ms. Q-band Acquisition parameters: temperature = 20 K; MW frequency = 34.06 GHz. Note, in both cases, the X-band spectra have been shifted along the field axis for plotting purposes only.

Low-Lying Excited States in {Fe_2(μ-CAr)}^{17}. Consistent with population of higher spin states at elevated temperatures, a solution magnetic measurement of **{Fe_2(μ-CAr)}^{17}** provided a χT value of 1.26 cm^3 K mol^{-1} ($\mu_{eff} = 3.19\mu_B$) at 298 K, considerably larger than that expected for an isolated $S = ½$ spin system ($\chi T = 0.37$ cm^3 K mol^{-1} and $\mu_{eff} = 1.73\mu_B$ for $g = 2.00$). Variable temperature magnetic susceptibility measurements on microcrystalline samples of **{Fe_2(μ-CAr)}^{17}** revealed a similar value for χT (1.31 cm^3 K mol^{-1}) at 298 K. The value of χT decreases as the sample is cooled down, reaching a value of 0.46 cm^3 K mol^{-1} ($\mu_{eff} = 1.92\mu_B$) at 3 K (Figure 7). Simulations according to the Heisenberg exchange Hamiltonian $H = -2J_{12}(S_1 \cdot S_2)$ assuming $S_1 = 1$ (intermediate spin Fe(II)) and either $S_2 = 1/2$ (low spin Fe(III) or Fe(I)) or 3/2 (intermediate spin Fe(III) or high spin Fe(I)) afford isotropic exchange constants $J_{12} = -104$ cm^{-1} and -112 cm^{-1}, respectively. Although both models afford fits which are in reasonable agreement with the experimental data, analysis of the ^{1}H hyperfine coupling by EPR spectroscopy indicates that **{Fe_2(μ-CAr)}^{17}** is valence delocalized. Efforts to simulate the magnetometry data using a more general model involving multiple spin states at arbitrary energies with $S > ½$ did not prove fruitful. In any case, the magnetometry data cannot be rationalized in terms of a low spin Fe(II)/low spin Fe(III) formulation, consistent with the analysis of the CW-EPR spectrum of **{Fe_2(μ-CAr)}^{17}**.

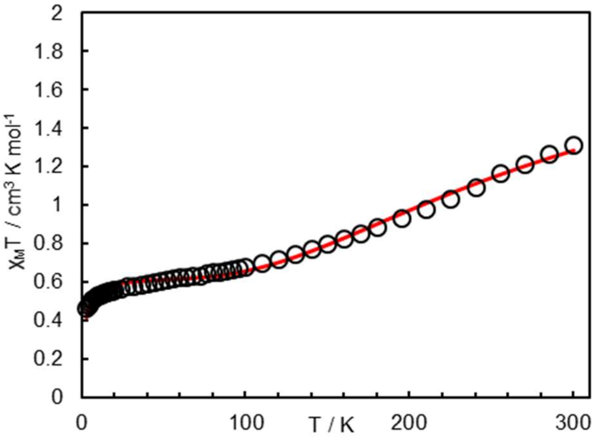

Figure 7. Variable temperature magnetic susceptibility measurements for $[(P_6ArC)Fe_2(\mu\text{-}H)][BAr^F{}_{24}]$ (**$\{Fe_2(\mu\text{-}CAr)\}^{17}$**) collected between 3 and 300 K with a 0.5 T field after diamagnetic correction (black circles). Parameters for the fit shown: $S_1 = 1$, $g_1 = 2.55$, $S_2 = 1/2$, $g_2 = 2.45$, $J = -111.6$ cm^{-1}, $zJ = -0.64$ cm^{-1}. Equally satisfactory fits can be obtained with $S_2 = 3/2$.

In Situ *Characterization of a Reactive $\{Fe_2(\mu\text{-}CAr)\}^{19}$ Species.* To determine the effect of redox chemistry on the structural and electronic features of the Fe(μ-C)(μ-H)Fe core, we pursued characterization of the **$\{Fe_2(\mu\text{-}CAr)\}^{19}$** species $[K(THF)_n][(P_6ArC)Fe_2(\mu\text{-}H)]$. Treatment of **$\{Fe_2(\mu\text{-}CAr)\}^{18}$** with potassium naphthalenide at -78 °C generates a new species that exhibits an EPR signal centered at $g \sim 2.04$ (Figure 8a). Q-band measurements reveal that although both **$\{Fe_2(\mu\text{-}CAr)\}^{17}$** and **$\{Fe_2(\mu\text{-}CAr)\}^{19}$** exhibit axial EPR spectra, the symmetries of their g tensors are distinct (Figure 8). Simulations indicate that $g_z > g_{x,y}$ for **$\{Fe_2(\mu\text{-}CAr)\}^{19}$** ($g$ = [2.0890 2.036 2.026]) whereas $g_{x,y} > g_z$ in **$\{Fe_2(\mu\text{-}CAr)\}^{17}$**. Solution phase structural characterization of this species via extended X-ray absorption fine structure (EXAFS) is consistent with its assignment as **$\{Fe_2(\mu\text{-}CAr)\}^{19}$**, with a geometry closely related to **$\{Fe_2(\mu\text{-}CAr)\}^{17\text{-}18}$** (Figure S2).

The signal attributed to **$\{Fe_2(\mu\text{-}CAr)\}^{19}$** persists and remains well-resolved for samples maintained at -78 °C for 30-60 minutes. Storing solutions of **$\{Fe_2(\mu\text{-}CAr)\}^{19}$** for > 1 hr. or warming above -78 °C results in loss of its characteristic EPR feature, concomitant with the appearance of several distinct $S = ½$ species (EPR, Figure 21). Thus far, efforts to characterize these decomposition products have proved challenging. All of the iron-containing products generated at higher temperatures are NMR silent; only resonances corresponding to diisopropylphenylphosphine, derived from C-P bond cleavage of the ligand, are observed in the ^{1}H and ^{31}P NMR spectra.

^{2}H-^{1}H Pulse EPR Supports a Symmetric Spin Distribution in $\{Fe_2(\mu\text{-}CAr)\}^{17}$ and $\{Fe_2(\mu\text{-}CAr)\}^{19}$. Complementary Q-band electron nuclear double resonance (ENDOR) and hyperfine sublevel correlation (HYSCORE) measurements of the ligand hyperfine coupling provide further insight into the spin distribution of **$\{Fe_2(\mu\text{-}CAr)\}^{17}$** and **$\{Fe_2(\mu\text{-}CAr)\}^{19}$**. In order to determine the ^{1}H and ^{13}C hyperfine coupling, the ^{2}H and ^{13}C isotopologues were prepared (see the footnote herein).[98] Although the natural abundance, ^{2}H-labelled, and ^{13}C-labelled isotopologues of **$\{Fe_2(\mu\text{-}CAr)\}^{19}$** exhibit X-band CW EPR spectra with slight differences among them (Figure 8), the X-band CW spectra of **$\{Fe_2(\mu\text{-}CAr)\}^{17}$** are broad and virtually identical. Simulation of the ^{2}H-^{1}H difference HYSCORE spectra of $[(P_6ArC)Fe_2(\mu\text{-}D)][BAr^{F}_{24}]$ affords an anisotropic deuterium hyperfine tensor $A(^{2}H) = \pm[2.1, 5.5, 7.4]$ MHz, with a small tensor frame rotation by $(\alpha,\beta,\gamma)^{o} = (15, 25, 0)^{o}$ relative to the coordinate frame of the g tensor. Scaling the ^{2}H hyperfine tensor by the proportion of the ^{1}H/^{2}H gyromagnetic ratios ($^{1}H\gamma/^{2}H\gamma = 6.514/1$) provides the ^{1}H hyperfine tensor $A(^{1}H) = \pm[14.0, 36.0, 48.0]$ MHz for **$\{Fe_2(\mu\text{-}CAr)\}^{17}$**, which is in accord with simulations of the ENDOR spectra for the natural abundance sample (Table 3). In a similar manner, simulation of the HYSCORE spectra of $[K(THF)_n][(P_6ArC)Fe_2(\mu\text{-}D)]$ provides, after scaling, the ^{1}H hyperfine tensor $A(^{1}H) = \pm[26.0, 18.0, 41.0]$ MHz for **$\{Fe_2(\mu\text{-}CAr)\}^{19}$** (Table 3), rotated by $(\alpha,\beta,\gamma)^{o} = (0,18,0)^{o}$ relative to the frame of the g tensor. Variable mixing time ^{2}H Mims ENDOR spectra were collected on $[(P_6ArC)Fe_2(\mu\text{-}D)][BAr^{F}_{24}]$ and $[K(THF)_n][(P_6ArC)Fe_2(\mu\text{-}D)]$, which allowed the absolute sign

of the ^{2}H hyperfine to be determined. Results were consistent with the sign of the ^{2}H$_{\mu}$ hyperfine (and by extension ^{1}H$_{\mu}$) being negative for both **{Fe$_2$(μ-CAr)}^{17}** and **{Fe$_2$(μ-CAr)}^{19}**.

Table 3. Hyperfine Coupling Constants in MHz Determined for {Fe$_2$(μ-CAr)}^{17} and {Fe$_2$(μ-CAr)}^{19}.

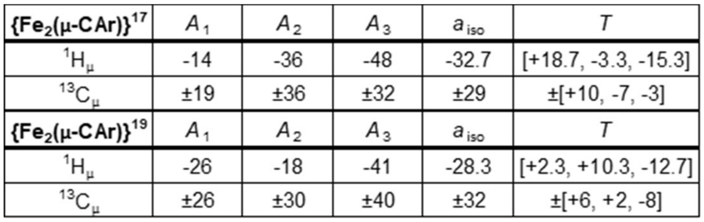

{Fe$_2$(μ-CAr)}^{17}	A_1	A_2	A_3	a_{iso}	T
^{1}H$_{\mu}$	-14	-36	-48	-32.7	[+18.7, -3.3, -15.3]
^{13}C$_{\mu}$	±19	±36	±32	±29	±[+10, -7, -3]
{Fe$_2$(μ-CAr)}^{19}	A_1	A_2	A_3	a_{iso}	T
^{1}H$_{\mu}$	-26	-18	-41	-28.3	[+2.3, +10.3, -12.7]
^{13}C$_{\mu}$	±26	±30	±40	±32	±[+6, +2, -8]

All hyperfine tensors are assumed to be collinear with *g* except A($^{1/2}$H). For **{Fe$_2$(μ-CAr)}^{17}** the Euler angles are (α,β,γ) ° = (15, 25, 0)°. For **{Fe$_2$(μ-CAr)}^{19}** the Euler angles are (α,β,γ)° = (0,18,0)°. The sign of A($^{1/2}$H) was determined by variable mixing time ^{2}H Mims ENDOR. The sign of A(^{13}C) is assumed to be negative based on DFT.

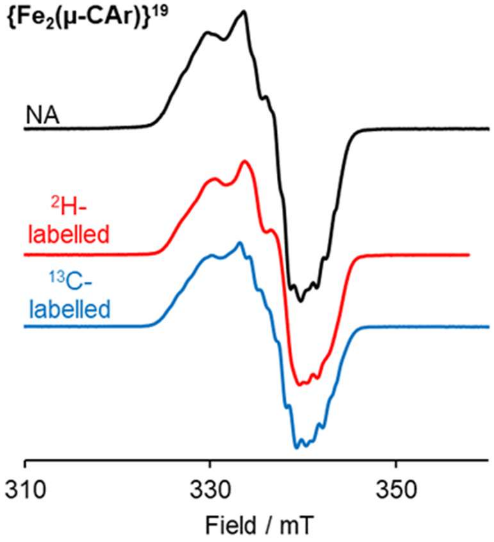

Figure 8. X-band CW EPR Spectra of [K(THF)$_n$][(P$_6$ArC)Fe$_2$H] (black), [K(THF)$_n$][(P$_6$ArC)Fe$_2$D] (red), and [K(THF)$_n$] [(P$_6$Ar^{13}C)Fe$_2$H] (blue), all 2 mM in 2-MeTHF. Acquisition parameters: temperature = 10 K; MW frequency = 9.639 GHz; MW power = 2 mW; modulation frequency = 100 kHz; modulation amplitude = 0.4 mT; conversion time = 82 ms.

The respective ^{1}H hyperfine tensors of **{Fe$_2$(μ-CAr)}^{17}** and **{Fe$_2$(μ-CAr)}^{19}**, respectively, can be decomposed into an isotropic component a_{iso}(^{1}H) (**{Fe$_2$(μ-CAr)}^{17}**: -32.7 MHz, **{Fe$_2$(μ-CAr)}^{19}**: -28.3 MHz) and an anisotropic component T(^{1}H) (**{Fe$_2$(μ-CAr)}^{17}**:

[+18.7, -3.3, -15.3] MHz, **{Fe$_2$(μ-CAr)}^{19}**: [+2.3, +10.3, -12.7] MHz). The isotropic ^{1}H hyperfine coupling arises from delocalization of spin density into the proton 1*s* orbital, either directly by a Fermi contact interaction or indirectly by spin polarization.[99-100] Given the large hyperfine constant expected for an electron localized in a hydrogen 1*s* orbital (a_{iso}^0 = 1420 MHz),[101-102] the small difference in the $a_{\mathrm{iso}}(^1\mathrm{H})$ values of **{Fe$_2$(μ-CAr)}^{17}** (-32.7 MHz) and **{Fe$_2$(μ-CAr)}^{19}** (-28.3 MHz) implies that the spin density on the μ-hydride ligand changes by only 0.003 e^- ($\rho_s(^1\mathrm{H}) \approx -0.023\ e^-$ and -0.020 e^-, respectively) upon a 2 e^- transfer, suggesting that redox chemistry does not substantially affect the Fe-H covalency. The isotropic ^{1}H hyperfine associated with the μ-hydride ligand in **{Fe$_2$(μ-CAr)}^{17}** can also be compared with that in the previously reported and isoelectronic μ-imide, μ-hydride species [([PhBP$_3$]Fe)$_2$(μ-NH)(μ-H)].[55] Although the $a_{\mathrm{iso}}(^1\mathrm{H})$ value determined for [([PhBP$_3$]Fe)$_2$(μ-NH)(μ-H)] (-38.9 MHz) is larger than that in **{Fe$_2$(μ-CAr)}^{17}** (32.7 MHz), the differences in the μ-hydride spin densities are minimal ($\rho_s(^1\mathrm{H}) \approx -0.027\ e^-$ and -0.023 e^-, respectively).

Due to the lack of any local *p*-orbital contribution, the anisotropic component of the ^{1}H hyperfine arises solely from dipolar interactions with the iron-based spin. For dimeric systems, it has been shown that the full dipolar coupling tensor can be analyzed in terms of a point dipole model,[103-105] with $T(^1\mathrm{H})$ calculated by summing over contributions from each metal site (Figure 9).

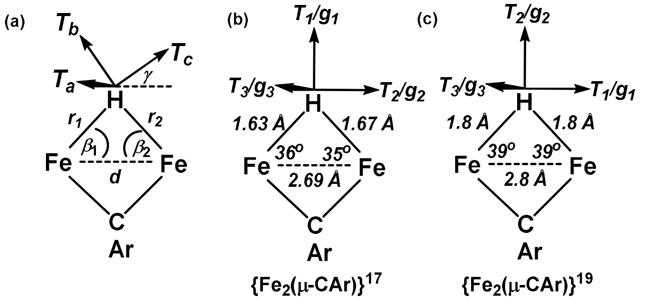

Figure 9. (a) Schematic representation of the metric parameters used to calculate the proton dipolar tensor within the defined molecular frame of $[(P_6ArC)Fe_2(\mu\text{-}H)]^n$ (n = -1 or +1). (b) Orientation of the principal components of $T(^1H)$ in the molecular frame of $[(P_6ArC)Fe_2(\mu\text{-}H)][BAr^F{}_{24}]$ (**$\{Fe_2(\mu\text{-}CAr)\}^{17}$**). (c) Orientation of the principal components of $T(^1H)$ in the molecular frame of $[K(THF)_n][(P_6ArC)Fe_2H]$ (**$\{Fe_2(\mu\text{-}CAr)\}^{19}$**).

$$T_a = -\tfrac{1}{2}(t_1 + t_2) \quad (1)$$

$$T_b = \tfrac{1}{2}(|T_a| + 3/2*(\cos2\gamma)^{-1}(t_1\cos2\beta_1 + t_2\cos2\beta_2)) \quad (2)$$

$$T_c = -(T_a + T_b) \quad (3)$$

$$\tan2\gamma = (\sin2\beta_1 - (t_2/t_1)*\sin2\beta_2)/(\cos2\beta_1 + (t_2/t_1)*\cos2\beta_2) \quad (4)$$

Where the values T_n (n = a, b, c) in MHz are the principal components of $T(^1H)$, β_1 and β_2 define the angle between r_1 and r_2, respectively, and the Fe1-Fe2 vector d. The angle γ describes the orientation of the coordinate axes T_b and T_c with respect to the Fe1-Fe2 vector d. The distance dependence of the magnetic dipole interaction of the μ-hydride with the individual iron centers Fe1 and Fe2, respectively, is defined by the elements t_1 and t_2 which take the classical form:

$$t_i = K_i c_i\left(\frac{2g_e\beta_e g_N\beta_N}{r_i^3}\right) \quad (5)$$

Where r_i represents the distance of the μ-hydride from Fe_i (i = 1,2), K_i is the spin projection coefficient for Fe_i (i = 1,2), and the effect of spin delocalization away from each Fe (such as onto the carbyne and P donor ligands) is parameterized by c_i with $0 \leq c_i \leq 1$.

It can be shown that a terminal hydride ligand should possess an axial anisotropic coupling tensor of the form $T(^1H) = t[-1, -1, +2]$.[43, 45, 106-107] On the other hand, this model predicts that a hydride which bridges two metal centers will exhibit a rhombic tensor of the form $T(^1H) = t[0, -2, +2]$.[33, 54-55, 108-109] For intermediate cases, the degree of rhombicity (ρ) can be quantified by decomposing the anisotropic hyperfine tensor into axial and rhombic terms, with $T = t[-(1-\varrho), -(1+\varrho), +2]$ and $\varrho \rightarrow 1$ for a fully rhombic interaction. The anisotropic ^{1}H hyperfine coupling tensors of **{Fe$_2$(μ-CAr)}^{17}** ($T(^1\mathrm{H}) = [+18.7, -3.3, -15.3]$ MHz) and **{Fe$_2$(μ-CAr)}^{19}** ($T(^1\mathrm{H}) = [+2.3, +10.3, -12.7]$ MHz) both exhibit a high degree of rhombicity (ϱ = 0.65 and 0.64, respectively), consistent with the presence of the μ-hydride ligand. For comparison, similar deviations of the through-space dipolar coupling from $\varrho \rightarrow 1$ have been reported for [([PhBP$_3$]Fe)$_2$(μ-NH)(μ-H)] (ϱ = 0.79)[55] and an Fe$^{1.5}_2$ bis(μ-hydride) complex (ϱ = 0.75).[54]

Based on equation 5, the contribution of each iron center to $T(^1\mathrm{H})$ depends on their spin projection factors. Thus, calculations of the dipolar coupling to the μ-hydride ligand in **{Fe$_2$(μ-CAr)}^{17}** and **{Fe$_2$(μ-CAr)}^{19}** using the point dipole model (equations 1-5) can shed light on the distribution of spin density and, thus, the degree of valence (de)localization in each complex. Most notably, the experimental tensor $T(^1\mathrm{H})_{\mathrm{exp}} = [+18.7, -3.3, -15.3]$ MHz is distinct from those expected if **{Fe$_2$(μ-CAr)}^{17}** was valence localized with either $S_1 = 1$, $S_2 = 1/2$ ($T(^1\mathrm{H})_{\mathrm{calc}} = [-18, -33, 52]$ MHz) or $S_1 = 3/2$, $S_2 = 1/2$ ($T(^1\mathrm{H})_{\mathrm{calc}} = [-19, -51, +70]$ MHz) spin coupling arrangements. On the other hand, good agreement between the experimental and calculated ($T(^1\mathrm{H})_{\mathrm{calc}} = [+17.8, -0.2, -17.6]$ MHz) tensors is obtained assuming **{Fe$_2$(μ-CAr)}^{17}** is valence delocalized ($K_1 = K_2 = +1/2$, $\gamma = 0^{\mathrm{o}}$) using the metric parameters r_1 = 1.63 Å, r_2 = 1.67 Å, and d = 2.69 Å (Figure 9b). These values of r_1 and r_2 compare favorably with those determined by crystallography (Fe1-H1: 1.63(3) Å, Fe2-H1: 1.64(3) Å) and are similar to those reported for [([PhBP$_3$]Fe)$_2$(μ-NH)(μ-H)] (1.64 Å and 1.68 Å).[55] This simulation indicates that the first principal component of $T(^1\mathrm{H})$ (T_3) and, thus, g_3 is normal to the Fe(μ-C)(μ-H)Fe plane ($T_{\mathrm{a}} = T_3$). The value of $\gamma = 0^{\mathrm{o}}$ indicates that the two in-plane components of $T(^1\mathrm{H})$ are oriented such that $T_{\mathrm{c}} = T_2$ (and, therefore, g_2) lies along the Fe-Fe vector, with $T_{\mathrm{b}} = T_1$ (and g_1) perpendicular to it. The orientation of $T(^1\mathrm{H})$ and g reported here for **{Fe$_2$(μ-CAr)}^{17}** is distinct from that in [([PhBP$_3$]Fe)$_2$(μ-NH)(μ-H)], where detailed analysis of the ^{1}H hyperfine coupling revealed that g_2, not g_1, is normal to the Fe(μ-N)(μ-H)Fe plane ($T_a = T_2$).[55]

Likewise, the orientation of $T(^1\text{H})$ and g in the molecular frame of [K(THF)$_n$][(P$_6$ArC)Fe$_2$H] can be determined by analysis of the dipolar coupling to the μ-hydride (Figure 9). Although a solid-state structure of [K(THF)$_n$][(P$_6$ArC)Fe$_2$H] was not obtained, the solution-state structure determined by EXAFS studies is in good agreement with that predicted by DFT geometry optimizations. As such, the computationally determined metric parameters were used in the calculation of $T(^1\text{H})$: $r_1 = r_2 = 1.79$ Å, $\beta_1 = \beta_2 = 38.7^\circ$, $d = 2.79$ Å. DFT calculations (*vide infra*) indicate that [K(THF)$_n$][(P$_6$ArC)Fe$_2$H] is valence-delocalized, which implies that the spin projection factors are $K_1 = K_2 = ½$ and $\gamma = 0^\circ$. The principal components of $T(^1\text{H})$ are calculated to be $T(^1\text{H})_{\text{calc}} = [T_c, T_b, T_a] = [+2.4, +11.4, -13.8]$ MHz, which compares favorably with the experimentally determined tensor $T(^1\text{H}) = +/-[+2.3, +10.3, -12.7]$ MHz and validates the structural and electronic parameters assumed in the simulation. This analysis indicates that $T_a = T_3$ and, thus, g_3 is normal to the Fe(μ-C)(μ-H)Fe plane (Figure 9c). The value of $\gamma = 0^\circ$ indicates that $T_c = T_1$ (and, therefore, g_1) lies along the Fe-Fe vector. Finally, $T_b = T_2$ and g_2 are perpendicular to the Fe-Fe vector in the Fe(μ-C)(μ-H)Fe plane. Combined, analysis of the anisotropic ^{1}H hyperfine coupling supports an electronically-delocalized description for both **{Fe$_2$(μ-CAr)}^{17}** and **{Fe$_2$(μ-CAr)}^{19}**, implying a symmetric distribution of α and β spin density.

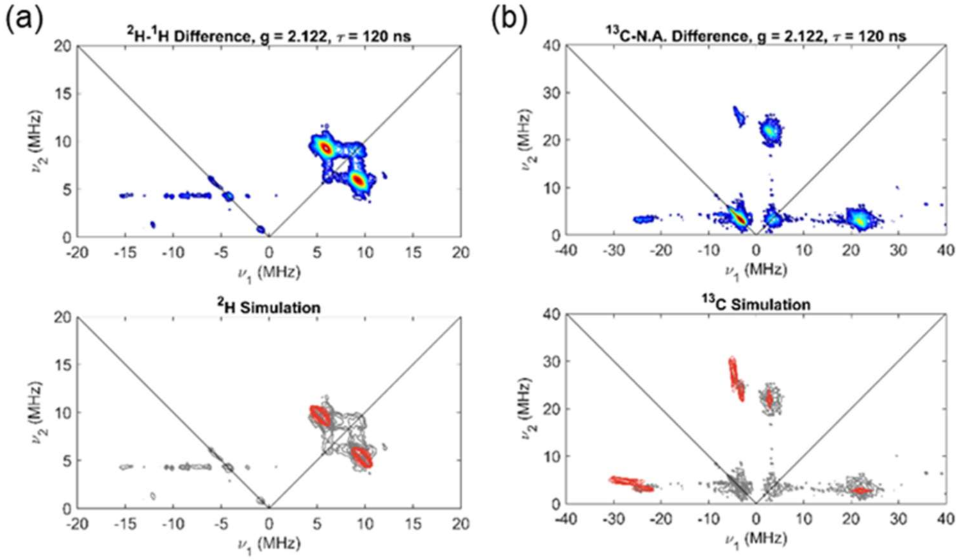

Figure 10. (a) Top panel: Q-band ^{2}H-^{1}H difference HYSCORE spectrum of $[(P_6ArC)Fe_2(\mu\text{-}D)][BAr^F_{24}]$ acquired at 1148 mT (g = 2.122). Bottom panel: Monochromatic representation of the HYSCORE data (grey) with ^{2}H simulations overlaid (red). Simulation parameters were derived by scaling the ^{1}H hyperfine tensor in Table 3 of the main text determined from Q-band ^{1}H ENDOR, and scaling by the proportion of ^{1}H/^{2}H gyromagnetic ratios ($\gamma^1H/\gamma^2H = 6.514$). Simulations also include ^{2}H nuclear quadrupole parameters $e^2qQ/h = 0.15$; $\eta = 0$. Acquisition parameters: temperature = 12 K; microwave frequency = 34.086 GHz; MW pulse length ($\pi/2$, π) = 12 ns, 24 ns; τ = 120 ns, $t_1 = t_2 = 100$ ns; $\Delta t_1 = \Delta t_2 = 12$ ns; shot repetition time (srt) = 1.5 ms). (b) Top panel: Q-band ^{13}C-natural abundance difference HYSCORE spectrum of $[(P_6Ar^{13}C)Fe_2H][BAr^F_{24}]$ acquired at 1148 mT (g = 2.122). Bottom: Monochromatic representation of the HYSCORE data (grey) with ^{13}C simulations overlaid (red) using parameters in Table 3. Acquisition parameters: temperature = 12 K; microwave frequency = 34.086 GHz; MW pulse length ($\pi/2$, π) = 12 ns, 24 ns; τ = 120 ns, $t_1 = t_2 = 100$ ns; $\Delta t_1 = \Delta t_2 = 12$ ns; shot repetition time (srt) = 1.5 ms).

^{13}C Pulse EPR Reveals a Decrease in Fe-C Covalency Upon Reduction. The HYSCORE spectra of the ^{13}C-labelled compounds $[(P_6Ar^{13}C)Fe_2(\mu\text{-}H)][BAr^F_{24}]$ (Figure 10, right) and $[K(THF)_n][(P_6Ar^{13}C)Fe_2(\mu\text{-}H)]$ clearly resolve the strong coupling interaction of the bridging carbon with the diiron unit (Figures S62-64). Simulations provide anisotropic hyperfine tensors $A(^{13}C) = \pm[19.0, 36.0, 32.0]$ MHz for **$\{Fe_2(\mu\text{-}CAr)\}^{17}$** and $A(^{13}C) = \pm[26.0, 30.0, 40.0]$

MHz for **{Fe$_2$(μ-CAr)}^{19}**, which can both be decomposed to a isotropic term $a_{\mathrm{iso}}(^{13}\mathrm{C})$ (**{Fe$_2$(μ-CAr)}^{17}**: ±29.0 MHz, **{Fe$_2$(μ-CAr)}^{19}** = ±32 MHz) and an anisotropic component $T(^{13}\mathrm{C})$ (**{Fe$_2$(μ-CAr)}^{17}**: ±[-10, +7, +3] MHz, **{Fe$_2$(μ-CAr)}^{19}**: ±[-6, -2, +8] MHz). The isotropic contribution to the ^{13}C coupling in **{Fe$_2$(μ-CAr)}^{19}** ($a_{\mathrm{iso}}(^{13}\mathrm{C})$ = ±32 MHz) is greater than that in **{Fe$_2$(μ-CAr)}^{17}** ($a_{\mathrm{iso}}(^{13}\mathrm{C})$ = ±29 MHz). However, the intrinsic coupling expected for a single electron localized in a carbon *2*s orbital ($a_{\mathrm{iso}}{}^{0}$ = 3110 MHz)[101] is much larger than these differences, signifying that the extent of Fe → C 2*s* spin delocalization ($\rho_s(^{13}\mathrm{C}) \approx 9.3 \times 10^{-3}\ e^-$ for **{Fe$_2$(μ-CAr)}^{17}** compared to $\approx 10.2 \times 10^{-3}\ e^-$ for **{Fe$_2$(μ-CAr)}^{19}**) varies moderately with redox changes. To the best of our knowledge, only one other synthetic iron complex featuring an anionic R_3C^-, R_2C^{2-}, or RC^{3-} type ligand has been ^{13}C enriched at the ligating carbon and interrogated by pulse EPR. This species, a terminal iron(V)-carbyne complex, was reported to have an $a_{\mathrm{iso}}(^{13}\mathrm{C})$ of ±32.7 MHz,[44] quite similar to the values observed here.

In contrast to that for the μ-hydride, the anisotropic component of the ^{13}C coupling arises from local 2*p* contributions, in addition to dipolar interactions with the spin localized at the adjacent Fe ions.[101] Assuming that spin polarization of the C 2*p* electrons is the dominant spin transfer mechanism,[110] the anisotropic ^{13}C hyperfine tensors of **{Fe$_2$(μ-CAr)}^{17}** and **{Fe$_2$(μ-CAr)}^{19}** can each be uniquely decomposed into two axial terms corresponding to spin transfer into the orthogonal C $2p_\sigma$ and C $2p_\pi$ orbitals. Deconvolution of the experimental $T(^{13}\mathrm{C})$ tensors affords b_σ = ±5.7 MHz and b_π = ±1.3 MHz for **{Fe$_2$(μ-CAr)}^{17}** compared to ±1.3 MHz and ±3.3 MHz for **{Fe$_2$(μ-CAr)}^{19}**. By comparison to the orientation of the *g* tensor in the molecular frame, it can be shown that b_π has its largest principal component normal to the Fe(μ-C)(μ-H)Fe plane for both **{Fe$_2$(μ-CAr)}^{17}** and **{Fe$_2$(μ-CAr)}^{19}** (Figure 9) and is associated with spin density in the out-of-plane C $2p_\pi$ orbital. On the other hand, b_σ has its largest component in the Fe(μ-C)(μ-H)Fe plane and arises from spin density in the C 2*p* orbital parallel to the Fe-Fe vector. Compared to the value expected for an electron localized in a ^{13}C $2p$ orbital (b^0 = 90.8 MHz),[101] the values of b_σ reported here correspond to spin densities of 0.063 e^- and 0.014 e^- in the C $2p_\sigma$ orbitals of **{Fe$_2$(μ-CAr)}^{17}** and **{Fe$_2$(μ-CAr)}^{19}**, respectively, reflecting a decrease in Fe-C σ-covalency upon reduction. Likewise, the values of b_π correspond to spin densities of 0.014 e^- and 0.036 e^- in the $2p_\pi$ orbitals of **{Fe$_2$(μ-CAr)}^{17}** and **{Fe$_2$(μ-CAr)}^{19}**, respectively, indicating an increase in Fe-C π-covalency upon reduction, most likely due to enhanced backbonding. For comparison, the degree of spin transfer into the $2p_\pi$ orbitals of the terminal carbyne ligand in $[(SiP_3)Fe^{V}CCH_3]^+$ ($\varrho_\pi(^{13}C) \approx +/-0.06\ e^-$)[44] is greater than that in either **{Fe$_2$(μ-CAr)}^{17}** or **{Fe$_2$(μ-CAr)}^{19}**. The effect of redox chemistry on b_σ and b_π is in good agreement with the qualitative MO picture derived from DFT calculations (*vide infra*), which indicates that the HOMO of **{Fe$_2$(μ-CAr)}^{17}** (Fe-Fe δ*) has the appropriate symmetry to interact with one of the in-plane C $2p_\sigma$, whereas the HOMO of**{Fe$_2$(μ-CAr)}^{19}** (Fe-Fe π*) has appropriate symmetry to overlap with the out-of-plane C $2p_\pi$ orbital. Combined with $\varrho(2s)$ derived from the isotropic ^{13}C coupling in **{Fe$_2$(μ-CAr)}^{19}**, the total spin density on the bridging carbon is ≈ +/-0.060 e^-. Notably, the total carbon spin density in **{Fe$_2$(μ-CAr)}^{17}** ($\varrho(^{13}C) \approx +/-0.086\ e^-$) is ~44% larger than that in **{Fe$_2$(μ-CAr)}^{19}**, suggesting that reduction leads to an overall decrease in Fe-C covalency.

It is also instructive to compare the $2s$ and $2p(\pi)$ spin densities determined by pulse EPR studies of the isoelectronic and structurally homologous complexes **{Fe$_2$(μ-CAr)}^{17}** and $[([PhBP_3]Fe)_2(\mu\text{-}NH)(\mu\text{-}H)]$ to assess the relative degree of Fe-C and Fe-N covalencies. The isotropic ^{13}C hyperfine coupling in **{Fe$_2$(μ-CAr)}^{17}** corresponds to a carbon $2s$ spin density ($\varrho_s(^{13}C) \approx 9.3 \times 10^{-3}\ e^-$) which is ~4.6 times larger than the nitrogen $2s$ spin density in $[([PhBP_3]Fe)_2(\mu\text{-}NH)(\mu\text{-}H)]$ ($\varrho_s(^{14}N) \approx 2 \times 10^{-3}\ e^-$).[55] Likewise, analysis of the anisotropic hyperfine coupling tensor yields a carbon $2p$ spin density ($\varrho_p(^{13}C) \approx +/-0.077\ e^-$) for **{Fe$_2$(μ-**

CAr)}^{17} which is ~3.9 times larger than the nitrogen 2*p* spin density in [([PhBP$_3$]Fe)$_2$(μ-NH)(μ-H)] (ϱ_p(^{14}N) ≈ -0.02 e^-).[55] Overall, the data convincingly demonstrates that the Fe-C covalency in **{Fe$_2$(μ-CAr)}**^{17} exceeds the Fe-N covalency in [([PhBP$_3$]Fe)$_2$(μ-NH)(μ-H)]. Consistent with the higher electronegativity of nitrogen compared to carbon, the carbyne is more easily oxidized and, therefore, develops more radical character in both its *s* and *p* orbitals.

X-ray Absorption Spectroscopy Supports Metal-Centered Redox Chemistry in {Fe$_2$(μ-CAr)}$^{17\text{-}19}$ and Reflects Redox-Induced Changes in Fe-C Covalency. The magnitude of the ^{13}C hyperfine coupling in **{Fe$_2$(μ-CAr)}**^{17} and **{Fe$_2$(μ-CAr)}**^{19} is inconsistent with a significant contribution of the μ-carbyne ligand to the redox-active orbital(s). To obtain a more refined picture of the changes that occur in relative iron oxidation state within the **{Fe$_2$(μ-CAr)}**$^{17\text{-}19}$ redox series, X-ray absorption spectra (XAS) were collected at the Fe K-edge. Consistent with redox predominantly localized at the metal sites,[111] the rising edge energies shift by 0.4-0.8 eV per oxidation event, increasing from 7118.0 eV for **{Fe$_2$(μ-CAr)}**^{19} to 7118.4 eV for **{Fe$_2$(μ-CAr)}**^{18} and 7119.2 eV for **{Fe$_2$(μ-CAr)}**^{17} (Figure 11a).[112] Systematic changes are also observed in the intensity of the pre-edge, with the feature at ~ 7111 eV gaining intensity upon oxidation while the features at ~7113-7115 eV lose intensity (Figure 11a). Pre-edge transitions most commonly arise from quadrupole-allowed metal 1*s* → 3*d* transitions, which gain intensity from 3*d*/4*p* mixing in the absence of centrosymmetry.[113-114] Oxidation results in a larger number of valence holes, thereby increasing the 1*s* → 3*d* transition probability. Because X-ray absorption spectroscopy at the Fe K edge probes metal-localized transitions, the pre-edge intensities are also sensitive to changes in covalency with the ligand.[114] As the proportion of metal-character in the acceptor orbital(s) decreases, so does the transition probability.

Time-dependent DFT calculations (TPSSh/CP(PPP) on Fe) were performed to determine the origin of the pre-edge features in **{Fe$_2$(μ-CAr)}**$^{17\text{-}19}$.[115-116] The computations reproduce the experimentally observed trends in the relative pre-edge intensities, as well as the increased splitting of the features between ~7113-7115 eV (Figure 11b). The feature at ~ 7111 eV corresponds to transitions into two low-lying, iron-based orbitals of δ and π-symmetry, respectively (Figure 11c). This pair of orbitals is predicted by DFT to be the redox-active set in **{Fe$_2$(μ-CAr)}$^{17-19}$** (*vide infra*). Due to the increasing number of valence holes, the intensity of this feature increases upon oxidation.

On the other hand, the features between 7113-7115 eV exhibit mixed Fe 1*s* → 3*d*/carbyne character[117] and are split by transitions into two distinct acceptor orbitals (Figure 11c). The lower energy side of this region is dominated by transitions into a fairly covalent Fe-C σ^* orbital, whereas the higher energy region involves transitions into the π*-system of the μ-arylcarbyne.[118-119] The loss of intensity that occurs between 7113-7115 eV in the pre-edge region is consistent with an increase in iron-ligand covalency upon oxidation, identical to what was inferred based on changes in the ^{13}C hyperfine coupling in **{Fe$_2$(μ-CAr)}^{17}** and **{Fe$_2$(μ-CAr)}^{19}**. The availability of low-lying orbitals with substantial ligand character suggests that the μ-carbyne ligand may serve a dual role as an electron-donor and an electron-acceptor, thereby diffusing the effects of redox chemistry at iron.

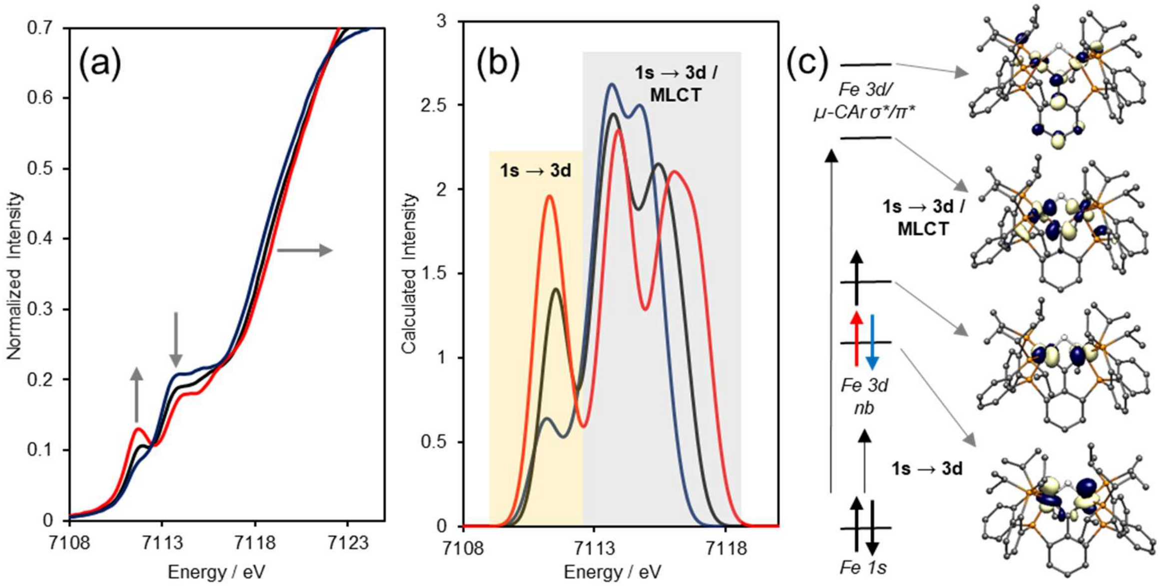

Figure 11. (a) Fe K-edge XAS spectra of [(P$_6$ArC)Fe$_2$(μ-H)][BAr$^F{}_{24}$] (**{Fe$_2$(μ-CAr)}^{17}**, red), (P$_6$ArC)Fe$_2$(μ-H) (**{Fe$_2$(μ-CAr)}^{18}**, black) and [K(THF)$_n$][(P$_6$ArC)Fe$_2$(μ-H)] (**{Fe$_2$(μ-CAr)}^{19}**, blue) with arrows indicating the trends observed upon sequential oxidation. All samples were measured as frozen solutions (2 mM in 2-MeTHF). (b) TD-DFT calculated pre-edge XAS spectra. (c) The first pre-edge feature is assigned to transitions into two Fe 3d non-bonding orbitals, rendered on the bottom right. The higher energy features arise from acceptor states with mixed Fe 3d/μ-CAr π* character. Quasi-restricted orbitals rendered at an isovalue of 0.05. The electrons in the non-bonding Fe 3*d* set are colored to denote the orbital population. The cation **{Fe$_2$(μ-CAr)}^{17}** has one electron (red) in the lower energy orbital, whereas **{Fe$_2$(μ-CAr)}^{18}** has an additional unpaired spin (black) in the higher energy orbital. Reduction to **{Fe$_2$(μ-CAr)}^{19}** places an additional electron (blue) in the lower energy orbital.

^{57}Fe Mössbauer Spectroscopy Suggests a Highly Covalent Fe-C Interaction. Similar to rising edge energies derived from Fe K-edge XAS spectra, Mössbauer isomer shifts are commonly used as an indicator of relative oxidation state.[120] Although substantial changes in isomer shift typically occur following one-electron redox changes (e.g. ~1 mm/s for high spin, six-coordinate Fe^{II} vs. ~0.4 mm/s for high spin, six-coordinate Fe^{III}),[120] the isomer shift range observed for a structurally homologous series of compounds is highly dependent on the degree of metal-

ligand covalency. Highly covalent metal-ligand interactions[78, 121] provide a mechanism to prevent the accumulation of excess charge density on the metal center by distributing it onto the ligand, mitigating the effect of redox chemistry on the isomer shift.

To assess the extent of iron-carbon covalency in **{Fe_2(μ-CAr)}$^{17\text{-}19}$**, the ^{57}Fe Mössbauer spectrum of **{Fe_2(μ-CAr)}^{17}** was measured as a frozen solution in 2-MeTHF with a 50 mT applied field (Figure 12, top). Although the signal can be simulated assuming only one subsite (δ = 0.23 mm s^{-1}, $|\Delta E_Q|$ = 0.70 mm s^{-1}, Mössbauer, Figure 12), moderately improved simulations (χ^2 = 0.63 vs. 1.24) were obtained by invoking two subsites. Two distinct models are obtained – one in which the two iron sites have different isomer shifts (Mössbauer, Figure 13) and one in which they have similar isomer shifts but distinct quadrupole splittings (Mössbauer, Figure 14). In either case, the Mössbauer signals from the individual subsites in **{Fe_2(μ-CAr)}^{17}** are largely overlapping, though a subtle shoulder may be discernable for the low velocity resonance. Overall, the model which attributes similar isomer shifts to the two iron sites comports best with the fact that **{Fe_2(μ-CAr)}^{17}** is electronically delocalized, implying that the iron centers bear similar charge density.[120]

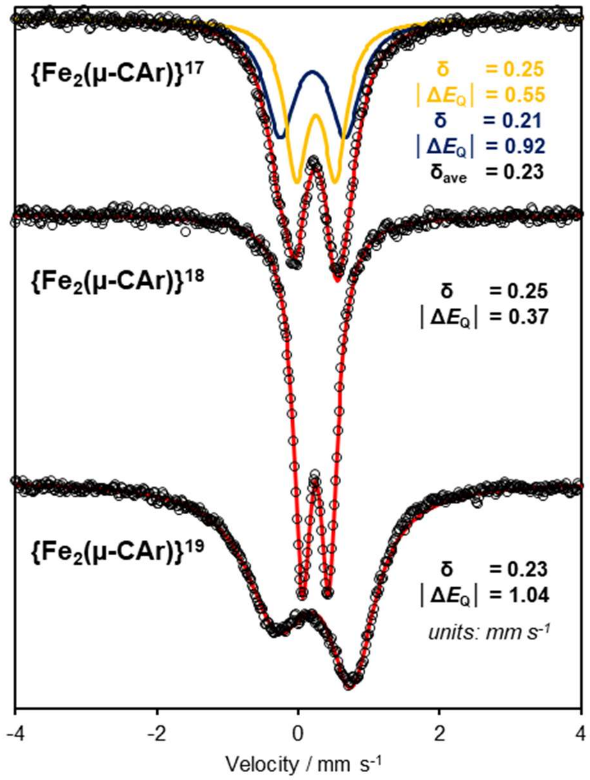

Figure 12. ^{57}Fe Mössbauer spectra of [(P$_6$ArC)Fe$_2$(μ-H)][BAr^F$_{24}$] (**{Fe$_2$(μ-CAr)}^{17}**, 24 mM in 2-MeTHF, top), (P$_6$ArC)Fe$_2$(μ-H) (**{Fe$_2$(μ-CAr)}^{18}**, microcrystalline solid, middle) and [K(THF)$_n$][(P$_6$ArC)Fe$_2$(μ-H)] (**{Fe$_2$(μ-CAr)}^{19}**, 29 mM in 2-MeTHF, bottom) collected at 80 K with a 50 mT field applied parallel to γ rays. Sum fits to the experimental spectra are shown in red, with individual subsites shown in orange and blue where relevant, with parameters included.

The reduced complex **{Fe$_2$(μ-CAr)}^{19}** was also evaluated by ^{57}Fe Mössbauer spectroscopy. At 80 K, the Mössbauer spectrum of **{Fe$_2$(μ-CAr)}^{19}** in zero applied field exhibits an asymmetric line shape and is substantially broadened (Mössbauer, Figure 15). The spectrum is significantly sharper in the presence of a weak applied field but retains the asymmetric line shape characteristic of a system in the intermediate spin relaxation regime (Figure 12, bottom). The Mössbauer data could be simulated to one asymmetrically broadened quadrupole doublet with δ = 0.23 mm s^{-1}, $|\Delta E_Q|$ = 1.04 mm s^{-1} (Figure 12).

We previously reported that **{Fe$_2$(μ-CAr)}^{18}** exhibits an isomer shift of 0.25 mm s^{-1} (Figure 12, middle),[66] which is nearly identical to those observed for **{Fe$_2$(μ-CAr)}^{17}** (δ_{ave} = 0.23 mm s^{-1}) and **{Fe$_2$(μ-CAr)}^{19}** (δ = 0.25 mm s^{-1}). The invariance of δ to one-electron redox chemistry in **{Fe$_2$(μ-CAr)}$^{17\text{-}19}$**, despite shifts in their rising edge energies, reflects a high degree of covalency within the Fe-C bonding. Effectively, the μ-carbyne can act as an electron source or sink, diffusing the effects of redox chemistry via through-bond interactions. As a rough gauge of how significant this influence is, a related series of mononuclear iron-carbonyl complexes [(SiP$_3$)Fe(CO)]$^{-1/0/+1}$ exhibit an isomer shift range that spans 0.09 – 0.31 mm s^{-1}.[78] More similar to that observed here, one electron oxidation of the formally Fe(IV)-carbyne complex [(SiP$_3$)FeCCH$_3$] is accompanied by a negligible change in isomer shift (-0.03 mm s^{-1} to 0.01 mm s^{-1}).[44] In both of these examples, an Fe-Si interaction provides an additional and significant pathway for covalent delocalization of charge, highlighting the relative importance of Fe-C covalency in **{Fe$_2$(μ-CAr)}$^{17\text{-}19}$**.

Computational Studies Support High Fe-C Covalency. A more quantitative description of the Fe-C covalency in **{Fe$_2$(μ-CAr)}$^{17\text{-}19}$** was obtained from DFT calculations. Consistent with the experimental results, geometry optimizations (TPSS/ZORA-def-2-TZVP) predict that **{Fe$_2$(μ-CAr)}^{18}** and **{Fe$_2$(μ-CAr)}^{19}** adopt a C_2-symmetric structure in which the central carbon retains a trigonal planar conformation. Comparison of the orbital contours obtained from single-point energy calculations (TPSSh/ZORA-def2-TZVPP) on the optimized geometries of **{Fe$_2$(μ-CAr)}^{18}** and **{Fe$_2$(μ-CAr)}^{19}** reveals a direct correspondence in their electronic structures. Both feature molecular orbitals that are delocalized across the Fe-(μ-C)-Fe linkage, leading to a symmetric distribution of spin density on Fe1 and Fe2 (ϱ(Fe) ~ 1.11 e^- for **{Fe$_2$(μ-CAr)}^{18}** and ϱ(Fe) ~ 0.63 e^- for **{Fe$_2$(μ-CAr)}^{19}** based on Löwdin population analysis). The computations predict that electron transfer chemistry involves two iron-localized orbitals -

one δ^* symmetry orbital derived from $3d_{x2\text{-}y2}$ and one π^* symmetry orbital of $3d_{yz}$ parentage (Figure 13). In **{Fe$_2$(μ-CAr)}^{18}**, both orbitals are singly occupied, resulting in the experimentally determined $S = 1$ ground state. Reduction of **{Fe$_2$(μ-CAr)}^{18}** occurs in the non-bonding Fe-Fe δ^* ($3d_{x2\text{-}y2}$) orbital, leaving a single unpaired α electron in the Fe-Fe π^* ($3d_{yz}$).

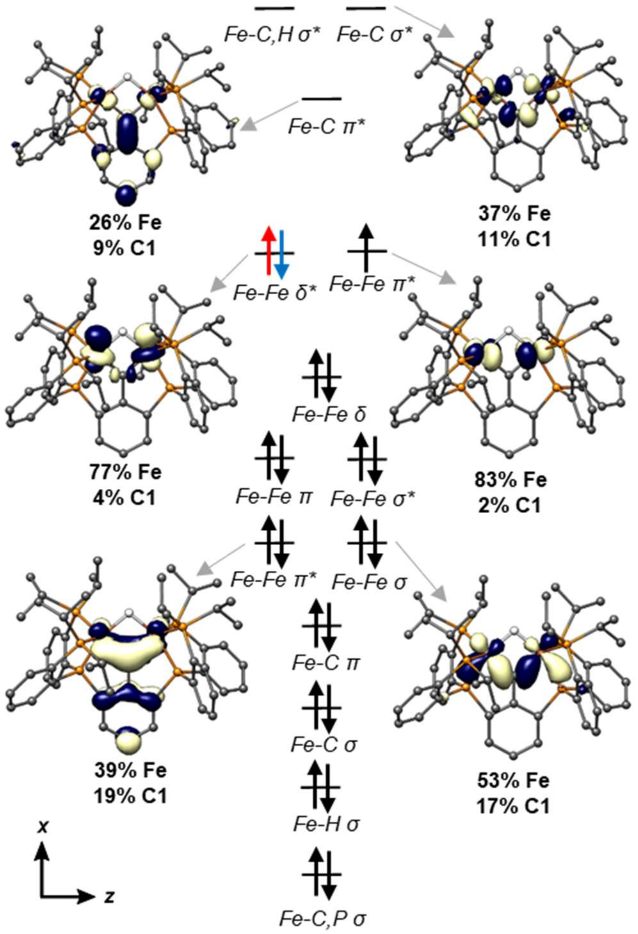

Figure 13. Qualitative molecular orbital diagram for [(P$_6$ArC)Fe$_2$(μ-H)][BAr$^F{}_{24}$] (**{Fe$_2$(μ-CAr)}^{17}**, red), (P$_6$ArC)Fe$_2$(μ-H) (**{Fe$_2$(μ-CAr)}^{18}**, black) and [K(THF)$_n$][(P$_6$ArC)Fe$_2$(μ-H)] (**{Fe$_2$(μ-CAr)}^{19}**, blue). The electrons in the non-bonding Fe 3*d* set are colored to denote the orbital population. The cation **{Fe$_2$(μ-CAr)}^{17}** has one electron (red) in the lower energy orbital, whereas **{Fe$_2$(μ-CAr)}^{18}** has an additional unpaired spin (black) in the higher energy orbital. Reduction to **{Fe$_2$(μ-CAr)}^{19}** places an additional electron (blue) in the lower energy orbital. Orbital plots (isovalue = 0.05) and population analysis are shown for key

Fe-C interactions and the redox-active orbitals in **{Fe$_2$(μ-CAr)}^{18}** by way of example. Orbitals labelled by Fe-Fe interaction indicate symmetry only and do not imply the relative significance of the bonding character.

Considering the μ-arylcarbyne in its closed-shell form would imply an Fe 3*d* electron count of 12 for **{Fe$_2$(μ-CAr)}^{18}** and 13 for **{Fe$_2$(μ-CAr)}^{19}**, corresponding to electronic structure descriptions of {Fe$^{II}_2$(μ-CAr^{3-})(μ-H$^-$)} and {Fe$^{+1.5}_2$(μ-CAr^{3-})(μ-H$^-$)}, respectively. However, Löwdin population analysis suggests that alternative resonance forms may be more appropriate. The Fe$_2$(μ-C) bonding in **{Fe$_2$(μ-CAr)}^{18}** and **{Fe$_2$(μ-CAr)}^{19}** engages a pair of non-degenerate ligand-based σ-symmetry orbitals, which are largely localized on the bridging carbon, as well as a series of π-symmetry orbitals delocalized over the μ-arylcarbyne motif. Bonding combinations with the appropriate iron-based SALCs produces two orbitals, one corresponding to an Fe-(μ-C)-Fe σ-interaction (HOMO-8) and the other an Fe-(μ-CAr)-Fe π-bond (HOMO-7), that are close in energy to the non-bonding Fe 3*d* manifold (Figure 13). Löwdin population analysis reveals that both of these orbitals exhibit substantial Fe-character (53% for HOMO-8 and 39% for HOMO-7), clearly demonstrating that the Fe-C interactions are highly covalent. As a result of this high degree of covalency, these orbitals should not be considered as predominantly ligand-based for electron counting purposes and may, in fact, be better described as part of the Fe 3*d* manifold. Including these electrons in the *d* count would result in oxidation states for of {Fe$^{I}_2$(μ-CAr$^-$)(μ-H$^-$)} or {Fe$^{0}_2$(μ-CAr$^+$)(μ-H$^-$)} for **{Fe$_2$(μ-CAr)}^{18}**. We favor the intermediate electronic structure descriptor {Fe$^{I}_2$(μ-CAr$^-$)(μ-H$^-$)}, which is most representative of both the Löwdin spin population (ϱ(Fe) ~ 1.11 e^-) and the calculated atomic charges (-1.48 on Fe and -0.14 on C1). This would imply that **{Fe$_2$(μ-CAr)}^{17}** and **{Fe$_2$(μ-CAr)}^{19}** are best represented as {Fe$^{+1.5}_2$(μ-CAr$^-$)(μ-H$^-$)} and {Fe$^{+0.5}_2$(μ-CAr$^-$)(μ-H$^-$)}, respectively.

DFT Calculations Support Valence Localization in {Fe$_2$(μ-CAr)}^{17}. Although the electronic ground state of **{Fe$_2$(μ-CAr)}^{17}** has $S = ½$, inversion recovery experiments and magnetometry studies revealed that states with $S > ½$ are energetically accessible. In accord with these findings, DFT calculations on **{Fe$_2$(μ-CAr)}^{17}** indicate that both $S = 1/2$ and $S = 3/2$ states are close in energy ($\Delta \sim$ 1-5 kcal/mol, Table S9). However, only the pure DFT functional BP86 correctly predicts an $S = ½$ ground state for **{Fe$_2$(μ-CAr)}^{17}**; all other functionals tested provide an $S = 3/2$ ground state. In general, the calculated bond metrics for both spin states compare favorably with those determined experimentally (Table S8). Notably, the $S = 1/2$ geometry reproduces the key distortions observed in the solid-state structure (Table S11), in contrast to the optimized geometry obtained for the $S = 3/2$ state of **{Fe$_2$(μ-CAr)}^{17}**, which displays C_2 symmetry. Efforts to converge to a C_2 symmetric geometry for the $S = ½$ state of **{Fe$_2$(μ-CAr)}^{17}**, either by starting from the optimized $S = 3/2$ geometry or from the solid state structure of **{Fe$_2$(μ-CAr)}^{18}**, were unsuccessful, consistent with the preference of **{Fe$_2$(μ-CAr)}^{17}** to adopt lower symmetry even in solution. Although only small perturbations in the individual bond lengths and angles are observed, even subtle geometrical changes can significantly alter metal-metal communication.[122-125]

Analysis of the electronic structures derived from single-point energy calculations on the $S = 1/2$ and $3/2$ states of **{Fe$_2$(μ-CAr)}^{17}** provide insight into the effect of structural distortion on electronic communication. As in **Fe$_2$(μ-CAr)}^{18}** and **Fe$_2$(μ-CAr)}^{19}**, the $S = 3/2$ state of **{Fe$_2$(μ-CAr)}^{17}** features molecular orbitals that are fully delocalized, leading to a symmetric distribution of spin density between the two iron centers (ϱ(Fe) ~ 1.65 e^- based on Löwdin population analysis). In contrast to the foregoing and at odds with ^{1}H ENDOR studies, spin-unrestricted DFT calculations on the $S = ½$ ground state of **{Fe$_2$(μ-CAr)}^{17}** yield a broken-symmetry solution with substantial spin contamination (Calc. $\langle S^2\rangle$: 1.57, Theory:

0.75). Analysis of the unrestricted corresponding orbitals obtained from calculations with the TPSSh functional (10% HF) reveals a single pair of magnetic orbitals with a spatial overlap significantly less than unity ($\langle\alpha|\beta\rangle = 0.52$).[126] Formally, this broken-symmetry state corresponds to antiferromagnetic coupling of an intermediate spin Fe(II) center ($S_1 = 1$) to a low spin Fe(III) ($S_2 = ½$). In light of the high degree of Fe-C covalency, an alternative description ($\{Fe^{I}Fe^{II}(\mu\text{-}CAr^{-})(\mu\text{-}H^{-})\}$) that invokes antiferromagnetic coupling to a low spin Fe(I) center ($S_2 = ½$) may be more appropriate.

IMPLICATIONS

Electronic (De)localization in Fe(μ-C)(μ-H)Fe Model Complexes. Calculations at the DFT level of theory suggest that the $S = ½$ ground state of **{Fe$_2$(μ-CAr)}^{17}** is biased toward electronic localization, whereas ^{1}H ENDOR studies clearly indicate that it is not. To understand the possible origins of this apparent discrepancy, the ratio of the delocalization energy $B(S + ½)$, where B is the double exchange parameter and is larger for delocalized systems, to the sum of the various trapping forces present in **{Fe$_2$(μ-CAr)}^{17}** must be considered.[127-128] The limited solubility of **{Fe$_2$(μ-CAr)}^{18}** as well as the thermal instability of **{Fe$_2$(μ-CAr)}^{19}** frustrated attempts to observe intervalence charge transfer transitions in the near-IR region, which could be used to directly assess the effect of redox chemistry on the magnitude of B. However, it has been shown that the magnitude of B is proportional to the Fe-Fe σ-overlap[128] and depends strongly on the Fe-Fe distance.[124] Although a solid state structure of **{Fe$_2$(μ-CAr)}^{19}** was not obtained, EXAFS studies suggest that the Fe-Fe separation in **{Fe$_2$(μ-CAr)}^{19}** is longer than that in **{Fe$_2$(μ-CAr)}^{17}**, a conclusion validated by DFT geometry optimizations. Based solely on this metric, the double exchange in **{Fe$_2$(μ-CAr)}^{17}** should be stronger, not weaker, than that in **{Fe$_2$(μ-CAr)}^{19}**. This can be verified computationally by following previously described protocols to estimate *B* by DFT methods,[129] which indicates a value of ~4400 cm^{-1} for **{Fe_2(μ-CAr)}^{17}** compared to only 1400 cm^{-1} for **{Fe_2(μ-CAr)}^{19}**, which is ~ 3-fold smaller. Although ligation differences may lead to non-linear trends in *B* vs. $r_{Fe\text{-}Fe}$, the magnitude of the double exchange interactions in **{Fe_2(μ-CAr)}^{17}** and **{Fe_2(μ-CAr)}^{19}** predicted by DFT are likely upper bounds for the true values based on comparison with the literature ($[Fe_2(\mu\text{-}OH)_3(Me_3TACN)_2]^{2+}$: $r_{Fe\text{-}Fe}$ = 2.51 Å, *B* = 1350 cm^{-1}; $[2Fe\text{-}2S]^+$: $r_{Fe\text{-}Fe}$ ~ 2.73 Å, *B* = 700-965 cm^{-1}).[124, 128] Notwithstanding, this analysis demonstrates that, if anything, the intrinsic delocalization energy is larger for **{Fe_2(μ-CAr)}^{17}** compared to **{Fe_2(μ-CAr)}^{19}**.

However, the sum of the dynamic and static contributions to the total trapping energy may be larger in **{Fe_2(μ-CAr)}^{17}** compared to **{Fe_2(μ-CAr)}^{19}**. Even in the absence of chemical asymmetry, electronic localization can be induced by a vibronic coupling mechanism, which involves coupling of electron and nuclear motion along a vibrational coordinate described as an antisymmetric combination of the local, metal-ligand breathing modes (*i.e.* as the coordination sphere of one metal relaxes, the other contracts).[128] The energy associated with this term ($\Delta E_{vib} = \lambda^2/k = 4\pi^2c^2\mu\upsilon^2 n(\Delta r)^2$ where μ is the reduced mass and *n* is the coordination number)[130] depends on the change in metal-ligand bond lengths induced by electron transfer (Δr) and the vibrational frequency (υ). If we assume, albeit crudely, that the effect per redox event on the vibrational frequency is similar to that reported for [2Fe-2S] clusters ($\upsilon_{ox}^2/\upsilon_{red}^2$ ~ 1.11-1.17),[131-132] we can estimate that the vibronic trapping energy of **{Fe_2(μ-CAr)}^{17}** is ~1.4 times (= $(\upsilon_{ox}^2/\upsilon_{red}^2)^2$) greater than that in **{Fe_2(μ-CAr)}^{19}**, which does not compensate for the increase in *B* predicted upon 2 e^- reduction.

Although geometry optimizations suggest that the iron sites of **{Fe_2(μ-CAr)}^{19}** are chemically equivalent, the same is not true of **{Fe_2(μ-CAr)}^{17}**. Consistent with DFT calculations, ^{1}H NMR studies suggest that **{Fe$_2$(μ-CAr)}^{17}** adopts a low symmetry solution phase structure which resembles that observed in the solid state. Comparison of the metric parameters about Fe1 and Fe2 in **{Fe$_2$(μ-CAr)}^{17}** reveals subtle differences in the Fe-P bond lengths (Table 2). These static contributions to the total trapping energy would reinforce the vibronic trapping effect in **{Fe$_2$(μ-CAr)}^{17}** and could promote valence localization, as predicted by DFT. However, analysis of the experimental ^{1}H hyperfine coupling clearly indicates that **{Fe$_2$(μ-CAr)}^{17}** is valence delocalized, suggesting that DFT may not adequately describe the electronic structure of **{Fe$_2$(μ-CAr)}^{17}**. Alternatively, the ground state of **{Fe$_2$(μ-CAr)}^{17}** *may be* localized, but at the temperature of the pulse EPR measurements (20 K), the barrier to electron hopping may be low enough that it *appears* delocalized on the EPR timescale.

Implications for Hydride-Bound Intermediates of FeMoco. A putative intermediate (E$_4$(4H)) in the reduction of N$_2$ by FeMoco has been freeze-trapped and characterized by EPR spectroscopy.[35] Cryoannealing experiments led the Hoffman and coworkers to conclude that this species has accumulated four reducing equivalents relative to the E$_0$ state of FeMoco.[32] Detailed ^{1}H ENDOR studies revealed the presence of two strongly coupled protons (a_{iso} ~ 22.3-24.3 MHz), which were assigned to two bridging hydrides based on the rhombic symmetry of their dipolar coupling tensor (ρ ~ 0.72-1).[33-34] More recently, the electronic structure of this intermediate was revisited using high-resolution ENDOR measurements in combination with quantum mechanical calculations.[34] This study revealed that although their hyperfine tensors are nearly coaxial, the symmetry of the dipolar coupling to each hydride is distinct, with a "null" component along g_2 for H1 (T(H1) = [-13.2, 0, +13.2]) compared to a zero-value along g_3 for H2 (T(H2) = [13.2, -13.2, 0]). Based on a point-dipole model for the through-space coupling of each μ-hydride to its anchor atoms, Hoffman and coworkers concluded that this permutation of the principal values of $T(^1$H) for H1 vs. H2 indicates that they bridge iron centers with distinct spin-coupling arrangements. Hoffman and coworkers suggest that H2 must bridge two metal atoms whose spins are ferromagnetically aligned (t_1, $t_2 > 0$) in order for $T(^1H)$ to have a vanishing element in the $Fe_2(\mu\text{-}H)$ plane (for $T_c = -(T_a + T_b) \sim 0$, T_a must be $\sim -T_b$). On the other hand, the "null" component of $T(H1)$ is believed to be normal to the $Fe_2(\mu\text{-}H)$ plane ($T_a = -\frac{1}{2}(t_1 + t_2)$), which requires that $t_1 \sim -t_2$ and, thus, H1 bridges two metal centers that are antiferromagnetically coupled.

Previous ^1H ENDOR studies on two distinct diiron μ-hydride model complexes seem to support the foregoing conclusions. Detailed analysis of the dipolar coupling to μ-hydride in $[([PhBP_3]Fe)_2(\mu\text{-}NH)(\mu\text{-}H)]$ mapped $T(^1H) = [19.4, -17.4, -2.0]$ MHz onto the molecular frame, with g_3 in the Fe(μ-N)(μ-H)Fe plane ($T_c = T_3 \sim 0$).[55] Likewise, studies of an $[(N_2)Fe^{1.5}(\mu\text{-}H)_2Fe^{1.5}(N_2)]^-$ complex oriented the "null" of component of $T(^1H) = [-21, 24, -3]$ MHz along the Fe-Fe axis.[54] Consistent with the predictions above, both complexes are formulated as fully delocalized Class III dimers and, thus, $K_1 = K_2 = +1/2$ and $t_1 = t_2 > 0$.[55, 133] As discussed herein, the same is true of **$\{Fe_2(\mu\text{-}CAr)\}^{17}$** and **$\{Fe_2(\mu\text{-}CAr)\}^{19}$** and, indeed, analysis of the anisotropic ^1H hyperfine coupling revealed that the vanishing element corresponds to T_c in the Fe(μ-C)(μ-H)Fe plane.

Until the present study, the effect of electronic localization on the symmetry of $T(^1H)$ associated with the $Fe_2(\mu\text{-}H)$ motif had not been discussed. Only one valence localized diiron μ-hydride complex is known in the literature, but pulse EPR studies have not been reported.[52] In contrast to the electronically delocalized species discussed above, a valence localized $Fe_2(\mu\text{-}H)$ dimer would have an asymmetric distribution of α and β spin density. As a result, the spin projection factors K_1 and K_2 (and, thus, t_1 and t_2) would have opposite signs and unequal magnitudes. Following the analysis of Hoffman and coworkers for the dihydride state of

FeMoco,[34] we would expect *a priori* that such a species would exhibit a "null" component normal to the $Fe_2(\mu\text{-H})$ plane ($T_a \sim 0$). However, it can be demonstrated, even if **{Fe₂(μ-CAr)}[17]** was electronically localized and antiferromagnetically coupled, T_a would *not* adopt a zero-value – in fact, none of the principal components of $T(^1H)$ would be zero. Rather, the signature of valence localization in **{Fe₂(μ-CAr)}[17]** is predicted to be $|T_b| >> |T_a|$, with $T_c \neq 0$.

To gain better physical understanding of why this is true, the effects of spin coupling must be considered carefully. Assuming local spins of $S_1 = 1$ and $S_2 = ½$, standard vector coupling methods[134-135] provide spin projection coefficients of $K_1 = 4/3$ and $K_2 = -1/3$, respectively, for a $S_T = ½$ state of **{Fe₂(μ-CAr)}[17]**. If the two Fe-H bond lengths are roughly equivalent ($r_1 \sim r_2$), the magnitude of the dipolar coupling to $S_1 = 1$ is four-fold larger than that from $S_2 = ½$ ($t_1 = -4t_2$, because $t_i \propto K_i$ from equation 5). In order to achieve exact cancellation of the through-space coupling normal to the $Fe_2(\mu\text{-H})$ plane ($T_a = -½(t_1 + t_2) \sim 0$ when $t_1 \sim -t_2$), the distance of the μ-hydride to the iron bearing the minority spin ($S_2 = ½$) must be ~1.6-fold smaller ($|K_1/K_2| = (r_1/r_2)^3 = 4$), which is not physically reasonable. A similar conclusion can be reached if instead the local spin states are $S_1 = 5/2$ (high spin Fe(III), $K_1 = +7/3$) and $S_2 = 2$ (high spin Fe(II), $K_2 = -4/3$), though the difference in the individual bond lengths necessary to achieve $T_a \sim 0$ is smaller ($|K_1/K_2| = (r_1/r_2)^3 = 7/4$; $r_1 \sim 1.2r_2$) but still substantial. It is important to note that the conclusion $T_a \neq 0$ for valence localized systems is valid for all values of γ because T_a has no angular dependence.

Simultaneously, the presence of two ions with spin projection factors of unequal magnitude leads to a ^1H dipolar coupling tensor with $|T_b| >> |T_a|$. Unlike the component of the anisotropic hyperfine normal to $Fe_2(\mu\text{-H})$ plane (T_a), the in-plane component T_b is very sensitive to the value of γ, which is determined from the ratio of t_2/t_1 and the angles β_1 and β_2. For a symmetrically-bridged, valence-delocalized $Fe_2(\mu\text{-}H)$ dimer, $\gamma \equiv 0$ because $t_1 = t_2$ (see equation 4). However, when $t_1 \neq t_2$, $\gamma \neq 0$, and a factor of $(\cos 2\gamma)^{-1}$ must be included in the calculation of T_b. The value of γ obtained by assuming a valence localized assignment for **$\{Fe_2(\mu\text{-}CAr)\}$**^{17} is such that $(\cos 2\gamma)^{-1}$ contributes a factor of 5 to the calculation of T_b, leading to $|T_b| >> |T_a|$. The relation $|T_b| >> |T_a|$ is also true if the local spin states are $S_1 = 5/2$ (high spin Fe(III), $K_1 = +7/3$) and $S_2 = 2$ (high spin Fe(II), $K_2 = -4/3$). In fact, in this case, the value of γ is such that the factor $(\cos 2\gamma)^{-1}$ in the calculation of T_b is ~13.

The possibility of making inferences regarding the distribution of electron density in reduced states of FeMoco is intriguing[13] since, thus far, direct information in this regard is available only for the resting state.[8] Consistent with the study by Hoffman and coworkers,[34] we show here that the orientation and symmetry of $T(^1H)$ for a bridging hydride ligand can provide valuable information about the electronic structure of the anchoring metal atoms. As concluded by Hoffman and coworkers,[34] exact cancellation of the out-of-plane element T_a does in fact demonstrate that the two anchor metal atoms are antiferromagnetically coupled. However, while this might be true of isovalent ions, our studies and analysis indicate that an antiferromagnetically coupled *mixed valent* pair will not exhibit this same symmetry. Given that $T_a = 0$ for the hydride denoted H1 in the $E_4(4H)$ state of FeMoco, it is *most likely* that H1 bridges a pair of Fe(III) metal centers ($K_1 = K_2$ so $t_1 \sim -t_2$).

On the other hand, the presence of a vanishing element of $T(^1H)$ oriented within the $Fe_2(\mu\text{-}H)$ plane ($T_c \sim 0$) indicates that the metal centers are ferromagnetically-aligned spins, either in the same oxidation state or as a delocalized pair. The symmetry of $T(H2) = [13.2, -13.2, 0]$ ($T_c = 0$) alone does not distinguish between these two cases for the electronic structure of the iron centers that bind H2 in the E_4(4H) state of FeMoco. Rather, as emphasized by Hoffman and coworkers, it is the fact that the principal components of T(H1) and T(H2) have identical magnitudes, though permuted, which suggests that the Fe_2(μ-H1) and Fe_2(μ-H2) motifs differ only in their spin coupling arrangement. Thus, it is likely that H2 also bridges two Fe(III) ions, only these are ferromagnetically aligned, in contrast to those which bind H1.

Insight into the Electronic Structure and Reactivity of FeMoco from ^{13}C Pulse EPR. Fundamental to elucidating the role of the interstitial carbide is an understanding of the nature of the Fe-C bonding and how this bonding may change during the catalytic cycle. Empirical force field simulations of nuclear resonance vibrational spectroscopic (NRVS) data for FeMoco yielded Fe-C force constants which were an order of magnitude smaller than those for low spin iron-carbide-carbonyl clusters.[136] Reduction and/or substrate binding to FeMoco may induce further weakening and elongation of the Fe-C bond(s).[137-139] This has been demonstrated for some monometallic iron-alkyl model complexes and has been attributed to the ionic character of the bond, which becomes more polarized upon reduction.[140-141] Notably, enhanced N_2 reduction reactivity was observed for systems featuring more flexible axial donors.[140] However, more recent QM/MM studies accounting for the effects of antiferromagnetic coupling within the cluster afforded Fe-C force constants roughly five times larger than suggested from computational modelling of NRVS data.[142] Further support of more highly covalent bonding to the interstitial carbide was obtained by XES studies, which revealed a decrease in the splitting of the Fe Kβ mainlines of FeMoco and FeVco compared to that in $MoFe_3S_4$ and VFe_3S_4 cubane models.[143]

The lack of a consistent description of the Fe-C bonding in FeMoco motivates complementary studies aimed at benchmarking Fe-C covalency. In principle, ligand superhyperfine couplings can provide a direct and comparable measure of metal-ligand interactions.[99, 144-146] However, theoretical studies of FeMoco revealed a significant dependence of $a_{\text{iso}}(\mu_6\text{-X})$ (assumed at that time to be N^{3-}, but equally valid for C^{4-}) on the specific spin coupling arrangement of the cofactor.[147] The lowest energy BS7 solution has a symmetric distribution of "spin-up" and "spin-down" density around the central atom, which results in a small isotropic coupling. As a result, the relative degree of Fe-C covalency in FeMoco cannot be assessed based on a comparison with the a_{iso} or $\varrho(^{13}\text{C})$ values reported here.

The present ^{13}C pulse EPR and XAS studies support the hypothesis that electron loading leads to a decrease in Fe-C covalency, at least in a $\text{Fe}_2(\mu\text{-C})$ model system. Quantitative analysis of the carbon $2s$ and $2p$ spin densities of **$\{\text{Fe}_2(\mu\text{-CAr})\}^{17}$** ($\varrho(^{13}\text{C}) \approx +/-0.086\ e^-$) and **$\{\text{Fe}_2(\mu\text{-CAr})\}^{19}$** ($\varrho(^{13}\text{C}) \approx +/-0.060\ e^-$) suggests that 2 e^- reduction leads to a ~44% decrease in Fe-C covalency. This value is in good agreement with the predicted change in the calculated covalency[148] of C1, which decreases from 31.7% in **$\{\text{Fe}_2(\mu\text{-CAr})\}^{17}$** to 15.6% in **$\{\text{Fe}_2(\mu\text{-CAr})\}^{19}$** based on DFT. Deconvolution of the anisotropic component of the ^{13}C hyperfine coupling in **$\{\text{Fe}_2(\mu\text{-CAr})\}^{17}$** and **$\{\text{Fe}_2(\mu\text{-CAr})\}^{19}$** revealed that redox chemistry disparately affects the Fe-C σ- and π-bonding, with a significant decrease in σ-covalency and a less substantial increase in π-covalency upon reduction. These changes can be rationalized in terms of the qualitative MO diagram shown in Figure 13 based on the symmetry of the HOMO's of **$\{\text{Fe}_2(\mu\text{-CAr})\}^{17}$** (Fe-Fe δ*) and **$\{\text{Fe}_2(\mu\text{-CAr})\}^{19}$** (Fe-Fe π*), which overlap best with the C $2p_\sigma$ and $2p_\pi$ orbitals of the carbyne, respectively. Notably, these changes in Fe-C covalency occur despite the fact that redox chemistry involves metal-localized orbitals. A similar observation has been made for some [Fe-S] clusters (13-16% decrease in Fe-S covalency upon 1e^- reduction) and has been attributed to electronic relaxation that accompanies the redox process.[148] Even in the absence of significant structural differences, changes in the electron-electron repulsion induced by metal-based redox chemistry can trigger a redistribution of the charge density to the ligands via changes in covalency. This model of electronic relaxation via changes in Fe-C covalency is clearly in accord with our ^{57}Fe Mossbauer studies, which revealed that **{Fe$_2$(μ-CAr)}$^{17-19}$** have nearly identical (average) isomer shifts. The interstitial carbide of FeMoco may also serve as a source or sink of electron density by modulating the degree of Fe-C covalency, helping to prevent the accumulation of excess charge density at iron and facilitating multi-electron transformations.

CONCLUSIONS

The diiron μ-carbyne complexes **{Fe$_2$(μ-CAr)}^{17}** and **{Fe$_2$(μ-CAr)}^{19}** are the first carbon-bridged, dinuclear iron complexes that feature odd numbers of valence electrons. Although both species populate S = ½ states at low temperature, spectroscopic studies reveal that both are valence delocalized. Computational estimates of the double exchange parameter B suggest that geometrical distortions observed only in **{Fe$_2$(μ-CAr)}^{17}** are largely responsible for this electronic localization. Both **{Fe$_2$(μ-CAr)}^{17}** and **{Fe$_2$(μ-CAr)}^{19}** were amenable to investigation by pulse EPR methods, affording a unique opportunity to assess the influence of valence (de)localization on the spectroscopic signature of the μ-hydride ligand. Caution must be exercised when interpreting the orientation and symmetry of T(^{1}H) for a bridging hydride in terms of the spin-coupling of the anchoring metal atoms. However, combined with a study by Hoffman and coworkers,[34] our results suggest that the hydride ligands in the {Fe$_2$(μ-H)}$_2$ intermediate E$_4$(4H) bridge isovalent (most probably Fe^{III}) metal centers, providing valuable insight into the distribution of electron density in a reduced state of FeMoco.

Although DFT calculations indicate that electron transfer involves metal-localized orbitals, ^{13}C pulse EPR investigations of **{Fe$_2$(μ-CAr)}^{17}** and **{Fe$_2$(μ-CAr)}^{19}** revealed that redox chemistry induces significant changes in Fe-C covalency (-21% upon 2 e^- reduction), a conclusion further supported by X-ray absorption spectroscopy, ^{57}Fe Mössbauer studies, and computational studies. Although the relative degree of Fe-C covalency in FeMoco cannot be directly assessed based on a comparison with the a_{iso} or $\varrho(^{13}C)$ values reported here, computational studies suggest that ^{13}C hyperfine interaction may still be a valuable reporter of structural and/or electronic deformations that reduce the symmetry of the cofactor.[137] Although use of ^{13}C-S-adenosylmethionine allows the biosynthesis of FeMoco with the interstitial carbide selectively labelled with ^{13}C, there is currently only one report of ^{13}C ESEEM targeting the central atom, specifically for the $S = 3/2$ resting state of FeMoco.[1] Further studies of the ^{13}C-labelled cofactor are expected to be informative, since pulse EPR methods have proven insightful for understanding the structural and electronic features of the cofactor in a variety of states.[28-30] These efforts, in concert with theoretical and synthetic modelling of the structural and spectroscopic features of FeMoco, may help to better elucidate the nature of the activation process.

EXPERIMENTAL DETAILS

General Considerations. All reactions were performed at room temperature in a nitrogen filled M. Braun glovebox or using standard Schlenk techniques unless otherwise specified. Glassware was oven dried at 140°C for at least two hours prior to use, and allowed to cool under vacuum. Complex $(P_6ArC)Fe_2H$ was prepared as previously described.[66] All other reagents were obtained commercially unless otherwise noted and typically stored over activated 4 Å molecular sieves. Tetrahydrofuran, toluene-d_8, and benzene-d_6 were dried using sodium/benzophenone ketyl, degassed with three freeze-pump-thaw cycles, vacuum transferred, and stored over 3 Å molecular sieves prior to use. Diethyl ether, benzene, toluene, acetonitrile, hexanes, and pentane were dried by sparging with nitrogen for at least 15 minutes, then passing through a column of activated A2 alumina under positive nitrogen pressure. ^{1}H and ^{31}P NMR spectra were recorded on a Varian 300 or 400 MHz spectrometer. All chemical shifts (δ) are reported in ppm, and coupling constants (*J*) are in hertz. The ^{1}H-NMR spectra were referenced using residual H impurity in the deuterated solvent. UV-Vis spectra were recorded on a Varian Cary Bio 50 spectrophotometer. Elemental analyses were performed at Caltech.

Physical Methods

Mössbauer Measurements. Zero field ^{57}Fe Mössbauer spectra were recorded in constant acceleration on a spectrometer from See Co (Edina, MN) equipped with an SVT-400 cryostat (Janis, Wilmington, WA). The quoted isomer shifts are relative to the centroid of the spectrum of α-Fe foil at room temperature. Samples were prepared in 2-MeTHF and transferred to a Delrin cup. The data were fitted to Lorentzian lineshapes using the program WMOSS (www.wmoss.org).

Magnetic Measurements. Magnetic measurements for $\{Fe_2(\mu\text{-CAr})\}^{17}$ were conducted with a Quantum Design MPMS3 SQUID Magnetometer at the University of California, Los Angeles. A polycrystalline sample of $\{Fe_2(\mu\text{-CAr})\}^{17}$ was measured in a gelatin capsule and mounted in a plastic straw. Magnetization data at 100 K from 0 to 4 T were collected to confirm the absence of ferromagnetic impurities. Direct current variable temperature magnetic susceptibility measurements were collected between 3 and 300 K with a 0.5 T field. Magnetic susceptibility data was corrected for diamagnetism of the sample, estimated using Pascal's constants. Magnetic susceptibility data was simulated with PHI.[149]

X-ray Crystallography. For compounds $\{Fe_2(\mu\text{-CAr})\}^{17}$, low-temperature (100 K) diffraction data (φ-and ω-scans) were collected on a Bruker AXS D8 VENTURE KAPPA diffractometer coupled to a PHOTON 100 CMOS detector with Mo Kα radiation (λ = 0.71073 Å) or with Cu Kα (λ = 1.54178 Å). All diffractometer manipulations, including data collection, integration, and scaling were carried out using the Bruker APEXII software.[150] Absorption corrections were applied using SADABS.[151] Structures were solved by direct methods using SHELXS[152] and refined against *F*2 on all data by full-matrix least squares with SHELXL-2014[153] interfaced with Olex2-1.2.8[154] and using established refinement techniques. All non-hydrogen atoms were refined anisotropically, except heavily disordered solvent in some cases. Hydrogen atoms were included into the model at geometrically calculated positions and refined using a riding model, except for the hydride ligands in $\{Fe_2(\mu\text{-CAr})\}^{17}$. The isotropic displacement parameters of all hydrogen atoms were fixed to 1.2 times the *U* value of the atoms they are linked to (1.5 times for methyl groups).

EPR. Continuous wave (CW) X-band EPR spectra were obtained on a Bruker EMX spectrometer. Cryogenic temperatures were achieved using an Oxford Instruments ESR-900 liquid helium flow cryostat and an ITC-503 temperature controller. Pulse EPR spectroscopy: All pulse Q-band (34 GHz) EPR, electron nuclear double resonance (ENDOR) and hyperfine sublevel correlation spectroscopy (HYSCORE) experiments were acquired using a Bruker ELEXSYS E580 pulse EPR spectrometer equipped a Bruker D-2 Q-band ENDOR resonator. Temperature control was achieved using an ER 4118HV-CF5-L Flexline Cryogen-Free VT cryostat manufactured by ColdEdge equipped with an Oxford Instruments Mercury ITC temperature controller.

Q-band pulse electron spin-echo detected EPR (ESE-EPR) field-swept spectra were acquired using the 2-pulse “Hahn-echo” sequence ($\boldsymbol{\pi/2}$ – $\boldsymbol{\tau}$ – $\boldsymbol{\pi}$ – echo).

Q-band inversion recovery data were acquired using the 3-pulse inversion recovery sequence sequence ($\boldsymbol{\pi - T - \pi/2}$ – $\boldsymbol{\tau}$ – $\boldsymbol{\pi}$ – echo), where T is varied and $\boldsymbol{\tau}$ is a fixed delay.

Q-band pulse ENDOR spectra were acquired using the Davies pulse sequence ($\boldsymbol{\pi - T_{RF} - \pi_{RF} - t_{RF} - \pi/2}$ – $\boldsymbol{\tau}$ – $\boldsymbol{\pi}$ – echo), where $\boldsymbol{T_{RF}}$ is the delay between mw pulses and RF pulses,

$\boldsymbol{\pi_{RF}}$ is the length of the RF pulse, and the RF frequency is randomly sampled during each pulse sequence. For all ENDOR scans, the same $\boldsymbol{t_{RF}}$ of 1 μs was used, all other acquisition parameters are detailed in the caption for each ENDOR figure.

Q-band HYSCORE spectra were acquired using the 4-pulse sequence ($\boldsymbol{\pi/2 - \tau - \pi/2 - t_1 - \pi - t_2 - \pi/2}$ – echo), where $\boldsymbol{\tau}$ is a fixed delay, while $\boldsymbol{t_1}$ and $\boldsymbol{t_2}$ are independently incremented by $\Delta\boldsymbol{t_1}$ and $\Delta\boldsymbol{t_2}$, respectively. The time domain data was baseline-corrected (third-order polynomial) to eliminate the exponential decay in the echo intensity, apodized with a Hamming window function, zero-filled to eight-fold points, and fast Fourier-transformed to yield the 2-dimensional frequency domain. For ^{2}H-^{1}H and ^{13}C-^{12}C difference spectra, the time domain of the HYSCORE spectrum of the natural abundance sample was subtracted from that of the isotopically-enriched sample, and the same data processing procedure detailed above was used to generate the frequency spectrum.

In general, the ENDOR spectrum for a given nucleus with spin $\boldsymbol{I}= 1/2$ (^{1}H) coupled to the S = ½ electron spin exhibits a doublet at frequencies

$$\boldsymbol{\nu_{\pm} = \left|\frac{A}{2} \pm \nu_N\right|} \tag{E1}$$

Where $\boldsymbol{\nu_N}$ is the nuclear Larmor frequency and $\boldsymbol{A}$ is the hyperfine coupling. For nuclei with $\boldsymbol{I \geq 1}$ (^{14}N, ^{2}H), an additional splitting of the $\boldsymbol{\nu_{\pm}}$ manifolds is produced by the nuclear quadrupole interaction (P)

$$\boldsymbol{\nu_{\pm,m_I} = \left|\nu_N \pm \frac{3P(2m_I - 1)}{2}\right|} \tag{E2}$$

In HYSCORE spectra, these signals manifest as cross-peaks or ridges in the 2-D frequency spectrum which are generally symmetric about the diagonal of a given quadrant. This technique allows hyperfine levels corresponding to the same electron-nuclear submanifold to be differentiated, as well as separating features from hyperfine couplings in the weak-coupling regime ($|\boldsymbol{A}| < \boldsymbol{2}|\boldsymbol{\nu_I}|$) in the (+,-) quadrant from those in the strong coupling regime ($|\boldsymbol{A}| > \boldsymbol{2}|\boldsymbol{\nu_I}|$) in the (-,-) quadrant. The (-,-) and (+,-) quadrants of these frequency spectra are symmetric to the (+,+) and (-,+) quadrants, thus only two of the quadrants are typically displayed in literature. For systems with appreciable hyperfine anisotropy in frozen solutions or solids, HYSCORE spectra typically do not exhibit sharp cross peaks, but show ridges that represent the sum of cross peaks from selected orientations at the magnetic field position at which the spectrum is collected. The length and curvature of these correlation ridges allow for the separation and estimation of the magnitude of the isotropic and dipolar components of the hyperfine tensor, as shown in Figure S1.

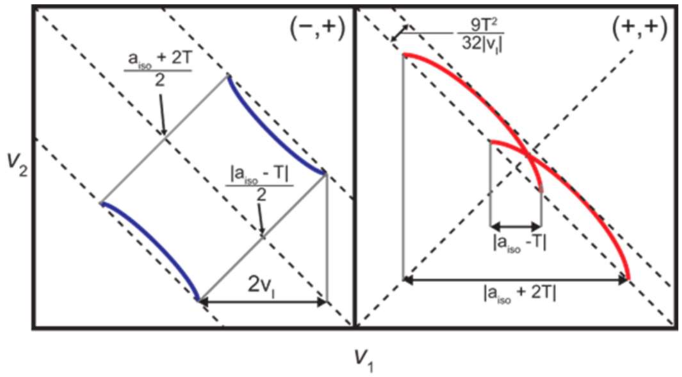

Figure S1. HYSCORE powder patterns for an $S = 1/2$, $I = 1/2$ spin system with an axial hyperfine tensor which contains isotropic ($\boldsymbol{a_{iso}}$) and dipolar ($\boldsymbol{T}$) contributions. Blue correlation ridges represent the strong coupling case; red correlation ridges represent the weak coupling case.

For weakly-coupled nuclei ($\boldsymbol{A < 2\nu_I}$), $\boldsymbol{\nu_\alpha}$ and $\boldsymbol{\nu_\beta}$ are both positive, appearing in the (+,+) quadrant, while for strongly-coupled nuclei, they will show up in the (−,+) quadrant. In the intermediate coupling regime where $\boldsymbol{A \approx 2\nu_I}$, peaks will often appear in both the (+,+) and (−,+) quadrants of the HYSCORE spectrum.

All EPR spectra (CW, ENDOR, HYSCORE) were simulated using the EasySpin[155] simulation toolbox (version 5.2.25) with Matlab 2019a using the following Hamiltonian:

$$\boldsymbol{\hat{H} = \mu_B \vec{B}_0 g \hat{S} + \mu_N g_N \vec{B}_0 \hat{I} + h\hat{S} \cdot A \cdot \hat{I} + h\hat{I} \cdot P \cdot \hat{I}} \tag{E3}$$

In this expression, the first term corresponds to the electron Zeeman interaction term where $\boldsymbol{\mu_B}$ is the Bohr magneton, g is the electron spin g-value matrix with principle components g = [g_{xx}, g_{yy}, g_{zz}], and $\boldsymbol{\hat{S}}$ is the electron spin operator; the second term corresponds to the nuclear Zeeman interaction term where $\boldsymbol{\mu_N}$ is the nuclear magneton, $\boldsymbol{g_N}$ is the characteristic nuclear g-value for each nucleus (e.g. ^{1}H,^{2}H,^{31}P), and $\boldsymbol{\hat{I}}$ is the nuclear spin operator; the third term corresponds to the electron-nuclear hyperfine term, where $\boldsymbol{A}$ is the hyperfine coupling tensor with principle components $\boldsymbol{A}$ = [A_{xx} A_{yy} A_{zz}]; and for nuclei with $\boldsymbol{I \geq 1}$, the final term corresponds to the nuclear quadrupole (NQI) term which arises from the interaction of the nuclear quadrupole moment with the local electric field gradient (efg) at the nucleus, where $\boldsymbol{P}$ is the quadrupole coupling tensor. In the principle axis system (PAS), $\boldsymbol{P}$ is traceless and parametrized by the quadrupole coupling constant $\boldsymbol{e^2Qq/h}$ and the asymmetry parameter $\boldsymbol{\eta}$ such that:

$$\boldsymbol{P = \begin{pmatrix} P_{xx} & 0 & 0 \\ 0 & P_{yy} & 0 \\ 0 & 0 & P_{zz} \end{pmatrix} = \frac{e^2Qq/h}{4I(2I-1)} \begin{pmatrix} -(1-\eta) & 0 & 0 \\ 0 & -(1+\eta) & 0 \\ 0 & 0 & 2 \end{pmatrix}} \tag{E4}$$

Where $\frac{e^2Qq}{h} = 2I(2I-1)P_{zz}$ and $\eta = \frac{P_{xx}-P_{yy}}{P_{zz}}$. The asymmetry parameter may have values between 0 and 1, with 0 corresponding to an electric field gradient with axial symmetry and 1 corresponding to a fully rhombic efg.

The orientations between the hyperfine and NQI tensor principle axis systems and the g-matrix reference frame are defined by the Euler angles (α, β, γ), with rotations performed within the zyz convention where α rotates xyz counterclockwise about z-axis to give x'y'z', β rotates x'y'z counterclockwise about y'-axis to give x",y",z", γ rotates xyz counterclockwise about z"-axis to give final frame orientation.

XAS/EXAFS. Data was collected at Stanford Synchrotron Radiation Lightsource, beamline 4-1, at SLAC National Accelerator Laboratory. The electron energy was 3.0 GeV and the average current was 500 mA. Beam intensity was monitored using nitrogen-filled ion chambers located before (I_0) and after (I_1, I_2) the sample. Sample was placed in an Oxford instruments, continuous flow liquid He cryostat maintained at 10 K. Samples were filled in 40-μL Lucite sample holders. The beam size (slit size) was 1 mm (v) and 12 mm (h). The X-ray was monochromatized by a Si(220) double-crystal monochromator. Data was collected as fluorescence excitation spectra using a 30-element Ge Solid state detector (Canberra). A Fe foil between I_1 and I_2 was used for calibration using a K-edge location of (7,112.0 eV).

Data reduction of XAS spectra was done with SamView (SixPack software available at https://www.sams-xrays.com/sixpack). Athena from the Demeter software package (Demeter version 0.9.26, B. Ravel) was used for merging, background subtraction (post and pre-edge) and normalization. A five-domain cubic spline was used to remove low-frequency background in k-space. Fitting for EXAFS data was done with Artemis from the Demeter software package using *ab initio* phases and amplitudes calculated with FEFF6 from crystal structure data.

During EXAFS curve fitting, the range was set to 3-12 Å^{-1} in k-space. The coordination number (N) and passive electron reduction factor ($S_0^2 = 0.85$) were held constant, while bond distances between the absorber and backscatterer (R) and mean square displacement of the bond distance (σ^2) were varied. The non-structural parameter E_0 (the zero-value energy of the photoelectron wave vector k) was a global variable across all pathways. The Fe-P pathways were merged for $\{Fe_2(\mu\text{-}CAr)\}^{18}$ and $\{Fe_2(\mu\text{-}CAr)\}^{17}$. For $\{Fe_2(\mu\text{-}CAr)\}^{19}$, the σ^2 variables were linked for the two Fe-P pathways, while the variable R was kept independent. This was done to highlight that there is no difference in Fe-P distance in the previous samples.

The fit results for samples $\{Fe_2(\mu\text{-}CAr)\}^{19}$, $\{Fe_2(\mu\text{-}CAr)\}^{18}$, and $\{Fe_2(\mu\text{-}CAr)\}^{17}$ is shown in Table S1, and Figure S2. Samples $\{Fe_2(\mu\text{-}CAr)\}^{17}$ and $\{Fe_2(\mu\text{-}CAr)\}^{18}$ were fit with their corresponding crystallography data. Sample $\{Fe_2(\mu\text{-}CAr)\}^{19}$ proposed structure was most similar to $\{Fe_2(\mu\text{-}CAr)\}^{17}$, therefore fits were done using $\{Fe_2(\mu\text{-}CAr)\}^{17}$crystallography data. For FT EXAFS figures, the x-axis represents the non-phase-shift corrected radial distance (R') that is shorter than the actual scattering distance by about 0.5 Å.

DFT Calculations. Calculations were carried out using version 4.0.2 of the ORCA package.[156] Geometry optimizations were conducted using the TPSS functionals in combination with the scalar relativistically recontracted versions of the def2-SVP (ZORA-def2-SVP) basis set on most C and H atoms. An enlarged basis set (ZORA-def2-TZVP) was employed for the Fe and P atoms, the iron-bound C and H ligands as well as any C atoms of the central aryl linker which undergo significant distortion in the solid state structure. For all atoms, the general-purpose segmented all-electron relativistically contracted auxiliary Coulomb-fitting basis (SARC/J) was employed. Solvation was modeled with CPCM in tetrahydrofuran.[157] Optimizations were followed by a frequency calculation to ensure a true minimum. Single-point energy calculations for $[(P_6ArC)Fe_2H][BAr^F{}_{24}]$ were conducted with a range of functionals (BP86, TPSS, TPSS + 5% HF, TPSSh) to evaluate the influence of the amount of Hartree-Fock exchange on the spin state energetics. These calculations employed the enlarged ZORA-def-TZVPP basis set on Fe, P, and special C/H atoms enumerated above. Calculations with hybrid functionals used the RIJCOSX approximation.[158] Broken symmetry calculations using the FlipSpin method were also conducted from the optimized $S = ½$ geometry and the character of the solution evaluated by analysis of the unrestricted corresponding orbitals.[159]

For DFT calculations of Mössbauer parameters,[160] the TPSSh functional was used in combination with the ZORA-def2-TZVP basis set on most C and H atoms. The CP(PPP) basis set was employed for Fe and the IGLO-III basis set was utilized for P and the iron-bound C and H ligands as well as any C atoms of the central aryl linker which undergo significant distortion in the solid state structure. The general purpose def2/J Coulomb fitting basis was employed on atoms using the def2-TZVPbasis, while the AutoAux feature of ORCA was used to generate auxiliary bases for the other atoms. All auxiliary bases were fully decontracted. To capture core polarization effects, the radial integration accuracy was increased around the Fe, P, and the iron-bound C and H ligands (IntAcc 7). A previously-reported calibration[161] was used to convert the computed Fe core electron density to the isomer shift (δ) in units of mm s^{-1}; estimates of the uncertainty in the computed values of δ and ΔE_Q were obtained from this calibration.

For time-dependent DFT calculations of XAS spectra,[115-116] the TPSSh functional was used in combination with the ZORA-def2-TZVP basis set on most C and H atoms. The CP(PPP) basis set was employed for Fe, and the ZORA-def2-TZVPP basis set was utilized for P and special C/H atoms. The AutoAux feature of ORCA was used to generate auxiliary bases and all auxiliary bases were fully decontracted. The radial integration accuracy was increased around the Fe (SpecialGridIntAcc 7). A total of 50 root excitations were calculated with a line broadening of 1 eV. The unrestricted Kohn-Sham orbitals generated from the calculations were subsequently transformed into quasi-restricted orbitals.[162]

Synthetic Procedures. *Preparation of [(P_6ArC)Fe_2H][BAr$^F{}_{24}$] ({Fe_2(μ-CAr)}^{17}).* A solution of (P_6ArC)Fe_2H (23.9 mg, 0.023 mmol) in tetrahydrofuran (10 mL) was chilled to -78 °C in a glovebox cold well. To this mixture, a chilled solution of [Cp_2Co][BAr$^F{}_{24}$] in tetrahydrofuran (1 mL) was added dropwise. After stirring for 1 hour at -78 °C, the reaction was removed from the cold well. After stirring for an additional 30 minutes at room temperature, the volatiles were removed under vacuum. The orange-brown residue was re-dissolved in diethyl ether (3 mL) and filtered over Celite. The filtrate was layered under pentane (10-12 mL) and stored at -35 °C for 2 days, affording {Fe_2(μ-CAr)}^{17} (30.6 mg, 70%) as orange-brown blades. ^{1}H NMR (400 MHz, C_6D_6/THF) δ = 82.69 (b), 50.32 (s), 38.25 (b), 27.57 (s), 19.15 (b), 15.67 (s), 9.36 (s), 8.55 (s), 7.87 (s), 7.43 (s), 6.93 (b), 6.66 (b), 6.32 (b), 6.20 (B), 6.07 (b), 5.80 (b), 5.04 (b), -3.84 (s), -19.27 (s). ^{19}F NMR (400 MHz, C_6D_6/THF) δ = -61.87 (s). UV-Vis (THF) [ε (M^{-1} cm^{-1})]: 341 nm (1.2 x 10^4), 416 nm (9.3 x 10^3), 750 nm (2.7 x 10^3). Anal. Calcd (%) for $C_{87}H_{88}BF_{24}Fe_2P_6$: C, 55.06; H, 4.67; N, 0.00. Found: C, 54.93; H, 5.20; N, 0.07.

Preparation of [K(THF)$_n$][(P_6ArC)Fe_2H] ({Fe_2(μ-CAr)}^{19}). Due to its thermal sensitivity, solutions of [K(THF)$_n$][(P_6ArC)Fe_2H] were prepared *in situ* for EPR spectroscopy, Mössbauer spectroscopy and X-ray absorption spectroscopy.

Preparation of 2,6-dibromotoluene-d_3. Dry diisopropylamine (1.749 g, 17.29 mmol, 1.1 equiv.) was dissolved in a 5:1 mixture of 2-MeTHF/THF (60 mL) and chilled to 0 °C. Under nitrogen, *n*BuLi (6.5 mL, 2.66 M, 17.29 mmol, 1.1 equiv.) was added dropwise. After stirring for 30 minutes, the lithium diisopropylamide solution was chilled to -110 °C in an ethanol/liquid nitrogen bath. Dibromobenzene (3.707 g, 15.72 mmol, 1 equiv.) was added dropwise via syringe. After stirring for 1.5 hours, iodomethane-d_3 (1.17 mL, 18.86 mmol, 1.2 equiv.) was added dropwise via syringe. The mixture was allowed to warm slowly to room temperature in the cold bath. After stirring overnight, the colorless solution was concentrated under vaccum at room temperature. A saturated ammonium chloride solution (40 mL) was added to the residue followed by dichloromethane (40 mL). After stirring for 10 minutes, the organic layer was collected, washed with water, and then, brine. The organics were dried over magnesium sulfate, filtered, and then concentrated *in vacuo*. The crude oil was then vacuum distilled, with 2,6-dibromotoluene-d_3 (1.39 g, 36%) transferring between 70-80 °C.

Preparation of 2,6-dibromotoluene-^{13}C. Using iodomethane-^{13}C, 2,6-dibromotoluene-^{13}C (1.54 g, 39%) was prepared via the same procedure outlined for 2,6-dibromotoluene-d_3.

Preparation of (3-bromo-2-methylphenyl)(bis(2-diisopropylphenylphosphino)phosphine-d_3. Using 2,6-dibromotoluene-d_3, (3-bromo-2-methylphenyl)(bis(2-diisopropylphenylphosphino)phosphine -d_3 (2.53 g, 82%) was prepared in a manner analogous to that reported for (3-bromo-2-methylphenyl)(bis(2-diisopropylphenylphosphino)phosphine.

Preparation of (3-bromo-2-methylphenyl)(bis(2-diisopropylphenylphosphino)phosphine-^{13}C. Using 2,6-dibromotoluene-^{13}C, (3-bromo-2-methylphenyl)(bis(2-diisopropylphenylphosphino)phosphine-^{13}C (2.92 g, 81%) was prepared in a manner analogous to that reported for (3-bromo-2-methylphenyl)(bis(2-diisopropylphenylphosphino)phosphine.

Preparation of 2,6-bis[bis(2-diisopropylphenylphosphino)phosphino)]toluene-d_3. Using (3-bromo-2-methylphenyl)(bis(2-diisopropylphenylphosphino)phosphine-d_3, 2,6-bis[bis(2-diisopropyl phenylphosphino)phosphino)]toluene-d_3 (3.36 g, 81%) was prepared in a manner analogous to that reported for 2,6-bis[bis(2-diisopropylphenylphosphino)phosphino)]toluene.

Preparation of 2,6-bis[bis(2-diisopropylphenylphosphino)phosphino)]toluene-^{13}C. Using (3-bromo-2-methylphenyl)(bis(2-diisopropylphenylphosphino)phosphine-^{13}C, 2,6-bis[bis(2-diisopropyl phenylphosphino)phosphino)]toluene-^{13}C (3.67 g, 80%) was prepared in a manner analogous to that reported for 2,6-bis[bis(2-diisopropylphenylphosphino)phosphino)]toluene.

Preparation of $(P_6ArCD_3)Fe_2Br_2$. Using 2,6-bis[bis(2-diisopropylphenyl phosphino)phosphino)]toluene-d_3, $(P_6ArCD_3)Fe_2Br_2$ (924 mg, 46%) was prepared in a manner analogous to that reported for $(P_6ArCH_3)Fe_2Br_2$.

Preparation of $(P_6Ar^{13}CH_3)Fe_2Br_2$. Using 2,6-bis[bis(2-diisopropylphenylphosphino) phosphino)]toluene-^{13}C, $(P_6Ar^{13}CH_3)Fe_2Br_2$ (813 mg, 42%) was prepared in a manner analogous to that reported for $(P_6ArCH_3)Fe_2Br_2$.

Preparation of $(P_6ArC)Fe_2(D)$. Using $(P_6ArCD_3)Fe_2Br_2$, $(P_6ArC)Fe_2(D)$ (37 mg, 11%) was prepared in a manner analogous to that reported for $(P_6ArC)Fe_2(H)$.

Preparation of $(P_6Ar^{13}C)Fe_2(H)$. Using $(P_6Ar^{13}CH_3)Fe_2Br_2$, $(P_6Ar^{13}C)Fe_2(H)$ (192 mg, 53%) was prepared in a manner analogous to that reported for $(P_6ArC)Fe_2(H)$.

Preparation of $[(P_6ArC)Fe_2D][BAr^F_{24}]$. Using $(P_6ArC)Fe_2D$, $[(P_6ArC)Fe_2D][BAr^F_{24}]$ was prepared in a manner analogous to that reported for $\{Fe_2(\mu\text{-}CAr)\}$[17]. After ^{1}H NMR analysis, the crude mixture was concentrated and re-dissolved in 2-MeTHF for EPR studies. As noted in the manuscript, H/D exchange occurs in the synthesis of $(P_6ArC)Fe_2D$, leading to a mixture of $[(P_6ArC)Fe_2D][BAr^F_{24}]$ and $[(P_6ArC)Fe_2H][BAr^F_{24}]$ upon oxidation. These two isotopologues exhibit some distinct resonances as a result of a paramagnetic isotope effect on chemical shifts (PIECS). Similar behavior has been reported for other μ-hydride complexes and has been attributed to the effect of the shorter M-D bonds (and therefore smaller M-M separation) on the M-M exchange interaction.[163-164] Based on the relative intensity of the related features, we estimate roughly 50% deuterium enrichment, in good agreement with simulations of the ENDOR and HYSCORE data.

Preparation of [(P$_6$Ar^{13}C)Fe$_2$H][BAr^F$_{24}$]. Using (P$_6$Ar^{13}C)Fe$_2$H, [(P$_6$Ar^{13}C)Fe$_2$H][BAr^F$_{24}$] was prepared in a manner analogous to that reported for {Fe$_2$(μ-CAr)}^{17}. After ^{1}H NMR analysis, the crude mixture was concentrated and re-dissolved in 2-MeTHF for EPR studies.

Supplemental Data

Table S1. Best-fitting results for Fe EXAFS of {Fe$_2$(μ-CAr)}^{19}, {Fe$_2$(μ-CAr)}^{18}, and {Fe$_2$(μ-CAr)}^{17}

Sample	Path	R(Å)		N	σ^3(10^{-3}Å^2)	R-factor(%)	ΔE$_0$ (eV)
		EXAFS	XRD				
{Fe$_2$(μ-CAr)}^{19}	Fe-C	1.79±0.01		1	2.4±4.5	2.59	7.5±2.7
	Fe-P	2.09±0.08		1	2.1±3.9		
	Fe-P	2.23±0.09		2	2.1±3.9		
	Fe-Fe	2.76±0.07		1	9.9±0.0		
{Fe$_2$(μ-CAr)}^{18}	Fe-C	1.78±0.01	1.79	1	0.7±3.2	2.73	8.8±1.4
	Fe-P	2.22±0.09	2.13-2.26	3	6.3±1.2		
	Fe-Fe	2.62±0.04	2.67	1	5.0±2.9		
{Fe$_2$(μ-CAr)}^{17}	Fe-C	1.77±0.02	1.79	1	3.5±3.8	2.82	7.0±1.6
	Fe-P	2.24±0.06	2.15-2.35	3	8.0±1.1		
	Fe-Fe	2.63±0.06	2.69	1	6.9±2.8		

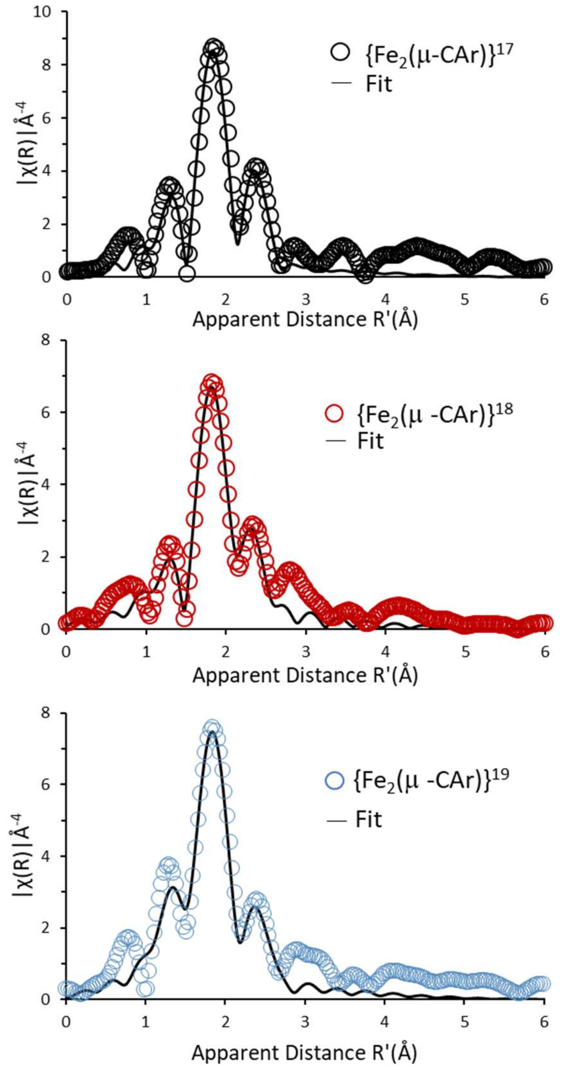

Figure S2. EXAFS R-space of $\{Fe_2(\mu\text{-}CAr)\}^{17}$ (black), $\{Fe_2(\mu\text{-}CAr)\}^{18}$ (red), and $\{Fe_2(\mu\text{-}CAr)\}^{19}$ (blue) with corresponding fits. Fitting parameters are outlined in table above.

Summary Tables

Table S2. Summary of statistics for diffraction data relevant for $\{Fe_2(\mu\text{-}CAr)\}^{17}$

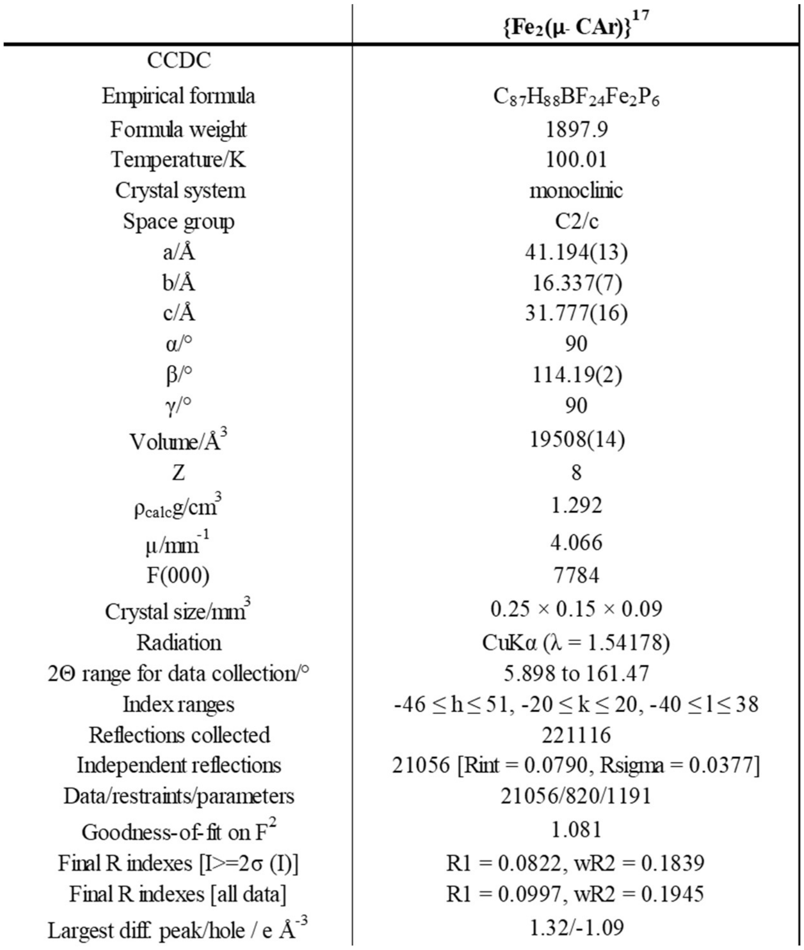

	$\{Fe_2(\mu\text{-} CAr)\}^{17}$
CCDC	
Empirical formula	$C_{87}H_{88}BF_{24}Fe_2P_6$
Formula weight	1897.9
Temperature/K	100.01
Crystal system	monoclinic
Space group	C2/c
a/Å	41.194(13)
b/Å	16.337(7)
c/Å	31.777(16)
α/°	90
β/°	114.19(2)
γ/°	90
Volume/Å^3	19508(14)
Z	8
ρ_{calc}g/cm^3	1.292
μ/mm^{-1}	4.066
F(000)	7784
Crystal size/mm^3	0.25 × 0.15 × 0.09
Radiation	CuKα (λ = 1.54178)
2Θ range for data collection/°	5.898 to 161.47
Index ranges	$-46 \leq h \leq 51$, $-20 \leq k \leq 20$, $-40 \leq l \leq 38$
Reflections collected	221116
Independent reflections	21056 [Rint = 0.0790, Rsigma = 0.0377]
Data/restraints/parameters	21056/820/1191
Goodness-of-fit on F^2	1.081
Final R indexes [I>=2σ (I)]	R1 = 0.0822, wR2 = 0.1839
Final R indexes [all data]	R1 = 0.0997, wR2 = 0.1945
Largest diff. peak/hole / e Å^{-3}	1.32/-1.09

Special Refinement Details for $[(P_6ArC)Fe_2H][BAr^F{}_{24}]$. Complex **$\{Fe_2(\mu\text{-}CAr)\}^{17}$** crystallizes in the space group *C*2/c with one molecule in the asymmetric unit. Electron density corresponding to the bridging hydride could be located in the diffraction map, but its position was variable during refinement. Its position was refined with the help of similarity restraints on the Fe-H distances. The $BAr^F{}_{24}$ counterion exhibits significant disorder in several $-CF_3$ groups. Efforts were made to model this as positional disorder due to rotation of the $-CF_3$ groups over two positions as best as possible. There is additionally some heavily disordered solvent which could not be modelled satisfactorily and was instead masked in Olex.

References

1. Spatzal, T.; Aksoyoglu, M.; Zhang, L.; Andrade, S. L. A.; Schleicher, E.; Weber, S.; Rees, D. C.; Einsle, O., Evidence for Interstitial Carbon in Nitrogenase FeMo Cofactor. *Science* **2011,** *334* (6058), 940-940.
2. Einsle, O.; Tezcan, F. A.; Andrade, S. L. A.; Schmid, B.; Yoshida, M.; Howard, J. B.; Rees, D. C., Nitrogenase MoFe-Protein at 1.16 Å Resolution: A Central Ligand in the FeMo-Cofactor. *Science* **2002,** *297* (5587), 1696-1700.
3. Kirn, J.; Rees, D. C., Crystallographic structure and functional implications of the nitrogenase molybdenum–iron protein from Azotobacter vinelandii. *Nature* **1992,** *360*, 553.
4. Lancaster, K. M.; Roemelt, M.; Ettenhuber, P.; Hu, Y.; Ribbe, M. W.; Neese, F.; Bergmann, U.; DeBeer, S., X-ray Emission Spectroscopy Evidences a Central Carbon in the Nitrogenase Iron-Molybdenum Cofactor. *Science* **2011,** *334* (6058), 974-977.
5. Rees, J. A.; Bjornsson, R.; Schlesier, J.; Sippel, D.; Einsle, O.; DeBeer, S., The Fe–V Cofactor of Vanadium Nitrogenase Contains an Interstitial Carbon Atom. *Angew. Chem. Int. Ed.* **2015,** *54* (45), 13249-13252.
6. Sippel, D.; Einsle, O., The structure of vanadium nitrogenase reveals an unusual bridging ligand. *Nat. Chem. Biol.* **2017,** *13*, 956.
7. Bjornsson, R.; Lima, F. A.; Spatzal, T.; Weyhermuller, T.; Glatzel, P.; Bill, E.; Einsle, O.; Neese, F.; DeBeer, S., Identification of a spin-coupled Mo(iii) in the nitrogenase iron-molybdenum cofactor. *Chem. Sci.* **2014,** *5* (8), 3096-3103.
8. Spatzal, T.; Schlesier, J.; Burger, E.-M.; Sippel, D.; Zhang, L.; Andrade, S. L. A.; Rees, D. C.; Einsle, O., Nitrogenase FeMoco investigated by spatially resolved anomalous dispersion refinement. *Nat. Commun.* **2016,** *7*, 10902.
9. Kowalska, J. K.; Henthorn, J. T.; Van Stappen, C.; Trncik, C.; Einsle, O.; Keavney, D.; DeBeer, S., X-ray Magnetic Circular Dichroism Spectroscopy Applied to Nitrogenase and Related Models: Experimental Evidence for a Spin-Coupled Molybdenum(III) Center. *Angew. Chem. Int. Ed.* **2019,** *58* (28), 9373-9377.
10. Bjornsson, R.; Neese, F.; DeBeer, S., Revisiting the Mössbauer Isomer Shifts of the FeMoco Cluster of Nitrogenase and the Cofactor Charge. *Inorg. Chem.* **2017,** *56* (3), 1470-1477.
11. Benediktsson, B.; Bjornsson, R., QM/MM Study of the Nitrogenase MoFe Protein Resting State: Broken-Symmetry States, Protonation States, and QM Region Convergence in the FeMoco Active Site. *Inorg. Chem.* **2017,** *56* (21), 13417-13429.
12. Kowalska, J. K.; Hahn, A. W.; Albers, A.; Schiewer, C. E.; Bjornsson, R.; Lima, F. A.; Meyer, F.; DeBeer, S., X-ray Absorption and Emission Spectroscopic Studies of $[L_2Fe_2S_2]^n$ Model Complexes: Implications for the Experimental Evaluation of Redox States in Iron–Sulfur Clusters. *Inorg. Chem.* **2016,** *55* (9), 4485-4497.
13. Henthorn, J. T.; Arias, R. J.; Koroidov, S.; Kroll, T.; Sokaras, D.; Bergmann, U.; Rees, D. C.; DeBeer, S., Localized Electronic Structure of Nitrogenase FeMoco Revealed by Selenium K-Edge High Resolution X-ray Absorption Spectroscopy. *J. Am. Chem. Soc.* **2019,** *141* (34), 13676-13688.
14. Buscagan, T. M.; Rees, D. C., Rethinking the Nitrogenase Mechanism: Activating the Active Site. *Joule* **2019,** *3* (11), 2662-2678.
15. Spatzal, T.; Perez, K. A.; Howard, J. B.; Rees, D. C., Catalysis-dependent selenium incorporation and migration in the nitrogenase active site iron-molybdenum cofactor. *eLife* **2015,** *4*, e11620.
16. Spatzal, T.; Perez, K. A.; Einsle, O.; Howard, J. B.; Rees, D. C., Ligand binding to the FeMo-cofactor: Structures of CO-bound and reactivated nitrogenase. *Science* **2014,** *345* (6204), 1620-1623.
17. Sippel, D.; Rohde, M.; Netzer, J.; Trncik, C.; Gies, J.; Grunau, K.; Djurdjevic, I.; Decamps, L.; Andrade, S. L. A.; Einsle, O., A bound reaction intermediate sheds light on the mechanism of nitrogenase. *Science* **2018,** *359* (6383), 1484-1489.
18. Morrison, C. N.; Spatzal, T.; Rees, D. C., Reversible Protonated Resting State of the Nitrogenase Active Site. *J. Am. Chem. Soc.* **2017,** *139* (31), 10856-10862.

19. Doan, P. E.; Telser, J.; Barney, B. M.; Igarashi, R. Y.; Dean, D. R.; Seefeldt, L. C.; Hoffman, B. M., ^{57}Fe ENDOR Spectroscopy and 'Electron Inventory' Analysis of the Nitrogenase E_4 Intermediate Suggest the Metal-Ion Core of FeMo-Cofactor Cycles Through Only One Redox Couple. *J. Am. Chem. Soc.* **2011,** *133* (43), 17329-17340.

20. Čorić, I.; Holland, P. L., Insight into the Iron–Molybdenum Cofactor of Nitrogenase from Synthetic Iron Complexes with Sulfur, Carbon, and Hydride Ligands. *J. Am. Chem. Soc.* **2016,** *138* (23), 7200-7211.

21. Wiig, J. A.; Lee, C. C.; Hu, Y.; Ribbe, M. W., Tracing the Interstitial Carbide of the Nitrogenase Cofactor during Substrate Turnover. *J. Am. Chem. Soc.* **2013,** *135* (13), 4982-4983.

22. Siegbahn, P. E. M., The mechanism for nitrogenase including all steps. *Phys. Chem. Chem. Phys.* **2019,** *21* (28), 15747-15759.

23. Siegbahn, P. E. M., Model Calculations Suggest that the Central Carbon in the FeMo-Cofactor of Nitrogenase Becomes Protonated in the Process of Nitrogen Fixation. *J. Am. Chem. Soc.* **2016,** *138* (33), 10485-10495.

24. McKee, M. L., A New Nitrogenase Mechanism Using a CFe_8S_9 Model: Does H_2 Elimination Activate the Complex to N_2 Addition to the Central Carbon Atom? *J. Phys. Chem. A* **2016,** *120* (5), 754-764.

25. Yano, J.; Yachandra, V., Mn_4Ca Cluster in Photosynthesis: Where and How Water is Oxidized to Dioxygen. *Chem. Rev.* **2014,** *114* (8), 4175-4205.

26. Van Stappen, C.; Thorhallsson, A. T.; Decamps, L.; Bjornsson, R.; DeBeer, S., Resolving the structure of the E_1 state of Mo nitrogenase through Mo and Fe K-edge EXAFS and QM/MM calculations. *Chem. Sci.* **2019,** *10* (42), 9807-9821.

27. Van Stappen, C.; Davydov, R.; Yang, Z.-Y.; Fan, R.; Guo, Y.; Bill, E.; Seefeldt, L. C.; Hoffman, B. M.; DeBeer, S., Spectroscopic Description of the E_1 State of Mo Nitrogenase Based on Mo and Fe X-ray Absorption and Mössbauer Studies. *Inorg. Chem.* **2019,** *58* (18), 12365-12376.

28. Hoffman, B. M.; Lukoyanov, D.; Yang, Z.-Y.; Dean, D. R.; Seefeldt, L. C., Mechanism of Nitrogen Fixation by Nitrogenase: The Next Stage. *Chem. Rev.* **2014,** *114* (8), 4041-4062.

29. Hoffman, B. M.; Lukoyanov, D.; Dean, D. R.; Seefeldt, L. C., Nitrogenase: A Draft Mechanism. *Acc. Chem. Res.* **2013,** *46* (2), 587-595.

30. Dos Santos, P. C.; Igarashi, R. Y.; Lee, H.-I.; Hoffman, B. M.; Seefeldt, L. C.; Dean, D. R., Substrate Interactions with the Nitrogenase Active Site. *Acc. Chem. Res.* **2005,** *38* (3), 208-214.

31. Lukoyanov, D.; Yang, Z.-Y.; Duval, S.; Danyal, K.; Dean, D. R.; Seefeldt, L. C.; Hoffman, B. M., A Confirmation of the Quench-Cryoannealing Relaxation Protocol for Identifying Reduction States of Freeze-Trapped Nitrogenase Intermediates. *Inorg. Chem.* **2014,** *53* (7), 3688-3693.

32. Lukoyanov, D.; Barney, B. M.; Dean, D. R.; Seefeldt, L. C.; Hoffman, B. M., Connecting nitrogenase intermediates with the kinetic scheme for N_2 reduction by a relaxation protocol and identification of the N_2 binding state. *Proc. Natl. Acad. Sci. U. S. A.* **2007,** *104* (5), 1451-1455.

33. Igarashi, R. Y.; Laryukhin, M.; Dos Santos, P. C.; Lee, H.-I.; Dean, D. R.; Seefeldt, L. C.; Hoffman, B. M., Trapping H- Bound to the Nitrogenase FeMo-Cofactor Active Site during H_2 Evolution: Characterization by ENDOR Spectroscopy. *J. Am. Chem. Soc.* **2005,** *127* (17), 6231-6241.

34. Hoeke, V.; Tociu, L.; Case, D. A.; Seefeldt, L. C.; Raugei, S.; Hoffman, B. M., High-Resolution ENDOR Spectroscopy Combined with Quantum Chemical Calculations Reveals the Structure of Nitrogenase Janus Intermediate E_4(4H). *J. Am. Chem. Soc.* **2019,** *141* (30), 11984-11996.

35. Lukoyanov, D.; Khadka, N.; Yang, Z.-Y.; Dean, D. R.; Seefeldt, L. C.; Hoffman, B. M., Reductive Elimination of H_2 Activates Nitrogenase to Reduce the N≡N Triple Bond: Characterization of the E_4(4H) Janus Intermediate in Wild-Type Enzyme. *J. Am. Chem. Soc.* **2016,** *138* (33), 10674-10683.

36. Rohde, M.; Sippel, D.; Trncik, C.; Andrade, S. L. A.; Einsle, O., The Critical E_4 State of Nitrogenase Catalysis. *Biochemistry* **2018,** *57* (38), 5497-5504.

37. Lees, N. S.; McNaughton, R. L.; Gregory, W. V.; Holland, P. L.; Hoffman, B. M., ENDOR Characterization of a Synthetic Diiron Hydrazido Complex as a Model for Nitrogenase Intermediates. *J. Am. Chem. Soc.* **2008,** *130* (2), 546-555.

38. Thompson, N. B.; Oyala, P. H.; Dong, H. T.; Chalkley, M. J.; Zhao, J.; Alp, E. E.; Hu, M.; Lehnert, N.; Peters, J. C., Electronic Structures of an $[Fe(NNR_2)]^{+/0/-}$ Redox Series: Ligand Noninnocence and Implications for Catalytic Nitrogen Fixation. *Inorg. Chem.* **2019,** *58* (5), 3535-3549.

39. Nesbit, M. A.; Oyala, P. H.; Peters, J. C., Characterization of the Earliest Intermediate of Fe-N_2 Protonation: CW and Pulse EPR Detection of an Fe-NNH Species and Its Evolution to Fe-NNH_2^+. *J. Am. Chem. Soc.* **2019,** *141* (20), 8116-8127.

40. Anderson, J. S.; Cutsail, G. E.; Rittle, J.; Connor, B. A.; Gunderson, W. A.; Zhang, L.; Hoffman, B. M.; Peters, J. C., Characterization of an $Fe{\equiv}N{-}NH_2$ Intermediate Relevant to Catalytic N_2 Reduction to NH_3. *J. Am. Chem. Soc.* **2015,** *137* (24), 7803-7809.

41. Saouma, C. T.; Kinney, R. A.; Hoffman, B. M.; Peters, J. C., Transformation of an $[Fe(\eta2\text{-}N_2H_3)]^+$ Species to π-Delocalized $[Fe_2(\mu\text{-}N_2H_2)]^{2+/+}$ Complexes. *Angew. Chem. Int. Ed.* **2011,** *50* (15), 3446-3449.

42. Horitani, M.; Grubel, K.; McWilliams, S. F.; Stubbert, B. D.; Mercado, B. Q.; Yu, Y.; Gurubasavaraj, P. M.; Lees, N. S.; Holland, P. L.; Hoffman, B. M., ENDOR characterization of an iron-alkene complex provides insight into a corresponding organometallic intermediate of nitrogenase. *Chem. Sci.* **2017,** *8* (9), 5941-5948.

43. Chiang, K. P.; Scarborough, C. C.; Horitani, M.; Lees, N. S.; Ding, K.; Dugan, T. R.; Brennessel, W. W.; Bill, E.; Hoffman, B. M.; Holland, P. L., Characterization of the Fe-H Bond in a Three-Coordinate Terminal Hydride Complex of Iron(I). *Angew. Chem. Int. Ed.* **2012,** *51* (15), 3658-3662.

44. Citek, C.; Oyala, P. H.; Peters, J. C., Mononuclear Fe(I) and Fe(II) Acetylene Adducts and Their Reductive Protonation to Terminal Fe(IV) and Fe(V) Carbynes. *J. Am. Chem. Soc.* **2019,** *141* (38), 15211-15221.

45. Gu, N. X.; Oyala, P. H.; Peters, J. C., An S = 1/2 Iron Complex Featuring N2, Thiolate, and Hydride Ligands: Reductive Elimination of H_2 and Relevant Thermochemical Fe–H Parameters. *J. Am. Chem. Soc.* **2018**, *140*, 6374.

46. Hickey, A. K.; Greer, S. M.; Valdez-Moreira, J. A.; Lutz, S. A.; Pink, M.; DeGayner, J. A.; Harris, T. D.; Hill, S.; Telser, J.; Smith, J. M., A Dimeric Hydride-Bridged Complex with Geometrically Distinct Iron Centers Giving Rise to an S = 3 Ground State. *J. Am. Chem. Soc.* **2019**, *141*, 11970.

47. Yang, D.; Xu, S.; Zhang, Y.; Li, Y.; Li, Y.; Wang, B.; Qu, J., Reactivity toward Unsaturated Small Molecules of Thiolate-Bridged Diiron Hydride Complexes. *Inorg. Chem.* **2018,** *57* (24), 15198-15204.

48. Yu, X.; Tung, C.-H.; Wang, W.; Huynh, M. T.; Gray, D. L.; Hammes-Schiffer, S.; Rauchfuss, T. B., Interplay between Terminal and Bridging Diiron Hydrides in Neutral and Oxidized States. *Organometallics* **2017,** *36* (11), 2245-2253.

49. Yang, D.; Li, Y.; Wang, B.; Zhao, X.; Su, L.; Chen, S.; Tong, P.; Luo, Y.; Qu, J., Synthesis and Electrocatalytic Property of Diiron Hydride Complexes Derived from a Thiolate-Bridged Diiron Complex. *Inorg. Chem.* **2015,** *54* (21), 10243-10249.

50. Lee, Y.; Anderton, K. J.; Sloane, F. T.; Ermert, D. M.; Abboud, K. A.; García-Serres, R.; Murray, L. J., Reactivity of Hydride Bridges in High-Spin [3M–3(μ-H)] Clusters (M = FeII, CoII). *J. Am. Chem. Soc.* **2015,** *137* (33), 10610-10617.

51. Rittle, J.; McCrory, C. C. L.; Peters, J. C., A 10^6-Fold Enhancement in N_2-Binding Affinity of an $Fe_2(\mu\text{-}H)_2$ Core upon Reduction to a Mixed-Valence $Fe^{II}Fe^{I}$ State. *J. Am. Chem. Soc.* **2014,** *136* (39), 13853-13862.

52. Wang, W.; Nilges, M. J.; Rauchfuss, T. B.; Stein, M., Isolation of a Mixed Valence Diiron Hydride: Evidence for a Spectator Hydride in Hydrogen Evolution Catalysis. *J. Am. Chem. Soc.* **2013,** *135* (9), 3633-3639.

53. Jablonskytė, A.; Wright, J. A.; Fairhurst, S. A.; Peck, J. N. T.; Ibrahim, S. K.; Oganesyan, V. S.; Pickett, C. J., Paramagnetic Bridging Hydrides of Relevance to Catalytic Hydrogen Evolution at Metallosulfur Centers. *J. Am. Chem. Soc.* **2011,** *133* (46), 18606-18609.

54. Yang, H.; Rittle, J.; Marts, A. R.; Peters, J. C.; Hoffman, B. M., ENDOR Characterization of $(N_2)Fe^{II}(\mu\text{-}H)_2Fe^{I}(N_2)^-$: A Spectroscopic Model for N_2 Binding by the Di-μ-hydrido Nitrogenase Janus Intermediate. *Inorg. Chem.* **2018,** *57* (19), 12323-12330.

55. Kinney, R. A.; Saouma, C. T.; Peters, J. C.; Hoffman, B. M., Modeling the Signatures of Hydrides in Metalloenzymes: ENDOR Analysis of a Di-iron Fe(μ-NH)(μ-H)Fe Core. *J. Am. Chem. Soc.* **2012,** *134* (30), 12637-12647.

56. Robin, M. B.; Day, P., Mixed Valence Chemistry-A Survey and Classification. In *Advances in Inorganic Chemistry and Radiochemistry*, Emeleus, H. J.; Sharpe, A. G., Eds. Academic Press: 1968; Vol. 10, pp 247-422.

57. Holton, J.; Lappert, M. F.; Pearce, R.; Yarrow, P. I. W., Bridged hydrocarbyl or hydrocarbon binuclear transition metal complexes: classification, structures, and chemistry. *Chem. Rev.* **1983,** *83* (2), 135-201.

58. Casey, C. P.; Fagan, P. J.; Miles, W. H., Synthesis and interconversions of dinuclear iron complexes with μ-methyl, μ-methylene, and μ-methylidyne ligands. *J. Am. Chem. Soc.* **1982,** *104* (4), 1134-1136.

59. Marchetti, F., Constructing Organometallic Architectures from Aminoalkylidyne Diiron Complexes. *Eur. J. Inorg. Chem.* **2018,** *2018* (36), 3987-4003.

60. Kuppuswamy, S.; Wofford, J. D.; Joseph, C.; Xie, Z.-L.; Ali, A. K.; Lynch, V. M.; Lindahl, P. A.; Rose, M. J., Structures, Interconversions, and Spectroscopy of Iron Carbonyl Clusters with an Interstitial Carbide: Localized Metal Center Reduction by Overall Cluster Oxidation. *Inorg. Chem.* **2017,** *56* (10), 5998-6012.

61. Vollmer, G. Y.; Wallasch, M. W.; Saurenz, D.; Eger, T. R.; Bauer, H.; Wolmershäuser, G.; Prosenc, M. H.; Sitzmann, H., Benzylidyne Bridges from Diphenylacetylene and a Methylidyne Bridge from Methylmagnesium Chloride. *Organometallics* **2015,** *34* (3), 644-652.

62. Wang, R.; Sun, J.; Chen, J.; Xu, Q.; Souma, Y., Unusual reactions of cationic bridging carbyne complexes of dimethylsilane-bridged bis(η5-cyclopentadienyl)diiron tricarbonyl with carbonylmetal anions. *J. Organomet. Chem.* **2002,** *658* (1), 214-227.

63. Mansuy, D.; Lecomte, J. P.; Chottard, J. C.; Bartoli, J. F., Formation of a complex with a carbide bridge between two iron atoms from the reaction of (tetraphenylporphyrin)iron(II) with carbon tetraiodide. *Inorg. Chem.* **1981,** *20* (9), 3119-3121.

64. Tachikawa, M.; Muetterties, E. L., Metal clusters. 25. A uniquely bonded C-H group and reactivity of a low-coordinate carbidic carbon atom. *J. Am. Chem. Soc.* **1980,** *102* (13), 4541-4542.

65. Churchill, M. R.; Wormald, J.; Knight, J.; Mays, M. J., Synthesis and crystallographic characterization of bis(tetramethylammonium) carbidohexadecacarbonylhexaferrate, a hexanuclear carbidocarbonyl derivative of iron. *J. Am. Chem. Soc.* **1971,** *93* (12), 3073-3074.

66. Arnett, C. H.; Agapie, T., Activation of an Open Shell, Carbyne-Bridged Diiron Complex Toward Binding of Dinitrogen. *J. Am. Chem. Soc.* **2020,** *142*, 10059.

67. Yogendra, S.; Weyhermüller, T.; Hahn, A. W.; DeBeer, S., From Ylides to Doubly Yldiide-Bridged Iron(II) High Spin Dimers via Self-Protolysis. *Inorg. Chem.* **2019,** *58* (14), 9358-9367.

68. Reesbeck, M. E.; Grubel, K.; Kim, D.; Brennessel, W. W.; Mercado, B. Q.; Holland, P. L., Diazoalkanes in Low-Coordinate Iron Chemistry: Bimetallic Diazoalkyl and Alkylidene Complexes of Iron(II). *Inorg. Chem.* **2017,** *56* (3), 1019-1022.

69. Sun, C.-L.; Krause, H.; Fürstner, A., A Practical Procedure for Iron-Catalyzed Cross-Coupling Reactions of Sterically Hindered Aryl-Grignard Reagents with Primary Alkyl Halides. *Adv. Synth. Catal.* **2014,** *356* (6), 1281-1291.

70. Ni, C.; Power, P. P., Methyl-Bridged Transition Metal Complexes (M = Cr−Fe) Supported by Bulky Terphenyl Ligands. *Organometallics* **2009,** *28* (22), 6541-6545.

71. Klose, A.; Solari, E.; Floriani, C.; Chiesi-Villa, A.; Rizzoli, C.; Re, N., Magnetic Properties Diagnostic for the Existence of Iron(II)-Iron(II) Bonds in Dinuclear Complexes Which Derive from Stepwise Insertion Reactions on Unsupported Iron-Aryl Bonds. *J. Am. Chem. Soc.* **1994,** *116* (20), 9123-9135.

72. Horitani, M.; Shisler, K.; Broderick, W. E.; Hutcheson, R. U.; Duschene, K. S.; Marts, A. R.; Hoffman, B. M.; Broderick, J. B., Radical SAM catalysis via an organometallic intermediate with an Fe–[5'-C]-deoxyadenosyl bond. *Science* **2016,** *352* (6287), 822-825.

73. Wang, W.; Wang, K.; Li, J.; Nellutla, S.; Smirnova, T. I.; Oldfield, E., An ENDOR and HYSCORE Investigation of a Reaction Intermediate in IspG (GcpE) Catalysis. *J. Am. Chem. Soc.* **2011,** *133* (22), 8400-8403.

74. Wang, W.; Li, J.; Wang, K.; Huang, C.; Zhang, Y.; Oldfield, E., Organometallic mechanism of action and inhibition of the 4Fe-4S isoprenoid biosynthesis protein GcpE (IspG). *Angew. Chem. Int. Ed.* **2010,** *107* (25), 11189-11193.

75. Ye, M.; Thompson, N. B.; Brown, A. C.; Suess, D. L. M., A Synthetic Model of Enzymatic [Fe_4S_4]–Alkyl Intermediates. *J. Am. Chem. Soc.* **2019,** *141* (34), 13330-13335.

76. Li, J.; Wang, K.; Smirnova, T. I.; Khade, R. L.; Zhang, Y.; Oldfield, E., Isoprenoid Biosynthesis: Ferraoxetane or Allyl Anion Mechanism for IspH Catalysis? *Angew. Chem. Int. Ed.* **2013,** *52* (25), 6522-6525.

77. For the sake of comparison, the isoelectronic and structurally similar diiron u-imide, u-hydride complex ([$PhBP_3$]Fe)$_2$(μ-NH)(μ-H)][Na(THF)$_5$] ($PhBP_3^-$ = $PhB(CH_2PPh_2)_3^-$) displays electrochemical features at -2.58 V and -1.25 V. These are shifted by +200 mV and +400 mV, respectively, compared to corresponding redox events in (P_6ArC)Fe_2(μ-H), consistent with the enhanced electron releasing character of the carbyne ligand and the dialkylarylphosphine donors

78. Lee, Y.; Peters, J. C., Silylation of Iron-Bound Carbon Monoxide Affords a Terminal Fe Carbyne. *J. Am. Chem. Soc.* **2011,** *133* (12), 4438-4446.

79. Bursten, B. E.; Cayton, R. H., Electronic structure of piano-stool dimers. 3. Relationships between the bonding and reactivity of the organically bridged iron dimers [CpFe(CO)]$_2$(μ-CO)(μ-L) (L = CO, CH_2, C=CH_2, CH^+). *J. Am. Chem. Soc.* **1986,** *108* (26), 8241-8249.

80. Dzik, W. I.; Zhang, X. P.; de Bruin, B., Redox Noninnocence of Carbene Ligands: Carbene Radicals in (Catalytic) C−C Bond Formation. *Inorg. Chem.* **2011,** *50* (20), 9896-9903.

81. Chan, S.-C.; Gupta, P.; Engelmann, X.; Ang, Z. Z.; Ganguly, R.; Bill, E.; Ray, K.; Ye, S.; England, J., Observation of Carbodicarbene Ligand Redox Noninnocence in Highly Oxidized Iron Complexes. *Angew. Chem. Int. Ed.* **2018,** *57* (48), 15717-15722.

82. Sharon, D. A.; Mallick, D.; Wang, B.; Shaik, S., Computation Sheds Insight into Iron Porphyrin Carbenes' Electronic Structure, Formation, and N–H Insertion Reactivity. *J. Am. Chem. Soc.* **2016,** *138* (30), 9597-9610.

83. Khade, R. L.; Fan, W.; Ling, Y.; Yang, L.; Oldfield, E.; Zhang, Y., Iron Porphyrin Carbenes as Catalytic Intermediates: Structures, Mössbauer and NMR Spectroscopic Properties, and Bonding. *Angew. Chem. Int. Ed.* **2014,** *53* (29), 7574-7578.

84. Russell, S. K.; Hoyt, J. M.; Bart, S. C.; Milsmann, C.; Stieber, S. C. E.; Semproni, S. P.; DeBeer, S.; Chirik, P. J., Synthesis, electronic structure and reactivity of bis(imino)pyridine iron carbene complexes: evidence for a carbene radical. *Chem. Sci.* **2014,** *5* (3), 1168-1174.

85. Jacobs, B. P.; Agarwal, R. G.; Wolczanski, P. T.; Cundari, T. R.; MacMillan, S. N., Fe(IV) alkylidenes are actually Fe(II), and a related octahedral Fe(II) "alkylidene" is a conjugated vinyl complex. *Polyhedron* **2016,** *116*, 47-56.

86. Lindley, B. M.; Swidan, A. a.; Lobkovsky, E. B.; Wolczanski, P. T.; Adelhardt, M.; Sutter, J.; Meyer, K., Fe(iv) alkylidenes via protonation of Fe(ii) vinyl chelates and a comparative Mössbauer spectroscopic study. *Chem. Sci.* **2015,** *6* (8), 4730-4736.

87. Hartwig, J. F., *Organotransition Metal Chemistry: From Bonding to Catalysis*. University Science Books: Mill Valley, California, 2010.

88. Enemark, J. H.; Feltham, R. D., Principles of structure, bonding, and reactivity for metal nitrosyl complexes. *Coord. Chem. Rev.* **1974,** *13* (4), 339-406.

89. Gibson, J. F.; Hall, D. O.; Thornley, J. H.; Whatley, F. R., The iron complex in spinach ferredoxin. *Proc. Natl. Acad. Sci. U. S. A.* **1966,** *56* (3), 987-990.

90. Bencini, A.; Gatteschi, D., *Electron Paramagnetic Resonance of Exchange Coupled Systems*. Springer-Verlag Berlin Heidelberg: 1990.

91. Bertrand, P.; Gayda, J.-P., A theoretical interpretation of the variations of some physical parameters within the [2Fe-2S] ferredoxin group. *Biochim. Biophys. Acta – Prot. Struct.* **1979,** *579* (1), 107-121.

92. McWilliams, S. F.; Bill, E.; Lukat-Rodgers, G.; Rodgers, K. R.; Mercado, B. Q.; Holland, P. L., Effects of N_2 Binding Mode on Iron-Based Functionalization of Dinitrogen to Form an Iron(III) Hydrazido Complex. *J. Am. Chem. Soc.* **2018,** *140* (27), 8586-8598.

93. Safo, M. K.; Walker, F. A.; Raitsimring, A. M.; Walters, W. P.; Dolata, D. P.; Debrunner, P. G.; Scheidt, W. R., Axial Ligand Orientation in Iron(III) Porphyrinates: Effect of Axial π-Acceptors. Characterization of the Low-Spin Complex $[Fe(TPP)(4\text{-}CNPy)_2]ClO_4$. *J. Am. Chem. Soc.* **1994,** *116* (17), 7760-7770.

94. Brown, S. D.; Betley, T. A.; Peters, J. C., A Low-Spin d^5 Iron Imide: Nitrene Capture by Low-Coordinate Iron(I) Provides the 4-Coordinate Fe(III) Complex $[PhB(CH_2PPh_2)_3]$Fe⁝N-p-tolyl. *J. Am. Chem. Soc.* **2003,** *125* (2), 322-323.

95. Rieger, P. H., Electron paramagnetic resonance studies of low-spin d^5 transition metal complexes. *Coord. Chem. Rev.* **1994,** *135-136*, 203-286.

96. McGarvey, B. R., Survey of ligand field parameters of strong field d^5 complexes obtained from the g matrix. *Coord. Chem. Rev.* **1998,** *170* (1), 75-92.

97. Hyde, J. S.; Pasenkiewicz-Gierula, M.; Jesmanowicz, A.; Antholine, W. E., Pseudo field modulation in EPR spectroscopy. *Appl. Magn. Reson.* **1990,** *1* (3), 483.

98. Although NMR demonstrates that the deuterium label was fully incorporated into methyl position of the ligand, ENDOR spectra of the cation and anion reveal that the μ-hydride site was only ~50% enriched. This discrepancy is attributed to slow isotopic scrambling during the synthesis of $(P_6ArC)Fe_2(\mu\text{-}D)$, which may be facilitated by the elevated reaction temperatures. However, due to the different Larmor frequencies, the ^{2}H-labelled hydride can be selectively interrogated by HYSCORE such that the simulated parameters are not affected by the incomplete enrichment.

99. Solomon, E. I., Inorganic Spectroscopy: High Resolution. *Comments Inorg. Chem.* **1984,** *3* (5), 288-300.

100. McGarvey, B. R., The isotropic hyperfine interaction. *J. Phys. Chem.* **1967,** *71* (1), 51-66.

101. Wertz, J. E.; Bolton, J. R., *Electron Spin Resonance: Elementary Theory and Practical Applications*. Chapman and Hall: New York, N.Y., 1986.

102. Morton, J. R.; Preston, K. F., Atomic parameters for paramagnetic resonance data. *J. Magn. Res.* **1978,** *30* (3), 577-582.

103. Willems, J.-P.; Lee, H.-I.; Burdi, D.; Doan, P. E.; Stubbe, J.; Hoffman, B. M., Identification of the Protonated Oxygenic Ligands of Ribonucleotide Reductase Intermediate X by Q-Band ^{1,2}H CW and Pulsed ENDOR. *J. Am. Chem. Soc.* **1997,** *119* (41), 9816-9824.

104. DeRose, V. J.; Liu, K. E.; Lippard, S. J.; Hoffman, B. M., Investigation of the Dinuclear Fe Center of Methane Monooxygenase by Advanced Paramagnetic Resonance Techniques: On the Geometry of DMSO Binding. *J. Am. Chem. Soc.* **1996,** *118* (1), 121-134.

105. Hoeke, V.; Tociu, L.; Case, D. A.; Seefeldt, L. C.; Raugei, S.; Hoffman, B. M., Correction to "High-Resolution ENDOR Spectroscopy Combined with Quantum Chemical Calculations Reveals the Structure of Nitrogenase Janus Intermediate E_4(4H)". *J. Am. Chem. Soc.* **2019,** *141* (50), 19950-19950.

106. Kinney, R. A.; Hetterscheid, D. G. H.; Hanna, B. S.; Schrock, R. R.; Hoffman, B. M., Formation of $\{[HIPTN_3N]Mo(III)H\}^-$ by Heterolytic Cleavage of H_2 as Established by EPR and ENDOR Spectroscopy. *Inorg. Chem.* **2010,** *49* (2), 704-713.

107. Drover, M. W.; Schild, D. J.; Oyala, P. H.; Peters, J. C., Snapshots of a Migrating H-Atom: Characterization of a Reactive Iron(III) Indenide Hydride and its Nearly Isoenergetic Ring-Protonated Iron(I) Isomer. *Angew. Chem. Int. Ed.* **2019,** *58* (43), 15504-15511.

108. Keizer, P. N.; Krusic, P. J.; Morton, J. R.; Preston, K. F., Thiolato- and selenato-bridged dinuclear iron carbonyl radicals. *J. Am. Chem. Soc.* **1991,** *113* (14), 5454-5456.

109. Rao, G.; Altman, A. B.; Brown, A. C.; Tao, L.; Stich, T. A.; Arnold, J.; Britt, R. D., Metal Bonding with 3d and 6d Orbitals: An EPR and ENDOR Spectroscopic Investigation of Ti^{3+}–Al and Th^{3+}–Al Heterobimetallic Complexes. *Inorg. Chem.* **2019,** *58* (12), 7978-7988.

110. The dipolar contribution to the coupling can be obtained from equations presented in the text using the carbon gyromagnetic ratio. This affords an estimate of [-3.5, +1.1, +2.3] MHz, with the orientation of this tensor in the molecular frame undefined. It is not possible to explicitly determine the orientation of the 13C hyperfine tensor in the molecular frame because of the convolution of both local and dipolar contributions. However, the largest principal component of T(13C) is expected to be perpendicular to the Fe(μ-C)(μ-H)Fe plane. Given their nearly identical Fe-C bond lengths, the dipolar contribution to the 13C hyperfine can be treated as a constant and neglected in the analysis. Although this may overestimate tpi, the redox-dependent trends should not be affected. In support of this assertion, the effect of redox on the DFT calculted Fe-C covalencies is in reasonable agreement with those inferred by EPR.

111. Musgrave, K. B.; Angove, H. C.; Burgess, B. K.; Hedman, B.; Hodgson, K. O., All-Ferrous Titanium(III) Citrate Reduced Fe Protein of Nitrogenase: An XAS Study of Electronic and Metrical Structure. *J. Am. Chem. Soc.* **1998,** *120* (21), 5325-5326.

112. Although edge energies are commonly regarded as an indicator of changes in relative oxidation state, the rising edge of some [Fe-S] clusters are invariant to redox chemistry. Detailed spectroscopic investigation of a series of [2Fe-2S] model complexes suggested that this behavior may arise as a consequence of valence localization (see ref. 12). From this perspective, the distinct edge energies observed here can be taken to infer electronic delocalization.

113. Baker, M. L.; Mara, M. W.; Yan, J. J.; Hodgson, K. O.; Hedman, B.; Solomon, E. I., K- and L-edge X-ray absorption spectroscopy (XAS) and resonant inelastic X-ray scattering (RIXS) determination of differential orbital covalency (DOC) of transition metal sites. *Coord. Chem. Rev.* **2017,** *345*, 182-208.

114. Westre, T. E.; Kennepohl, P.; DeWitt, J. G.; Hedman, B.; Hodgson, K. O.; Solomon, E. I., A Multiplet Analysis of Fe K-Edge 1s → 3d Pre-Edge Features of Iron Complexes. *J. Am. Chem. Soc.* **1997,** *119* (27), 6297-6314.

115. Chandrasekaran, P.; Stieber, S. C. E.; Collins, T. J.; Que, J. L.; Neese, F.; DeBeer, S., Prediction of high-valent iron K-edge absorption spectra by time-dependent Density Functional Theory. *Dalton Trans.* **2011,** *40* (42), 11070-11079.

116. DeBeer George, S.; Petrenko, T.; Neese, F., Prediction of Iron K-Edge Absorption Spectra Using Time-Dependent Density Functional Theory. *J. Phys. Chem. A* **2008,** *112* (50), 12936-12943.

117. Note that while TD-DFT performs well for metal localized transitions, charge transfer artifacts are common for systems with extended arylic π systems. For this reason, we focus on the true on the carbyne ligand, which can act as a true pi acceptor.

118. Rees, J. A.; Martin-Diaconescu, V.; Kovacs, J. A.; DeBeer, S., X-ray Absorption and Emission Study of Dioxygen Activation by a Small-Molecule Manganese Complex. *Inorg. Chem.* **2015,** *54* (13), 6410-6422.

119. Roemelt, M.; Beckwith, M. A.; Duboc, C.; Collomb, M.-N.; Neese, F.; DeBeer, S., Manganese K-Edge X-Ray Absorption Spectroscopy as a Probe of the Metal–Ligand Interactions in Coordination Compounds. *Inorg. Chem.* **2012,** *51* (1), 680-687.

120. Gütlich, P.; Bill, E.; Trautwein, A. X., *Mössbauer Spectroscopy and Transition Metal Chemistry: Fundamentals and Applications*. Springer: Berlin, 2011.

121. Chalkley, M. J.; Peters, J. C., A Triad of Highly Reduced, Linear Iron Nitrosyl Complexes: {FeNO}$^{8–10}$. *Angew. Chem. Int. Ed.* **2016,** *55* (39), 11995-11998.

122. Hay, P. J.; Thibeault, J. C.; Hoffmann, R., Orbital interactions in metal dimer complexes. *J. Am. Chem. Soc.* **1975,** *97* (17), 4884-4899.

123. Brunold, T. C.; Gamelin, D. R.; Solomon, E. I., Excited-State Exchange Coupling in Bent Mn(III)−O−Mn(III) Complexes: Dominance of the π/σ Superexchange Pathway and Its Possible Contributions to the Reactivities of Binuclear Metalloproteins. *J. Am. Chem. Soc.* **2000,** *122* (35), 8511-8523.

124. Gamelin, D. R.; Bominaar, E. L.; Kirk, M. L.; Wieghardt, K.; Solomon, E. I., Excited-State Contributions to Ground-State Properties of Mixed-Valence Dimers: Spectral and Electronic-Structural Studies of $[Fe_2(OH)_3(tmtacn)_2]^{2+}$ Related to the $[Fe_2S_2]^+$ Active Sites of Plant-Type Ferredoxins. *J. Am. Chem. Soc.* **1996,** *118* (34), 8085-8097.

125. Summerville, R. H.; Hoffmann, R., Tetrahedral and other M_2L_6 transition metal dimers. *J. Am. Chem. Soc.* **1976,** *98* (23), 7240-7254.

126. Increasing the amount of exact exchange in the functional to 25% (TPSS0) affords an additional pair of magnetic orbitals (0.89). Inspection of the corresponding orbitals suggests that an additional resonance form, involving spin coupling of two S =1 Fe(II) sites to a ligand-based radical, may also contribute to the ground state.

127. Blondin, G.; Girerd, J. J., Interplay of electron exchange and electron transfer in metal polynuclear complexes in proteins or chemical models. *Chem. Rev.* **1990,** *90* (8), 1359-1376.

128. Orio, M.; Mouesca, J.-M., Variation of Average g Values and Effective Exchange Coupling Constants among [2Fe−2S] Clusters: A Density Functional Theory Study of the Impact of Localization (Trapping Forces) versus Delocalization (Double-Exchange) as Competing Factors. *Inorg. Chem.* **2008,** *47* (12), 5394-5416.

129. Dey, A.; Glaser, T.; Moura, J. J. G.; Holm, R. H.; Hedman, B.; Hodgson, K. O.; Solomon, E. I., Ligand K-edge X-ray Absorption Spectroscopy and DFT Calculations on $[Fe_3S_4]^{0,+}$ Clusters: Delocalization, Redox, and Effect of the Protein Environment. *J. Am. Chem. Soc.* **2004,** *126* (51), 16868-16878.

130. Glaser, T.; Rose, K.; Shadle, S. E.; Hedman, B.; Hodgson, K. O.; Solomon, E. I., S K-edge X-ray Absorption Studies of Tetranuclear Iron−Sulfur Clusters: μ-Sulfide Bonding and Its Contribution to Electron Delocalization. *J. Am. Chem. Soc.* **2001,** *123* (3), 442-454.

131. Fu, W.; Drozdzewski, P. M.; Davies, M. D.; Sligar, S. G.; Johnson, M. K., Resonance Raman and magnetic circular dichroism studies of reduced [2Fe-2S] proteins. *J. Biol. Chem.* **1992,** *267* (22), 15502-15510.

132. Han, S.; Czernuszewicz, R. S.; Kimura, T.; Adams, M. W. W.; Spiro, T. G., Fe_2S_2 protein resonance Raman spectra revisited: structural variations among adrenodoxin, ferredoxin, and red paramagnetic protein. *J. Am. Chem. Soc.* **1989,** *111* (10), 3505-3511.

133. Brown, S. D.; Mehn, M. P.; Peters, J. C., Heterolytic H_2 Activation Mediated by Low-Coordinate L_3Fe-(μ-N)-FeL_3 Complexes to Generate Fe(μ-NH)(μ-H)Fe Species. *J. Am. Chem. Soc.* **2005,** *127* (38), 13146-13147.

134. Noodleman, L.; Peng, C. Y.; Case, D. A.; Mouesca, J. M., Orbital interactions, electron delocalization and spin coupling in iron-sulfur clusters. *Coord. Chem. Rev.* **1995,** *144*, 199-244.

135. Boča, R., Zero-field splitting in metal complexes. *Coord. Chem. Rev.* **2004,** *248* (9), 757-815.

136. Scott, A. D.; Pelmenschikov, V.; Guo, Y.; Yan, L.; Wang, H.; George, S. J.; Dapper, C. H.; Newton, W. E.; Yoda, Y.; Tanaka, Y.; Cramer, S. P., Structural Characterization of CO-Inhibited Mo-Nitrogenase by Combined Application of Nuclear Resonance Vibrational Spectroscopy, Extended X-ray Absorption Fine Structure, and Density Functional Theory: New Insights into the Effects of CO Binding and the Role of the Interstitial Atom. *J. Am. Chem. Soc.* **2014,** *136* (45), 15942-15954.

137. Pelmenschikov, V.; Case, D. A.; Noodleman, L., Ligand-Bound S = 1/2 FeMo-Cofactor of Nitrogenase: Hyperfine Interaction Analysis and Implication for the Central Ligand X Identity. *Inorg. Chem.* **2008,** *47* (14), 6162-6172.

138. George, S. J.; Barney, B. M.; Mitra, D.; Igarashi, R. Y.; Guo, Y.; Dean, D. R.; Cramer, S. P.; Seefeldt, L. C., EXAFS and NRVS Reveal a Conformational Distortion of the FeMo-cofactor in the MoFe Nitrogenase Propargyl Alcohol Complex. *J. Inorg. Biochem.* **2012,** *112*, 85-92.

139. Dance, I., Ramifications of C-centering rather than N-centering of the active site FeMo-co of the enzyme nitrogenase. *Dalton Trans.* **2012,** *41* (16), 4859-4865.

140. Creutz, S. E.; Peters, J. C., Catalytic Reduction of N_2 to NH_3 by an Fe–N_2 Complex Featuring a C-Atom Anchor. *J. Am. Chem. Soc.* **2014,** *136* (3), 1105-1115.

141. Rittle, J.; Peters, J. C., Fe–N_2/CO complexes that model a possible role for the interstitial C atom of FeMo-cofactor (FeMoco). *Proc. Natl. Acad. Sci. U. S. A.* **2013,** *110* (40), 15898-15903.

142. Grunenberg, J., The Interstitial Carbon of the Nitrogenase FeMo Cofactor is Far Better Stabilized than Previously Assumed. *Angew. Chem. Int. Ed.* **2017,** *56* (25), 7288-7291.

143. Rees, J. A.; Bjornsson, R.; Kowalska, J. K.; Lima, F. A.; Schlesier, J.; Sippel, D.; Weyhermuller, T.; Einsle, O.; Kovacs, J. A.; DeBeer, S., Comparative electronic structures of nitrogenase FeMoco and FeVco. *Dalton Trans.* **2017,** *46* (8), 2445-2455.

144. Formanuik, A.; Ariciu, A.-M.; Ortu, F.; Beekmeyer, R.; Kerridge, A.; Tuna, F.; McInnes, E. J. L.; Mills, D. P., Actinide covalency measured by pulsed electron paramagnetic resonance spectroscopy. *Nat. Chem.* **2017,** *9* (6), 578-583.

145. Potapov, A.; Lancaster, K. M.; Richards, J. H.; Gray, H. B.; Goldfarb, D., Spin Delocalization Over Type Zero Copper. *Inorg. Chem.* **2012,** *51* (7), 4066-4075.

146. Bersohn, R.; Shulman, R. G., Measures of Covalency in Transition-Metal Chlorides. *J. Chem. Phys.* **1966,** *45* (6), 2298-2303.

147. Lukoyanov, D.; Pelmenschikov, V.; Maeser, N.; Laryukhin, M.; Yang, T. C.; Noodleman, L.; Dean, D. R.; Case, D. A.; Seefeldt, L. C.; Hoffman, B. M., Testing if the Interstitial Atom, X, of the Nitrogenase Molybdenum−Iron Cofactor Is N or C: ENDOR, ESEEM, and DFT Studies of the S = 3/2 Resting State in Multiple Environments. *Inorg. Chem.* **2007,** *46* (26), 11437-11449.

148. Dey, A.; Glaser, T.; Couture, M. M. J.; Eltis, L. D.; Holm, R. H.; Hedman, B.; Hodgson, K. O.; Solomon, E. I., Ligand K-Edge X-ray Absorption Spectroscopy of $[Fe_4S_4]^{1+,2+,3+}$ Clusters: Changes in Bonding and Electronic Relaxation upon Redox. *J. Am. Chem. Soc.* **2004,** *126* (26), 8320-8328.

149. Chilton, N. F.; Anderson, R. P.; Turner, L. D.; Soncini, A.; Murray, K. S., PHI: A powerful new program for the analysis of anisotropic monomeric and exchange-coupled polynuclear d- and f-block complexes. *J. Comput. Chem.* **2013,** *34* (13), 1164-1175.

150. *APEX-II Version 2 User Manual, M86-E01078*. Bruker Analytical X-ray Systems: Madison, WI, 2006.

151. Sheldrick, G., *SADABS (version 2008/1): Program for Absorption Correction for Data from Area Detector Frames*. University of Göttingen: 2008.

152. Sheldrick, G., A short history of SHELX. *Acta Crystall. Sec. A* **2008,** *64* (1), 112-122.

153. Sheldrick, G., Crystal structure refinement with SHELXL. *Acta Crystall. Sec. C* **2015,** *71* (1), 3-8.

154. Dolomanov, O. V.; Bourhis, L. J.; Gildea, R. J.; Howard, J. A. K.; Puschmann, H., OLEX2: a complete structure solution, refinement and analysis program. *J. Appl. Crystallogr.* **2009,** *42* (2), 339-341.

155. Stoll, S.; Schweiger, A., EasySpin, a comprehensive software package for spectral simulation and analysis in EPR. *J. Magn. Res.* **2006,** *178* (1), 42-55.

156. Neese, F., The ORCA program system. *WIREs Comput. Mol. Sci.* **2012,** *2* (1), 73-78.

157. Klamt, A.; Schüürmann, G., COSMO: a new approach to dielectric screening in solvents with explicit expressions for the screening energy and its gradient. *J. Chem. Soc., Perkin Trans. 2* **1993,** (5), 799-805.

158. Neese, F.; Wennmohs, F.; Hansen, A.; Becker, U., Efficient, approximate and parallel Hartree–Fock and hybrid DFT calculations. A 'chain-of-spheres' algorithm for the Hartree–Fock exchange. *Chem. Phys.* **2009,** *356* (1), 98-109.

159. Neese, F., Definition of corresponding orbitals and the diradical character in broken symmetry DFT calculations on spin coupled systems. *J. Phys. Chem. Solids* **2004,** *65* (4), 781-785.

160. Neese, F., Prediction and interpretation of the 57Fe isomer shift in Mössbauer spectra by density functional theory. *Inorg. Chim. Acta* **2002,** *337*, 181-192.

161. Thompson, N. B.; Green, M. T.; Peters, J. C., Nitrogen Fixation via a Terminal Fe(IV) Nitride. *J. Am. Chem. Soc.* **2017,** *139* (43), 15312-15315.

162. Neese, F., Importance of Direct Spin−Spin Coupling and Spin-Flip Excitations for the Zero-Field Splittings of Transition Metal Complexes: A Case Study. *J. Am. Chem. Soc.* **2006,** *128* (31), 10213-10222.

163. Dugan, T. R.; Bill, E.; MacLeod, K. C.; Brennessel, W. W.; Holland, P. L., Synthesis, Spectroscopy, and Hydrogen/Deuterium Exchange in High-Spin Iron(II) Hydride Complexes. *Inorg. Chem.* **2014,** *53* (5), 2370-2380.

164. Heintz, R. A.; Theopold, K. H.; Neiss, T. G., Unusually Large Isotope Effects on NMR Chemical Shifts of Paramagnetic Organometallic Compounds. *Angew. Chem. Int. Ed.* **1994,** *33* (22), 2326-2328.

CHAPTER 6

PROBING REDOX NON-INNOCENCE IN $\{Fe=C(H)Ar\}^{10-11}$ COMPLEXES BY $^{1,2}H$ AND ^{13}C PULSE EPR

ABSTRACT

We report the synthesis and spectroscopic characterization of a series of iron-carbene complexes in redox states $\{Fe=C(H)Ar\}^{10\text{-}11}$. Pulse EPR studies of the $^{1,2}H$ and ^{13}C isotopologues of $\{Fe=C(H)Ar\}^{11}$ reveal the high covalency of the Fe-carbene bonding, leading to a more even spin distribution than commonly observed for reduced Fischer carbenes.

INTRODUCTION

One-electron reduced Fischer-type carbene species have been implicated as intermediates in a variety of organic transformations, including C-C coupling and olefin cyclopropanation.[1-2] These proposals have motivated efforts to correlate the reactivity of open-shell metal carbenoid complexes with their electronic structure. Reactivity studies reveal that reduced Fischer carbenes behave like carbon-centered radicals, engaging in hydrogen atom abstraction, radical-radical coupling, and additions to unsaturated substrates.[1-2] In accordance with these findings, computational studies indicate that the singly-occupied molecular orbitals (SOMOs) of these species are predominantly ligand-centered, with the largest contribution coming from the $2p_\pi$ orbital on the ligating carbon.[3-5] To date, however, very few radical metal-carbene complexes have been spectroscopically characterized due to their transient nature. Following reduction of $[(CO)_5M{=}C(OCH_3)Ar]$ (M = Cr, Mo, W) at low temperatures, Krusic and coworkers were able to measure the CW-EPR spectra of the corresponding metal-carbene radical anions.[5] The small deviation of the observed g values (g_{obs} = 2.0031-2.0064) from the free electron value (g_e = 2.0023) as well as the magnitude of the ^1H hyperfine coupling constants provided experimental support for the redox non-innocence of the carbene ligand. More recently, Zhang and de Bruin reported a combined DFT-EPR study on the electronic structure of two porphyrin Co-carbene radical complexes.[3] These species can be generated by the reaction of ethyldiazoacetate with a Co(II) porphyrin and detected by CW-EPR, albeit as part of a mixture with two other species.

Although computational studies uniformly indicate substantial ligand redox non-innocence in radical metal-carbene complexes, it is not yet clear on the basis of experimental data whether this trend is valid or whether there is a broad spectrum of metal vs. carbene-based redox. Pulse EPR spectroscopy has the potential to provide detailed information about the distribution of spin density in open-shell metal carbenoid species, particularly if the ligating carbon can be ^{13}C-enriched.[6-7] Herein, we describe the synthesis and spectroscopic characterization of a series of terminal iron-carbene complexes. The ^{1,2}H and ^{13}C isotopologues were studied by pulse EPR spectroscopy which, in combination with DFT calculations, revealed that Fe-carbene bonding is highly covalent, leading to a more even distribution of spin density between the metal and the ligand than is commonly observed for traditional reduced Fischer carbenes.

RESULTS AND DISCUSSION

Exposure of a black-brown solution of the diiron μ-carbyne, μ-hydride complex ($P_6ArC)Fe_2(\mu$-H)[8] in tetrahydrofuran to an atmosphere of CO is accompanied by an immediate color change to red. The ^{1}H NMR spectrum of the reaction mixture indicates clean conversion to a new diamagnetic species identified by X-ray diffraction studies as the diiron carbene, tricarbonyl complex $(P_6ArCH)Fe_2(CO)_3$ (**{Fe=C(H)Ar}^{10}** in Enemark-Feltham type notation, with the superscript denoting the sum of the iron 3*d* and carbene $\sigma+\pi$ electrons for the iron-carbene unit). The solid-state structure of **{Fe=C(H)Ar}^{10}** (Figure 1) reveals that, although both iron centers retain a trigonal bipyramidal geometry, only Fe1 remains bound to the central carbon with a short Fe1-C1 distance of 1.922(3) Å. The second iron (Fe2) is no longer bridged, and instead binds two molecules of CO. A single proton can be located in the Fourier difference map attached to C1, consistent with the observation of a diagnostic Fe=C(*H*)Ar ^{1}H NMR resonance at δ = 10.90 (d, *J* = 4 Hz, 1H). As further confirmation of this linkage, the ^{13}C resonance associated with the carbene ligand appears at δ = 229 ppm and exhibits coupling to a single proton ($^1J_{C\text{-}H}$ = 137 Hz) by gate-decoupled ^{13}C NMR.

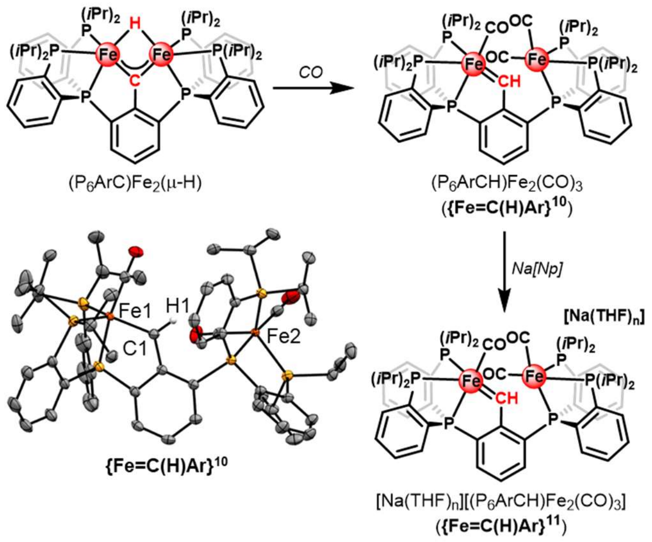

Figure 1. Synthesis and solid state structure of (P_6ArCH)$Fe_2(CO)_3$ (**{Fe=C(H)Ar}^{10}**.

When *c.a.* 50% ^{2}H-enriched (P_6ArC)Fe_2(μ-H) is reacted with CO, the intensity of the ^{1}H resonance at $\delta = 10.90$ resonance is halved, indicating that the μ-hydride ligand is the source of the Fe=C(*H*)Ar proton. We previously reported that hydrogenation of (P_6ArC)Fe_2(μ-H) proceeds through an isolable diiron carbene, dihydride species (P_6ArCH)$Fe_2(N_2)_2(H)_2$,[8] which is structurally related to **{Fe=C(H)Ar}^{10}**. In that study, however, deuterium-labeling experiments revealed that the μ-hydride ligand is *not* incorporated into the central carbon, distinct from what is observed here. Whereas H_2 activation by (P_6ArC)Fe_2(μ-H) proceeds via proton transfer or σ-bond metathesis, coordination of CO by (P_6ArC)Fe_2(μ-H) is evidently accommodated by direct C-H reductive elimination. To the best of our knowledge, this mode of reactivity has not been reported previously for diiron μ-carbyne complexes.

Insight into the electronic structure of **{Fe=C(H)Ar}^{10}** was obtained by ^{57}Fe Mössbauer spectroscopy in combination with DFT calculations. Three limiting electronic structure descriptions can be envisioned for **{Fe=C(H)Ar}^{10}**. Formally, at least, the ligand is dianionic, which would imply that the metal oxidation states are either 2Fe(I) or Fe(II)Fe(0). Alternatively, however, the arylcarbene ligand may be considered as a neutral *L*-type donor (i.e. a Fischer carbene),[9] leading to an oxidation state assignment of 2Fe(0). The ^{57}Fe Mössbauer spectrum of **{Fe=C(H)Ar}^{10}** (Figure 2) is composed of two sharp quadrupole doublets with δ_1 = -0.03 mm s^{-1}, $|\Delta E_Q|_1$ = 2.01 mm s^{-1} (orange) and δ_2 = -0.11 mm s^{-1}, $|\Delta E_Q|_2$ = 0.94 mm s^{-1} (blue). DFT calculations on the *mononuclear* fragments $(P_3)Fe^0(CO)_2$ (δ_{calc} = -0.00 mm s^{-1}, $|\Delta E_Q|_{calc}$ = 2.04 mm s^{-1}) and (P_3)Fe=C(H)Ar (δ_{calc} = -0.11 mm s^{-1}, $|\Delta E_Q|_{calc}$ = 0.77 mm s^{-1}) accurately reproduce the experimental parameters, inconsistent with a 2Fe(I) oxidation state assignment.

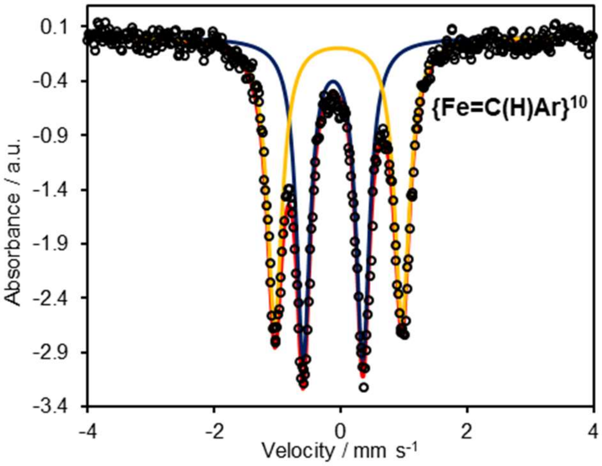

Figure 2. Zero-field ^{57}Fe Mössbauer spectrum of $(P_6ArCH)Fe_2(CO)_3$ (**{Fe=C(H)Ar}^{10}**) collected at 80 K.

Ambiguity remains, however, regarding the *d* electon count of the iron-carbene motif. The calculated frontier molecular orbitals of the (P_3)Fe=C(H)Ar fragment (Figure 3) include three filled orbitals with predominant Fe character (53-70%). These include orbitals of $3d_{xz,yz}$ parentage (HOMO-2 and HOMO-3) that engage in π-backbonding with the axial CO ligand as well as an orbital derived from Fe $3d_{x^2-y^2}$ (HOMO), which is largely non-bonding due to d/p mixing. In addition to these, the Fe=C(H)Ar π-bonding orbital (HOMO-1) appears just below the HOMO in energy and also has substantial Fe character (30%). The lowest unoccupied orbital (LUMO) associated with the (P_3)Fe=C(H)Ar motif is the iron-carbene πantibonding orbital. In contrast to most Fischer-type carbene complexes, this orbital is not predominantly localized on the ligating carbon, but is more evenly distributed between Fe (24%), C1 (14%) and the aryl substituent. These calculations indicate that the bonding within the Fe=C(H)Ar fragment of **{Fe=C(H)Ar}^{10}** is considerably more covalent than that in traditional Fischer-type carbene complexes, suggesting that both d^6 Fe^{II}=C(H)Ar and d^8 Fe^0←:C(H)Ar are significant resonance contributors.

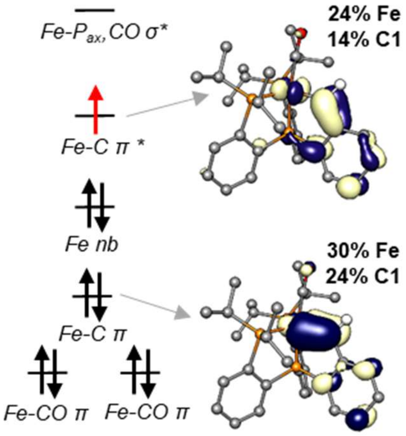

Figure 3. Qualitative molecular orbital diagram for $(P_6ArCH)Fe_2(CO)_3$ (**{Fe=C(H)Ar}^{10}**, black) and $[Na(THF)_n][(P_6ArCH)Fe_2(CO)_3]$ (**{Fe=C(H)Ar}^{11}**, red). Reduction to **{Fe=C(H)Ar}^{11}** places an additional electron (red) in the Fe-C π* orbital. Orbital plots (isovalue = 0.05) and population analysis are shown for key Fe-C interactions.

The accessibility of the low-lying Fe=C(H)Ar π^* orbital motivated us to target the radical anion $[(P_6ArCH)Fe_2(CO)_3]^-$ (**{Fe=C(H)Ar}^{11}**). The cyclic voltammogram of **{Fe=C(H)Ar}^{10}** in tetrahydrofuran (0.1 M $[n\text{Bu}_4\text{N}][\text{PF}_6]$) exhibits three reversible redox events, including two oxidative features at -0.64 V and -0.99 V (vs. Fc/Fc$^+$), respectively, and one reductive feature at -2.70 V (vs. Fc/Fc$^+$). Reduction of **{Fe=C(H)Ar}^{10}** on preparative scale with sodium napthalenide (Na[Np]) leads to a shift in the vibrational frequency associated with only one of the coordinate CO ligands, suggesting that reduction is localized on the (P_3)Fe=C(H)Ar fragment. Although the presumed product $[Na(THF)_n][(P_6ArCH)Fe_2(CO)_3]$

(**{Fe=C(H)Ar}^{11}**) is NMR-silent, it exhibits a characteristic EPR signal (Figure 4) with *g* = [2.048, 2.018, 2.0125], as determined by simulation of both X- and Q-band data. This species proved challenging to crystallize and does not appear to be indefinitely stable, so further characterization was conducted on samples prepared *in situ* at low temperatures.

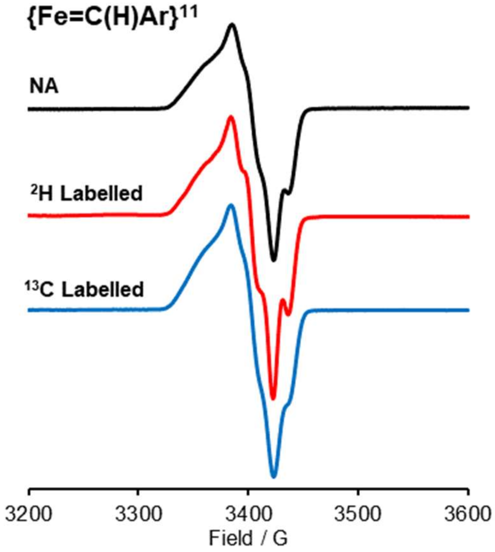

Figure 4. X-band CW EPR Spectra of [Na(THF)$_n$][(P$_6$ArCH)Fe$_2$(CO)$_3$] (**{Fe=C(H)Ar}^{11}**, black), [Na(THF)$_n$][(P$_6$ArC^{2}H)Fe$_2$(CO)$_3$] (**{Fe=C(^{2}H)Ar}^{11}**, red), and [Na(THF)$_n$][(P$_6$Ar^{13}CH)Fe$_2$(CO)$_3$] (**{Fe=^{13}C(H)Ar}^{11}**, blue), all 2 mM in 2-MeTHF. Acquisition parameters: temperature = 77 K; MW frequency = 9.639 GHz; MW power = 2 mW; modulation frequency = 100 kHz; modulation amplitude = 0.4 mT; conversion time = 82 ms.

The *g* tensor associated with **{Fe=C(H)Ar}^{11}** exhibits anisotropy indicative of substantial metal-based spin. To directly evaluate the degree of metal vs. ligand radical character, EPR studies were conducted on the ^{2}H and ^{13}C isotopologues **{Fe=C(^{2}H)Ar}^{11}** and **{Fe=^{13}C(H)Ar}^{11}**, respectively. The continuous-wave (CW) EPR spectra of the natural abundance, ^{2}H-enriched, and ^{13}C-labelled samples are nearly identical (Figure 4), indicating that the observed splitting is due to ^{31}P hyperfine coupling alone. Instead, the smaller ^{2}H and ^{13}C couplings were determined by Q-band electron nuclear double resonance (ENDOR) and hyperfine sublevel correlation (HYSCORE) measurements. Simulation of the ^{2}H-^{1}H difference HYSCORE spectra of **{Fe=C(^{2}H)Ar}^{11}** affords an anisotropic deuterium hyperfine tensor $A(^2\mathrm{H}) = \pm[0.8, 2.3, 2.0]$ MHz, rotated by $(\alpha,\beta,\gamma)^{\circ} = (40, 30, 0)^{\circ}$ relative to the coordinate frame of the g tensor. Scaling the ^{2}H hyperfine tensor by the proportion of the ^{1}H/^{2}H gyromagnetic ratios ($^1\mathrm{H}\gamma/^2\mathrm{H}\gamma = 6.514/1$) provides the ^{1}H hyperfine tensor $A(^1\mathrm{H}) = \pm[5.5, 15, 13]$ MHz for **{Fe=C(H)Ar}^{11}**, which is consistent with simulations of the ENDOR spectra for the natural abundance sample.

The proton hyperfine tensor of **{Fe=C(H)Ar}^{11}** can be decomposed into an isotropic contribution $a_{\mathrm{iso}}(^1\mathrm{H}) = \pm11.2$ MHz and a nearly axial anisotropic component $T(^1\mathrm{H}) = \pm[-5.7, 3.8, 1.8]$ MHz. The isotropic coupling arises from spin polarization of the core H 1*s* electrons and, compared to the expected value for a hydrogen atom ($a_{\mathrm{iso}}^{0} = 1420$ MHz),[10-11], corresponds to a H 1*s* spin density of only *c.a.* 0.008 e^-. On the other hand, the anisotropic ^{1}H hyperfine is attributable to dipolar interactions with the metal- and ligand-based spin. In the principal axis system of the proton hyperfine interaction, the through-space coupling can be calculated according to equation 1-2:

$$T(^1\mathrm{H})_{\mathrm{calc}} = t_{\mathrm{dioolar}}[2\ -1\ -1] \quad (1)$$

$$t_{\mathrm{dipolar}} = K\mu_0\mu_{\mathrm{B}}\mu_{\mathrm{N}}g_{\mathrm{e}}g_{\mathrm{N}}/4\pi\mathrm{h}r^3 \quad (2)$$

Where K is the spin projection factor of the spin-bearing atom, μ_0 is the vacuum permeability, μ_{B} is the Bohr magneton, μ_{N} is the nuclear magneton, g_{e} is the electronic g-factor, g_{N} is the nuclear g-factor and r is the distance between the proton and the spin-bearing atom.

Thus, in combination with DFT calculations, simulation of $T(^1\mathrm{H})$ using a point dipole model provides a means to validate structural and electronic assignments for **{Fe=C(H)Ar}^{11}**. Geometry optimization of the *mononuclear* fragment $[(\mathrm{P}_3)\mathrm{Fe{=}C(H)Ar}]^-$ provides an estimate for the Fe-H distance of 2.7 Å, from which $T(^1\mathrm{H})_{\mathrm{calc}} = [16, -8, -8]$ MHz can be determined assuming Fe1 bears all of the α spin. However, Loewdin population analysis for the truncated model $[(P_3)Fe{=}C(H)Ar]^-$ suggests that the spin density of Fe1 is only *c.a.* 0.40 e^-. This implies that $K_{Fe} = 0.4$ and, neglecting all other spin-carrying atoms, reduces the magnitude of the principal components of $T(^1H)_{calc}$ to [6.6, -3.3, -3.3] MHz, which is in reasonable agreement with the experimental tensor $T(^1H) = [5.7, -3.8, -1.8]$ MHz.

Simulations of the HYSCORE spectra (Figure 5) of the ^{13}C-labelled compound **{Fe=^{13}C(H)Ar}**^{11} provide an anisotropic hyperfine tensor $A(^{13}C) = \pm[14, -2, -12]$ MHz for the ligating carbon. From $A(^{13}C)$, it can be inferred that the isotropic coupling to the carbene ligand in **{Fe=^{13}C(H)Ar}**^{11} is negligible ($a_{iso}(^{13}C) \approx 0$ MHz). Although ^{13}C hyperfine couplings have not been reported for any metal-carbene species, comparison can be made to the benzyl radical, for which a proton replaces iron. Room temperature CW-EPR studies of the 90% $^{13}C_7$-enriched benzyl radical revealed a significantly larger isotropic coupling ($a_{iso}(^{13}C_7) \approx 68.7$ MHz) to the tolyl carbon.[12] Two synthetic iron-carbyne complexes have also been ^{13}C enriched and exhibit non-negligible isotropic couplings of *c.a.* 32 MHz.[6-7] Evidently, spin polarization of the C 2*s* electrons in **{Fe=^{13}C(H)Ar}**^{11} is minimal, perhaps due to the relatively small C $2p_\pi$ spin density (*vide infra*).

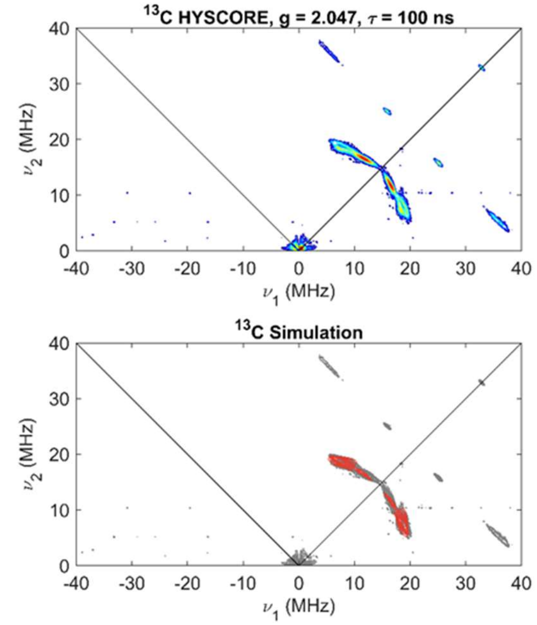

Figure 5. Q-band ^{13}C-natural abundance difference HYSCORE spectrum of $[Na(THF)_n][(P_6Ar^{13}CH)Fe_2(CO)_3]$ (**{Fe=^{13}C(H)Ar}^{11}**) acquired at g = 2.047. Bottom: Monochromatic representation of the HYSCORE data (grey) with ^{13}C simulations overlaid (red) using parameters given in the text.

The anisotropic contribution to the ^{13}C hyperfine in **{Fe=^{13}C(H)Ar}^{11}** $T(^{13}C) = \pm[14, -2, -12]$ MHz arises from local 2*p* contributions, in addition to dipolar interactions with the spin localized at the adjacent atoms.[10] The anisotropic tensor $T(^{13}C)$ can be decomposed into two axial terms, affording $b_\pi(^{13}C) = 8.7$ MHz and $t_{dipolar}(^{13}C) = 3.3$ MHz. The latter term reflects the strength of the through-space interactions with iron-based spin and is in reasonable agreement with a value of 2.2 MHz predicted using the point dipole model assuming $K_{Fe} = 0.4$. On the other hand, the magnitude of $b_\pi(^{13}C) = 8.7$ MHz reflects the local C $2p_\pi$ spin density at the ligating carbon, which can be estimated at *c.a.* 0.1 e^- by comparison to the intrinsic coupling expected for an electron localized in a C 2*p* orbital ($b_\pi^0 = 90.8$ MHz)[10].

CONCLUSIONS

Consistent with our interpretation of the ^{13}C EPR data, DFT calculations predict an isotropic ^{13}C coupling of only 2 MHz and a total C1 spin density of only 0.15 e^- for the mononuclear model $[(P_3)Fe{=}C(H)Ar]^-$. Instead, DFT indicates that there is substantial spin density localized at the carbene-bound Fe center (*c.a.* 0.4 e^-), in line with simulations of $T(^1H)$. These findings are in contrast with what has been reported for radical metal-carbenoid species to date.[1, 3-5] For example, calculations by Krusic and coworkers on the radical anion $[(CO)_5Cr{=}C(OCH_3)Ar]^-$ indicate that the spin density is biased toward the ligating carbon (65%), with little accumulated at the metal center (*c.a.* 4% on Cr).[5] This description is validated by the fact that the experimental ^1H couplings in $[(CO)_5Cr{=}C(OCH_3)Ar]^-$ are nearly identical to those observed in the benzylic radical $[HC(OCH_3)Ar]^\cdot$, as well as the lack of large ^{53}Cr coupling in $[(CO)_5Cr{=}C(OCH_3)Ar]^-$. This dichotomy highlights the enhanced Fe-C covalency in **$\{Fe{=}C(H)Ar\}^{10/11}$** compared to more traditional Fischer-type carbenes. The unique electronic structure of **$\{Fe{=}C(H)Ar\}^{10/11}$** may lead to unusual reactivity in both redox states, which will be the subject of future investigations.

EXPERIMENTAL DETAILS

General Considerations. All reactions were performed at room temperature in a nitrogen filled M. Braun glovebox or using standard Schlenk techniques unless otherwise specified. Glassware was oven dried at 140°C for at least two hours prior to use, and allowed to cool under vacuum. Complex $(P_6ArC)Fe_2H$ was prepared as previously described.[8] All other reagents were obtained commercially unless otherwise noted and typically stored over activated 4 Å molecular sieves. Tetrahydrofuran, toluene-d_8 and benzene-d_6 were dried using sodium/benzophenone ketyl, degassed with three freeze-pump-thaw cycles, vacuum transferred, and stored over 3 Å molecular sieves prior to use. Diethyl ether, benzene, toluene, acetonitrile, hexanes, and pentane were dried by sparging with nitrogen for at least 15 minutes, then passing through a column of activated A2 alumina under positive nitrogen pressure. ^{1}H and ^{31}P NMR spectra were recorded on a Varian 300 or 400 MHz spectrometer. All chemical shifts (δ) are reported in ppm, and coupling constants (*J*) are in hertz. The ^{1}H-NMR spectra were referenced using residual H impurity in the deuterated solvent. UV-Vis spectra were recorded on a Varian Cary Bio 50 spectrophotometer. Elemental analyses were performed at Caltech.

Physical Methods

Mössbauer Measurements. Zero field ^{57}Fe Mössbauer spectra were recorded in constant acceleration on a spectrometer from See Co (Edina, MN) equipped with an SVT-400 cryostat (Janis, Wilmington, WA). The quoted isomer shifts are relative to the centroid of the spectrum of α-Fe foil at room temperature. Samples were prepared in 2-MeTHF and transferred to a Delrin cup. The data were fitted to Lorentzian lineshapes using the program WMOSS (www.wmoss.org).

X-ray Crystallography. For compounds **{Fe=C(H)Ar}$^{\mathbf{10}}$**, low-temperature (100 K) diffraction data (φ-and ω-scans) were collected on a Bruker AXS D8 VENTURE KAPPA diffractometer coupled to a PHOTON 100 CMOS detector with Mo Kα radiation (λ = 0.71073 Å) or with Cu Kα (*λ* = 1.54178 Å). All diffractometer manipulations, including data collection, integration, and scaling were carried out using the Bruker APEXII software.[14] Absorption corrections were applied using SADABS.[15] Structures were solved by direct methods using SHELXS[16] and refined against *F*2 on all data by full-matrix least squares with SHELXL-2014[17] interfaced with Olex2-1.2.8[18] and using established refinement techniques. All non-hydrogen atoms were refined anisotropically, except heavily disordered solvent in some cases. Hydrogen atoms were included into the model at geometrically calculated positions and refined using a riding model, except for the carbene C-*H*. The isotropic displacement parameters of all hydrogen atoms were fixed to 1.2 times the *U* value of the atoms they are linked to (1.5 times for methyl groups).

EPR. Continuous wave (CW) X-band EPR spectra were obtained on a Bruker EMX spectrometer. Cryogenic temperatures were achieved using an Oxford Instruments ESR-900 liquid helium flow cryostat and an ITC-503 temperature controller. Pulse EPR spectroscopy: All pulse Q-band (34 GHz) EPR, electron nuclear double resonance (ENDOR) and hyperfine sublevel correlation spectroscopy (HYSCORE) experiments were acquired using a Bruker ELEXSYS E580 pulse EPR spectrometer equipped a Bruker D-2 Q-band ENDOR resonator. Temperature control was achieved using an ER 4118HV-CF5-L Flexline Cryogen-Free VT cryostat manufactured by ColdEdge equipped with an Oxford Instruments Mercury ITC temperature controller.

Q-band pulse electron spin-echo detected EPR (ESE-EPR) field-swept spectra were acquired using the 2-pulse "Hahn-echo" sequence ($\pi/2 - \tau - \pi$ – echo).

Q-band inversion recovery data were acquired using the 3-pulse inversion recovery sequence sequence ($\pi - T - \pi/2 - \tau - \pi$ – echo), where T is varied and τ is a fixed delay.

Q-band pulse ENDOR spectra were acquired using the Davies pulse sequence ($\pi - T_{RF} - \pi_{RF} - t_{RF} - \pi/2 - \tau - \pi$ – echo), where T_{RF} is the delay between mw pulses and RF pulses, π_{RF} is the length of the RF pulse and the RF frequency is randomly sampled during each pulse sequence. For all ENDOR scans the same t_{RF} of 1 μs was used, all other acquisition parameters are detailed in the caption for each ENDOR figure.

Q-band HYSCORE spectra were acquired using the 4-pulse sequence ($\pi/2 - \tau - \pi/2 - t_1 - \pi - t_2 - \pi/2$ – echo), where τ is a fixed delay, while t_1 and t_2 are independently incremented by Δt_1 and Δt_2, respectively. The time domain data was baseline-corrected (third-order polynomial) to eliminate the exponential decay in the echo intensity, apodized with a Hamming window function, zero-filled to eight-fold points, and fast Fourier-transformed to yield the 2-dimensional frequency domain. For ^{2}H-^{1}H and ^{13}C-^{12}C. difference spectra, the time domain of the HYSCORE spectrum of the natural abundance sample was subtracted from that of the isotopically-enriched sample, and the same data processing procedure detailed above was used to generate the frequency spectrum.

In general, the ENDOR spectrum for a given nucleus with spin I= ½ (^{1}H) coupled to the S = ½ electron spin exhibits a doublet at frequencies

$$\nu_{\pm} = \left|\frac{A}{2} \pm \nu_N\right| \tag{E1}$$

where ν_N is the nuclear Larmor frequency, and A is the hyperfine coupling. For nuclei with $I \geq 1$ (^{14}N, ^{2}H), an additional splitting of the $\nu_{\pm}$ manifolds is produced by the nuclear quadrupole interaction (P).

$$\nu_{\pm,m_I} = \left|\nu_N \pm \frac{3P(2m_I - 1)}{2}\right| \tag{E2}$$

In HYSCORE spectra, these signals manifest as cross-peaks or ridges in the 2-D frequency spectrum which are generally symmetric about the diagonal of a given quadrant. This technique allows hyperfine levels corresponding to the same electron-nuclear submanifold to be differentiated, as well as separating features from hyperfine couplings in the weak-coupling regime ($|A| < 2|\nu_I|$) in the (+,-) quadrant from those in the strong coupling regime ($|A| > 2|\nu_I|$) in the (-,-) quadrant. The (-,-) and (+,-) quadrants of these frequency spectra are symmetric to the (+,+) and (-,+) quadrants, thus only two of the quadrants are typically displayed in literature. For systems with appreciable hyperfine anisotropy in frozen solutions or solids, HYSCORE spectra typically do not exhibit sharp cross peaks, but show ridges that represent the sum of cross peaks from selected orientations at the magnetic field position at which the spectrum is collected. The length and curvature of these correlation ridges allow for the separation and estimation of the magnitude of the isotropic and dipolar components of the hyperfine tensor, as shown in Figure S1.

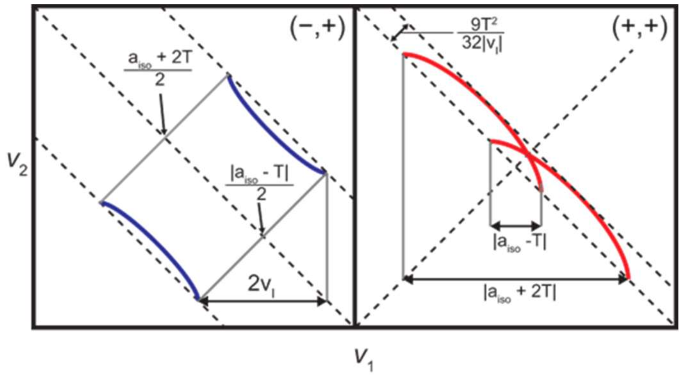

Figure S1. HYSCORE powder patterns for an $S = 1/2$, $I = 1/2$ spin system with an axial hyperfine tensor which contains isotropic (a_{iso}) and dipolar (T) contributions. Blue correlation ridges represent the strong coupling case; red correlation ridges represent the weak coupling case.

For weakly-coupled nuclei ($A < 2\nu_I$), ν_α and ν_β are both positive, appearing in the (+,+) quadrant, while for strongly-coupled nuclei they will show up in the (−,+) quadrant. In the intermediate coupling regime where $A \approx 2\nu_I$, peaks will often appear in both the (+,+) and (−,+) quadrants of the HYSCORE spectrum.

All EPR spectra (CW, ENDOR, HYSCORE) were simulated using the EasySpin[19] simulation toolbox (version 5.2.25) with Matlab 2019a using the following Hamiltonian:

$$\hat{H} = \mu_B \vec{B}_0 g \hat{S} + \mu_N g_N \vec{B}_0 \hat{I} + h\hat{S} \cdot \boldsymbol{A} \cdot \hat{I} + h\hat{I} \cdot \boldsymbol{P} \cdot \hat{I} \qquad \text{(E3)}$$

In this expression, the first term corresponds to the electron Zeeman interaction term where μ_B is the Bohr magneton, g is the electron spin g-value matrix with principle components g =

$[g_{xx}, g_{yy}, g_{zz}]$, and $\hat{S}$ is the electron spin operator; the second term corresponds to the nuclear Zeeman interaction term where μ_N is the nuclear magneton, g_N is the characteristic nuclear g-value for each nucleus (e.g. ^{1}H,^{2}H,^{31}P), and $\hat{I}$ is the nuclear spin operator; the third term corresponds to the electron-nuclear hyperfine term, where $\boldsymbol{A}$ is the hyperfine coupling tensor with principle components $\boldsymbol{A}$ = [A_{xx} A_{yy} A_{zz}]; and for nuclei with $I \geq 1$, the final term corresponds to the nuclear quadrupole (NQI) term which arises from the interaction of the nuclear quadrupole moment with the local electric field gradient (efg) at the nucleus, where $\boldsymbol{P}$ is the quadrupole coupling tensor. In the principle axis system (PAS), $\boldsymbol{P}$ is traceless and parametrized by the quadrupole coupling constant e^2Qq/h, and the asymmetry parameter η such that:

$$\boldsymbol{P} = \begin{pmatrix} P_{xx} & 0 & 0 \\ 0 & P_{yy} & 0 \\ 0 & 0 & P_{zz} \end{pmatrix} = \frac{e^2Qq/h}{4I(2I-1)} \begin{pmatrix} -(1-\eta) & 0 & 0 \\ 0 & -(1+\eta) & 0 \\ 0 & 0 & 2 \end{pmatrix} \tag{E4}$$

where $\frac{e^2Qq}{h} = 2I(2I-1)P_{zz}$ and $\eta = \frac{P_{xx}-P_{yy}}{P_{zz}}$. The asymmetry parameter may have values between 0 and 1, with 0 corresponding to an electric field gradient with axial symmetry and 1 corresponding to a fully rhombic efg.

The orientations between the hyperfine and NQI tensor principle axis systems and the g-matrix reference frame are defined by the Euler angles (α, β, γ), with rotations performed within the zyz convention, where α rotates xyz counterclockwise about z-axis to give x'y'z', β rotates x'y'z counterclockwise about y'-axis to give x",y",z", γ rotates xyz counterclockwise about z"-axis to give final frame orientation.

DFT Calculations. Calculations were carried out using version 4.0.2 of the ORCA package.[20] Geometry optimizations were conducted using the TPSS functionals in combination with the scalar relativistically recontracted versions of the def2-SVP (ZORA-def2-SVP) basis set on most C and H atoms. An enlarged basis set (ZORA-def2-TZVP) was employed for the Fe and P atoms, the iron-bound C and H ligands as well as any C atoms of the central aryl linker which undergo significant distortion in the solid-state structure. For all atoms, the general-purpose segmented all-electron relativistically contracted auxiliary Coulomb-fitting basis (SARC/J) was employed. Solvation was modeled with CPCM in tetrahydrofuran.[21] Optimizations were followed by a frequency calculation to ensure a true minimum. Single point energy calculations for were conducted TPSS and employed the enlarged ZORA-def-TZVPP basis set on Fe, P, and special C/H atoms enumerated above. Calculations with hybrid functionals used the RIJCOSX approximation.[22]

For DFT calculations of Mössbauer parameters,[24] the TPSSh functional was used in combination with the ZORA-def2-TZVP basis set on most C and H atoms. The CP(PPP) basis set was employed for Fe and the IGLO-III basis set was utilized for P and the iron-bound C and H ligands as well as any C atoms of the central aryl linker which undergo significant distortion in the solid-state structure. The general purpose def2/J Coulomb fitting basis was employed on atoms using the def2-TZVPbasis, while the AutoAux feature of ORCA was used to generate auxiliary bases for the other atoms. All auxiliary bases were fully decontracted. To capture core polarization effects, the radial integration accuracy was increased around the Fe, P, and the iron-bound C and H ligands (IntAcc 7). A previously-reported calibration[25] was used to convert the computed Fe core electron density to the isomer shift (δ) in units of mm s^{-1}; estimates of the uncertainty in the computed values of δ and ΔE_Q were obtained from this calibration.

Synthetic Procedures. *Preparation of* $(P_6ArCH)Fe_2(CO)_3$ *(*$\{Fe{=}C(H)Ar^{10}$*).* A Schlenk tube was charged with $(P_6ArC)Fe_2H$, which was then dissolved in tetrahydrofuran (10 mL). The tube was degassed on the Schlenk line with three freeze-pump-thaw cycles. Carbon monoxide was admitted to the tube at room temperature, resulting in an immediate color change from black-brown to red-brown. After stirring for 30 minutes, the soluton was concentrated *in vacuo*, affording **{Fe=C(H)Ar^{10}}** quantitatively in spectroscopically pure form. Crystals suitable for X-ray diffraction were obtained by diffusion of pentane vapors into a concentrated solution of **{Fe=C(H)Ar^{10}}** in tetrahydrofuran at -35 °C. ^{1}H NMR (400 MHz, C_7D_8) δ = 10.90 (d, *J* = 4 Hz, 1H), 8.12 (t, *J* = 8 Hz, 2H), 7.47 (t, *J* = 8 Hz, 1H), 7.41 (d, *J* = 4 Hz, 2H), 7.32 (t, *J* = 4 Hz, 2H), 7.14 (s, 2H), 7.09-7.00 (m, 6H), 6.87-6.79 (m, 3H), 6.60 (t, *J* = 8 Hz, 1H), 2.61 (broad septet, 2H), 2.46 (broad septet, 2H), 2.11 (broad septet, 2H), 1.88 (broad septet, 2H), 1.51 (m, 12H), 1.23 (dd, *J* = 4 Hz, 8 Hz, 6H), 1.09-1.00 (m, 12H), 0.87-0.79 (m, 12H), 0.39 (dd, *J* = 4 Hz, 8 Hz, 6H). ^{31}P{^{1}H} NMR (162 MHz, C_6D_6) δ = 129.58 (td, *J* = 5 Hz, 37 Hz, 1P), 123.64 (td, *J* = 5 Hz, 58 Hz, 1P), 110.39 (broad d, *J* = 60 Hz, 2P), 105.64 (d, *J* = 37 Hz, 2P). UV-Vis (THF) [ε (M^{-1} cm^{-1})]: 293 nm (1.5 x 10^4), 414 nm (1.2 x 10^4).

Preparation of $[Na(THF)_n][(P_6ArCH)Fe_2(CO)_3]$ *({Fe=C(H)Ar}^{11}).* Due to its thermal sensitivity, solutions of $[Na(THF)_n][(P_6ArCH)Fe_2(CO)_3]$ were prepared *in situ* for spectroscopic study.

Preparation of $(P_6ArCD)Fe_2(CO)_3$. Using $(P_6ArC)Fe_2(D)$, $(P_6ArCD)Fe_2(CO)_3$ was prepared in a manner analogous to that reported for $(P_6ArCH)Fe_2(CO)_3$.

Preparation of $(P_6Ar^{13}CH)Fe_2(CO)_3$. Using $(P_6Ar^{13}C)Fe_2(H)$, $(P_6Ar^{13}CH)Fe_2(CO)_3$ was prepared in a manner analogous to that reported for $(P_6ArCH)Fe_2(CO)_3$.

Preparation of $[Na(THF)_n][(P_6ArCD)Fe_2(CO)_3]$. Using $(P_6ArCD)Fe_2(CO)_3$, $[Na(THF)_n][(P_6ArCD)Fe_2(CO)_3]$ was prepared in a manner analogous to that reported for $[Na(THF)_n][(P_6ArCH)Fe_2(CO)_3]$.

Preparation of $[Na(THF)_n][(P_6Ar^{13}CH)Fe_2(CO)_3]$. Using $(P_6Ar^{13}CH)Fe_2(CO)_3$, $[Na(THF)_n][(P_6Ar^{13}CH)Fe_2(CO)_3]$ was prepared in a manner analogous to that reported for $[Na(THF)_n][(P_6ArCH)Fe_2(CO)_3]$.

Special Refinement Details for (P_6ArCH)$Fe_2(CO)_3$. Complex **{Fe=C(H)Ar^{10}}** crystallizes in the space group *P*-1 with one molecule in the asymmetric unit and one molecule of co-crystallized tetrahydrofuran. Electron density corresponding to the carbene C-H could be located in the diffraction map. There is additionally some heavily disordered solvent which could not be modelled satisfactorily and was instead masked in Olex.

References

1. Dzik, W. I.; Zhang, X. P.; de Bruin, B., Redox Noninnocence of Carbene Ligands: Carbene Radicals in (Catalytic) C−C Bond Formation. *Inorg. Chem.* **2011,** *50* (20), 9896-9903.
2. Sierra, M. A.; Gómez-Gallego, M.; Martínez-Álvarez, R., Fischer Carbene Complexes: Beautiful Playgrounds To Study Single Electron Transfer (SET) Reactions. *Eur. J. Chem.* **2007,** *13* (3), 736-744.
3. Dzik, W. I.; Xu, X.; Zhang, X. P.; Reek, J. N. H.; de Bruin, B., 'Carbene Radicals' in CoII(por)-Catalyzed Olefin Cyclopropanation. *J. Am. Chem. Soc.* **2010,** *132* (31), 10891-10902.
4. Dzik, W. I.; Reek, J. N. H.; de Bruin, B., Selective C-C Coupling of Ir–Ethene and Ir–Carbenoid Radicals. *Chem. Eur. J.* **2008,** *14* (25), 7594-7599.
5. Krusic, P. J.; Klabunde, U.; Casey, C. P.; Block, T. F., An electron spin resonance study of the radical anions derived from metal carbene complexes of chromium, molybdenum, and tungsten. *J. Am. Chem. Soc.* **1976,** *98* (7), 2015-2018.
6. Citek, C.; Oyala, P. H.; Peters, J. C., Mononuclear Fe(I) and Fe(II) Acetylene Adducts and Their Reductive Protonation to Terminal Fe(IV) and Fe(V) Carbynes. *J. Am. Chem. Soc.* **2019,** *141* (38), 15211-15221.
7. Arnett, C. H.; Bogacz, I.; Chatterjee, R.; Yano, J.; Oyala, P. H.; Agapie, T., Mixed Valent Diiron μ-Carbyne, μ-Hydride Complexes: Implications for Nitrogenase. *J. Am. Chem. Soc.* **2020,** *In Revision.*
8. Arnett, C. H.; Agapie, T., Activation of an Open Shell, Carbyne-Bridged Diiron Complex Toward Binding of Dinitrogen. *Journal of the American Chemical Society* **2020,** *142*, 10059-10068.
9. Hartwig, J. F., *Organotransition Metal Chemistry: From Bonding to Catalysis*. University Science Books: Mill Valley, California, 2010.
10. Wertz, J. E.; Bolton, J. R., *Electron Spin Resonance: Elementary Theory and Practical Applications*. Chapman and Hall: New York, N.Y., 1986.
11. Morton, J. R.; Preston, K. F., Atomic parameters for paramagnetic resonance data. *J. Magn. Res.* **1978,** *30* (3), 577-582.
12. Ihrig, A. M.; Jones, P. R.; Jung, I. N.; Lloyd, R. V.; Marshall, J. L.; Wood, D. E., Electron paramagnetic resonance and INDO study of carbon-13 hyperfine splitting constants in benzyl radical and toluene radical anion. *J. Am. Chem. Soc.* **1975,** *97* (16), 4477-4482.
13. Chilton, N. F.; Anderson, R. P.; Turner, L. D.; Soncini, A.; Murray, K. S., PHI: A powerful new program for the analysis of anisotropic monomeric and exchange-coupled polynuclear d- and f-block complexes. *J. Comput. Chem.* **2013,** *34* (13), 1164-1175.
14. *APEX-II Version 2 User Manual, M86-E01078*. Bruker Analytical X-ray Systems: Madison, WI, 2006.
15. Sheldrick, G., *SADABS (version 2008/1): Program for Absorption Correction for Data from Area Detector Frames*. University of Göttingen: 2008.
16. Sheldrick, G., A short history of SHELX. *Acta Crystall. Sec. A* **2008,** *64* (1), 112-122.
17. Sheldrick, G., Crystal structure refinement with SHELXL. *Acta Crystall. Sec. C* **2015,** *71* (1), 3-8.

18. Dolomanov, O. V.; Bourhis, L. J.; Gildea, R. J.; Howard, J. A. K.; Puschmann, H., OLEX2: a complete structure solution, refinement and analysis program. *J. Appl. Crystallogr.* **2009,** *42* (2), 339-341.

19. Stoll, S.; Schweiger, A., EasySpin, a comprehensive software package for spectral simulation and analysis in EPR. *J. Magn. Res.* **2006,** *178* (1), 42-55.

20. Neese, F., The ORCA program system. *WIREs Comput. Mol. Sci.* **2012,** *2* (1), 73-78.

21. Klamt, A.; Schüürmann, G., COSMO: a new approach to dielectric screening in solvents with explicit expressions for the screening energy and its gradient. *J. Chem. Soc., Perkin Trans. 2* **1993,** (5), 799-805.

22. Neese, F.; Wennmohs, F.; Hansen, A.; Becker, U., Efficient, approximate and parallel Hartree–Fock and hybrid DFT calculations. A 'chain-of-spheres' algorithm for the Hartree–Fock exchange. *Chem. Phys.* **2009,** *356* (1), 98-109.

23. Neese, F., Definition of corresponding orbitals and the diradical character in broken symmetry DFT calculations on spin coupled systems. *J. Phys. Chem. Solids* **2004,** *65* (4), 781-785.

24. Neese, F., Prediction and interpretation of the ^{57}Fe isomer shift in Mössbauer spectra by density functional theory. *Inorg. Chim. Acta* **2002,** *337*, 181-192.

25. Thompson, N. B.; Green, M. T.; Peters, J. C., Nitrogen Fixation via a Terminal Fe(IV) Nitride. *J. Am. Chem. Soc.* **2017,** *139* (43), 15312-15315.

26. Chandrasekaran, P.; Stieber, S. C. E.; Collins, T. J.; Que, J. L.; Neese, F.; DeBeer, S., Prediction of high-valent iron K-edge absorption spectra by time-dependent Density Functional Theory. *Dalton Trans.* **2011,** *40* (42), 11070-11079.

27. DeBeer George, S.; Petrenko, T.; Neese, F., Prediction of Iron K-Edge Absorption Spectra Using Time-Dependent Density Functional Theory. *J. Phys. Chem. A* **2008,** *112* (50), 12936-12943.

28. Neese, F., Importance of Direct Spin−Spin Coupling and Spin-Flip Excitations for the Zero-Field Splittings of Transition Metal Complexes: A Case Study. *J. Am. Chem. Soc.* **2006,** *128* (31), 10213-10222.

29. Dugan, T. R.; Bill, E.; MacLeod, K. C.; Brennessel, W. W.; Holland, P. L., Synthesis, Spectroscopy, and Hydrogen/Deuterium Exchange in High-Spin Iron(II) Hydride Complexes. *Inorg. Chem.* **2014,** *53* (5), 2370-2380.

30. Heintz, R. A.; Theopold, K. H.; Neiss, T. G., Unusually Large Isotope Effects on NMR Chemical Shifts of Paramagnetic Organometallic Compounds. *Angew. Chem. Int. Ed.* **1994,** *33* (22), 2326-2328.

APPENDIX A

TOWARDS SITE-DIFFERENTIATED MODELS OF THE IRON-MOLYBDENUM COFACTOR FEATURING CARBON OR SULFUR DONORS

INTRODUCTION

This appendix describes efforts to prepare and study the reactivity of site-differentiated models of FeMoco incorporating biologically relevant carbon and/or sulfur based donors.

RESULTS AND DISCUSSION

Towards Small Molecule Activation by Site-Differentiated Tetranuclear Iron Clusters. The ability of the imidazolate-supported tetranuclear iron clusters $[LFe_3O(RIm)_3Fe][OTf]_n$ (R = Ar or alkyl, n = 0-3) discussed in Chapters 2 and 3 to bind and activate small molecules other than CO was investigated in detail. Given the low CO binding affinities observed for $[LFe_3O(ArIm)_3Fe][OTf]_n$ (n = 0-3), efforts to promote coordination of N_2 were undertaken at elevated pressures. A sapphire NMR tube epoxied to an HPLC check valve was charged with the monocationic species $[LFe_3O(PhIm)_3Fe][OTf]_n$ (n = 1) and pressurized to ~2000 psi of N_2. The ^{1}H NMR spectra of the pressurized sample were invariant between 25 °C and -80 °C and identical to a spectrum taken at ambient pressures, indicating that N_2 could not be achieved under these conditions. More electron-rich isopropyl-substituted variants of the cluster, $[LFe_3O(iPrIm)_3Fe][OTf]_n$ (n = 1-2) were prepared. However, these displayed similar affinities for CO to their aryl-substituted counterparts and showed no propensity for binding of N_2.

In light of the ability of the less-reducing pyrazolate bridged clusters $[LFe_3O(PhPz)_3Fe][OTf]_2$ to accept an oxygen-atom and to hydroxylate a proximal C-H bond,[1] the reactivity of $[LFe_3O(PhIm)_3Fe][OTf]_2$ with iodosylbenzenes was explored. Surprisingly, addition of an excess of either insoluble iodosylbenzene (PhIO) or the soluble variant sPhIO to $[LFe_3O(PhIm)_3Fe][OTf]_2$ leads to little or no reaction (Scheme 1). The analogous reaction with the structurally homologous cluster $[LFe_3O(PhPz)_3Fe][OTf]_2$ proceeds instanteously with sPhIO, suggesting that lack of reactivity observed in the present case is electronic in origin.

Based on the results discussed in Chapters 2 and 3 of this thesis, it is surmised that the energy associated with internal electron transfer in [LFe$_3$O(PhIm)$_3$Fe][OTf]$_2$ may passivate the cluster toward reaction with neutral oxidants. In contrast, however, addition of tetrabutylammonium nitrite to [LFe$_3$O(PhIm)$_3$Fe][OTf]$_2$ slowly generates the 1 e$^-$ oxidized nitrosyl-bound species [LFe$_3$O(PhIm)$_3$Fe(NO)]$^{3+}$ (υ_{NO} = 1829 cm^{-1}, Scheme 1). Based on this observation, it seems that the apical Fe(III) site of [LFe$_3$O(PhIm)$_3$Fe][OTf]$_2$ has a higher affinity for anionic ligands compared to neutral donors and that substrate binding at the coordinatively unsaturated site must proceed electron transfer.

Scheme 1: Reactions of [LFe$_3$O(PhIm)$_3$Fe][OTf]$_2$ with oxidizing reagents.

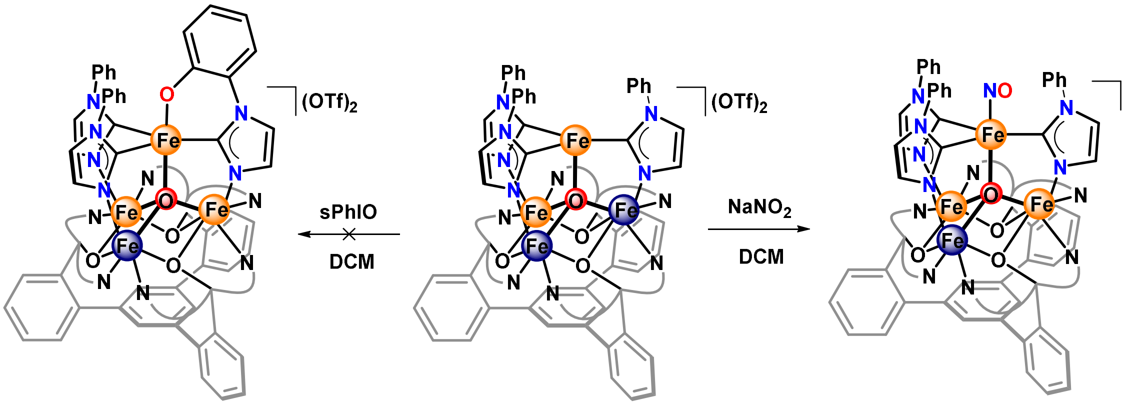

Encouraged by the ability of [LFe$_3$O(PhIm)$_3$Fe][OTf]$_2$ to reductively activate nitrite, we pursued reactivity with the azide anion. Addition of tetrabutylammonium azide to a thawing solution of [LFe$_3$O(PhIm)$_3$Fe][OTf]$_2$ immediately generates a new paramagnetic species based on changes in the ^{1}H NMR spectrum. X-ray diffraction studies demonstrated the formation of the expected azide adduct (Figure 1). Binding of the anionic N$_3^-$ ligand at the apical iron center leads to an elongation of the Fe4-O1 distance from 1.812(2) Å to 1.942(4) Å. This is accompanied by a significant contraction of one of the core Fe-O1 bond lengths from 1.984(2) Å to 1.892(4) Å. The iron-azide moiety is substantially more linear (Fe4-N-N angle: 164°) than is commonly observed (c.a. 120-140°), likely due to the steric pressure exerted by the flanking aryl substituents.

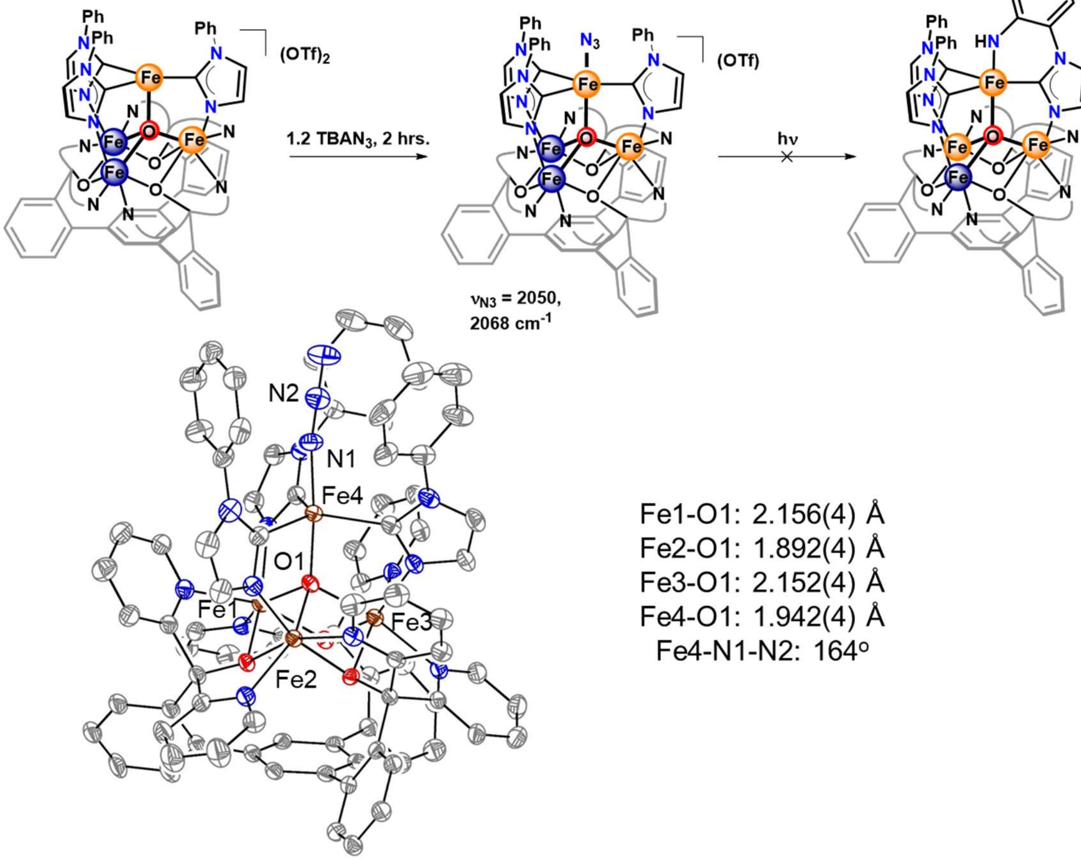

Figure 1. Preparation of [LFe$_3$O(PhIm)$_3$Fe(N$_3$)][OTf] (top). Solid state structure of [LFe$_3$O(PhIm)$_3$Fe(N$_3$)][OTf]. Ellipsoids shown at the 50% probability level. Hydrogen atoms, counterions and co-crystallized solvent omitted for clarity (bottom).

The azide adduct [LFe$_3$O(PhIm)$_3$Fe(N$_3$)][OTf] exhibited limited thermal stability. Unlike [LFe$_3$O(PhPz)$_3$Fe][OTf]$_2$, however, which becomes reduced upon exposure to azide, [LFe$_3$O(PhIm)$_3$Fe(N$_3$)][OTf] does not convert to [LFe$_3$O(PhIm)$_3$Fe)][OTf], but instead reverts back to [LFe$_3$O(PhIm)$_3$Fe][OTf]$_2$ over the course of hours. In an effort to promote more desirable reactivity, the azide complex [LFe$_3$O(PhIm)$_3$Fe(N$_3$)][OTf] was photolyzed in a frozen solvent glass. However, ^{1}H-NMR and EPR spectroscopy revealed that little if any of the azide complex is decomposed under these conditions.

Towards a Weak-Field $Fe_4(\mu_4$-C) Cluster. Previous members of our group had prepared the structurally homologous clusters $[LFe_3O(PhPz)_3Fe][OTf]_n$ (*n* = 0-3) and $[LFe_3F(PhPz)_3Fe][OTf]_n$ (*n* = 1-3), which feature interstitial oxo[2] and fluoride ligands,[3] respectively. In an effort to better understand the effect of the identity of the interstitial atom on the reactivity and electronic structure of FeMoco, which hosts a μ_6-C^{4-} donor in its core,[4] we sought to prepare clusters of the form $[LFe_3C(PhPz)_3Fe][OTf]_n$. These attempts proved unsuccessful, in spite of surveying a wide variety of potential C_1 precursors (Scheme 2). Reactions of the trinuclear complexes $LFe_3(OAc)_3$ or $LFe_3(OTf)_2(OAc)$ with several different halomethanes, including but not limited to CI_4 and $CHBr_3$, and reductants were explored but failed to yield tractable product mixtures. This was true even when a fourth iron equivalent and/or pyrazolate ligands were included from the outset of the reaction though, on occasion, the oxo cluster $[LFe_3O(PhPz)_3Fe][OTf]_n$ could be detected in small quantities. In other cases, ligand or metal scrambling was observed, affording products such as $LFe_3(OAc)_2(OTf)$ following treatment of $LFe_3(OTf)_2(OAc)$ with trimethylsilyldiazomethane or $[LFe_3O(OAc)_3Fe]$ upon reaction of $LFe_3(OAc)_3$ with $LiC(SiMe_3)_3$. In the latter case, there was no evidence for the formation of trimethylsilyl acetate by ^{1}H NMR spectroscopy. New paramagnetic products were obtained from the reaction of $LFe_3(OTf)_2(OAc)$ with 3 equiv. of either methyl lithium or trimethylsilylmethyl lithium. However, efforts to obtain solid state structural characterization of these species or to elaborate them into higher nuclearity clusters proved unsuccessful.

Scheme 2: Summary of efforts to prepare the μ_4-carbide cluster $[LFe_3C(PhPz)_3Fe]^{n+}$

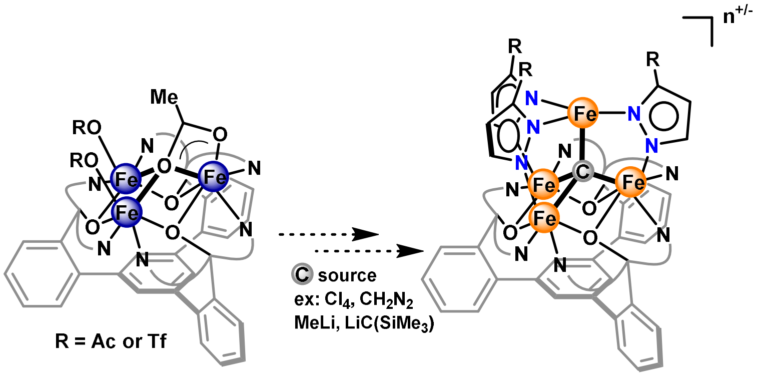

Towards Site-Differentiated Tetranuclear Clusters Incorporating Sulfur-Based Donors. Clusters featuring S-based donor ligands were prepared using *N*-aryl-2-thioimidazolate (SIm) bridging ligands. Treatment of $LFe_3(OTf)_2(OAc)$ with 3 equiv. of the sodium salte of the SIm anion followed by $Fe(OTf)_2$ and PhIO afforded a new paramagnetic species formulated as $[LFe_3O(SIm)_3Fe][OTf]$ based on ESI-MS (m/z = 1704). X-ray diffraction studies confirmed the identity of this species and revealed that each thioimidazolate ligand orients itself such that the S-based donor is coordinated to the basal iron centers (Figure 2), with relatively long Fe-S distances (2.52-2.55 Å). Within the triiron core, there are two long (2.130(4) and 2.122(3) Å) Fe-O1 distances and one short (1.934(3) Å) Fe-O1 bond length, implying a core redox level of $[Fe^{II}_2Fe^{III}]$. The unique, apical iron center adopts a pseudo-tetrahedral N_3O coordination geometry with a relatively short Fe4-O1 distance (1.868(3) Å). Charge balance requires the presence of three Fe(II) centers, implying that the apical iron is best assigned as Fe(II) in spite of the short Fe4-O1 distance. The lack of an apparent substrate binding site on the cluster motivated us to pursue other avenues of research.

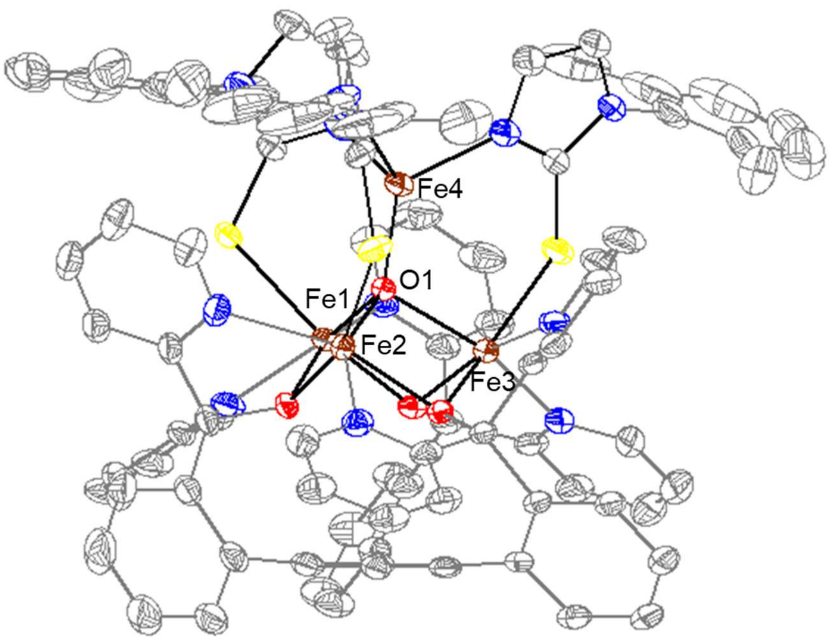

Figure 2. Solid-state structure of [$LFe_3O(SIm)_3Fe$][OTf]. Ellipsoids shown at the 50% probability level. Hydrogen atoms, counterions, and solvent omitted for clarity.

An alternative approach to incorporating S-donors was also pursued through the preparation of the tris(benzylthiolate) ligand framework $L^{SH}{}_{tBu}$. This was readily accessed by monobromination of each tolyl substituent in **A** followed by bromide displacement with thiourea and base deprotection (Scheme 3). New paramagnetic species were generated in the reaction of $L^{SH}{}_{tBu}$ with Fe{N($SiMe_3$)$_2$}, for example, but none proved amenable to structural characterization. As such, work on this ligand framework was abandoned. A related platform incorporating multiple phosphine donors was sought, but proved challenging to access.

Scheme 3. Synthesis of the tris(benzylthiolate) ligand $L^{SH}{}_{tBu}$ and efforts to prepare a hexaphosphine ligand

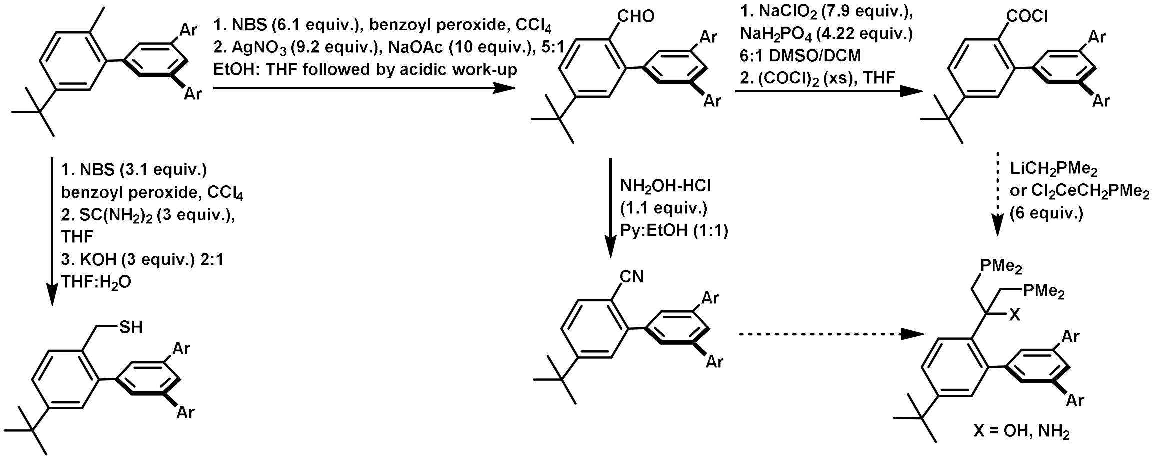

Site-Differentiated Trinuclear Clusters. In the course of studying $[LFe_3O(RIm)_3Fe][OTf]_n$ (R = Ar or alkyl, n = 0-3) series of clusters, it was discovered that adding $K\{N(SiMe_3)_2\}$ to the triiron oxo-tris(imidazole) clusters $[LFe_3O(H\text{-}Rim)_3][OTf]_3$ in the absence of an additional iron source promotes metal scrambling, yielding clusters of the form $LFe_2O(RIm)_2Fe\{N(SiMe_3)_2\}$ (Figure 3). Attempts were made to use these clusters as precursors for the synthesis of heterometallic clusters and/or clusters featuring two different bridging ligands. Unfortunately, however, only intractable product mixtures where obtained. It did prove possible to generate the all-ferric cluster $[LFe_2O(iPrIm)_2Fe\{N(SiMe_3)_2\}][OTf]$ by one-electron oxidation of $[LFe_2O(iPrIm)_2Fe\{N(SiMe_3)_2\}]$. Efforts were directed toward accessing terminal iron-imido and iron-nitrido clusters following F^- promoted removal of the $SiMe_3$ groups. EPR spectroscopy revealed the formation of a new S = 5/2 species following treatment of $[LFe_2O(iPrIm)_2Fe\{N(SiMe_3)_2\}][OTf]$ with tetrabutylammonium fluoride, but it is possible this only arises from binding of F^- at a coordinatively unsaturated basal iron site (Figure 4).

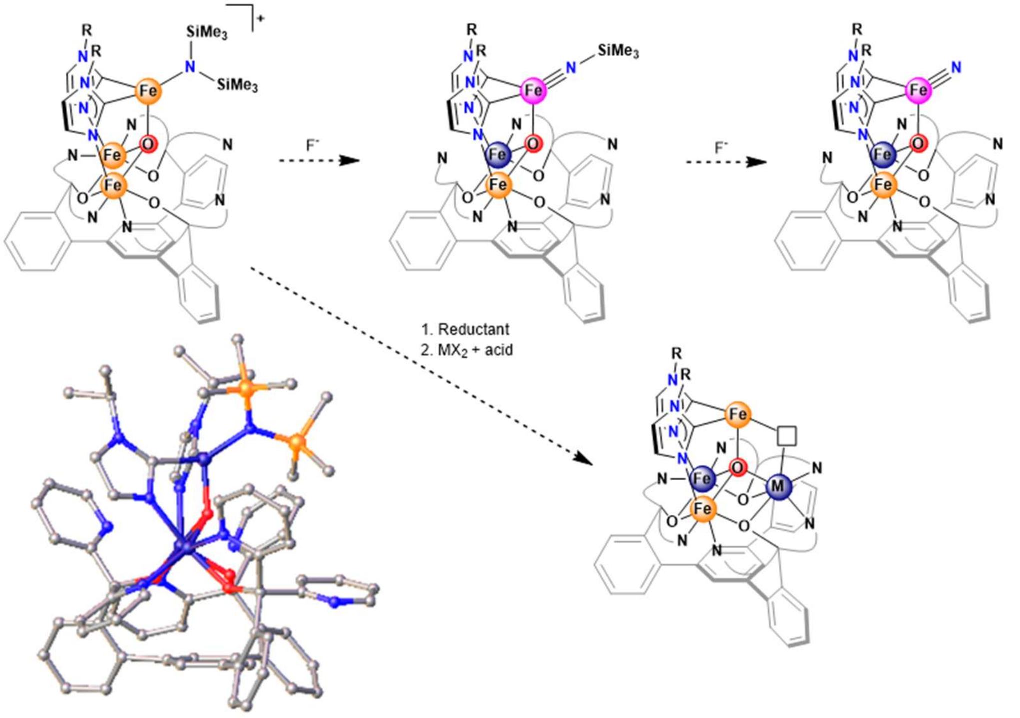

Figure 3. Targeted reactivity of a site-differentiated trinuclear iron cluster. Crystal structure of [$LFe_2O(iPrIm)_2Fe\{N(SiMe_3)_2\}$]. Hydrogen atoms and co-crystallized solvent omitted for clarity.

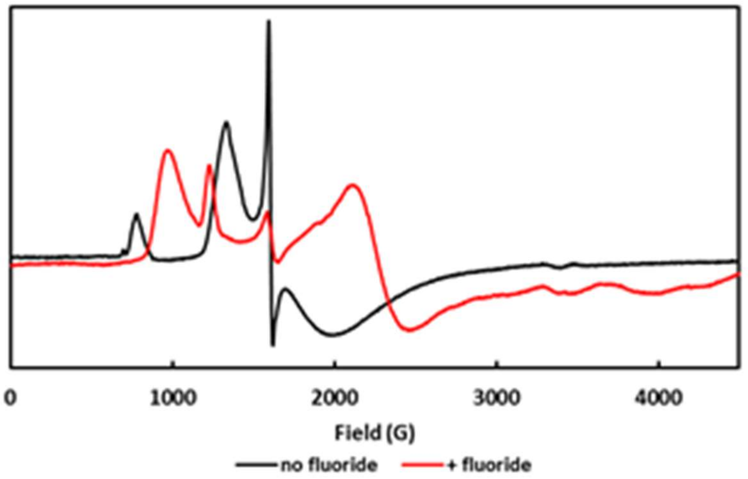

Figure 4. EPR spectrum of [$LFe_2O(iPrIm)_2Fe\{N(SiMe_3)_2\}$][OTf] before (black) and after (red) addition of 1 equiv. of [$n$$Bu_4N$][F].

EXPERIMENTAL DETAILS

General Considerations. All reactions were performed at room temperature in a nitrogen filled M. Braun glovebox or using standard Schlenk techniques unless otherwise specified. Glassware was oven dried at 140°C for at least two hours prior to use, and allowed to cool under vacuum. $[LFe_3O(PhIm)_3Fe][OTf]_2$,[5] tritolylbenzene **A**,[6] $LFe_3(OTf)_2(OAc)$[2] and $[LFe_3O(H\text{-}RIm)_3][OTf]_3$[5] were prepared as previously described. All other reagents were obtained commercially unless otherwise noted and typically stored over activated 4 Å molecular sieves. Tetrahydrofuran, toluene-d_8 and benzene-d_6 were dried using sodium/benzophenone ketyl, degassed with three freeze-pump-thaw cycles, vacuum transferred, and stored over 3 Å molecular sieves prior to use. Diethyl ether, benzene, toluene, acetonitrile, hexanes, and pentane were dried by sparging with nitrogen for at least 15 minutes, then passing through a column of activated A2 alumina under positive nitrogen pressure. ^1H and ^{31}P NMR spectra were recorded on a Varian 300 or 400 MHz spectrometer. All chemical shifts (δ) are reported in ppm, and coupling constants (J) are in hertz. The ^1H-NMR spectra were referenced using residual H impurity in the deuterated solvent. UV-Vis spectra were recorded on a Varian Cary Bio 50 spectrophotometer. Infrared (ATR-IR) spectra were recorded on a Bruker ALPHA ATR-IR spectrometer. Elemental analyses were performed at Caltech.

Physical Methods

X-ray Crystallography. Low-temperature (100 K) diffraction data (φ-and ω-scans) were collected on a Bruker AXS D8 VENTURE KAPPA diffractometer coupled to a PHOTON 100 CMOS detector with Mo Kα radiation (λ = 0.71073 Å) or with Cu Kα (λ = 1.54178 Å). All diffractometer manipulations, including data collection, integration, and scaling were carried out using the Bruker APEXII software.[7] Absorption corrections were applied using SADABS.[8] Structures were solved by direct methods using SHELXS[9] and refined against $F2$ on all data by full-matrix least squares with SHELXL-2014[10] interfaced with Olex2-1.2.8[11] and using established refinement techniques. All non-hydrogen atoms were refined anisotropically, except heavily disordered solvent in some cases. Hydrogen atoms were included into the model at geometrically calculated positions and refined using a riding model. The isotropic displacement parameters of all hydrogen atoms were fixed to 1.2 times the *U* value of the atoms they are linked to (1.5 times for methyl groups).

Synthetic Procedures.

Preparation of $[LFe_3O(PhIm)_3Fe(N_3)][OTf]$. A solution of tetrabutylammonium azide (5.3 mg, 0.019 mmol, 1.1 equiv) in dichloromethane was added to a thawing solution of $[LFe_3O(PhIm)_3Fe][OTf]_2$ (30.9 mg, 0.017 mmol, 1 equiv). After 20 minutes, the solution was layered with diethyl ether and placed in the freezer, precipitating $[LFe_3O(PhIm)_3Fe(N_3)][OTf]$ as mixture with other species. ^1H NMR (400 MHz, CH_2Cl_2) δ = 102.94 (b), 64.28 (s), 46.93 (s), 42.60 (s), 19.38 (s), 12.57 (s), 12.38 (s), 7.78 (s), -6.14 (s).

Preparation of $[LFe_3O(SIm)_3Fe][OTf]$. A solution of sodium *N*-(2,6-dimethylphenyl)-2-thioimidazolate (83.8 mg, 0.37 mmol, 3.3 equiv) was added dropwise to a chilled solution of $LFe_3(OTf)_2(OAc)$ (155 mg, 0.11 mmol, 1 equiv) in tetrahydrofuran. After stirring for two hours, $Fe(OTf)_2$ (39.7 mg, 0.11 mmol, 1 equiv) was added as a solid. After stirring for an additional two hours, iodosylbenzene (24.8 mg, 0.11 mmol, 1 equiv) was added as a solid. After stirring overnight, the solution was concentrated to ~5-6 mL and then filtered over Celite. The precipitate was washed with minimal tetrahydrofuran and then eluted with acetonitrile. The product was obtained by concentration of the acetonitrile filtrate. ^1H NMR (400 MHz, CH_2Cl_2) δ = 147.54 (s), 77.02 (s), 66.26 (s), 43.86 (s), 42.30 (s), 33.92 (s), 24.49 (s), 18.30 (s), 15.64 (s), 12.77 (s), 7.38 (s), 6.94 (s), 1.96 (s), -22.90 (s).

Preparation of L^{SH}_{tBu}. purification. Thiourea (74.3 mg, 0.98 mmol, 3 equiv) and L^{Br}_{tBu} (245 mg, 0.33 mmol, 1 equiv) were charged into an oven-dried Schlenk tube. These were dried briefly under vacuum, then dissolved in 5 mL of dry tetrahydrofuran and refluxed for 12 hours. After cooling to room temperature, the precipitate was collected on a fine frit in a wet box and dried under vacuum. The solid was then dissolved in 14 mL of 2:1 tetrahydrofuran/water, to which potassium hydroxide (54 mg, 3 equiv) was added. After refluxing overnight, the solution was acidified with 0.5 mL of 2 M HCl. The mixture was concentrated *in vacuo* and extracted with DCM. Concentration of the organic fraction yields the product in spectroscopically pure form (72 mg). ^{1}H NMR (400 MHz, CD_2Cl_2) δ = 7.71 (s, 3 H), 7.56 (s, 3 H), 7.24 (s, 6 H), 3.71 (d, 6 H), 1.62 (t, 3 H), 1.20 (s, 27 H).

Preparation of $[LFe_2O(iPrIm)_2Fe\{N(SiMe_3)_2\}]$. A solution of potassium hexamethyldisilazide (81.6 mg, 0.41 mmol, 3.2 equiv) was added to a thawing suspension of $[LFe_3O(iPrIm)_3][OTf]_3$ (232.4 mg, 0.13 mmol, 1 equiv) in tetrahydrofuran (1.9 mL). After stirring for 1 hour, the mixture was re-frozen. A suspension of $FeCl_2(THF)_{1.5}$ (21.8 mg, 0.13 mmol, 1.05 equiv) was added to the thawing mixture. After stirring overnight, the solution was concentrated and the resulting tar washed with pentane and diethyl ether. The desired product (54 mg) was eluted with benzene. ^{1}H NMR (400 MHz, C_6D_6) δ = 134.74 (b), 123.65 (b), 81.61 (s), 63.72 (s), 58.63 (s), 58.63 (s), 51.42 (s), 48.88 (s), 47.79 (s), 43.99 (s), 41.40 (s), 40.75 (s), 38.99 (s), 36.66 (s), 35.85 (s), 33.05 (s), 31.23 (s), 30.73 (s), 28.85 (s), 25.86 (s), 22.39 (s), 21.68 (s), 20.10 (s), 18.06 (s), 15.88 (s), 15.08 (s), -7.34 (s), -18.16 (s).

References

1. de Ruiter, G.; Thompson, N. B.; Takase, M. K.; Agapie, T., Intramolecular C–H and C–F Bond Oxygenation Mediated by a Putative Terminal Oxo Species in Tetranuclear Iron Complexes. *J. Am. Chem. Soc.* **2016,** *138* (5), 1486-1489.
2. de Ruiter, G.; Thompson, N. B.; Lionetti, D.; Agapie, T., Nitric Oxide Activation by Distal Redox Modulation in Tetranuclear Iron Nitrosyl Complexes. *J. Am. Chem. Soc.* **2015,** *137* (44), 14094-14106.

3. Reed, C. J.; Agapie, T., Tetranuclear Fe Clusters with a Varied Interstitial Ligand: Effects on the Structure, Redox Properties, and Nitric Oxide Activation. *Inorg. Chem.* **2017,** *56* (21), 13360-13367.

4. Lancaster, K. M.; Roemelt, M.; Ettenhuber, P.; Hu, Y.; Ribbe, M. W.; Neese, F.; Bergmann, U.; DeBeer, S., X-ray Emission Spectroscopy Evidences a Central Carbon in the Nitrogenase Iron-Molybdenum Cofactor. *Science* **2011,** *334* (6058), 974-977.

5. Arnett, C. H.; Chalkley, M. J.; Agapie, T., A Thermodynamic Model for Redox-Dependent Binding of Carbon Monoxide at Site-Differentiated, High Spin Iron Clusters. *J. Am. Chem. Soc.* **2018,** *140* (16), 5569-5578.

6. Suseno, S.; Agapie, T., Intramolecular Arene C–H to C–P Functionalization Mediated by Nickel(II) and Palladium(II). *Organometallics* **2013,** *32* (11), 3161-3164.

7. *APEX-II Version 2 User Manual, M86-E01078*. Bruker Analytical X-ray Systems: Madison, WI, 2006.

8. Sheldrick, G., *SADABS (version 2008/1): Program for Absorption Correction for Data from Area Detector Frames*. University of Göttingen: 2008.

9. Sheldrick, G., A short history of SHELX. *Acta Crystall. Sec. A* **2008,** *64* (1), 112-122.

10. Sheldrick, G., Crystal structure refinement with SHELXL. *Acta Crystall. Sec. C* **2015,** *71* (1), 3-8.

11. Dolomanov, O. V.; Bourhis, L. J.; Gildea, R. J.; Howard, J. A. K.; Puschmann, H., OLEX2: a complete structure solution, refinement and analysis program. *J. Appl. Crystallogr.* **2009,** *42* (2), 339-341.

APPENDIX B

TOWARDS A FE$_2$(μ-N$_2$) MODEL OF FEMOCO SUPPORTED BY LIGANDS WITH A ONE OR TWO CARBON BRIDGE

INTRODUCTION

This appendix describes efforts to prepare models of a dinuclear subsite of FeMoco and to evaluate cooperative modes of N_2 activation.

RESULTS AND DISCUSSION

Several ligand architectures were targeted and explored towards the preparation of well-defined diiron complexes competent for N_2 activation and functionalization. Our initial efforts focused on the metalation of a ditopic, *p*-phenylene-bridged bis(carbene)borate ligand. The ligand itself was readily assembled in four steps starting from 1,4-bis(trimethylsilyl)benzene (Scheme 1). Boron tribromide (BBr_3, 3 equiv) was addeded to a solution of bis(trimethylsilyl)benzene in toluene and refluxed to generate 1,4-bis(dibromoboryl)benzene. Selective halide/dimethyamino-exchange was accomplished by treating 1,4-bis(dibromoboryl)benzene with 2 equiv of (trimethylsilyl)dimethylamine at low temperatures. Substitution of the remaining bromide substituents with 2 equiv of phenyllithium afforded the diborane **4**. Finally, the ditopic bis(imidazolium)borate salt **5** was accessed by protonolysis of **4** with a mixture of *t*-butylimidazolium triflate (2 equiv) and *t*-butylimidazole (2 equiv).

Scheme 1. Synthesis of ditopic, *p*-phenylene-bridged bis(carbene)borate ligand

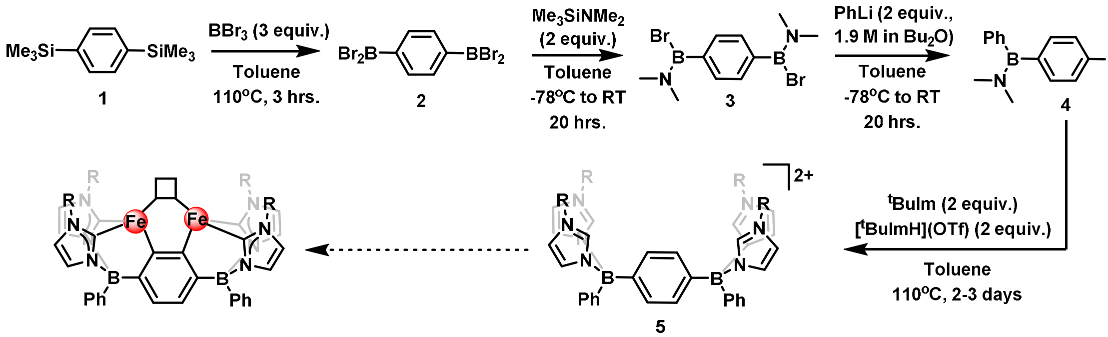

Efforts were directed toward deprotonation of **5** with a variety of bases, including benzyl potassium and *n*-butyl lithium, followed by metalation with iron halide precursors. The metalated products proved to be insoluble in all common organic solvents, which was attributed to the generation of coordination polymers. The generation of these species can be explained in light of a solid state structure of the deprotonated intermediate, which revealed that deprotonation occurs twice at the central C2 carbon atoms and twice at the backbone C4 carbon centers.

In light of the foregoing challenges, efforts were directed toward the preparation of a 2-methylimidazole linked variant inspired by the emergence of *N*-heterocyclic olefin-type ligands.[1] We envisioned that the proligand could be assembled in a manner analogous to that described above, namely, by Si/B exchange followed by protonolysis (Scheme 2). The *N*-atoms of the heterocycle were silylated in a stepwise fashion, first by reaction of 2-methylimidazole with trimethylsilyl chloride and trimethylamine followed by reaction of the mono-silylated product with trimethylsilyl triflate. The bis(silylated) 2-methylimidazolium salt **8** so obtained was then reacted with 2 equiv of bromo(dimethylamino)phenyl borane, which readily undergoes Si/B metathesis. However, subsequent treatment of the 2-methylimidazolium linked bis(borane) **9** with a mixture of isopropylimidazolium triflate (2 equiv) and isopropylimidazole (2 equiv) does not afford the desired proligand, but instead leads to B-N cleavage, generating tris(*t*-butylimidazolium)borate as an undesired product. Alternative conditions, including stepwise and low-temperature additions of the imidazole arms, were explored but to no avail. As such, this ligand framework was abandoned.

Scheme 2. Attempted synthesis of ditopic, 2-methylimidazole-bridged bis(carbene)borate ligand

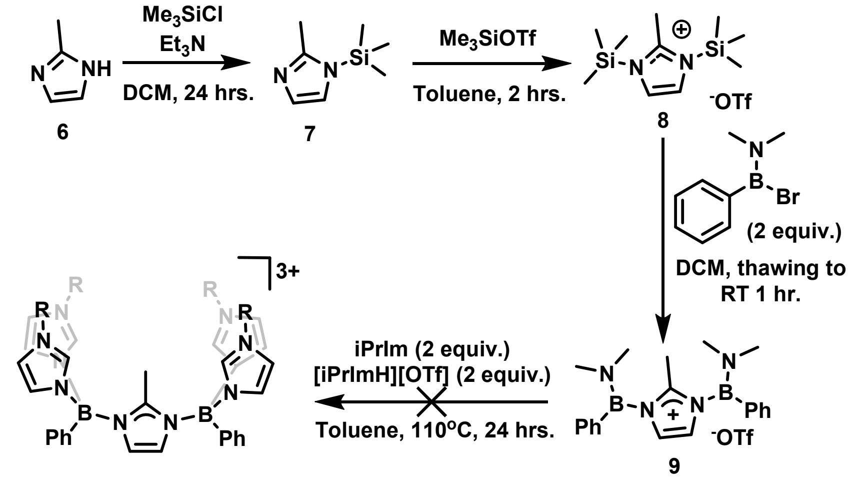

Motivated by a recent report from Bertrand and coworkers on the use of an anionic 1,2,3-triazole-4,5-diylidene as a 1,2-dihapto ligand to support binuclear complexes,[2] we prepared the 2-phenylimidazole linked (bis)imidazolium proligand to support well-defined diiron complexes. The proligand was assembled by first reacting *N*-(diisopropylphenyl) imidazole with chloroiodomethane to generate *N*-(chloromethyl),N'-(diisopropylphenyl) imidazolium iodide. A mixture of potassium 2-phenylimidazolate and 2 equiv of *N*-(chloromethyl),N'-(diisopropylphenyl) imidazolium iodide was heated to reflux for several days in acetonitrile, affording iodide-salt of the desired proligand **11** in low yields after separation by column chromatography (Scheme 3). Iodide/triflate exchange was accomplished by reaction of **11** with trimethylsilyl triflate in dichloromethane. Attempts to metalate **11** by deprotonation followed by reaction with iron halide salts lead to the generation of tetrametallic clusters, as indicated by ESI-MS. Unfortunately, we were unable to obtain diffraction-quality crystals of these species.

Scheme 3. Synthesis of 2-phenylimidazole linked (bis)imidazolium ligand.

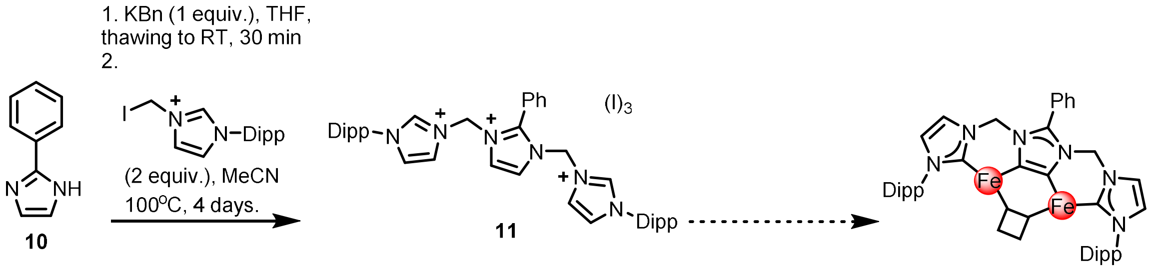

To better control the metal-ligand stoichiometry, we pursued a more sterically encumbered ligand scaffold. With this in mind, a phenanthroline-bridged hexaphosphine ligand framework was prepared starting from a 9,10-dibromophenanthroline derivative **12**. Monolithiation of **12** with 1 equiv *n*-butyllithium followed by quenching with bis(*o*-diisopropylphosphinophenyl)-chlorophosphine (P_2P^{Cl}) affords the mono-substituted product 9-bromo-10-(*o*-diisopropylphophinophenyl)phenanthroline (Scheme 4). Subsequent lithiation of **13** with *n*-butyllithium followed by addition of bis(*o*-diisopropylphosphinophenyl)-chlorophosphine (P_2P^{Cl}) yields the desired ligand 9,10-bis(*o*-diisopropylphophinophenyl)phenanthroline (**panthr**), albeit in low yields.

Scheme 4. Synthesis of phenanthroline-bridged hexaphosphine (**panthr**) ligand.

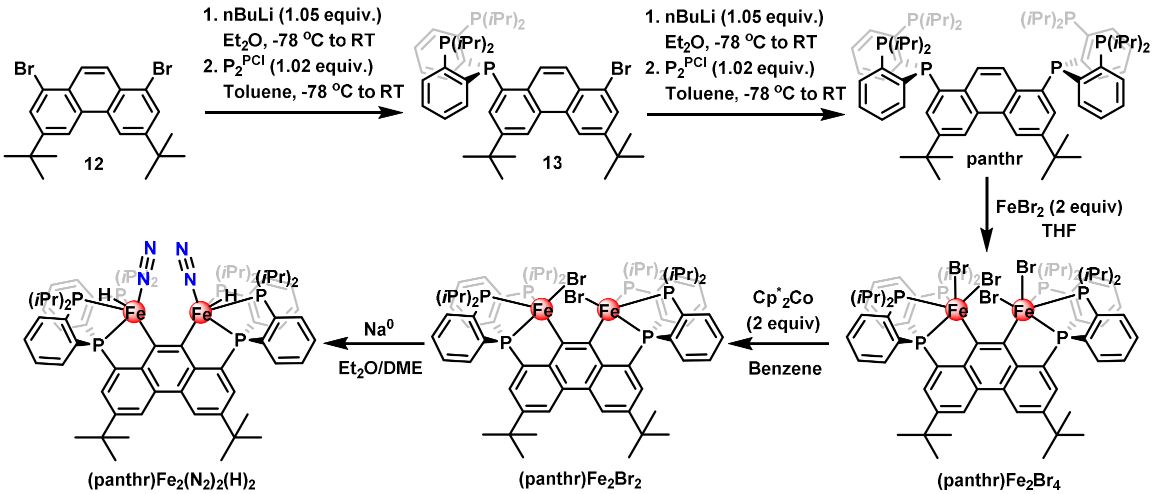

Reaction of **panthr** with 2 equiv of $FeBr_2$ generates the diiron tetrabromide complex $(panthr)Fe_2Br_4$ as revealed by X-ray diffraction studies (Figure 1a). Reduction of (panthr)Fe_2Br_4 with 2 equiv of decamethylcobaltocene affords the diiron(I) congener (panthr)Fe_2Br_2 (Figure 1b), which is sensitive to disproportionation in the presence of donor solvents such as tetrahydrofuran. Stirring a solution of (panthr)Fe_2Br_2 in Et_2O/DME over a sodium mirror at -78 °C generates a new species with a hydridic resonance at -13 ppm in its ^1H NMR spectrum. An IR spectrum of the product contains an Fe-N_2 stretch at 2100 cm^{-1} in addition to the Fe-H vibration at 1826 cm^{-1} (Figure 2). The ^{31}P NMR spectrum of the desired product indicates the presence of C_2-symmetry, leading to a formulation of (panthr)$Fe_2(N_2)(H)_2$ for the product. Based on the relatively high Fe-N_2 stretching frequency, the dinitrogen ligands are likely bound in a terminal rather than bridging fashion. Since cooperative N_2 activation was not observed, this ligand framework was abandoned in favor of that discussed in Chapter 4.

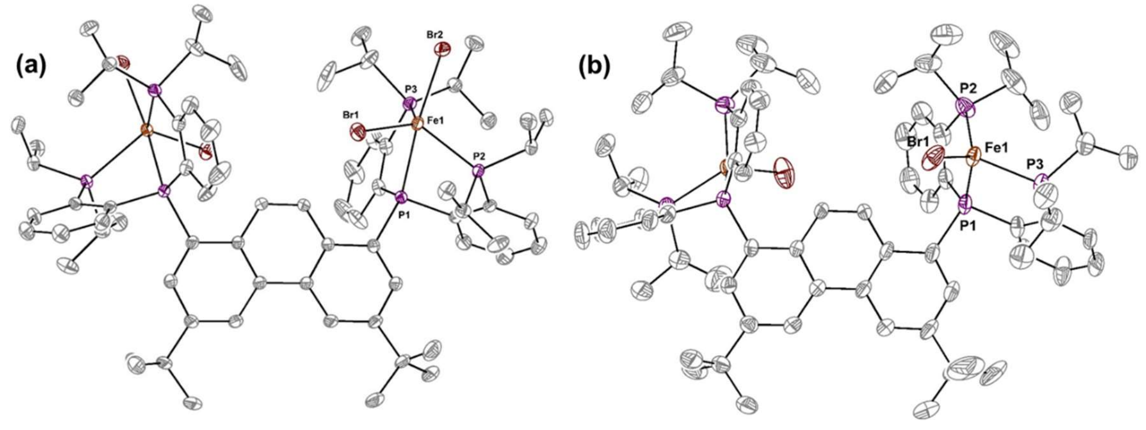

Figure 1. Solid state structures of (panthr)Fe_2Br_4 (a) and (panthr)Fe_2Br_2 (b). Hydrogen atoms and co-crystallized solvent not shown for clarity. Thermal ellipsoids shown at 50% probability level.

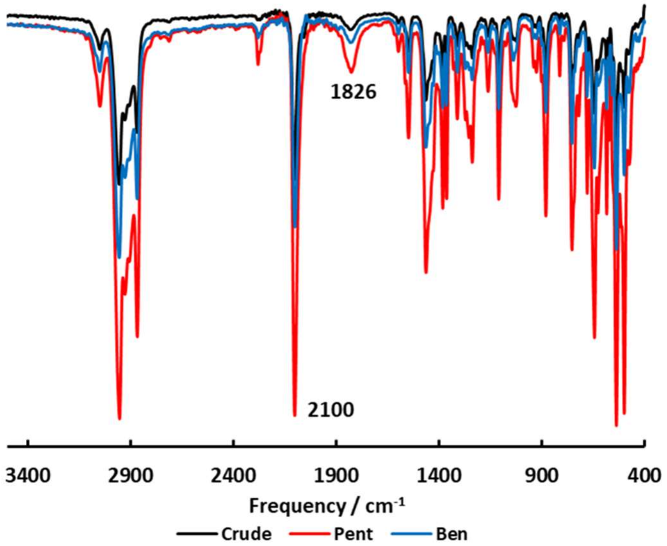

Figure 2. IR spectrum of (panthr)$Fe_2(N_2)_2(H)_2$ obtained following reaction of (panthr)Fe_2Br_2 with Na^0.

EXPERIMENTAL DETAILS

General Considerations. All reactions were performed at room temperature in a nitrogen filled M. Braun glovebox or using standard Schlenk techniques unless otherwise specified. Glassware was oven dried at 140°C for at least two hours prior to use, and allowed to cool under vacuum. Compounds **4**[3] and **12**[4], bromo(dimethylamino)phenyl borane[5] and bis(*o*-diisopropylphosphinophenyl)-chlorophosphine (P_2P^{Cl})[6] were prepared using procedures adapted from the literature. All other reagents were obtained commercially unless otherwise noted and typically stored over activated 4 Å molecular sieves. Tetrahydrofuran, toluene-d_8 and benzene-d_6 were dried using sodium/benzophenone ketyl, degassed with three freeze-pump-thaw cycles, vacuum transferred, and stored over 3 Å molecular sieves prior to use. Diethyl ether, benzene, toluene, acetonitrile, hexanes, and pentane were dried by sparging with nitrogen for at least 15 minutes, then passing through a column of activated A2 alumina under positive nitrogen pressure. ^1H and ^{31}P NMR spectra were recorded on a Varian 300 or 400 MHz spectrometer. All chemical shifts (δ) are reported in ppm, and coupling constants (J) are in hertz. The ^{1}H-NMR spectra were referenced using residual H impurity in the deuterated solvent. UV-Vis spectra were recorded on a Varian Cary Bio 50 spectrophotometer. Infrared (ATR-IR) spectra were recorded on a Bruker ALPHA ATR-IR spectrometer. Elemental analyses were performed at Caltech.

Physical Methods

X-ray Crystallography. Low-temperature (100 K) diffraction data (φ-and ω-scans) were collected on a Bruker AXS D8 VENTURE KAPPA diffractometer coupled to a PHOTON 100 CMOS detector with Mo Kα radiation (λ = 0.71073 Å) or with Cu Kα (λ = 1.54178 Å). All diffractometer manipulations, including data collection, integration, and scaling were carried out using the Bruker APEXII software.[7] Absorption corrections were applied using SADABS.[8] Structures were solved by direct methods using SHELXS[9] and refined against *F*2 on all data by full-matrix least squares with SHELXL-2014[10] interfaced with Olex2-1.2.8[11] and using established refinement techniques. All non-hydrogen atoms were refined anisotropically, except heavily disordered solvent in some cases. Hydrogen atoms were included into the model at geometrically calculated positions and refined using a riding model. The isotropic displacement parameters of all hydrogen atoms were fixed to 1.2 times the *U* value of the atoms they are linked to (1.5 times for methyl groups).

Synthetic Procedures.

*Preparation of **5***. To a toluene solution (30 mL) of **4** (371 mg, 1.09 mmol, 1 equiv) in a Schlenk tube was added *t*-butylimidazole (271 mg, 218 mmol, 2 equiv) and *t*-butylimidazolium triflate (599 mg, 218 mmol, 2 equiv). The mixture was refluxed for 3 days and then the precipitate was collected on a medium frit, providing the desired product as a spectroscopically pure material. ^{1}H NMR (400 MHz, CH_2Cl_2) δ = 8.36 (s, 4H), 7.33-7.21 (m), 7.01 (s, 4 H), 1.62 (s, 48 H).

Preparation of ***11****.* A solution benzyl potassium (30.5 mg, 0.23 mmol, 1 equiv) was added to a thawing solution of 2-phenyl imidazole (33.7 mg, 0.23 mmol, 1 equiv) in tetrahydrofuran. After stirring for 30 minutes, the mixture was concentrated to dryness and then resuspended in 3 mL of acetonitrile in a Schlenk tube. An acetonitrile solution of *N*-(chloromethyl),N'-(diisopropylphenyl) imidazolium iodide (232.1 mg, 0.48 mmol, 2 equiv) was added dropwise and the mixture was refluxed to completion, typically >4 days. The mixture was concentrated and purified by gradient elution (DCM to 2:1 ACN/DCM to CAN) over silica gel, affording the product as spectroscopically pure material (26 mg). ^{1}H NMR (400 MHz, CH_2Cl_2) $\delta = 9.67$ (2H), 8.63 (2H), 8.18 (2H), 7.78 (2H), 7.57 (2H), 7.41 (2H), 7.39 (4H), 6.83 (4H), 2.31 (4H), 1.19 (12H), 1.11 (12H).

Preparation of ***13****.* A solution of *n*BuLi (0.37 mL, 0.59 mmol, 1.05 equiv.) was added dropwise to a stirring solution of **12** (253.8 mg, 0.57 mmol, 1 equiv.) in 5 mL of diethyl ether at -78 ºC. After stirring for 1 hour at -78 ºC, the resulting colorless suspension was removed from the cold bath and stirred for an additional hour. The mixture was then concentrated under vacuum, redissolved in toluene (5.4 mL), and chilled to -78 ºC. A suspension of bis(*o*-diisopropylphosphinophenyl)-chlorophosphine (261.6 mg, 0.58 mmol, 1.02 equiv.) in minimal toluene was then added dropwise. After stirring for 30 minutes at -78 ºC, the mixture was allowed to warm slowly to room temperature. The next day, the solution was concentrated to dryness and used in the next step without further purification.

Preparation of ***panthr****.* A solution of *n*BuLi (0.31 mL, 0.50 mmol, 1.05 equiv.) was added dropwise to a stirring solution of **13** (374.6 mg, 0.48 mmol, 1 equiv) in 5 mL of diethyl ether at -78 ºC. After stirring for 1 hour at -78 ºC, the resulting colorless suspension was removed from the cold bath and stirred for an additional hour. The mixture was then concentrated under vacuum, redissolved in toluene (5.4 mL), and chilled to -78 ºC. A suspension of bis(*o*-

diisopropylphosphinophenyl)-chlorophosphine (220.2 mg, 0.49 mmol, 1.02 equiv.) in minimal toluene was then added dropwise. After stirring for 30 minutes at -78 ºC, the mixture was allowed to warm slowly to room temperature. The next day, the solution was concentrated to dryness and extracted between pentane and acetonitrile. The pentane fraction was concentrated inside a Schlenk tube and then the residue was washed with hot acetonitrile. The precipitate was collected, affording **panthr** in spectroscopically pure form.

Preparation of ***(panthr)Fe$_2$Br$_4$***. A solution of **panthr** (101.2 mg, 0.09 mmol, 1.0 equiv.) in tetrahydrofuran (2 mL) was added to a suspension of $FeBr_2$ (38.9 mg, 0.18 mmol, 2.0 equiv.) in tetrahydrofuran (1 mL). After stirring for 2 hours, the mixture was concentrated to ~1 mL and pentane was added to precipitate a yellow-green solid. The precipitate was collected on a fine frit and washed with additional tetrahydrofuran/pentane, affording **(panthr)Fe$_2$Br$_4$** (75 mg) in spectroscopically pure form. ^1H NMR (400 MHz, CH_2Cl_2) δ = 178.26 (b), 139.84 (b), 84.61 (b), 14.86 (s), 14.14 (s), 12.54 (s), 11.71 (s), 10.88 (s), -3.04 (s), -10.68 (s).

Preparation of ***(panthr)Fe$_2$Br$_2$***. A suspension of Cp^*_2Co (17.8 mg, 0.05 mmol, 2.0 equiv.) in minimal benzene was added to a suspension of **(panthr)Fe$_2$Br$_4$** (41.3 mg, 0.026 mmol, 1.0 equiv.) in benzene. After stirring for three hours, the resulting brick red suspension was filtered over Celite and concentrated in vacuo. The residue was used without further purification. ^1H NMR (400 MHz, C_6D_6) δ = -3.50 (b), -11.08 (b), -23 (b).

Preparation of ***(panthr)Fe$_2$(N$_2$)$_2$(H)$_2$***. A suspension of **(panthr)Fe$_2$Br$_2$** (17.8 mg, 0.05 mmol, 2.0 equiv.) in diethyl ether/dimethoxyethane was transferred to a chilled vial mirrored with Na^0. After stirring for two hours, the solution was filtered over Celite and concentrated in vacuo. The product could not be isolated cleanly, but was characterized by a hydride resonance at -13 ppm in the ^1H NMR and characteristic Fe-N_2 and Fe-H features in the IR spectrum.

References

1. Roy, M. M. D.; Rivard, E., Pushing Chemical Boundaries with N-Heterocyclic Olefins (NHOs): From Catalysis to Main Group Element Chemistry. *Acc. Chem. Res.* **2017**, *50*, 2017.

2. Yan, X.; Bouffard, J.; Guisado-Barrios, G.; Donnadieu, B.; Bertrand, G., Anionic 1,2,3-Triazole-4,5-diylidene: A 1,2-Dihapto Ligand for the Construction of Bimetallic Complexes. *Chem. Eur. J.* **2012,** *18* (46), 14627-14631.

3. Bieller, S.; Zhang, F.; Bolte, M.; Bats, J. W.; Lerner, H.-W.; Wagner, M., Bitopic Bis- and Tris(1-pyrazolyl)borate Ligands: Syntheses and Structural Characterization. *Organometallics* **2004,** *23* (9), 2107-2113.

4. Uchida, Y.; Hirose, T.; Nakashima, T.; Kawai, T.; Matsuda, K., Synthesis and Photophysical Properties of a 13,13'-Bibenzo[b]perylenyl Derivative as a π-Extended 1,1'-Binaphthyl Analog. *Org. Lett.* **2016,** *18* (9), 2118-2121.

5. Spasyuk, D. M.; Carpenter, S. H.; Kefalidis, C. E.; Piers, W. E.; Neidig, M. L.; Maron, L., Facile hydrogen atom transfer to iron(iii) imido radical complexes supported by a dianionic pentadentate ligand. *Chem. Sci.* **2016,** *7* (9), 5939-5944.

6. Mankad, N. P.; Rivard, E.; Harkins, S. B.; Peters, J. C., Structural Snapshots of a Flexible Cu_2P_2 Core that Accommodates the Oxidation States Cu^ICu^I, $Cu^{1.5}Cu^{1.5}$, and $Cu^{II}Cu^{II}$. *J. Am. Chem. Soc.* **2005,** *127* (46), 16032-16033.

7. *APEX-II Version 2 User Manual, M86-E01078*. Bruker Analytical X-ray Systems: Madison, WI, 2006.

8. Sheldrick, G., *SADABS (version 2008/1): Program for Absorption Correction for Data from Area Detector Frames*. University of Göttingen: 2008.

9. Sheldrick, G., A short history of SHELX. *Acta Crystall. Sec. A* **2008,** *64* (1), 112-122.

10. Sheldrick, G., Crystal structure refinement with SHELXL. *Acta Crystall. Sec. C* **2015,** *71* (1), 3-8.

11. Dolomanov, O. V.; Bourhis, L. J.; Gildea, R. J.; Howard, J. A. K.; Puschmann, H., OLEX2: a complete structure solution, refinement and analysis program. *J. Appl. Crystallogr.* **2009,** *42* (2), 339-341.

NMR Data

Chapter 2

General introduction: For details concerning the determination of the thermodynamic parameters for CO binding, see Arnett, C.H.; Chalkley, M.J.; Agapie, T. *J. Am. Chem. Soc.* **2018**, *140*, 5569-5578.

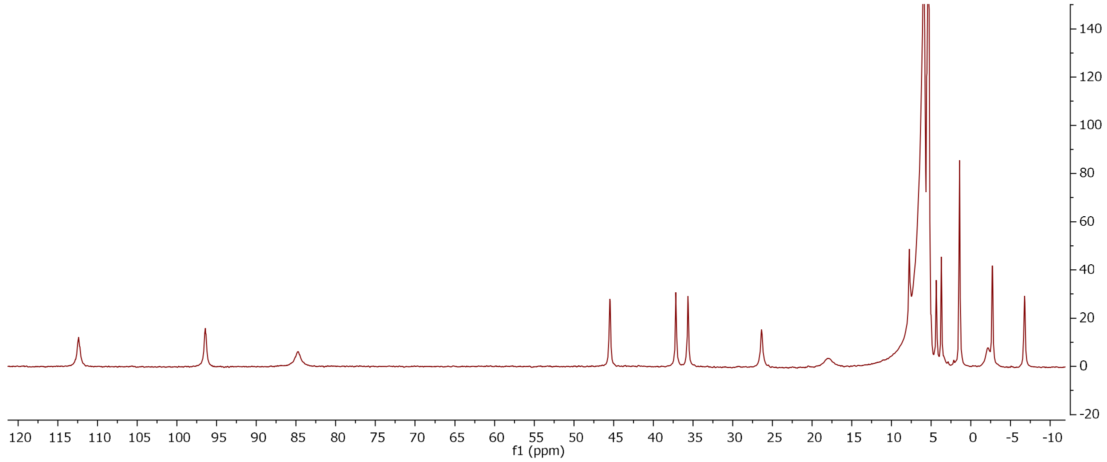

Figure 1. ^{1}H NMR (300 MHz) of $LFe_3(OTf)_3$ **(1)** in CD_2Cl_2

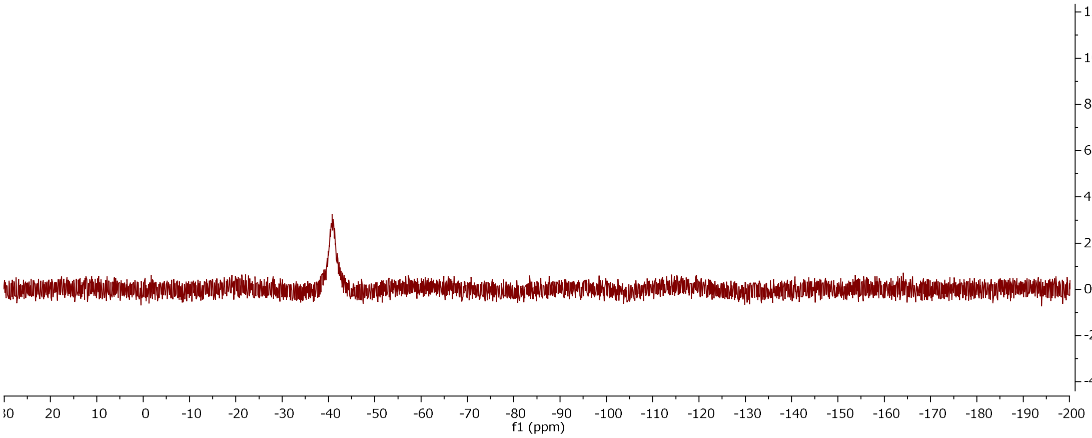

Figure 2. ^{19}F NMR (300 MHz) of $LFe_3(OTf)_3$ **(1)** in CD_2Cl_2

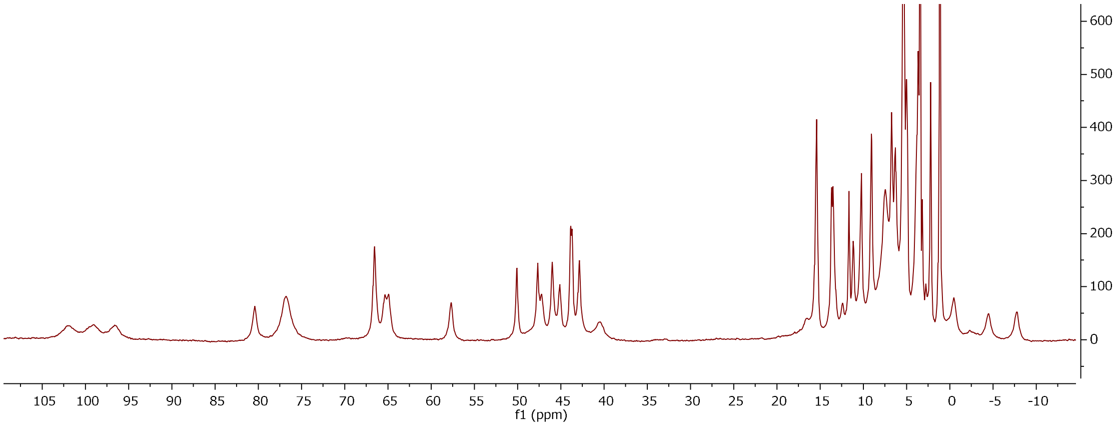

Figure 3. ^{1}H NMR (300 MHz) of $[LFe_3O(PhIm\text{-}H)_3][OTf]_3$ **(2)** in CD_2Cl_2

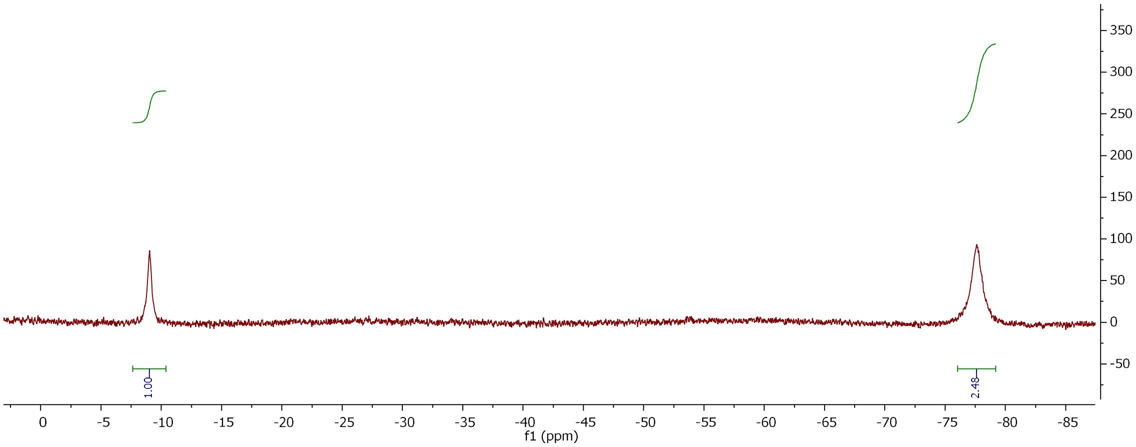

Figure 4. ^{19}F NMR (300 MHz) of [LFe$_3$O(PhIm-H)$_3$][OTf]$_3$ **(2)** in CD$_2$Cl$_2$. We attribute the presence of two triflate signals to dissociation of one PhIm-H ligand and triflate binding to the cluster in solution.

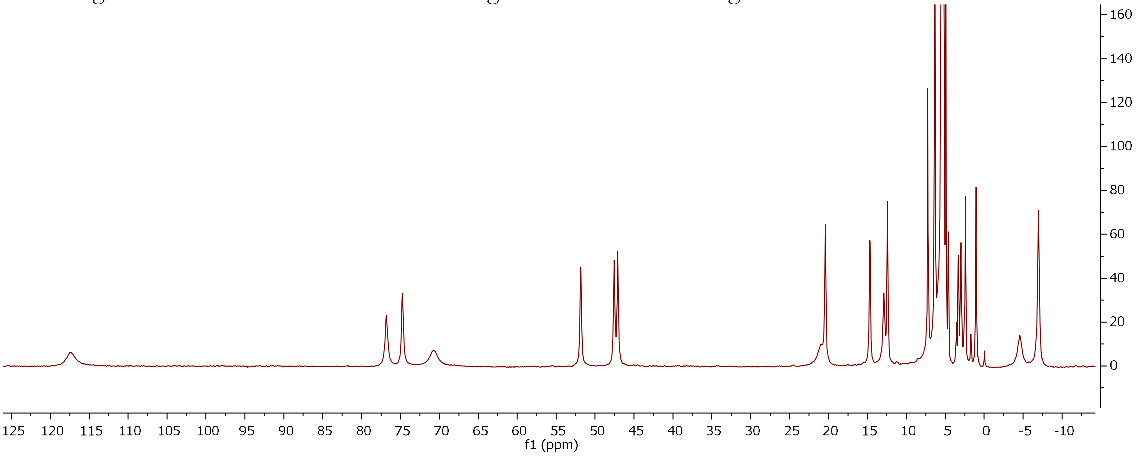

Figure 5. ^{1}H NMR (300 MHz) of [LFe$_3$O(PhIm)$_3$Fe][OTf]$_2$ **(3)** in CD$_2$Cl$_2$

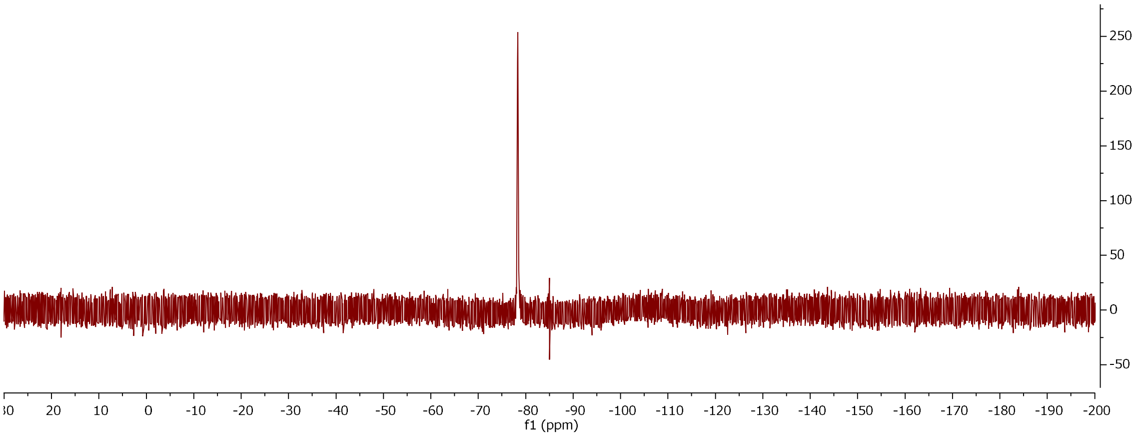

Figure 6. ^{19}F NMR (300 MHz) of [LFe$_3$O(PhIm)$_3$Fe][OTf]$_2$ **(3)** in CD$_2$Cl$_2$

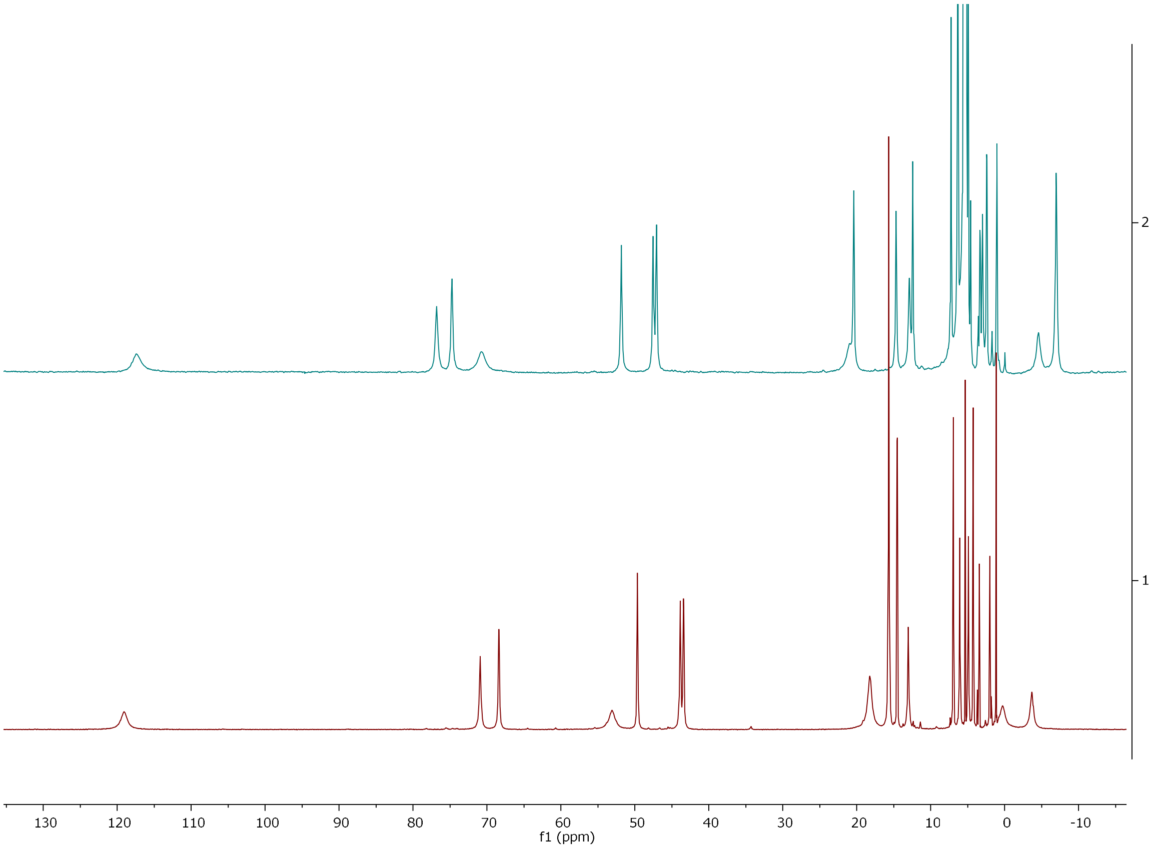

Figure 7. Comparison of ^{1}H NMR Spectra (300 MHz) for [LFe$_3$O(PhIm)$_3$Fe][OTf]$_2$ (**3**) (top) and [LFe$_3$O(PhPz)$_3$Fe][OTf]$_2$ (bottom) in CD$_2$Cl$_2$

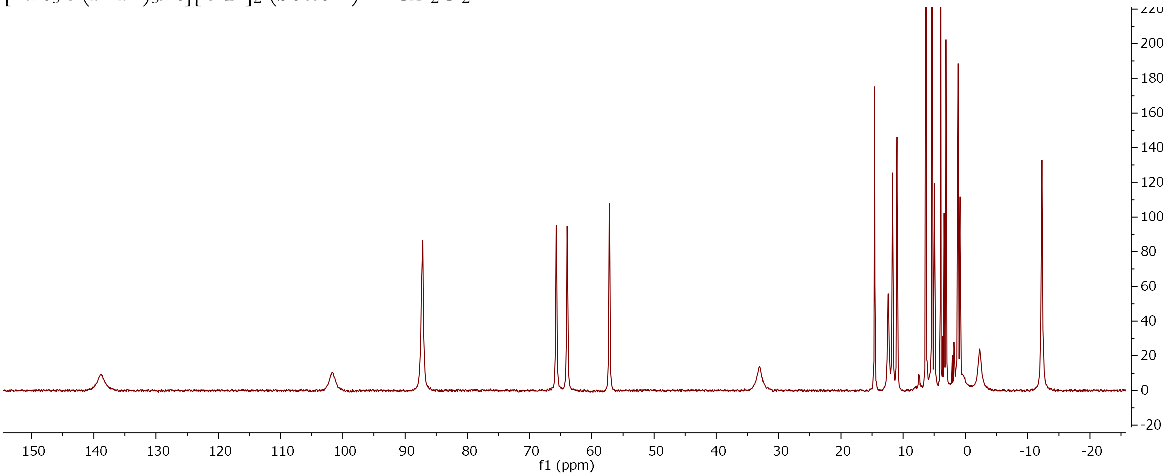

Figure 8. ^{1}H NMR (400 MHz) of [LFe$_3$O(PhIm)$_3$Fe][OTf]$_3$ **(4)** in CD$_2$Cl$_2$

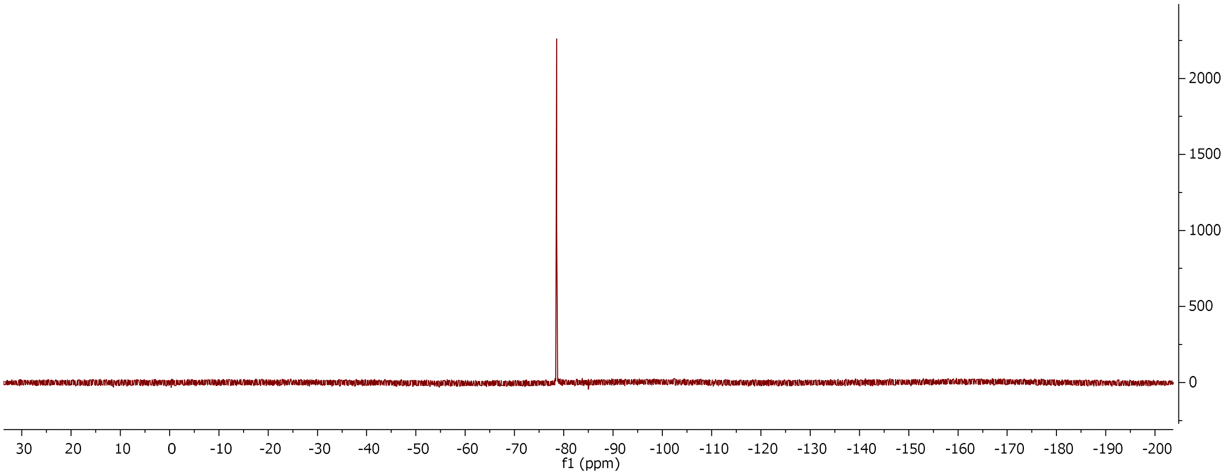

Figure 9. ^{19}F NMR (400 MHz) of $[LFe_3O(PhIm)_3Fe][OTf]_3$ **(4)** in CD_2Cl_2

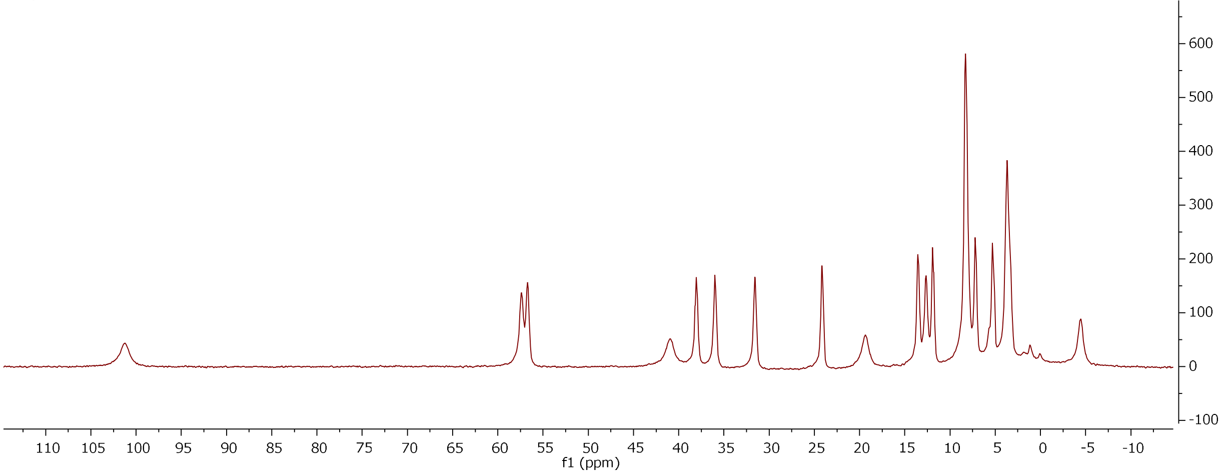

Figure 10. ^{1}H NMR (300 MHz) of $[LFe_3O(PhIm)_3Fe][OTf]$ **(5)** in CD_2Cl_2

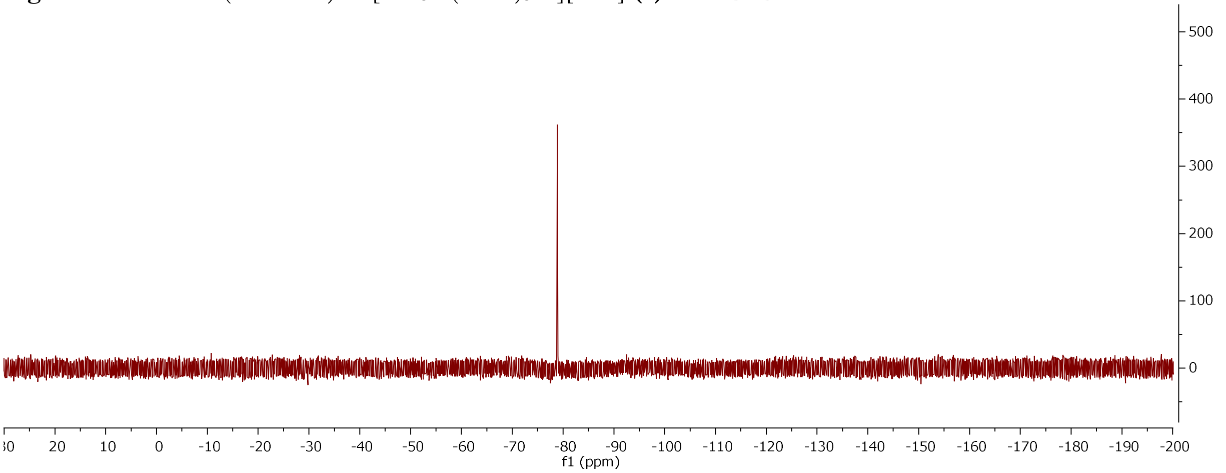

Figure 11. ^{19}F NMR (300 MHz) of $[LFe_3O(PhIm)_3Fe][OTf]$ **(5)** in CD_2Cl_2

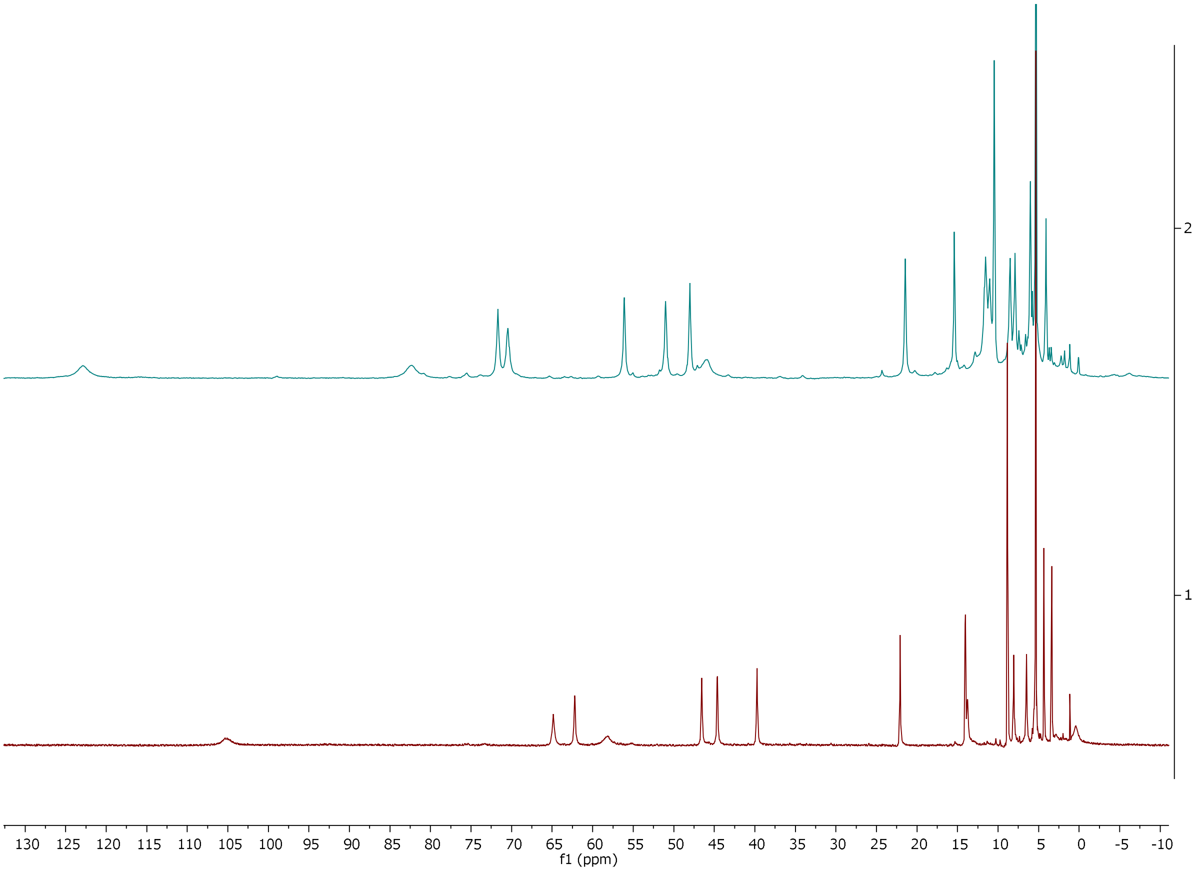

Figure 12. Comparison of ^{1}H NMR (300 MHz) of [LFe$_3$O(PhIm)$_3$Fe(CO)][OTf] (**5-CO**) (top) and [LFe$_3$O(PhPz)$_3$Fe(NO)](OTf) (bottom) at room temperature reveals similar splitting pattern, though absolute peak positions vary.

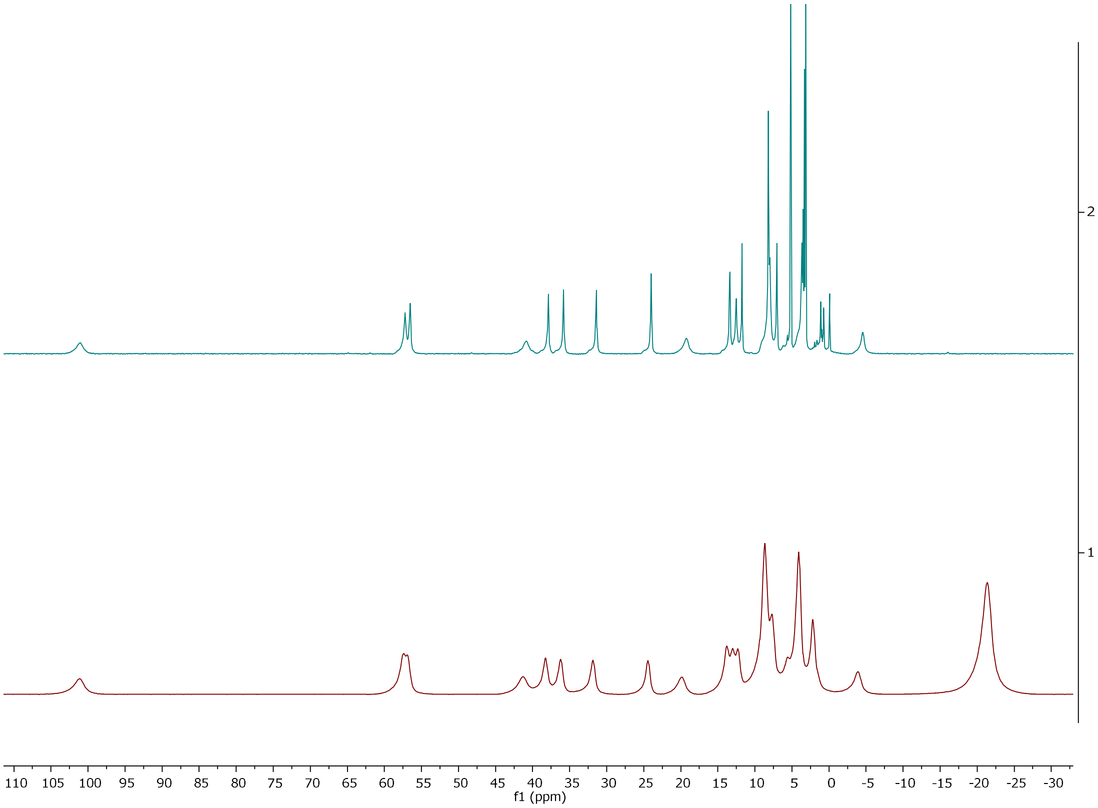

Figure 13. Comparison of ^{1}H NMR (400 MHz) of [LFe$_3$O(PhIm)$_3$Fe][OTf] (**5**) obtained by reduction of [LFe$_3$O(PhIm)$_3$Fe][OTf] (**3**) (top) and by oxidation of [LFe$_3$O(PhIm)$_3$Fe] (**6**) (bottom). The peak at ~ -20 ppm is from residual Cp$_2$Co/[Cp$_2$Co][OTf].

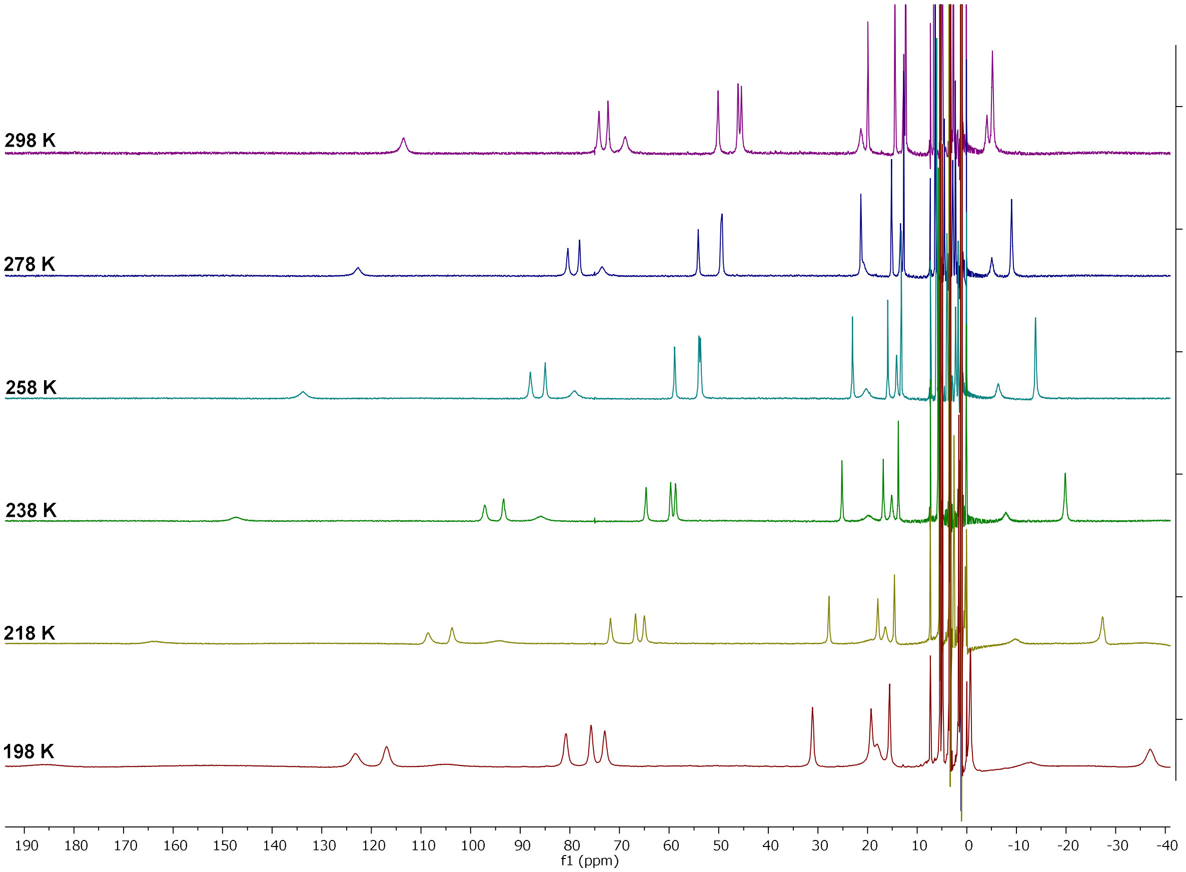

Figure 14. VT-^{1}H NMR (500 MHz) of [LFe$_3$O(PhIm)$_3$Fe][OTf]$_2$ (**3**) in CD$_2$Cl$_2$ under N$_2$ between 298 K (top) and 198 K (bottom) in 20 K intervals.

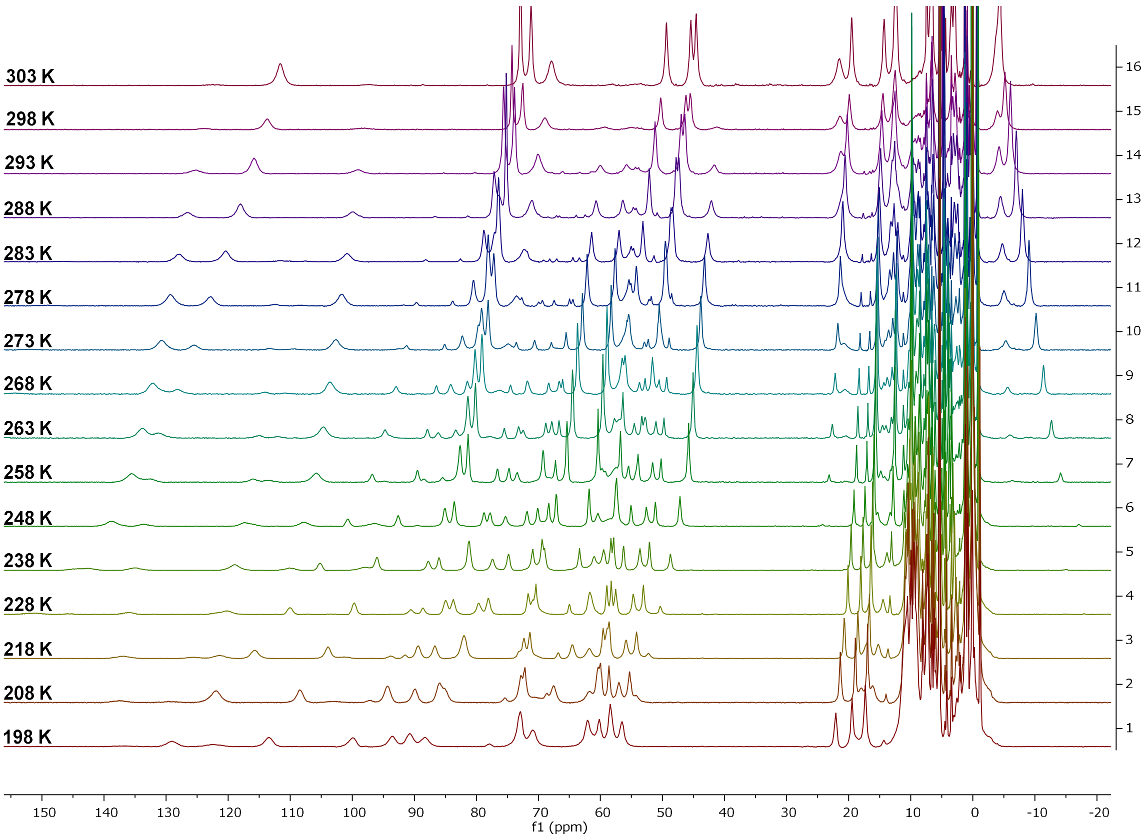

Figure 15. VT-^{1}H NMR (500 MHz) of $[LFe_3O(PhIm)_3Fe][OTf]_2$ (**3**) in CD_2Cl_2 under CO (1 atm.) between 303 K (top) and 198 K (bottom).

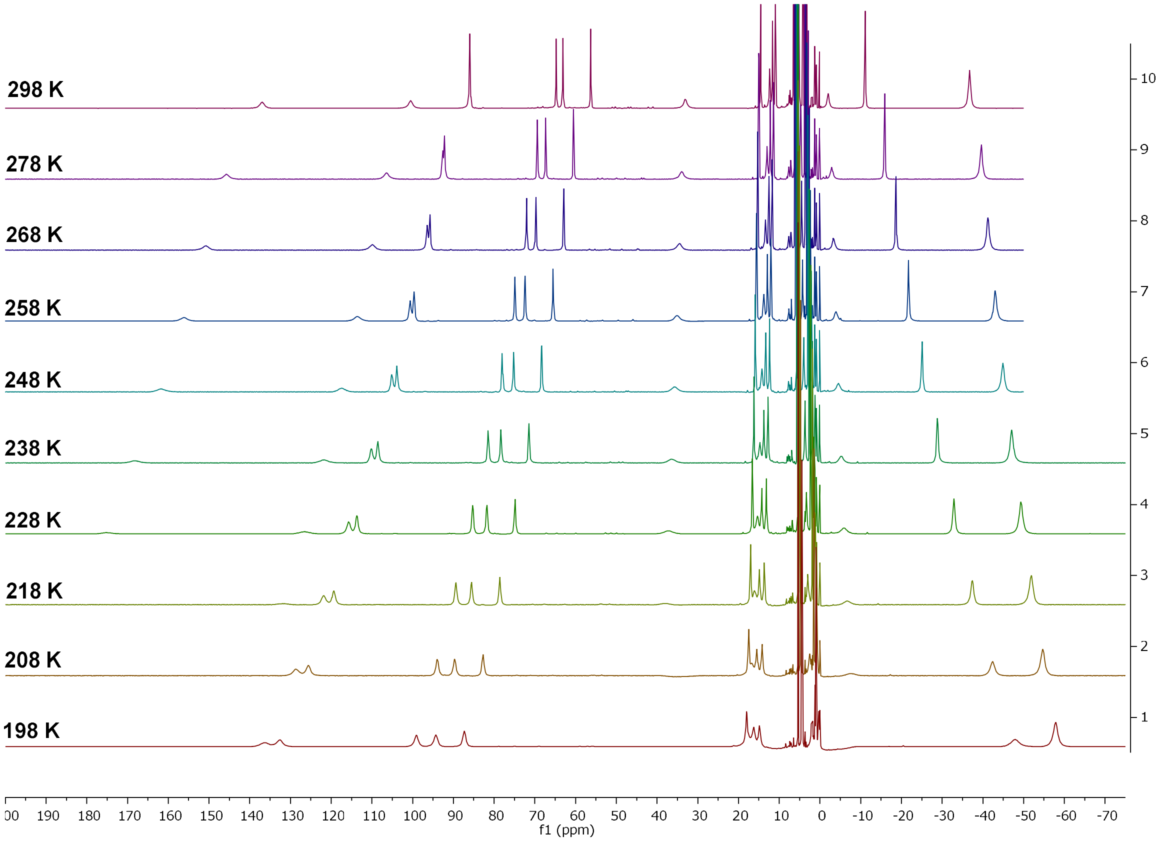

Figure 16. VT-^{1}H NMR (500 MHz) of [LFe$_3$O(PhIm)$_3$Fe][OTf]$_3$ (**4**) in CD$_2$Cl$_2$ under N$_2$ between 298 K (top) and 198 K (bottom).

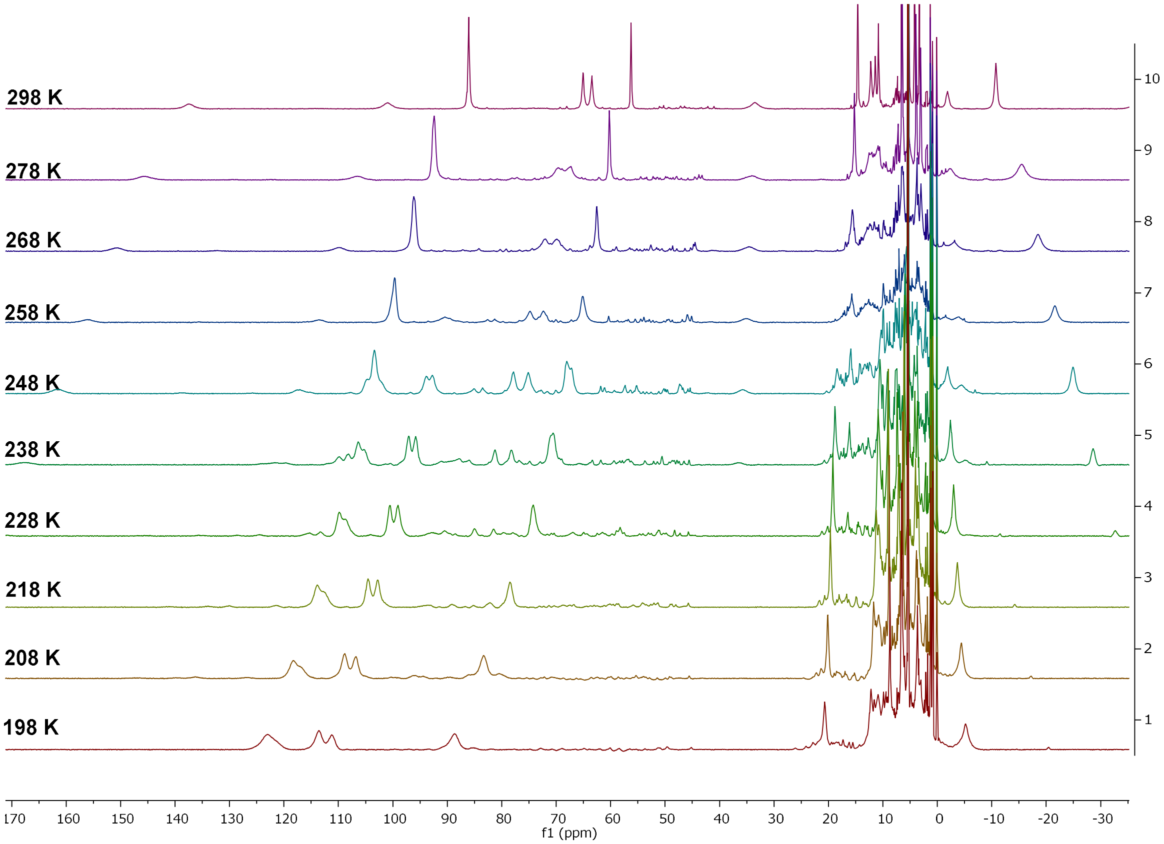

Figure 17. VT-^{1}H NMR (500 MHz) of [LFe$_3$O(PhIm)$_3$Fe][OTf]$_3$ (**4**) in CD$_2$Cl$_2$ under CO (1 atm.) between 298 K (top) and 198 K (bottom). Note, decomposition is observed following exposure to CO (~13%). Allowing the sample to stand overnight results in additional decomposition, including oxidation to **3** and other unidentified products. While some decomposition (~13%) is observed upon exposure of **4** to CO, this decomposition appears to be relatively slow at lower temperatures such that over the timescale of the experiment little additional decomposition occurs (<5%). Allowing the sample to stand overnight results in additional decomposition, including oxidation to **3** and other unidentified products. Similar decomposition, albeit much faster, is observed in the presence of donating solvents such as acetonitrile and acetone.

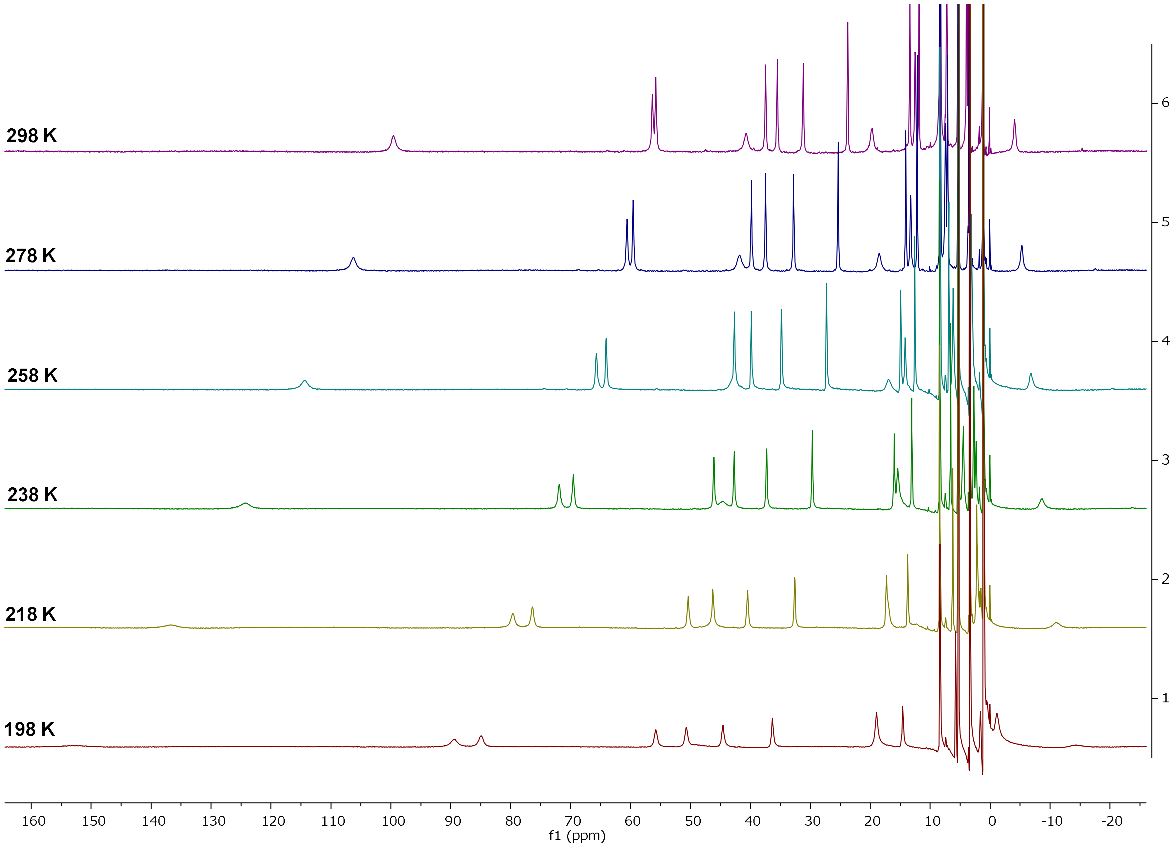

Figure 18. VT-^{1}H NMR (500 MHz) of [LFe$_3$O(PhIm)$_3$Fe][OTf] (**5**) in CD$_2$Cl$_2$ under N$_2$ between 298 K (top) and 198 K (bottom) in 20 K intervals.

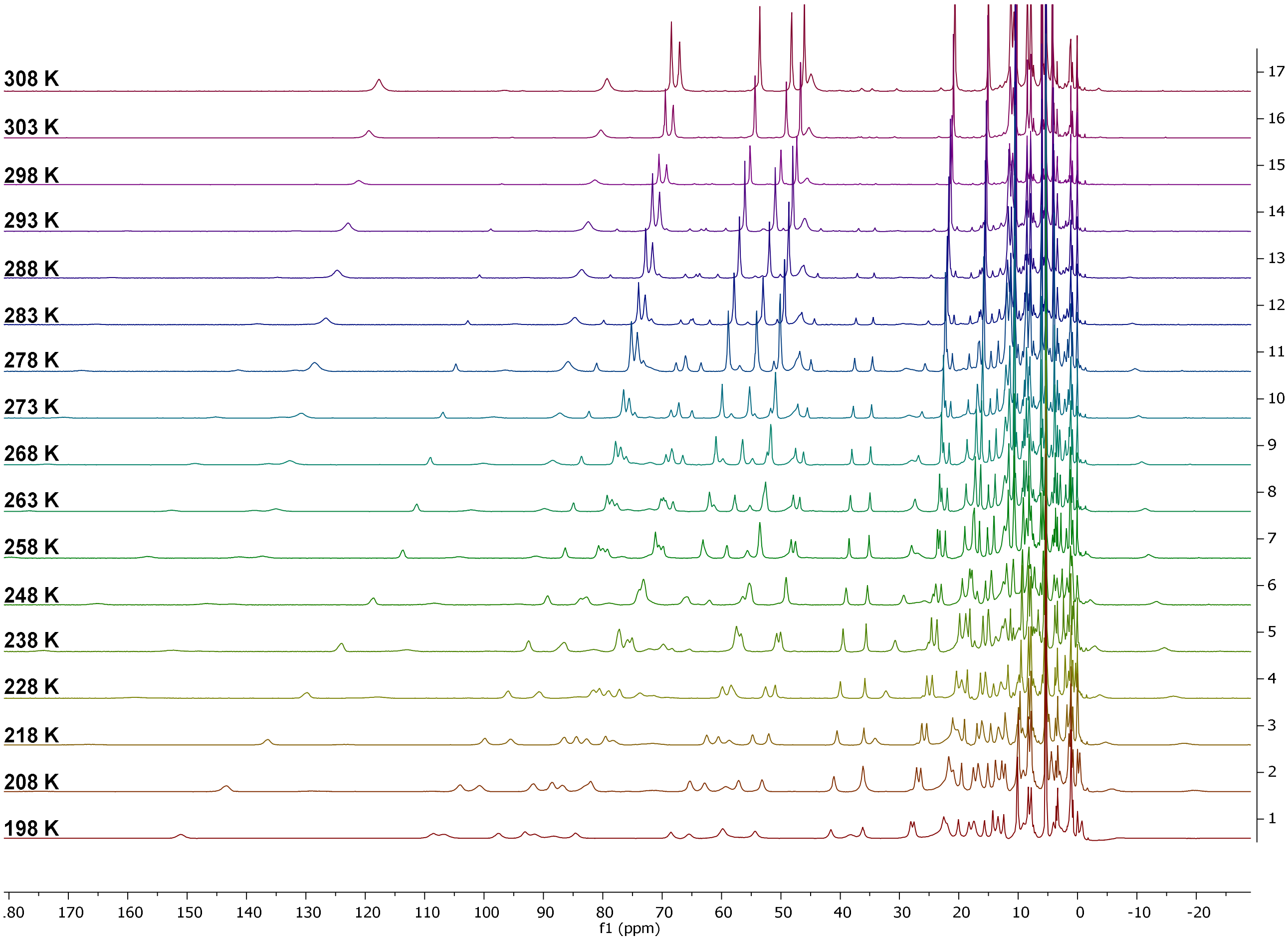

Figure 19. VT-^{1}H NMR (500 MHz) of [LFe$_3$O(PhIm)$_3$Fe][OTf] (**5**) in CD$_2$Cl$_2$ under CO (1 atm.) between 308 K (top) and 198 K (bottom).

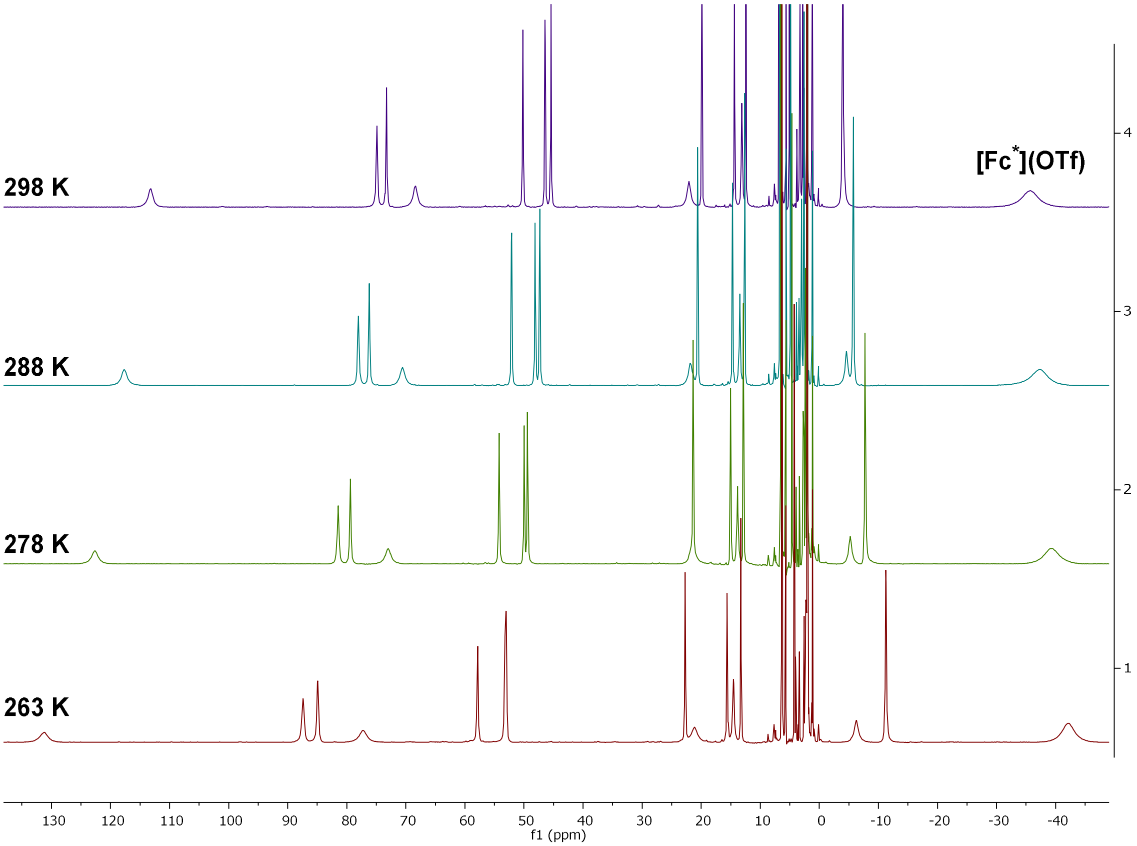

Figure 20. VT-^{1}H NMR (500 MHz) of $[LFe_3O(PhIm)_3Fe][OTf]_2$ (**3**) in acetone-*d*$_6$ under N_2 (1 atm.) between 298 K (top) and 263 K (bottom).

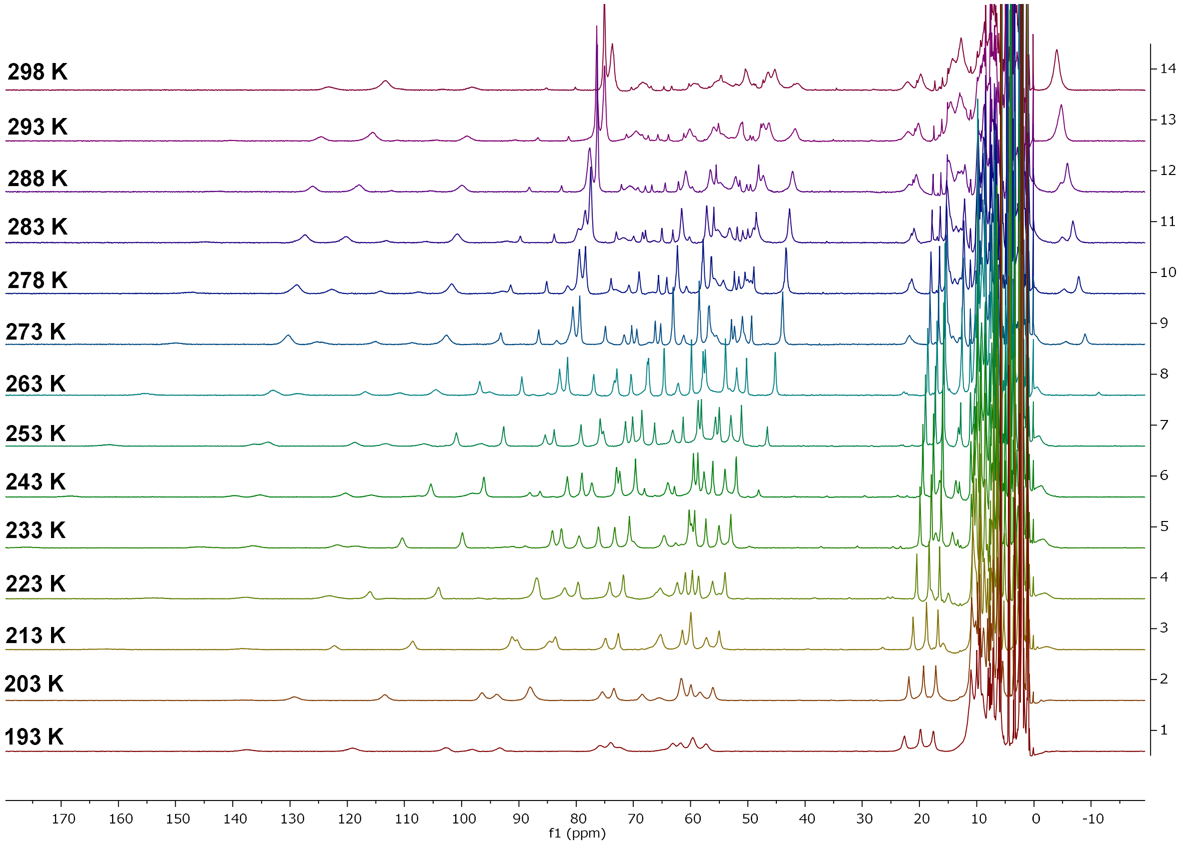

Figure 21. VT-^{1}H NMR (500 MHz) of [LFe$_3$O(PhIm)$_3$Fe][OTf]$_2$ (**3**) in acetone-d_6 under CO (1 atm.) between 298 K (top) and 193 K (bottom).

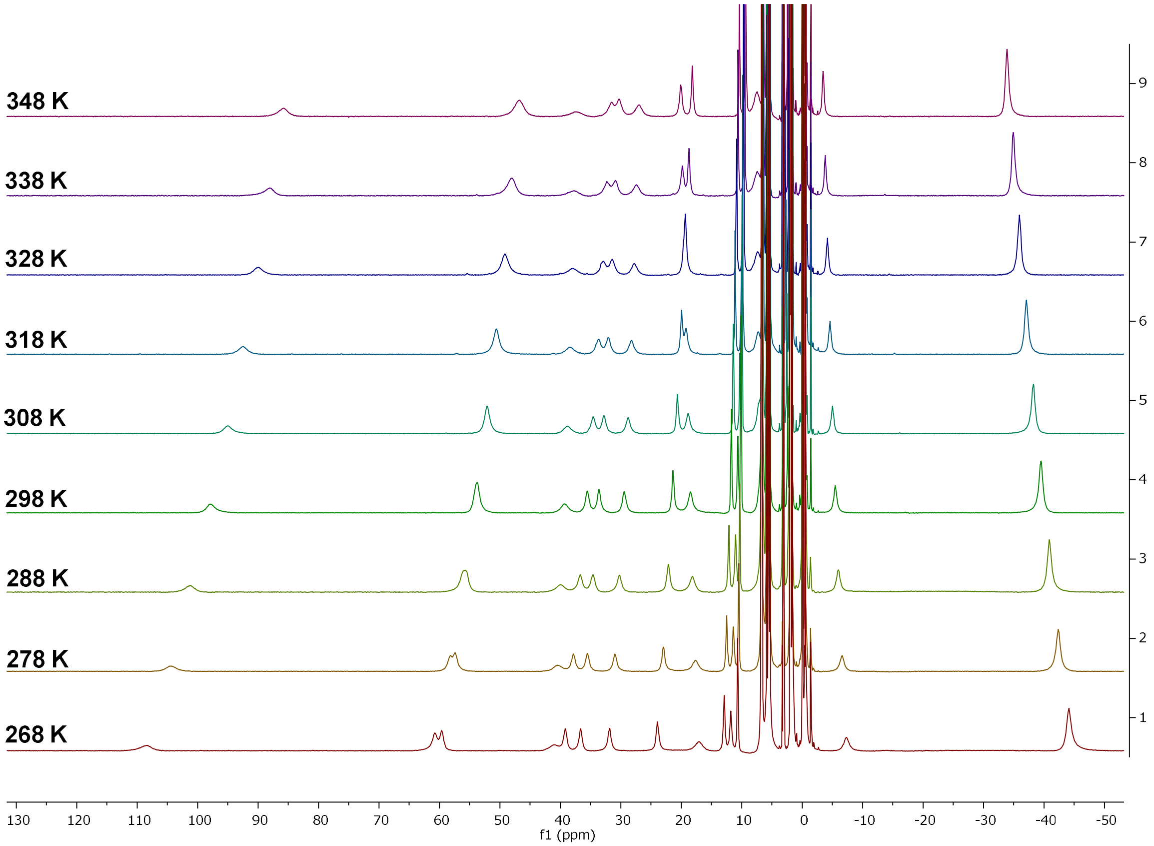

Figure 22. VT-^{1}H NMR (500 MHz) of [LFe$_3$O(PhIm)$_3$Fe][OTf] (**5**) in chlorobenzene-*d*$_5$ under N$_2$ (1 atm.) between 348 K (top) and 268 K (bottom).

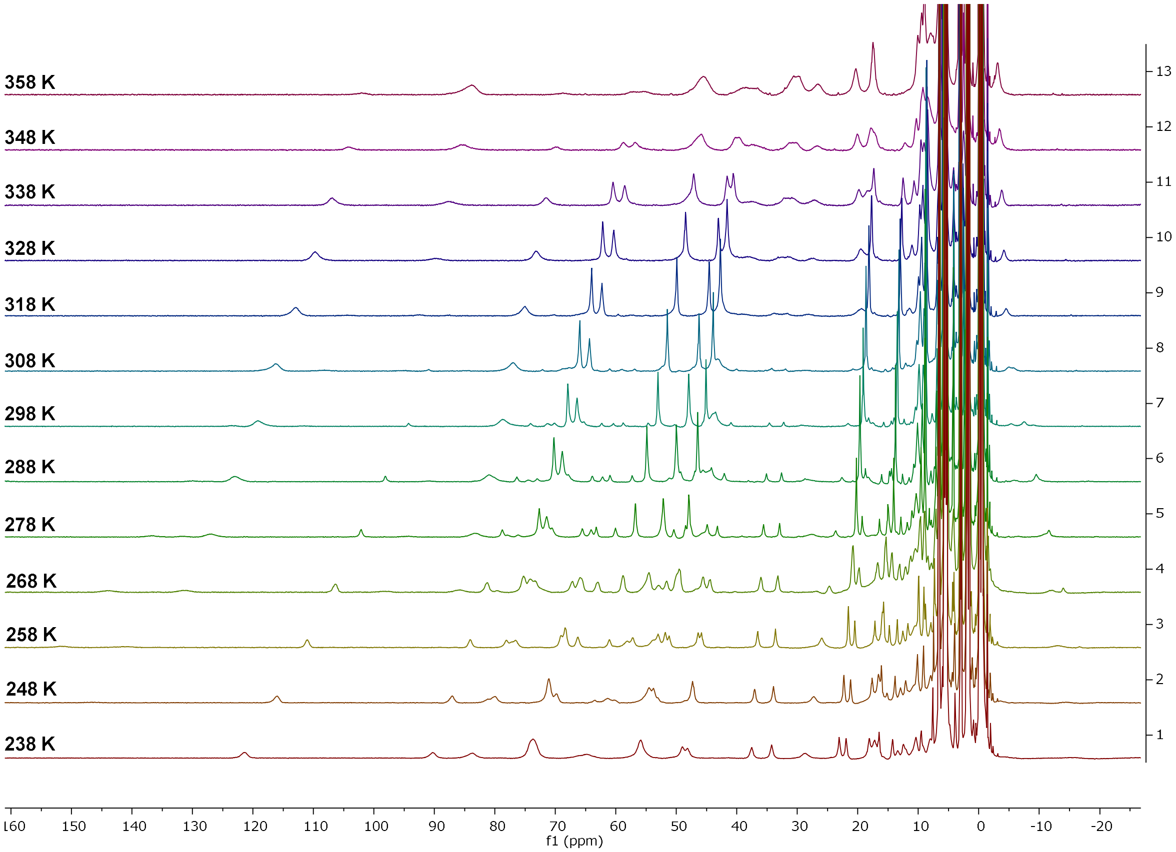

Figure 23. VT-^{1}H NMR (500 MHz) of [LFe$_3$O(PhIm)$_3$Fe][OTf] (**5**) in chlorobenzene-*d*$_5$ under CO (1 atm.) between 358 K (top) and 238 K (bottom).

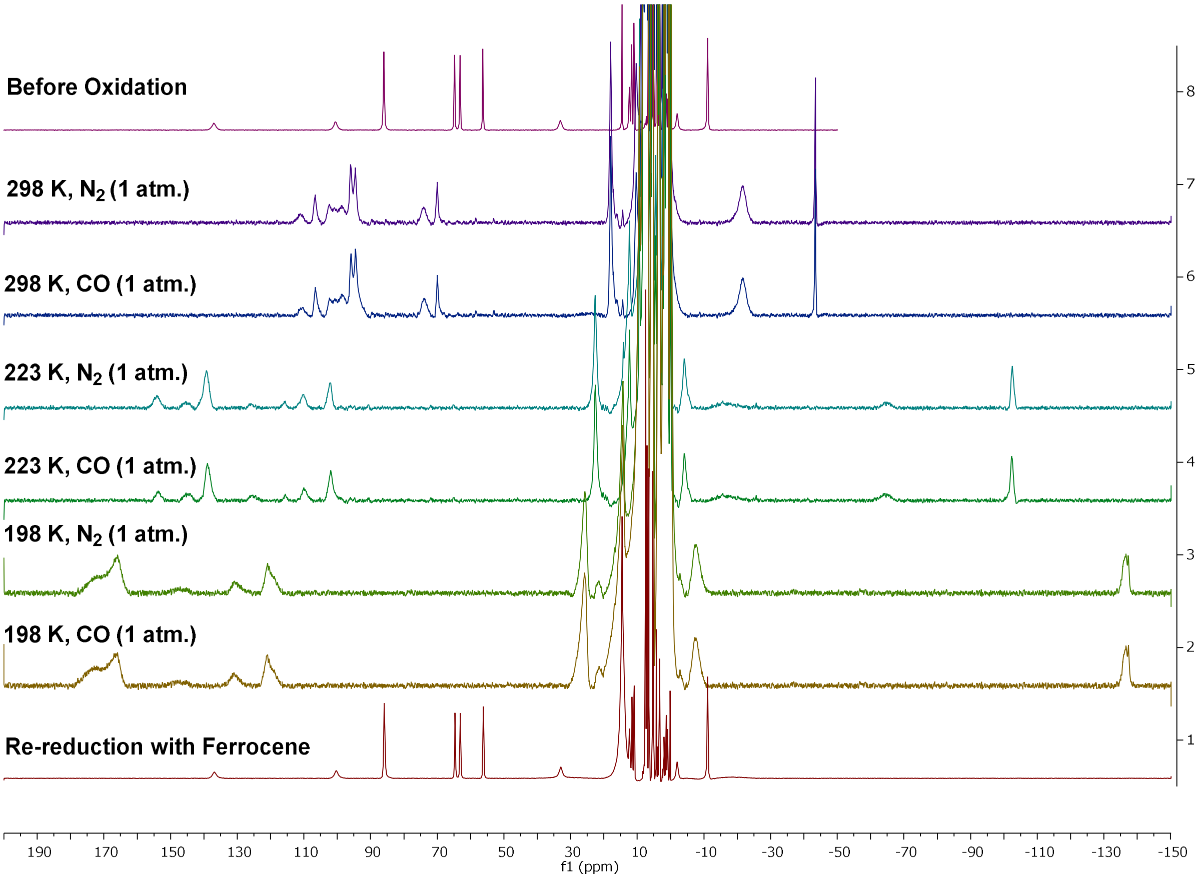

Figure 24. *In situ* oxidation of [LFe$_3$O(PhIm)$_3$Fe][OTf]$_3$ (**4**) and lack of CO binding. The oxidized product is believed to be [LFe$_3$O(PhIm)$_3$Fe][OTf]$_4$ based on the reversibility of this redox transformation. Based on the similarity of the NMR spectra under N$_2$ or CO, this oxidized product does not appear to bind CO.

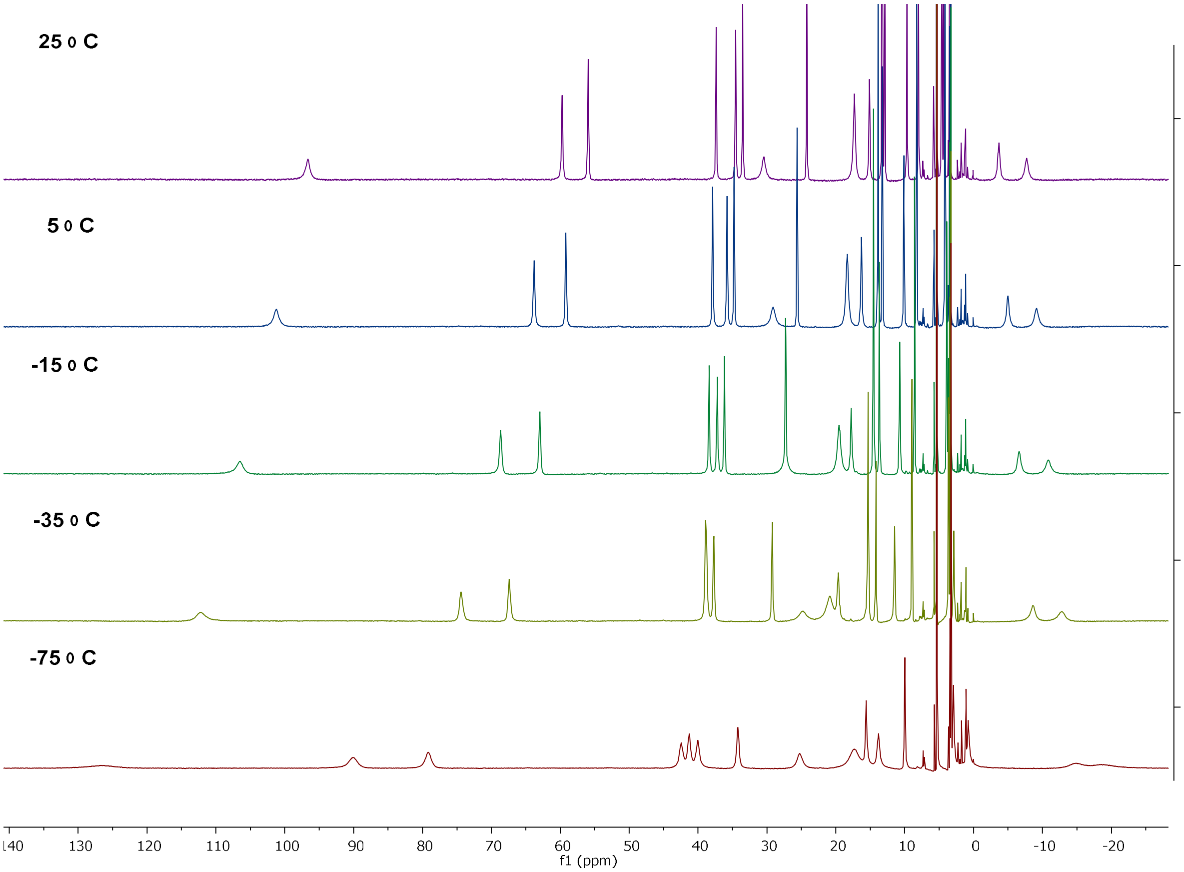

Figure 25. Variable Temperature ^{1}H-NMR (500 MHz) of [LFe$_3$O(PhPz)$_3$Fe][OTf] in CD$_2$Cl$_2$ under 1 atm. of CO. All temperature dependent shifts match those reported previously for [LFe$_3$O(PhPz)$_3$Fe][OTf] at the listed temperature, demonstrating no reaction with CO even at low temperatures.

Chapter 3

General introduction: For details concerning the determination of the thermodynamic parameters for CO binding, see Arnett, C.H.; Kaiser, J.T.; Agapie, T. *Inorg. Chem.*, **2019**, *58*, 15971-15982.

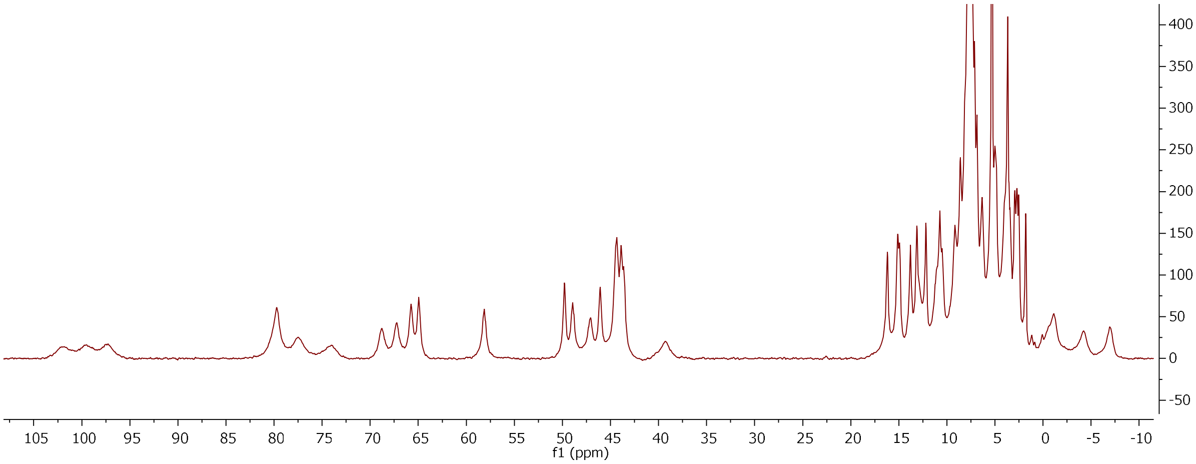

Figure 26. ^{1}H NMR (300 MHz) of [LFe$_3$O(^{pCF3}ArIm-H)$_3$][OTf]$_3$ (A) in CD$_2$Cl$_2$

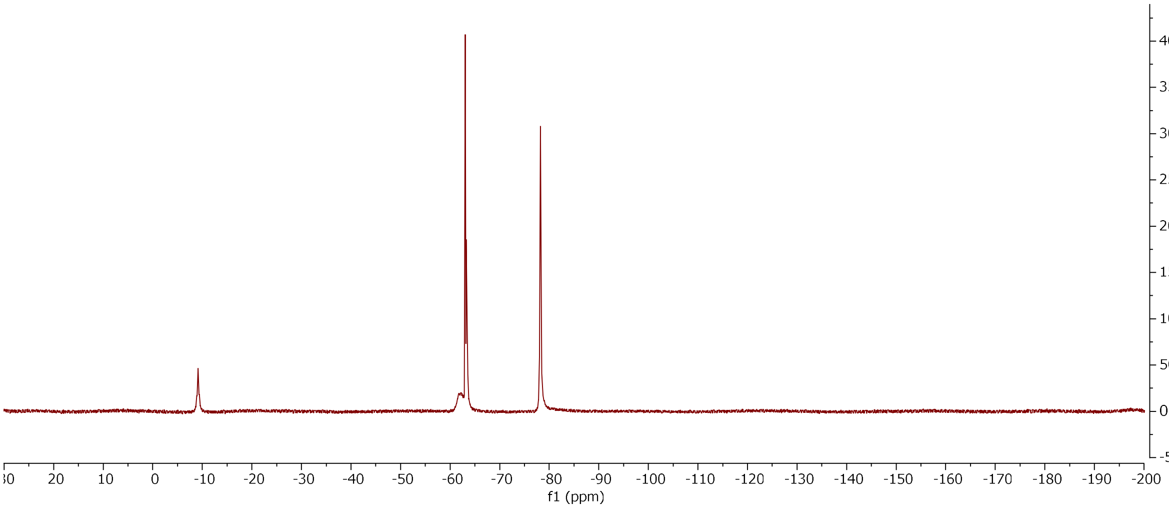

Figure 27. ^{19}F NMR (300 MHz) of [LFe$_3$O(^{pCF3}ArIm-H)$_3$][OTf]$_3$ (A) in CD$_2$Cl$_2$

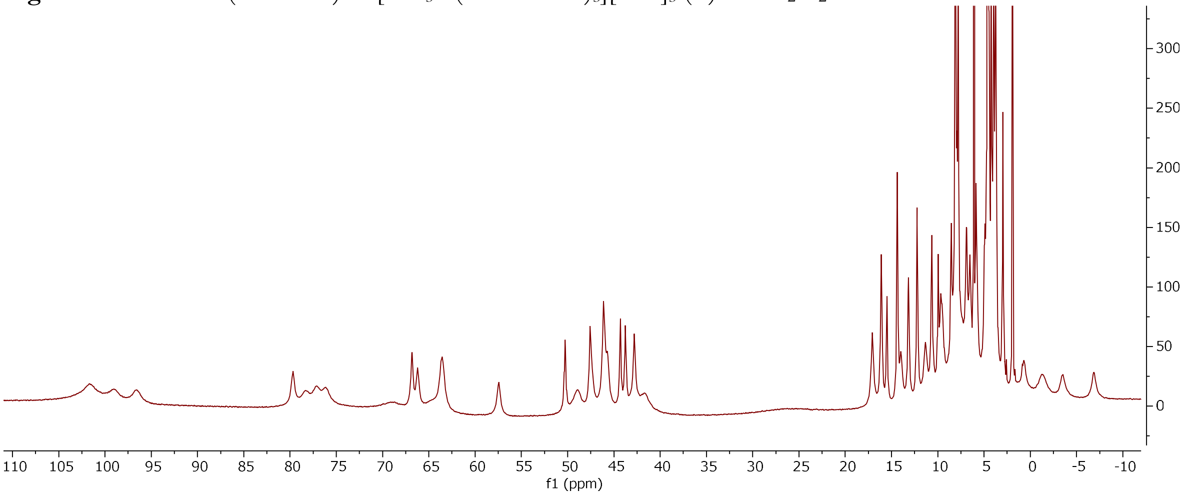

Figure 28. ^{1}H NMR (300 MHz) of [LFe$_3$O(^{pOMe}ArIm-H)$_3$][OTf]$_3$ (B) in CD$_2$Cl$_2$

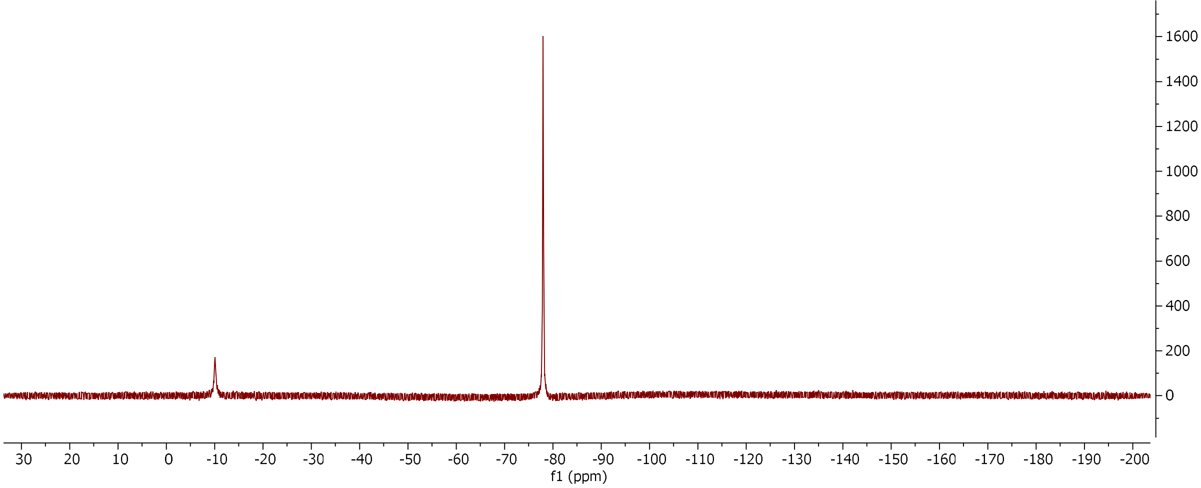

Figure 29. ^{19}F NMR (300 MHz) of [LFe$_3$O(^{pOMe}ArIm-H)$_3$][OTf]$_3$ (B) in CD$_2$Cl$_2$

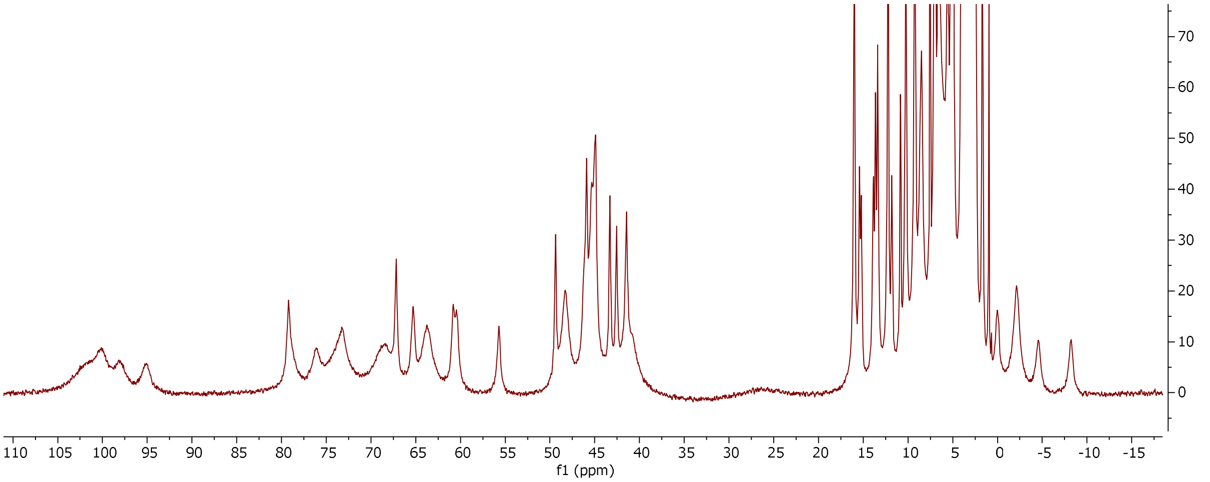

Figure 30. ^{1}H NMR (300 MHz) of [LFe$_3$O(^{pNMe2}ArIm-H)$_3$][OTf]$_3$ (C) in CD$_2$Cl$_2$

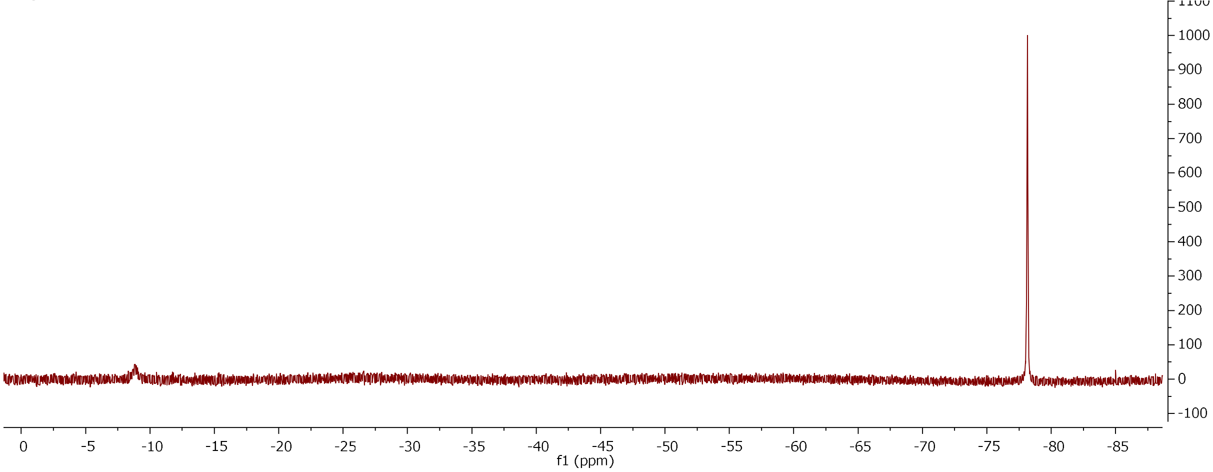

Figure 31. ^{19}F NMR (300 MHz) of [LFe$_3$O(^{pNMe2}ArIm-H)$_3$][OTf]$_3$ (C) in CD$_2$Cl$_2$

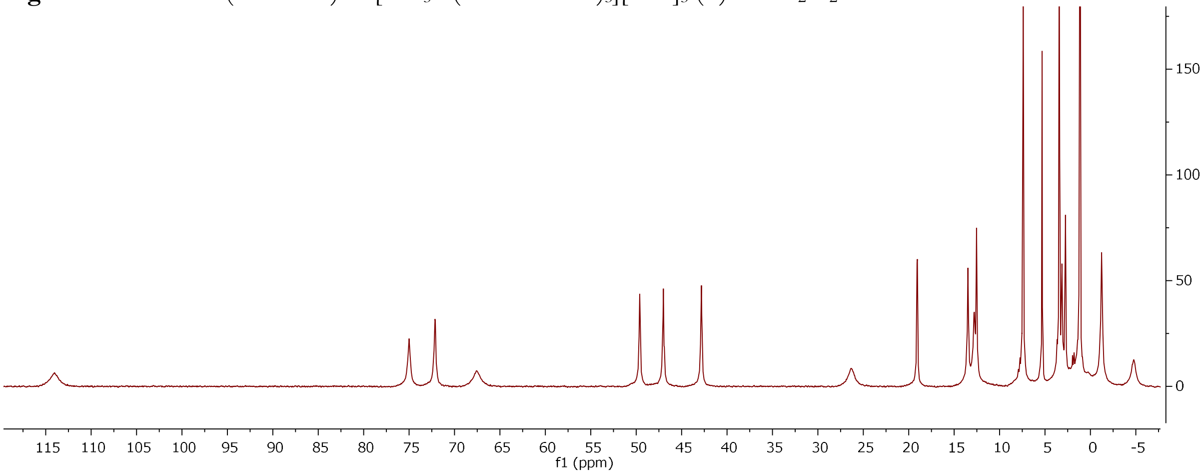

Figure 32. ^{1}H NMR (300 MHz) of [LFe$_3$O(^{pCF3}ArIm)$_3$Fe][OTf]$_2$ (1^{CF3}) in CD$_2$Cl$_2$

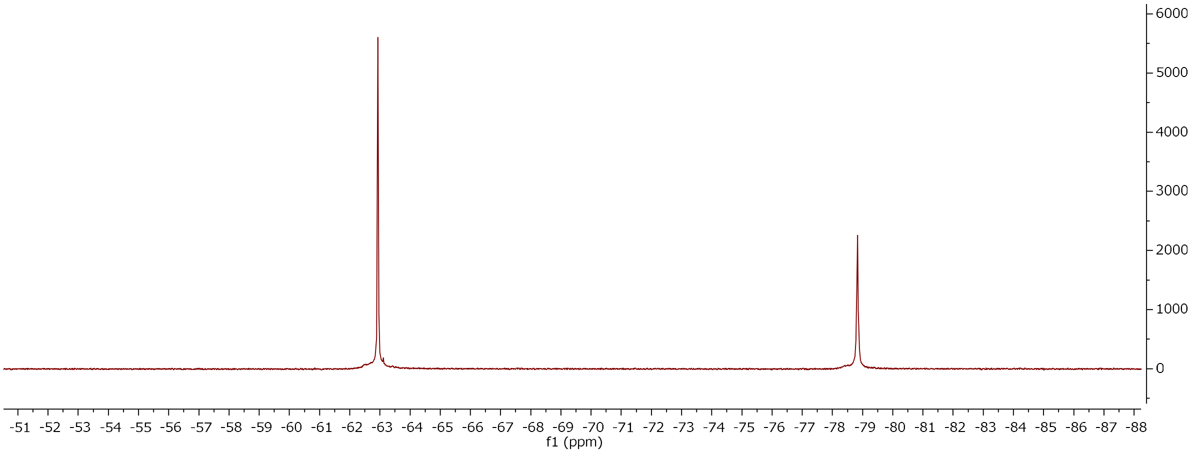

Figure 33. ^{19}F NMR (300 MHz) of [LFe$_3$O(^{pCF3}ArIm)$_3$Fe][OTf]$_2$ (1^{CF3}) in CD$_2$Cl$_2$

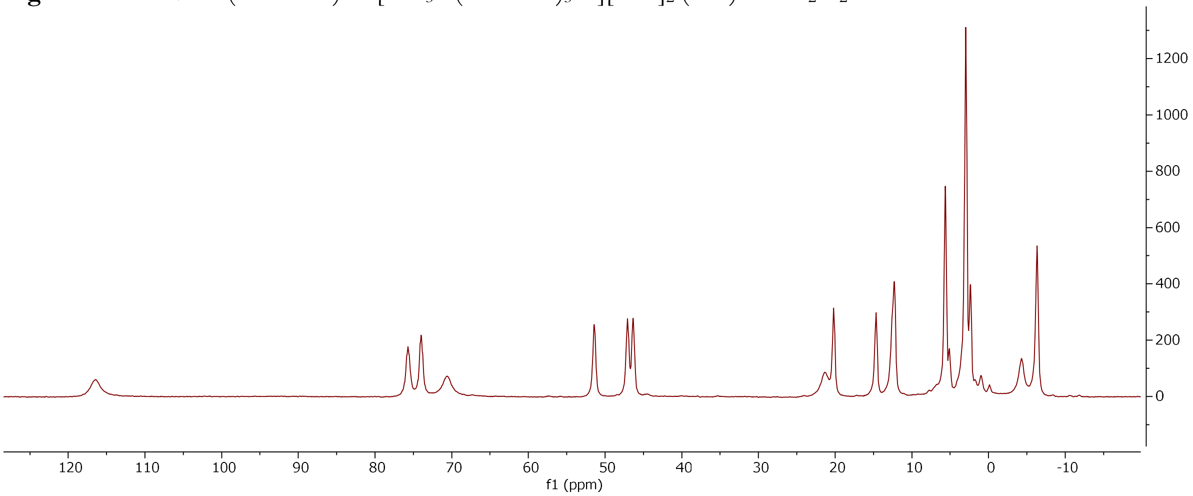

Figure 34. ^{1}H NMR (300 MHz) of [LFe$_3$O(^{pOMe}ArIm)$_3$Fe][OTf]$_2$ (1^{OMe}) in CD$_2$Cl$_2$

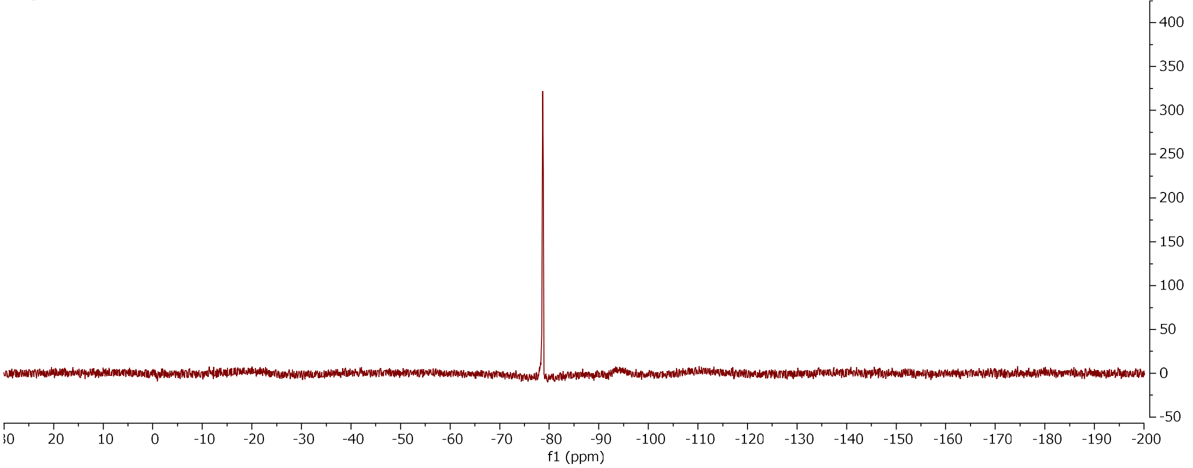

Figure 35. ^{19}F NMR (300 MHz) of [LFe$_3$O(^{pOMe}ArIm)$_3$Fe][OTf]$_2$ (1^{OMe}) in CD$_2$Cl$_2$

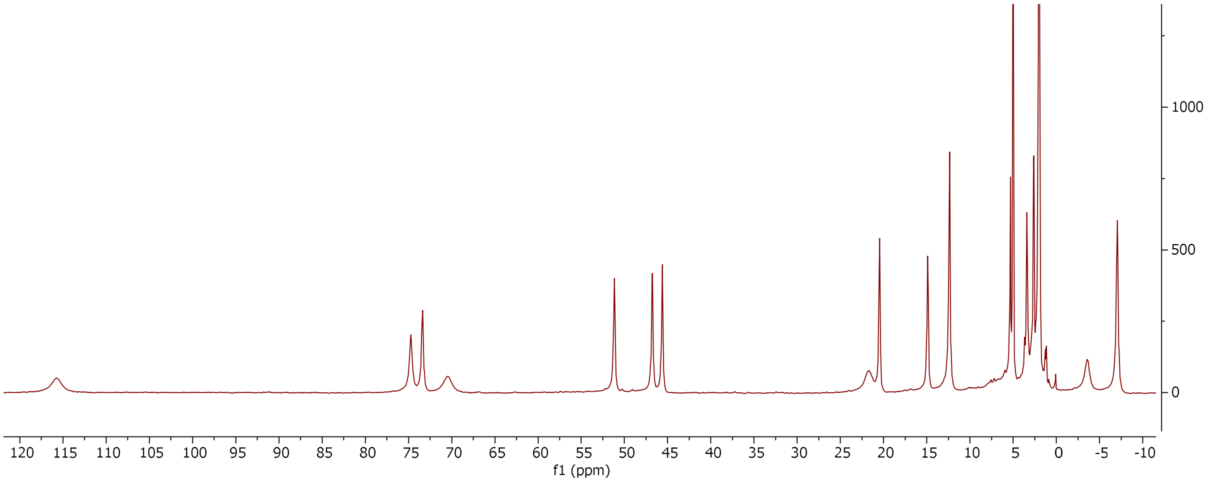

Figure 36. ^{1}H NMR (300 MHz) of [LFe$_3$O(^{pNMe2}ArIm)$_3$Fe][OTf]$_2$ (1^{NMe2}) in CD$_2$Cl$_2$

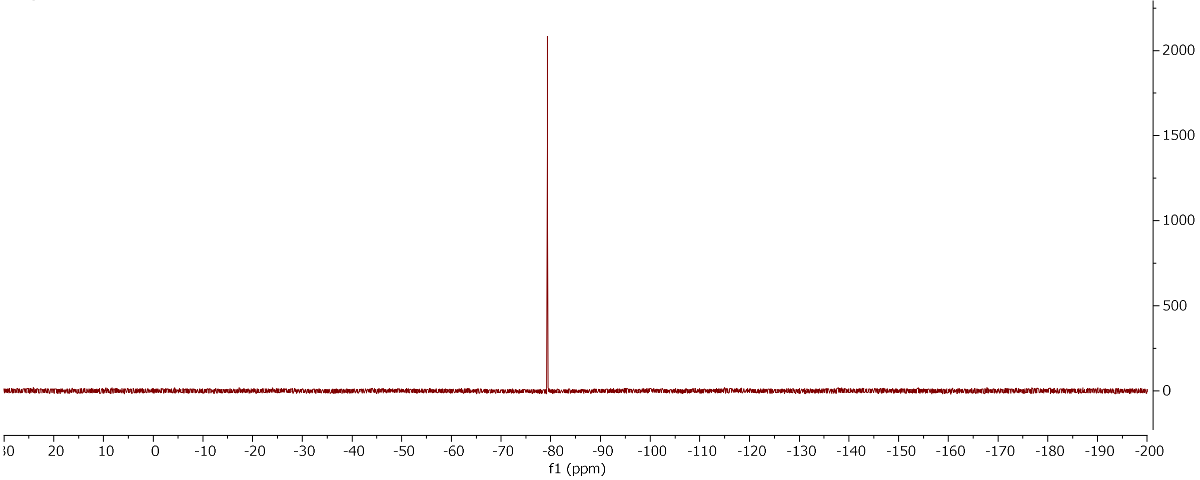

Figure 37. ^{19}F NMR (300 MHz) of [LFe$_3$O(^{pNMe2}ArIm)$_3$Fe][OTf]$_2$ (1^{NMe2}) in CD$_2$Cl$_2$

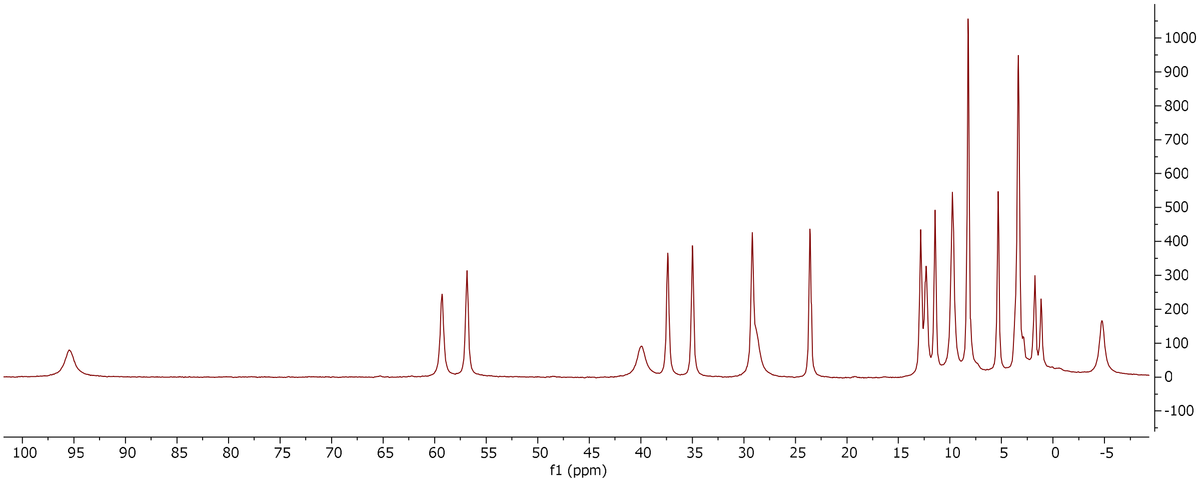

Figure 38. ^{1}H NMR (300 MHz) of [LFe$_3$O(^{pCF3}ArIm)$_3$Fe][OTf] (2^{CF3}) in CD$_2$Cl$_2$

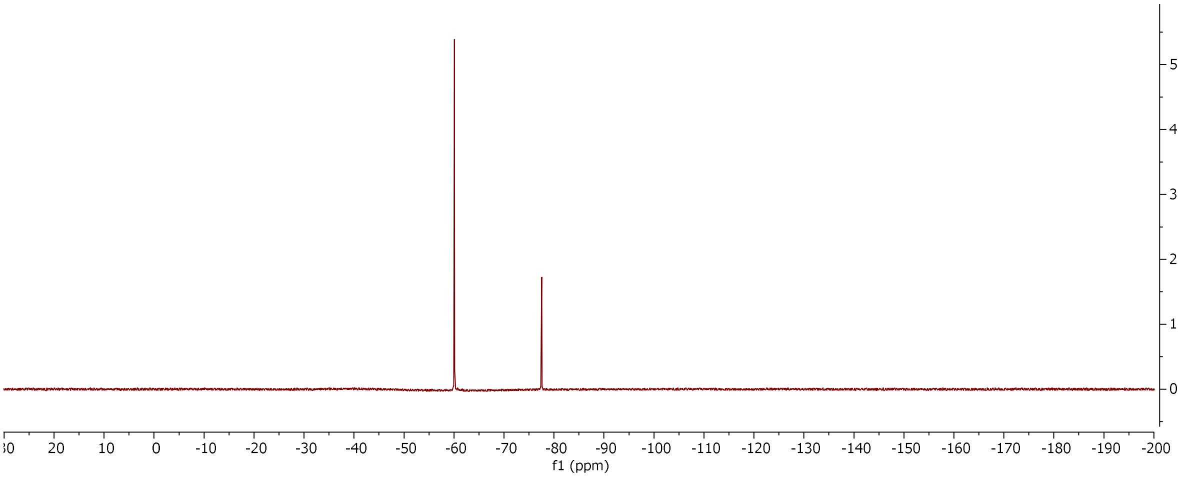

Figure S39. ^{19}F NMR (300 MHz) of [LFe$_3$O(^{pCF3}ArIm)$_3$Fe][OTf] (2^{CF3}) in CD$_2$Cl$_2$

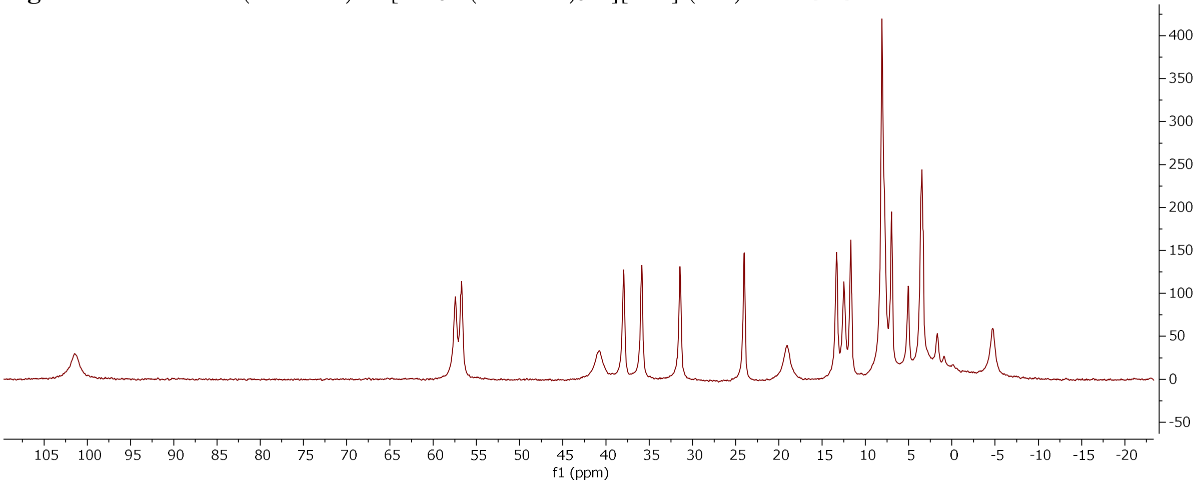

Figure S40. ^{1}H NMR (300 MHz) of [LFe$_3$O(PhIm)$_3$Fe][BF$_4$] (2^{H}) in CD$_2$Cl$_2$

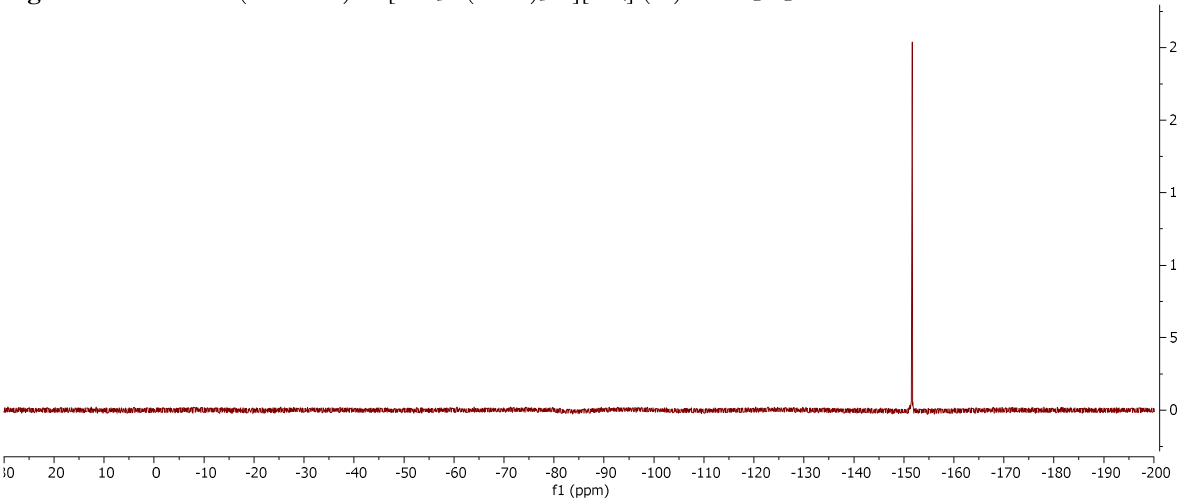

Figure 41. ^{19}F NMR (300 MHz) of [LFe$_3$O(PhIm)$_3$Fe][BF$_4$] (2^{H}) in CD$_2$Cl$_2$

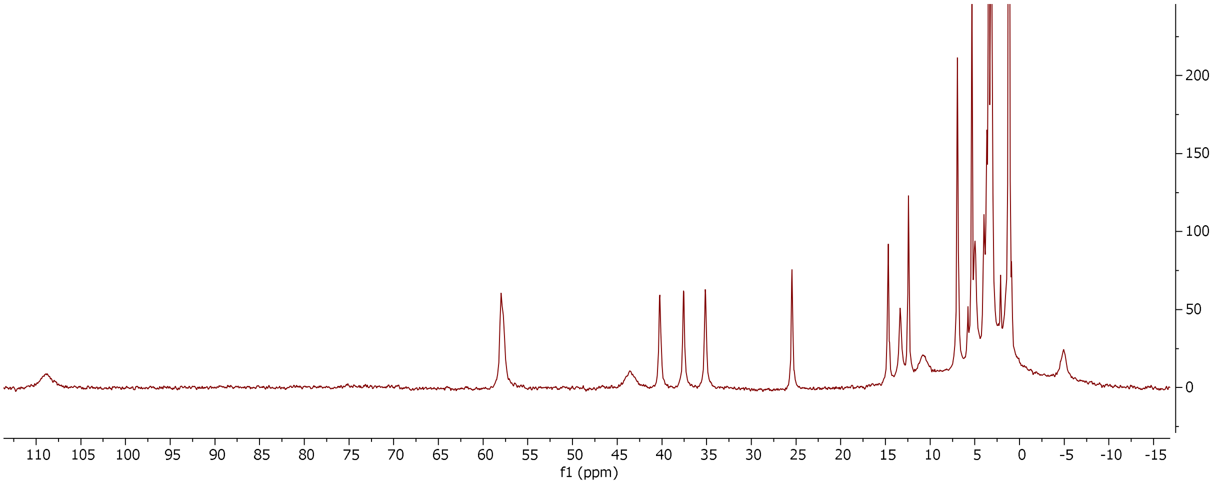

Figure 42. ^{1}H NMR (300 MHz) of [LFe$_3$O(^{pNMe2}ArIm)$_3$Fe][OTf] (2^{NMe2}-OTf) in CD$_2$Cl$_2$

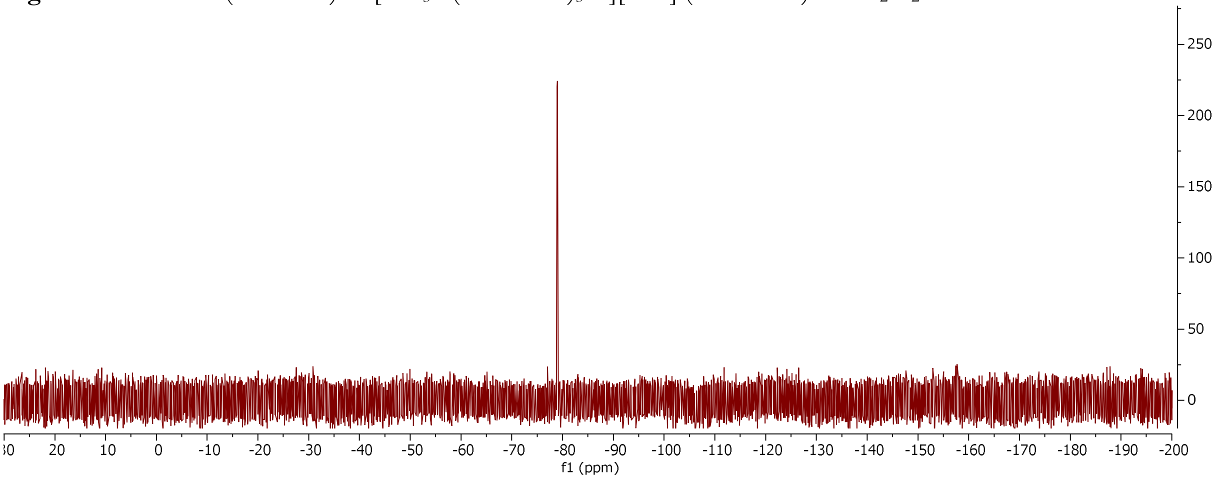

Figure 43. ^{19}F NMR (300 MHz) of [LFe$_3$O(^{pNMe2}ArIm)$_3$Fe][OTf] (2^{NMe2}-OTf) in CD$_2$Cl$_2$

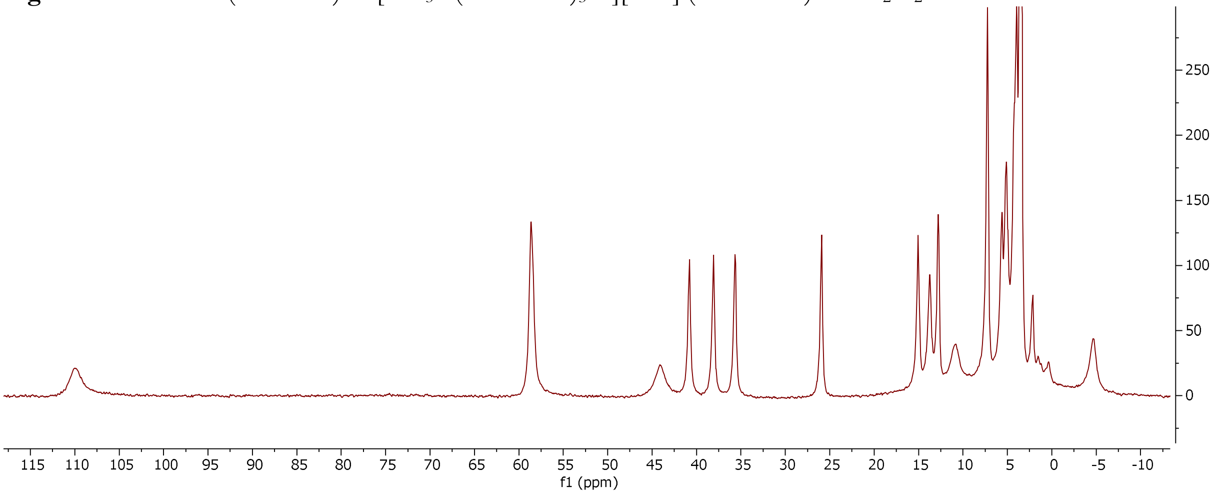

Figure 44. ^{1}H NMR (300 MHz) of [LFe$_3$O(^{pNMe2}ArIm)$_3$Fe][BF$_4$] (2^{NMe2}-BF$_4$) in CD$_2$Cl$_2$

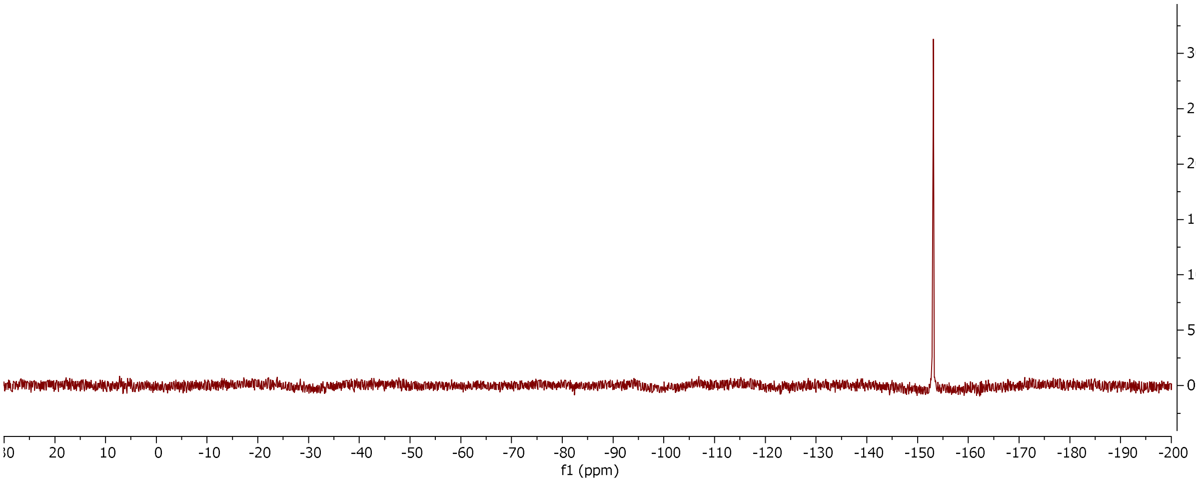

Figure 45. ^{19}F NMR (300 MHz) of [LFe$_3$O(^{pNMe2}ArIm)$_3$Fe][BF$_4$] (2^{NMe2}-BF$_4$) in CD$_2$Cl$_2$

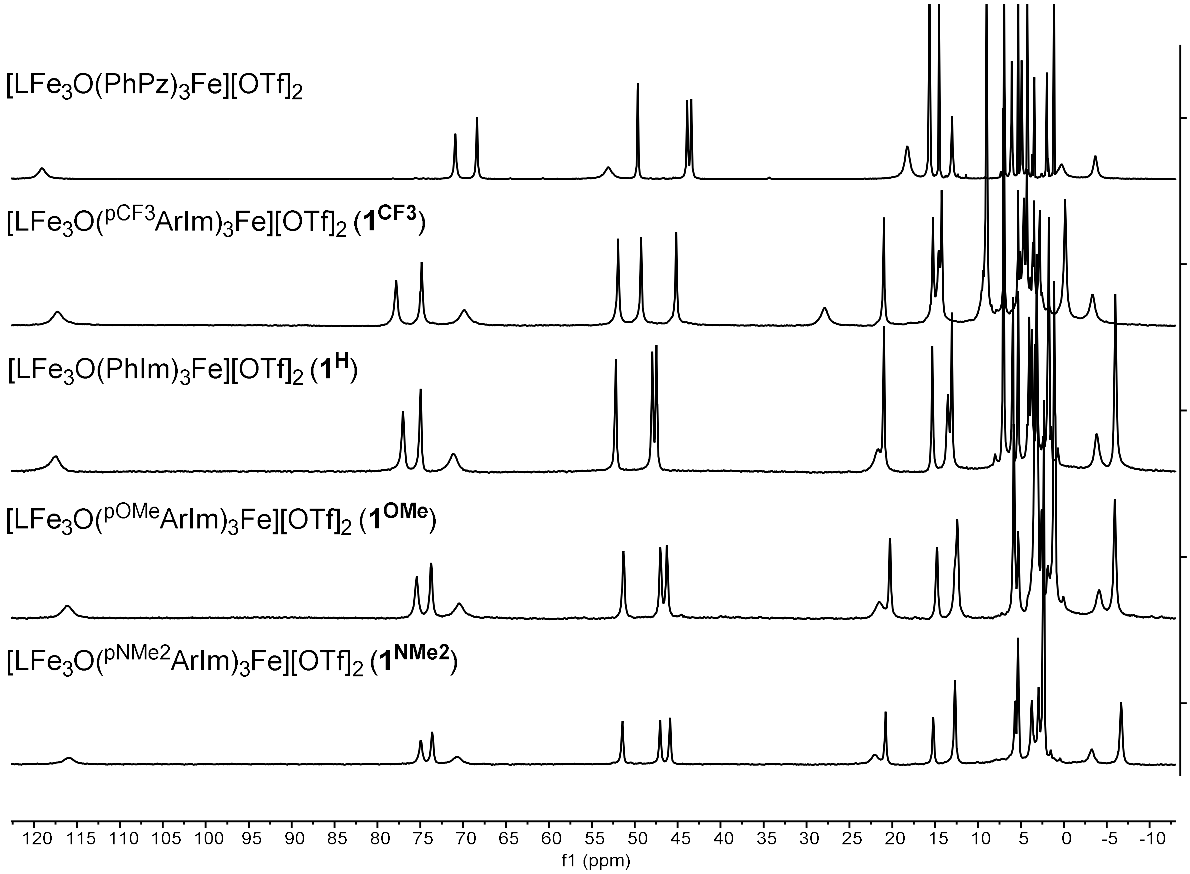

Figure 46. Comparison of ^{1}H NMR (300 MHz) of [LFe$_3$O(PhPz)$_3$Fe][OTf]$_2$, [LFe$_3$O(^{pCF3}ArIm)$_3$Fe][OTf]$_2$ (1^{CF3}), [LFe$_3$O(PhIm)$_3$Fe][OTf]$_2$ (1^{H}), [LFe$_3$O(^{pOMe}ArIm)$_3$Fe][OTf]$_2$ (1^{OMe}), and [LFe$_3$O(^{pNMe2}ArIm)$_3$Fe][OTf]$_2$ (1^{NMe2}) in CD$_2$Cl$_2$

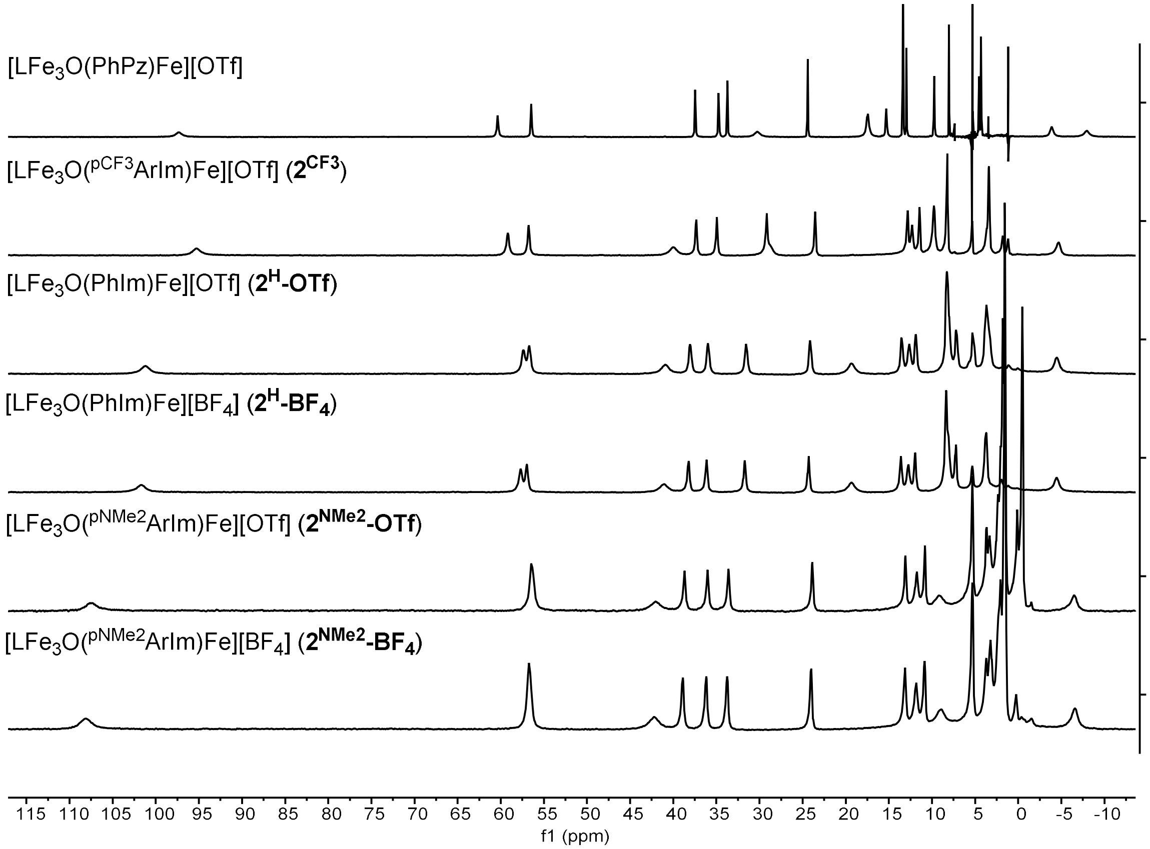

Figure 47. Comparison of ^{1}H NMR (300 MHz) of [LFe$_3$O(PhPz)$_3$Fe][OTf], [LFe$_3$O(^{pCF3}ArIm)$_3$Fe][OTf] (2^{CF3}), [LFe$_3$O(PhIm)$_3$Fe][OTf] (2^{H}-OTf), [LFe$_3$O(PhIm)$_3$Fe][BF$_4$] (2^{H}-BF$_4$), [LFe$_3$O(^{pNMe2}ArIm)$_3$Fe][OTf] (2^{NMe2}-OTf), and [LFe$_3$O(^{pNMe2}ArIm)$_3$Fe][BF$_4$] (2^{NMe2}-BF$_4$) in CD$_2$Cl$_2$

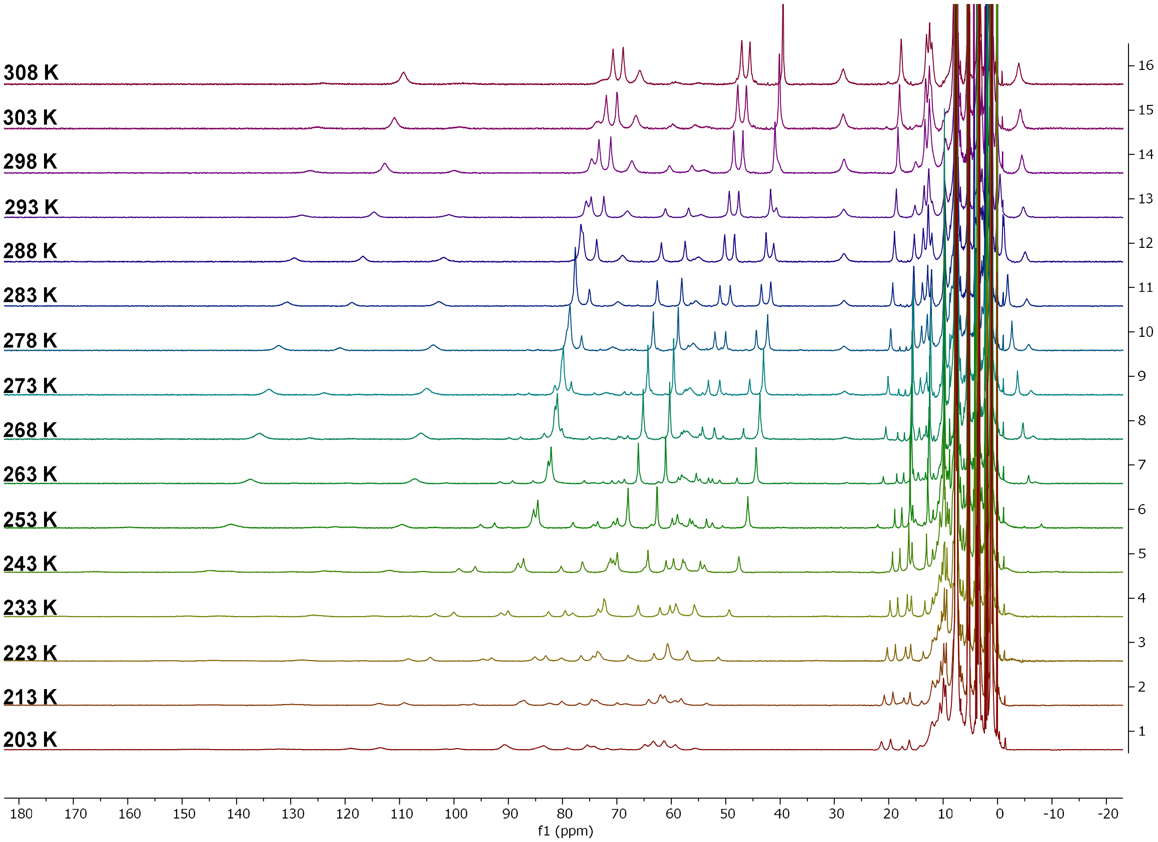

Figure 48. VT-^{1}H NMR (400 MHz) of [LFe$_3$O(^{pCF3}ArIm)$_3$Fe][OTf]$_2$ (1^{CF3}) in CD$_2$Cl$_2$ under CO (1 atm.) between 308 K (top) and 203 K (bottom).

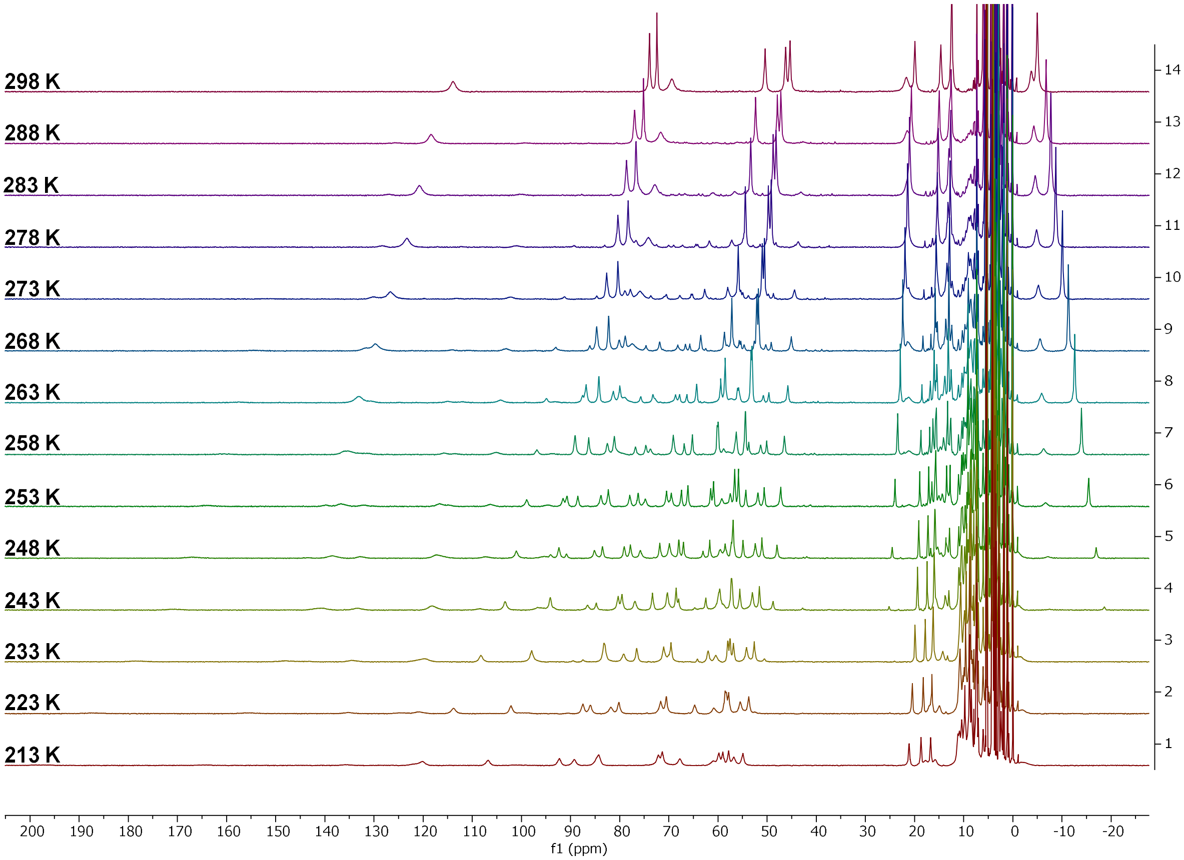

Figure 49. VT-^{1}H NMR (400 MHz) of [LFe$_3$O(^{pOMe}ArIm)$_3$Fe][OTf]$_2$ (1^{OMe}) in CD$_2$Cl$_2$ under CO (1 atm.) between 298 K (top) and 213 K (bottom).

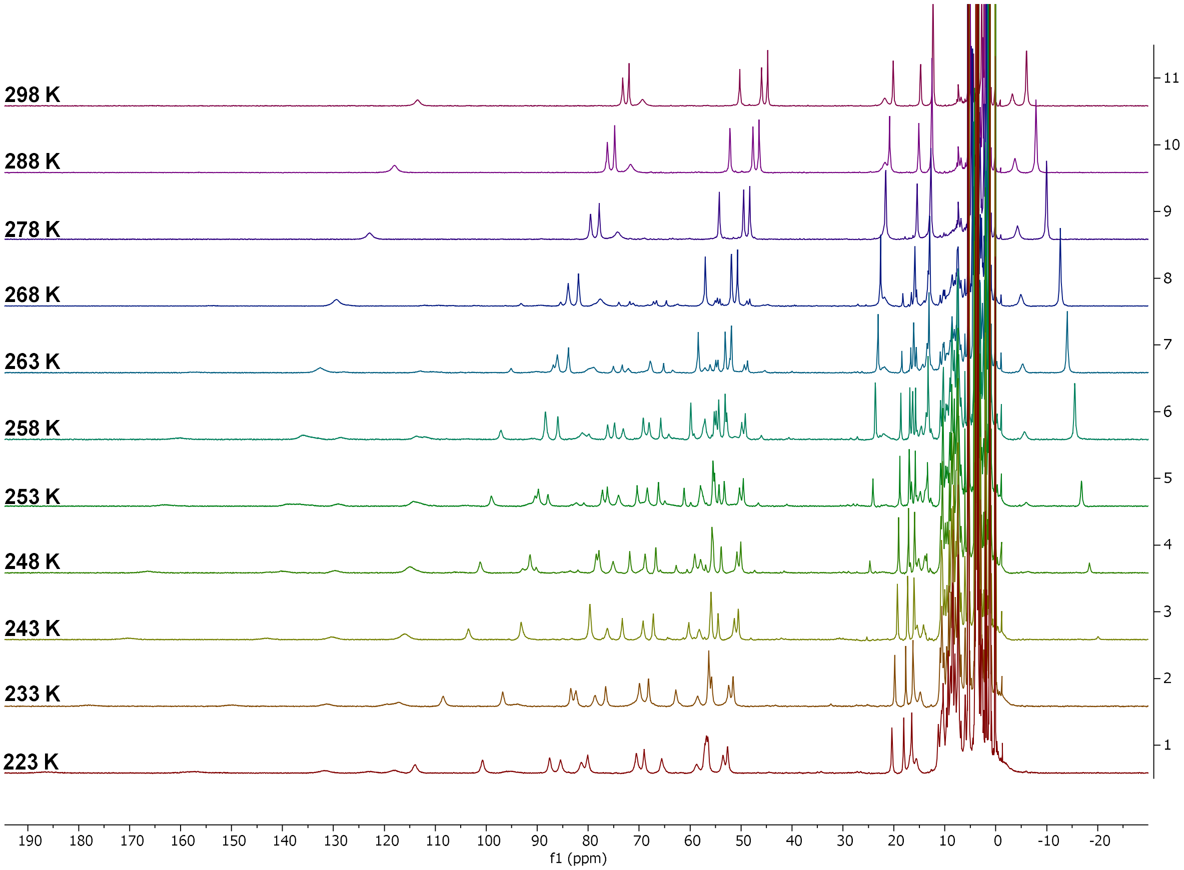

Figure 50. VT-^{1}H NMR (400 MHz) of [LFe$_3$O(^{pNMe2}ArIm)$_3$Fe][OTf]$_2$ (1^{NMe2}) in CD$_2$Cl$_2$ under CO (1 atm.) between 298 K (top) and 223 K (bottom).

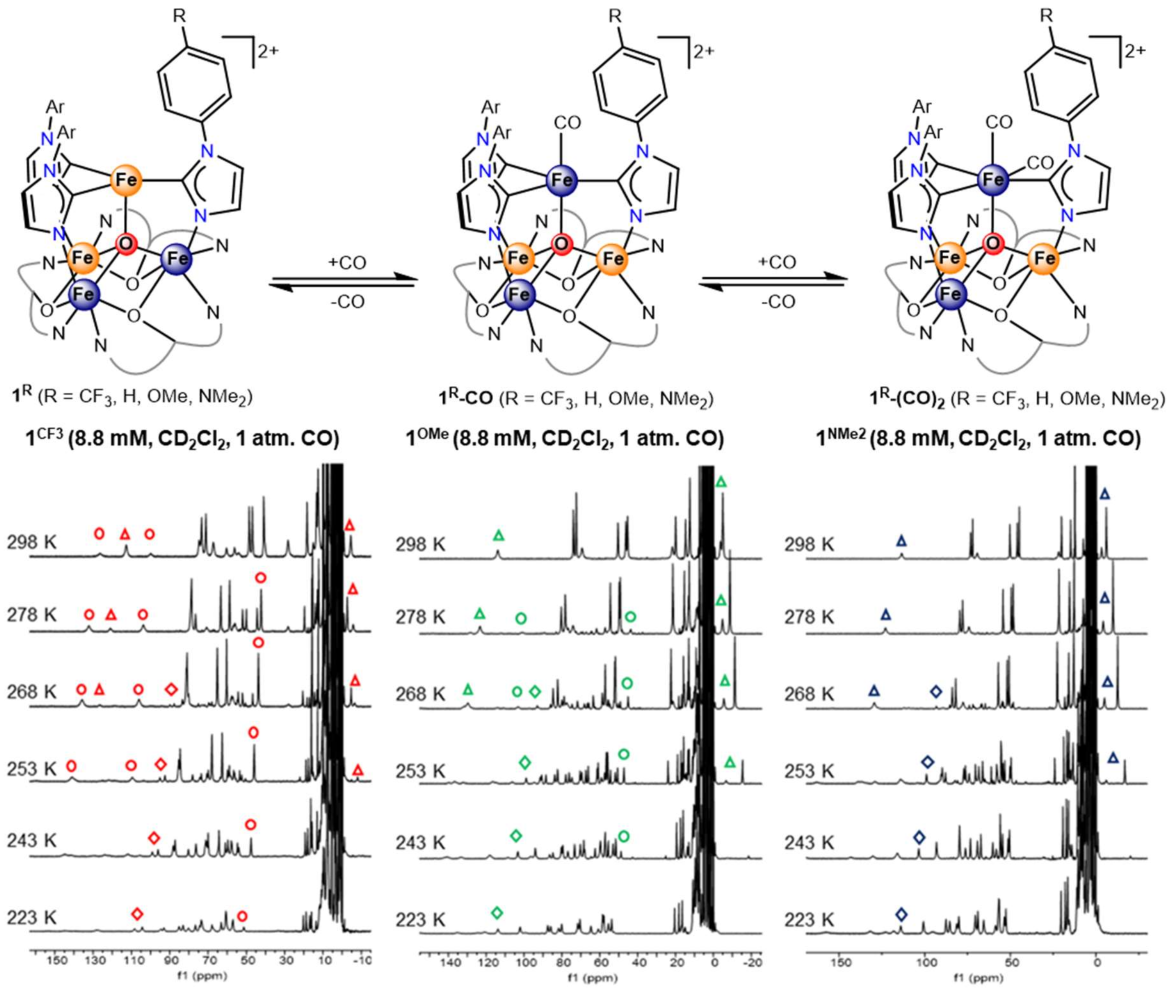

Figure 51. Variable temperature ^{1}H-NMR spectroscopy illustrates the influence of ligand modifications on the affinity of 1^R (R = CF$_3$, H, OMe, NMe$_2$) for binding one vs. two molecules of CO. Diagnostic spectral features: 1^R (triangles), 1^R-CO (circles), 1^R-(CO)$_2$ (diamonds).

Chapter 4

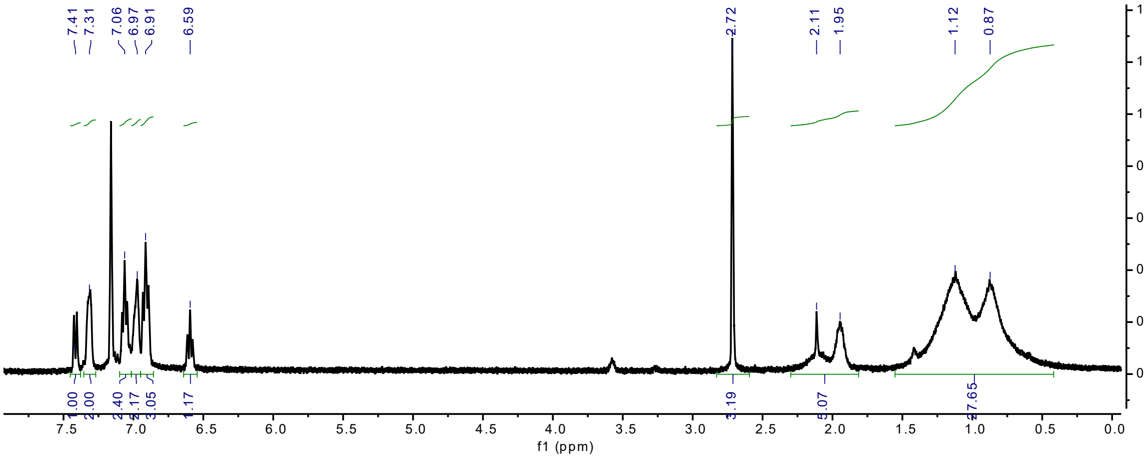

Figure 52. ^{1}H NMR (400 MHz) of **1** in C$_6$D$_6$

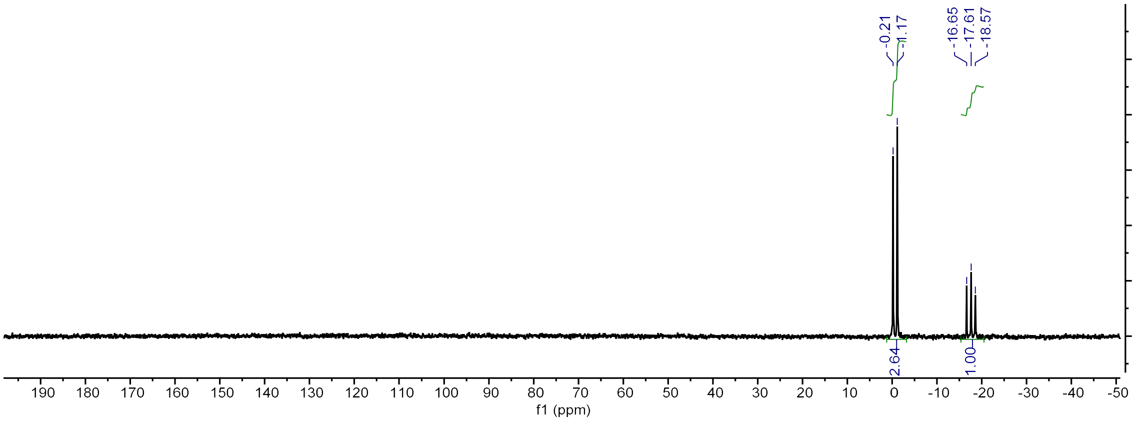

Figure 53. $^{31}P\{^1H\}$ NMR (162 MHz) of **1** in C_6D_6

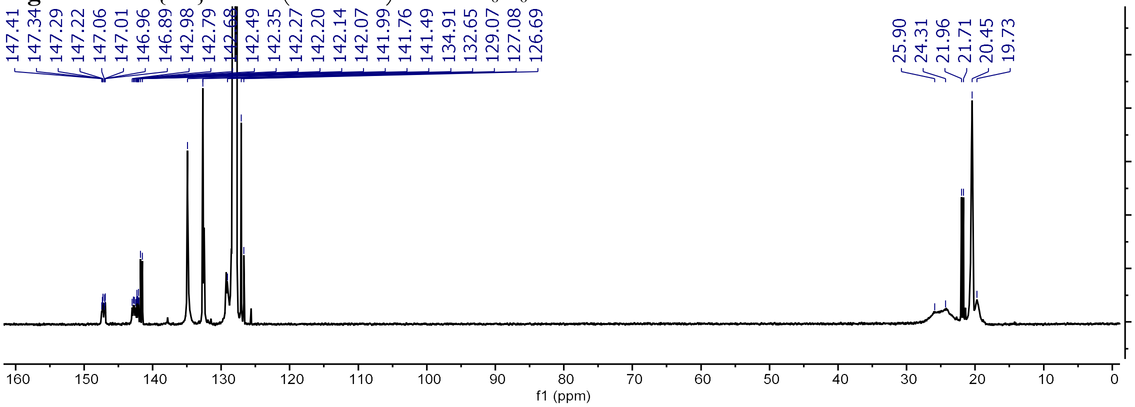

Figure 54. $^{13}C\{^1H\}$ NMR (101 MHz) of **1** in C_6D_6

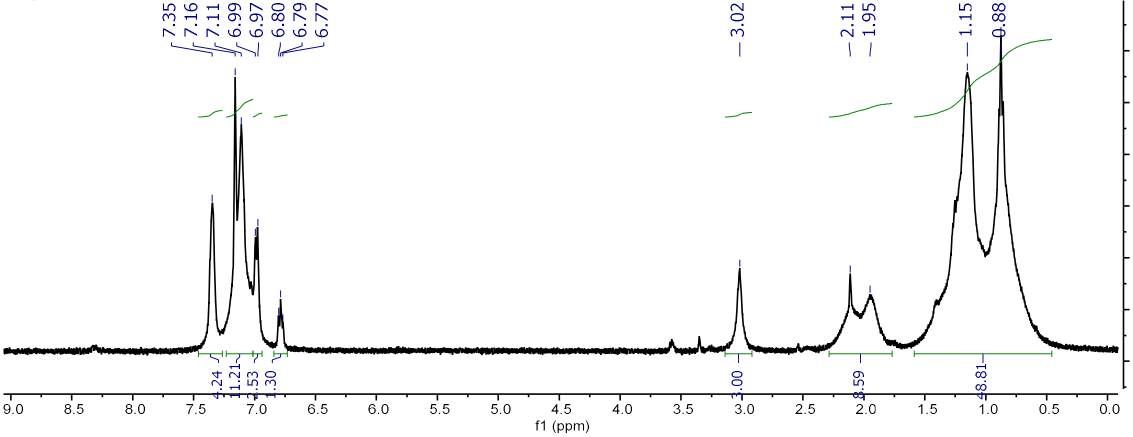

Figure 55. ^1H NMR (400 MHz) of **2** in C_6D_6

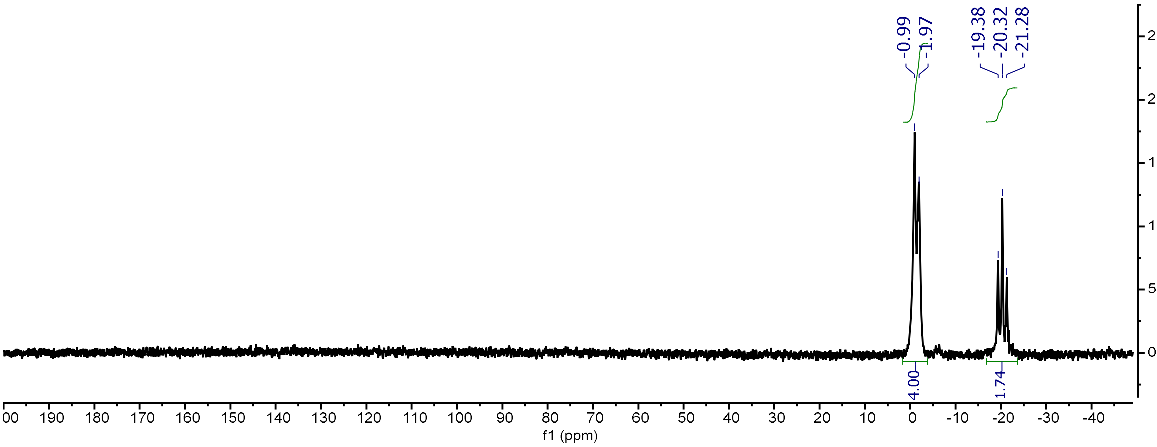

Figure 56. $^{31}P\{^1H\}$ NMR (162 MHz) of **2** in C_6D_6

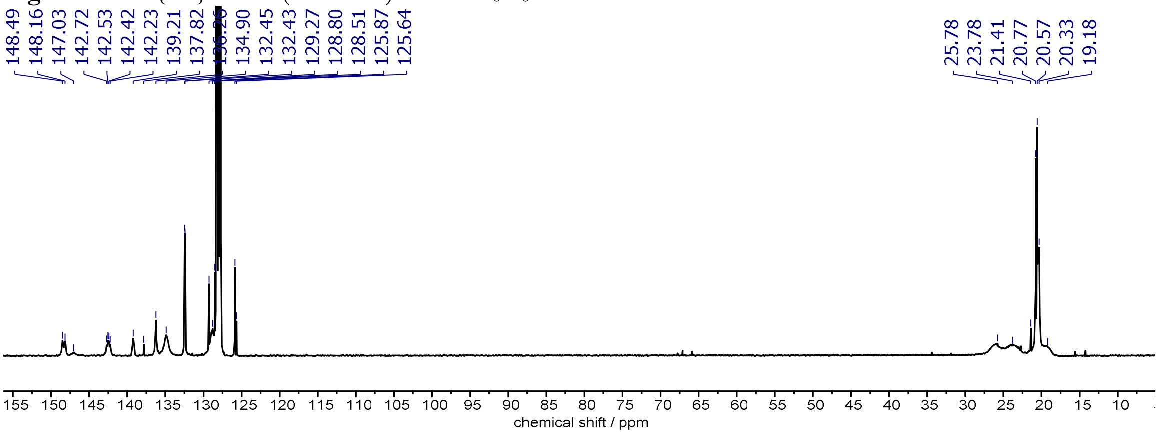

Figure 57. $^{13}C\{^1H\}$ NMR (101 MHz) of **2** in C_6D_6

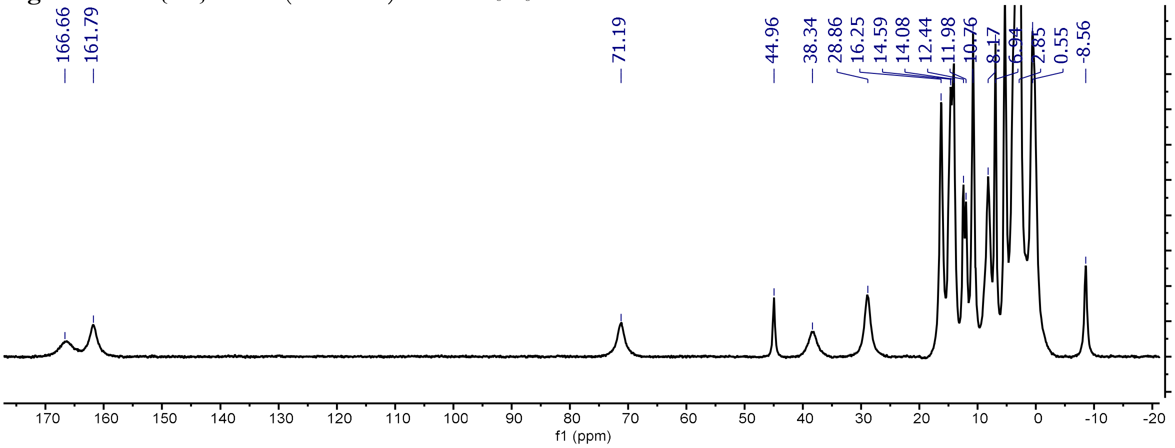

Figure 58. ^1H NMR (400 MHz) of $(P_6ArCH_3)Fe_2Br_4$ **(3)** in CD_2Cl_2

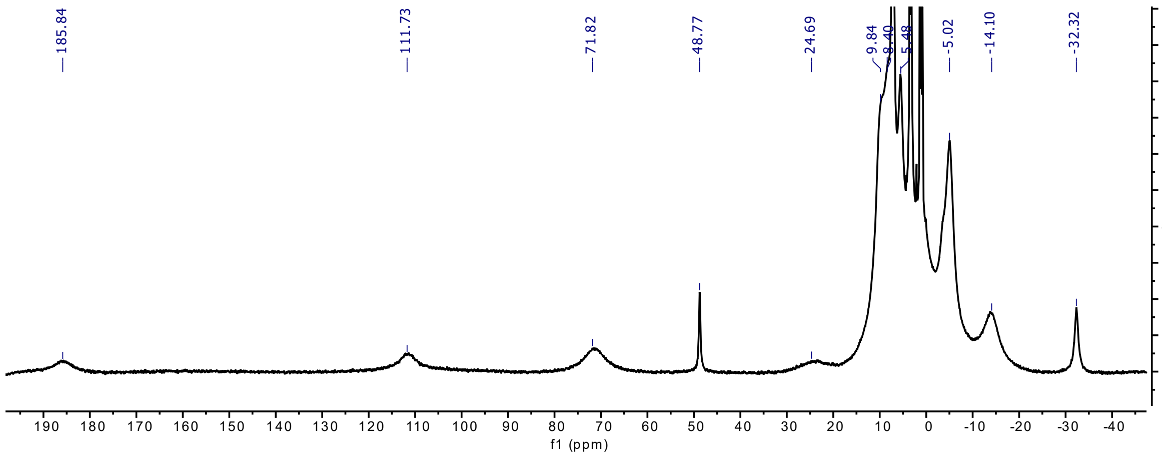

Figure 59. ^1H NMR (400 MHz) of $(P_6ArCH_3)Fe_2Br_2$ **(4)** in C_6D_6

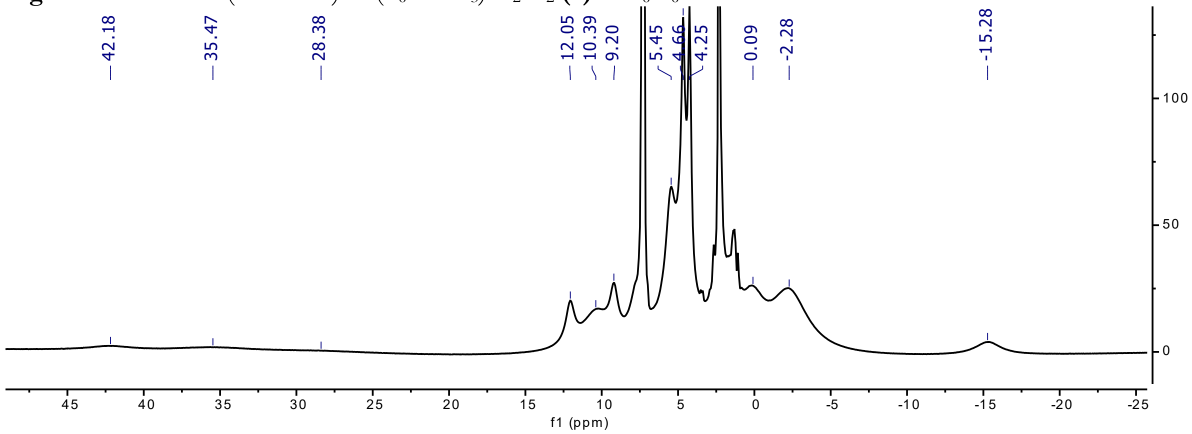

Figure 60. ^1H NMR (400 MHz) of $(P_6ArC)Fe_2H$ (**5**) in C_6D_6.

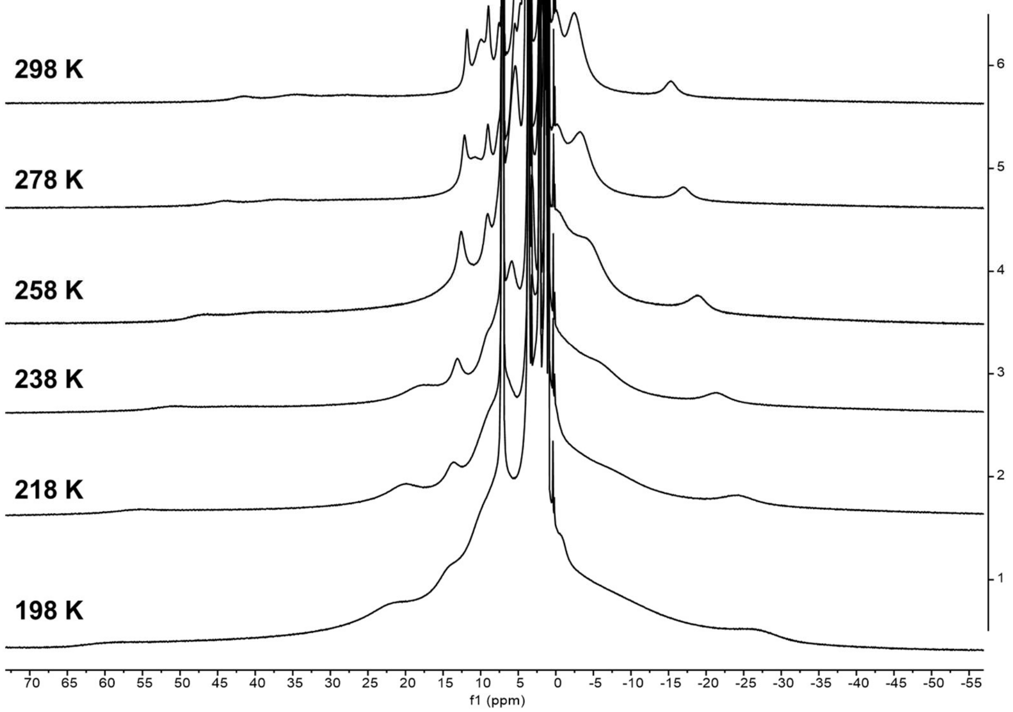

Figure 61. Variable Temperature ^1H NMR (400 MHz) of $(P_6ArC)Fe_2H$ (**5**) in C_7D_8.

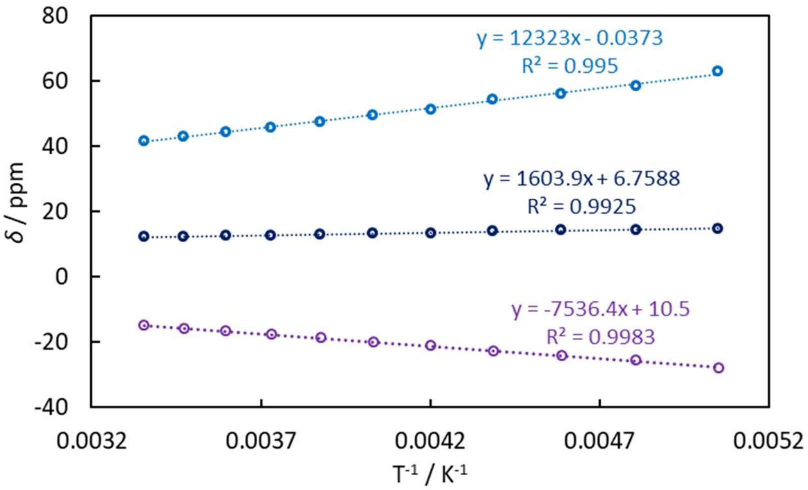

Figure 62. ^{1}H NMR chemical shifts of (P_6ArC)Fe_2H (**5**) in C_7D_8 plotted as a function of 1/T display ideal Curie-behavior.

Figure 63. ^{1}H NMR (400 MHz) of (P_6ArCH_3)$Fe_2(H_2)_2(H)_4$ (6-H_2) in C_7D_8

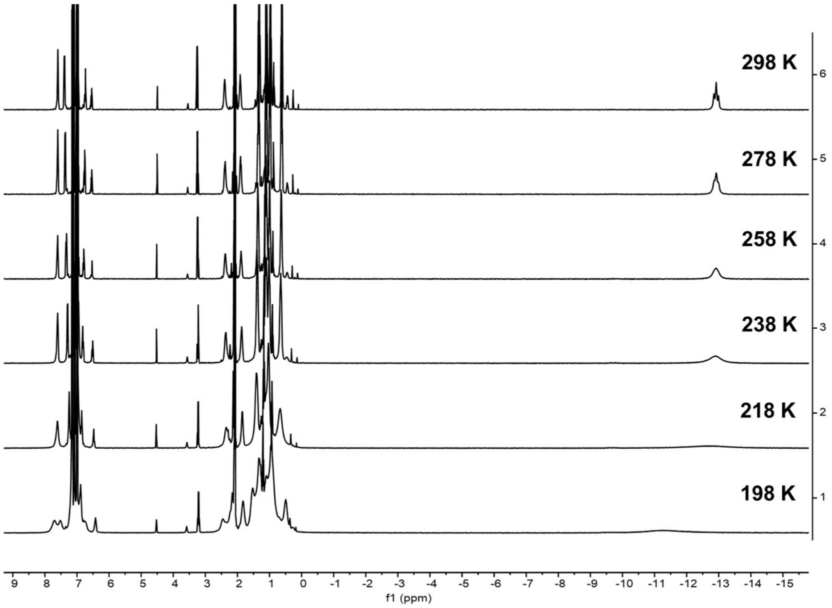

Figure 64. Variable Temperature ^{1}H NMR (400 MHz) of (P_6ArCH_3)$Fe_2(H_2)_2(H)_4$ (6-H_2) in C_7D_8

Figure 65. $^{31}P\{^{1}H\}$ NMR (162 MHz) of $(P_6ArCH_3)Fe_2(H_2)_2(H)_4$ (6-H_2) in C_7D_8. Asterisks denote ^{31}P resonances associated with $(P_6ArCH_3)Fe_2(N_2)_2(H)_4$ (6-N_2).

Figure 66. ^{1}H NMR (400 MHz) of $(P_6ArCH_3)Fe_2(N_2)_2(H)_4$ (6-N_2) in C_7D_8

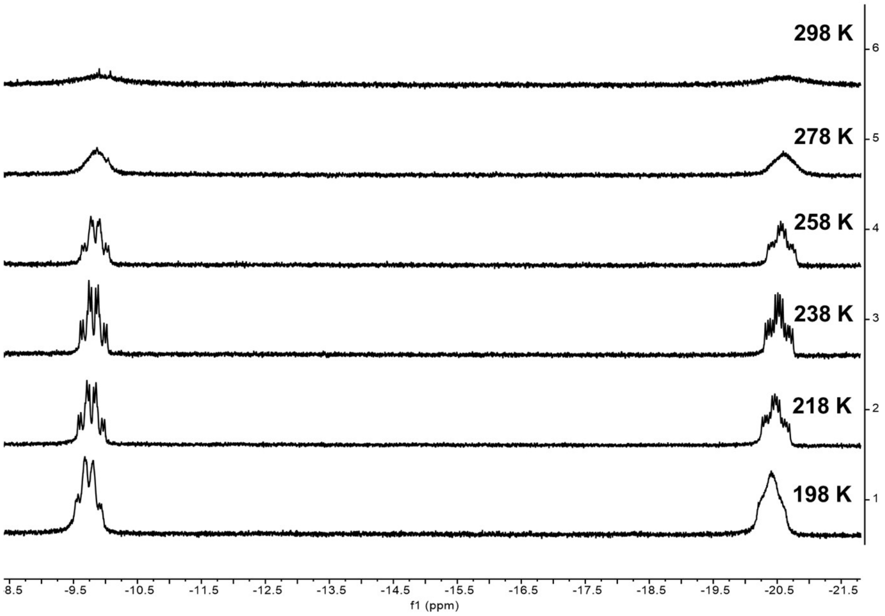

Figure 67. Variable Temperature ^{1}H NMR (400 MHz) of $(P_6ArCH_3)Fe_2(N_2)_2(H)_4$ (6-N_2) in C_7D_8 focusing on hydridic region.

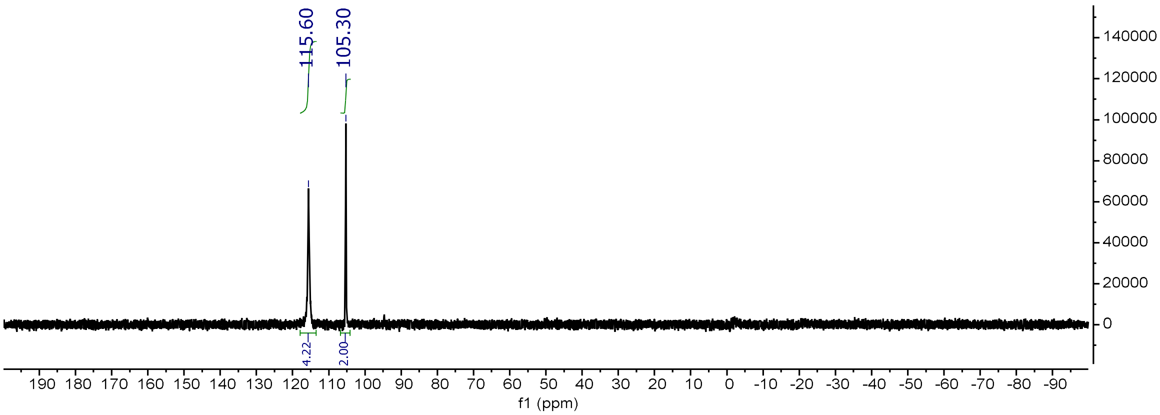

Figure 68. $^{31}P\{^1H\}$ NMR (162 MHz) of $(P_6ArCH_3)Fe_2(N_2)_2(H)_4$ (6-N_2) in C_7D_8.

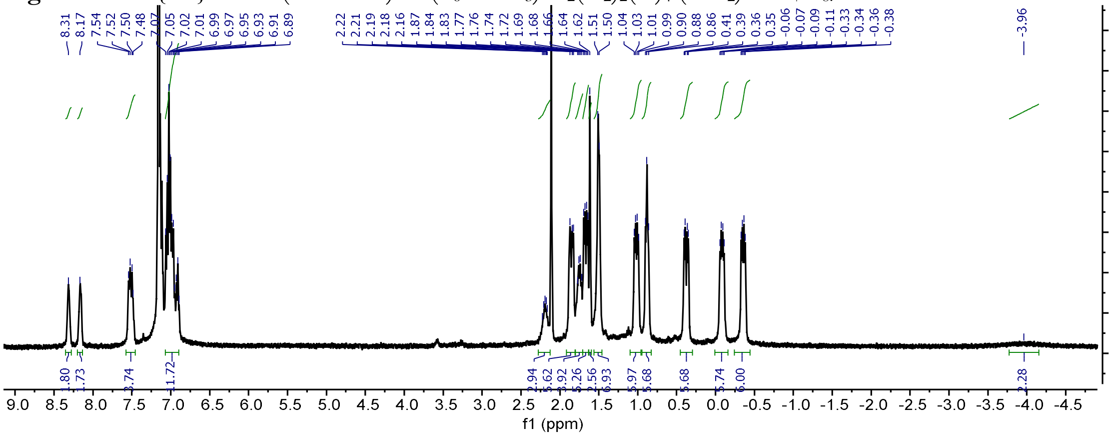

Figure 69. ^1H NMR (400 MHz) of $[P_6ArCH_3](FeH)_2(\mu\text{-}N_2)$ (7) in C_6D_6.

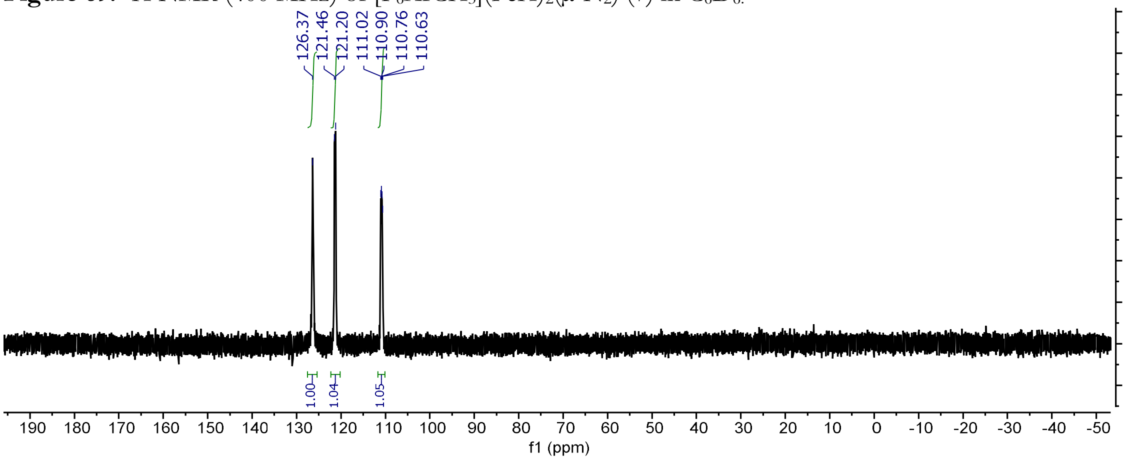

Figure 70. $^{31}P\{^1H\}$ NMR (162 MHz) of $[P_6ArCH_3](FeH)_2(\mu\text{-}N_2)$ (7) in C_6D_6.

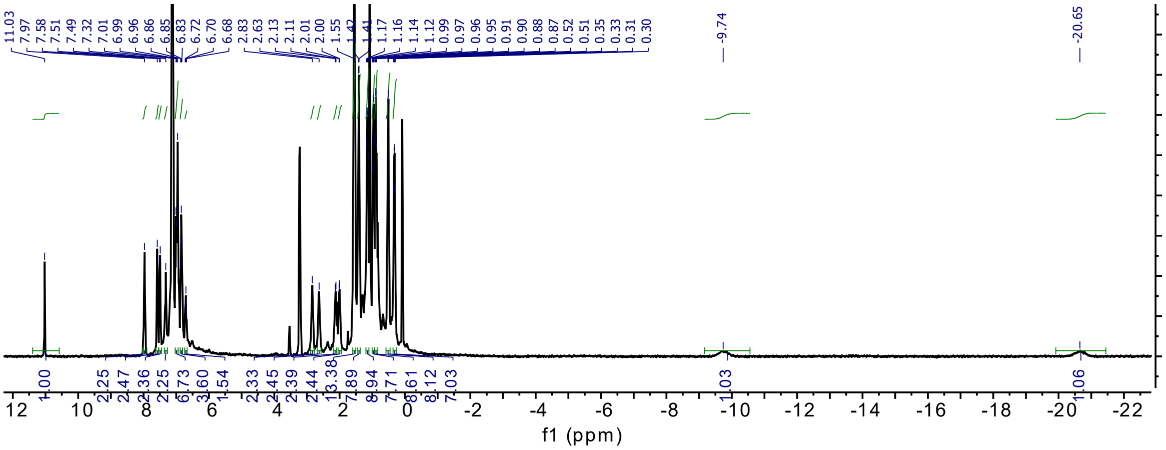

Figure 71. ^1H NMR (400 MHz) of $(P_6ArCH)Fe_2(N_2)_2(H)_2$ (8) in C_6D_6

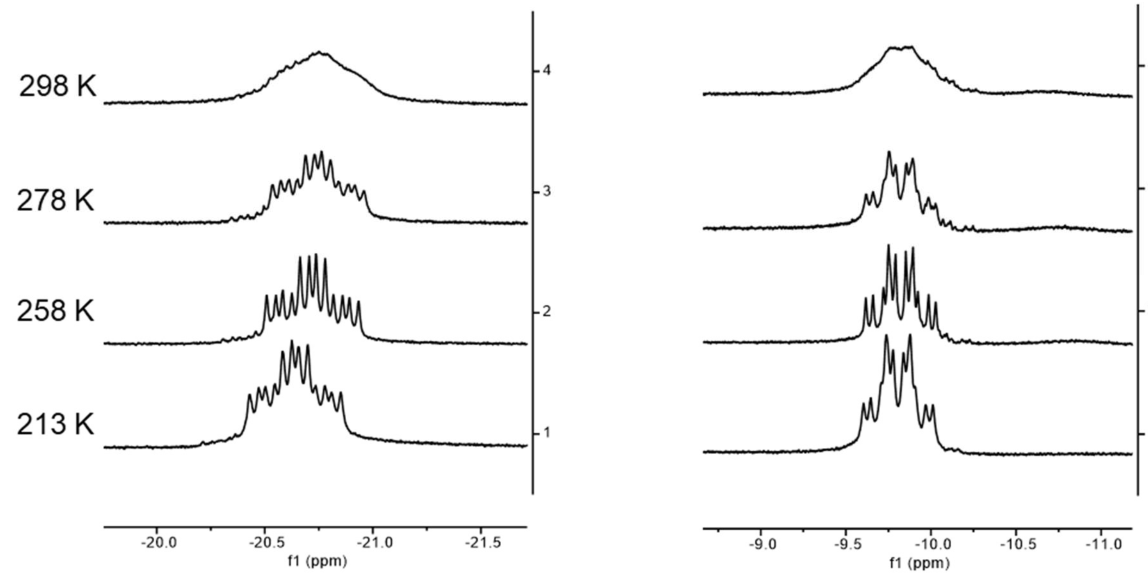

Figure 72. ^1H NMR (400 MHz) of $(P_6ArCH)Fe_2(N_2)_2(H)_2$ (8) in C_7D_8 at variable temperatures to resolve $^2J_{HP}$.

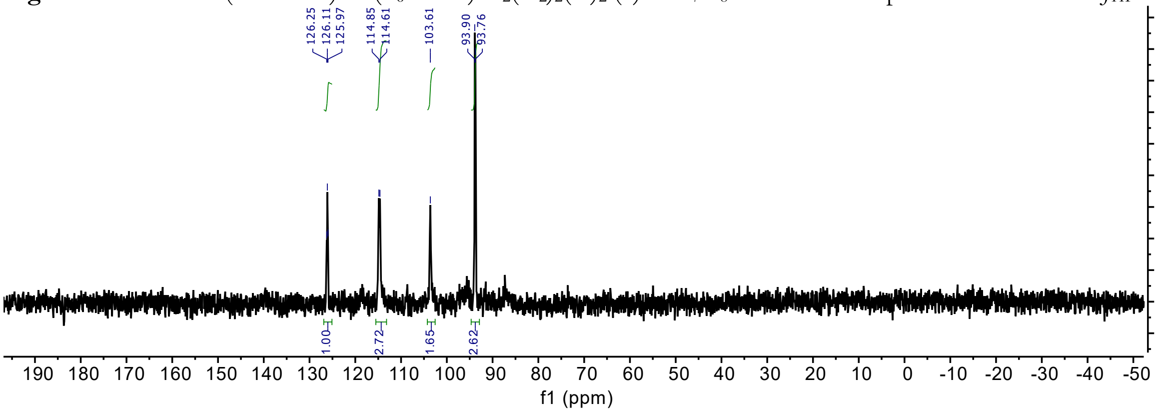

Figure 73. $^{31}P\{^1H\}$ NMR (162 MHz) of $(P_6ArCH)Fe_2(N_2)_2(H)_2$ (8) in C_6D_6

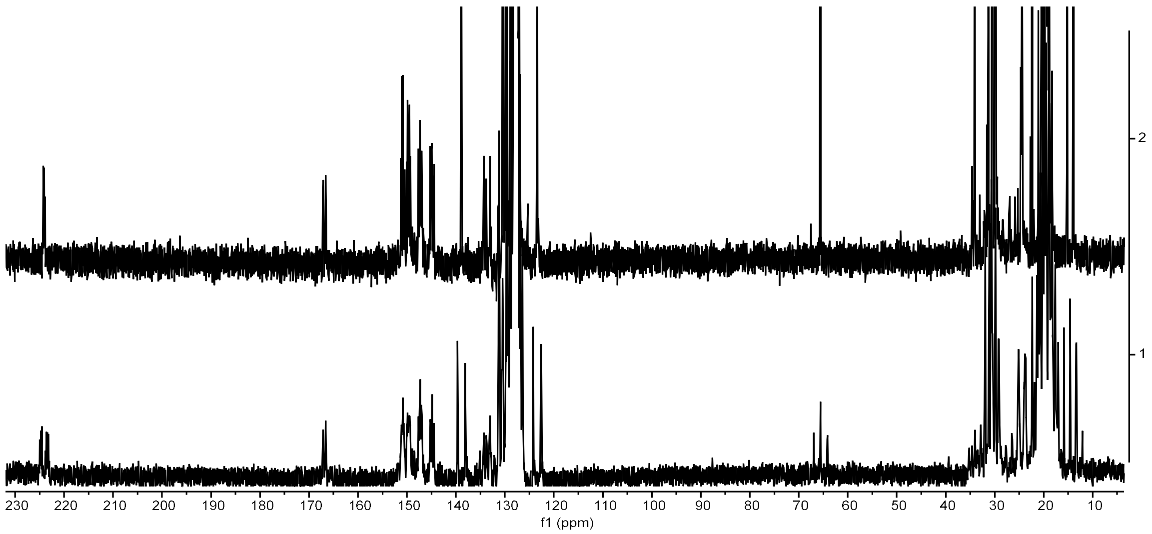

Figure 74. $^{13}C\{^1H\}$ NMR (101 MHz) of $(P_6ArCH)Fe_2(N_2)_2(H)_2$ (8) in C_6D_6 (top). Gate decoupled ^{13}C NMR (101 MHz) of $(P_6ArCH)Fe_2(N_2)_2(H)_2$ (8) in C_6D_6 (Bottom).

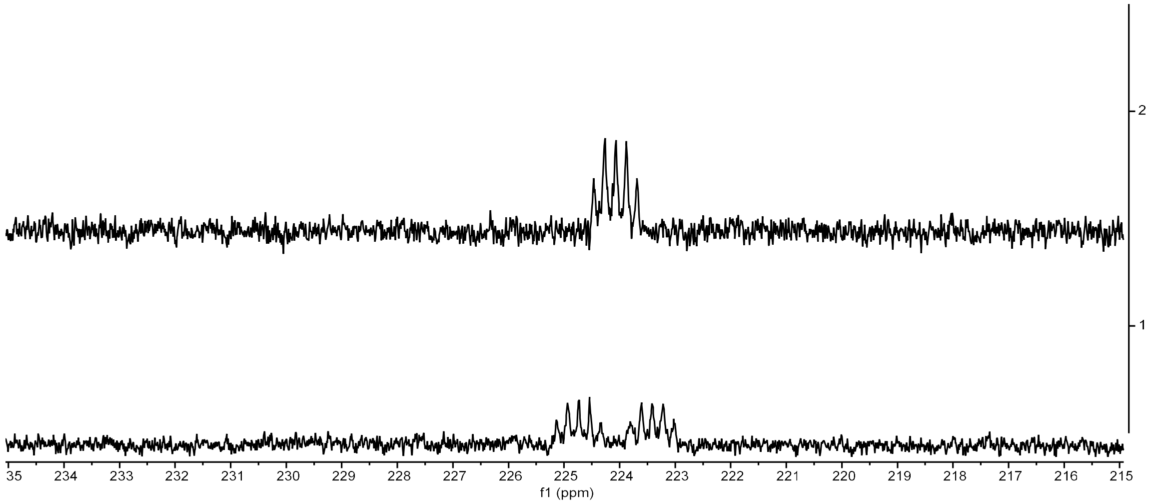

Figure 75. $^{13}C\{^1H\}$ NMR (101 MHz) of $(P_6ArCH)Fe_2(N_2)_2(H)_2$ (8) in C_6D_6 (top) focusing on the carbene resonance. Gate decoupled ^{13}C NMR (101 MHz) of $(P_6ArCH)Fe_2(N_2)_2(H)_2$ (8) in C_6D_6 (Bottom). From this data: $\delta = 224$ ppm, $^1J_{CH} = 134$ Hz, $^2J_{CP} = 20$ and 39 Hz.

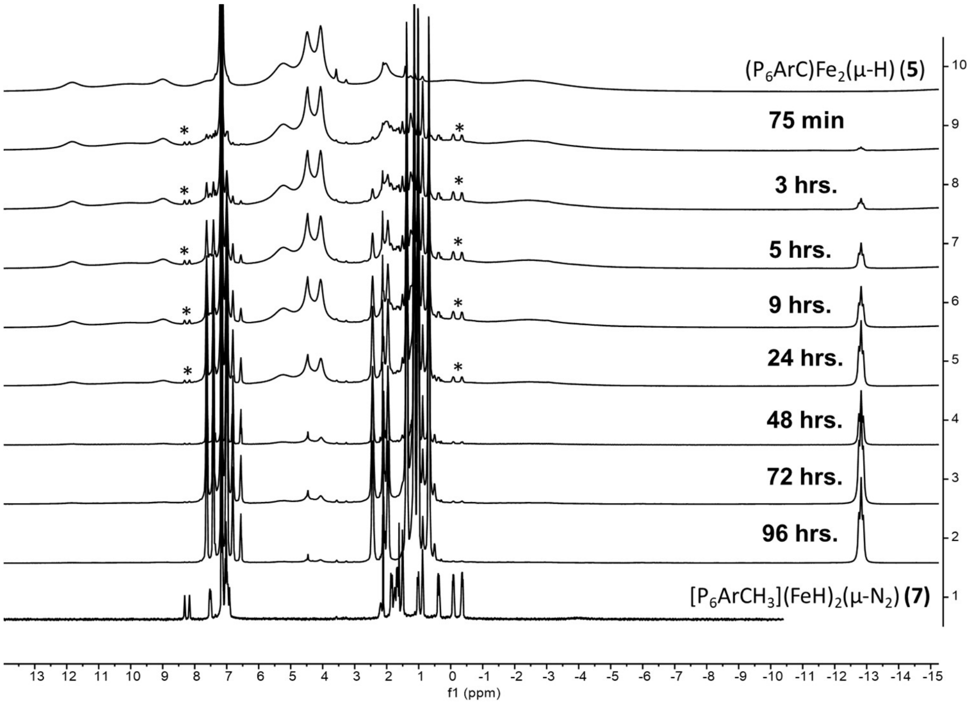

Figure 76. ^{1}H NMR spectra collected during the course of the reaction of (P$_6$ArC)Fe$_2$H (5) with a mixture of H$_2$ and N$_2$ in a sealed J Young tube. Asterisks denote characteristic resonances of [P$_6$ArCH$_3$](FeH)$_2$(μ-N$_2$) (7), observed as an intermediate in the reaction.

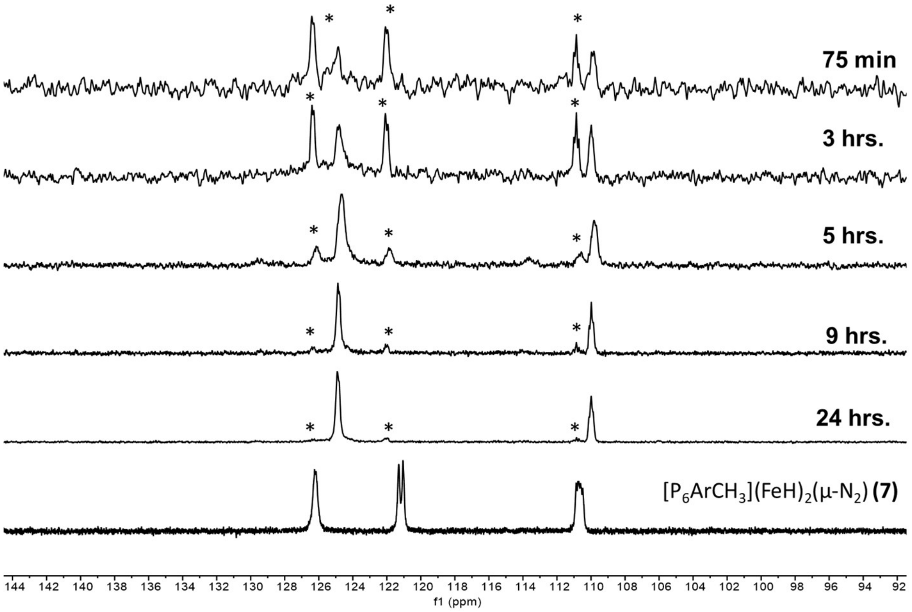

Figure 77. ^{31}P NMR spectra collected during the course of the reaction of (P$_6$ArC)Fe$_2$H (5) with a mixture of H$_2$ and N$_2$ in a sealed J Young tube. Asterisks denote characteristic resonances of [P$_6$ArCH$_3$](FeH)$_2$(μ-N$_2$) (7), observed as an intermediate in the reaction.

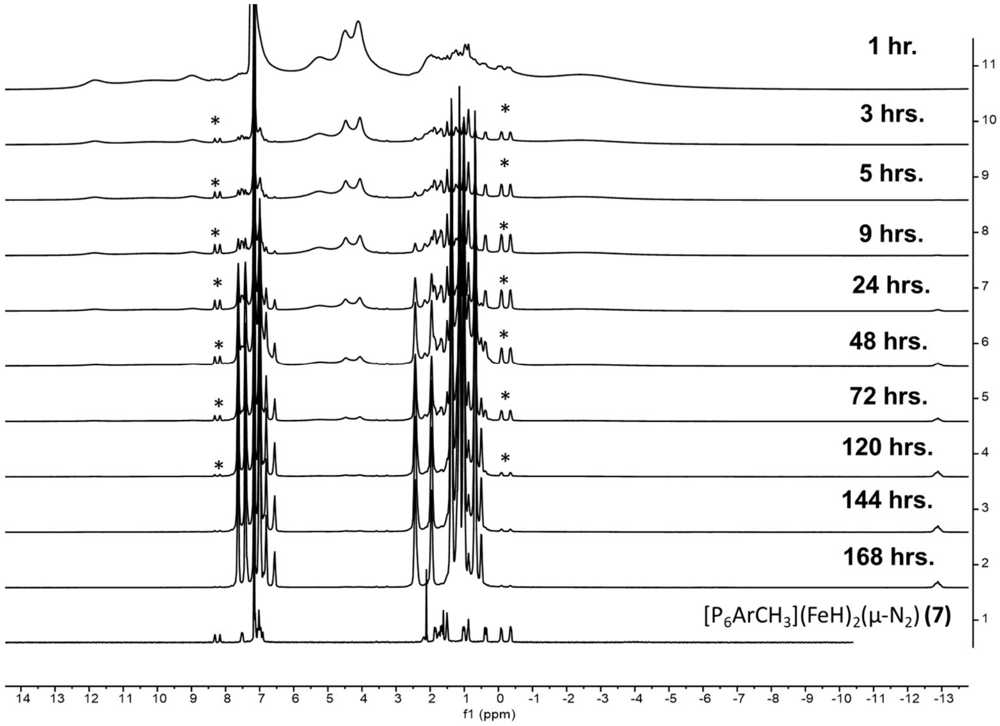

Figure 78. ^{1}H NMR spectra collected during the course of the reaction of (P_6ArC)Fe_2H (5) with a mixture of D_2 and N_2 in a sealed J Young tube. Asterisks denote characteristic resonances of [P_6ArCH_3](FeX)$_2$(μ-N_2) (7-H/D, X = H or D), observed as an intermediate in the reaction.

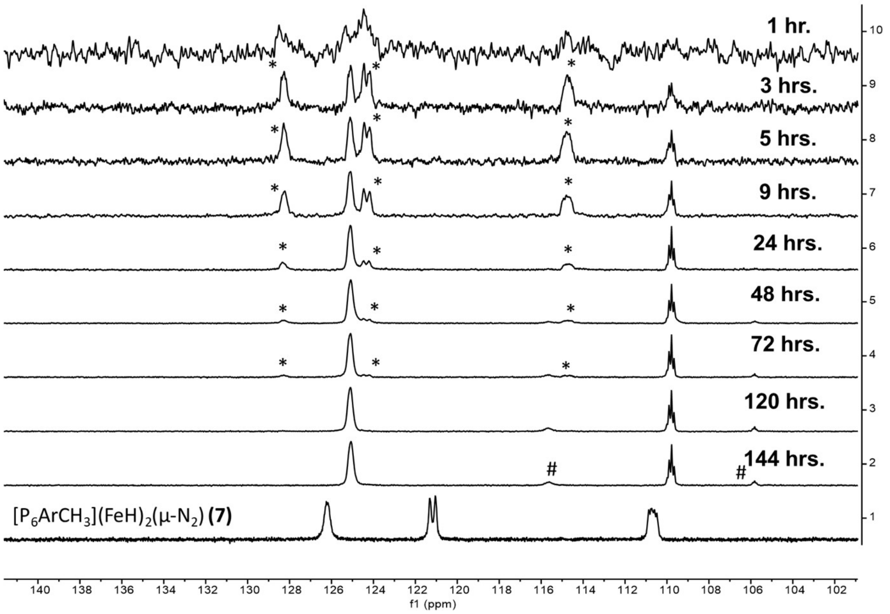

Figure 79. ^{31}P NMR spectra collected during the course of the reaction of (P_6ArC)Fe_2H (5) with a mixture of D_2 and N_2 in a sealed J Young tube. Asterisks denote characteristic resonances of [P_6ArCH_3](FeX)$_2$(μ-N_2) (7-H/D, X = H or D), observed as an intermediate in the reaction. Note these resonances are shifted with respect to [P_6ArCH_3](FeH)$_2$(μ-N_2) (7), which is not observed in the case of H_2. The # marked resonances correspond to (P_6ArCH_3)Fe_2(N_2)$_2$(D)$_3$(H) (6-N_2).

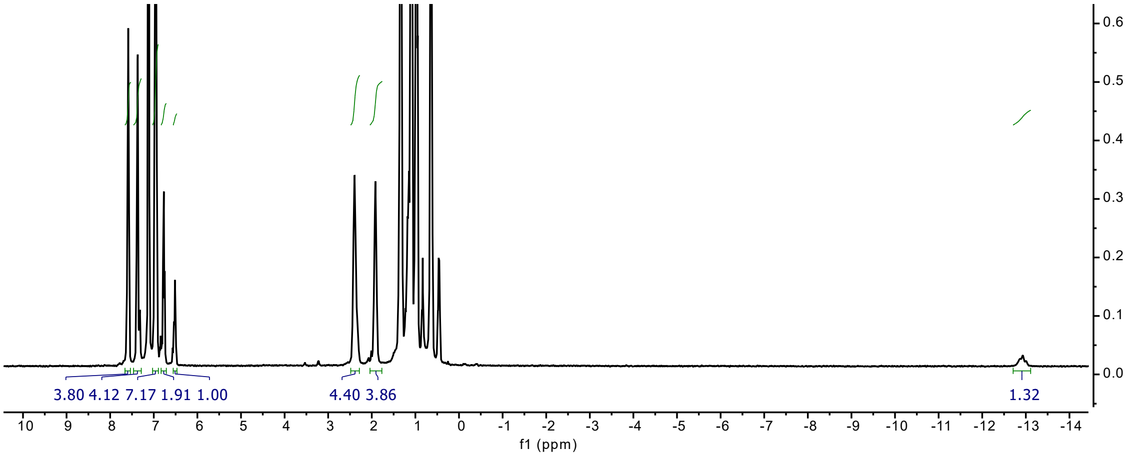

Figure 80. ^{1}H NMR spectra collected at the end of the reaction of (P_6ArC)Fe_2H (5) with a mixture of D_2 and N_2 in a sealed J Young tube. Note especially the observation of the hydridic/HD resonance at -12.9 and the lack of a –CHD_2 resonance from the central methyl group. Integration indicates that the first equivalent of D_2 adds regioselectively across the Fe-C bond such that the original hydride ligand remains bound to Fe and is not delivered to the carbyne carbon. Under thermal conditions, this reaction is not reversible and the hydride ligand does not exchange with D_2 in the headspace.

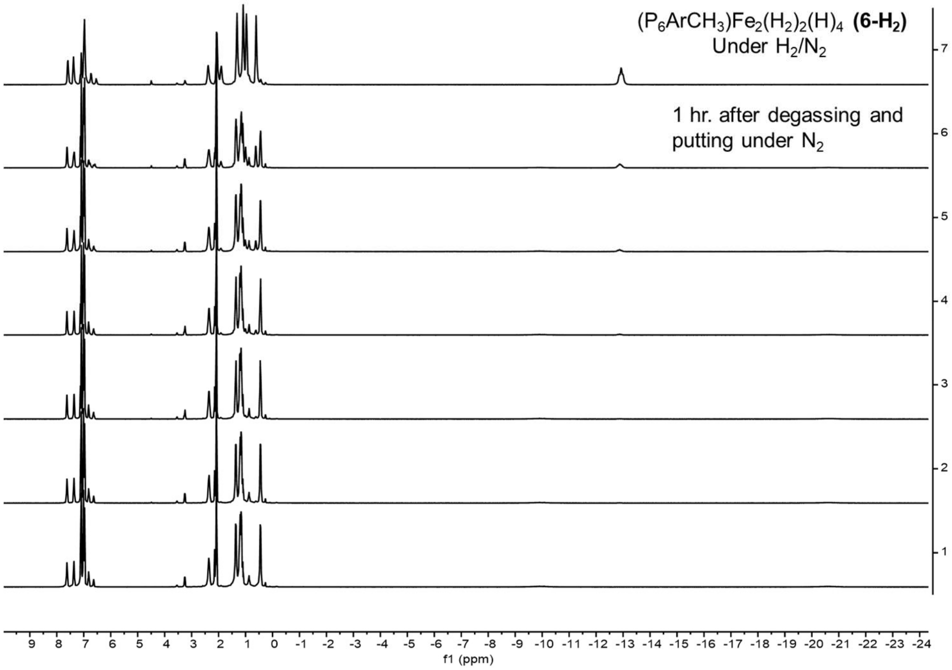

Figure 81. ^{1}H NMR spectra collected during the course of converting of (P_6ArCH_3)$Fe_2(H_2)_2(H)_4$ (6-H_2) to (P_6ArCH_3)$Fe_2(N_2)_2(H)_4$ (6-N_2) under N_2 in a sealed J Young tube.

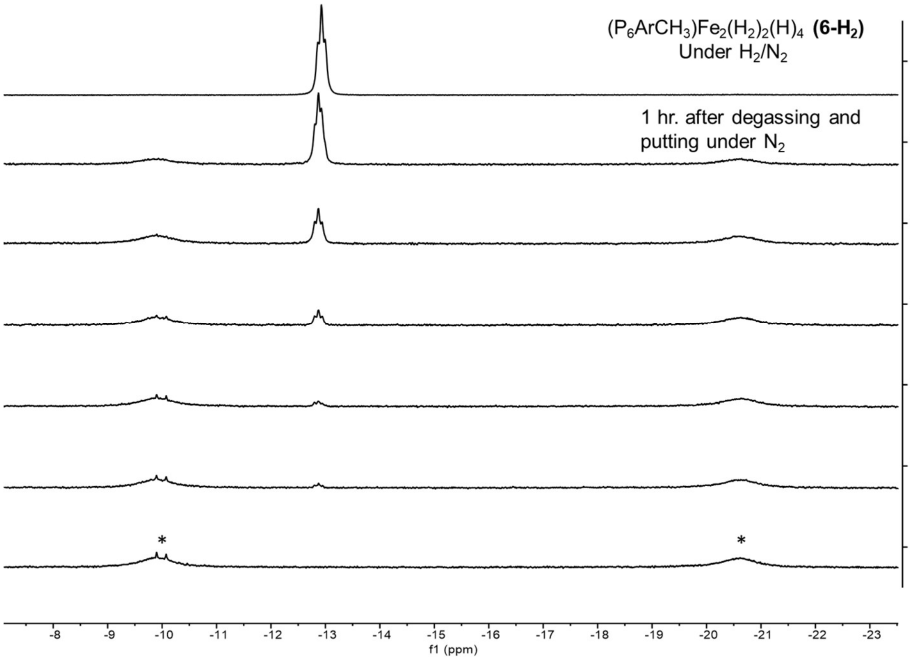

Figure 82. ^{1}H NMR spectra collected during the course of converting of (P$_6$ArCH$_3$)Fe$_2$(H$_2$)$_2$(H)$_4$ (6-H$_2$) to (P$_6$ArCH$_3$)Fe$_2$(N$_2$)$_2$(H)$_4$ (6-N$_2$) under N$_2$ in a sealed J Young tube, focusing on the hydridic region. Asterisks denote the position of the resonances for 6-N$_2$.

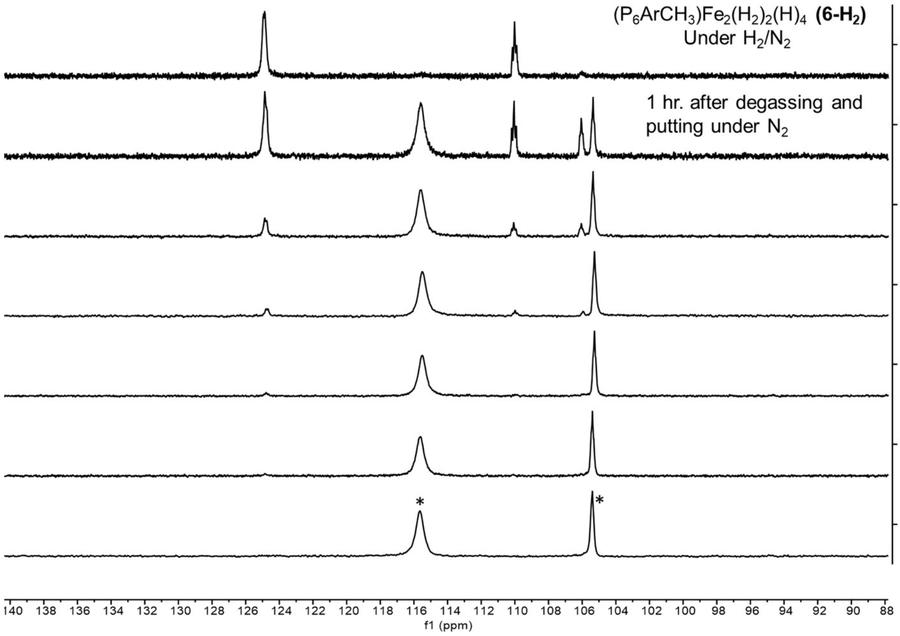

Figure 83. ^{31}P NMR spectra collected during the course of converting of (P$_6$ArCH$_3$)Fe$_2$(H$_2$)$_2$(H)$_4$ (6-H$_2$) to (P$_6$ArCH$_3$)Fe$_2$(N$_2$)$_2$(H)$_4$ (6-N$_2$) under N$_2$ in a sealed J Young tube. Asterisks denote the position of the resonances for 6-N$_2$.

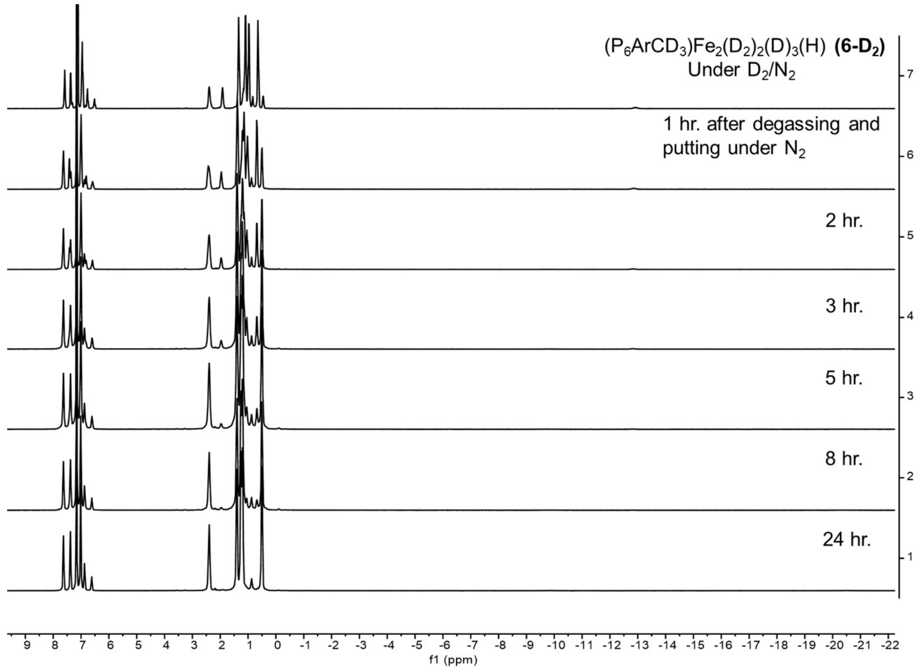

Figure 84. ^1H NMR spectra collected during the course of converting of $(P_6ArCD_3)Fe_2(D_2)_2(D)_3(H)$ (6-D_2) to $(P_6ArCD_3)Fe_2(N_2)_2(D)_3(H)$ (6-N_2), under N_2 in a sealed J Young tube.

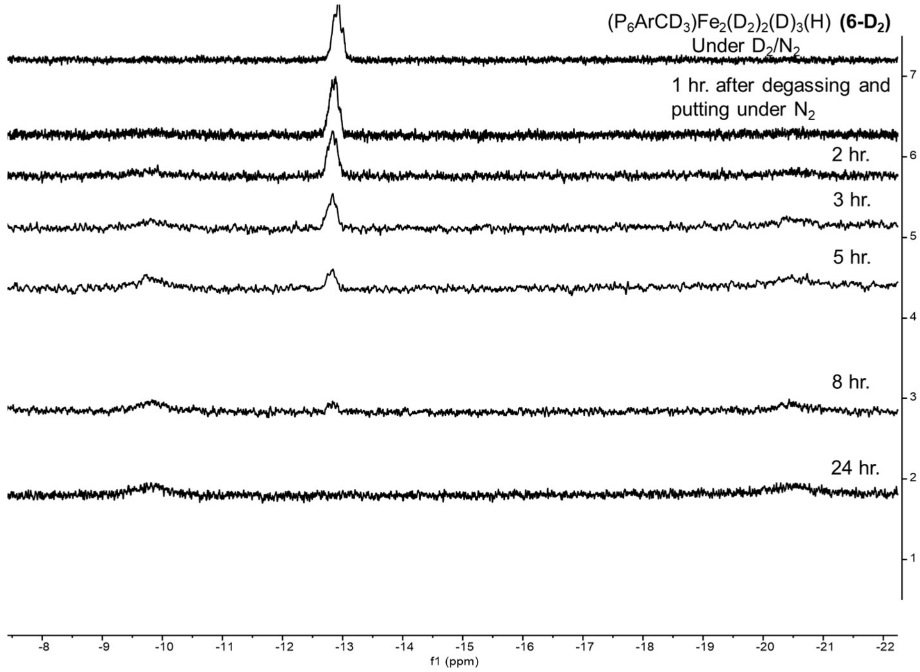

Figure 85. ^1H NMR spectra collected during the course of converting of $(P_6ArCD_3)Fe_2(D_2)_2(D)_3(H)$ (6-D_2) to $(P_6ArCD_3)Fe_2(N_2)_2(D)_3(H)$ (6-N_2), under N_2 in a sealed J Young tube, focusing on the hydridic region.

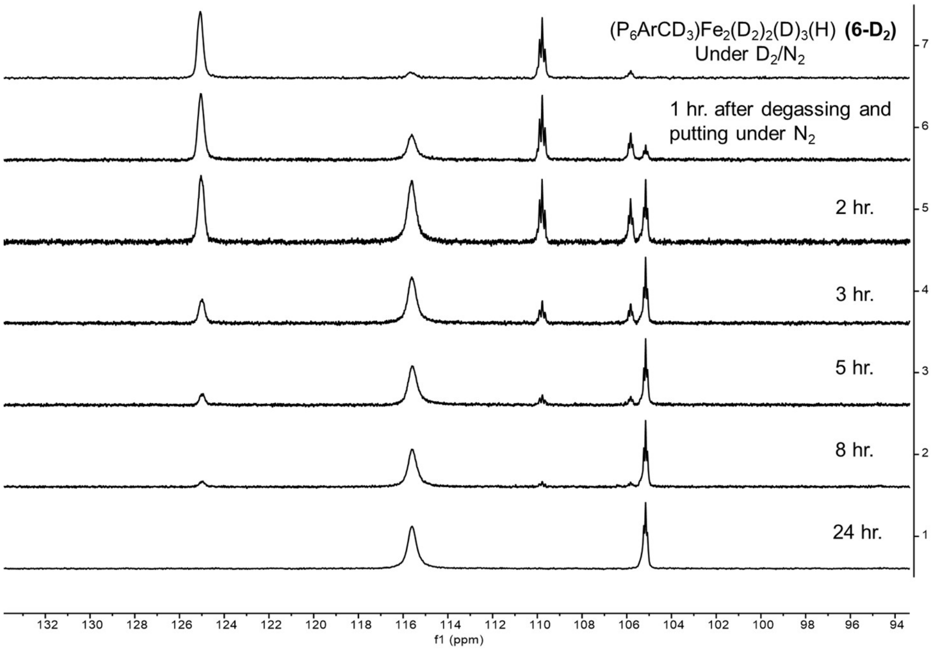

Figure 86. ^{31}P NMR spectra collected during the course of converting of $(P_6ArCD_3)Fe_2(D_2)_2(D)_3(H)$ (6-D$_2$) to $(P_6ArCD_3)Fe_2(N_2)_2(D)_3(H)$ (6-N$_2$), under N_2 in a sealed J Young tube.

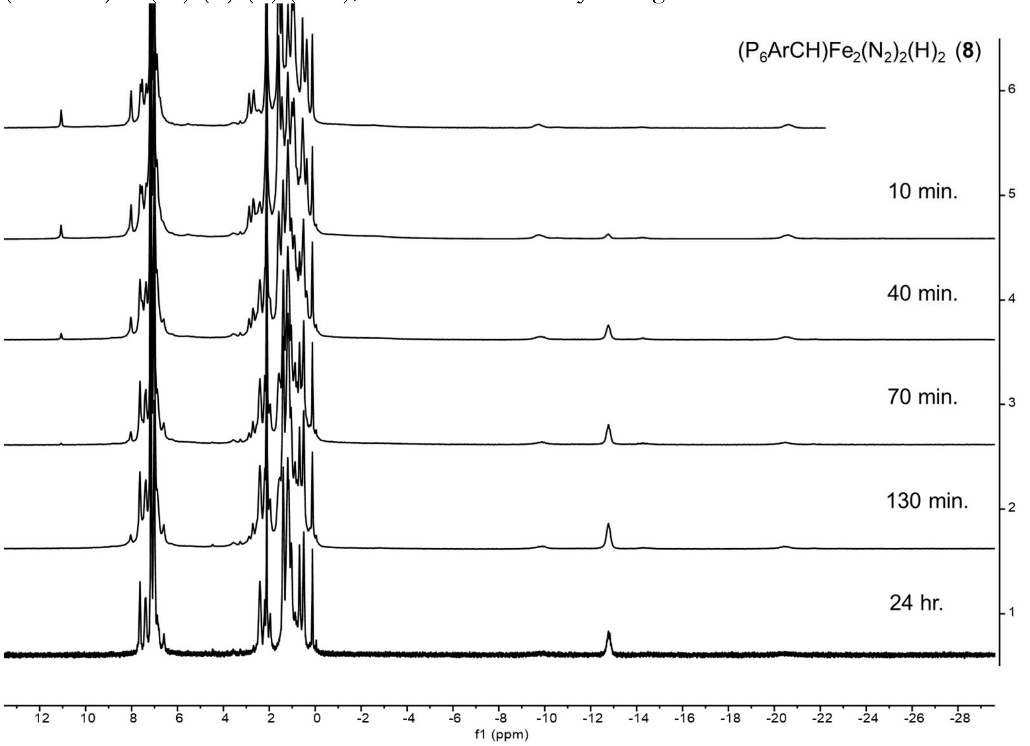

Figure 87. ^{1}H NMR spectra collected during the course of the reaction of $(P_6ArCH)Fe_2(N_2)_2(H)_2$ (8) with a mixture of H_2 and N_2 in a sealed J Young tube.

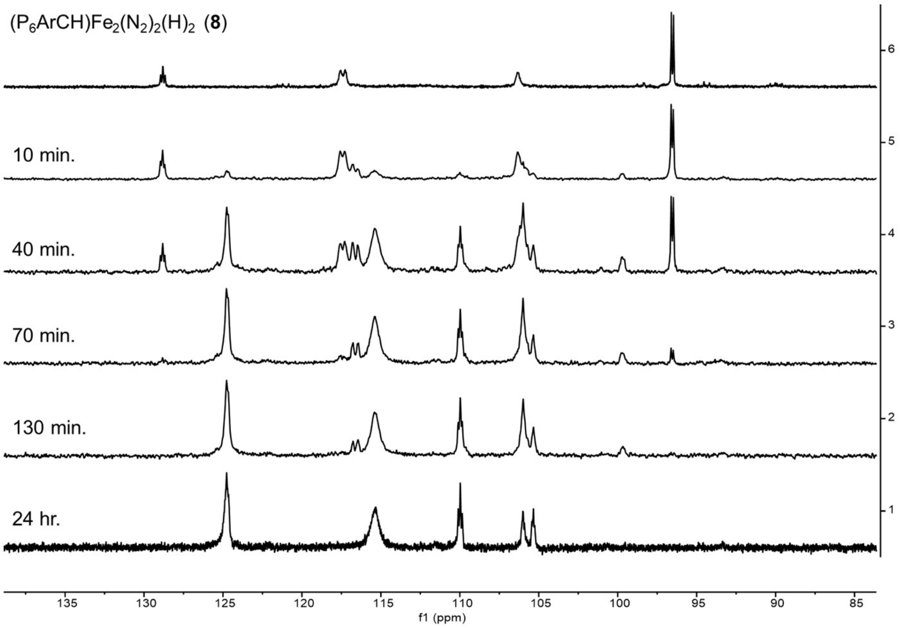

Figure 88. ^{31}P NMR spectra collected during the course of the reaction of $(P_6ArCH)Fe_2(N_2)_2(H)_2$ (8) with a mixture of H_2 and N_2 in a sealed J Young tube.

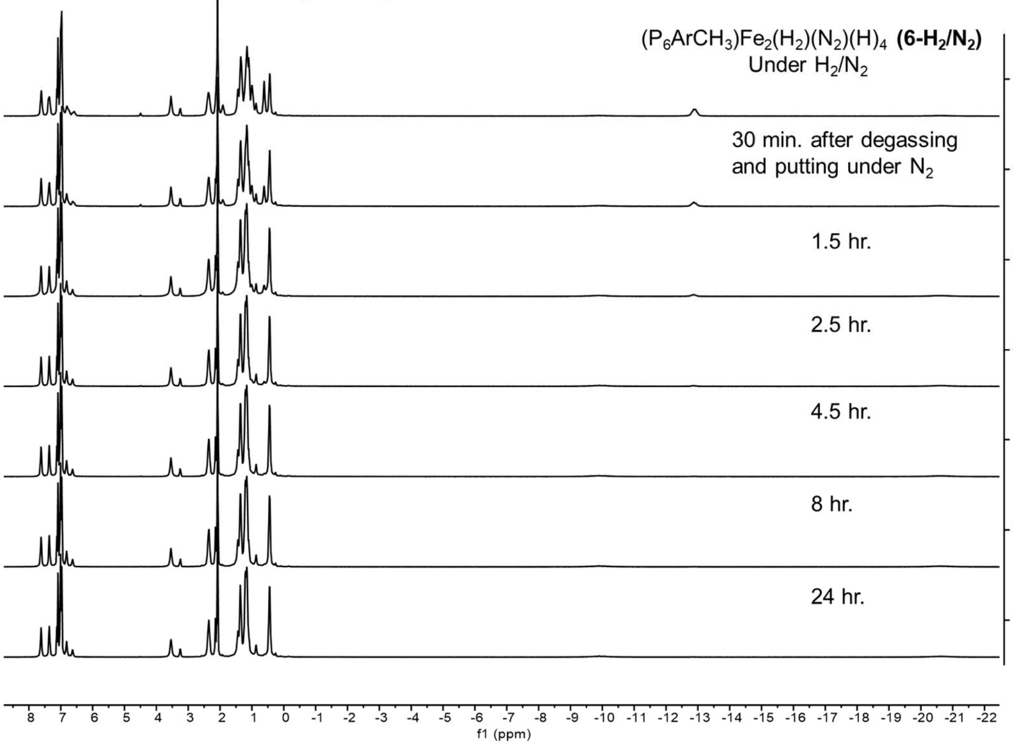

Figure 89. ^{1}H NMR spectra collected during the course of converting of $(P_6ArCH_3)Fe_2(H_2)(N_2)(H)_4$ ($6\text{-}H_2/N_2$) to $(P_6ArCH_3)Fe_2(N_2)_2(H)_4$ ($6\text{-}N_2$), under N_2 in a sealed J Young tube.

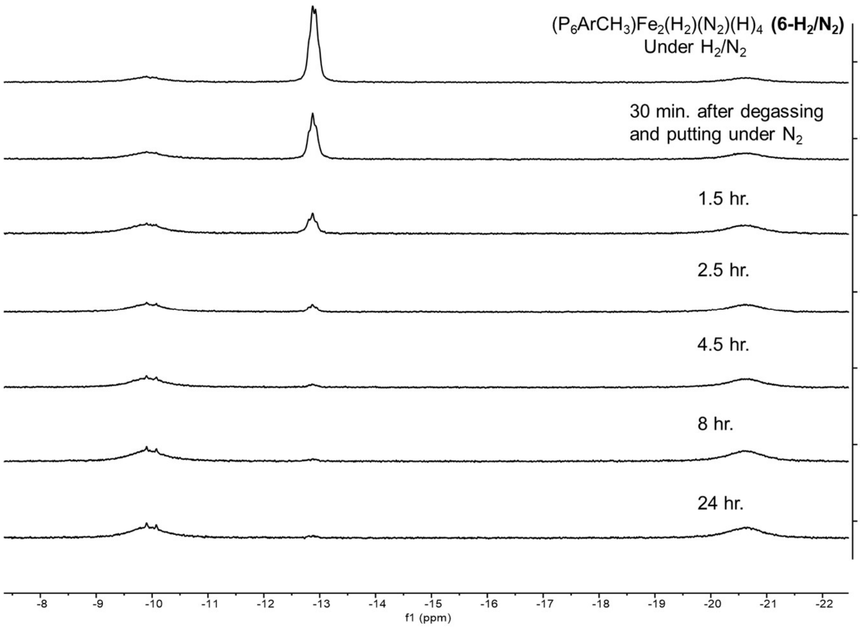

Figure 90. ^{1}H NMR spectra collected during the course of converting of $(P_6ArCH_3)Fe_2(H_2)(N_2)(H)_4$ (6-H_2/N_2) to $(P_6ArCH_3)Fe_2(N_2)_2(H)_4$ (6-N_2), under N_2 in a sealed J Young tube.

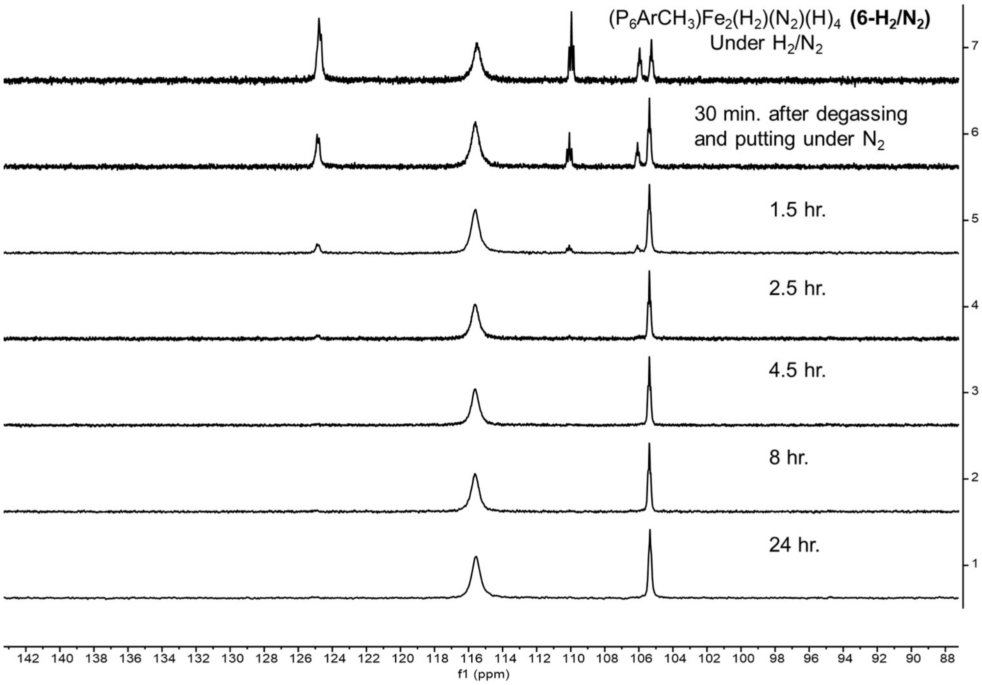

Figure 91. ^{31}P NMR spectra collected during the course of converting of $(P_6ArCH_3)Fe_2(H_2)(N_2)(H)_4$ (6-H_2/N_2) to $(P_6ArCH_3)Fe_2(N_2)_2(H)_4$ (6-N_2), under N_2 in a sealed J Young tube.

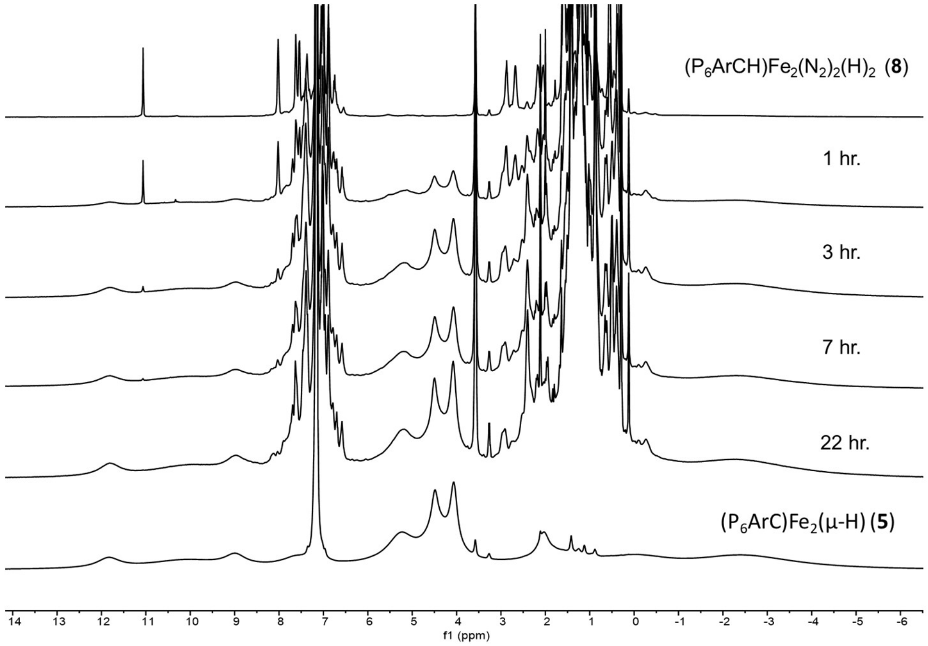

Figure 92. ^{1}H NMR spectra collected during the course of the room temperature photolysis of $(P_6ArCH)Fe_2(N_2)_2(H)_2$ (8), yielding as the major product $(P_6ArC)Fe_2H$ (5).

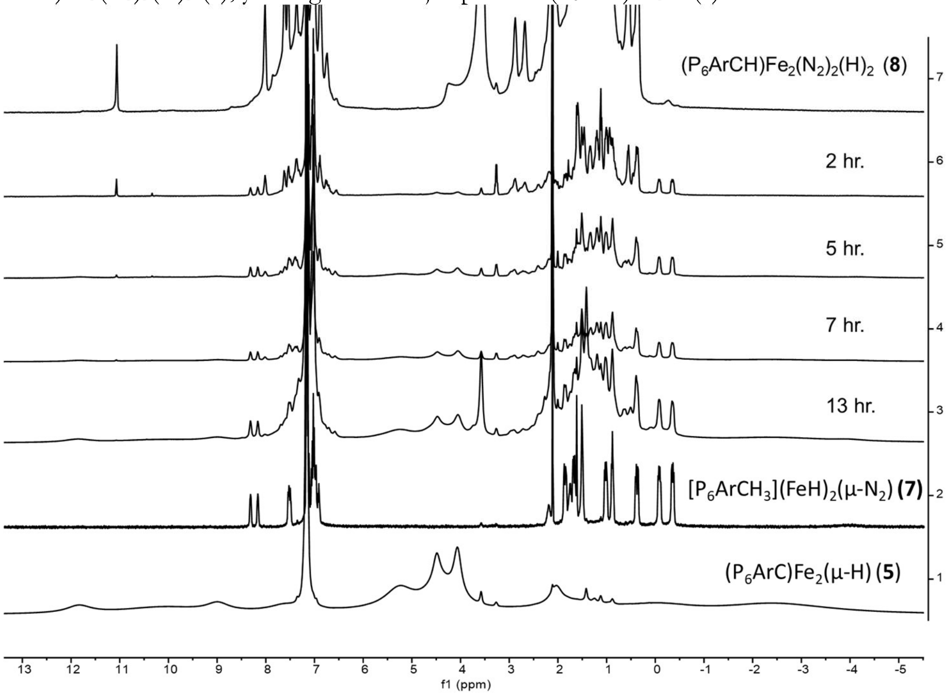

Figure 93. ^{1}H NMR spectra collected during the course of the low temperature photolysis of $(P_6ArCH)Fe_2(N_2)_2(H)_2$ (8), yielding as the major diamagnetic product $[P_6ArCH_3](FeH)_2(\mu\text{-}N_2)$ (7) as well as $(P_6ArC)Fe_2H$ (5).

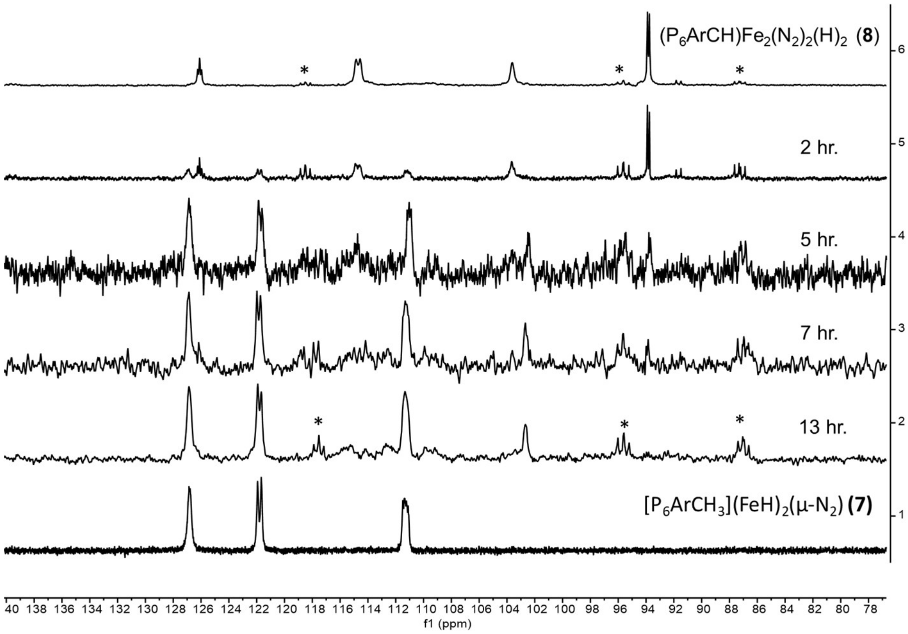

Figure 94. ^{31}P NMR spectra collected during the course of the low temperature photolysis of $(P_6ArCH)Fe_2(N_2)_2(H)_2$ (8), yielding as the major diamagnetic, phosphorus containing product $[P_6ArCH_3](FeH)_2(\mu\text{-}N_2)$ (7). Asterisks denote resonances originating from impurities in 8.

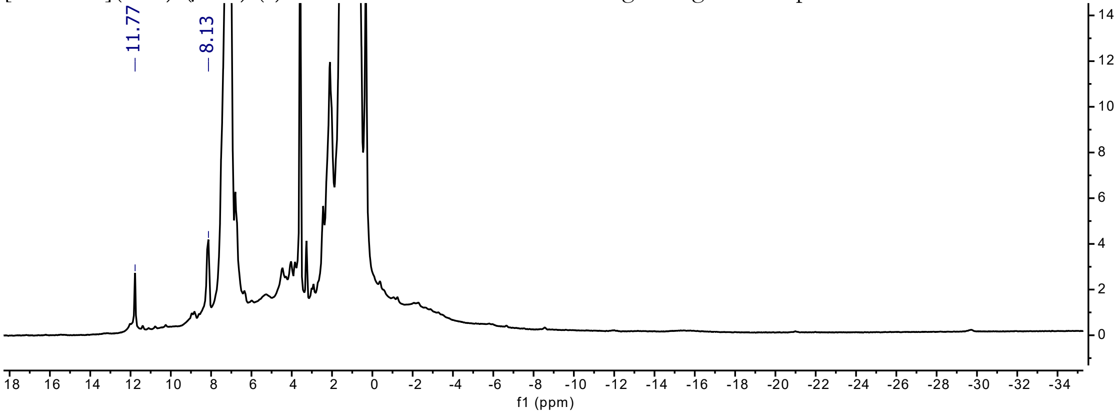

Figure 95. ^{1}H NMR spectrum following reaction of $(P_6ArC)Fe_2H$ (5) with TEMPO-H.

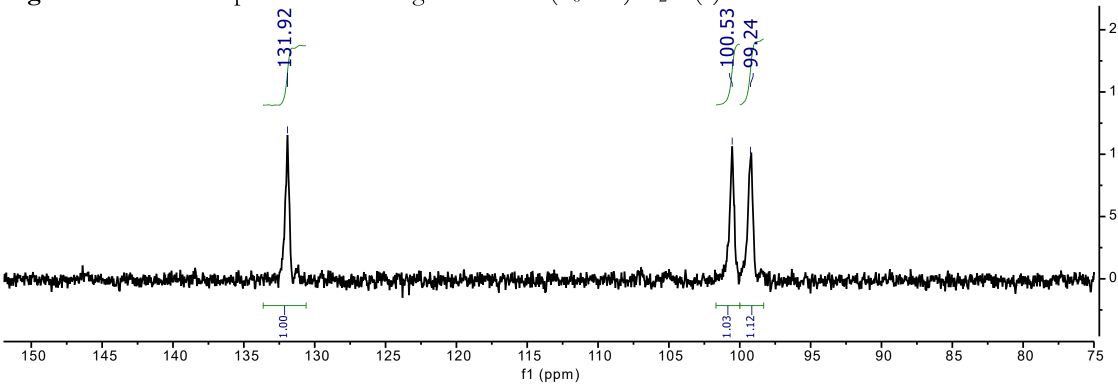

Figure 96. ^{31}P NMR spectrum following reaction of $(P_6ArC)Fe_2H$ (5) with TEMPO-H.

Chapter 5

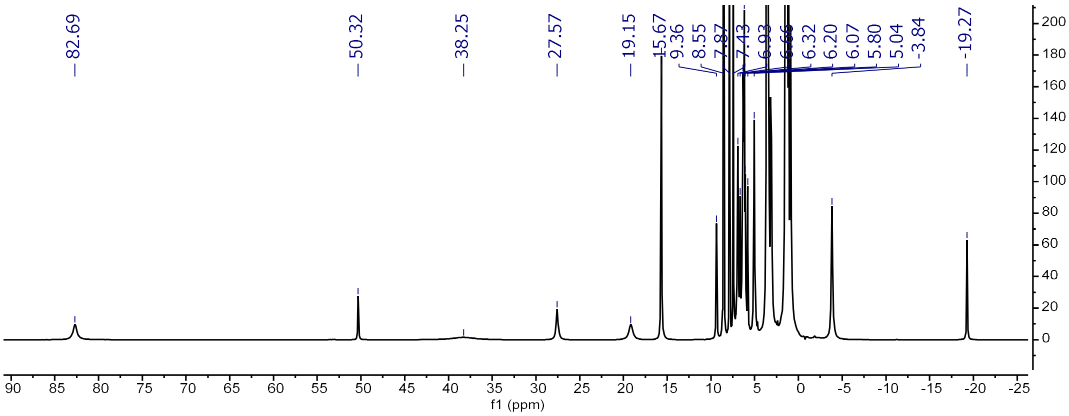

Figure 97. ^{1}H NMR (400 MHz) of **{Fe$_2$(μ-CAr)}^{17}** in C_6D_6/THF

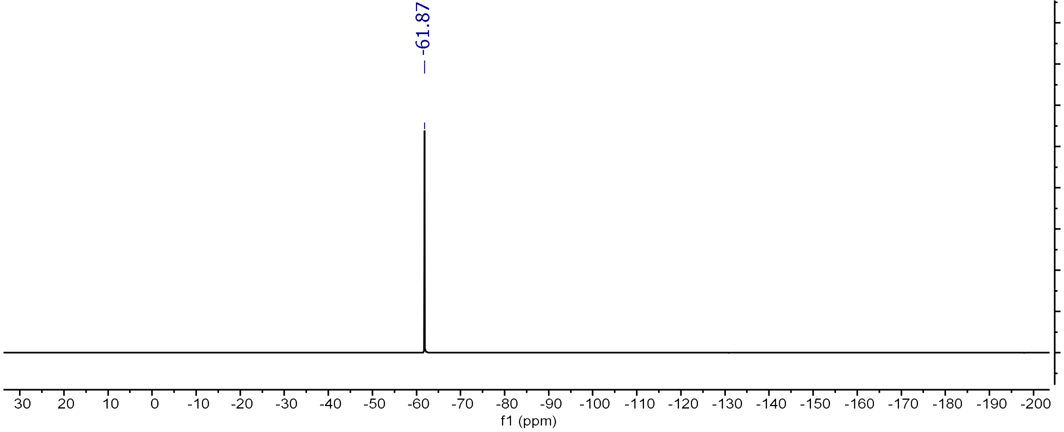

Figure 98. ^{19}F NMR (400 MHz) of **{Fe$_2$(μ-CAr)}^{17}** in C_6D_6/THF

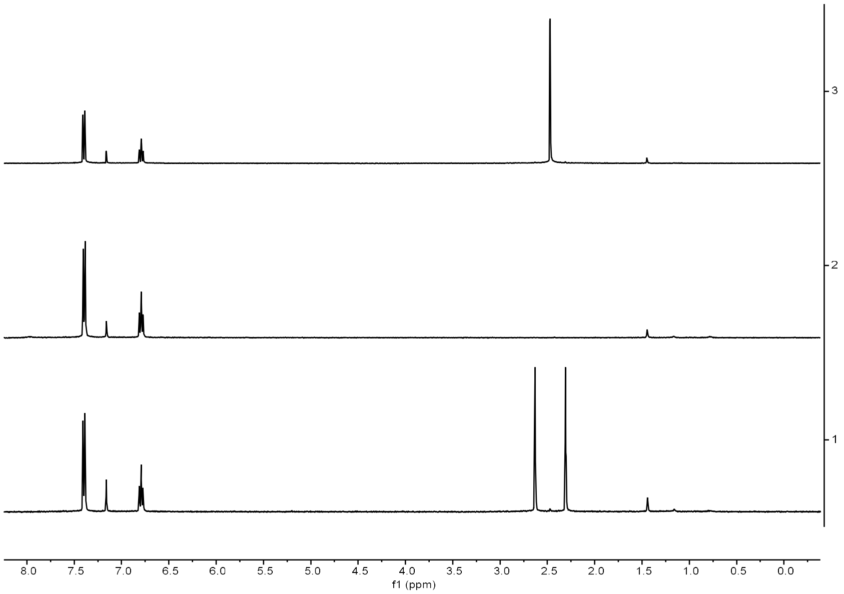

Figure 100. Comparison of ^{1}H NMR (400 MHz) of 2,6-dibromotoluene (top), 2,6-dibromotoluene-d_3 (middle) and 2,6-dibromotoluene-^{13}C (bottom) in C_6D_6

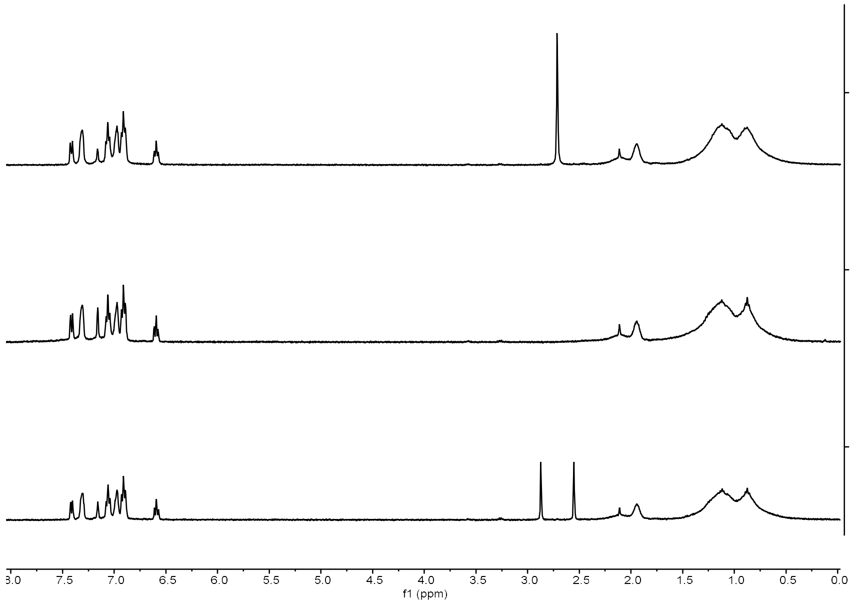

Figure 101. Comparison of ^{1}H NMR (400 MHz) of (3-bromo-2-methylphenyl)(bis(2-diisopropylphenylphosphino)phosphine (top), (3-bromo-2-methylphenyl)(bis(2-diisopropylphenylphosphino)phosphine-*d*$_3$ (middle) and (3-bromo-2-methylphenyl)(bis(2-diisopropylphenylphosphino)phosphine-^{13}C (bottom) in C_6D_6

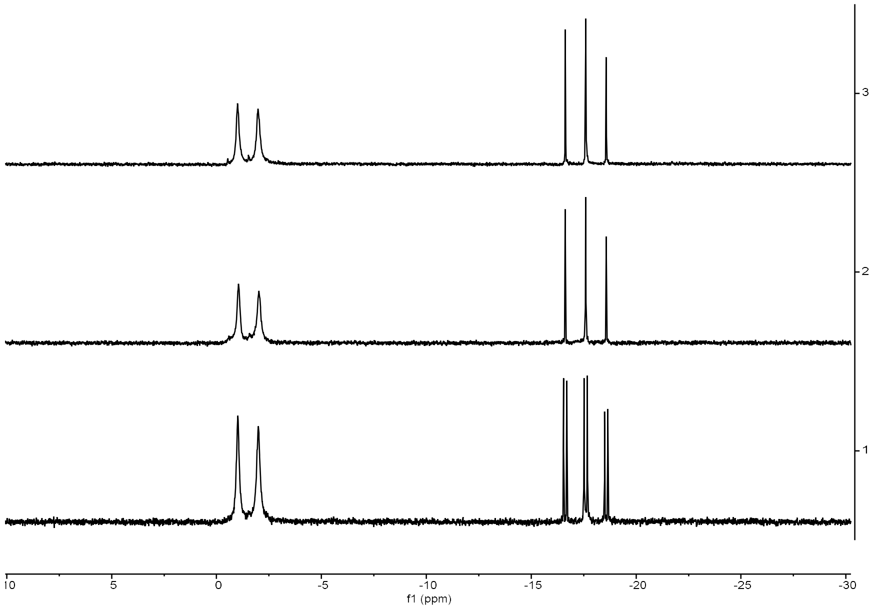

Figure 102. Comparison of ^{31}P NMR (162 MHz) of (3-bromo-2-methylphenyl)(bis(2-diisopropylphenylphosphino)phosphine (top), (3-bromo-2-methylphenyl)(bis(2-diisopropylphenylphosphino)phosphine-*d*$_3$ (middle) and (3-bromo-2-methylphenyl)(bis(2-diisopropylphenylphosphino)phosphine-^{13}C (bottom) in C_6D_6

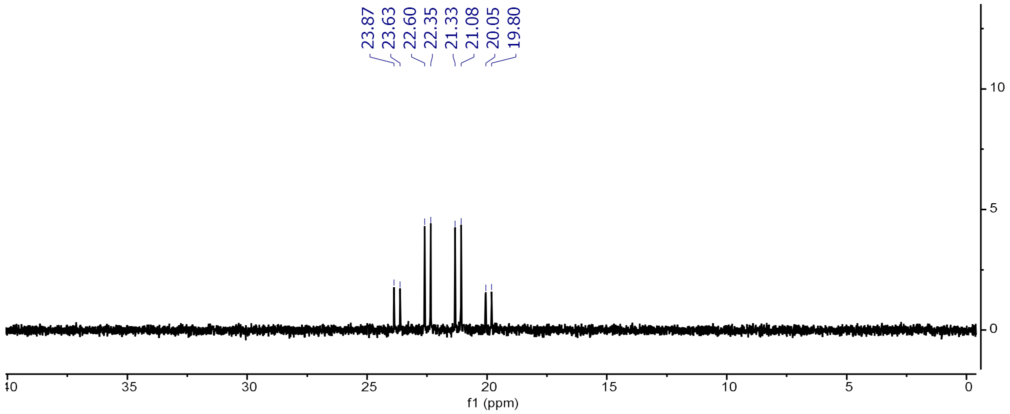

Figure 103. ^{13}C NMR (101 MHz) of (3-bromo-2-methylphenyl)(bis(2-diisopropylphenylphosphino)phosphine-^{13}C in C_6D_6

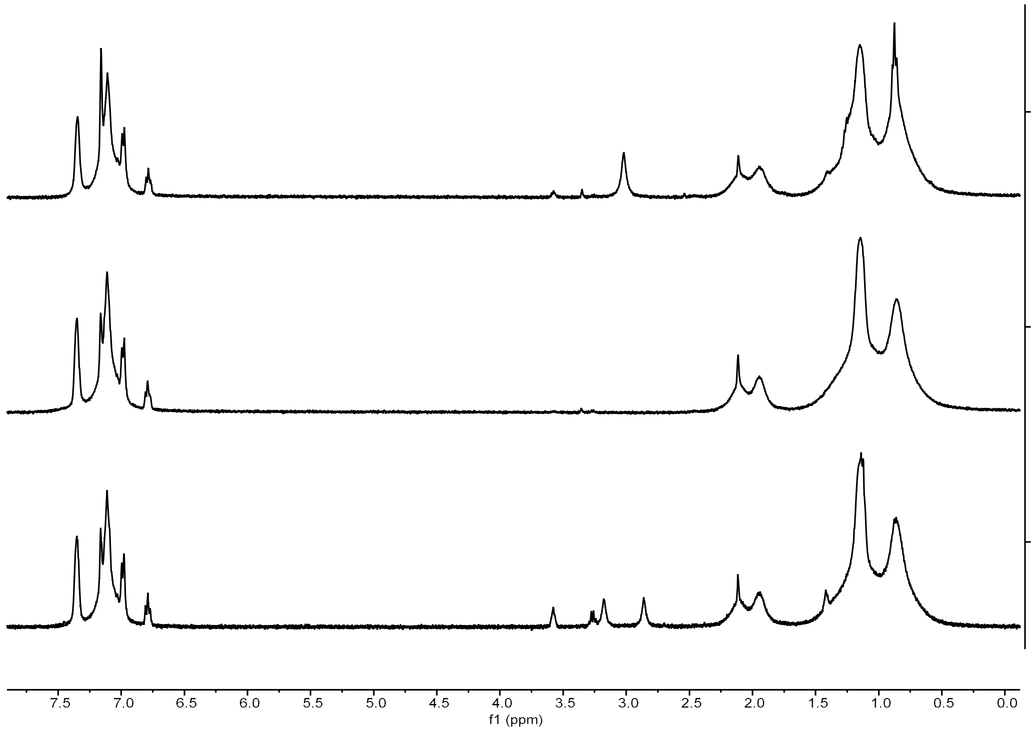

Figure 104. Comparison of ^{1}H NMR (400 MHz) of 2,6-bis[bis(2-diisopropylphenylphosphino)phosphino)]toluene (top), 2,6-bis[bis(2-diisopropylphenylphosphino)phosphino)]toluene-*d*$_3$ (middle) and 2,6-bis[bis(2-diisopropylphenylphosphino)phosphino)]toluene-^{13}C (bottom) in C_6D_6

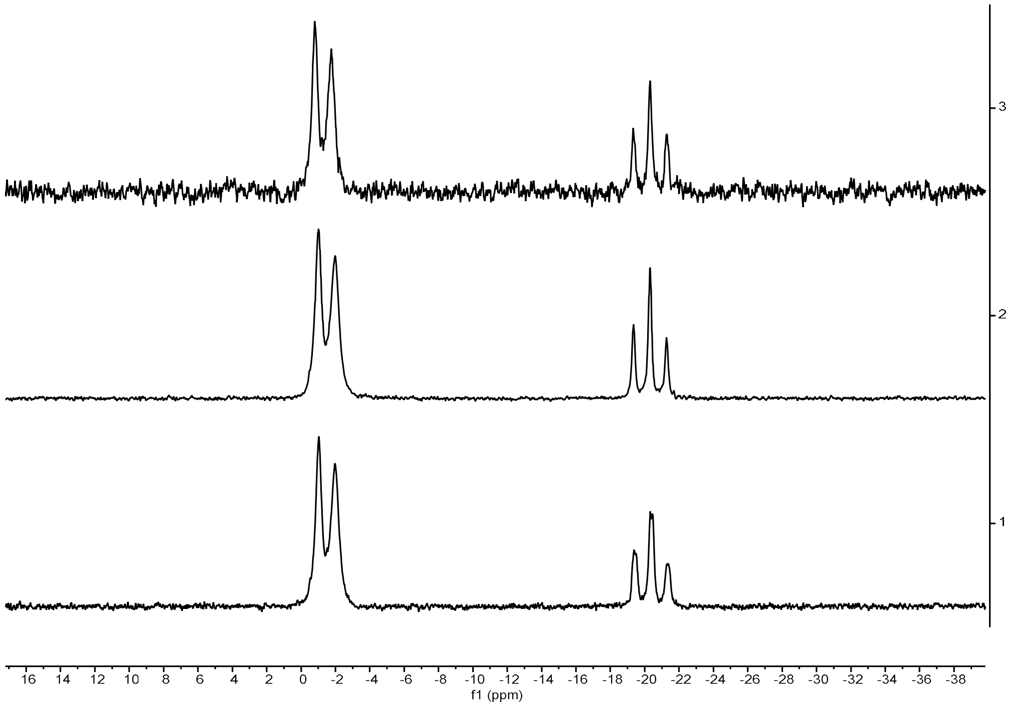

Figure 105. Comparison of ^{31}P NMR (162 MHz) of 2,6-bis[bis(2-diisopropylphenylphosphino)phosphino)]toluene (top), 2,6-bis[bis(2-diisopropylphenylphosphino)phosphino)]toluene-*d*$_3$ (middle) and 2,6-bis[bis(2-diisopropylphenylphosphino)phosphino)]toluene-^{13}C (bottom) in C_6D_6

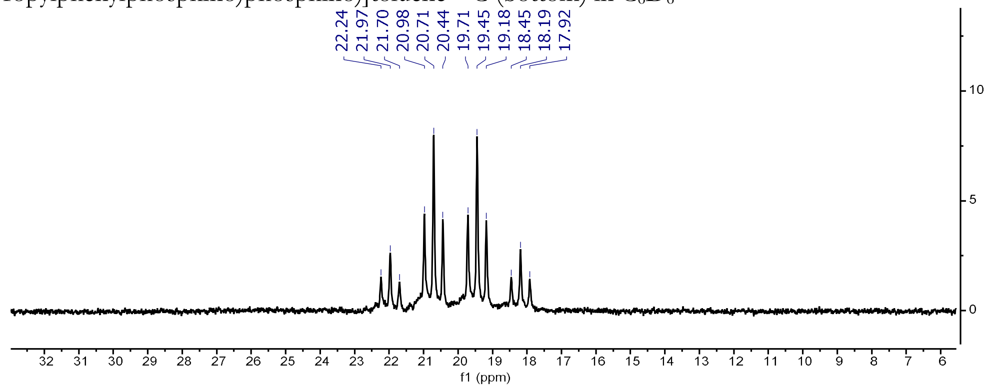

Figure 106. ^{13}C NMR (101 MHz) of 2,6-bis[bis(2-diisopropylphenylphosphino)phosphino)]toluene-^{13}C in C_6D_6

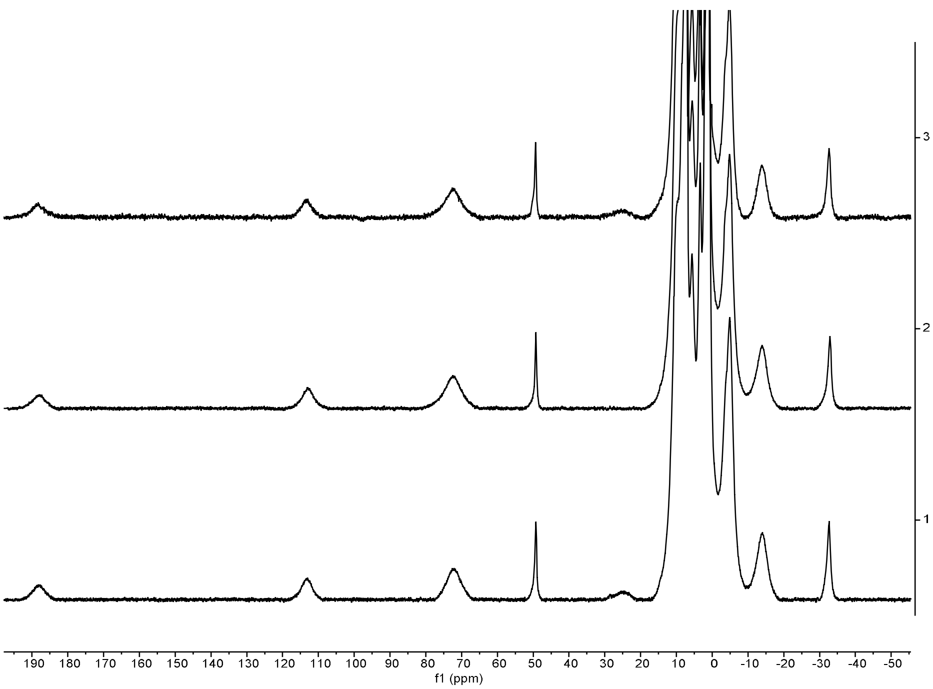

Figure 107. Comparison of ^1H NMR (400 MHz) of $(P_6ArCH_3)Fe_2Br_2$ (top), $(P_6ArCD_3)Fe_2Br_2$ (middle) and $(P_6Ar^{13}CH_3)Fe_2Br_2$ (bottom) in C_6D_6

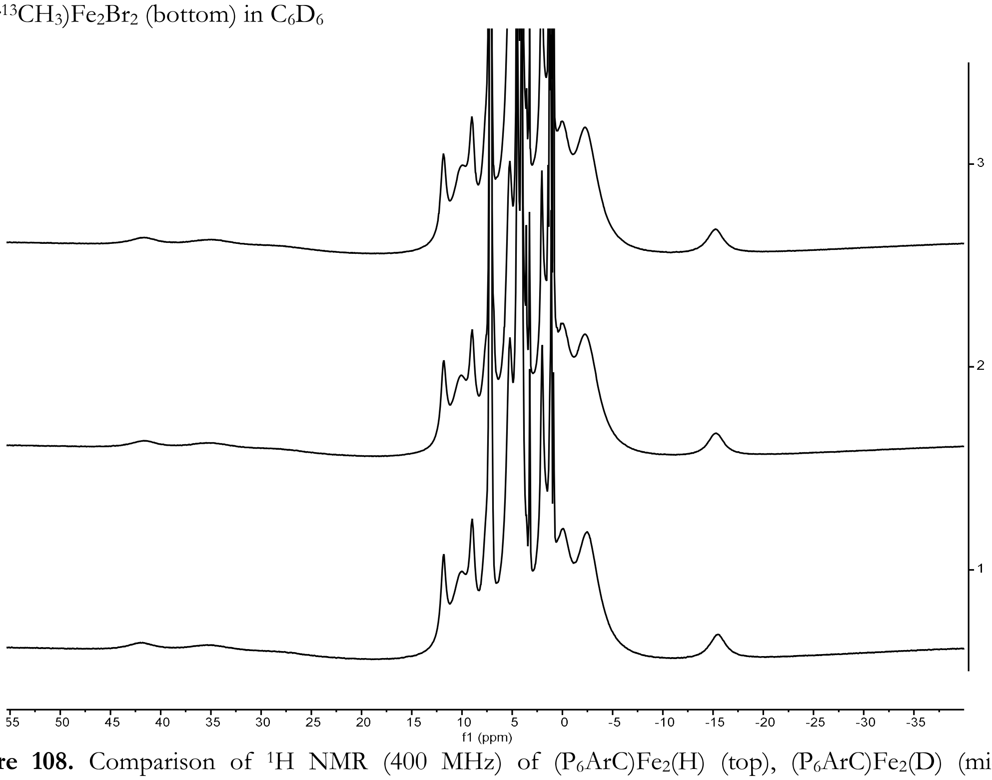

Figure 108. Comparison of ^1H NMR (400 MHz) of $(P_6ArC)Fe_2(H)$ (top), $(P_6ArC)Fe_2(D)$ (middle) and $(P_6Ar^{13}C)Fe_2(H)$ (bottom) in C_6D_6

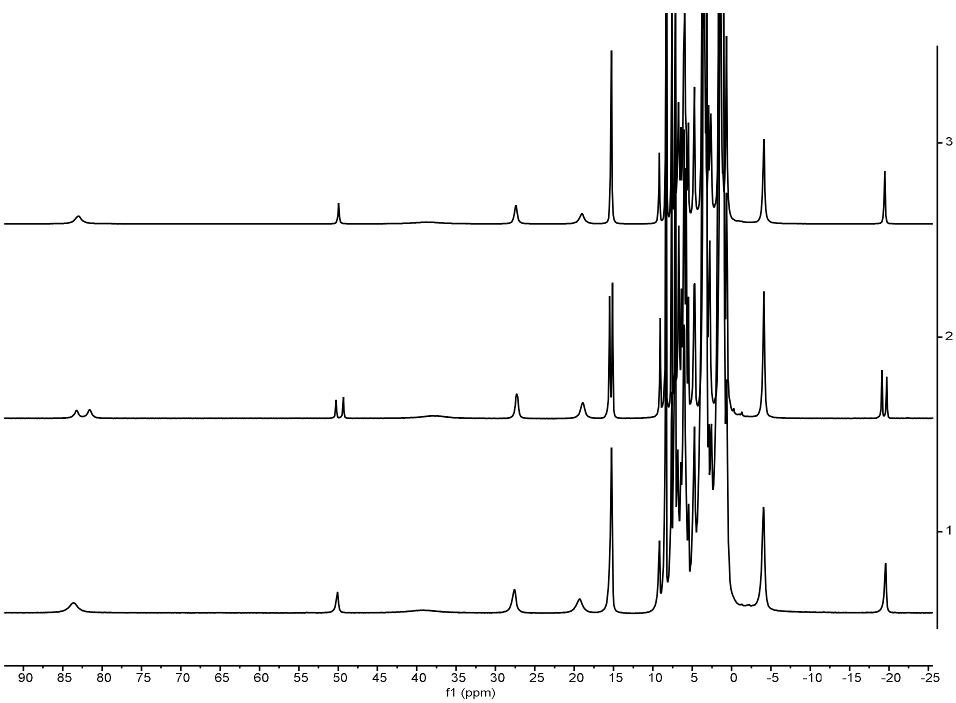

Figure 109. Comparison of ^{1}H NMR (400 MHz) of [(P$_6$ArC)Fe$_2$H][BAr^F$_{24}$] (top), [(P$_6$ArC)Fe$_2$D][BAr^F$_{24}$] (middle) and [(P$_6$Ar^{13}C)Fe$_2$H][BAr^F$_{24}$] (bottom) in C$_6$D$_6$

Chapter 6

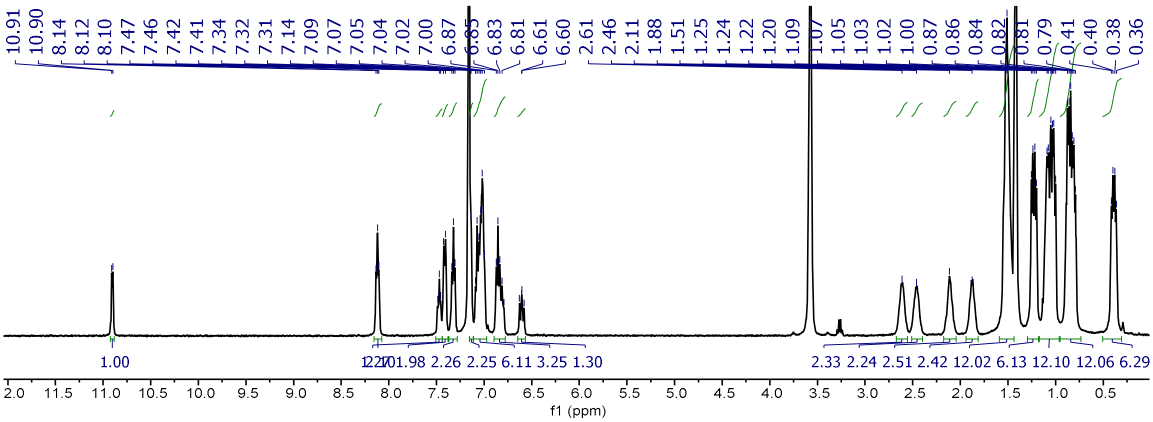

Figure S110. ^{1}H NMR (400 MHz) of **{Fe=C(H)Ar}^{10}** in C$_6$D$_6$/THF

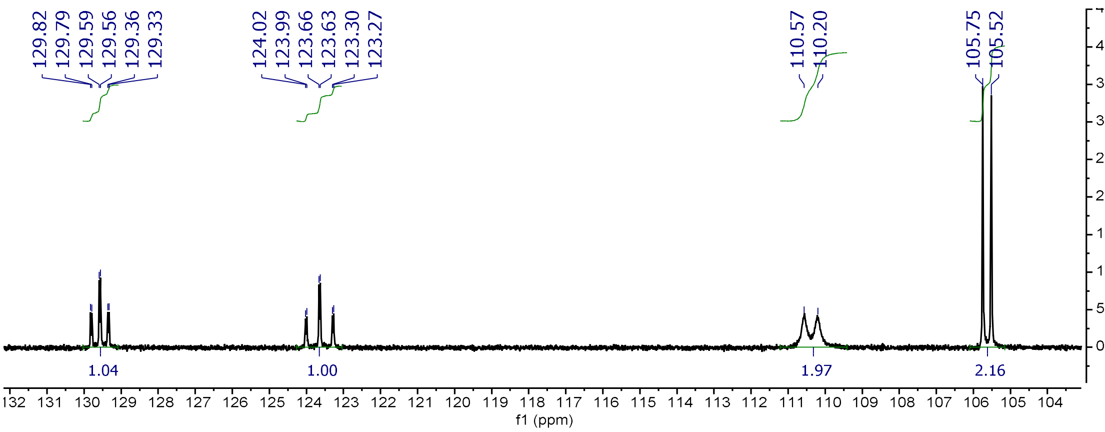

Figure S111. $^{31}P\{^1H\}$ NMR (400 MHz) of **{Fe=C(H)Ar}¹⁰** in C_6D_6

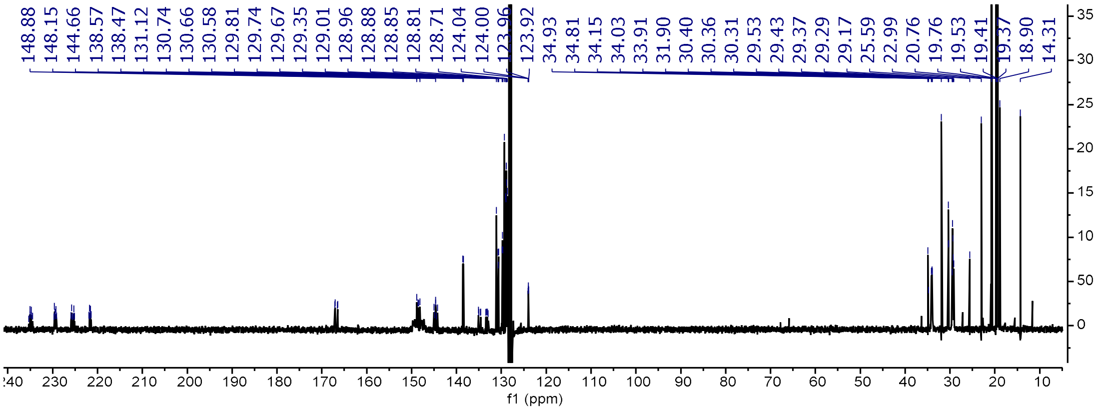

Figure S112. $^{13}C\{^1H\}$ NMR (400 MHz) of **{Fe=C(H)Ar}¹⁰** in C_6D_6

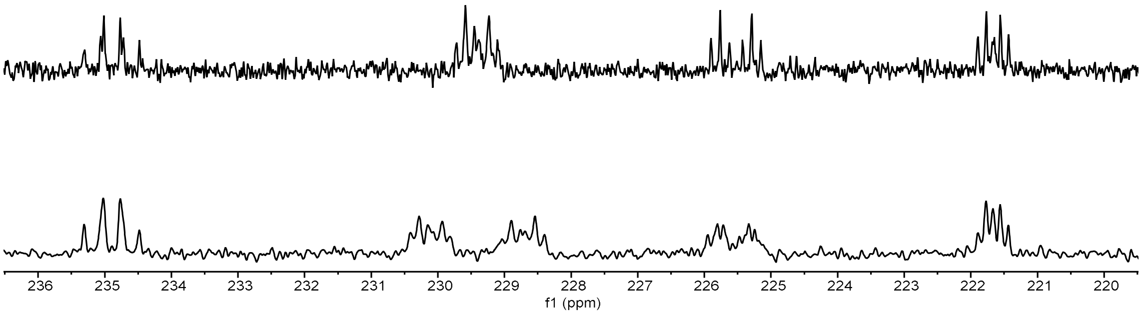

Figure S113. $^{13}C\{^1H\}$ NMR (101 MHz) of $(P_6ArCH)Fe_2(CO)_3$ **({Fe=C(H)Ar}¹⁰)** in C_6D_6 (top) focusing on the carbene resonance. Gate decoupled ^{13}C NMR (101 MHz) of $(P_6ArCH)Fe_2(CO)_3$ **({Fe=C(H)Ar}¹⁰)** in C_6D_6 (Bottom). From this data: $\delta = 229$ ppm, $^1J_{CH} = 137$ Hz.

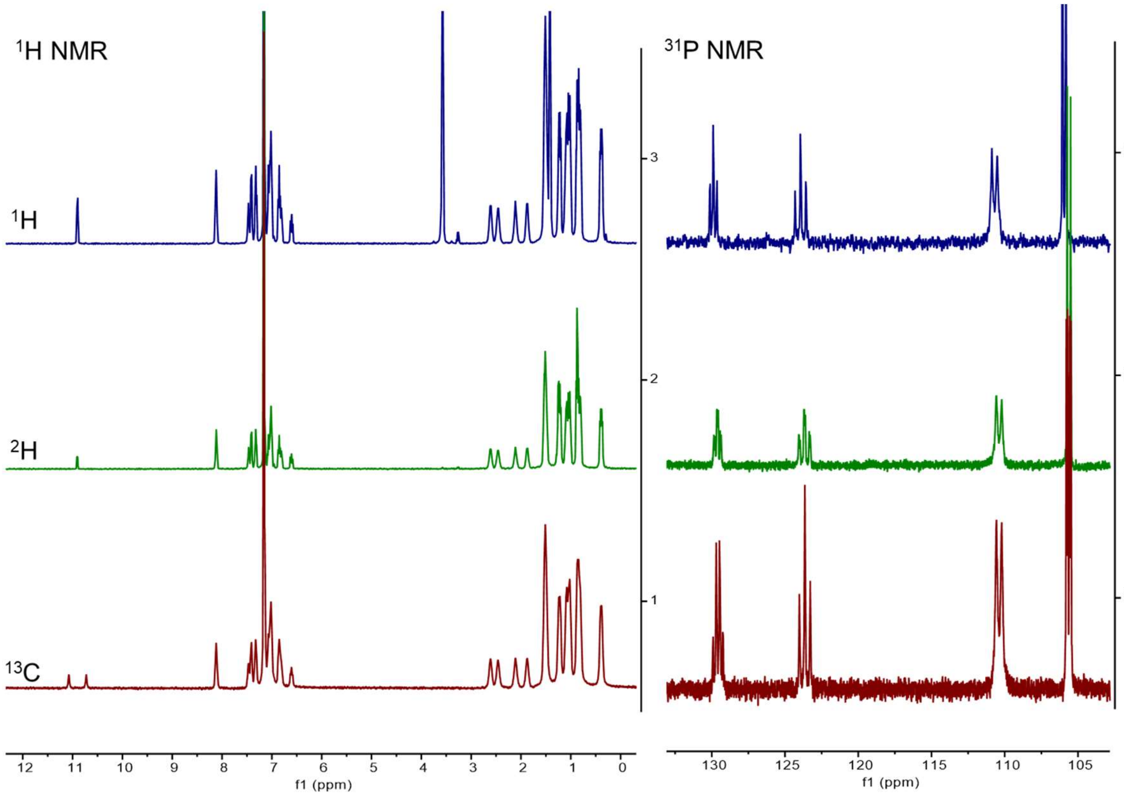

Figure S114. ^{1}H (400 MHz) and ^{31}P (162 MHz) NMR of **{Fe=C(H)Ar}^{10}** (top, blue), **{Fe=C(^{2}H)Ar}^{10}** (green, middle) and **{Fe=^{13}C(H)Ar}^{10}** in C_6D_6/THF

Appendix A

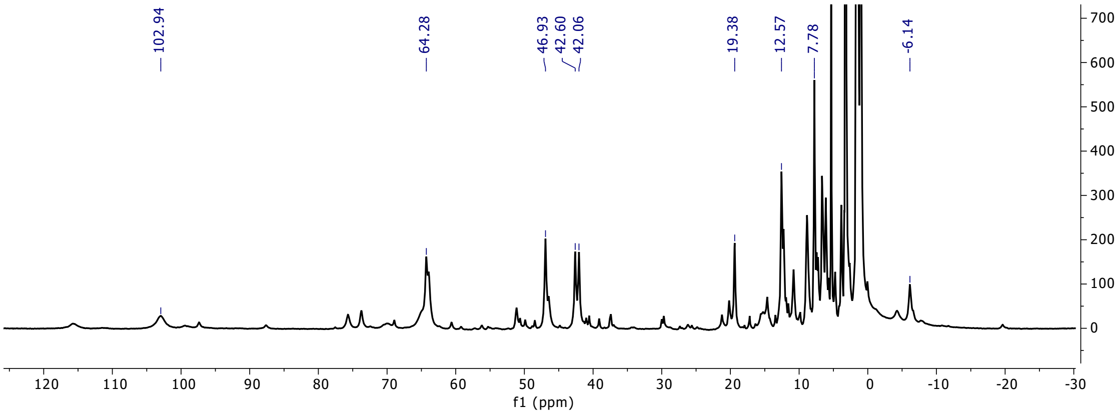

Figure S115. ^{1}H NMR (400 MHz) of $[LFe_3O(PhIm)_3Fe(N_3)][OTf]$ in CD_2Cl_2.

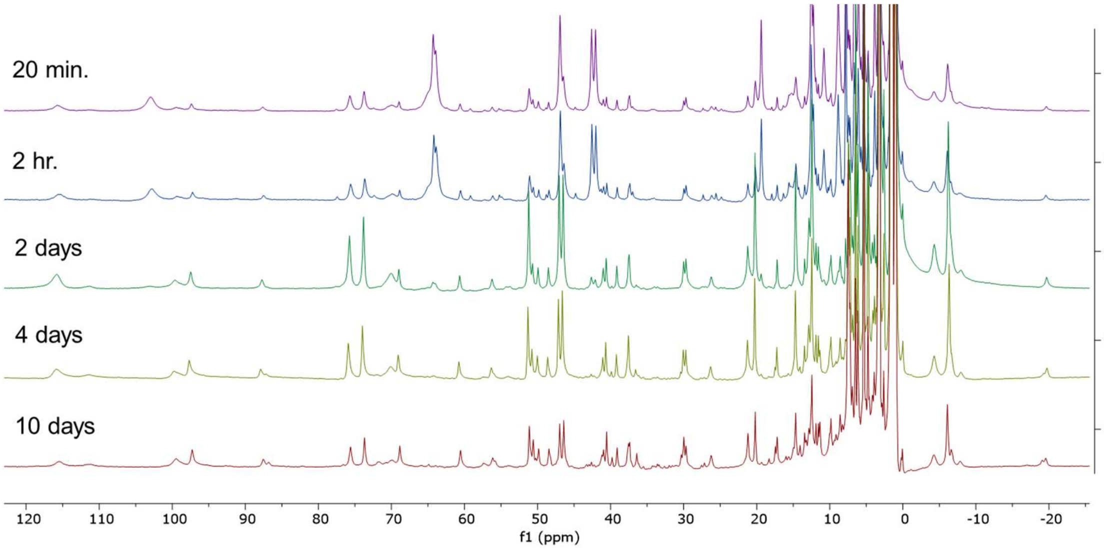

Figure S116. ^{1}H NMR (400 MHz) spectra following the decomposition of [LFe$_3$O(PhIm)$_3$Fe(N$_3$)][OTf] at room temperature in CD$_2$Cl$_2$.

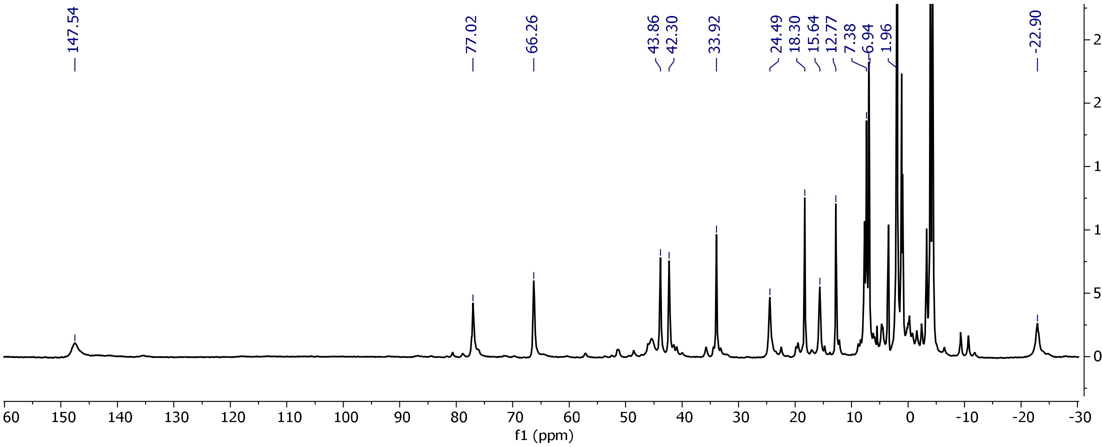

Figure S117. ^{1}H NMR (400 MHz) of [LFe$_3$O(SIm)$_3$Fe][OTf] in CD$_2$Cl$_2$.

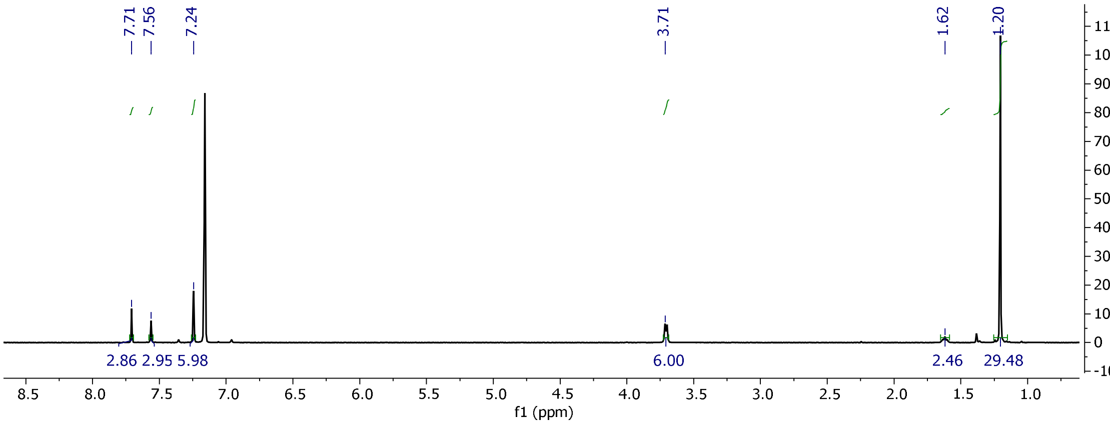

Figure S118. ^{1}H NMR (400 MHz) of L^{SH}_{tBu} in C$_6$D$_6$.

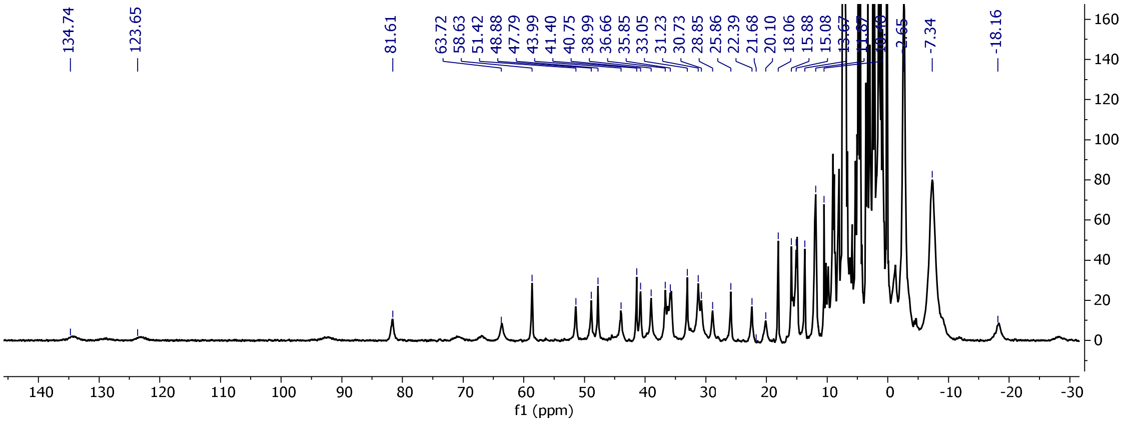

Figure S119. ^{1}H NMR (400 MHz) of [LFe$_2$O(iPrIm)$_2$Fe{N(SiMe$_3$)$_2$}] in C$_6$D$_6$.

Appendix B

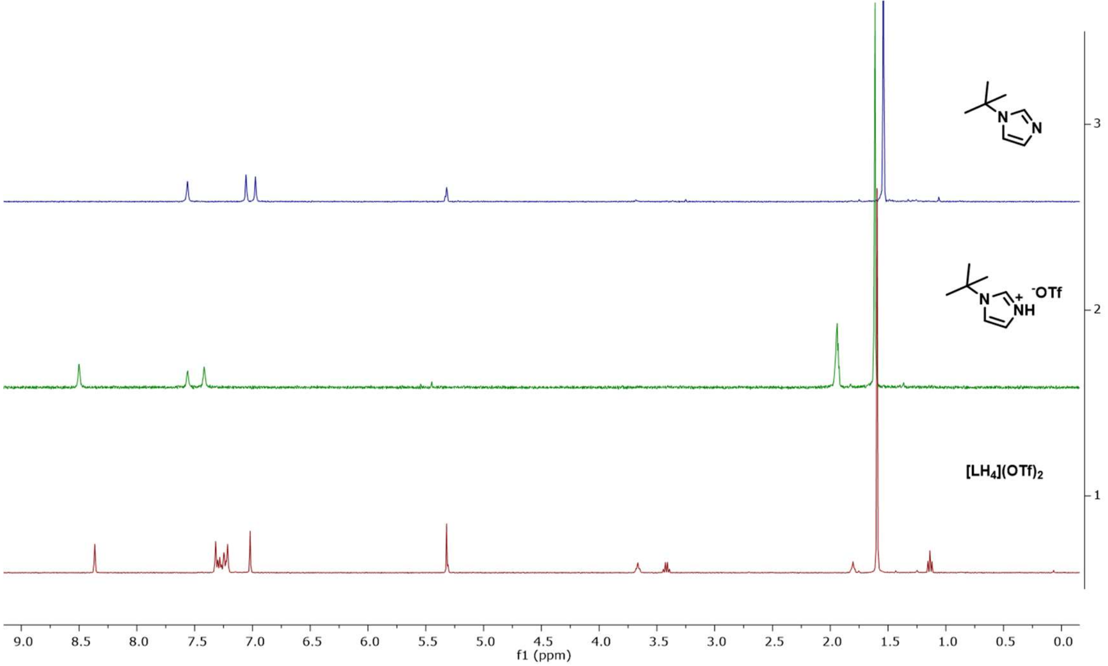

Figure S120. ^{1}H NMR (400 MHz) of **5** (bottom, red) in CD$_2$Cl$_2$.

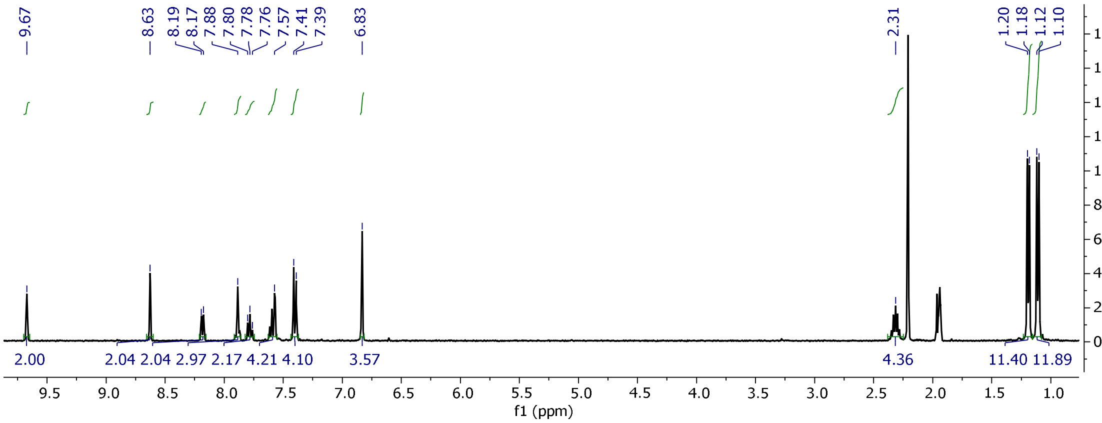

Figure S121. ^{1}H NMR (400 MHz) of **11** (bottom, red) in CD$_2$Cl$_2$.

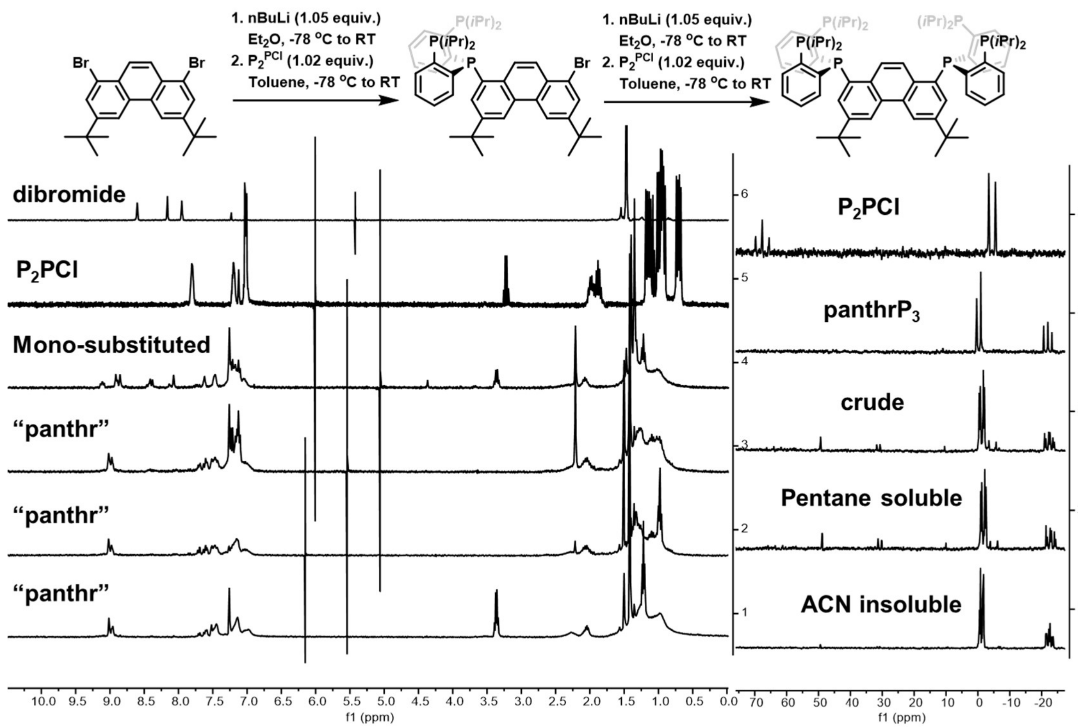

Figure S122. ^{1}H (400 MHz, left) and ^{31}P NMR (162 MHz, right) of **13** (3rd from top) and **panthr** in C_6D_6.

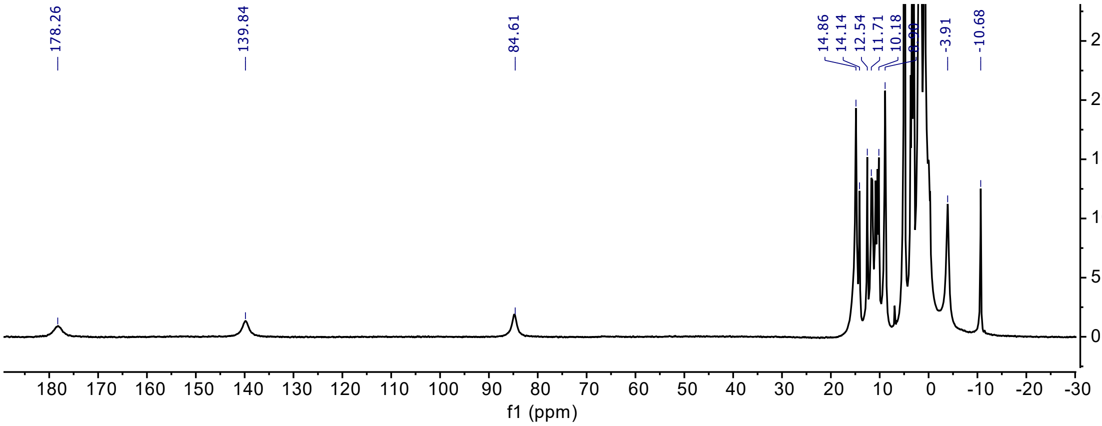

Figure S123. ^{1}H NMR (400 MHz) of (**panthr)Fe$_2$Br$_4$** in CD_2Cl_2.

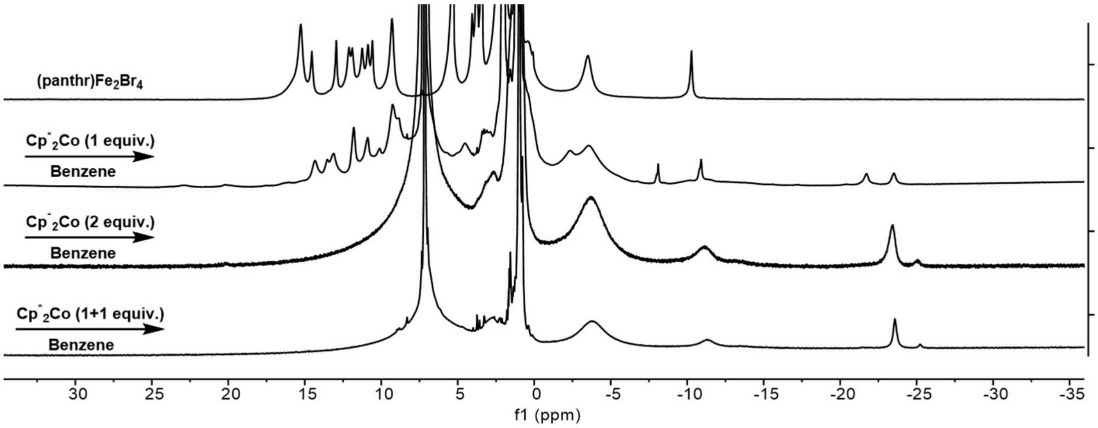

Figure S124. ^{1}H NMR (400 MHz) of (**panthr)Fe$_2$Br$_2$** (bottom two spectra) in C_6D_6.

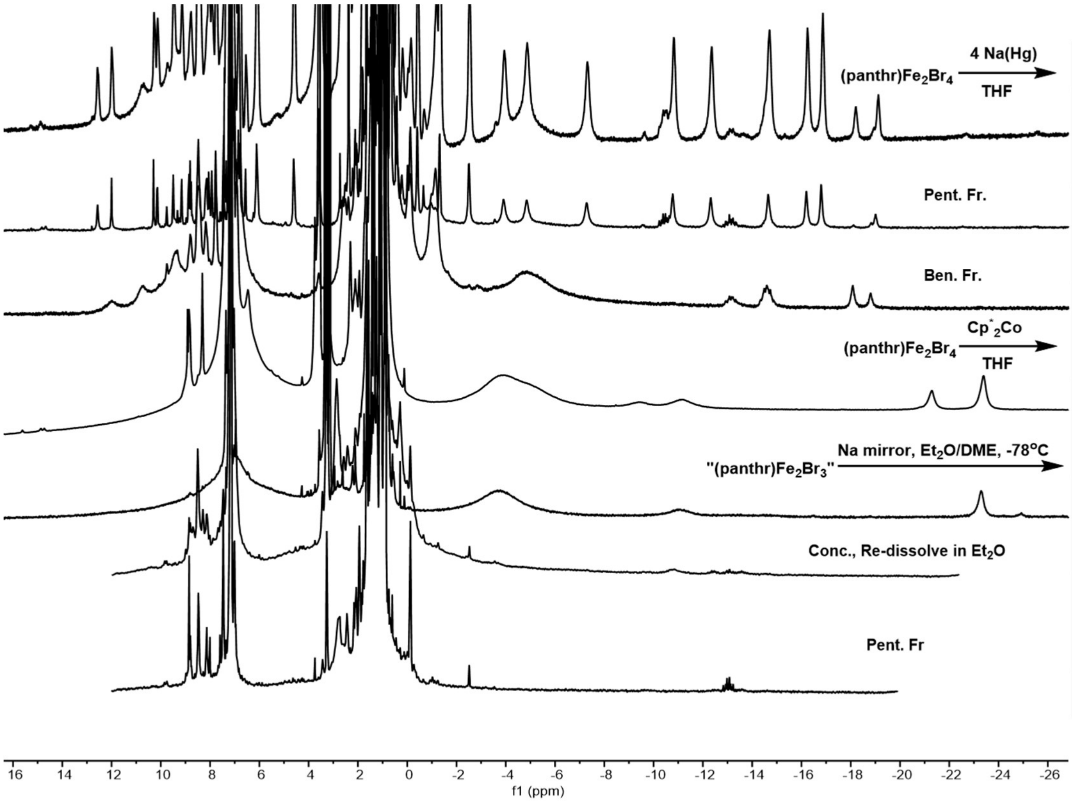

Figure S125. ^{1}H NMR (400 MHz) of (**panthr)Fe$_2$(N$_2$)$_2$(H)$_2$** (bottom spectrum) in C_6D_6.

Mössbauer

Chapter 2

General introduction: For simulation details, see Arnett, C.H.; Chalkley, M.J.; Agapie, T. *J. Am. Chem. Soc.* **2018**, *140*, 5569-5578.

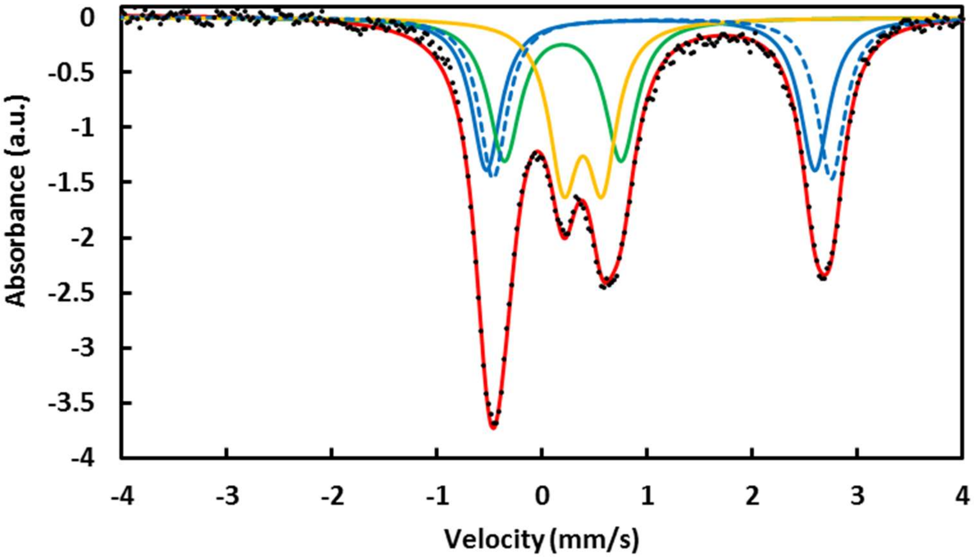

Figure 1. Zero field ^{57}Fe Mössbauer spectra (80 K) of [LFe$_3$O(PhIm)$_3$Fe][OTf]$_2$ (microcrystalline material, black dots). The simulation assuming four distinct subsites is shown in red, with parameters: (i): $\delta = 1.03$ mm/s, $|\Delta E_Q| = 3.13$ mm/s (solid blue trace, 25%); (ii): $\delta = 1.14$ mm/s, $|\Delta E_Q| = 3.22$ mm/s (dashed blue trace, 25%); (iii): $\delta = 0.39$ mm/s, $|\Delta E_Q| = 0.38$ mm/s (solid orange trace, 25%); (iv): $\delta = 0.19$ mm/s, $|\Delta E_Q| = 1.11$ mm/s (solid green trace, 25%).

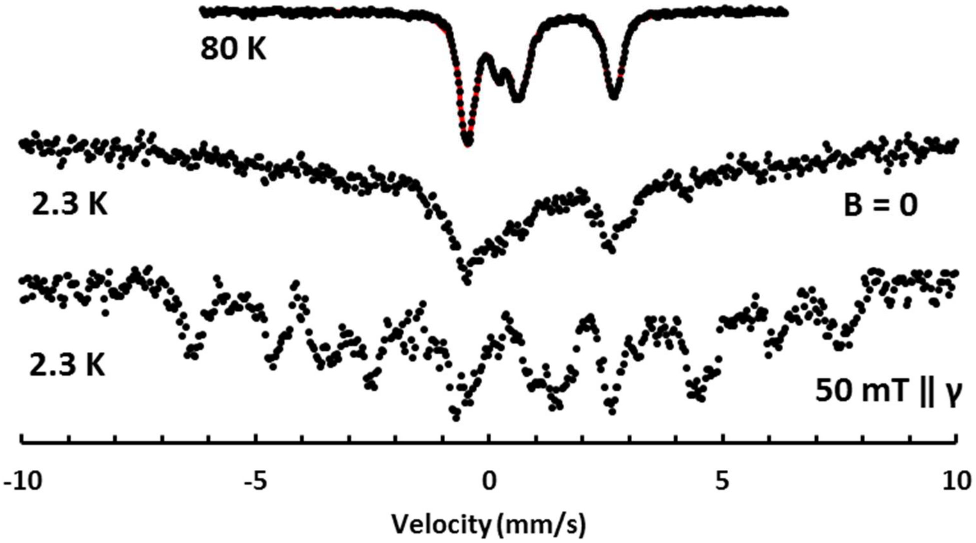

Figure 2. VTVH ^{57}Fe Mössbauer spectra of [LFe$_3$O(PhIm)$_3$Fe][OTf]$_2$ (**3**, microcrystalline material, black dots). Spectrum at 80 K in zero field (top). Spectrum at 2.3 K in zero field (middle). Spectrum at 2.3 K with a 50 mT field applied parallel to γ rays (bottom). All spectra collected with the same sample of **3**.

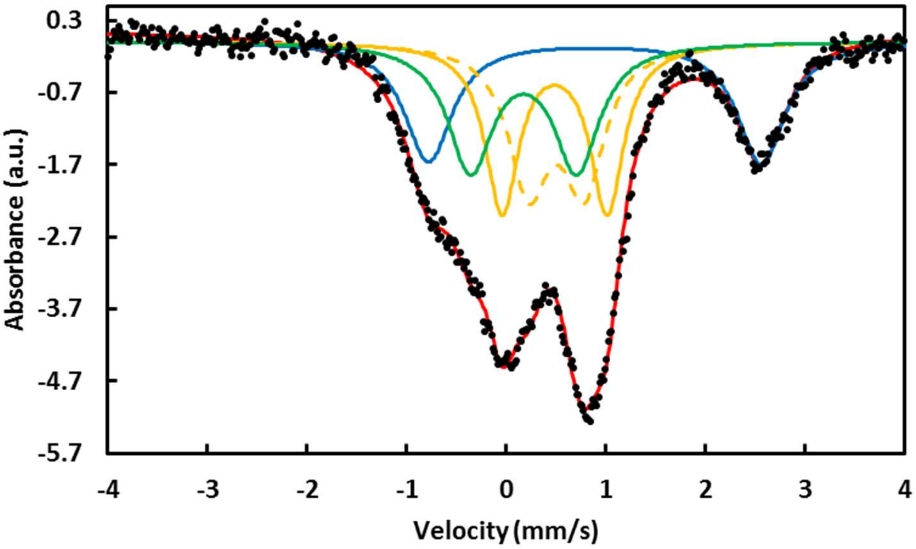

Figure 3. Zero field ^{57}Fe Mössbauer spectra (80 K) of [LFe$_3$O(PhIm)$_3$Fe][OTf]$_3$ (**4**, microcrystalline material, black dots). The simulation assuming four distinct subsites is shown in red, with parameters: (i): δ = 0.89 mm/s, |ΔE$_Q$| = 3.34 mm/s (solid blue trace, 25%); (ii): δ = 0.48 mm/s, |ΔE$_Q$| = 1.05 mm/s (solid orange trace, 25%); (iii): δ = 0.50 mm/s, |ΔE$_Q$| = 0.56 mm/s (dashed orange trace, 25%); (iv): δ = 0.17 mm/s, |ΔE$_Q$| = 1.07 mm/s (solid green trace, 25%)

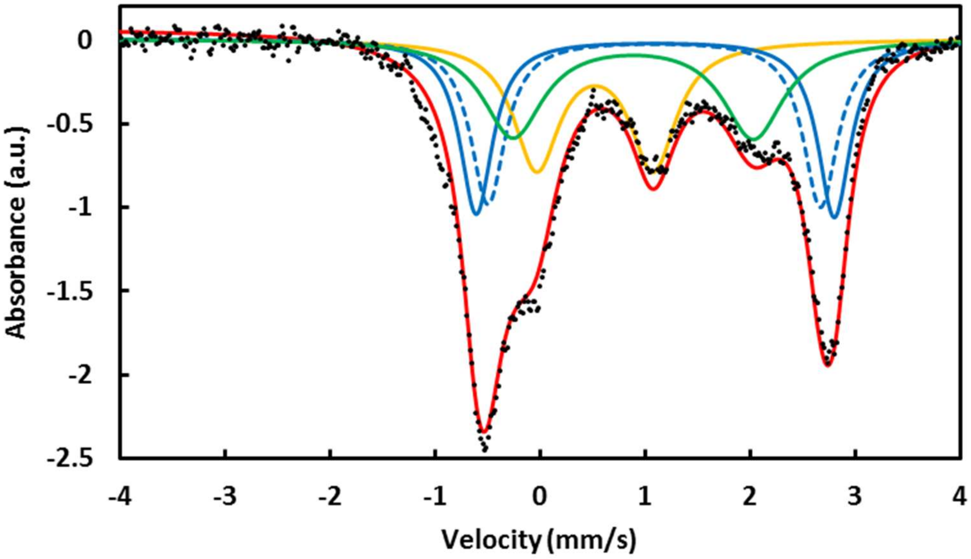

Figure 4. Zero field ^{57}Fe Mössbauer spectra (80 K) of [LFe$_3$O(PhIm)$_3$Fe][OTf] (**5**, microcrystalline material, black dots). The simulation assuming four distinct subsites is shown in red, with parameters: (i): δ = 1.09 mm/s, |ΔE$_Q$| = 3.17 mm/s (dashed blue trace, 25%); (ii): δ = 1.10 mm/s, |ΔE$_Q$| = 3.41 mm/s (solid blue trace, 25%); (iii): δ = 0.53 mm/s, |ΔE$_Q$| = 1.11 mm/s (solid orange trace, 25%); (iv): δ = 0.89 mm/s, |ΔE$_Q$| = 2.29 mm/s (solid green trace, 25%).

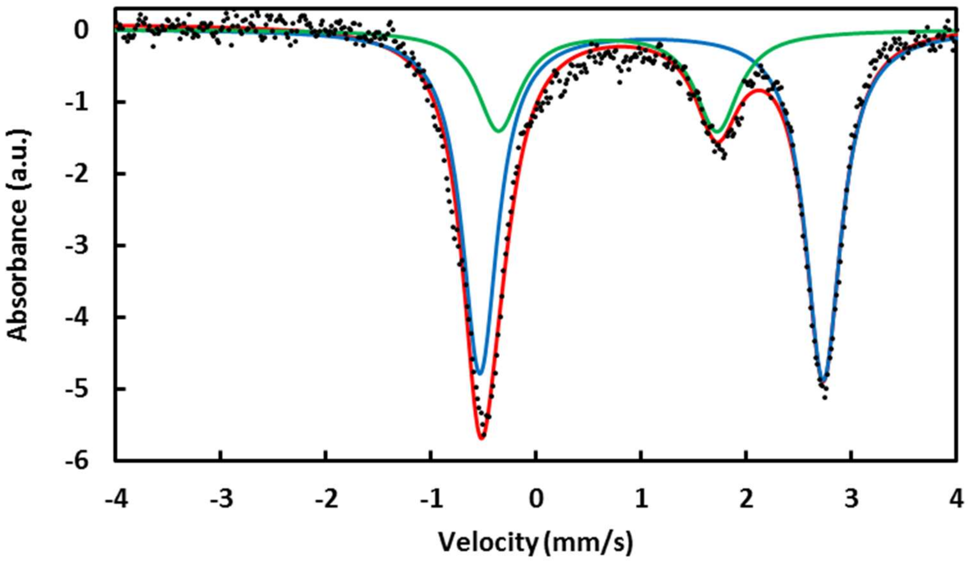

Figure 5. Zero field ^{57}Fe Mössbauer spectra (80 K) of [LFe$_3$O(PhIm)$_3$Fe] (**6**, powder, black dots). The simulation assuming two subsites is shown in red, with parameters: (i): δ = 1.13 mm/s, $|\Delta E_Q|$ = 3.19 mm/s (solid blue trace, 75%); (ii): δ = 0.68 mm/s, $|\Delta E_Q|$ = 2.08 mm/s (solid green trace, 25%).

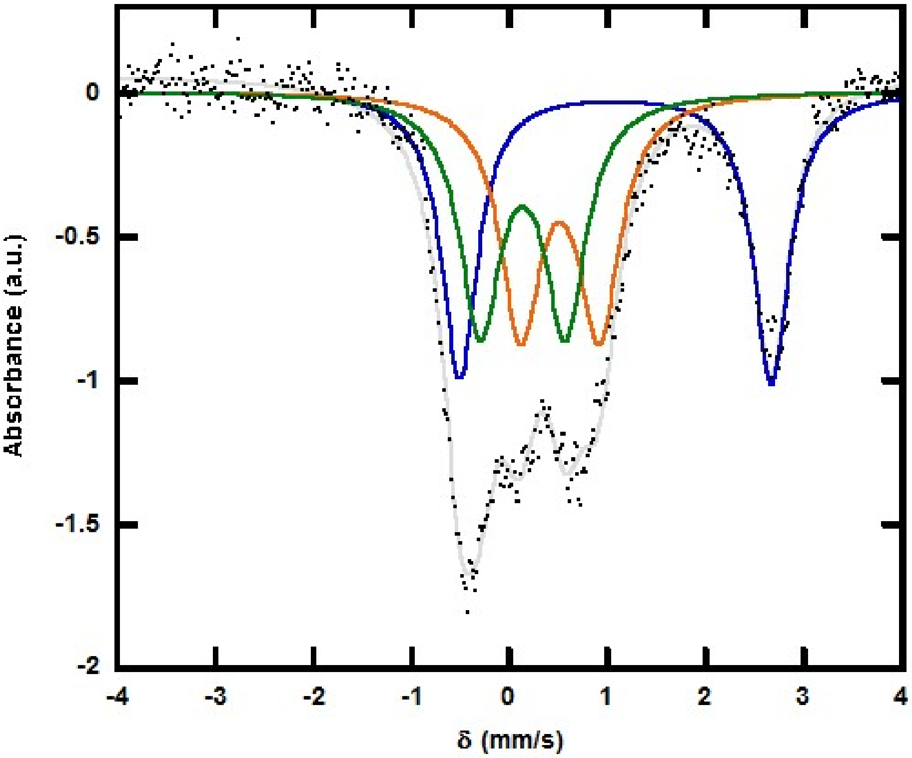

Figure 6. Zero field ^{57}Fe Mössbauer spectra (80 K) of [LFe$_3$O(PhIm)$_3$Fe][OTf]$_2$ (**3**) following exposure to CO (1 atm., solution in 2,6-lutidine, black dots). The simulation assuming three distinct subsites is shown in grey, with parameters: (i): δ = 1.09 mm/s, $|\Delta E_Q|$ = 3.18 mm/s (solid blue trace, 35.2%); (ii): δ = 0.51 mm/s, $|\Delta E_Q|$ = 0.80 mm/s (solid orange trace, 32.5%); (iii): δ = 0.14 mm/s, $|\Delta E_Q|$ = 0.87 mm/s (solid green trace, 32.3%). Comparison with the spectra in Figures S64 or S65 reveals a significant loss (15% total iron content) of core Fe(II) upon binding of CO.

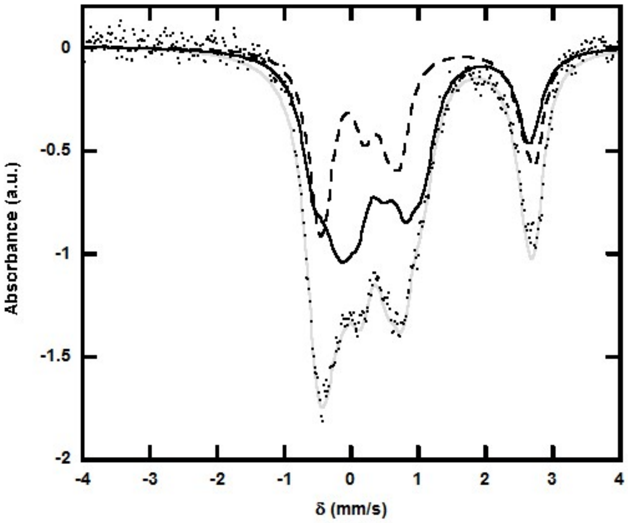

Figure 7. Zero field ^{57}Fe Mössbauer spectra (80 K) of [$LFe_3O(PhIm)_3Fe$][OTf]$_2$ (**3**) following exposure to CO (1 atm. solution in 2,6-lutidine, black dots). The simulation (shown in grey) assuming eight distinct subsites, four from [$LFe_3O(PhIm)_3Fe$][OTf]$_2$ (**3**) with fixed isomer shift and quadrupole splitting parameters, and four from [$LFe_3O(PhIm)_3Fe(CO)_n$][OTf]$_2$ (**3-(CO)$_n$**). The parameters associated with the [$LFe_3O(PhIm)_3Fe(CO)$][OTf]$_2$ (**3-CO**) simulated subspectrum (solid black trace): (i): δ = 1.05 mm/s, $|\Delta E_Q|$ = 3.22 mm/s (15.4%); (ii): δ = 0.47 mm/s, $|\Delta E_Q|$ = 0.71 mm/s (15.4%); (iii): δ = 0.48 mm/s, $|\Delta E_Q|$ = 1.18 mm/s (15.4%); (iv): δ = 0.10 mm/s, $|\Delta E_Q|$ = 0.78 mm/s (15.4%). The parameters associated with the [$LFe_3O(PhIm)_3Fe$](OTf)$_2$ subspectrum (dashed black trace): (v): δ = 1.03 mm/s, $|\Delta E_Q|$ = 3.13 mm/s (9.6%); (vi): δ = 1.14 mm/s, $|\Delta E_Q|$ = 3.22 mm/s (9.6%); (vii): δ = 0.39 mm/s, $|\Delta E_Q|$ = 0.37 mm/s (9.6%); (viii): δ = 0.19 mm/s, $|\Delta E_Q|$ = 1.11 mm/s (9.6%).

Chapter 3

General introduction: For simulation details, see Arnett, C.H.; Kaiser, J.T.; Agapie, T. *Inorg. Chem.*, **2019**, *58*, 15971-15982.

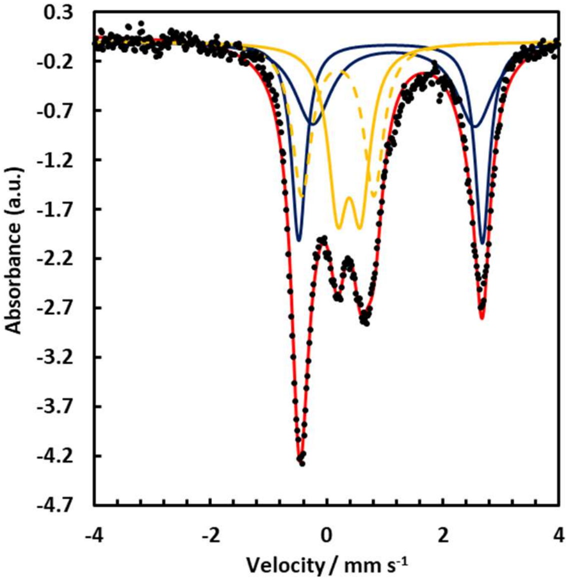

Figure 8. Zero field ^{57}Fe Mössbauer spectra (80 K) of $[LFe_3O(^{pCF3}ArIm)_3Fe][OTf]_2$ ($\mathbf{1^{CF3}}$, microcrystalline material, black dots). The simulation assuming four distinct subsites is shown in red, with parameters: (i): δ = 1.10 mm/s, $|\Delta E_Q|$ = 3.17 mm/s (solid blue trace, 25%); (ii): δ = 1.16 mm/s, $|\Delta E_Q|$ = 2.80 mm/s (solid blue trace, 25%); (iii): δ = 0.39 mm/s, $|\Delta E_Q|$ = 0.39 mm/s (solid orange trace, 25%); (iv): δ = 0.19 mm/s, $|\Delta E_Q|$ = 1.24 mm/s (dashed orange trace, 25%).

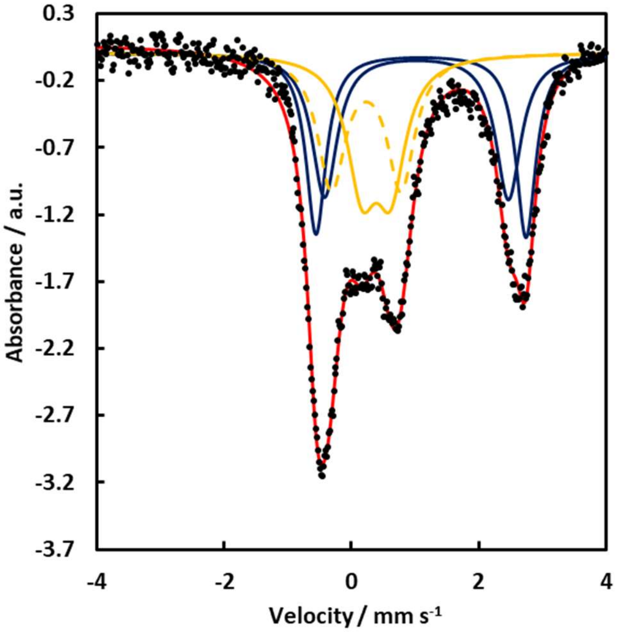

Figure 9. Zero field ^{57}Fe Mössbauer spectra (80 K) of $[LFe_3O(^{pNMe2}ArIm)_3Fe][OTf]_2$ ($\mathbf{1^{NMe2}}$, microcrystalline material, black dots). The simulation assuming four distinct subsites is shown in red, with parameters: (i): δ = 1.02 mm/s, $|\Delta E_Q|$ = 2.89 mm/s (solid blue trace, 25%); (ii): δ = 1.09 mm/s, $|\Delta E_Q|$ = 3.30 mm/s (solid blue trace, 25%); (iii): δ = 0.39 mm/s, $|\Delta E_Q|$ = 0.45 mm/s (solid orange trace, 25%); (iv): δ = 0.22 mm/s, $|\Delta E_Q|$ = 1.10 mm/s (dashed orange trace, 25%).

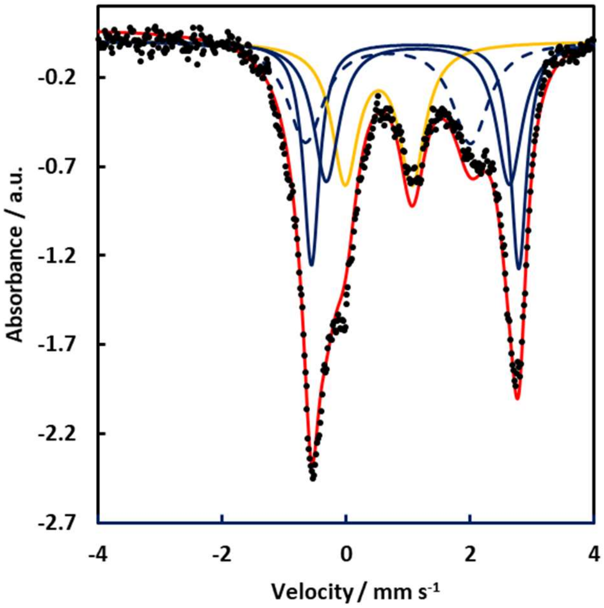

Figure 10. Zero field ^{57}Fe Mössbauer spectra (80 K) of $[LFe_3O(PhIm)_3Fe][OTf]$ ($\mathbf{2^H}$, microcrystalline material, black dots). The simulation assuming four distinct subsites is shown in red, with parameters: (i): δ = 1.12 mm/s,

|ΔE$_Q$| = 3.34 mm/s (solid blue trace, 25%); (ii): δ = 1.17 mm/s, |ΔE$_Q$| = 2.95 mm/s (solid blue trace, 25%); (iii): δ = 0.53 mm/s, |ΔE$_Q$| = 1.08 mm/s (solid orange trace, 25%); (iv): δ = 0.68 mm/s, |ΔE$_Q$| = 2.66 mm/s (dashed blue trace, 25%).

Chapter 4

General introduction: For simulation details, see Arnett, C.H.; Agapie, T. *J. Am. Chem. Soc.*, **2020**, *142*, 10059-10068

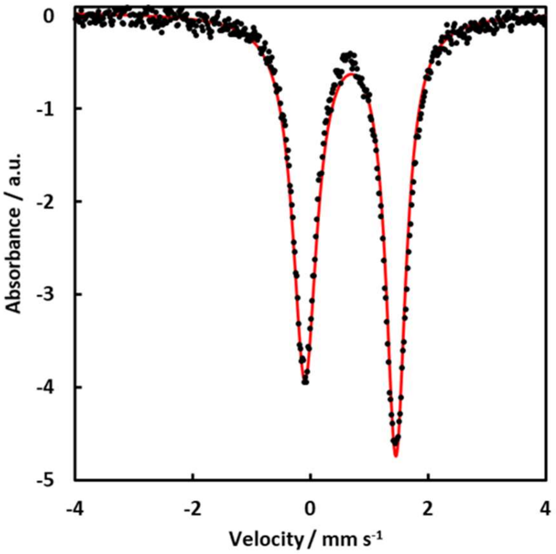

Figure 11. Solid-state ^{57}Fe Mössbauer spectrum of (P_6ArCH_3)Fe_2Br_2 (**4**) collected at 80 K with a 50 mT field applied parallel to the γ rays. Data presented in black points, simulation represented by solid red line. Fit with δ = 0.68 mm s^{-1}, |ΔE_Q| = 1.55 mm s^{-1}, Γ_L = 0.50 mm s^{-1}, Γ_R = 0.41 mm s^{-1}.

Chapter 5

General introduction: For simulation details, see Arnett, C.H.; Bogacz, I.; Chatterjee, R.; Yano, J.; Oyala, P.H.; Agapie, T. *J. Am. Chem. Soc.* **2020**, *In Revision*.

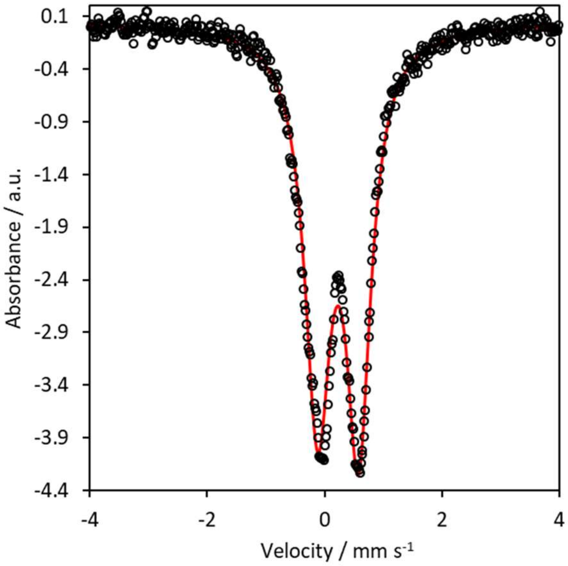

Figure 12. ^{57}Fe Mössbauer spectrum of [(P_6ArC)Fe_2H][BAr$^F_{24}$] (**{Fe$_2$(μ-CAr)}^{17},** 24 mM in 2-MeTHF) collected at 80 K with a 50 mT field applied parallel to the γ rays. Data presented in black points, simulation represented by solid red line. Fit with δ = 0.23 mm s^{-1}, $|\Delta E_Q|$ = 0.70 mm s^{-1}, Γ_L = 0.54 mm s^{-1}, Γ_R = 0.51 mm s^{-1}. Reduced χ^2 = 1.235.

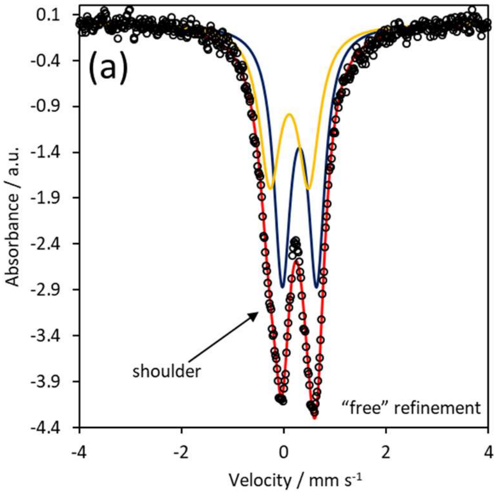

Figure 13. ^{57}Fe Mössbauer spectrum of [(P_6ArC)Fe_2H][BAr$^F_{24}$] (**{Fe$_2$(μ-CAr)}^{17},** 24 mM in 2-MeTHF) collected at 80 K with a 50 mT field applied parallel to the γ rays. Data presented in black points, simulation represented by solid red line. (a) Fit with two subsites with no restraint on relative populations: δ = 0.30 mm s^{-1}, $|\Delta E_Q|$ = 0.67 mm s^{-1}, Γ = 0.39 mm s^{-1}, Area = 56%; δ = 0.10 mm s^{-1}, $|\Delta E_Q|$ = 0.76 mm s^{-1}, Γ = 0.50 mm s^{-1}, Area = 44%. Reduced χ^2 = 0.620 (b) Fit with two subsites with both sites restrained to have equal populations: δ = 0.30 mm s^{-1}, $|\Delta E_Q|$ = 0.67 mm s^{-1}, Γ = 0.38 mm s^{-1}, Area = 50%; δ = 0.12 mm s^{-1}, $|\Delta E_Q|$ = 0.76 mm s^{-1}, Γ = 0.53 mm s^{-1}, Area = 50%. Reduced χ^2 = 0.628.

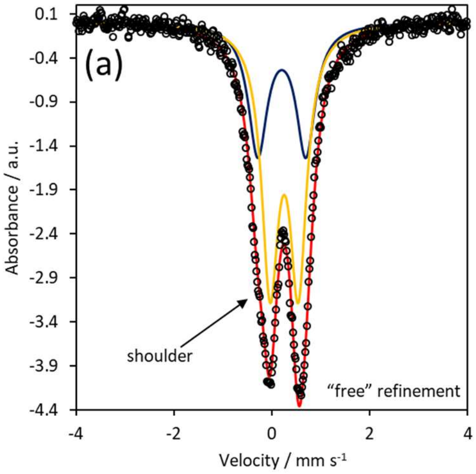

Figure 14. ^{57}Fe Mössbauer spectrum of [(P_6ArC)Fe_2H][BAr$^F_{24}$] (**{Fe$_2$(μ-CAr)}^{17},** 24 mM in 2-MeTHF) collected at 80 K with a 50 mT field applied parallel to the γ rays. Data presented in black points, simulation represented by solid red line. (a) Fit with two subsites with no restraint on relative populations: δ = 0.20 mm s^{-1}, $|\Delta E_Q|$ = 0.98 mm s^{-1}, Γ = 0.47 mm s^{-1}, Area = 36%; δ = 0.24 mm s^{-1}, $|\Delta E_Q|$ = 0.57 mm s^{-1}, Γ = 0.42 mm s^{-1}, Area = 64%. (b) Fit with two subsites with both sites restrained to have equal populations: δ = 0.21 mm s^{-1}, $|\Delta E_Q|$ = 0.92 mm s^{-1}, Γ = 0.47 mm s^{-1}, Area = 50%; δ = 0.25 mm s^{-1}, $|\Delta E_Q|$ = 0.55 mm s^{-1}, Γ = 0.42 mm s^{-1}, Area = 50%.

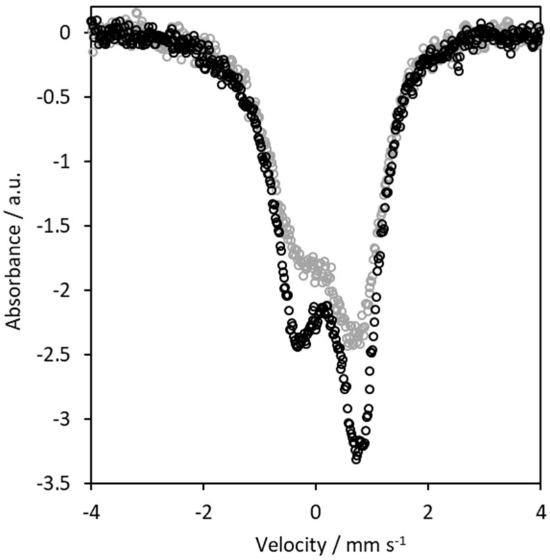

Figure 15. ^{57}Fe Mössbauer spectrum of [K(THF)$_n$][(P$_6$ArC)Fe$_2$H] (**{Fe$_2$(μ-CAr)}^{19},** 29 mM in THF) collected at 80 K with zero applied field (grey) and a 50 mT field applied parallel to the γ rays (black).

EPR

Chapter 2

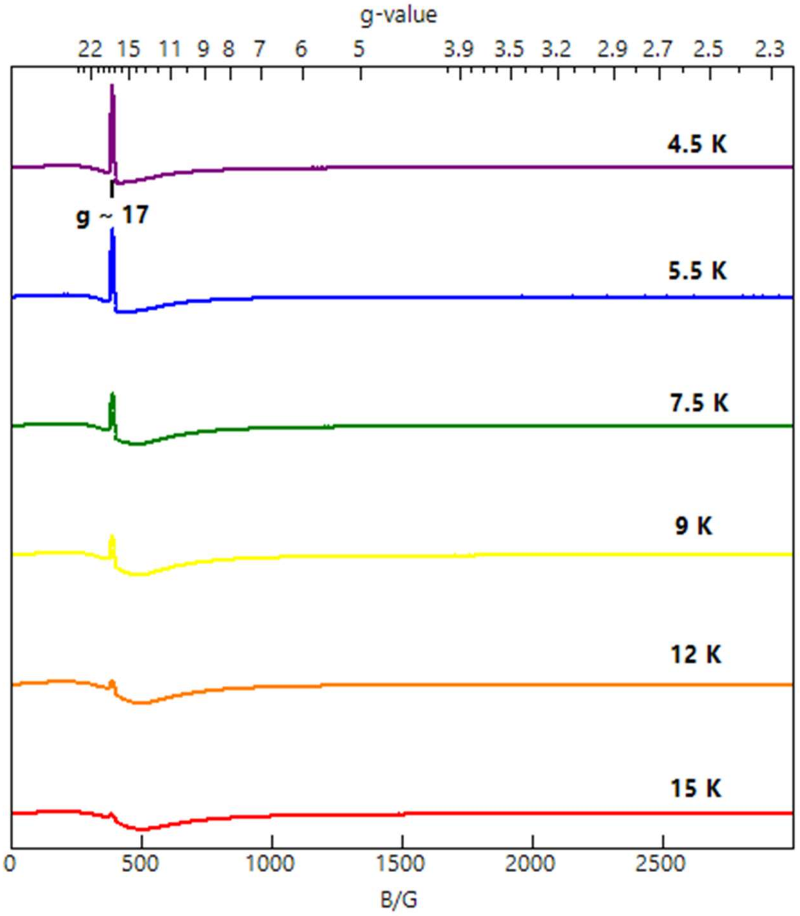

Figure 1. Variable temperature X-band EPR spectrum of [$LFe_3O(PhIm)_3Fe$][OTf]$_2$ (**3**) in 4:5 propionitrile:butyronitrile (2 mM).

Chapter 3

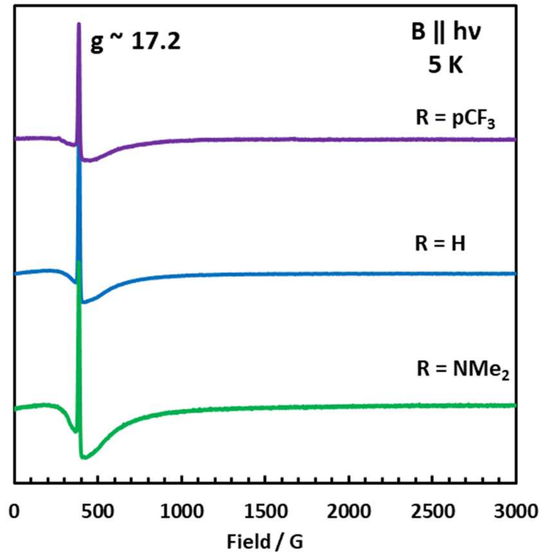

Figure 2. Parallel-mode EPR Spectra of $[LFe_3O(^{pCF3}ArIm)_3Fe][OTf]_2$ ($\mathbf{1^{CF3}}$, purple), $[LFe_3O(PhIm)_3Fe][OTf]_2$ ($\mathbf{1^{H}}$, blue) and $[LFe_3O(^{pNMe2}ArIm)_3Fe][OTf]_2$ ($\mathbf{1^{NMe2}}$, green) at 4.5 K in a propionitrile/butryonitrile (4:5) glass.

Chapter 5

General introduction: For simulation details, see Arnett, C.H.; Bogacz, I.; Chatterjee, R.; Yano, J.; Oyala, P.H.; Agapie, T. *J. Am. Chem. Soc.* **2020**, *In Revision.*

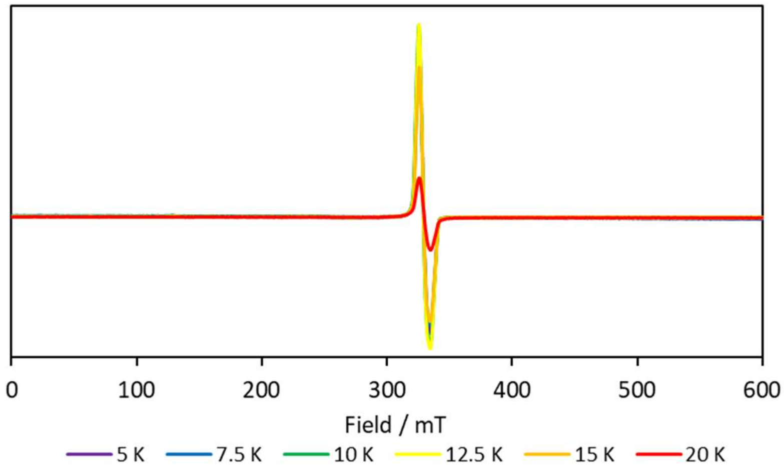

Figure 3. X-band CW EPR Spectrum of $[(P_6ArC)Fe_2H][BAr^F{}_{24}]$ (2 mM, 2-MeTHF) collected a function of temperature. A decrease in signal intensity and broadening is observed upon warming to 15-20 K.

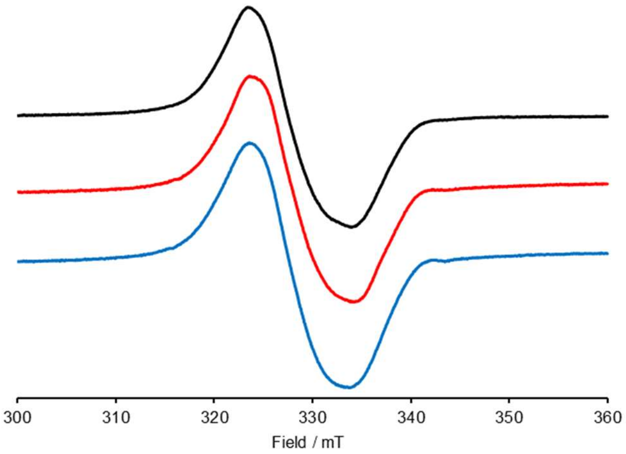

Figure 4. X-band CW EPR Spectra of [(P_6ArC)Fe_2H][BAr^F_{24}] (black), [(P_6ArC)Fe_2D][BAr^F_{24}] (red), and [($P_6Ar^{13}C$)Fe_2H][BAr^F_{24}] (blue), all 2 mM, 2-MeTHF. X-band CW-EPR acquisition parameters: temperature = 5 K; MW frequency = 9.639 GHz; MW power = 2 mW; modulation frequency = 100 kHz; modulation amplitude = 0.4 mT; conversion time = 82 ms.

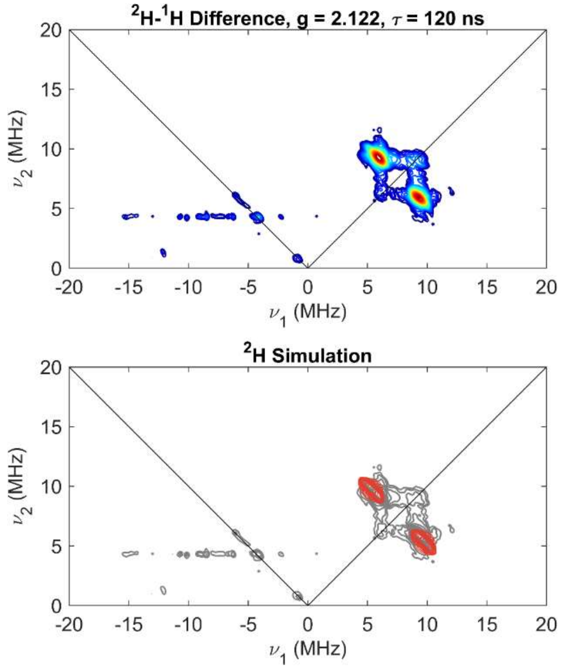

Figure 5. (top panel) Q-band ^{2}H-^{1}H difference HYSCORE spectrum of [(P_6ArC)Fe_2D][BAr^F_{24}] acquired at 1148 mT (g = 2.122). (bottom) Monochromatic representation of the HYSCORE data (grey) with ^{2}H simulations overlaid (red). Simulation parameters were derived by scaling the ^{1}H hyperfine tensor in Table 2 of the main text determined from Q-band ^{1}H ENDOR, and scaling by the proportion of ^{1}H/^{2}H gyromagnetic ratios ($\gamma^1H/\gamma^2H = 6.514$). Simulations also include ^{2}H nuclear quadrupole parameters $e^2qQ/h = 0.15$; $\eta = 0$. Acquisition parameters: temperature = 12 K; microwave frequency = 34.086 GHz; MW pulse length (π/2, π) = 12 ns, 24 ns; τ = 120 ns, $t_1 = t_2 = 100$ ns; $\Delta t_1 = \Delta t_2 = 12$ ns; shot repetition time (srt) = 1.5 ms).

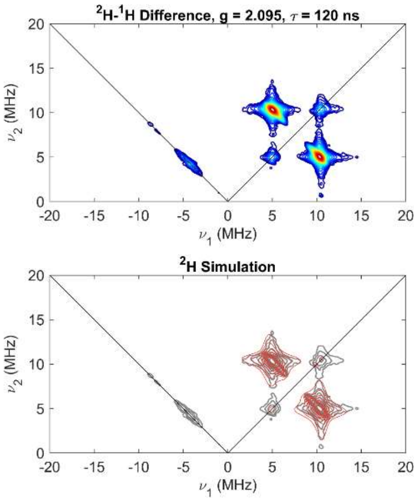

Figure 6. (top panel) Q-band ^{2}H-^{1}H difference HYSCORE spectrum of [(P$_6$ArC)Fe$_2$D][BAr^F$_{24}$] acquired at 1162.5 mT (g = 2.095). (bottom) Monochromatic representation of the HYSCORE data (grey) with ^{2}H simulations overlaid (red). Simulation parameters were derived by scaling the ^{1}H hyperfine tensor in Table 2 determined from Q-band ^{1}H ENDOR, and scaling by the proportion of ^{1}H/^{2}H gyromagnetic ratios (γ^1H/γ^2H = 6.514). Simulations also include ^{2}H nuclear quadrupole parameters e^2qQ/h = 0.15; η = 0. Acquisition parameters: temperature = 12 K; microwave frequency = 34.086 GHz; MW pulse length (π/2, π) = 12 ns, 24 ns; τ = 120 ns, t$_1$ = t$_2$ = 100 ns; Δt$_1$ = Δt$_2$ = 12 ns; shot repetition time (srt) = 1.5 ms).

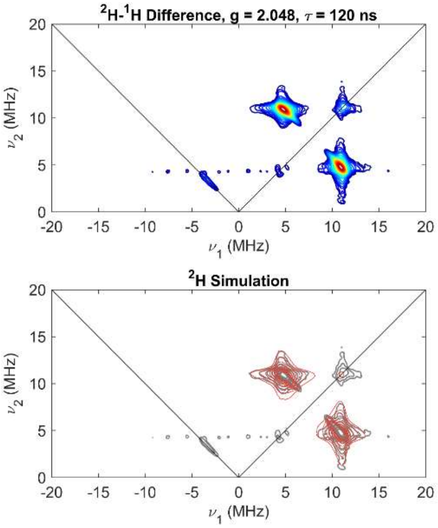

Figure 7. (top panel) Q-band ^{2}H-^{1}H difference HYSCORE spectrum of [(P$_6$ArC)Fe$_2$D][BAr^F$_{24}$] acquired at 1189 mT (g = 2.048). (bottom) Monochromatic representation of the HYSCORE data (grey) with ^{2}H simulations overlaid (red). Simulation parameters were derived by scaling the ^{1}H hyperfine tensor in Table 2 determined from Q-band ^{1}H ENDOR, and scaling by the proportion of ^{1}H/^{2}H gyromagnetic ratios (γ^1H/γ^2H = 6.514). Simulations also include ^{2}H nuclear quadrupole parameters e^2qQ/h = 0.15; η = 0. Acquisition parameters:

temperature = 12 K; microwave frequency = 34.086 GHz; MW pulse length ($\pi/2$, π) = 12 ns, 24 ns; τ = 120 ns, $t_1 = t_2$ = 100 ns; $\Delta t_1 = \Delta t_2$ = 12 ns; shot repetition time (srt) = 1.5 ms).

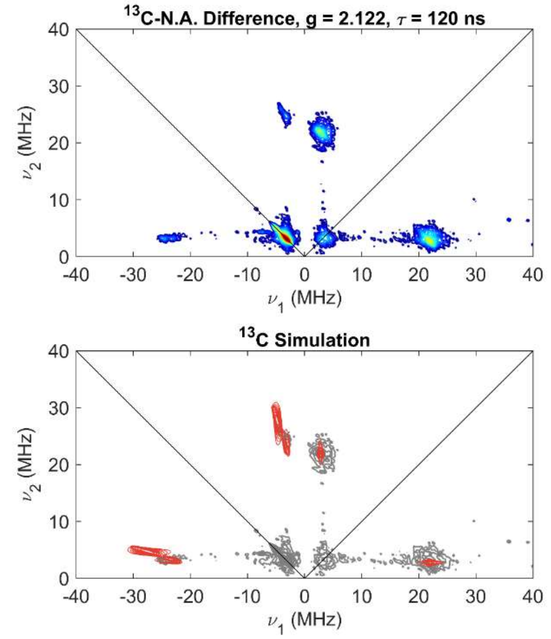

Figure 8. (top panel) Q-band ^{13}C-natural abundance difference HYSCORE spectrum of [(P$_6$Ar^{13}C)Fe$_2$H][BAr$^F{}_{24}$] acquired at 1148 mT (g = 2.122). (bottom) Monochromatic representation of the HYSCORE data (grey) with ^{13}C simulations overlaid (red) using parameters in Table 2. Acquisition parameters: temperature = 12 K; microwave frequency = 34.086 GHz; MW pulse length ($\pi/2$, π) = 12 ns, 24 ns; τ = 120 ns, $t_1 = t_2$ = 100 ns; $\Delta t_1 = \Delta t_2$ = 12 ns; shot repetition time (srt) = 1.5 ms).

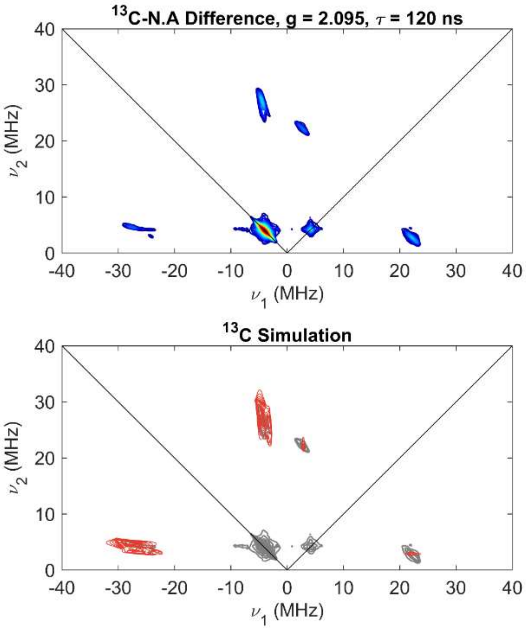

Figure 9. (top panel) Q-band ^{13}C-natural abundance difference HYSCORE spectrum of $[(P_6Ar^{13}C)Fe_2H][BAr^F{}_{24}]$ acquired at 1162.5 mT (g = 2.095). (bottom) Monochromatic representation of the HYSCORE data (grey) with ^{13}C simulations overlaid (red) using parameters in Table 2. Acquisition parameters: temperature = 12 K; microwave frequency = 34.086 GHz; MW pulse length (π/2, π) = 12 ns, 24 ns; τ = 120 ns, $t_1 = t_2$ = 100 ns; $\Delta t_1 = \Delta t_2$ = 12 ns; shot repetition time (srt) = 1.5 ms).

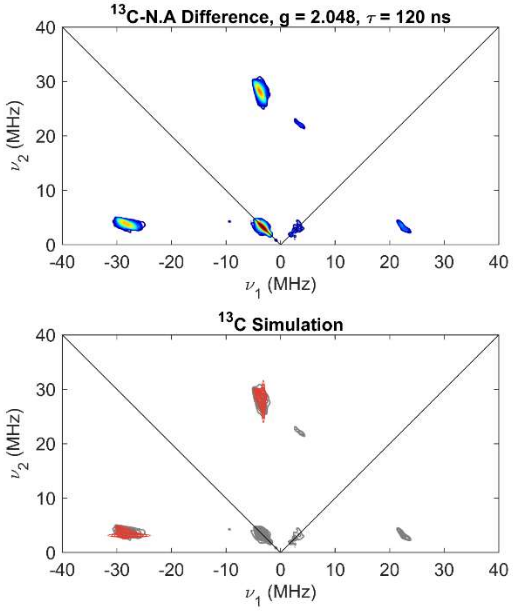

Figure 10. (top panel) Q-band ^{13}C-natural abundance difference HYSCORE spectrum of $[(P_6Ar^{13}C)Fe_2H][BAr^F{}_{24}]$ acquired at 1189 mT (g = 2.048). (bottom) Monochromatic representation of the HYSCORE data (grey) with ^{13}C simulations overlaid (red) using parameters in Table 2. Acquisition parameters:

temperature = 12 K; microwave frequency = 34.086 GHz; MW pulse length (π/2, π) = 12 ns, 24 ns; τ = 120 ns, $t_1 = t_2 = 100$ ns; $\Delta t_1 = \Delta t_2 = 12$ ns; shot repetition time (srt) = 1.5 ms).

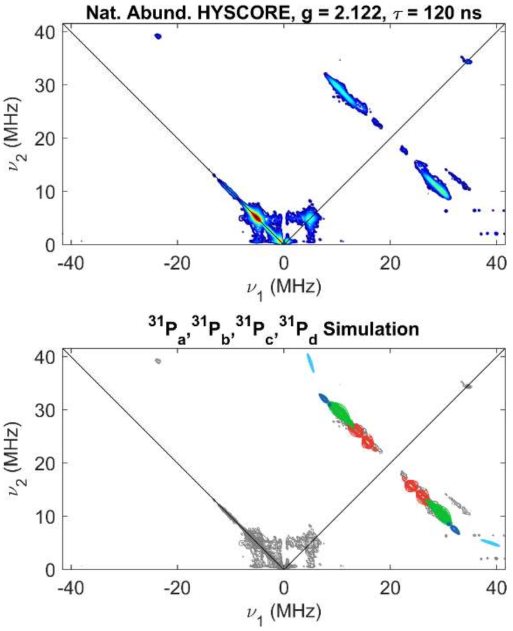

Figure 11. (top panel) Q-band HYSCORE spectrum of natural abundance $[(P_6Ar^{13}C)Fe_2H][BAr^F{}_{24}]$ acquired at 1148 mT (g = 2.122). (bottom) Monochromatic representation of the HYSCORE data (grey) with ^{31}P simulations overlaid (P_a = red, P_b = green, P_c = blue, P_d = cyan) using parameters in Table 2. Acquisition parameters: temperature = 12 K; microwave frequency = 34.086 GHz; MW pulse length (π/2, π) = 12 ns, 24 ns; τ = 120 ns, $t_1 = t_2 = 100$ ns; $\Delta t_1 = \Delta t_2 = 12$ ns; shot repetition time (srt) = 1.5 ms).

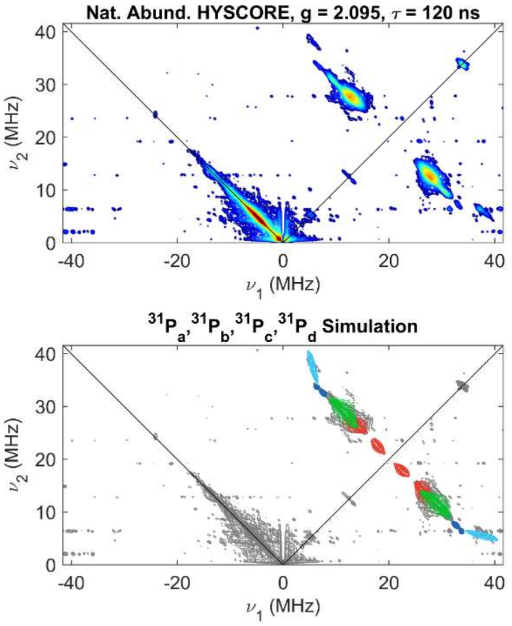

Figure 12. (top panel) Q-band HYSCORE spectrum of natural abundance [(P$_6$Ar^{13}C)Fe$_2$H][BAr$^F{}_{24}$] acquired at 1162.5 mT (g = 2.095). (bottom) Monochromatic representation of the HYSCORE data (grey) with ^{31}P simulations overlaid (P$_a$ = red, P$_b$ = green, P$_c$ = blue, P$_d$ = cyan) using parameters in Table 2. Acquisition parameters: temperature = 12 K; microwave frequency = 34.086 GHz; MW pulse length (π/2, π) = 12 ns, 24 ns; τ = 120 ns, t$_1$ = t$_2$ = 100 ns; Δt$_1$ = Δt$_2$ = 12 ns; shot repetition time (srt) = 1.5 ms).

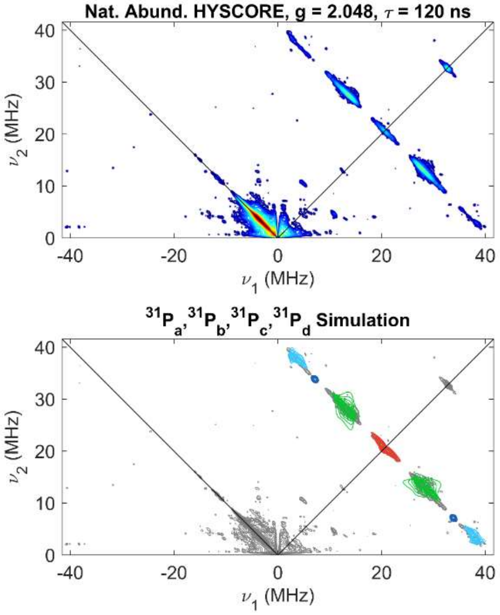

Figure 13. (top panel) Q-band HYSCORE spectrum of natural abundance [(P$_6$Ar^{13}C)Fe$_2$H][BAr$^F{}_{24}$] acquired at 1189 mT (g = 2.048). (bottom) Monochromatic representation of the HYSCORE data (grey) with ^{31}P simulations overlaid (P$_a$ = red, P$_b$ = green, P$_c$ = blue, P$_d$ = cyan) using parameters in Table 2. Acquisition parameters: temperature = 12 K; microwave frequency = 34.086 GHz; MW pulse length (π/2, π) = 12 ns, 24 ns; τ = 120 ns, t$_1$ = t$_2$ = 100 ns; Δt$_1$ = Δt$_2$ = 12 ns; shot repetition time (srt) = 1.5 ms).

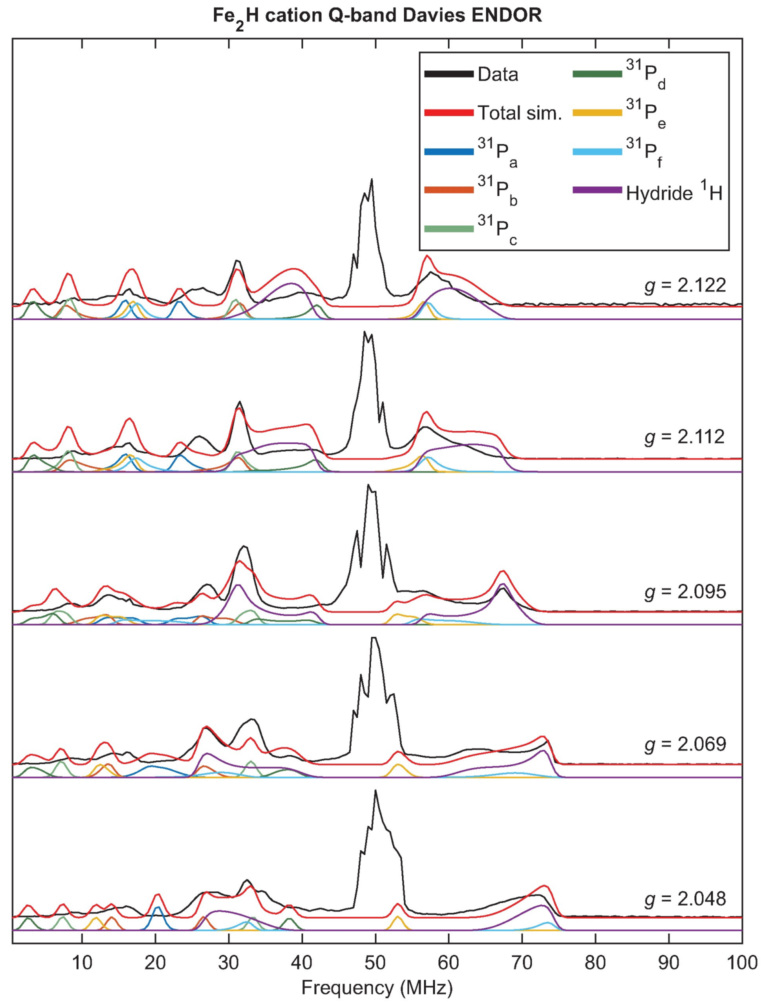

Figure 14. Field-dependent Q-band Davies ENDOR spectra of $[(P_6ArC)Fe_2H][BAr^F{}_{24}]$ (black) with simulations using parameters in Table 2. Acquisition parameters: temperature = 10 K; MW frequency = 34.086 GHz; MW pulse length ($\pi/2$, π) = 40 ns, 80 ns; τ = 200 ns; RF pulse length = 15 μs; T_{RF} = 2 μs; shot repetition time = 6 ms.

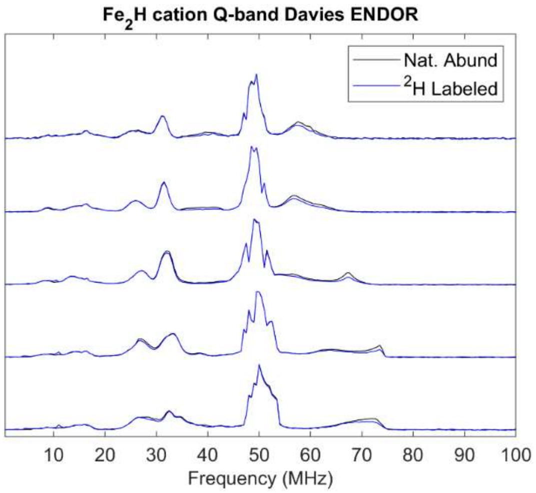

Figure 15. Comparison of the ENDOR spectra of $[(P_6ArC)Fe_2H][BAr^F_{24}]$ and $[(P_6ArC)Fe_2D][BAr^F_{24}]$. Acquisition parameters: temperature = 10 K; MW frequency = 34.086 GHz; MW pulse length ($\pi/2$, π) = 40 ns, 80 ns; τ = 200 ns; RF pulse length = 15 μs; T_{RF} = 2 μs; shot repetition time = 6 ms.

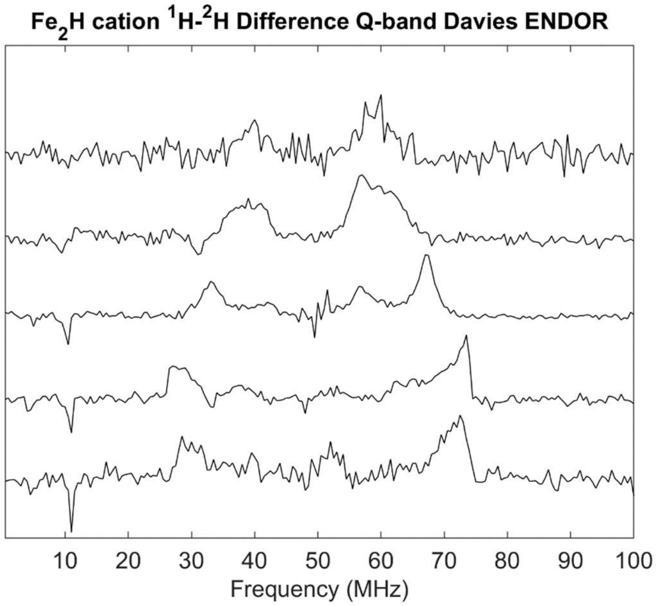

Figure 16. Difference ENDOR spectra of $[(P_6ArC)Fe_2H][BAr^F_{24}]$ and $[(P_6ArC)Fe_2D][BAr^F_{24}]$ showing the signals arising from the μ-deutride. Acquisition parameters: temperature = 10 K; MW frequency = 34.086 GHz; MW pulse length ($\pi/2$, π) = 40 ns, 80 ns; τ = 200 ns; RF pulse length = 15 μs; T_{RF} = 2 μs; shot repetition time = 6 ms.

Analysis of Anisotropic ^{1}*H Hyperfine Tensor for* $[(P_6ArC)Fe_2H][BAr^F_{24}]$. The corresponding values of $T(^1\mathrm{H})$ can be calculated from the following equations:

$$T_a = -\frac{1}{2}(t_1 + t_2) \quad \text{(E1)}$$

$$T_b = \frac{1}{2}\left[\frac{t_1+t_2}{2} + \frac{3}{2}\left(\frac{1}{cos2\gamma}\right)(t_1cos2\beta_1 + t_2cos2\beta_2)\right] \quad \text{(E2)}$$

$$T_c = -(T_1 + T_2) \quad \text{(E3)}$$

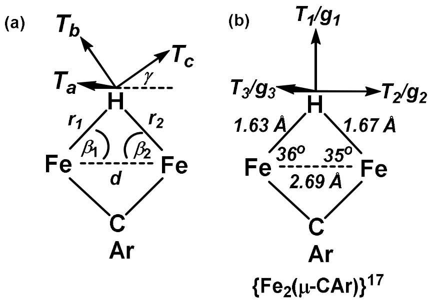

Figure 17. (a) Schematic representation of the metric parameters used to calculate the proton dipolar tensor within the defined molecular frame and definition of the principal components of $T(^1H)$ in that frame. (b) Values of the metric parameters which reproduce the experimental $T(^1H)$. Not shown: $d = 2.69$ Å (fixed from XRD), $\beta_1 = 35.9°$ and $\beta_2 = 34.9°$.

Where β_1 and β_2 define the angle between r_1 and r_2, respectively, and the *Fe1-Fe2* vector *d*. The angle γ describes the orientation of the coordinate axes T_b and T_c with respect to the *Fe1-Fe2* vector *d*. The distance dependence of the magnetic dipole interaction of the μ-hydride with Fe1 and Fe2, respectively, is defined by the elements t_1 and t_2 which take the classical form:

$$t_i = K_i d_i\left(\frac{2g_e\beta_e g_N\beta_N}{r_i^3}\right) \quad \text{(E4)}$$

Where r_i represents the distance of the μ-hydride from Fe_i (i = 1,2), K_i is the spin projection coefficient for Fe_i (i = 1,2), and d_i parameterizes the effect of covalent delocalization of spin density way from Fe_i (i = 1,2), adopting a value between 0 and 1. The spin projection factors for a two metal system are uniquely defined by standard vector coupling methods, yielding $K_1 = 4/3$ for the $S = 1$ center Fe_1 and $K_2 = -1/3$ for the $S = ½$ center Fe_2. In the analysis that follows, it is assumed that $d_1 = d_2 \sim 1$, which is reasonable given the relatively small amount of ligand-based spin density indicated by their respective hyperfine couplings.

Analysis of equations E1-E3 reveals that only T_a, which is normal to the Fe(μ-C)(μ-H)Fe plane, has no direct angular dependence. Thus, it is possible to construct equations that define allowable combinations of r_1 and r_2 which would yield values of T_a corresponding to one (or more) of principal components of the experimental $T(^1H)$ tensor +/-[-18.7, +3.3, +15.3] MHz.

$$\text{If } T_a = +/\text{-}18.7 \text{ MHz then: } \frac{1}{r_2^3} = \pm\frac{112.2}{a} + \frac{4}{r_1^3} \quad \text{(E5)}$$

$$\text{If } T_a = +/\text{-}3.3 \text{ MHz then: } \frac{1}{r_2^3} = \pm\frac{19.8}{a} + \frac{4}{r_1^3} \quad \text{(E6)}$$

$$\text{If } T_a = +/\text{-}15.3 \text{ MHz then: } \frac{1}{r_2^3} = \pm\frac{91.8}{a} + \frac{4}{r_1^3} \quad \text{(E7)}$$

$$\text{Where } a = 2g_e\beta_e g_N\beta_N \quad \text{(E8)}$$

Graphs corresponding to E5-E7 are shown in Figures 18-20 below. From the data it is clear T_a does *not* correspond to the second principal component of $T(^1H)$ (T_2 = +/- 3.3 MHz) – reasonable values of r_2 require unreasonably short r_1 distances. Therefore, g_2 lies in the Fe(μ-C)(μ-H)Fe plane, not perpendicular to it. On the other hand, T_a could correspond to either the first or third principal components of $T(^1H)$ so long as that tensor value is negative. This constraint can be illustrated by examination of Figure 18, which shows that assuming T_a = -18.7 MHz (left graph) yields reasonable values for both r_1 and r_2. The same is true for T_a = -15.3 MHz (Figure 20, right graph).

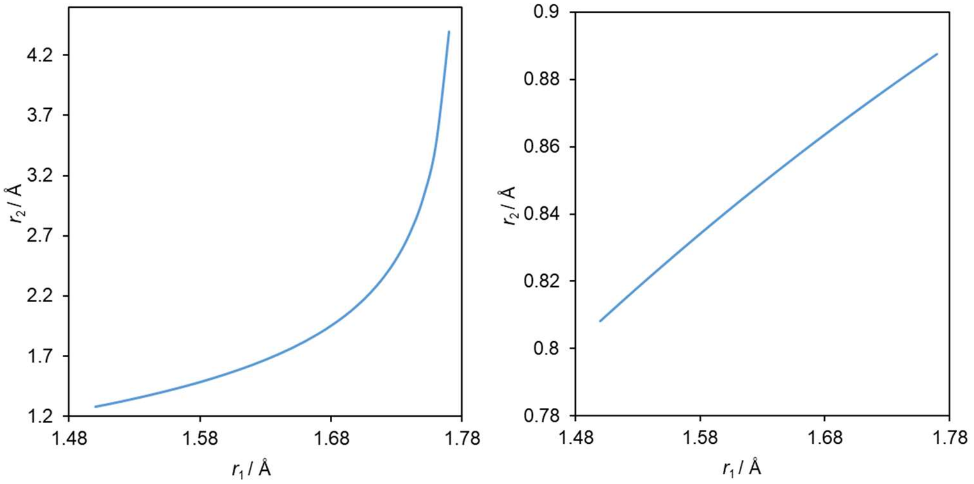

Figure 18. Plots of E6 assuming T_a = -18.7 MHz (left) and T_a = +18.7 MHz (right).

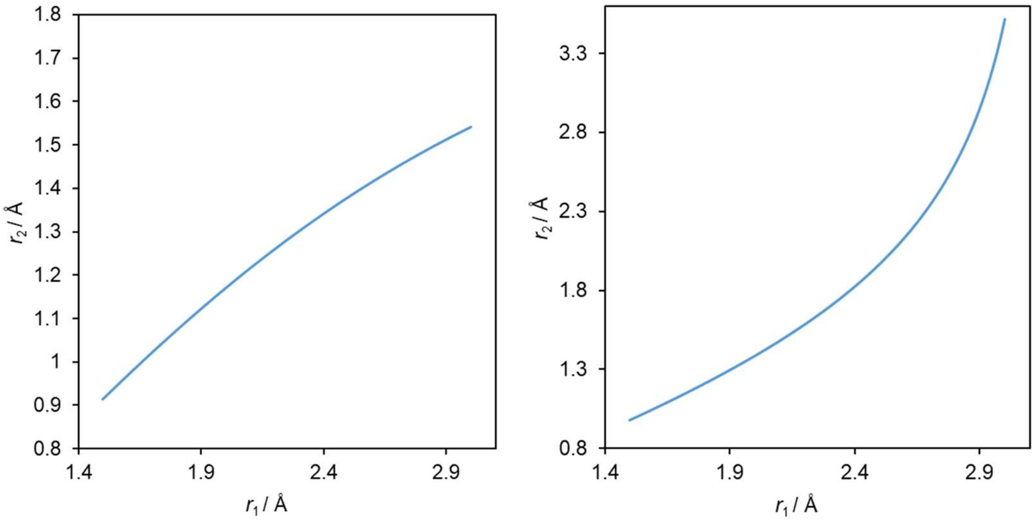

Figure 19. Plots of E5 assuming T_a = +3.3 MHz (left) and T_a = -3.3 MHz (right).

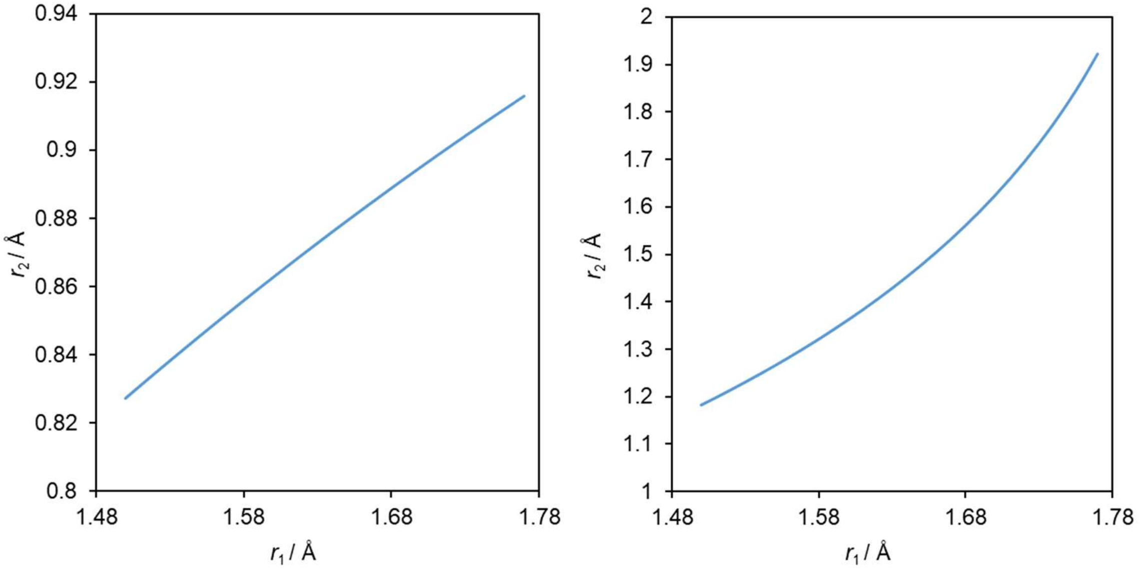

Figure 20. Plots of E7 assuming T_a = +15.3 MHz (left) and T_a = -15.3 MHz (right).

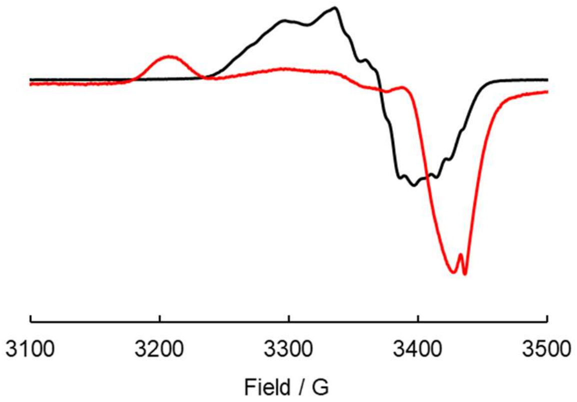

Figure 21. Decomposition of [K(THF)$_n$][(P$_6$ArC)Fe$_2$H]. X-band CW EPR Spectrum of [K(THF)$_n$][(P$_6$ArC)Fe$_2$H] generated by reduction of (P$_6$ArC)Fe$_2$H with potassium napthalenide (KNp, black). After thawing sample to room temperature (red).

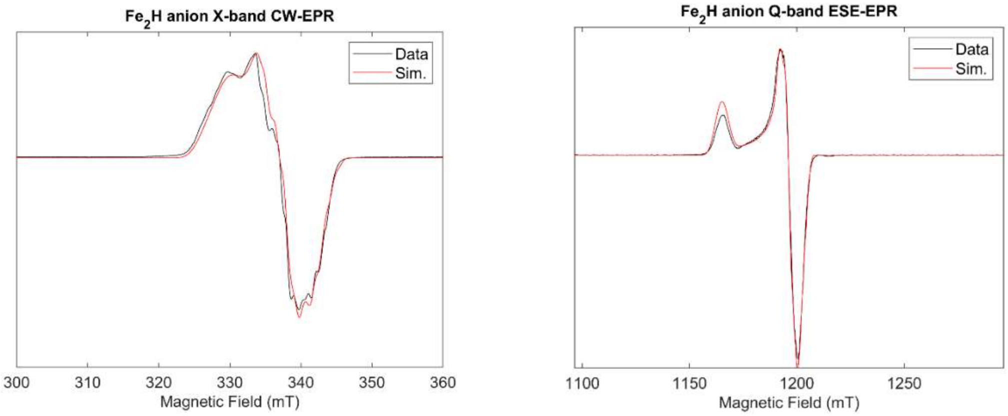

Figure 22. X-band CW EPR (left panel) and pseudomodulated[8] Q-band ESE-EPR (right panel) spectra of $[K(THF)_n][(P_6ArC)Fe_2H]$ in 2-MeTHF (2 mM). Experimental data shown in black and simulations are shown in red. Simulation parameters: S = ½, g = [2.089, 2.036, 2.026], Sys.lw = 1, ^{31}P and ^{1}H hyperfine parameters detailed in Table 3 of main text, with broadening parameters: HStrain = [20 10 10], gStrain = [0.012, 0.0015, 0.001].
X-band CW-EPR acquisition parameters: temperature = 10 K; MW frequency = 9.639 GHz; MW power = 2 mW; modulation frequency = 100 kHz; modulation amplitude = 0.4 mT; conversion time = 82 ms.
Q-band ESE-EPR acquisition parameters: temperature = 10 K; MW frequency = 34.086 GHz; MW pulse length ($\pi/2$, π) = 40 ns, 80 ns; τ = 200 ns; shot repetition time = 6 ms.

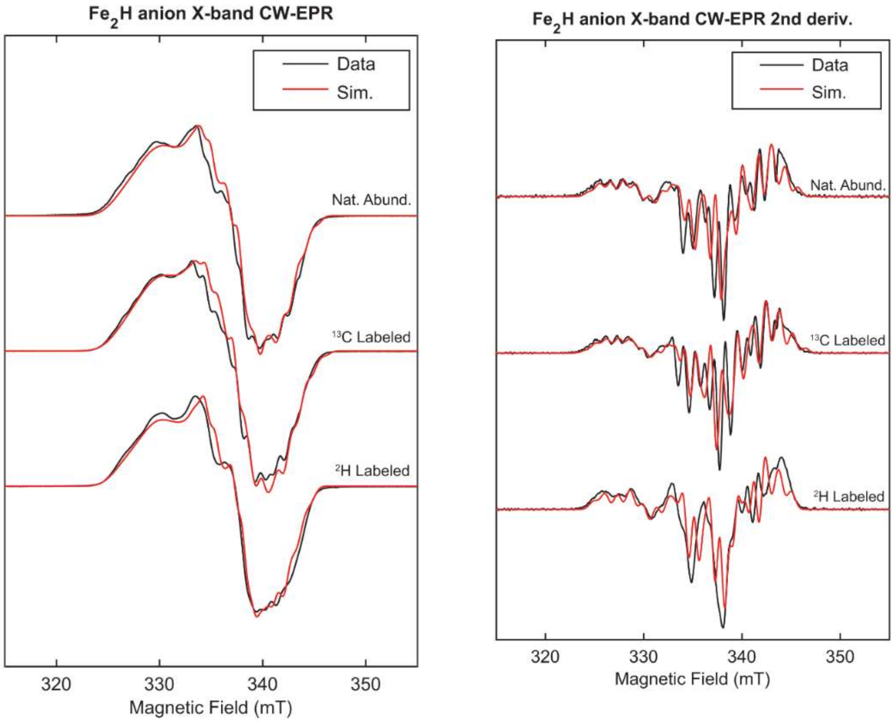

Figure 23. X-band CW EPR Spectra of $[K(THF)_n][(P_6ArC)Fe_2H]$, $[K(THF)_n][(P_6ArC)Fe_2D]$, and $[K(THF)_n][(P_6Ar^{13}C)Fe_2H]$ (left panel, in black), all 2 mM, 2-MeTHF. Simulations are shown in red with parameters: S = ½, g = [2.089, 2.036, 2.026], Sys.lw = 1, ^{31}P, ^{1}H and ^{13}C hyperfine parameters detailed in Table 3 of main text, with broadening parameters: HStrain = [20 10 10], gStrain = [0.012, 0.0015, 0.001]. Derivative spectra of X-band CW-EPR for each isotopologue with simulations overlaid in red (right panel). X-band CW-

EPR acquisition parameters: temperature = 10 K; MW frequency = 9.639 GHz; MW power = 2 mW; modulation frequency = 100 kHz; modulation amplitude = 0.4 mT; conversion time = 82 ms.

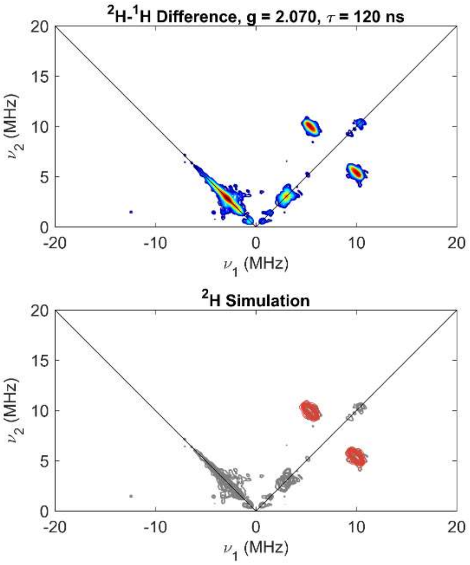

Figure 24. (top panel) Q-band ^{2}H-^{1}H difference HYSCORE spectrum of [K(THF)$_n$][(P$_6$ArC)Fe$_2$D] acquired at 1175.5 mT (g = 2.070). (bottom) Monochromatic representation of the HYSCORE data (grey) with ^{2}H simulations overlaid (red). Simulation parameters were derived by scaling the ^{1}H hyperfine tensor in Table 3 of main text determined from Q-band ^{1}H ENDOR, and scaling by the proportion of ^{1}H/^{2}H gyromagnetic ratios (γ^1H/γ^2H = 6.514). Simulations also include ^{2}H nuclear quadrupole parameters e^2qQ/h = 0.15; η = 0. Acquisition parameters: temperature = 20 K; microwave frequency = 34.086 GHz; MW pulse length (π/2, π) = 12 ns, 24 ns; τ = 120 ns, t_1 = t_2 = 100 ns; Δt_1 = Δt_2 = 12 ns; shot repetition time (srt) = 1 ms).

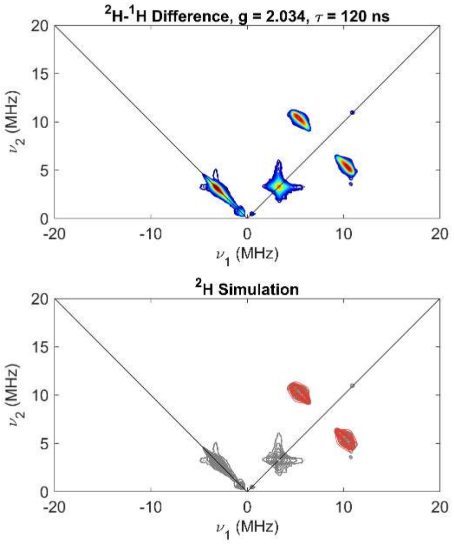

Figure 25. (top panel) Q-band ^{2}H-^{1}H difference HYSCORE spectrum of [K(THF)$_n$][(P$_6$ArC)Fe$_2$D] acquired at 1196.5 mT (g = 2.034). (bottom) Monochromatic representation of the HYSCORE data (grey) with ^{2}H simulations overlaid (red). Simulation parameters were derived by scaling the ^{1}H hyperfine tensor in Table 3 of main text determined from Q-band ^{1}H ENDOR, and scaling by the proportion of ^{1}H/^{2}H gyromagnetic ratios

(γ^1H/γ^2H = 6.514). Simulations also include ^{2}H nuclear quadrupole parameters e^2qQ/h = 0.15; η = 0. Acquisition parameters: temperature = 20 K; microwave frequency = 34.086 GHz; MW pulse length (π/2, π) = 12 ns, 24 ns; τ = 120 ns, t_1 = t_2 = 100 ns; Δt_1 = Δt_2 = 12 ns; shot repetition time (srt) = 1 ms).

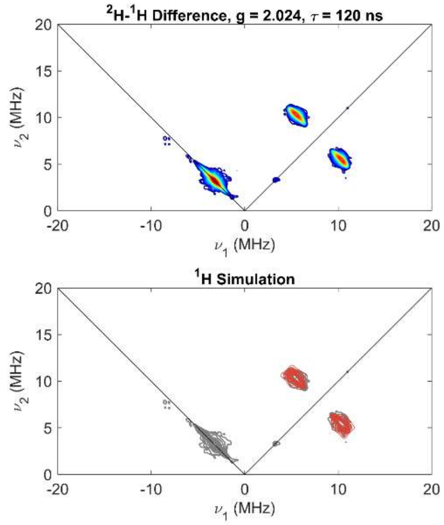

Figure 26. (top panel) Q-band ^{2}H-^{1}H difference HYSCORE spectrum of [K(THF)$_n$][(P$_6$ArC)Fe$_2$D] acquired at 1202.5 mT (g = 2.024). (bottom) Monochromatic representation of the HYSCORE data (grey) with ^{2}H simulations overlaid (red). Simulation parameters were derived by scaling the ^{1}H hyperfine tensor in Table 3 of main text determined from Q-band ^{1}H ENDOR, and scaling by the proportion of ^{1}H/^{2}H gyromagnetic ratios (γ^1H/γ^2H = 6.514). Simulations also include ^{2}H nuclear quadrupole parameters e^2qQ/h = 0.15; η = 0. Acquisition parameters: temperature = 20 K; microwave frequency = 34.086 GHz; MW pulse length (π/2, π) = 12 ns, 24 ns; τ = 120 ns, t_1 = t_2 = 100 ns; Δt_1 = Δt_2 = 12 ns; shot repetition time (srt) = 1 ms).

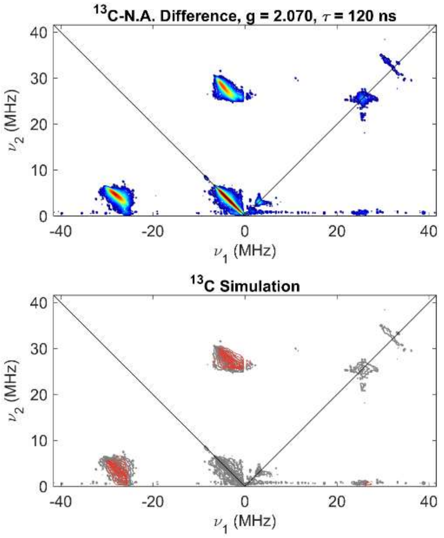

Figure 27. (top panel) Q-band ^{13}C-natural abundance difference HYSCORE spectrum of [K(THF)$_n$][(P$_6$Ar^{13}C)Fe$_2$H] acquired at 1175.5 mT (g = 2.070). (bottom) Monochromatic representation of the

HYSCORE data (grey) with ^{13}C simulations overlaid (red) using parameters in Table 3 of main text. Acquisition parameters: temperature = 20 K; microwave frequency = 34.058 GHz; MW pulse length (π/2, π) = 12 ns, 24 ns; τ = 120 ns, $t_1 = t_2 = 100$ ns; $\Delta t_1 = \Delta t_2 = 12$ ns; shot repetition time (srt) = 1ms).

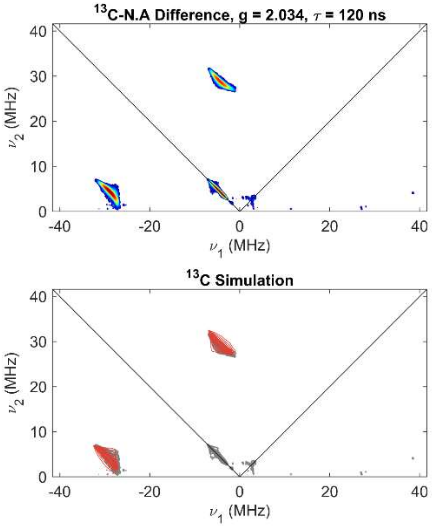

Figure 28. (top panel) Q-band ^{13}C-natural abundance difference HYSCORE spectrum of $[K(THF)_n][(P_6Ar^{13}C)Fe_2H]$ acquired at 1196.5 mT (g = 2.034). (bottom) Monochromatic representation of the HYSCORE data (grey) with ^{13}C simulations overlaid (red) using parameters in Table 3 of main text. Acquisition parameters: temperature = 20 K; microwave frequency = 34.058 GHz; MW pulse length (π/2, π) = 12 ns, 24 ns; τ = 120 ns, $t_1 = t_2 = 100$ ns; $\Delta t_1 = \Delta t_2 = 12$ ns; shot repetition time (srt) = 1ms).

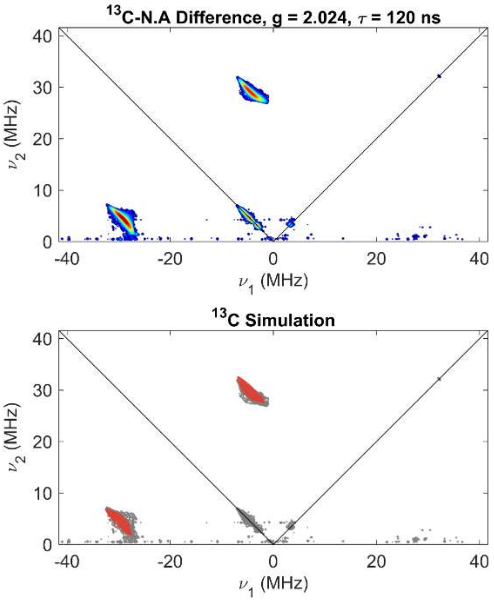

Figure 29. (top panel) Q-band ^{13}C-natural abundance difference HYSCORE spectrum of $[K(THF)_n][(P_6Ar^{13}C)Fe_2H]$ acquired at 1202.5 mT (g = 2.024). (bottom) Monochromatic representation of the HYSCORE data (grey) with ^{13}C simulations overlaid (red) using parameters in Table 3 of main text. Acquisition parameters: temperature = 20 K; microwave frequency = 34.058 GHz; MW pulse length (π/2, π) = 12 ns, 24 ns; τ = 120 ns, $t_1 = t_2$ = 100 ns; $\Delta t_1 = \Delta t_2$ = 12 ns; shot repetition time (srt) = 1ms).

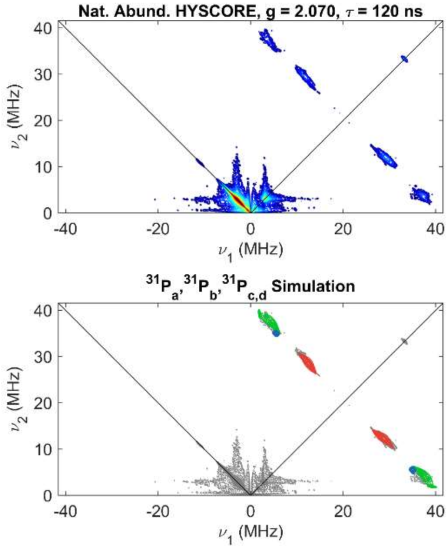

Figure 30. (top panel) Q-band HYSCORE spectrum of natural abundance $[K(THF)_n][(P_6ArC)Fe_2H]$ acquired at 1175.5 mT (g = 2.070). (bottom) Monochromatic representation of the HYSCORE data (grey) with ^{31}P simulations overlaid (P_a = red, P_b = green, $P_{c,d}$ = blue) using parameters in Table 3 of main text. Acquisition parameters: temperature = 20 K; microwave frequency = 34.058 GHz; MW pulse length (π/2, π) = 12 ns, 24 ns; τ = 120 ns, $t_1 = t_2$ = 100 ns; $\Delta t_1 = \Delta t_2$ = 12 ns; shot repetition time (srt) = 1 ms).

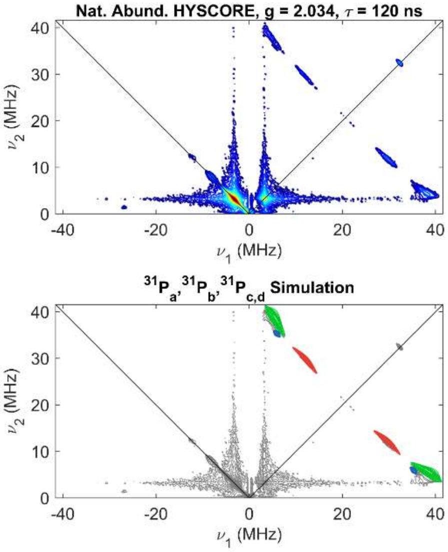

Figure 31. (top panel) Q-band HYSCORE spectrum of natural abundance $[K(THF)_n][(P_6ArC)Fe_2H]$ acquired at 1196.5 mT (g = 2.034). (bottom) Monochromatic representation of the HYSCORE data (grey) with ^{31}P simulations overlaid (P_a = red, P_b = green, $P_{c,d}$ = blue) using parameters in Table 3 of main text. Acquisition parameters: temperature = 20 K; microwave frequency = 34.058 GHz; MW pulse length ($\pi/2$, π) = 12 ns, 24 ns; τ = 120 ns, $t_1 = t_2$ = 100 ns; $\Delta t_1 = \Delta t_2$ = 12 ns; shot repetition time (srt) = 1 ms).

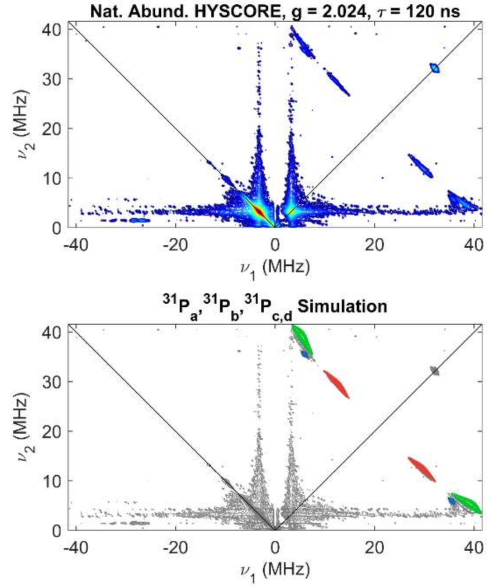

Figure 32. (top panel) Q-band HYSCORE spectrum of natural abundance $[K(THF)_n][(P_6ArC)Fe_2H]$ acquired at 1202.5 mT (g = 2.024). (bottom) Monochromatic representation of the HYSCORE data (grey) with ^{31}P simulations overlaid (P_a = red, P_b = green, $P_{c,d}$ = blue) using parameters in Table 3 of main text. Acquisition parameters: temperature = 20 K; microwave frequency = 34.058 GHz; MW pulse length ($\pi/2$, π) = 12 ns, 24 ns; τ = 120 ns, $t_1 = t_2$ = 100 ns; $\Delta t_1 = \Delta t_2$ = 12 ns; shot repetition time (srt) = 1 ms).

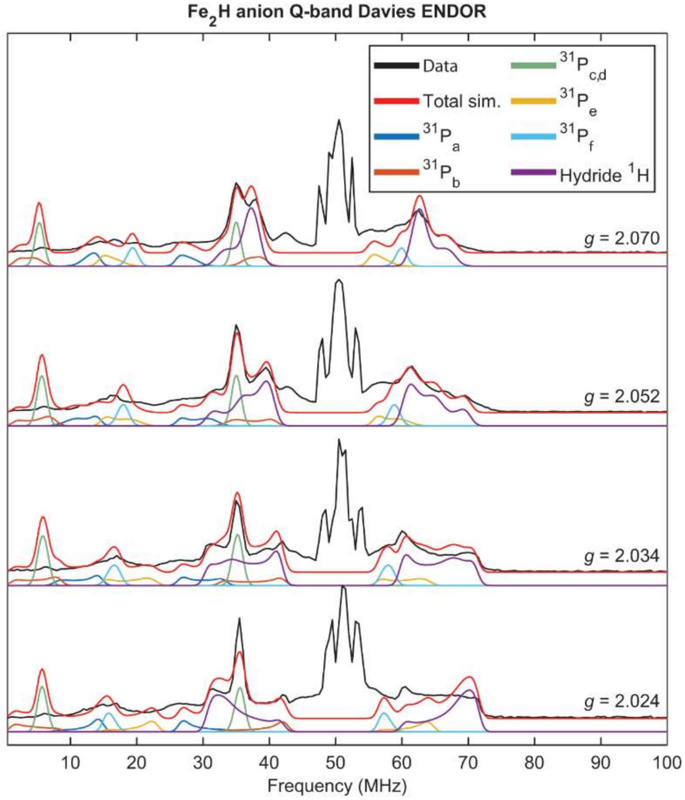

Figure 33. Field-dependent Q-band Davies ENDOR spectra of [K(THF)$_n$][(P$_6$ArC)Fe$_2$H] (black) with simulations using parameters in Table 3 of main text. Acquisition parameters: temperature = 15 K; MW frequency = 34.058 GHz; MW pulse length (π/2, π) = 40 ns, 80 ns; τ = 200 ns; RF pulse length = 15 μs; T$_{RF}$ = 2 μs; shot repetition time = 6 ms.

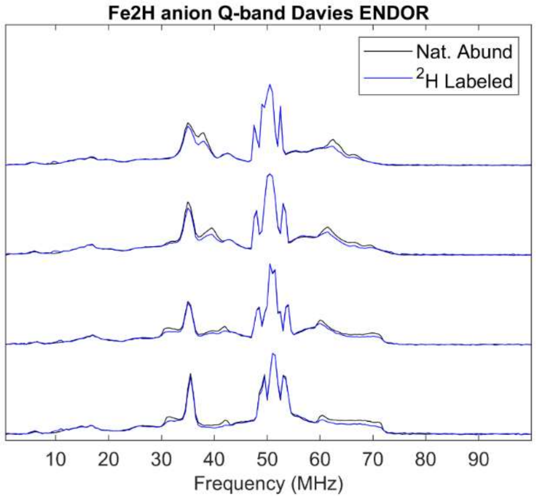

Figure 34. Comparison of the ENDOR spectra of [K(THF)$_n$][(P$_6$ArC)Fe$_2$H] and [K(THF)$_n$][(P$_6$ArC)Fe$_2$D]. Acquisition parameters: temperature = 15 K; MW frequency = 34.058 GHz; MW pulse length (π/2, π) = 40 ns, 80 ns; τ = 200 ns; RF pulse length = 15 μs; T_{RF} = 2 μs; shot repetition time = 6 ms.

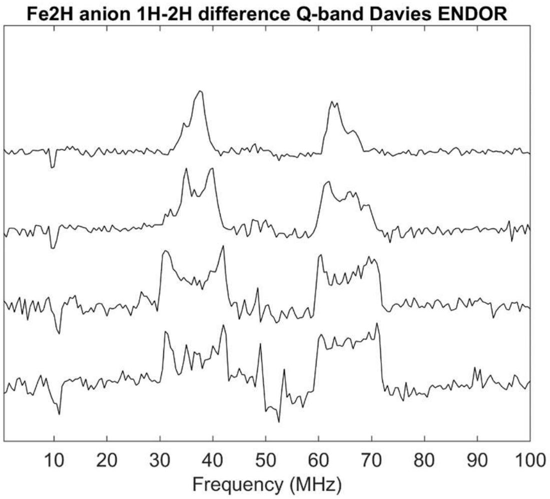

Figure 35. Difference ENDOR spectra of [K(THF)$_n$][(P$_6$ArC)Fe$_2$H] and [K(THF)$_n$][(P$_6$ArC)Fe$_2$D] showing the signals arising from the μ-deutride. Acquisition parameters: temperature = 15 K; MW frequency = 34.058 GHz; MW pulse length (π/2, π) = 40 ns, 80 ns; τ = 200 ns; RF pulse length = 15 μs; T_{RF} = 2 μs; shot repetition time = 6 ms.

Chapter 6

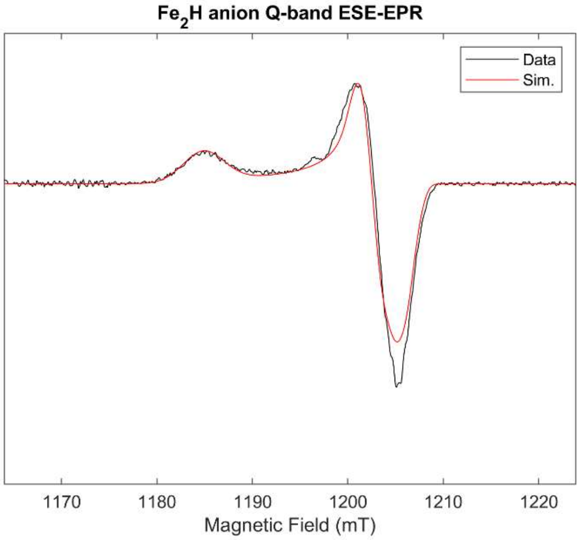

Figure 36. Pseudomodulated[8] Q-band ESE-EPR spectrum of [Na(THF)$_n$][(P$_6$ArCH)Fe$_2$(CO)$_3$] in 2-MeTHF (2 mM). Experimental data shown in black and simulations are shown in red. Simulation parameters: S = ½, g = [2.048, 2.018, 2.0125], ^{1}H hyperfine parameters detailed in the main text.

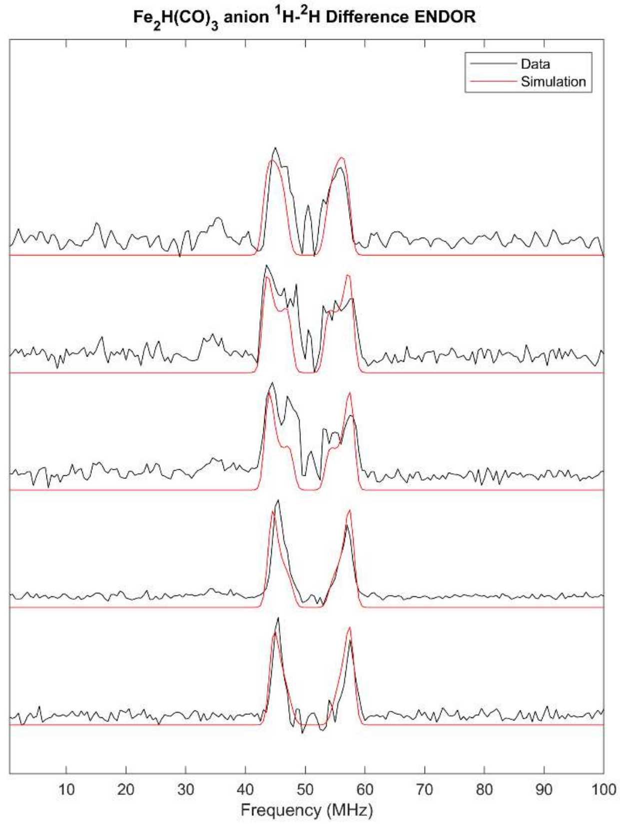

Figure 37. Difference ENDOR spectra of [Na(THF)$_n$][(P$_6$ArCH)Fe$_2$(CO)$_3$] and [Na(THF)$_n$][(P$_6$ArCD) Fe$_2$(CO)$_3$] showing the signals arising from the μ-deutride.

Appendix A

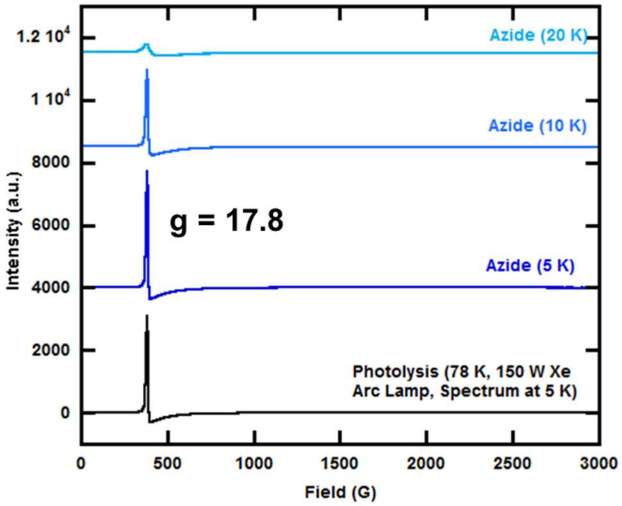

Figure 38. Photolysis of a frozen glass of [LFe$_3$O(PhIm)$_3$Fe(N$_3$)][OTf] at 78 K does not lead to disappearance of its characteristic EPR signal.

References

1. Willems, J.-P.; Lee, H.-I.; Burdi, D.; Doan, P. E.; Stubbe, J.; Hoffman, B. M., Identification of the Protonated Oxygenic Ligands of Ribonucleotide Reductase Intermediate X by Q-Band ^{1,2}H CW and Pulsed ENDOR. *J. Am. Chem. Soc.* **1997,** *119* (41), 9816-9824.
2. DeRose, V. J.; Liu, K. E.; Lippard, S. J.; Hoffman, B. M., Investigation of the Dinuclear Fe Center of Methane Monooxygenase by Advanced Paramagnetic Resonance Techniques: On the Geometry of DMSO Binding. *J. Am. Chem. Soc.* **1996,** *118* (1), 121-134.
3. Hoeke, V.; Tociu, L.; Case, D. A.; Seefeldt, L. C.; Raugei, S.; Hoffman, B. M., High-Resolution ENDOR Spectroscopy Combined with Quantum Chemical Calculations Reveals the Structure of Nitrogenase Janus Intermediate E_4(4H). *J. Am. Chem. Soc.* **2019,** *141* (30), 11984-11996.
4. Yang, H.; Rittle, J.; Marts, A. R.; Peters, J. C.; Hoffman, B. M., ENDOR Characterization of $(N_2)Fe^{II}(\mu\text{-}H)_2Fe^{I}(N_2)^{-}$: A Spectroscopic Model for N_2 Binding by the Di-μ-hydrido Nitrogenase Janus Intermediate. *Inorg. Chem.* **2018,** *57* (19), 12323-12330.
5. Kinney, R. A.; Saouma, C. T.; Peters, J. C.; Hoffman, B. M., Modeling the Signatures of Hydrides in Metalloenzymes: ENDOR Analysis of a Di-iron Fe(μ-NH)(μ-H)Fe Core. *J. Am. Chem. Soc.* **2012,** *134* (30), 12637-12647.
6. Randall, D. W.; Gelasco, A.; Caudle, M. T.; Pecoraro, V. L.; Britt, R. D., ESE-ENDOR and ESEEM Characterization of Water and Methanol Ligation to a Dinuclear Mn(III)Mn(IV) Complex. *J. Am. Chem. Soc.* **1997,** *119* (19), 4481-4491.
7. Wertz, J. E.; Bolton, J. R., *Electron Spin Resonance: Elementary Theory and Practical Applications*. Chapman and Hall: New York, N.Y., 1986.
8. Hyde, J. S.; Pasenkiewicz-Gierula, M.; Jesmanowicz, A.; Antholine, W. E., Pseudo field modulation in EPR spectroscopy. *Appl. Magn. Reson.* **1990,** *1* (3), 483.

Crystal Structures

Chapter 2

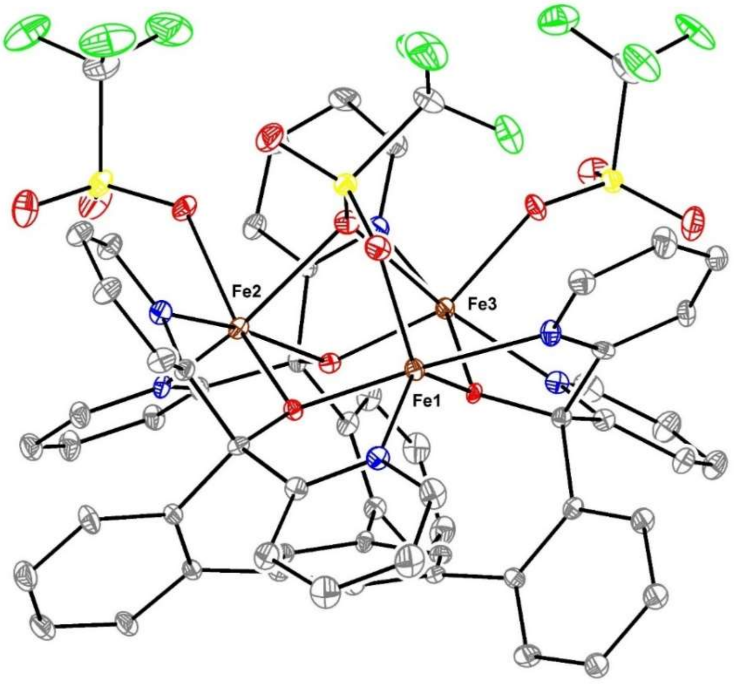

Figure 1. Crystal structure of $LFe_3(OTf)_3$ (**1**). Ellipsoids are shown at the 50% probability level. Hydrogen atoms and co-crystallized solvent molecules are not shown for clarity.

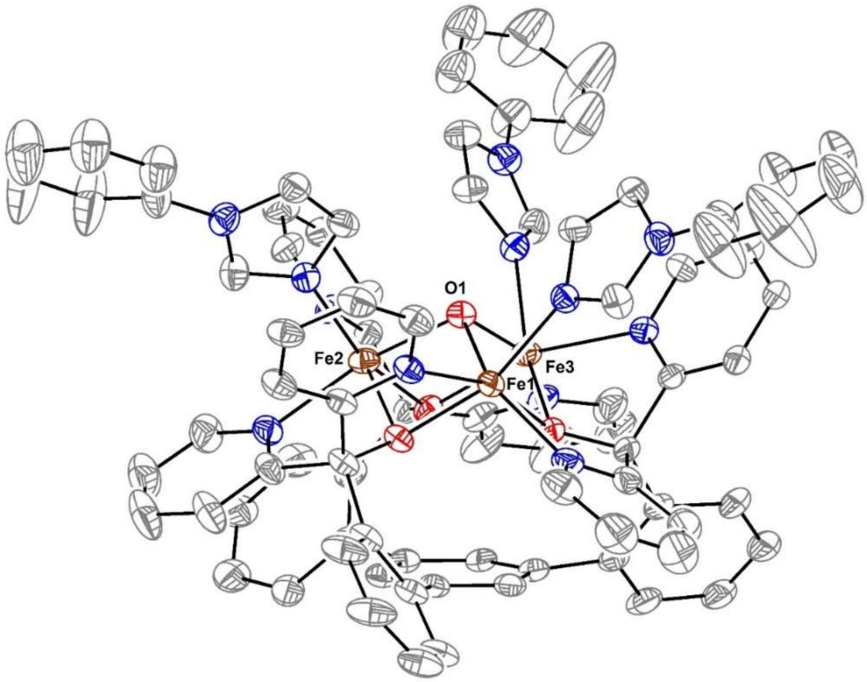

Figure 2. Crystal structure of [$LFe_3O(PhIm\text{-}H)_3$][OTf]$_3$ (**2**). Ellipsoids are shown at the 50% probability level. Hydrogen atoms, co-crystallized solvent molecules, and outer sphere counter ions are not shown for clarity.

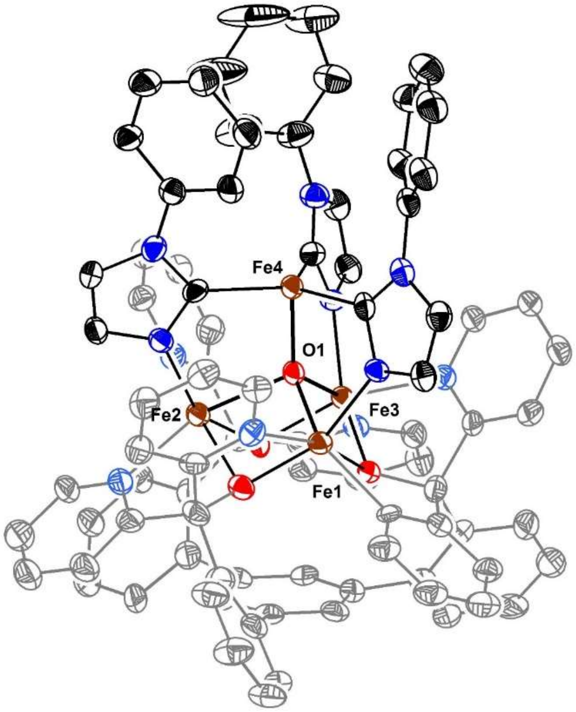

Figure 3. Crystal structure of [$LFe_3O(PhIm)_3Fe$][OTf]$_3$ (**4**). Ellipsoids are shown at the 50% probability level. Hydrogen atoms, co-crystallized solvent molecules, and outer sphere counter ions are not shown for clarity.

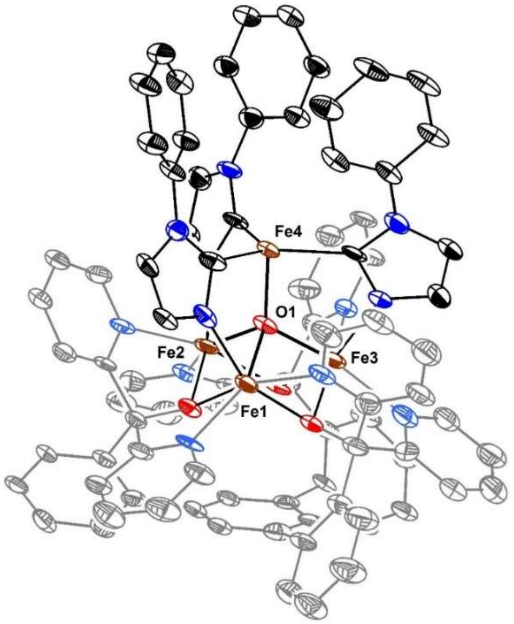

Figure 4. Crystal structure of [$LFe_3O(PhIm)_3Fe$][OTf] (**5**). Ellipsoids are shown at the 50% probability level. Hydrogen atoms, co-crystallized solvent molecules, and outer sphere counter ions are not shown for clarity.

Chapter 3

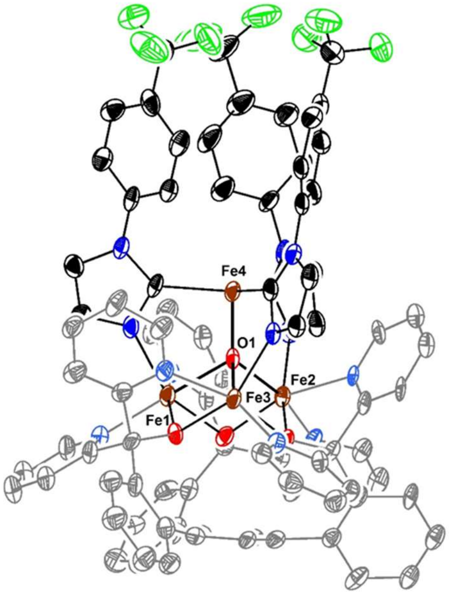

Figure 5. Crystal structure of $[LFe_3O(^{pCF3}ArIm)_3Fe][OTf]_2$ (**1^{CF3}**). Ellipsoids are shown at the 50% probability level. Hydrogen atoms and co-crystallized solvent molecules are not shown for clarity.

Chapter 4

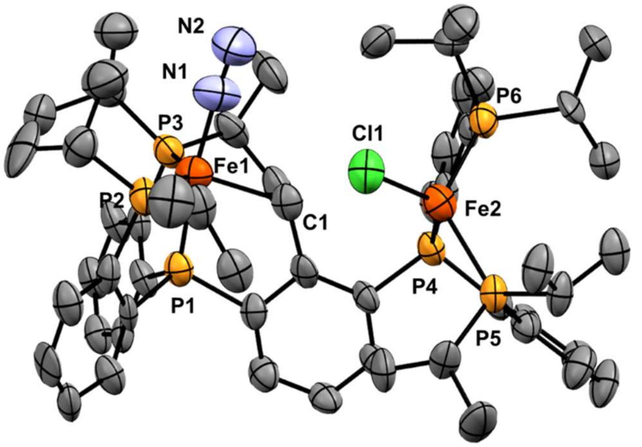

Figure 6. Crystal structure obtained from the reaction of $(P_6ArC)Fe_2H$ (**5**) with HCl. Data quality is only sufficient to identify the species as $(P_6ArCH_2)Fe(N_2)FeCl$.

Misc. Structures

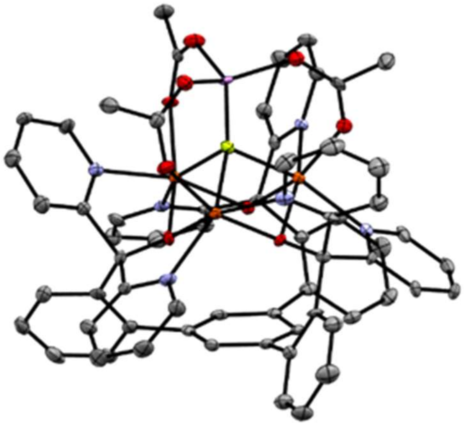

Figure 7. Crystal structure obtained from the reaction of [LFe$_3$F(OAc)$_3$Li].

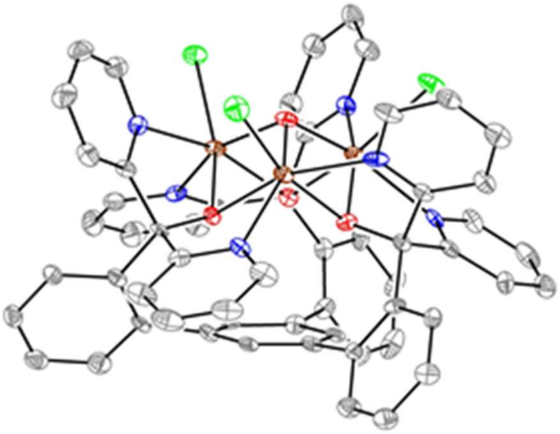

Figure 8. Crystal structure obtained from the reaction of [LFe$_3$Cl$_3$(μ_3-O)].

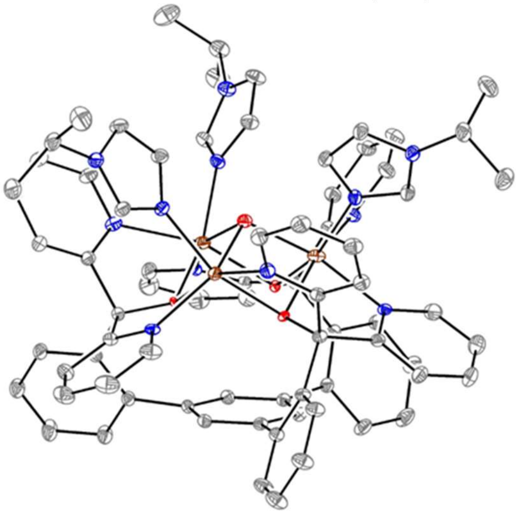

-

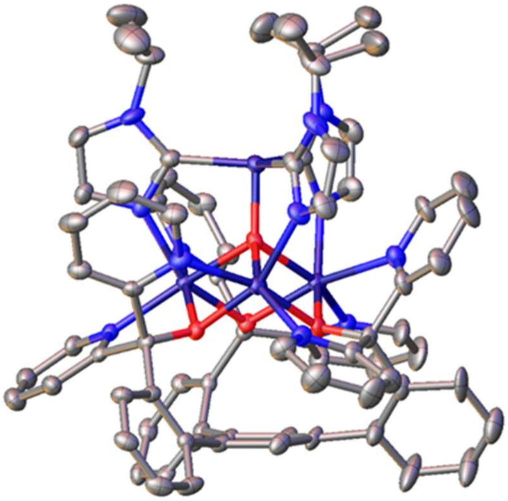

Figure 10. Crystal structure obtained from the reaction of [$LFe_3O(iPrIm)_3Fe$]($OTf)_2$.

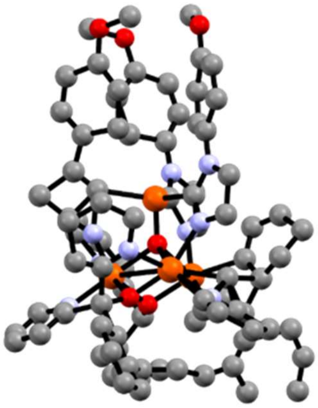

Figure 11. Crystal structure obtained from the reaction of [$LFe_3O(pOMeArIm)_3Fe$]($OTf)_2$.

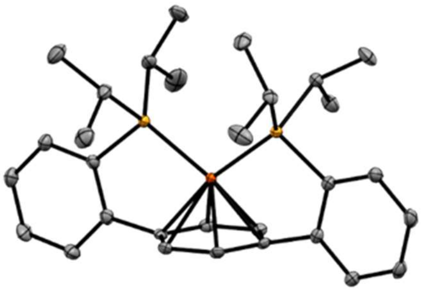

Figure 12. Crystal structure obtained from the reaction of P_2Fe.

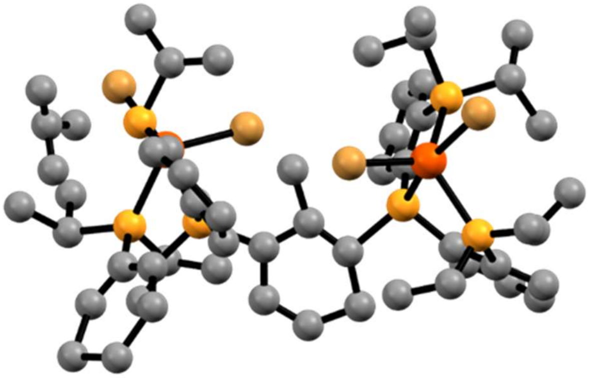

Figure 13. Crystal structure obtained from the reaction of $(P_6ArCH_3)Fe_2Br_4$.

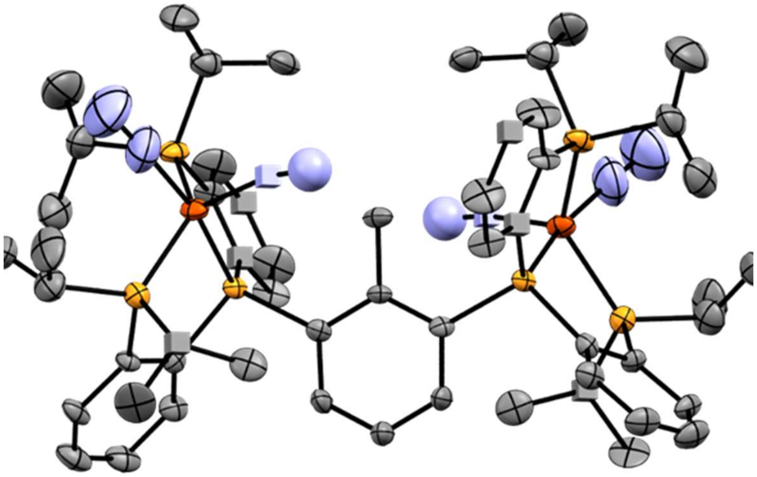

Figure 14. Crystal structure obtained from the reaction of $(P_6ArCH_3)Fe_2(N_2)_4$.

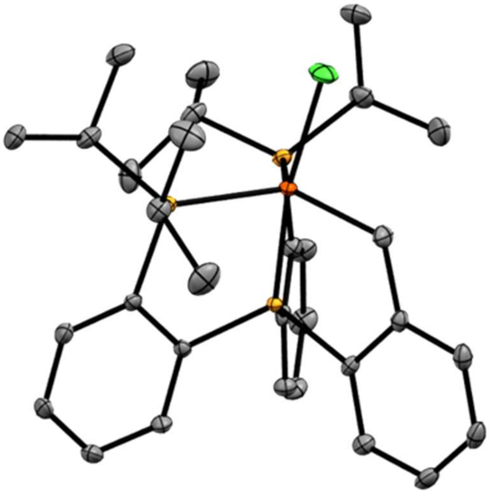

Figure 15. Crystal structure obtained from the reaction of $(P_3ArCH_2)FeCl$.

ABOUT THE AUTHOR

Charles “Charlie” H. Arnett is a native of Rockville, MD, a suburb of the nation’s capital, and he lived there for almost 23 years. He completed his undergraduate studies at Georgetown University, which overlooks the majestic Potomac River on the outskirts of Washington, D.C. He developed a passion for synthetic chemistry while working in the laboratory of Prof. Timothy H. Warren where he studied copper(II)-phenolate intermediates in the etherification of hydrocarbon substrates with acyl-protected phenols. His undergraduate research was supported by an ARCS fellowship and an ACS scholarship. The summer prior to his senior year at Georgetown, Charlie flew across the country for the first time and spent three months as a research fellow in the laboratory of Prof. Jonas C. Peters at Caltech studying heterobimetallic models of *carbon monoxide dehydrogenase*. In 2015, Charlie graduated from Georgetown with a B.S. in Chemistry, *summa cum laude*, and was recognized with the Milijevic Award for highest academic standing in his field. That same year, he joined the laboratory of Prof. Theodor Agapie at Caltech studying multimetallic models of the *nitrogenase* active site. In 2016, Charlie received a Graduate Research Fellowship from the National Science Foundation to support his ongoing endeavors in the Agapie lab. He completed his Ph.D. studies at Caltech in 2020. He plans to pursue a career in patent law and has accepted a position with the law firm Jones Day in Washington, D.C., where he will work as an intellectual property specialist while attending law school.

RESUME

EDUCATION

California Institute of Technology Pasadena, CA
Ph.D., Chemistry, GPA: 4.20 2020
National Science Foundation Graduate Research Fellow
Dissertation: Multimetallic Model Complexes of the *Nitrogenase* Active Site

Georgetown University Washington, DC
B.S., Chemistry with Honors, *Summa cum laude*, Phi Betta Kappa, GPA: 3.98 2015
Thesis: Copper Catalyzed sp^3 C-H Etherification with Acyl Protected Phenols

RESEARCH EXPERIENCE

California Institute of Technology, Division of Chemistry and Chemical Engineering
Pasadena, CA
Graduate Student Researcher in Inorganic Chemistry 2015-2020

- Synthesized small molecule multi-iron clusters as models of the iron-molybdenum cofactor of *nitrogenase* and interrogated their reactivity
- Co-authored 6 peer reviewed publications (5 first author) and presented at 3 international conferences

Georgetown University, Department of Chemistry
Washington, DC
Undergraduate Research Assistant in Organic Chemistry and Catalysis 2013-2015

- Developed a copper-catalyzed method for the production of pharmaceutically important alkyl aryl ethers
- Co-authored 1 peer reviewed publication and presented at the National Academy of Sciences

PUBLICATIONS

Graduate Studies

- **Arnett, C.H.**; Oyala, P.H.; Agapie, T. Probing Redox Non-innocence in $\{Fe{=}C(H)Ar\}^{10\text{-}11}$ Complexes by ^{1,2}H and ^{13}C Pulse EPR. *Manuscript in Preparation.*
- **Arnett, C.H.**; Bogacz, I.; Chatterjee, R.; Yano, J.; Oyala, P.H.; Agapie, T. Mixed-Valent Diiron μ-Carbyne, μ-Hydride Complexes: Implications for Nitrogenase. *Manuscript in Revision.*
- Hirscher, N.A.; **Arnett, C.H.**; Oyala, P.H.; Agapie, T. Characterization of Cr-Hydrocarbyl Species via Pulse EPR in the Study of Ethylene Tetramerization Catalysis. *Manuscript in Revision.*
- **Arnett, C.H.**; Agapie, T. Activation of an Open Shell, Carbyne-Bridged Diiron Complex Toward Binding of Dinitrogen. *J. Am. Chem. Soc.* **2020**, *142*, 10059–10068.

- **Arnett, C.H.**; Kaiser, J.; Agapie, T. Remote Ligand Modifications Tune Electronic Distribution and Reactivity in Site-Differentiated, High Spin Iron Clusters: Flipping Scaling Relationships. *Inorganic Chemistry,* **2019**, *58*, 15971-15982.
- **Arnett, C.H.**; Chalkley, M.J.; Agapie, T. A Thermodynamic Model for Redox-Dependent Binding of Carbon Monoxide at Site-Differentiated, High Spin Iron Clusters. *J. Am. Chem. Soc.* **2018**, *140*, 5569-5578.

Undergraduate Studies

- Salvador, T. K.; **Arnett, C. H.**; Kundu, S.; Sapiezynski, N. G.; Bertke, J. A.; Boroujeni, M. R.; Warren, T. H. Copper Catalyzed sp^3 C-H Etherification with Acyl Protected Phenols. *J. Am. Chem. Soc.,* **2016**, *138*, 16580-16583.

SELECTED SCHOLARLY PRESENTATIONS

Graduate Studies

- **Arnett, C.H.**; Agapie, T. Remote Ligand Modifications Tune Electronic Distribution and Redistribution in Site-Differentiated, High Spin Iron Clusters. Gordon Research Conference in Inorganic Reactions Mechanisms, Galveston, TX: March 9-15, 2019. (International, Poster presentation)
- **Arnett, C.H.**; Agapie, T. A Thermodynamic Model for Redox-Dependent Binding of Carbon Monoxide at Site-Differentiated, High Spin Iron Clusters. *Gordon Research Conference in Metallocofactors*, South Hadley, MA: June 10-15, 2018. (International; **One of six short talks selected from poster abstracts**)
- **Arnett, C.H.**; Agapie, T. Site-Differentiated, High Spin Tetranuclear Iron Clusters Reversibly Bind CO in Four Redox States. Gordon Research Seminar in Bioinorganic Chemistry, Ventura, CA: January 25-28, 2018. (International; One of twenty-eight short talks selected from poster abstracts)